



UNIVERSIDAD AUTÓNOMA DE MADRID
FACULTAD DE CIENCIAS
INSTITUTO IMDEA NANOCIENCIA

TESIS DOCTORAL

**Insights Into Hydrogen Bonded Systems:
From Single Molecule To The Bulk**

Teresa Naranjo Sánchez

Memoria presentada para optar al título de Doctor en
Química Orgánica



FACULTAD DE
CIENCIAS

instituto
imdea
nanociencia

PhD supervisors

Thesis Director:

Emilio M. Pérez

IMDEA Nanociencia

Chemistry of low
dimensional Materials Lab

Thesis Director:

Borja Ibarra

IMDEA Nanociencia

Molecular motors
manipulations Lab

Thesis Tutor:

Diego Cárdenas

Facultad de ciencias

Universidad Autónoma de
Madrid

CONTENTS

LIST OF ABBREVIATIONS	1
RESUMEN	3
ABSTRACT	7
1. INTRODUCTION	11
1.1. What is supramolecular chemistry?	11
1.1.1.1. Noncovalent interactions in Nature	12
1.2. Noncovalent interactions: an energetic approach	13
1.2.1. Induction interactions	13
1.2.2. Electrostatic interactions	13
1.2.3. Dispersion interactions	14
1.2.4. Interactions with participation of Hydrogen	14
1.3. Why is it important to study supramolecular chemistry at the single molecule level?	15
1.4. Single molecule force spectroscopy techniques (SMFS)	18
1.4.1. Atomic Force Microscopy	19
1.5.1.a Technical requirements for AFM measurements	20
1.5.1.b Measurements of elasticity and force	20
1.5.1.c Applications	21
1.5.1.d Drawbacks and limitations of AFM	27
1.4.2. Optical Tweezers	28
1.5.2.a Optical trapping and manipulation	28
1.5.2.b Dual-beam optical tweezers	29
1.5.2.c Mechanical properties and unfolding kinetics of NA	30
1.5.2.d Molecular motors dynamics	33
1.5.2.e Limitations and drawbacks of optical tweezers	34
OBJECTIVES	37
2. MECHANICAL MEASUREMENT OF H-BONDED HOST-GUEST SYSTEMS UNDER NON-EQUILIBRIUM, NEAR PHYSIOLOGICAL CONDITIONS	39
2.1. Introduction	39
2.2. Results and Discussion	43
2.2.1. Chemical Design	43

2.2.2.	Bulk characterization of the end host-guest system	45
2.2.3.	Single molecule experiments	47
2.3.	Experimental Section	51
2.3.1.	Synthesis of the Hamilton receptor derivative	53
2.3.2.	Preparation of modified solid supports	67
2.3.3.	Cyanuric acid derivate synthesis	68
2.3.4.	Automated oligonucleotide synthesis and analytical data of oligonucleotides	78
2.3.5.	Mass spectral data of synthesized oligonucleotides	78
2.3.6.	Melting temperatures of duplexes	84
2.3.7.	Synthesis of DNA construct	84
2.3.8.	Optical Tweezers experiments	84
2.3.9.	Experimental force-extension curves	85
2.3.10.	Computational Details	87
3.	MEASUREMENT AND MANIPULATION OF SUTTLING MOTION OF AN INDIVIDUAL MOLECULAR SHUTTLE	91
3.1.	Introduction	91
3.2.	Results and Discussion	99
3.2.1.	Chemical design	99
3.2.2.	Single molecule experiments	102
3.2.3.	Force-dependent kinetic rates	110
3.3.	Experimental Section	113
3.3.1.	Rotaxane Synthesis	114
3.3.2.	Oligonucleotide synthesis	142
3.3.3.	Copper-free click reaction	143
3.3.4.	Mass spectral data of synthesized oligonucleotides	144
3.3.5.	Synthesis of DNA construct	146
3.3.6.	Optical Tweezers experiments	146
3.3.7.	Kinetic rates in the Bell-Evans model	147
4.	HYDROGEN BONDS ARE NOT SHIELDED IN ROOM TEMPERATURE IONIC LIQUID	149
4.1.	Introduction	149
4.2.	Results and Discussion	151
4.2.1.	Experimental approach	151
4.2.2.	Bulk studies	152

4.2.3. Single molecule experiments	159
4.3. Experimental section	163
4.3.1. Synthesis of HR-cy couple	164
4.3.1.a. Cy synthesis	164
4.3.1.b. HR synthesis	172
4.3.2. Synthesis of Am derivative	178
4.3.3. Synthesis HR-barb couple for AFM studies	182
4.3.3.a. HR synthesis	182
4.3.3.b. Barb synthesis	188
4.3.3.c. Synthesis of 11-azidoundecane-1-thiol	192
4.3.4. AFM Tip and surface functionalization	196
4.3.4.a. Barb functionalization of AFM gold-coated Si cantilevers	196
4.3.4.b. HR functionalization of gold-coated surface	196
4.3.5. SAM characterization	197
4.3.5.a. ATR experiments	197
4.3.5.b. Contact angle measurements	197
4.3.6. AFM measurements	197
4.3.7. Description of UV/vis titration experiments	198
4.3.8. Description of IR-ATR experiments	198
5. INGENIERING OF Sso7d PROTEIN LOOKING FOR A NEW SOLVATOCHROMIC BIOSENSOR	201
5.1. Introduction	201
5.2. Results and Discussion	207
5.2.1. Sso7d selection by magnetic bead sorting	209
5.2.2. Protein expression and purification. Titration studies by interferometry	211
5.2.3. Expression and purification of cysteine mutants	214
5.2.4. Labeling of Sso7d cysteine mutants with 4-DMN derivatives	215
5.2.5. Fluorescence assays with 4-DMN labelled Sso7d-based cysteine mutants	216
5.3. Experimental section	217
5.3.1. Yeast surface display	218
5.3.1.a. Reagents set up	218
5.3.1.b. Naïve library growth	218
5.3.1.c. Magnetic beads selection	219
5.3.1.d. Full-length protein expression confirmation	220

5.3.1.e. Colony forming units counting	220
5.3.1.f. Flow cytometry assays	220
5.3.2. Identification of individual clones	223
5.3.3. Expression and purification of Sso7d proteins	224
5.3.4. Protein labelling with 4-DMN	225
5.3.5. Fluorescence spectroscopy assays	225
5.3.6. Sso7d vs hEGF titration studies on Octet	225
CONCLUSIONS	227
CONCLUSIONES	231
REFERENCES	235

LIST OF ABBREVIATIONS

AFM	Atomic force microscopy
Am	Ammonium
ATR	Attenuated total reflectance
Ben	Benzamidine
BLI	Bio-Layer Interferometry
BSSE	Basis set superposition error
BzO ⁻	Benzoate
CAM	Chloramphenicol
CB-PQT ⁴⁺	Cyclobis(paraquat- <i>p</i> -phenylene)
CD	Cyclodextrin
18_crown_6	1,4,7,10,13,16-Hexaoxacyclooctadecane
CP	Counterpoise
Cy	Cyaniric acid derivative
DFS	Dynamic force spectroscopy
DFT	Density functional theory
DMTU	<i>N,N'</i> -dimethyl thiourea
4-DMN	4- <i>N,N</i> -dimethylamino-1,8-naphthalimide
DNP	1,5-Dioxynaphthalene
Dig	Digoxigenin
α -Dig	Anti-digoxigenin
DCM	Dichloromethane
DMAP	4-Dimethylaminopyridine
DMF	<i>N,N</i> -dimethylformamide
dsDNA	Double strand DNA
EDA	Energy decomposition analysis
[emim][FAP]	1-Ethyl-3-methylimidazolium tris(pentafluoroethyl)trifluoro phosphate
EDCI	1-Ethyl-3-(3-dimethylaminopropyl)carbodiimide hydrochloride
FSC	Forward-scattered
hEGF	Human Epidermal Growth Factor
HR	Hamilton receptor

IEF	Integral equation formalism
IPTG	Isopropyl β -D-1-thiogalactopyranoside
IR	Infrared
KAN	Kanamycin
NBO	Natural bond orbital
NA	Nucleic acids
o-DCB	Orto-diclorobenceno
PECs	Potential energy curves
OT	Optical tweezers
PSD	Position sensitive detectors
RTIL	Room temperature ionic liquid
SAM	Self-assembled monolayers
SMFS	Single-molecule force spectroscopy
ssDNA	Single strand DNA
SSC	Side-scattered
STM	Scanning tunnelling microscopy
TBAF	Tetrabutylammonium fluoride
TLC	Thin-layer chromatography
TNP	Trinaphto [3.3.3]propellane
THF	Tetrahydrofuran
TTF ²⁺	Tetrathiafulvalene
WLC	Worm-like chain
YSD	Yeast surface display

RESUMEN

La química supramolecular es conocida como la “química más allá de la molécula” y se centra en el estudio de las interacciones débiles y reversibles que se dan entre las moléculas, conocidas como interacciones no covalentes. La importancia de la química supramolecular fue puesta de manifiesto con el Premio Nobel en Química de 1987, que fue otorgado a Cram, Lehn y Pedersen en reconocimiento a su trabajo en esta área. Décadas después del nacimiento de la química supramolecular, se pueden encontrar muchas técnicas para medir las interacciones no covalentes en condiciones de equilibrio. Debido a que los conjuntos de moléculas pierden coherencia rápidamente, no podemos extrapolar los datos en bulk a eventos de una sola molécula en condiciones de no equilibrio, de mayor relevancia para la dinámica de los sistemas biológicos. El tema central de esta tesis, consiste en el estudio de la química supramolecular, y en particular sistemas unidos por enlaces de hidrógeno, desde una perspectiva de una sola molécula.

Los capítulos 2 y 4 se centran en la naturaleza misma de los enlaces de hidrógeno, a través del estudio de sistemas huésped-receptor unidos por enlace de hidrógeno. Los enlaces de hidrógenos, son posiblemente la interacción no covalente más importante. Las propiedades físicas del agua y el almacenamiento de información en el ADN dependen de los enlaces de hidrógeno, por nombrar tan solo dos ejemplos cruciales. En el capítulo 2 hemos desarrollado un nuevo método que explota la alta resolución de fuerza de las pinzas ópticas (OT) para medir, a nivel de una sola molécula, la resistencia mecánica de sistemas huésped-receptor unidos por enlaces de hidrógeno, fuera del equilibrio y bajo condiciones cuasi-fisiológicas. Para aislar inequívocamente eventos de unión individuales, utilizamos un espaciador de ADN. El sistema receptor de Hamilton-ácido cianúrico, que se mantiene unido a través de seis enlaces de hidrógeno, fue el sistema huésped-receptor estudiado. La fuerza requerida para romper el sistema es ~17 pN y aumenta con la velocidad de estiramiento como se espera para un sistema en condiciones de no equilibrio. El bloqueo de uno de los sitios de enlace de hidrógeno da como resultado una disminución significativa de la fuerza para romper el sistema en 1-2 pN, lo que indica la capacidad del método para resolver cambios sutiles en la resistencia mecánica del enlace debido a componentes individuales de enlaces de hidrógeno.

Hasta el día de hoy, todavía existe un debate acalorado sobre el equilibrio entre las contribuciones Coulombicas y covalentes a los enlaces de hidrógeno. En esta línea, el objetivo principal del capítulo 4 fue contribuir experimentalmente a una mejor comprensión de la

naturaleza de los enlaces de hidrógeno. Para ello, comparamos las constantes de asociación (K_a) de cuatro sistemas huésped-receptor unidos por enlaces de hidrógeno, que presentan dadores y aceptores fuertes enlaces de hidrógeno, en disolventes orgánicos y en tris(pentafluoroetil) trifluoro fosfato de 1-etil-3-metilimidazolio ([emim][FAP]), un líquido iónico a temperatura ambiente (RTIL), a través de valoraciones UV-vis espectroscópicas. Los RTILs son sales puras con punto de fusión por debajo de la temperatura ambiente, en las cuales las interacciones electrostáticas dipolo-dipolo (proporcionales a r^{-6}) deberían ser insignificantes en comparación con las interacciones carga-dipolo (proporcionales a r^{-2}). Obtuvimos K_a más pequeñas en [emim][FAP] que en disolventes orgánicos ($K_a(\text{Ben-AcOH}) = 2.51 \times 10^3 \text{ M}^{-1}$ en CH_3Cl ; $K_a(\text{HR-cy}) = 6.31 \times 10^5 \text{ M}^{-1}$ en acetonitrilo; $K_a(18_crown_6\text{-Am}) = 3.98 \times 10^3 \text{ M}^{-1}$ en acetonitrilo; $K_a(\text{DMTU-BzO}^-) = 3.98 \times 10^4 \text{ M}^{-1}$ en CH_3Cl), como se esperaba, pero sorprendentemente, del mismo orden de magnitud. Además, observamos desplazamientos en la huella dactilar en los espectros ATR-IR para las parejas HR-cy y Ben-AcOH en RTIL; por lo tanto, la caracterización espectroscópica de estos sistemas huésped-receptor confirmó su formación a través de enlaces H, en lugar de interacciones solvofóbicas inespecíficas. También comparamos mediciones a nivel de una sola molécula en uno de los sistemas huésped-receptor en orto-diclorobenceno (o-DCB) y [emim][FAP], usando espectroscopía de fuerza de una sola molécula basada en AFM. El evento de asociación fue claramente detectable y mostró valores de fuerza de ruptura comparables en ambos disolventes, y de nuevo menores en RTIL ($230 \pm 37 \text{ pN}$ en o-DCB frente a $94 \pm 30 \text{ pN}$ en RTIL). Nuestros resultados indican que la fuerza de los enlaces de hidrógeno se ve afectada por el cambio en el disolvente, pero no se suprime por completo en entornos compuestos completamente de moléculas cargadas, lo que sugiere que el equilibrio entre contribuciones Coulombicas y covalentes en los enlaces de hidrógeno, no se inclina hacia el primero en el caso de enlaces de hidrógeno fuertes. En comparación, observamos que el agua, con dadores y aceptores de enlaces de hidrógeno más débil se une exclusivamente al anión del RTIL, como se espera para los enlaces H dominados por interacciones electrostáticas.

El estudio de motores moleculares sintéticos ha dado lugar a que recientemente Sauvage, Stoddart y Feringa recibieran el Premio Nobel de Química 2016. Los motores moleculares naturales rectifican el movimiento Browniano aleatorio para generar fuerzas direccionales y llevar a cabo tareas macroscópicas. Inspirados en los ejemplos naturales, se han desarrollado dispositivos sintéticos que exhiben control sobre el movimiento rotatorio o lineal. Incluso hay algunos ejemplos seleccionados de sistemas sintéticos capaces de utilizar el movimiento Browniano rectificado para realizar trabajos e inducir colectivamente el movimiento de objetos mucho más grandes. Sin embargo, observar los mecanismos de trabajo de tales sistemas a nivel de una sola molécula sigue siendo un gran desafío. En el

capítulo 3, hemos manipulado mecánicamente rotaxanos individuales de dos estaciones unidos por enlace de hidrógeno, aprovechando la gran sensibilidad en fuerza, espacio y tiempo que caracteriza a las OT. Pudimos estudiar el ciclo mecano-químico de esta molécula en condiciones cuasi-fisiológicas. Hemos sido capaces de controlar la posición promedio del macrociclo aplicando una carga mecánica en el sistema. Sorprendentemente, aplicando fuerzas próximas a la fuerza de coexistencia, es decir, la fuerza a la cual el macrociclo presenta la misma probabilidad de encontrarse en ambas estaciones, observamos el movimiento de desplazamiento inducido térmicamente de macrociclos individuales durante minutos, registrando cientos de eventos de “salto”. Estas mediciones nos han permitido caracterizar la dinámica del sistema de operación en términos de la diferencia de energía libre de Gibbs ($\Delta G = 34 \pm 2 k_B T$), la fuerza de coexistencia ($F_{1/2} = 8.92$ pN), la coordenada del estado de transición ($x_s^\ddagger = 7 \pm 2$ nm) y las velocidades cinéticas a un rango amplio de fuerzas.

Finalmente en el capítulo 5, estudiamos la química supramolecular desde un punto de vista biológico, durante una estancia de investigación (3 meses) en el laboratorio de Barbara Imperiali en MIT. Nos centramos en el estudio de ligandos basados en proteínas para desarrollar un nuevo biosensor solvatocrómico. Específicamente, en este capítulo nos centramos en la ingeniería de la proteína ultraestable Sso7d (de la archaeon hyperthermophilic *Sulfolobus solfataricus*), buscamos Sso7d que fueran capaces de unir selectivamente el factor de crecimiento epidérmico humano (hEGF), y que dieran lugar a un aumento de la fluorescencia cuando se produce la unión de hEGF. Para ello, hemos llevado la evolución dirigida del scaffold Sso7d, y obtuvimos un binder que enlazaba selectivamente hEGF y que presentaba constantes de disociación en el rango de 10^{-8} M. Una vez encontrado este binder, lo decoramos con el fluoróforo 4-*N,N*-dimetilamino-1,8-naftalimida (4-DMN) en las posiciones 31 y 33, lo que dio como resultado aumentos de 15 veces en la fluorescencia tras la unión de hEGF. Estos son resultados prometedores y están cerca de encontrar un excelente biosensor solvatocrómico.

ABSTRACT

Supramolecular chemistry has been defined as “chemistry beyond the molecule” and focuses on the examination of the weaker and reversible noncovalent interactions between molecules. The importance of supramolecular chemistry was highlighted by the 1987 Nobel Prize for Chemistry which was awarded to Cram, Lehn, and Pedersen in recognition of their work in this area. Decades after the birth of supramolecular chemistry, there are many techniques to measure noncovalent interactions in the bulk and under equilibrium conditions. As ensembles of molecules rapidly lose coherence, we cannot extrapolate bulk data to single-molecule events under non-equilibrium conditions, more relevant to the dynamics of biological systems. The central topic of this thesis is the study supramolecular chemistry, in particular hydrogen-bonded systems, and with a focus on the single-molecule level.

Chapters 2 and 4 focus on the very nature of the H-bond and H-bonded host-guest systems. H-bonds are arguably the most important of noncovalent interactions, the physical properties of water and the information storage in DNA depend on H-bonds, to name just two crucial examples. In chapter 2 we have developed a new method that exploits the high force resolution of optical tweezers (OT) to measure, at the single-molecule level, the mechanical strength of H-bonded host-guest systems out of equilibrium and under near-physiological conditions. To unambiguously isolate single binding events we utilize a DNA reporter. The Hamilton receptor-cyanuric acid host-guest system, which is holding through six hydrogen bonds was the host-guest system under study. The force required to dissociate the host-guest system is ~17 pN and increases with the pulling rate as expected for a system under non-equilibrium conditions. Blocking one of the hydrogen bonding sites results in a significant decrease of the force-to-break by 1–2 pN, pointing out the ability of the method to resolve subtle changes in the mechanical strength of the binding due to the individual H-bonding components.

To this day, there is still a heated debate about the balance between the Coulombic and covalent contributions to H-bonds. In this line, the main objective of chapter 4 was to contribute experimentally to the better understanding of the nature of H-bonds. We compared binding constants (K_a) of four H-bonded host-guest systems, featuring strong H-bond donors and acceptors, benzamidine-acetic acid (Ben-AcOH, neutral-neutral), the Hamilton receptor-cyanuric acid derivative pair (HR-cy, neutral-neutral), the 1,4,7,10,13,16-hexaoxacyclooctadecane-ammonium derivative (18_crown_6-Am, neutral-cation) and *N,N'*-

dimethyl thiourea-sodium benzoate (DMTU-BzO⁻, neutral-anion); in non-polar organic solvents and 1-ethyl-3-methylimidazolium tris(pentafluoroethyl)trifluoro phosphate ([emim][FAP]), a room temperature ionic liquid (RTIL), through UV-vis spectroscopic titrations. RTILs are pure salts with melting point below room temperature, in which dipole-dipole electrostatic interactions (proportional to r^{-6}) should be negligible in comparison with dipole-point charge interactions (proportional to r^{-2}). Our study yielded smaller K_a in [emim][FAP] ($K_a(\text{Ben-AcOH}) = 1.99 \times 10^3 \text{ M}^{-1}$; $K_a(\text{HR-cy}) = 3.16 \times 10^6 \text{ M}^{-1}$; $K_a(18_crown_6\text{-Am}) = 3.16 \times 10^3 \text{ M}^{-1}$; $K_a(\text{DMTU-BzO}^-) = 1.99 \times 10^4 \text{ M}^{-1}$) than in organic solvents ($K_a(\text{Ben-AcOH}) = 2.51 \times 10^3 \text{ M}^{-1}$ in CH₃Cl; $K_a(\text{HR-cy}) = 6.31 \times 10^5 \text{ M}^{-1}$ in acetonitrile; $K_a(18_crown_6\text{-Am}) = 3.98 \times 10^3 \text{ M}^{-1}$ in acetonitrile; $K_a(\text{DMTU-BzO}^-) = 3.98 \times 10^4 \text{ M}^{-1}$ in CH₃Cl), as expected, but somewhat surprisingly, they were of the same order of magnitude. Moreover, we observed the fingerprint shifts in the ATR-IR spectra for the HR-cy and Ben-AcOH couples in RTIL; therefore, spectroscopic characterization of these host-guest systems supported their formation through H-bonds, rather than unspecific solvophobic interactions. We also compared measurements at the single-molecule level on one of the host-guest systems, HR-cy couple, in ortho-dichlorobenzene (o-DCB) and [emim][FAP], using AFM-based Single-Molecule Force Spectroscopy. The association event was clearly detectable and showed comparable breaking force values in both solvents, although smaller in RTIL ($230 \pm 37 \text{ pN}$ in o-DCB versus $94 \pm 30 \text{ pN}$ in RTIL). Our results indicate that the strength of H-bonds is affected by the change in solvent, but is not completely suppressed in surroundings composed entirely of charged molecules, suggesting that the balance of Coulombic to covalent contributions H-bonds is not tipped towards the former in strong H-bonds. In comparison, water, a weaker H-bond donor and acceptor is found to bind exclusively to the anion of the RTIL, as expected for H-bonds dominated by electrostatic interactions.

The study of synthetic molecular motors recently resulted in Sauvage, Stoddart and Feringa being awarded with the Nobel Prize in Chemistry 2016. Natural molecular motors rectify random Brownian motion to generate directional forces and carry out macroscopic tasks. Inspired by the natural examples, synthetic devices exhibiting control over rotary or linear motion have been developed. There are even some selected examples of synthetic systems able to use biased Brownian motion to perform work and collectively induce movement of much larger objects. However, looking at the working mechanisms of such systems at the single-molecule level remains a phenomenal challenge. In chapter 3, we manipulated individual H-bonded two-station molecular shuttles, taking advantage of the extreme force, space and time sensitivity of OT. We were able to study the mechano-chemical cycle of this molecule under near-physiological conditions. We controlled the average position of the macrocycle by applying a mechanical load on the system. Remarkably, by applying

forces, in which the macrocycle populates both stations, we observed the thermally induced shuttling motion of single macrocycles during minutes, recording several hundreds of shuttling events. These measurements have allowed us to characterize the dynamics of the shuttling process in terms of the free energy difference ($\Delta G = 34 \pm 2 k_B T$), coexistence force ($F_{1/2} = 8.92$ pN), the position of the transition state ($x_s^\ddagger = 7 \pm 2$ nm) and the kinetic rates in a wide range of forces.

Finally in chapter 5, we looked into supramolecular chemistry from a biological point of view, during a research internship (3 months) in the laboratory of Barbara Imperiali at MIT. We focused on the study of protein-based ligands in order to develop a new solvatochromic biosensor. Specifically, in this chapter we focused on engineering the ultrastable Sso7d protein (from the hyperthermophilic archaeon *Sulfolobus solfataricus*) to find human Epidermal Growth Factor (hEGF) binders, looking for fluorescence increase upon hEGF binding. For this, we have carried directed evolution on the Sso7d scaffold, obtaining a selective hEGF binder which present dissociation constants in the 10^{-8} M range; then we introduced the 4-*N,N*-dimethylamino-1,8-naphthalimide (4-DMN) fluorophore in 31 and 33 positions of the Sso7d protein, what resulted in 15-fold increases in fluorescence upon hEGF binding. These are promising results and close to find an excellent solvatochromic biosensor.

CHAPTER 1.

INTRODUCTION

1.1. What is supramolecular chemistry?

Chemistry is the science of matter and of transformations, and life is its highest expression. In its method, chemistry is a science of interactions, of transformations and of models. Chemical synthesis has the power to produce new molecules and new materials with new properties. New indeed, because they did not exist before being created by the recomposition of atomic arrangements into novel and infinitely varied combinations and structures.¹

For more than 180 years, since the synthesis of urea by Wohler in 1828, molecular chemistry has developed a vast array of highly sophisticated and powerful methods for the construction of ever more complex molecular structures by the making or breaking of covalent bonds between atoms in a controlled and precise fashion. Molecular chemistry, thus, has established its power over the covalent bond. The time has come to do the same for noncovalent intermolecular forces.

Although the word “supramolecular” made an early appearance in Webster’s Dictionary in 1903, “supramolecular chemistry” in its modern sense was introduced only in 1978 by Lehn, who defined it as the “chemistry of molecular assemblies and of the intermolecular bond.”² Classic explanations of supramolecular chemistry describe it as “chemistry beyond the molecule,” “the chemistry of the noncovalent bond,” and “non-molecular chemistry,” or even “Lego chemistry.” According to Lehn, a supermolecule is an organized complex entity that is created from the association of two or more chemical species held together by intermolecular forces (Figure I-1). Supermolecular structures are the result of not only additive but also cooperative interactions, including H-bond, hydrophobic interactions and coordination, and their properties are different (ideally better) than the sum of the properties of each individual component.^{1, 3-6}

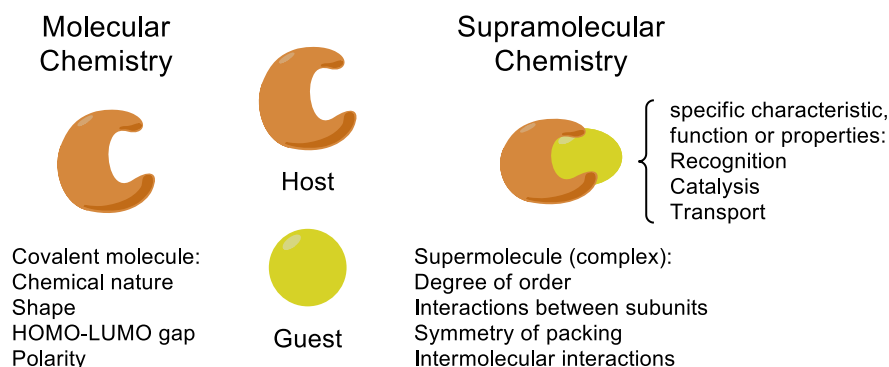


Figure I-1. Definition of traditional supramolecular “host-guest” chemistry according to J. M. Lehn.⁷

The noncovalent supramolecular approach demands a very careful design of the monomeric building blocks to ensure the self-assembly into a specific, desired supramolecular aggregate. Generally, this can be achieved by a fine-tuning of the geometrical requirements of the host and guest molecules and/or by equipping the monomers with specific noncovalent binding sites following the molecular recognition principle. This fact was first introduced as the “lock and key” principle for the specific interactions between enzymes and substrates by Nobel laureate Hernan Emil Fischer, in 1894.⁸ In 1967, the molecular recognition principle was successfully introduced for the template directed synthesis of crown ethers by Charles John Pedersen.⁹ The following years, further development of the molecular recognition principle led to the establishment of host-guest chemistry by Donald James Cram.¹⁰ Lehn, Pedersen and Cram were awarded the 1987 Nobel Prize in Chemistry for “*for their development and use of molecules with structure-specific interactions of high selectivity*”.

1.2. Noncovalent interactions in Nature

The existence of a condensed phase probably represents the most important example of noncovalent interactions. The vast majority of chemical processes occur in solution, and the condensed phase affects the structure, properties, and reactivity of a system dramatically and plays an even more important role in biology, since life originated in the liquid water phase.

Besides the structure of water, noncovalent interactions play other key roles in Nature. An important example is the structure of proteins. The twenty natural amino acids present different structures with more or less acidic or basic, hydrophilic or hydrophobic functionalities, capable of different intermolecular interactions. The secondary, tertiary and quaternary structures of proteins are determined mostly by noncovalent interactions, together with reversible disulfide covalent bonds. A protein function is determined more directly by its three-dimensional structure and dynamics than by its sequence of amino acids. Noncovalent interactions are also responsible for the structure and function of other important biological

macromolecules such as DNA or RNA. The double-helical structure of DNA, which is of key importance for the transfer of genetic information, is mainly due to noncovalent interactions, among nucleic acid bases. These bases are polar, aromatic heterocycles which interact both via H-bonds between base pairs, perpendicular to the helix, and π - π interactions that extend all along the helix axis.

Three-dimensional biomolecular structures are strongly influenced by weak noncovalent interactions between side functionalities, but the central importance of these weak interactions is by no means limited to structural effects. Life relies on biological specificity, which arises from the fact that individual biomolecules communicate through noncovalent interactions.

1.3. Noncovalent interactions: an energetic approach

Noncovalent bonds range from coordinative bonds with a strength of several hundreds of kJ mol^{-1} to weak van der Waals interactions worth only a few kJ mol^{-1} .¹¹ On the basis of perturbation theory,¹² the total stabilization energy of noncovalent complexes can be partitioned into various energy contributions. The electrostatic, induction, and dispersion terms form the dominant attractive contributions. In rare cases only one particular energy term is dominant. We therefore prefer not to classify supramolecular interactions according to the interacting chemical groups, but rather according to their energy. More often, several attractive terms contribute to the overall stabilization of noncovalent systems. The most relevant contributions to noncovalent interactions are listed below.

1.3.1. Induction interactions

The formation of intensely coloured charge-transfer complexes in nonpolar solvents was first theoretically inferred by Mulliken.¹³ The condition for the formation of a charge-transfer interaction in a complex requires that an electron flows from one of its components, with a low ionization potential, to the other, with a high electron affinity. Electron donors and acceptors are classified according to the type of orbital donating or accepting the electrons as follows: donors, n , σ , π (n = nonbonding orbitals); acceptors, v , σ^* , π^* (v = vacant orbitals). The strongest charge-transfer complexes are of n - v type, whereas the π - π^* type are the weakest.¹⁴

1.3.2. Electrostatic interactions

The presence of a charged component (electron, anion, cation, proton, or metal ion) in a cluster represents an important source of electrostatic stabilization for the other components. This is particularly true for aromatic ions wherein the charge is highly delocalized. Because cations usually possess high electron affinity and anions low ionization potential, the charge-

transfer energy term can be an important attractive contribution. Attractive or repulsive electrostatic interactions are found when two (partial) charges interact either with opposite polarity (attraction) or the same polarity (repulsion). Ion–ion interactions are strongest with bond energies in the range of ca. 100 to 350 kJ mol⁻¹. The distance between the charges and the extent of delocalization over a part of a molecule, or even the whole molecule, have an effect on the strength of the interaction.¹¹ Consequently, the minimization of the distance between two oppositely charged ions will be a geometric factor when it comes to the structure of the supramolecular aggregate, even though there is no particular directionality in the ion-ion interaction. Interactions between ions and dipoles are somewhat weaker (ca. 50-200 kJ mol⁻¹). A typical example for such an ion–dipole complex is the interaction of alkali metal ions with crown ethers.

Electrostatic interactions also play a dominant role in weak molecular clusters between components exhibiting quadrupole moment q , like arenes. The global minimum of the benzene dimer corresponds to a structure with the monomers located in perpendicular planes (T-shape structure¹⁵). This structure is favoured by attractive q - q interactions between the two benzene molecules. These qualitative estimates are now fully supported by highly accurate *ab initio* calculations.¹⁶ The same q - q interactions determine the structure of crystalline phenylalanine.¹⁷

1.3.3 Dispersion interactions

The London dispersion force is the weakest Van der Waals interaction (<5 kJ mol⁻¹). It is a temporary attractive force that results when the electrons in two adjacent atoms occupy positions that make the atoms form temporary dipoles. This force is sometimes called an induced dipole-induced dipole attraction. London forces are the attractive forces that cause nonpolar substances to condense to liquids and to freeze into solids when the temperature is lowered sufficiently. While the structure of clusters responds to directionally specific electrostatic interactions, their stabilization energy reflects also the intervention of less specific dispersion interactions. For example, this is the case for stacked DNA base pairs. Stability of these pairs stems from dispersion energy while their structure is determined by dipole-dipole electrostatic interactions. Dispersion energy plays an important role in stabilizing clusters of biological macromolecules, where it may be the dominant attractive term.

1.3.4. Interactions with participation of Hydrogen

Hydrogen bonds (H-Bonds) are the main focus of this thesis, for this reason we are going to explain them in detail bellow.

More than 90 years have lapsed from 1920, when the concept of “H-Bond” was born. During this long period innumerable papers and books have been written on the subject.¹⁸⁻²¹

The great importance of H-bond in all fields of chemistry and biochemistry is due to their key role in most conformational equilibria, chemical reactions, supramolecular structures, life processes, molecular assemblies and so on.²²

Complexes with H-bonds are stabilized by electrostatic, induction, and dispersion energy terms. The formation of an H-bond of the $XH\cdots Y$ (X and Y electronegative atoms) type is accompanied by an elongation of the X-H bond, which causes a decrease (red-shift) of the respective X-H stretching frequency. The red-shift is easily observable and provides unambiguous evidence about the formation of a noncovalent complex.¹⁴

It is important to distinguish between strong H-bonds with binding energies in the range of 60-120 kJ mol⁻¹ and heteroatom-heteroatom distances between $d= 2.2$ - 2.5 Å, moderate H-bonds (15-60 kJ mol⁻¹, $d= 2.5$ - 3.2 Å), and weak H-bonds (15 kJ mol⁻¹, $d= 4$ Å).¹¹ Also, the range of possible H-bond angles is narrow in strong H-bonds (175°-180°) so that there is excellent spatial control here, while moderate (130°-180°) and weak (90°-150°) H-bonds are more flexible. The fact that H-bond is of electrostatic nature remains controversial and several chemical calculations about it have been performed.²³⁻²⁵

The other two types of intermolecular bonds with participation of hydrogen are the improper (blue-shifting) H-bond and the dihydrogen bond. The $C-H\cdots\pi$ improper (blue-shifting) H-bond was theoretically predicted²⁶ in carbon proton donor \cdots benzene complexes. The manifestation of this bond is completely opposite to that of a normal H-bond, i.e., instead of an elongation of the X-H bond and a red-shift of the X-H stretch vibrational frequency upon complex formation, there is a contraction of the bond length and a blue-shift of the stretch frequency. The existence of a $C-H\cdots\pi$ improper H-bond in the chloroform \cdots fluorobenzene complex was confirmed experimentally by double resonance infrared ion-depletion spectroscopy.²⁷ The dihydrogen bond of the type $M-H\cdots H-Y$ was originally found in metal complexes (M = metal element) and later detected in the H_3BNH_3 dimer.²⁸⁻³⁰ The explanation of this unconventional H-bond is straightforward,³¹ two hydrogens may interact weakly if one is bound to an electropositive element and the other to a very electronegative element. Consequently, one hydrogen has positive and the other has negative partial charge, which generates a multipole attraction between them.

1.4. Why is it important to study supramolecular chemistry at the single molecule level?

It is said that, when Feynman was bothered while looking through one of the first scanning tunnelling microscopes, he said he was upset to be interrupted because seeing the images of single atoms was a "religious experience". For many generations of scientists, the molecule was both the concrete, ultimate entity on which our understanding of the everyday

world was based, and an elusive intellectual construct the very existence of which could only be inferred circumstantially by experiments on macroscopic samples. Seeing an individual atom or molecule going through its motions brings immediate, emotional impact to this central concept of modern thought.

The study of single molecules has become a major theme of research in modern science. The history of single-molecule experiments is related to that of single-molecule imaging and has its roots in the invention of the scanning tunnelling microscope, the first tool that allowed scientists to “see” individual molecules. The possibility of manipulating single molecular entities has always attracted the scientist. Since the experimental discovery of the nucleus of the atom by Rutherford, it has become a major goal in physics to search for the ultimate constituents of matter. A similar trend is followed in modern biology. There, the main goal has been to quantify the molecular mechanisms governing the operation of the constituent parts of living organisms and, ultimately, the chemistry of life.³²

Single-molecule experiments provide a new tool in physical chemistry that allows us to explore chemical processes at an unprecedented level. They offer a quantitative description of chemical processes reminiscent of the physicist’s approach. The principal reason for using novel physical methods and analyses for studying chemical processes at the single molecule level is the prevalence of molecular heterogeneity. One might suppose that the mean average property of approximately 10^{19} molecules (roughly the number of molecules in 1 μl of water, equivalent to $1/(18 \times 1000)$ th of a mole), is an adequate representation of the properties of any given single molecule. In some exceptional chemical systems this is true; however, in general this is not the case. This is because single molecules usually exist in multiple states, intrinsically related to their functions.³³ Moreover, thermal fluctuations in the molecules that form a population result in broadening the distribution of a measured parameter from a bulk ensemble experiment, which can be difficult to interpret individually. These fluctuations are driven by collisions from the surrounding solvent molecules, which can drive molecules into different, transient intermediate states. In single molecule experiments, these states can often be probed individually. The idealized dynamic picture envisaged from these experiments is a ‘movie’ at long timescales, in which molecular trajectories are smooth and well defined. At short timescales, this movie is very different: dynamics are fast and random (stochastic). Molecules dwell in a background of thermal agitation that affects their dynamic performance. This inherent dynamics can only be captured by real-time monitoring of individual processes. Fluctuations represent an integral part of molecular function, and single-molecule information must therefore be included in the overall description of molecular processes.

Bulk experiments, in which a large number of identical (but unavoidably unsynchronized) reactions take place, hinder access to signals from intermediate states of the specimens because they are averaged out. In most ensemble experiments the population is

in steady state. If the system is briefly taken out of equilibrium, then transient molecular synchrony can be obtained, such as by forcing all molecules into just a single state; however, this by definition is a transient effect (since the molecular population rapidly loses coherence) so practical measurements are likely to be short-lived and technically challenging. Also, structural methods such as electron microscopy, vibrational spectroscopies or nuclear magnetic resonance (NMR) allow 'taking snapshots' of specific instants in the temporal flow of events for a certain type of molecule, but only the average state is eventually reconstructed from the data.

All these considerations become even more relevant for the chemistry of life. The real strength of single-molecule techniques is that these subpopulations of molecular states can be investigated. The importance to biochemistry is that this multiple-state heterogeneity is actually an essential characteristic of the normal functioning of biological molecular motors; there is a fundamental instability in these molecules that allows them to switch between multiple states as part of their underlying physiological function. These biological molecular motors use external energy sources to drive directed motion and convert chemical energy into mechanical work. Therefore, the mechanical forces and displacements play a very important role in their mechanism of operation. Taking inspiration from these tiny and powerful biomachines, a relevant field of chemistry was born, which studies artificial molecular motors; in these devices, non-covalent transient interactions are fundamental in the development of their system operation. Significant advances in obtaining directional motion on the nanoscale performed by synthetic molecular machines have been made. To understand the operation of this molecular machinery, a new exciting and interdisciplinary research field called mechanochemistry arose; which studies the essential role that forces play in chemical and biochemical processes. The mechanical properties at the single-molecule level are key parameters for these systems. In order to measure the mechanical properties of biological molecules directly, several single-molecule force spectroscopy (SMFS) techniques were invented in the 1990s, such as optical tweezers (OT), magnetic tweezers, and atomic force spectroscopy (AFM). Moreover, a number of important problems in supramolecular chemistry, such as the strength of the intermolecular interactions, or the elasticity of an isolated polymer chain, cannot be addressed by bulk measurements. By solving these problems during the last two decades, SMFS has become widely accepted as a powerful tool to study inter- and intra-molecular interactions of individual molecules.³⁴⁻³⁹

It should be noted that the force measured through these SMFS techniques is intrinsically related to the pulling rate at which the experiment is performed. This is the focus of Dynamic Force Spectroscopy (DFS). DFS probes molecular bonds at different force loads (applied force over time), thereby allowing the approximation of the transition state and kinetic rate of the energy barrier of the bonds.⁴⁰ Such energy barriers form the energy landscape used

to describe reaction pathways of protein unfolding, folding, binding and function.⁴¹ When isolated, bonds are ruptured under steady ramps of force, barriers diminish in time and, thus, rupture force depends on rate of loading (= force/time).⁴² In this way, the method of DFS probes the inner world of molecular interactions to reveal barriers that are difficult or impossible to detect in assays of near equilibrium dissociation. These inner barriers are the determinants of bond lifetime and strength under rapid detachment.

SMFS have unique advantages over ensemble approaches in studies of molecular machines and assemblies.⁴³⁻⁴⁸ Moreover, the analysis of rupture force, or force spectra of single molecules provides a measure of bond energies, lifetimes, and more recently, entire energy landscapes.^{49, 50} SMFS in turn spurred the development of, and benefited greatly from, theoretical approaches that permit the extraction of detailed equilibrium thermodynamic parameters from inherently non-equilibrium pulling experiments.^{40, 49, 51}

1.5. Single molecule force spectroscopy techniques (SMFS)

Although there is an ever-expanding repertoire of single-molecule manipulation techniques, including OT, magnetic tweezers, AFM, micro-needle manipulation,⁵² biomembrane force probe⁵³ and flow-induced stretching,^{54, 55} we are going to focus on OT and AFM, which are the two techniques that have been used in this thesis (Table I-1).

Table I-1. Comparison of SMFS techniques.

	Optical Tweezers	Atomic Force Microscopy
Spatial resolution (nm)	0.1 - 2	0.5 - 1
Temporal resolution (s)	10 ⁻⁴	10 ⁻³
Stiffness (pN nm ⁻¹)	0.005 - 1	10 - 10 ⁵
Force range (pN)	0.1 - 100	10 - 10 ⁴
Displacement range (nm)	0.1 - 10 ⁵	0.5 - 10 ⁴
Probe size (mm)	0.25 - 0.5	100 - 200
Typical applications	3D manipulation Tethered assay Interaction assay	High-force pulling and interactions assays
Features	Low-noise and low-drift dumbbell geometry	High-resolution imaging
Limitations	Photodamage Nonspecific Sample heating	Large high-stiffness probe Large minimal force Nonspecific

1.5.1. Atomic Force Microscopy

The invention of the AFM in 1986 by Binnig, Quate and Gerber⁵⁶ defined a new way of imaging structures well below the resolution limit of optical microscopy. Unlike the conventional high-resolution electron microscope, which must operate in vacuum, the unique characteristics of imaging with a position-sensitive probe attached to a microcantilever allow the AFM to be operated in any environment. AFM (Figure I-2) was initially developed to overcome limitations of the scanning tunnelling microscope in imaging nonconductive samples.^{57, 58} However, the possibility of modifying the surface and manipulating individual molecules in solution made AFM an ideal tool for biological applications.⁵⁹⁻⁶²

In general, the AFM studies can be divided in topographical and non-topographical applications. In the first group, we can include the studies focused on getting an image of the sample surface, for its structural or dynamic characterization. The non-topographical applications are one of the most promising and interesting areas of this microscopy,^{40, 63-67} allowing the study of inter and intramolecular forces, as well as the manipulation of the sample. When AFM is used for one-dimensional force measurements, the AFM cantilever is moved only in the vertical direction, perpendicular to the specimen plane.^{68, 69} The vertical motion of the cantilever is controlled by piezoelectric actuators affording sub-nanometer resolution. The displacement of the cantilever is monitored directly with either a capacitor or a linear voltage differential transformer. As a result, high-resolution force-versus-extension curves of single molecules can be recorded.

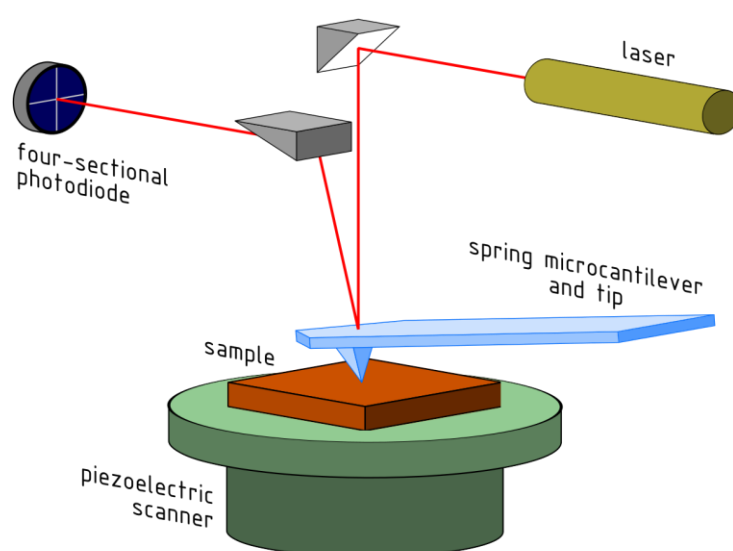


Figure I-2. Cartoon of the atomic force microscope, which consists of a cantilever with a sharp tip (blue) held above a piezoelectric scanning stage (green). Deflection of the cantilever is measured from the displacement of a low power laser (red beam) reflected off the cantilever on a position-sensitive detector (PSD).

1.5.1.a. Technical requirements for AFM measurements

From a one-dimensional force measurement we can extract two characteristic data: force and extension. The extension is the distance between the anchoring points at which the two ends of the molecule under study are attached, such as the surface of a coverslip and the cantilever tip. Force is generally calculated from the bending of a cantilever of known spring constant. The cantilever stiffness depends on the material properties and shape of the cantilever, with typical values of $10\text{-}10^5$ pN/nm. To obtain precise force data, each cantilever must be properly calibrated before use.⁷⁰ The extension data are obtained by measuring the change in displacement between the molecular force probe tip and the sample surface. The accuracy of this data is determined by the quality of the piezoelectric stage. Piezoelectric stages used in AFM provide Angstrom-level resolution (Table I-2).⁴⁸

1.5.1.b. Measurements of elasticity and force

For stretching measurements, the ends of the molecule under study are attached specifically between the cantilever and the surface, which are chemically modified to form specific bonds with the molecule of interest. For example, antibody-antigen interactions,^{71, 72} streptavidin-biotin bonds⁷³, avidin-biotin bonds,⁷⁴ hexahistidine–Ni-NTA⁷⁵ and gold–thiol⁷⁶ interaction can be used.

Single-molecule force-extension measurements are obtained by stretching mechanically an individual molecule along a particular coordinate. The force-extension curves provide valuable information on the structure, the folding and unfolding kinetics and the folding energy landscape. Measurement of the stretching curve is relatively straightforward. The AFM tip is lowered toward the surface or the sample is lifted toward the cantilever tip by piezoelectric actuators. After the initial contact with the surface, the cantilever is pressed into the surface on which the sample is deposited with a predetermined constant force. The tip is then retracted. Attachment of the sample (molecules under study) tethers the cantilever tip to the surface, causing the cantilever to bend toward the surface as the tip is retracted (Figure I-3). The value of this force is calculated using Hooke's Law.⁴⁸

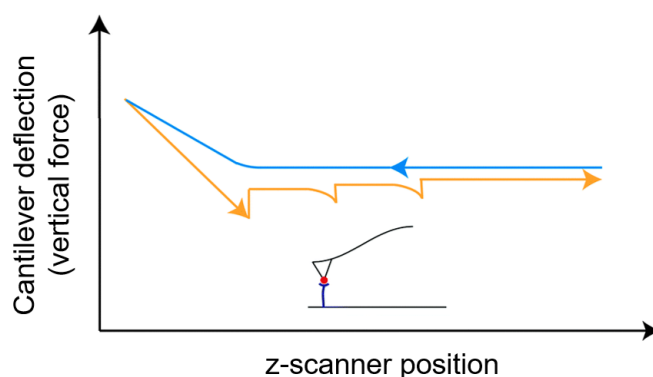


Figure I-3. A typical force-extension curve for a molecule–molecule detachment process with three unbinding events. When approaching the surface, the cantilever is in an equilibrium position and the curve is flat. As the tip approaches the surface, the cantilever is pushed up to the surface – being deflected upwards, which is seen as a sharp increase in the measured force. Once the tip starts retracting, the deflection starts to decrease and passes its equilibrium position. Moving away from the surface, the tip snaps in due to interaction with the surface and the cantilever is deflected downwards. Once the tip-sample interactions are terminated due to increased distance, the tip snaps out and returns to its equilibrium position.

The problem of pulling an ensemble of molecules instead of a single molecule can be addressed in several ways (dilution, using a tip with suitable geometry or statistical analysis of the data), but perhaps the most direct method is the use of handles with special mechanical characteristics. In a method termed ‘mechanical fingerprinting’⁷³ the protein of interest is serially linked with a well characterized oligomer of Titin I27 domains (see below). In the case of the I27 oligomer linkage, the characteristic sawtooth pattern in stretching curves resulting from the unfolding of individual Titin domains ensures that a single molecule is being stretched.³⁶ Another approach for specific attachment of single molecules exploits the properties of extremely sharp functionalized carbon nanotubes.⁷⁷

1.5.1.c. Applications

In the field of SMFS, AFM techniques were pioneered by the groups of Colton and Gaub, commencing with studies of molecular recognition events between ligand-receptor couples and studies on DNA,^{69, 74, 78} polysaccharides,^{79, 80} determination of mechanical properties of surface macromolecules on fungi and measurement of elastic response of biopolymers membrane in bacterial surfaces.⁸¹ In the last years this technique has been widely used to study the mechanical folding/unfolding individual protein molecules. The first protein unfolded by AFM, and probably the best-studied protein so far, is the immunoglobulin titin.⁶⁹ In humans, the titin filament represents an adjustable molecular spring in muscle sarcomeres, the repeating unit of myofibrils of striated muscles. About 90% of titin is made of immunoglobulin domains. AFM showed that simply applying a mechanical pulling force to both peptide ends induced the fully reversible unfolding of an oligomeric titin construct. Recording

the applied force over the stretching distance revealed a characteristic sawtooth-like pattern of force peaks. Each force peak of this pattern reflected the unfolding of a single immunoglobulin molecule and the sequence of force peaks described the unfolding pathways of all immunoglobulin molecules within the oligomeric titin construct. This is the reason why titin is used as a mechanical fingerprint in single molecule measurements, as pointed out before. However, most other proteins unfold in complex three-dimensional trajectories.⁴¹ Mechanically stretching proteins at different sites showed that their resistance to unfolding strongly depends on the pulling direction.⁸²⁻⁸⁴ Other AFM force measurements were used to characterize the properties of cellular machineries.⁸⁵⁻⁸⁸

We have shown how AFM is an extremely useful technique for the study of biological systems. Now we will show some important examples in which AFM has been utilized to investigate supramolecular systems at the single-molecule level.⁸⁹⁻⁹² The strategy of the experiment involves two steps. The first step is to chemically modify the AFM tip and substrate with host and guest molecules, respectively. The second step is to enable the formation of host-guest complex by bringing together the two surfaces, and rupturing the complex by separating them. During the latter step, the force curve is recorded, which provides extensive information on the system, such as the rupture force of the host-guest complex. In an ideal case, an individual rupture event is observed in one force curve. However, in most cases, multiple rupture events occur simultaneously, which makes it difficult to isolate single-molecule events. As mentioned before, the use of handles (like long PEG polymers, Titin oligomer) attached to the molecules of interest has been recently used to overcome this problem.

Schönherr and coworkers⁸⁹ studied the unbinding force between ferrocene moieties immobilized on AFM tips and β -cyclodextrin (β -CD) receptors in highly ordered self-assembled monolayers on Au(111) (Figure I-4). Due to multiple rupture events taking place simultaneously, statistical analysis on plenty of similar force curves shown that the observed rupture forces were integer multiples of one fundamental force unit of 55 ± 10 pN, which was attributed to the rupture of an individual ferrocene-CD complex. Further investigation of ferrocene-CD complexes showed that this force quantum is independent of the spacer length, and independent of the unloading rate.⁹³ These results indicate that the host-guest complex rupture forces were probed under conditions of thermodynamic equilibrium. This is different from the previously studied biological systems, which are dependent of the loading rate.⁹⁴⁻⁹⁶

Other guest molecules for β -CD, such as adamantane and benzene were studied by AFM showing similar results as ferrocene.⁹¹ The analysis of the histograms revealed periodic distributions of forces with loading-rate independent maxima at integer multiples of a certain force quantum characteristic of each guest. For instance, the observed force quanta were 39 ± 15 pN for benzene and 102 ± 15 pN for adamantane, respectively. The force values followed the same trend as the free binding energy ΔG measured for model guest compounds in

solution or on β -CD monolayers, as determined by microcalorimetry and surface plasmon resonance measurements, respectively.

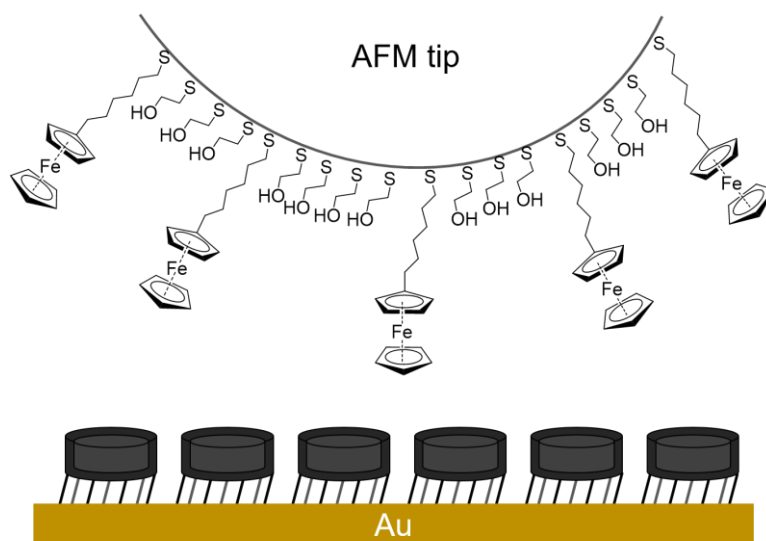


Figure I-4. Schematic representation of AFM-SMFS of ferrocene guest immobilized in a hydroxyl terminated self-assembled monolayer (SAM) on an AFM tip and a SAM of β -cyclodextrin adsorbate on Au (111). Figure adapted from *J. Am. Chem. Soc.* **2000**, 122 (20), 4963-4967.

Other important noncovalent interactions are metal–ligand interactions. Some systems on the topic of metallo-supramolecules have been studied by AFM.^{97, 98} For such purpose, Cudera et al.⁹⁷ designed unsymmetrical α,ω -functionalized poly(ethylene oxide) for mono-termination with a terpyridine ligand and subsequently for the attachment onto AFM tips and microscopy slide substrates (Figure I-5). Using ruthenium (III)-ruthenium (II) chemistry metallo-supramolecular complexes were formed. The rupture of these coordinative bonds showed a rupture force at 95 pN for individual complexes, which was supported by elasticity model fitting and Monte Carlo simulations.

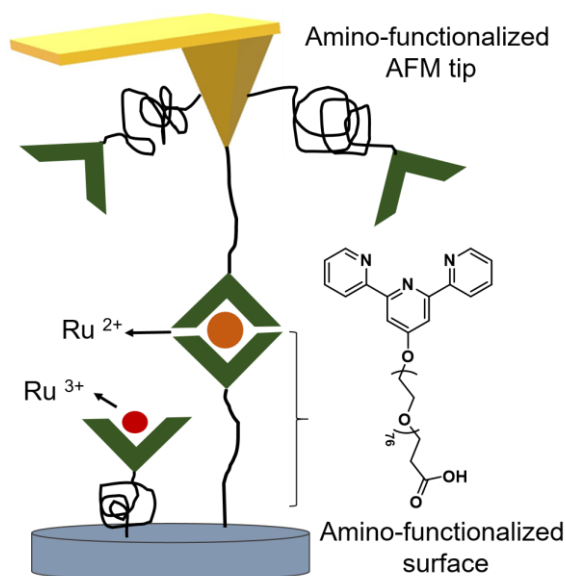


Figure I-5. Schematic representation of AFM-SMFS. The substrate is coated with terpyridine ruthenium (III) mono-complexes, otherwise the tip is coated with free terpyridine units. The bis complexes can only be formed between the free terpyridines at the tip and the mono-complexes bound to the substrate. Ruthenium (III) is reduced to ruthenium (II) during this process (solvent DMSO). Figure adapted from *Adv. Func. Mater.* **2003**, 13 (8), 615-620.

Zou et al. studied the mechanical strength of supramolecular quadruple H-bond bis(2-ureido-4[1*H*]-pyrimidinone) (UPy)₂ complexes under quasi-equilibrium and non-equilibrium states in situ by controlling the temperature (Figure I-6).^{99, 100} The determination of the rupture forces at 301 K was carried out for loading rates between ~5 nN/s and ~500 nN/s, and were found to depend logarithmically on the loading rate, consistent with the prediction by Evans et al.^{40, 95} In contrast, for measurements carried out in situ at 330 K, no loading-rate dependence was observed for rates between 5 and 200 nN/s. This observation indicates that the corresponding experiment was carried out under quasiequilibrium conditions.

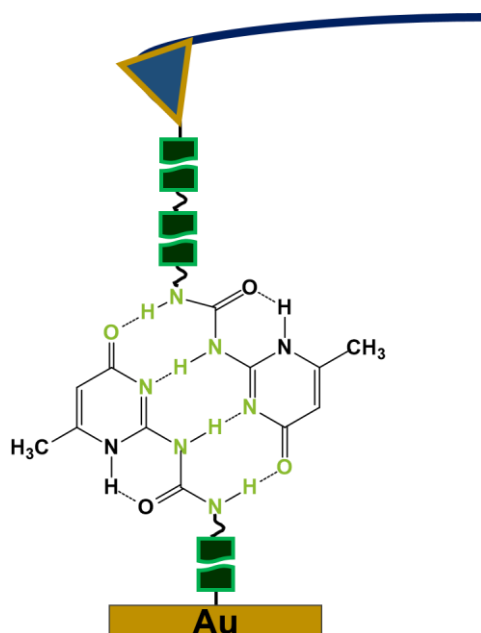


Figure I-6. Schematic of the AFM-SMFS experiment for the supramolecular quadruple H-bond bis(2-ureido-4[1H]-pyrimidinone), obtained in hexadecane. Figure adapted from *J. Am. Chem. Soc.* **2005**, 127 (32), 11230-11231.

More recently, the mechanical strength of another self-complementary quadruple H-bond motif, urea-aminotriazine (UAT), was investigated by SMFS (Figure I-7).^{101, 102} The bond rupture was probed at three different, fixed piezo retraction rates in far from equilibrium conditions. The number of supramolecular bonds (N) between AFM tip and the surface was determined by independent knowledge of the linker length. The observed rupture force of urea-aminotriazine (UAT)-based supramolecular polymer chains was found to decrease with increasing rupture length. The dependence of the most probable rupture force (102 ± 32 pN and loading rate $r_f = (134.7 \pm 50.9) \times 10^3$ pN/s) on N was in quantitative agreement with the theory of uncooperative bond rupture for supramolecular linkages switched in series. Moreover, relevant parameters of the bond energy landscape and kinetic off-rates, were obtained from a single data set of rupture events at a fixed loading rate for these supramolecular linkages switched in series.

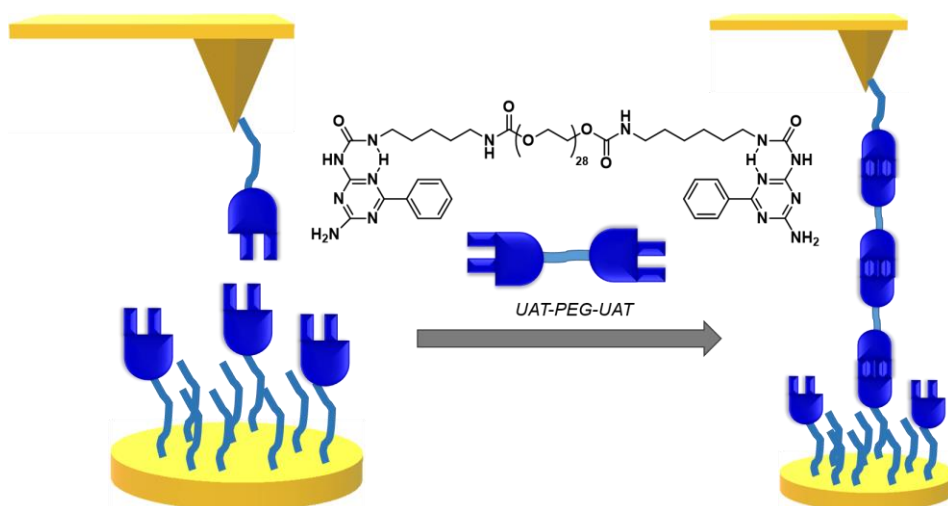


Figure I-7. Schematic of AFM-SMFS of supramolecular UAT polymers in hexadecane. A gold-coated surface and a gold-coated AFM probe are functionalized with PEG and PEG-UAT moieties. The bifunctional UAT-PEG-UAT linker is added to the solution to form supramolecular polymers. Figure adapted from *J. Phys. Chem. B* **2012**, 116 (1), 565-570.

The first direct measurement of π - π Interactions between pyrene and a graphite surface was performed by Zhang et al.¹⁰³ Modifying the AFM tip with a pyrene tailored polymer chain and measuring the desorption force of a single pyrene unit from a graphite surface (Figure I-8). They observed a breaking force of 55 ± 16 pN, which was independent of the loading rate, implying that the measurement is carried out under quasi-equilibrium conditions. In other words, the adsorption force between the pyrene unit and the graphite surface is equal to the desorption force obtained.

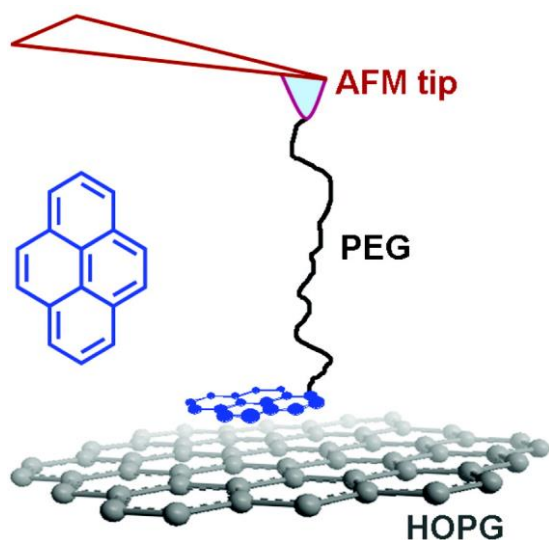


Figure I-8. Schematic of AFM-SMFS setup for measuring the π - π interactions between pyrene and graphite in aqueous medium. Figure reproduced with permission from *Langmuir* **2007**, 23 (15), 7911-7915. Copyright (2007) American Chemical Society.

More recently, similar experiments were carried out with single-walled carbon nanotubes (Figure I-9),¹⁰⁴ Iliafar and coworkers used AFM to measure the force required to remove single-stranded DNA (ssDNA) homopolymers from single-walled carbon nanotubes (SWCNTs) deposited on methyl-terminated self-assembled monolayers (SAMs). They showed that the free energy of binding of these ssDNA sequences to the SAM-modified substrate is quite similar to their free energy of binding to graphite, which is in contrary to the expectation that the binding of ssDNA with carbon surfaces should decrease with surface curvature, the peeling forces in fact are greater by a factor of 2–3 on SWCNTs. These results were supported by replica-exchange molecular dynamics simulations.

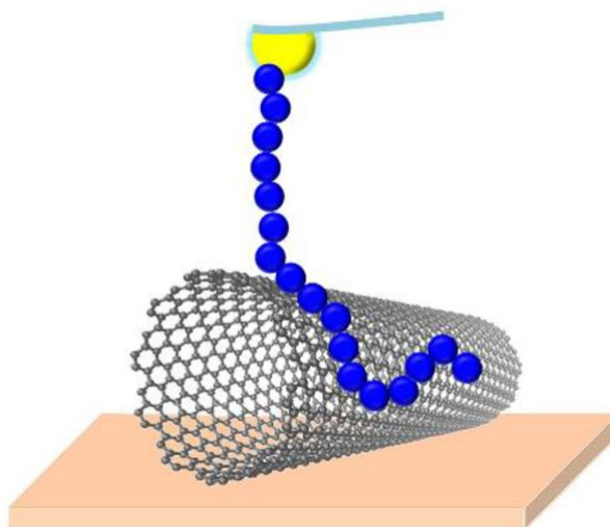


Figure I-9. Schematic representation of AFM-SMFS of single-walled carbon nanotubes (SWCNTs) deposited on methyl-terminated SAMs and an AFM tip modified with single-stranded DNA (ssDNA) homopolymers. Figure reproduced with permission from *J. Am. Chem. Soc.* **2014**, *136* (37), 12947-12957. Copyright (2014) American Chemical Society.

1.5.1.d. Drawbacks and limitations of AFM

The main drawbacks and limitations of AFM stem from the large size (100-200 μm in length) and relatively high stiffness ($10\text{-}10^5$ pN nm^{-1}) of the cantilevers, which impose a lower bound on the useful force range, and a reduced bandwidth, particularly in aqueous conditions. Therefore, the minute forces (below 10 pN) and rapid dynamics characteristics of non-covalent interactions under physiological conditions are difficult to access with this technique.

Specificity is a second major concern in many AFM pulling experiments. It can be difficult to discriminate interactions of the AFM tip with the molecule of interest from nonspecific interactions or inappropriate contacts with the molecule of interest, such as binding at an intermediate position rather than at one of the ends.

1.5.2. Optical tweezers

OT were first realized 31 years ago by Arthur Ashkin and co-workers at the Bell Telephone Laboratories,¹⁰⁵ and provided scientists with a tool that is ideally suited for biophysical studies at the molecular level. By selecting a wavelength in the near-infrared region of 800-1.100 nm, where light is poorly absorbed by most living matter,¹⁰⁶ optical tweezers can be used to grasp, capture and manipulate micrometre-scale dielectric objects non-invasively and with exquisite precision. The loads exerted by optical traps fall conveniently into the pN range, and are therefore perfectly suited to studying the forces between and within biomolecules (see Table I-1). Combined with position sensitive detectors (PSD) that can monitor the displacements of trapped objects accurately down to the subnanometre level,¹⁰⁷ optical tweezers have revolutionized the nascent field of single-molecule biophysics, making it now possible to study the processes of life at the level of individual molecules. However, there is still a considerable challenge ahead to apply this technique to study chemistry at the level of individual molecules.

1.5.2.a. Optical trapping and manipulation

Optical traps involve the balance of two types of optical forces: scattering forces, which push objects along the direction of propagation of the light, and gradient forces, which pull objects along the spatial gradient of light intensity.¹⁰⁵ When gradient optical forces exceed those from scattering, an object is attracted to the point of highest intensity formed by focused light and can be stably trapped at this position in all three dimensions. In practical implementations of an optical trap, a near-infrared laser beam is tightly focused by a high-numerical aperture microscope objective to create the large spatial gradient in light intensity necessary to form a stable trap.¹⁰⁷ In the vicinity of this focus, the optical trap behaves as a linear “Hookean” spring, generating forces on an object proportional to its displacement from the centre of the trap.

The magnitude of these optical forces is adequate for manipulating microscopic dielectric objects¹⁰⁸⁻¹¹⁰ such as micron-sized polystyrene beads, which can be biochemically linked to the molecules of interest serving in this way as probes by which the movements and forces on the system can be measured in real time. Exerting calibrated forces on the molecule of interest requires having it attached between the bead on the trap and a second surface. Typically this second attachment point is a second bead which may be held atop of a micropipette by suction (Figure I-10). In this fashion, the system can be manipulated (stretched) by moving the optical trap relative to the micropipette.

1.5.2.b. Dual-beam optical tweezers

In the last years, different type of optical tweezers has been developed to study and manipulate biological systems at the single molecule level.⁴⁶ Following we describe a dual-beam optical tweezers instrument used in this thesis, Figure I-10. Although the range of OT experimental configurations is diverse and keeps growing, the basic elements in the optical tweezers can be grouped into those common to an optical microscope and those related to the generation of the optical trap.¹⁰⁶ The microscope elements are an objective, a fluidics chamber and a condenser lens. The trap elements are a laser and a photodetector that registers the light at the exit of the condenser.

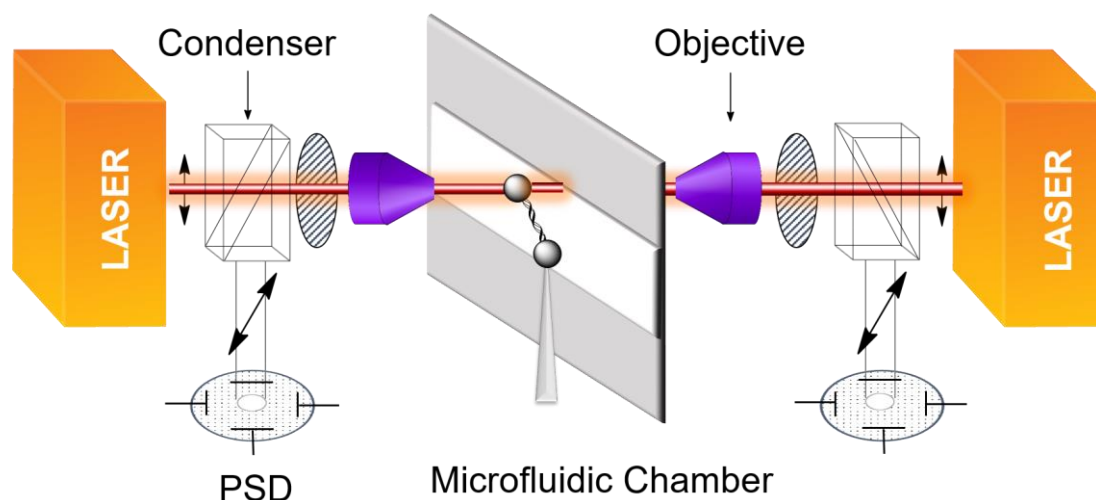


Figure I-10. Basic elements in a dual-beam OT instrument. Laser light (typically infrared) is highly focused by a microscope objective and collected by a condenser lens. A bead can be trapped in the focal region, which is produced inside a fluidics chamber. A micropipette inserted in the chamber can hold a second bead by suction. Micrometer-sized beads are typically used as mechanical handles to hold a biopolymer by both ends. The collected exiting rays are registered by a position-sensitive photodetector (PSD). The scheme shows a single-molecule experiment in which a DNA fiber is stretched between two beads.

Basic elements in the OT instrument:

- ❖ **Laser illumination.** Laser power in the focal region of several hundred milliwatts provides a good balance that prevents photodamage and produces forces up to a few hundreds of pN. In dual-beam systems, two equal counter-propagating laser beams are brought to the same focus.
- ❖ **Strongly-focusing objective lens.** To achieve the steep focus needed to create a stable optical trap, the numerical aperture of the trapping microscope objective should be near or above 1.0. This requirement is met by both water and oil immersion objectives. However, and although the latter offers the highest numerical aperture, water immersion objectives are the most commonly used for optical trapping since they

do not introduce spherical aberrations that degrade the optical trap performance deep in solution.

- ❖ **Microfluidics chamber** (Figure I-11). It is the test tube for the assays. It is usually built using two microscope coverslips sandwiching parafilm layers with imprinted channels. The design allows specimens to be flowed through a top and a bottom channel connected with the central channel by glass capillaries. The tip of a micropipette and the optical trap are located close together (within a distance of less than 5-10 μm) at the central channel. As described above, the micropipette is used to hold beads by suction. Buffers can be easily exchanged and flowed at a controlled rate, thus adding the ability to exert hydrodynamic pressure. Additional glass capillaries can be used to dispense different chemicals directly to the vicinity of the optical trap (not shown in Figure I-11). Therefore, the system allows exchanging experimental conditions rapidly and easily (for example, chemical concentration and pH) without affecting the performance of the instrument, which allows the detection in real time of processes triggered by such changes in conditions.

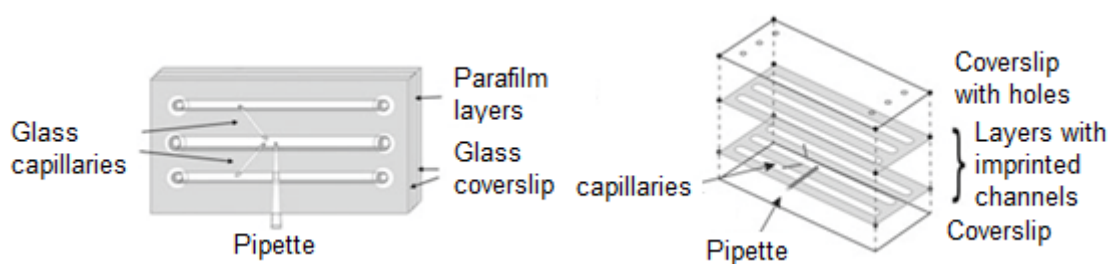


Figure I-11. Fluidics chamber. Micron-sized polystyrene beads are passed sequentially through a system of channels. In this design, the experiment takes place in the central channel, which is connected to the top and the bottom channels by glass capillaries. The scheme also shows the disposition of a micropipette. Mounting a custom-made fluidics chamber for optical tweezers. After assembling the tubes and parafilm layers, the components are heat-sealed.

- ❖ **Condenser lens.** It is used to collect the light scattered by the optically trapped biological specimen and convert it into a parallel beam.
- ❖ **Light-detection system.** The interference between the light scattered by the trapped bead and unscattered light is measured with a quadrant photodiode or position-sensitive photodetector (PSD).

1.5.2.c. Mechanical properties and unfolding kinetics of nucleic acids

Thanks to the advent of the OT technique, elastic properties and folding dynamics of diverse nucleic acid structures have been investigated from their characteristic force-extension curves.¹¹¹⁻¹¹³ In these experiments, a single nucleic acid molecule is grabbed by two different,

specific sites by means of two short nucleic acid stretches, to properly functionalized dielectric microspheres. Typically, nucleic acid fibres are prepared containing modified nucleotides with biotin groups at one end and digoxigenin at the opposite, so that they can bind to streptavidin- and anti-digoxigenin-coated beads, respectively (Figure I-12a). Force-extension curves are obtained by the stretching and subsequent relaxation of a single nucleic acid molecule by moving the micropipette relative to the laser trap at a constant rate (Figure I-12b). The extension of the nucleic acid molecule is determined from the distance between the beads with a video camera, whereas the force acting on it is calculated from the displacement of the laser beams on the PSDs.⁷³ Herein, we present to examples, which are relevant for this thesis: A) the mechanical properties of double-stranded DNA (dsDNA) and B) the real-time folding/unfolding kinetics studies of DNA hairpins.

A) Mechanical properties of dsDNA. In a typical force-extension curve of a single dsDNA molecule, three different elasticity regimes can be distinguished during its stretching pathway (Figure I-12):^{73, 114}

- ❖ **Entropic elasticity regime.** Below some 5 pN, the molecule, initially bent over itself in a random way as a result of thermal fluctuations, is stretched like a Hookean spring until it reaches its characteristic contour-length.
- ❖ **Enthalpic or intrinsic elasticity regime.** From 5 to 60 pN, approximately, the molecule is stretched beyond its contour length.
- ❖ **Overstretching transition.** At about 65 pN –in non-torsionally constrained molecules and depending on ionic strength, pH and sequence–, the molecule undergoes a structural transition to an almost totally unwound state with an elongation of 1.7 times its contour length. This sudden change happens over a very narrow force range (~2 pN) and involves an increase in the rise per phosphate from 3.4 to 5.8 Å. The bases unstack and, depending on environmental conditions, the strands may either remain linked by partial base pairing -like a parallel ladder (S-form)-, or separate into a totally molten state (force-induced melting) or in a heterogeneous combination of both. When more than one molecule are stretched, overstretching transition occurs at higher forces (e.g. 120 pN if two molecules are stretched at the same time). Therefore, the force-extension curve of the dsDNA serves as a marker for single molecule identification.

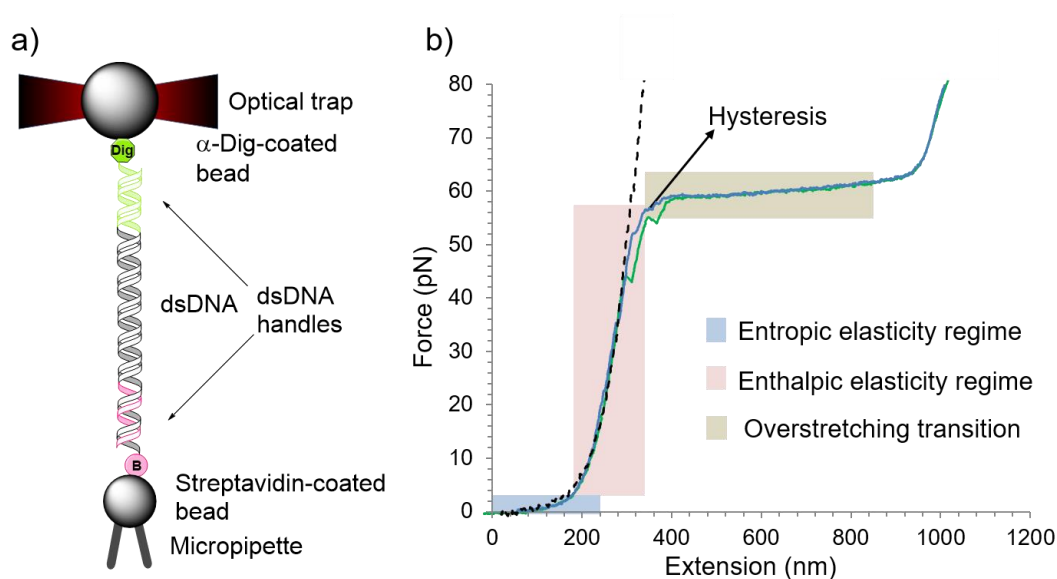


Figure I-12. a) Scheme of the experimental setup in OT measurements of the mechanical properties of dsDNA. A single dsDNA molecule is tethered by different DNA duplex ends between two polystyrene microspheres: an anti-digoxigenin (α -Dig)-coated bead, optically trapped, and a streptavidin-coated bead, held by suction on top of a micropipette. B symbolizes D-biotin, meanwhile, Dig represents Digoxigenin. b) Characteristic force-extension curve of a single dsDNA molecule; displaying WLC behaviour (dashed black line). The graph shows an individual dsDNA molecule from pUC19 (2686 bp) in 150 mM NaCl, 10 mM Tris-Cl, 1 mM EDTA, pH 7.5. Boxes illustrate the strand arrangement in each elasticity regime according to the literature.

When the stress on the molecule decreases, it begins to return to its equilibrium state but following a slightly different pathway, inducing a certain hysteresis between the stretching and the relaxation traces. This absence of overlapping in the force-extension curve is a hallmark of the reannealing of the strands out of equilibrium.

These pulling/relaxing profiles can be modelled using the worm-like chain (WLC) model that predicts the relationship between the extension of a linear dsDNA polymer and the entropic restoring force (dashed line Figure I-12b).

B) In the literature we can find large number of examples of the **real-time folding/unfolding kinetics studies of DNA hairpins**, here we present the one described by Woodside and co-workers¹¹⁵ (Figure I-13). They reported a systematic study of the kinetics and thermodynamics of the folding transition for individual DNA hairpins of varying stem length, loop length, and stem GC content. Unfolding was induced mechanically in a high resolution optical trap; by moving one optical trap with respect to the other at fixed pulling rates. They measured folding transitions of 20 different hairpin sequences. For all hairpins studied, folding and unfolding were characterized by a single transition. From the force dependence of these rates, they determined the position and height of the energy barrier. By measuring unfolding

energies spanning one order of magnitude, transition rates covering six orders of magnitude, and hairpin opening distances with subnanometer precision, their results define the essential features of the energy landscape for folding.

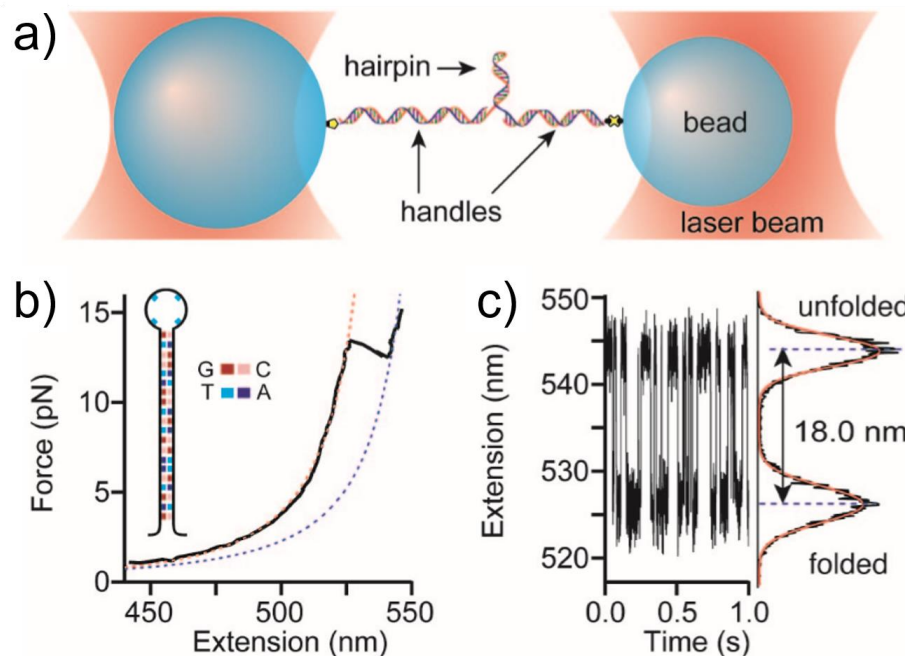


Figure I-13. Measurements of hairpin folding/unfolding. a) Illustration of the experimental geometry: A hairpin is attached by means of dsDNA handles to beads held in two traps (not to scale). b) Force-extension curve for one representative hairpin, displaying WLC behaviour of handles (dotted red line) followed by hairpin unfolding at ~ 13 pN. WLC fit to the contour length increase after hairpin unfolding (dotted blue line). c) DNA extension vs. time at constant force reveals two-state behaviour. Fit of extension histogram (black) to two Gaussian curves (red) gives the distance between the folded and unfolded states. Figure reproduced with permission from *Proc. Nat. Acad. Sci. USA* **2006**, 103 (16), 6190-6195.

1.5.2.d. Molecular motors dynamics

In last years, it has become clear that all living cells contain a wide variety of molecular motors that convert chemical energy into to mechanical work. They perform a multitude of functions that are essential to life, from DNA replication, RNA transcription and protein synthesis to cell division, vesicle trafficking, cell locomotion, endocytosis and of course, the best known example, muscle contraction. There are two types of biological molecular motors: “rotary motors” are usually embedded in membranes and are driven by the flow of ions across transmembrane electrochemical gradients; the bacterial flagellar motor and the ATP-synthase are good examples; and “linear motors” that work in an isotropic chemical environment and derive energy from chemical reactions, usually the hydrolysis of the chemical ATP to adenosine diphosphate (ADP) and inorganic phosphate. Linear motors move along anisotropic

(or polarized) tracks that confer directionality to the movement; a prototypical example is the kinesin protein.

In 1993 Block and coworkers¹¹⁶ measured the individual steps of kinesin, a molecular porter that walks directionally along a microtubule track. They obtain high spatial and temporal sensitivity combining optical tweezers with a dual-beam interferometer. They captured silica beads with kinesin molecules bound to their surface out of a suspension and deposited them onto microtubules immobilized on a coverslip. They then observed the fine structure of the motion as beads developed load by moving away from the centre of the trap. In the presence of ATP, when the kinesin motor and microtubule track interacted, the bead was pulled along by the kinesin and the nanometre scale displacements and pN forces produced were measured. The crucial observation made, and indeed a testament to the incredible sensitivity of their method, was that they could identify discrete 8 nm steps taken by the kinesin molecule. Rather than moving smoothly like an ensemble would do, the single molecule moved in a stochastic jerky fashion. They found that the motor paused for a random interval after taking each step as it waited for a fresh ATP molecule to diffuse into its catalytic site.

1.5.2.e. Limitations and drawbacks of optical tweezers

The versatility and precision afforded by optical tweezers are accompanied by important limitations and drawbacks that must be carefully considered before and during their use. There are some important difficulties associated with using light to generate force. As trap stiffness depends on the gradient of the optical field, optical perturbations that affect the intensity or the intensity distribution of light will degrade the performance of the optical tweezers. High-resolution optical trapping is therefore limited to optically homogeneous preparations and highly purified samples.

Optical tweezers also lack selectivity and exclusivity. Any dielectric particle near the focus of the trapping laser will be trapped, and the number of particles that can be simultaneously trapped can be quite large. For this reason, samples in which the objects that will be trapped are freely diffusing must be kept at extremely low concentrations to prevent additional objects from being trapped once the first object is captured.

Local heating in the vicinity of the optical trap due to the high intensity at the focus of the trapping laser, 10^9 - 10^{12} W cm⁻¹, is another drawback but it can be quantified, both theoretically and experimentally,¹¹⁷⁻¹¹⁹ and kept limited.

Optical damage induced in trapped specimens is less well understood. Although the use of trapping lasers operating in the near-infrared spectrum minimizes photo damage, singlet oxygen or other reactive oxygen species can be generated within this wavelength range,¹²⁰ and might be damaging to the sample.

Finally, the artificial nature of the single-molecule linkage strategy has to be considered. Whereas individual cells can be held directly in an optical trap, handling single molecules requires the use of molecular handles as explained before. The absence of this type of configuration in living conditions is considered as a handicap for in vivo applications of this technique.^{48, 121}

OBJECTIVES

This thesis aims to address fundamental issues in supramolecular chemistry. We began with a general introduction to supramolecular chemistry and why it is important to study it at the single-molecule level. Following the premises introduced in the first chapter, we find the fundamental objectives of this thesis:

- 1) The first objective was to develop a novel experimental set-up to unequivocally isolate H-bonded host-guest systems and study their mechanical strength under non-equilibrium, near-physiological conditions and at the single molecule level.
- 2) The second objective was to measure and manipulate the mechanics and real time kinetics of individual synthetic molecular shuttles under biocompatible aqueous conditions. In order to:
 - Investigate the mechanochemical cycle and dynamics of the system operation when it is driven out of equilibrium by a mechanical load. As a consequence we will extract conclusions about the design of molecular machines at the theoretical level, both to help analyse existing examples and to propose simpler, more efficient machines.
 - Obtain useful information to compare synthetic to natural molecular machines under identical conditions, since the majority of synthetic molecular motors reported to date have been investigated in organic solvents.
- 3) Our third objective was to contribute to the debate between the balance of the Coulombic and covalent contributions to H-bonds. In chapter 4 we have addressed this question from an experimental point of view, both in the bulk and at the single-molecule level.
- 4) Finally, the fourth objective of this thesis emerges as a result of a predoctoral internship at MIT, in the laboratory of Prof. Barbara Imperiali. We focused on the study of protein-based ligands in order to develop a new solvatochromic biosensor.

CHAPTER 2.

Mechanical Measurement of H-bonded Host–Guest Systems Under Non-equilibrium, Near Physiological Conditions

2.1. Introduction

Decades after the birth of supramolecular chemistry, there are many techniques to measure noncovalent interactions, such as hydrogen bonding, under equilibrium conditions. As ensembles of molecules rapidly lose coherence, we cannot extrapolate bulk data to single-molecule events under non-equilibrium conditions, more relevant to the dynamics of biological systems. For this reason our interest was focused on the development of a new method that exploits the high force resolution of optical tweezers to measure at the single molecule level the mechanical strength of a hydrogen bonded host-guest pair out of equilibrium and under near-physiological conditions.

Hydrogen bonds are arguably the most prominent of noncovalent interactions,^{122, 123} as the very foundations of life as we know it depend crucially on H-bonding.¹ From a synthetic point of view, a wealth of host-guest systems,¹²⁴⁻¹²⁶ supramolecular polymers,¹²⁷⁻¹³² and molecular machines¹³³⁻¹³⁸ based on H-bonding has been described.¹³⁹⁻¹⁴³ Unsurprisingly, measuring and understanding H-bonds has been the subject of intensive research efforts, and it still busies the scientific community.^{144, 145} Most measurements of H-bonded systems are based on the determination of association constants,^{146, 147} and therefore provide ΔG data obtained under equilibrium conditions, and are the average over very many interactions, in the order of Avogadro's number. As molecules in an ensemble are not synchronized, these data are not necessarily related to the behaviour of a single molecule under non-equilibrium conditions.^{148, 149-151} In addition, the growing interest in molecular nanotechnology has increased the need for knowledge regarding molecular stability and bond mechanical strength from a single-molecule perspective and under near-physiological aqueous conditions. These conditions are required for the proper operation of next generation hybrid molecular motors; biological mechano-enzymes modified with synthetic molecules in order to control their activity and motion at the molecular level.¹⁵²

The development of methods to manipulate individual molecules in the last couple of decades offers the opportunity to directly observe single molecule events for the first time.¹⁵³⁻¹⁵⁵ SMFS methods have been particularly successful for the observation of noncovalent interactions in organic solvents.¹⁵⁶⁻¹⁵⁹

Very recently Kawai et al. obtained direct quantitative observations of weak H-bonds, using high-resolution AFM with a CO functionalized tip, they could resolve the outmost hydrogen atoms of single molecules directly via the C=O...H-C intermolecular interaction.¹⁶⁰ They used a linear O...H-C system for the direct detection of this very weak, intermolecular interaction, which is responsible for the spatially localized contrast of the hydrogen atom and was used as a marker to identify the adsorption geometry of the three-dimensional hydrocarbon, Trinaphto [3.3.3]propellane (TNP), (Figure II-1).

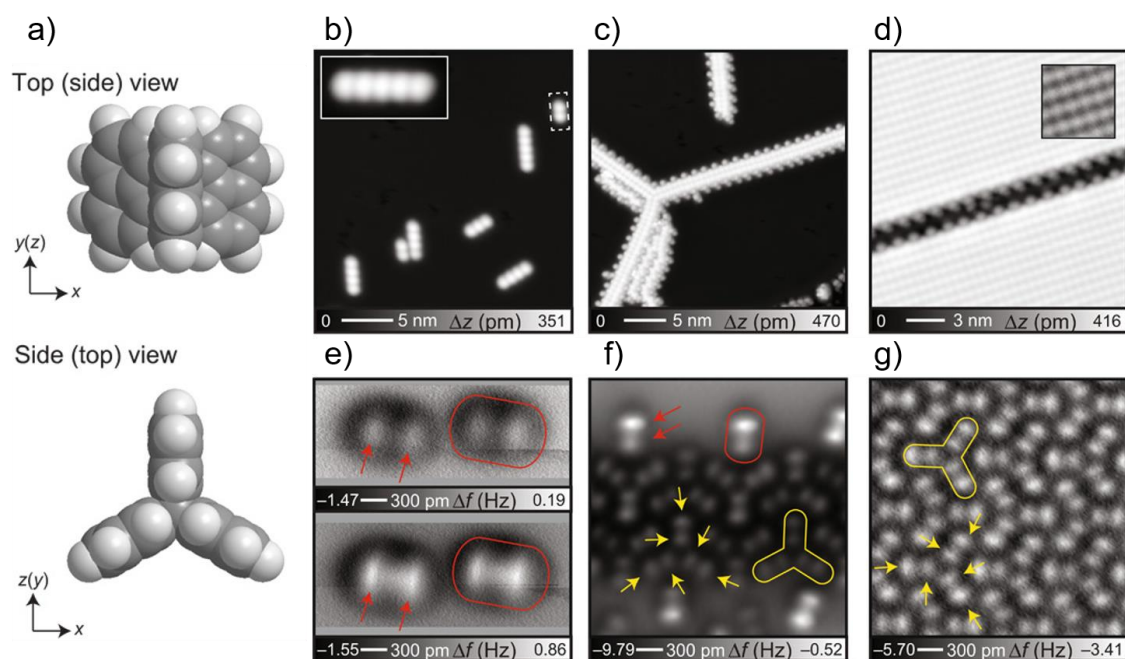


Figure II-1. a) Trinaphto [3.3.3]propellane (TNP): the top panel shows the top (side) view, and the bottom panel shows the side (top) view for the upright (sidelying) configuration. A, C and E are short one-dimensional structures observed in scanning tunnelling microscopy (STM) topography of TNP deposited on a clean Ag(111) surface. b) to g): Experimental observations of TNP on Ag(111). Series of scanning tunnelling microscopy (STM) topographies (b, c and d) of TNP deposited on the Ag(111) surface with increasing coverage and corresponding AFM images (e, f and g). As the coverage of TNP increases, the ratio of the upright (red arrows) and side-lying (yellow arrow) TNP becomes larger. Figure reproduced with permission from *Sci. Adv.* **2017**, 3 (5).

When a small amount of TNP was used, counting these shapes, it was found that most of them were composed of TNPs, up to a maximum of a pentamer assembly, inset (Figure II-1b). Through AFM studies (e, f and g) the configuration was analysed in detail, they observed the dimer TNPs, as indicated by a dashed box in Figure II-1b.

Figure II-1e shows the corresponding AFM image, in which two bright spots appear in each molecule, as indicated by red arrows and ovals. Assuming that the contrast relates to the hydrogen atoms, the TNPs are adsorbed as upright (Figure II-1a). An increase in the number of deposited TNPs results in larger one-dimensional chain-like structures (Figure II-1c). The corresponding AFM image, Figure II-1f, shows that the dots at the sides of the chains correspond to upright TNPs, as indicated by the red arrows and oval, and it is also observed many dots within the chain structure. Recalling the chemical structure of TNP showed in a, six dots can be assigned as the hydrogen atoms in the side-lying TNP, as indicated by the yellow arrows and the trigonal-shaped visual guide. Because the height of the side-lying TNPs is shorter than that of the upright TNPs by 140 pm, they appear darker (more negative frequency shift) in constant height mode. Further TNP deposition leads to the formation of films with a 1×1 structure of side-lying TNPs, terminating with upright TNPs at the edges (Figure II-1d and g).

This example represents a direct observation of weak H-bonds. However, there are scarce examples in literature related with direct measurements of the strength of H-bonds at the single-molecule level; one example that we can find was reported by Bassani et al.¹⁶¹ They studied the strength of a H-bonded host-guest system, the Hamilton receptor (in blue in Figure II-2a) and a barbituric derivative (in red in Figure II-2a), that are linked through six strong H-Bonds. They performed force spectroscopy measurements using 1,2-dichlorobenzene as solvent at room temperature. They recorded force/distance curves at approach and retraction velocities of 250 nms^{-1} with contact time of 5 s. After statistical analysis the force related to the rupture of a single H-bonded system was found to be 169 pN. The experimental set up and an example of a force/distance curve obtained are depicted in Figure II-2.

However, under aqueous conditions, H-bonds are typically disrupted by forces of a few pN. For instance $\sim 10\text{-}15$ pN are required to pull apart the H-bonds holding the double helix of DNA.¹⁶² This force range is at the detection limit of classical SPM methods.¹⁶³ In addition, the non-specific adsorption of the sample, typically used by these methods and, in many cases, the lack of a proper reporter, hinders the unambiguous identification of single molecule events. In the biological sciences, this problem is circumvented by using repetitions of the unit peptide under study, and discarding the initial distance changes (typically the first 30 to 75 nm) and associated force peaks, which are systematically overestimations.⁶⁴

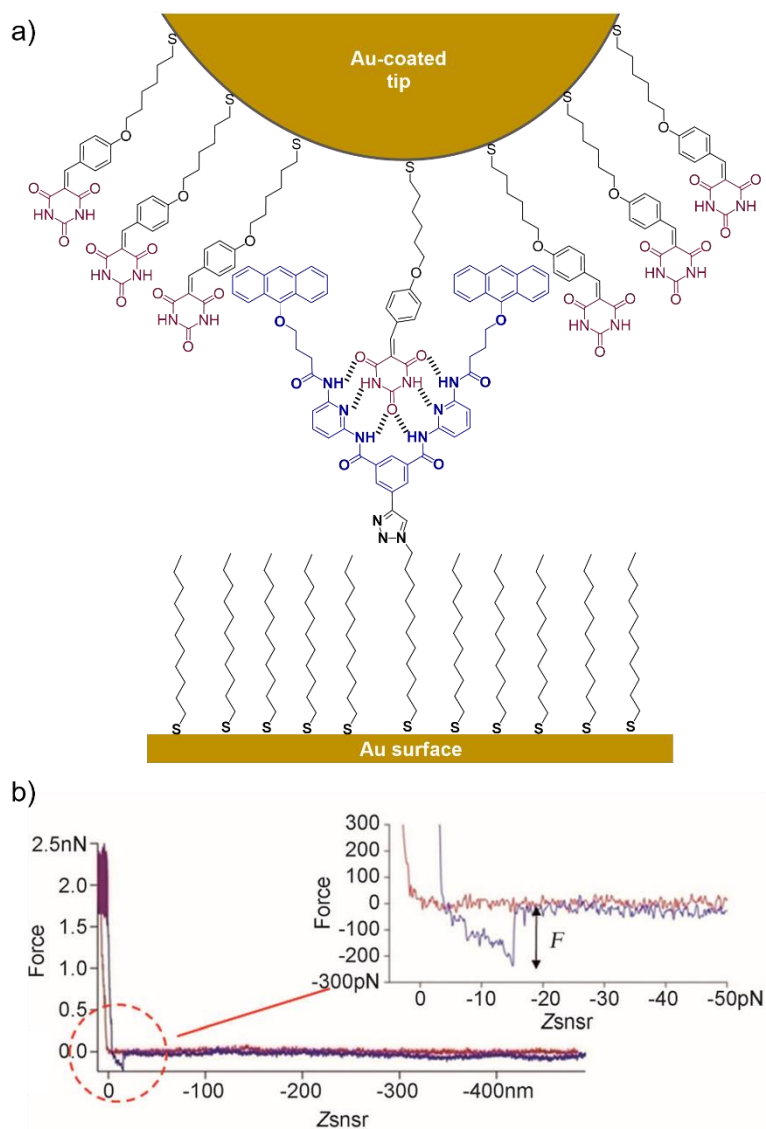


Figure II-2. a) Schematic representation of AFM-SMFS. The gold-coated substrate is functionalized with the Hamilton receptor, in blue, otherwise the gold-coated tip is functionalized with the barbituric derivative, in red. The formation host-guest couple is ensured applying contact time of 5 s (solvent 1,2-dichlorobenzene). b) Force/distance curves at approach and retraction velocities of 250 nm s^{-1} . Upon approach (red trace) no peaks were observed, while upon retraction (blue trace) it was observed a peak corresponding to the strength necessary to break the H-Bonds that hold the system together. Figure adapted with permission from *Chem. Eur. J.* **2013**, *19* (38), 12748-12758.

At this point, we arrive at the main objective of this chapter; we are looking for a novel experimental set-up to unequivocally isolate H-bonded host-guest systems and study their mechanical strength under non-equilibrium, near-physiological conditions; as single molecule manipulation technique we have selected OT.⁴⁶ The ability of OT to resolve forces as small as 0.1-1 pN makes this technique ideally suited to measure the mechanical strength of noncovalent interactions in aqueous solutions.

2.2. Results and Discussion

2.2.1. Chemical Design

In order to unambiguously identify single host-guest interactions we use a hairpin-like DNA construct as a 'single-molecule reporter'. The well-defined mechanical properties of DNA make this biological polymer an excellent reporter for identification and manipulation of single molecules.^{54, 162} As a model H-bonded system, we focused on the receptor for barbiturates developed by Hamilton¹⁶⁴ and a cyanuric acid derivative as guest (HR-cy in Figure II-3), which features six strong H-bonds. We based our choice on several reasons: 1) the system has been thoroughly studied in bulk; 2) benchmark data using SMFS for a similar system in organic solvents are available;¹⁶¹ 3) the synthesis of the building blocks is well-known and versatile, for instance it is possible to block one of the cyanuric acids' H-bond donors by methylation (HR-cyCH₃ in Figure II-3a).

To study the mechanical strength of the H-bonds of a single host-guest system, the receptor (HR) and the cyanuric acid were linked covalently to the 3'- and 5'- termini, respectively, of self-complementary DNA oligonucleotides (Figure II-3a and Experimental section). Briefly, an amino alkyl chain-controlled pore glass (LCAA-CPG) solid support was modified with the HR (compound **II-9**, Experimental section) and used as a ground to synthesize, in the 3' to 5' direction, one of the oligonucleotides (oligonucleotide 6, Figure II-3a and Experimental section). The 5'-terminus of the complementary oligonucleotide (oligonucleotides 7 and 8, Figure II-3a and Experimental section) was linked covalently to a cyanuric acid phosphoramidite (compound **II-11** and **II-15**, Experimental section) on the last step of a solid support DNA chemical synthesis. The oligonucleotide sequences were designed to provide a 5' protruding end after annealing (Figure II-3a), which was used to ligate the modified oligonucleotide couple to one end of a 410 bp dsDNA molecule (or unzipping segment). The other end of the unzipping segment was modified at the 5'-terminus with a single biotin and at the 3'-terminus with a dsDNA spacer (~1 μ m) finished with multiple digoxigenins (Dig) (Figure II-3a and Experimental section).¹⁶⁵

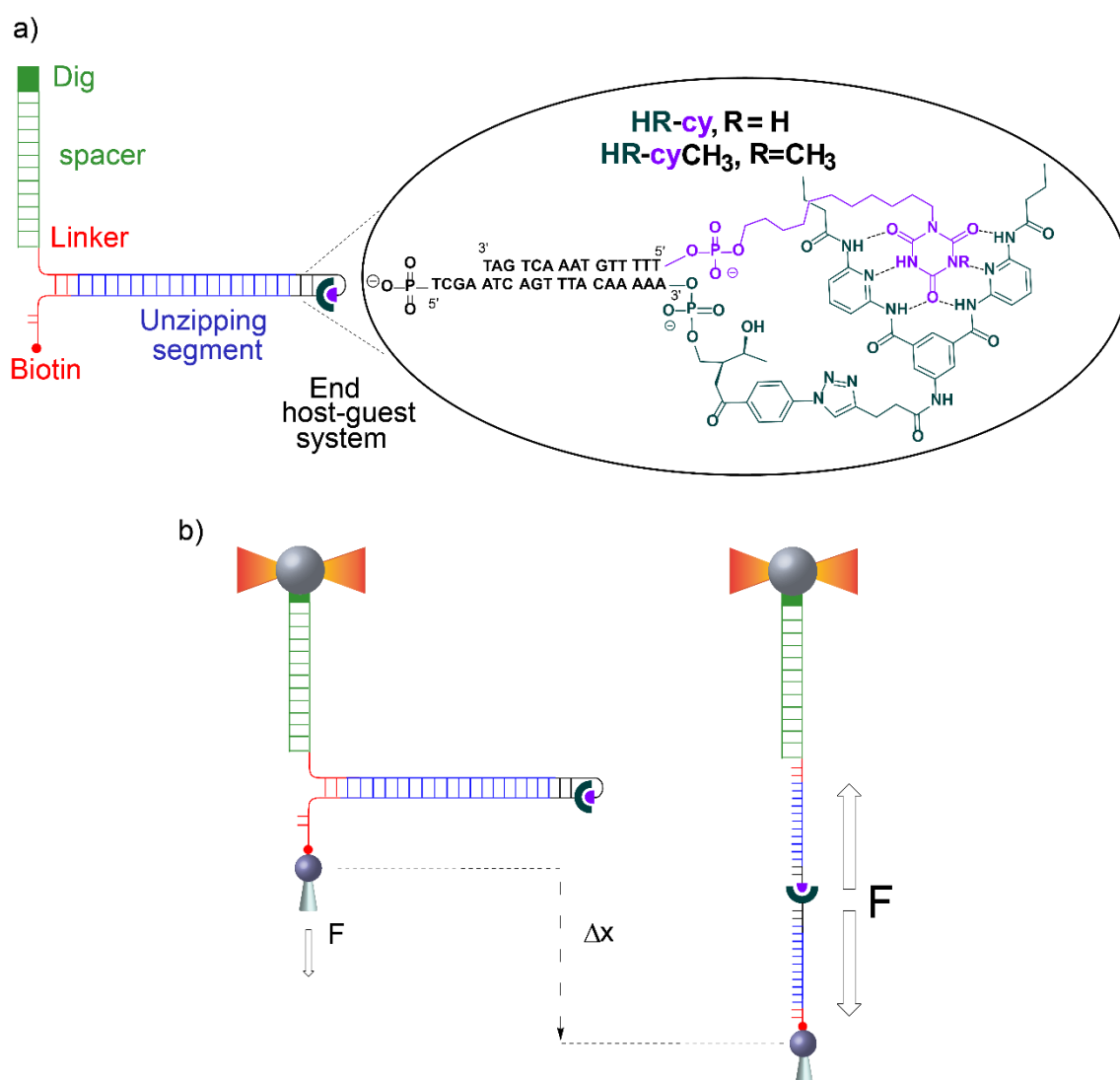


Figure II-3. Schematic of experimental setup: a) Diagram illustrating the DNA construct (not to scale). One end of the main DNA unzipping segment (blue) was ligated to complementary DNA oligonucleotides bearing the receptor (HR, dark green) and the cyanuric acid (cy, purple). The other end of the unzipping segment was ligated through a short DNA linker (red) to a dsDNA (2686bp) labelled with digoxigenin (Dig, green). The 5' end of the linker was labelled with biotin. The insert shows the structure of the HR–cy couple and the sequence of the complementary DNA oligonucleotides. b) A single DNA construct was tethered to functionalized beads via Dig-antiDig (green) and biotin-streptavidin (red) connections: one strand of the unzipping segment was attached to a bead (grey sphere) held in the laser trap (dark yellow beams) and the complementary strand to a bead on top of a mobile micropipette (light grey cone). The dsDNA spacer (green) provides separation ($\sim 1 \mu\text{m}$) between the two attachment points. Pulling the beads in opposite directions promotes the unzipping of the DNA (Δx) and allows applying controlled, axial mechanical force (F) to the host–guest couple located at one end of the unzipping segment.

We used a counter propagating dual-beam optical tweezers instrument¹⁶⁶ to unzip mechanically individual DNA constructs tethered between an optically trapped

anti-Dig-coated bead and a streptavidin-coated bead immobilized on top of a micropipette (Figure II-3b and Experimental section). This configuration allows applying controlled directional mechanical force to the opposite strands of the DNA construct and to determine ultimately the mechanical strength of the transient, out of equilibrium, H-bond interactions holding together the single host-guest couple located at the end of the unzipping segment. Therefore, the DNA construct was designed to pull the HR-cy couple in an axial direction along the extension of the host-guest couple (Figure II-3b).

2.2.2. Bulk characterization of the host-guest system

Before going to single molecule manipulation, we further characterized the ended dsDNA; where are placed our host-guest systems under study. For this, we measured melting temperatures (T_m), recording the dependence of the absorbance versus the temperature at 260 nm:

When a DNA solution is heated enough, the dsDNA unwinds, and the H-bonds that hold the two strands together weaken and finally break. The process of breaking a dsDNA into ssDNA is known as DNA melting, or DNA denaturation. The temperature at which the DNA strands are half denatured, meaning half dsDNA, half ssDNA, is called the melting temperature (T_m). The amount of strand separation, or melting, can be measured by the absorbance of the DNA solution at 260 nm. Nucleic acids absorb light at this wavelength because of the electronic structure in their bases, but when two strands of DNA come together, the close proximity of the bases in the two strands quenches some of this absorbance. When the two strands separate, this quenching disappears and the absorbance rises 30-40 %. This is called hyperchromicity. The hypochromic effect is the effect of stacked bases in a double helix absorbing less ultra-violet light. Thus, T_m depends on the oligonucleotide composition (G-C base pairing (bp) have 3 H-bonds, while A-T bp have only two); it is also affected by its environment: increasing salt concentrations helps diffuse negative repulsions between the phosphates in the DNA's backbone, conversely, pH can have a negative effect on DNA's stability which may lead to a lowering of its melting temperature.

Very briefly, buffered aqueous solutions of oligonucleotides were prepared in phosphate buffered saline (PBS) with oligonucleotide concentrations of 0.2 μ M. The samples were heated at a rate of 1 $^{\circ}$ C/ min. Melting curves were recorded at a wavelength of 260 nm and were obtained by calculating the inflexion points of the melting curves. Thus, we determined the melting point for the duplexes a-f, which are structural analogues of the final system (sequences and T_m are summarized in Table II-1).

Duplexes b (ended in HR-cy couple) and c (ended in HR-cyCH₃ couple) reveal an increment in the melting point of 3.9 and 2.6 $^{\circ}$ C (Table II-1 and Figure II-4) with respect to

duplex a (without HR-cy couples). We also recorded melting temperatures of duplexes d (ended in HR), e (ended cy) and f (ended in cyCH₃) to discard possible effect of the free HR, cy and cyCH₃ to the melting temperatures.

These measurements provide evidence that the HR-cy and the HR-cyCH₃ are held together through H-Bonds. We were also able to observe that there is a significant difference in the melting point of the duplex c (ended in HR-cyCH₃ couple) with respect to the duplex b (ended in HR-cy couple) of 1.3 °C, this point reflects the existence of fewer H-Bonds between the HR-cyCH₃ couple.

Table II-1. Duplexes sequences and its melting points, ΔT_m values are referenced to duplex a

n°.	Sequence	T _m (°C)	ΔT_m (°C)
a	5'-TCGA ATC AGT TTA CAA AAA-3' 5'-TTT TTG TAA ACT GAT TCGA-3'	56.3 ± 0.2	0
b	5'-TCGA ATC AGT TTA CAA AAA-HR-3' 5'-cy-TTT TTG TAA ACT GAT TCGA-3'	60.2 ± 0.3	3.9
c	5'-TCGA ATC AGT TTA CAA AAA-HR-3' 5'-cyCH ₃ -TTT TTG TAA ACT GAT TCGA-3'	58.9 ± 0.4	2.6
d	5'-TCGA ATC AGT TTA CAA AAA-HR-3' 5'-TTT TTG TAA ACT GAT TCGA-3'	55.9 ± 0.2	0.4
e	5'-TCGA ATC AGT TTA CAA AAA-3' 5'-cy-TTT TTG TAA ACT GAT TCGA-3'	56.2 ± 0.4	0.1
f	5'-TCGA ATC AGT TTA CAA AAA-3' 5'- cyCH ₃ -TTT TTG TAA ACT GAT TCGA-3'	56.9 ± 0.3	0.6

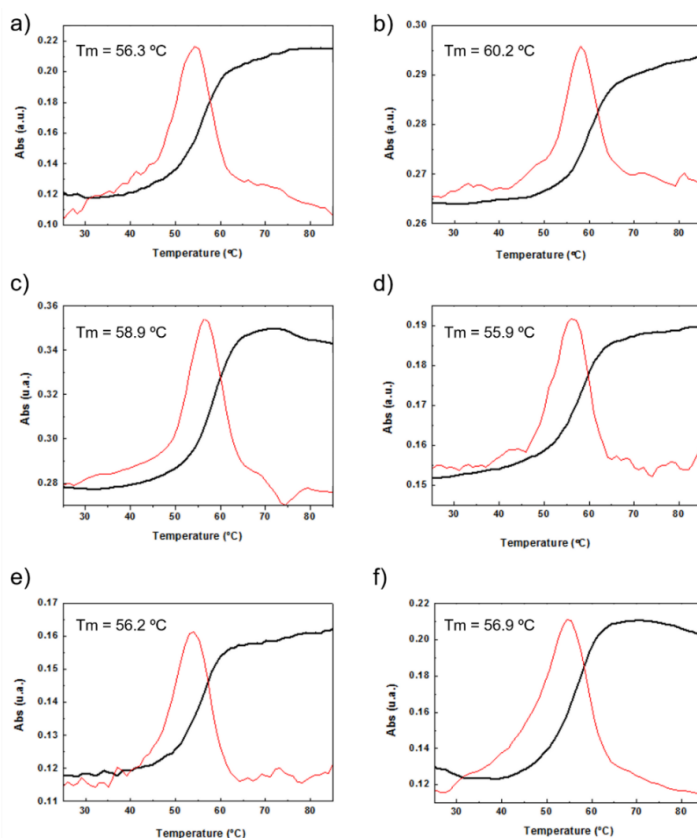


Figure II-4. Absorbance versus Temperature curves (black traces) at 260 nm wavelength for duplexes a-f. The melting points were obtained by calculating the inflexion points of the melting curves (red traces).

2.2.3. Single molecule experiments

Under near-physiological NaCl and pH conditions (Tris-HCl 20 mM pH 7.5, 50 mM NaCl) mechanical unzipping of a single DNA construct started at a force of ~ 12 piconewtons (pN) (Figure II-5a). The characteristic force-extension curve of the molecule permitted the unequivocal identification of single attachments between the beads.^{162,167} The initial and final extensions of the DNA constructs corresponded to their expected lengths before and after unzipping, respectively.¹⁶⁸ The unzipping segment contained three guanine-cytosine (GC) base pair clusters with 1 to 3 repetitions of the GCC sequence, separated by a ~ 100 nucleotide low-GC content, the three GCC clusters are clearly visible as distinct increments in force as we move from the initial GCC cluster to $(GCC)_2$ and $(GCC)_3$ (Figure II-5a). These sequences were used as fiducial markers to align independent force-extension curves (Experimental Section) and further identify the end of the DNA unzipping segment where the host-guest interactions should occur.

Mechanical unzipping of the DNA was typically carried out with a pulling rate of 50 nm s^{-1} . When the HR component of the host-guest system was not included at the

end of the unzipping segment, disassembly was completed shortly after unzipping of the last (GC)₃ position at an average force of 11.5 ± 0.3 pN (number of experiments, N = 20, Figure II-5b). However, when the HR-cy host-guest system was included, after full unzipping of the DNA segment the force increased to 16.7 ± 1.6 pN (N = 100, 12% of which showed unequivocal signs of binding), reflecting the mechanical strength of the H-bonds between the HR-cy couple under these experimental conditions (Figure II-5b). Disruption of one of the H-bonding interactions by a methyl group (HR-cyCH₃) decreased the rupture force to 15.6 ± 0.7 pN (N = 100, 10%, Figure II-5b). We note that although mechanical stability is not necessarily related to thermodynamic stability,¹⁶⁹ our results are in agreement with the effect of these modifications on the thermal stability of oligonucleotide duplexes in the bulk.

We confirmed with a 95% probability that the difference between the rupture forces measured for the HR-cy and HR-cyCH₃ couples is statistically significant (this is clearly explained in the Experimental section). These results highlight the remarkable ability of our method to resolve subtle changes in the mechanical strength of the complex due to the H-bond components. However, we note that the mechanical stability of the HR-cy couple depends on the location of the transition state along the mechanical reaction coordinate used in our experiments, the height of the barrier and the loading rate.¹⁶⁹⁻¹⁷¹ Therefore, the H-bonds of the host-guest system are probably not equivalent in terms of resistance to the applied force, and our measurements reflect an average for the mechanical strength of the HR-cy couple. In fact, the difference in the rupture force between the HR-cy and HR-cyCH₃ couples (1-2 pN) suggests that the applied force is distributed over the whole binding site of the host-guest couple and is not representative of a single H-bond.

Previously reported average rupture forces for the HR-cy system were measured at ~170 pN with Atomic Force Microscopy (AFM) at a pulling rate of 250 nm s^{-1} in an organic solvent.¹⁶¹ As discussed above, the discrepancy in experimental results may arise from differences in the pulling geometry, effective pulling rates, contact forces¹⁷² and/or from an enhancement in binding strength of H-bonded complexes in organic solvents compared to aqueous environment.

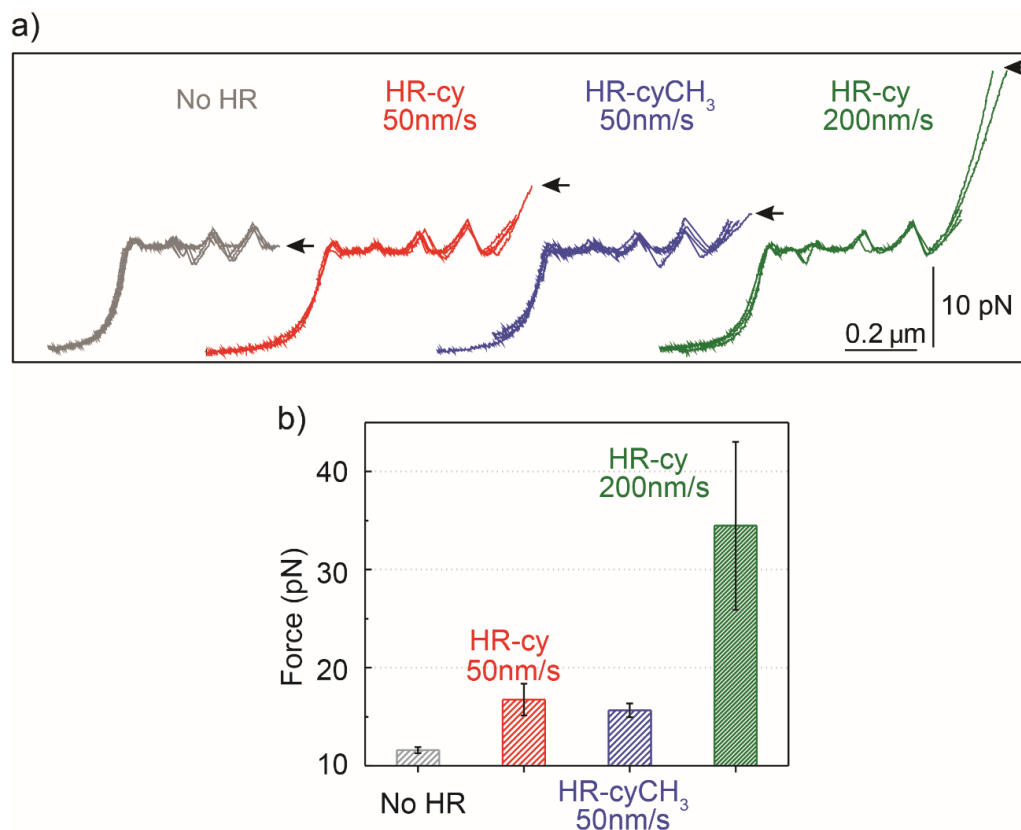


Figure II-5. Rupture forces of the HR-cy couple. a) Representative experiments showing the force extension curves of DNA constructs harbouring at their ends the HR-cy (red, 50 nm/ s, green 200 nm/ s) or HR-cyCH₃ (blue, 50 nm/ s) couples. The mechanical unzipping of DNA constructs without the HR component is shown in grey. Four independent curves are shown in each case (see Experimental section for additional curves). The positions of the GC clusters are revealed as peaks in the unzipping pattern. Arrows indicate the force and position of the rupture events. b) Average rupture forces for DNA constructs without the HR-cy couple (grey), with the HR-cy couple (red, 50 nm/ s, green 200 nm/ s) and with the HR-cyCH₃ couple (blue, 50 nm/ s). Error shows standard deviations; see the main text for populations. Data were taken at 100 Hz (22 ± 1 °C).

Our experimental results were corroborated by DFT calculations. The potential energy curves (PECs) for HR-cy and HR-cyCH₃ couples were calculated performing single point energy calculations at different distances in an axial direction, along the extension of the host-guest couple. Specifically, we increase the host-guest distance (see Experimental section for the definition of the axial direction) 50 times with a variation of 0.2 Å between them. The long range corrected ω B97xD density functional¹⁷³ was employed in combination with the basis-set 6-31g(d,p) and the IEF-PCM water solvation model. This methodology has been chosen following the literature in the field.^{23, 24, 174, 175} The PECs for HR-cy and HR-cyCH₃ systems and the optimized structures for the completely bonded and non-interacting states in water are displayed in Figure II-6.

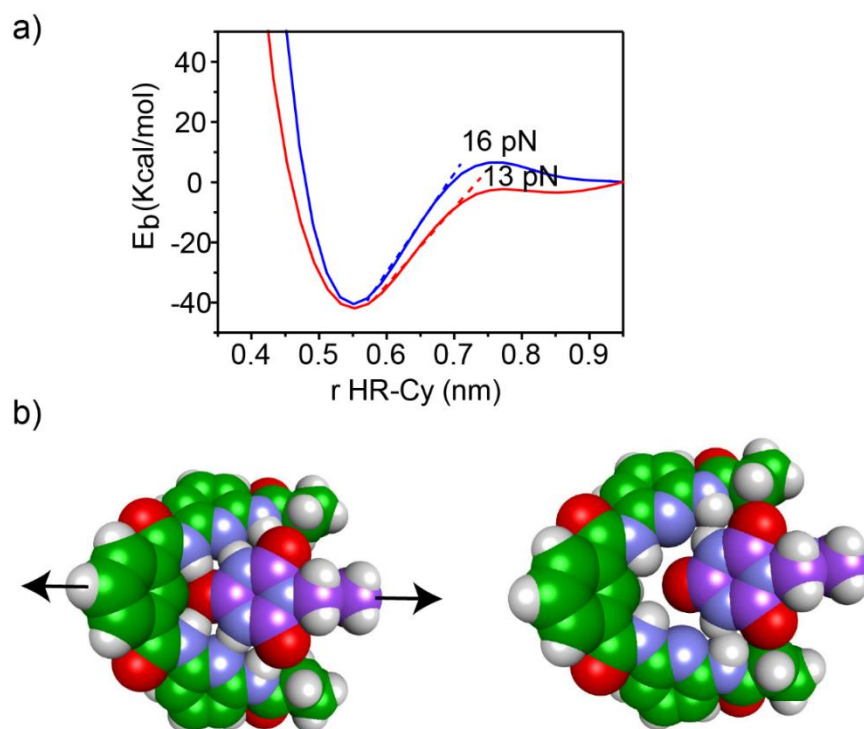


Figure II-6. a) Potential energy curves for HR-cy (blue) and HR-cyCH₃ (red) employing IEF-PCM water solvation model. b) Energy-minimized molecular models showing the geometry of the bound (left) and unbound (right) HR-cy system.

In Figure II-6a, we observe that at large distances, interactions are negligible ($E_b = 0$) but attractive interactions grow as host and guest approach each other, reaching a state of equilibrium where the net force (the sum of both attractive and repulsive components) is zero. The PECs indicate the energy of the host-guest interaction based on the depth of the potential well, and the force (F) is the slope of the curve, according to: $F = -dE_b/dr$, where E_b is the binding energy and r the distance between host and guest. At equilibrium, the binding energy for the systems HR-cy and HR-cyCH₃ are calculated to be 40.51 and 41.92 Kcal mol⁻¹ respectively, which are expected binding energies for systems with six and five strong hydrogen bonds in aqueous conditions.

At short distances from the equilibrium state (0-0.03 nm) the potential energy is not affected by a change in the intermolecular distance, but at larger values of r a change in the slope is observed. From this point to the next change in slope, where the cyanuric acid is completely dissociated from the HR (see Figure II-6b right), a value of 16 pN for the force is obtained. This value is directly related with the force required to split the couple, and is in good agreement with our experimental data. In the case of the HR-cyCH₃ system, the calculated force was 13 pN, a noticeably lower value than HR-cy, following the same tendency of our experimental results. We also calculated the rupture force using 1,2-dichlorobenzene as model of organic solvent (see Experimental Section). We observe a slight increase in the force: 17 pN for HR-cy system and 14 pN

for HR-cyCH₃. DFT calculations corroborate that the average rupture forces measured in our work under aqueous conditions are in the correct order of magnitude, and support a relatively minor role of solvent composition in the breaking of an already formed H-bonded host-guest couple.

To sum up, we have developed a new method to measure the average mechanical strength of H-bonded supramolecular complexes, at the single-molecule level, under non-equilibrium conditions. Our method expands the capabilities of previously described SPM methods by exploiting the force resolution of optical tweezers (0.1-100 pN), which allows measuring the characteristic strength of H-bonds under near-physiological conditions, and by including a DNA reporter that guarantees that the force measurements refer to a single binding event. The modularity and addressability of the DNA construct described here also opens up the possibility of targeting synthetic host-guest couples in controlled orientations and stoichiometry. In this case, we have focused on aqueous conditions, but the system is in principle adaptable to other sets of conditions. This renders our method a versatile and precise tool to address key questions in supramolecular chemistry, like the mechanical strength of H-bonded systems, and its relationship with their thermodynamic stability.

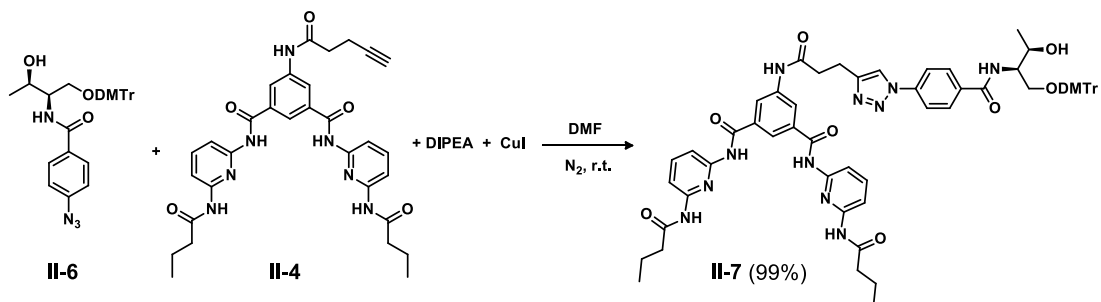
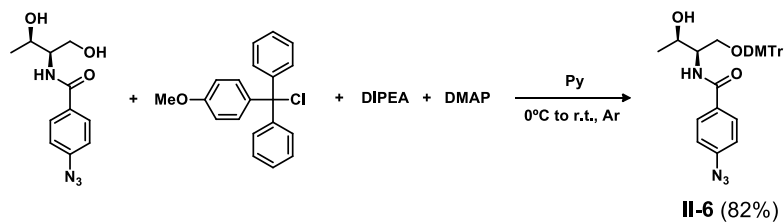
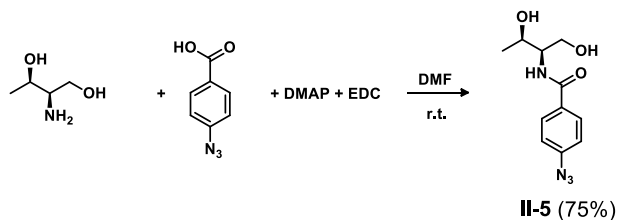
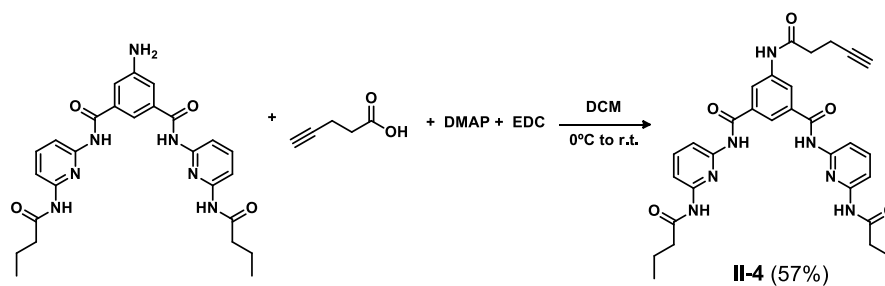
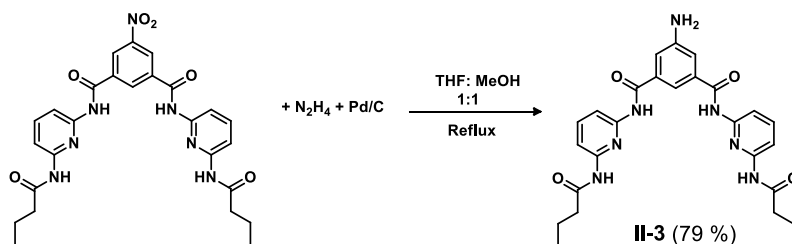
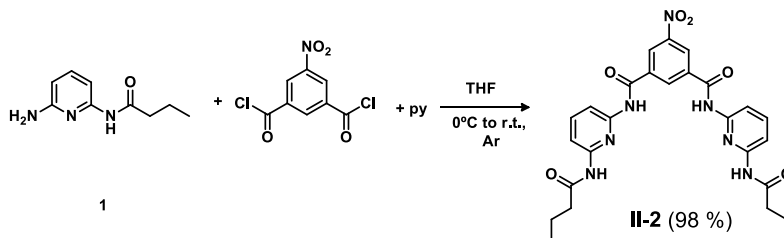
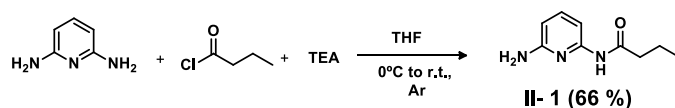
2.3. Experimental section

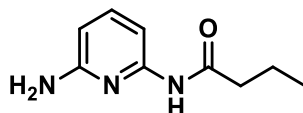
Contents:

- 2.3.1.** Synthesis of the Hamilton receptor derivative
- 2.3.2.** Preparation of modified solid supports
- 2.3.3.** Cyanuric acid derivate synthesis
- 2.3.4.** Oligonucleotide synthesis and analytical data of oligonucleotides
- 2.3.5.** Mass spectral data of synthesized oligonucleotides
- 2.3.6.** Melting temperatures of duplexes
- 2.3.7.** Synthesis of DNA construct
- 2.3.8.** Optical Tweezers experiments
- 2.3.9.** Experimental force-extension curves
- 2.3.10.** Computational details

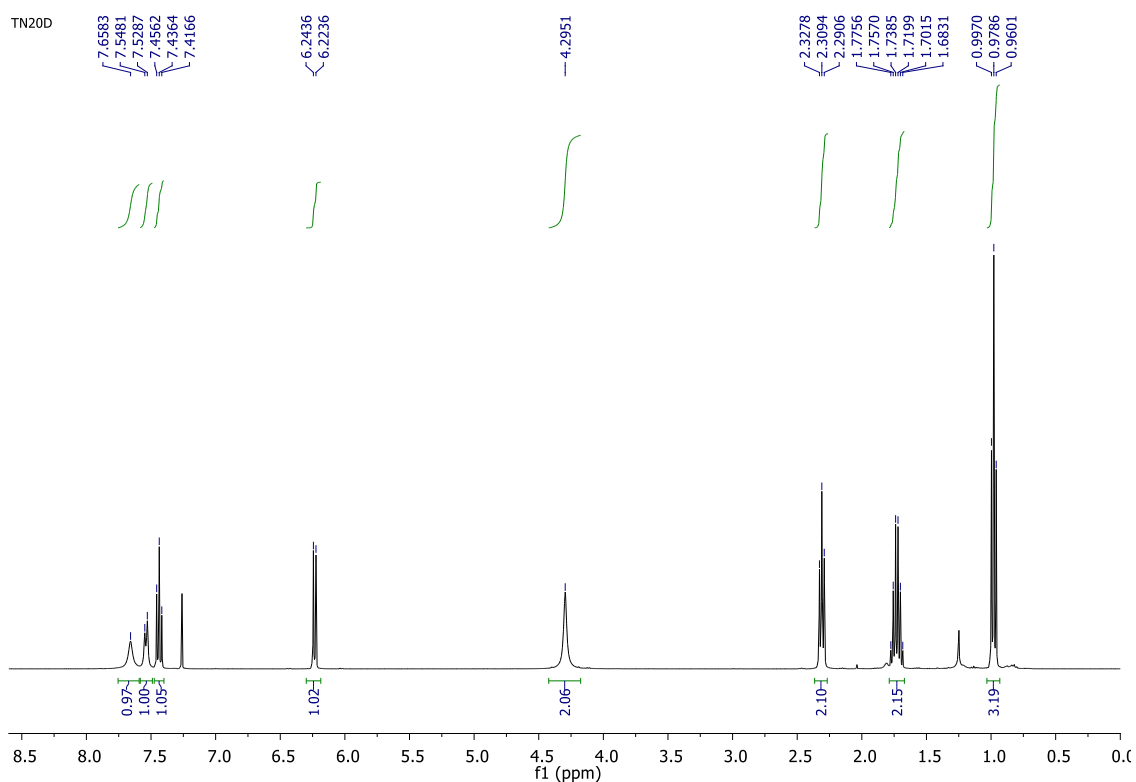
General. All solvents were dried according to standard procedures. Reagents were used as purchased. All air-sensitive reactions were carried out under argon atmosphere. Flash chromatography was performed using silica gel (Merck, Kieselgel 60, 230-240 mesh, or Scharlau 60, 230-240 mesh). Analytical thin layer chromatographies (TLC) were performed using aluminium-coated Merck Kieselgel 60 F254 plates. NMR spectra were recorded on a BrukerAvance 400 (^1H : 400 MHz; ^{13}C : 100 MHz), spectrometer at 298 K, unless otherwise stated, using partially deuterated solvents as internal standards. Coupling constants (J) are denoted in Hz and chemical shifts (δ) in ppm. Multiplicities are denoted as follows: s = singlet, d = doublet, t = triplet, sx = sextuplet, m = multiplet, br = broad. Fast Atom Bombardment (FAB) and Matrix-assisted Laser desorption ionization (coupled to a Time-Of-Flight analyzer) experiments (MALDI-TOF) were recorded on a VS AutoSpec spectrometer and a Bruker ULTRAFLEX III spectrometer, respectively.

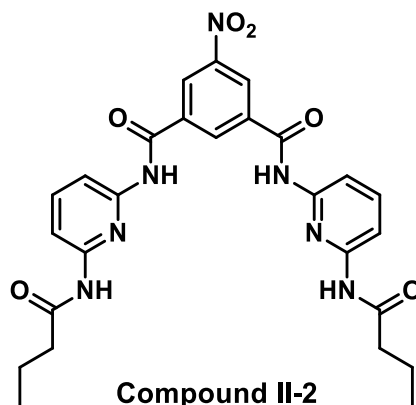
2.3.1. Synthesis of the Hamilton receptor derivative



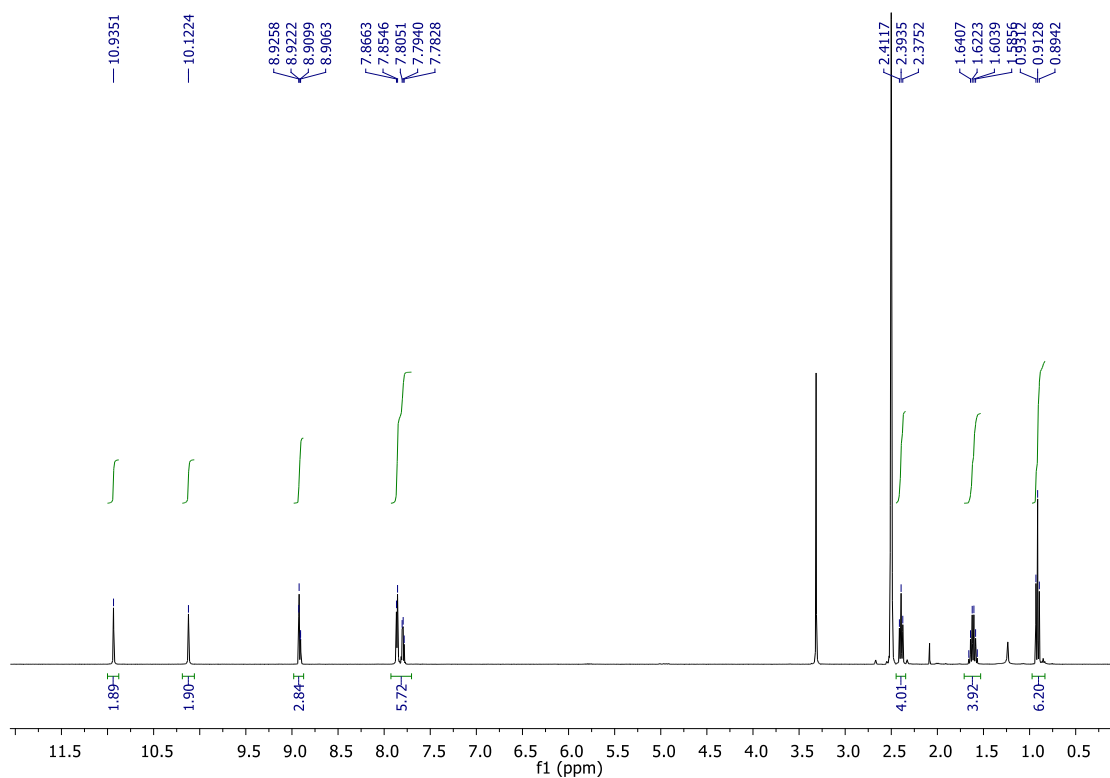
***N*-(6-aminopyridin-2-yl)butyramide****Compound II-1**

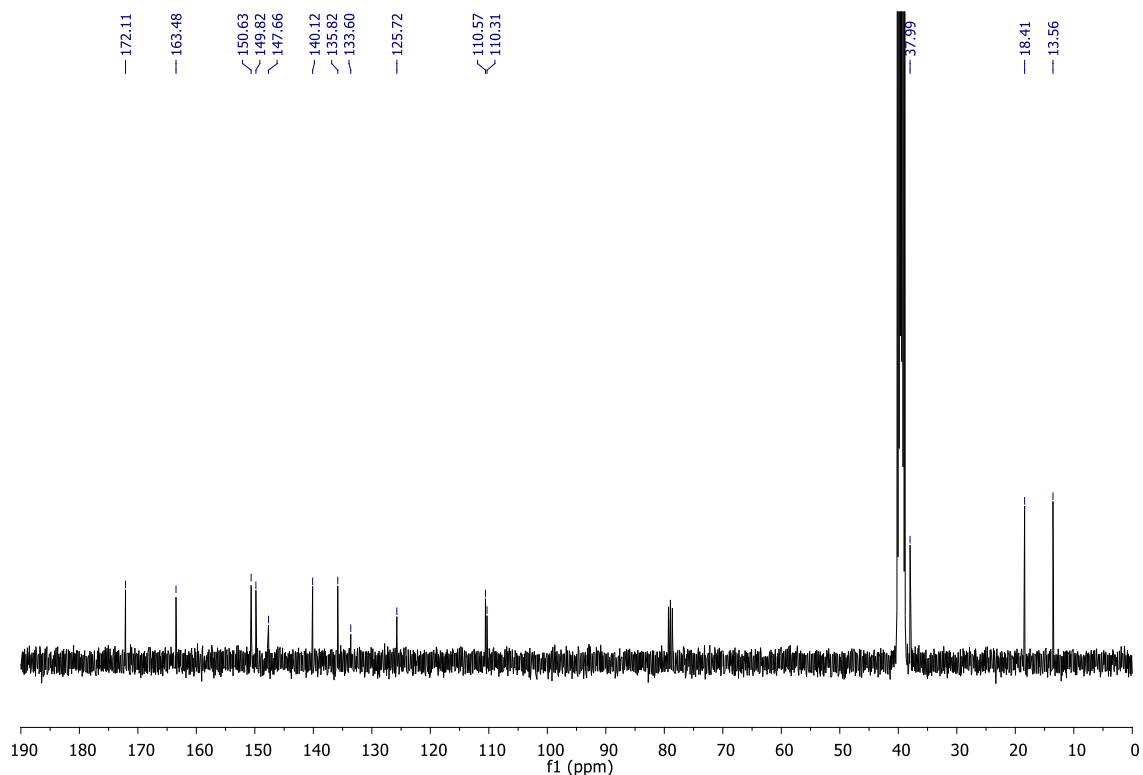
A solution of butyryl chloride (2 g, 18.8 mmol) in dry THF (10 mL) was added to a solution of 2,6-diaminopyridine (2.05 g, 18.8 mmol) and trimethylamine (1.9 g, 18.8 mmol) in dry THF (20 mL) at 0 °C under nitrogen atmosphere over a period of 2h. The solution was stirred overnight, at room temperature; the residue was filtered off and the solvent removed under reduced pressure. The product was purified by column chromatography to give **II-1** as yellow solid, 2.23 g, 66%. ¹H NMR (CDCl₃): δ = 7.65 (s, 1H), 7.54 (br d, *J* = 7.8 Hz, 1 H), 7.44 (t, *J* = 7.9 Hz, 1 H), 7.44 (t, *J* = 7.9 Hz, 1 H), 7.23 (d, *J* = 8 Hz, 1 H), 4.29 (br s, 2H), 2.31 (t, *J* = 7.4 Hz, 2 H), 1.73 (s, *J* = 7.4 Hz, 2 H), 0.98 (t, *J* = 7.4 Hz, 3 H). This data is in accordance with *Chem. Eur. J.* **2007**, 13, 5466.



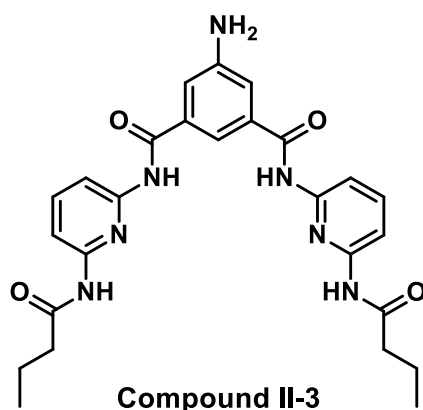
***N'*,*N*³-bis(6-butylamidopyridin-2-yl)-5-nitroisophthalamide**

A solution of 5-nitroisophthaloyl dichloride (0.9 g, 3.62 mmol) in dry THF was added dropwise to a solution of monosubstituted diaminopyridine **II-1** (1.5 g, 7.24 mmol) and trimethylamine (0.7 g, 7.24 mmol) in dry THF (15 mL) at 0°C under argon atmosphere. The solution was stirred at room temperature overnight, the residue filtered off and the solvent removed under reduced pressure. Purification by column chromatography on silica gel (DCM: AcOEt 10:1 to 3:1) gave **II-2** as a yellow solid, 1.89 g, 98%. ¹H NMR ([D₆]dimethyl sulfoxide): δ = 10.94 (s, 2H), 10.12 (s, 2H), 8.92 (m, 2H), 8.91 (m, 1H), 7.86 (d, *J* = 4.7 Hz, 3 H), 7.79 (m, 2H), 2.39 (t, *J* = 7.3 Hz, 2 H), 1.61 (sx, *J* = 7.4 Hz, 2 H), 0.91 (t, *J* = 7.4 Hz, 3 H); ¹³C NMR ([D₆]dimethyl sulfoxide): δ = 172.1 (2C), 163.5 (2C), 150.6 (2C), 149.8 (2C), 147.7 (2C), 140.1 (2C), 135.8 (2C), 133.6, 125.7 (2C), 110.6, 110.3 (2C), 38.0 (2C), 18.4 (2C), 13.6 (2C) ppm. This data is in accordance with *J. Am. Chem. Soc.*, **1990**, 26, 9589.

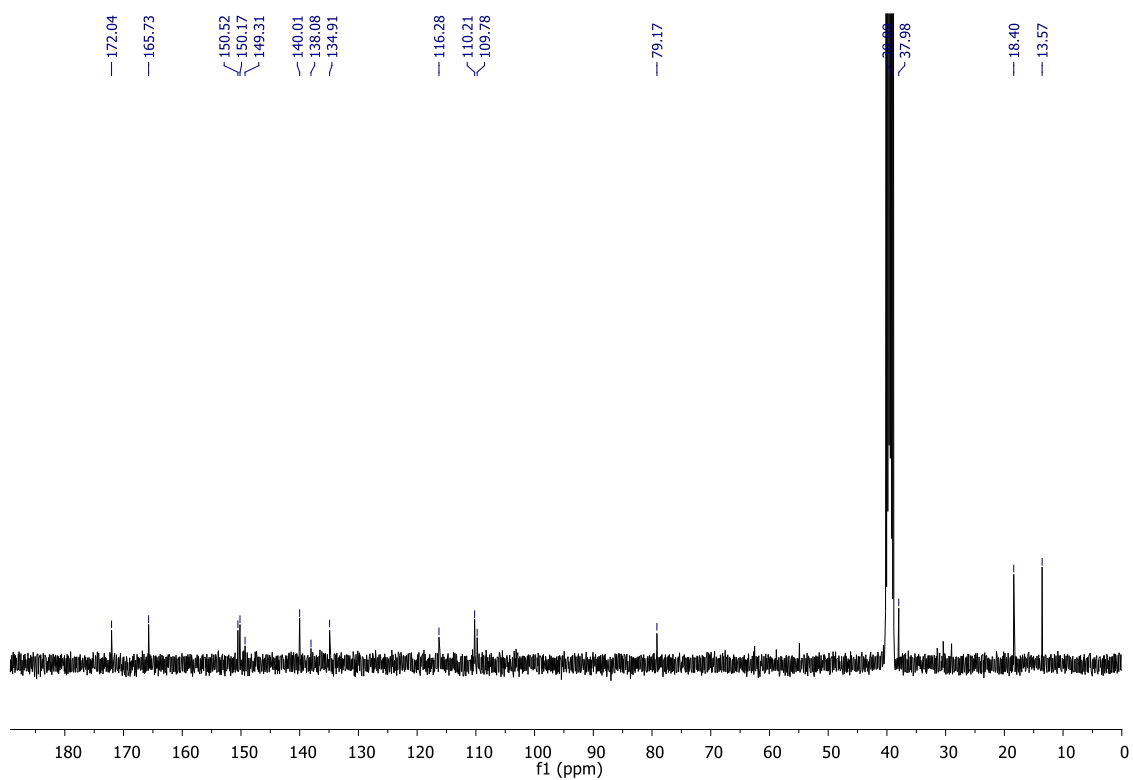
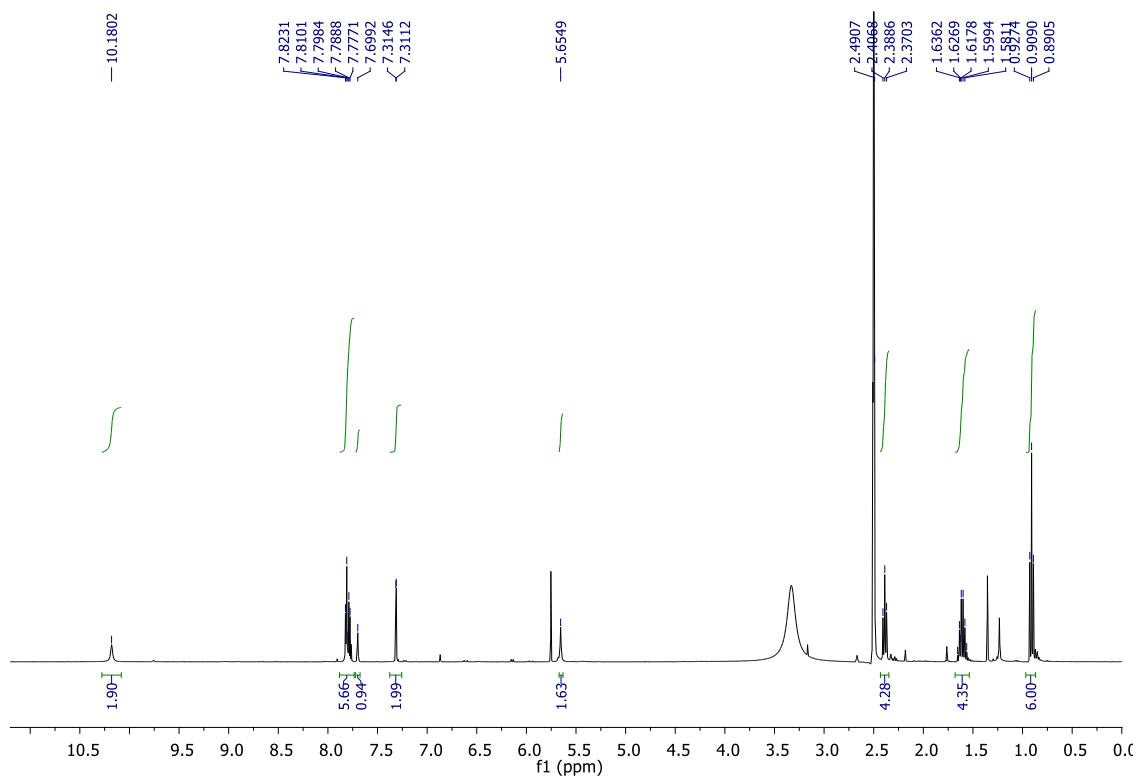


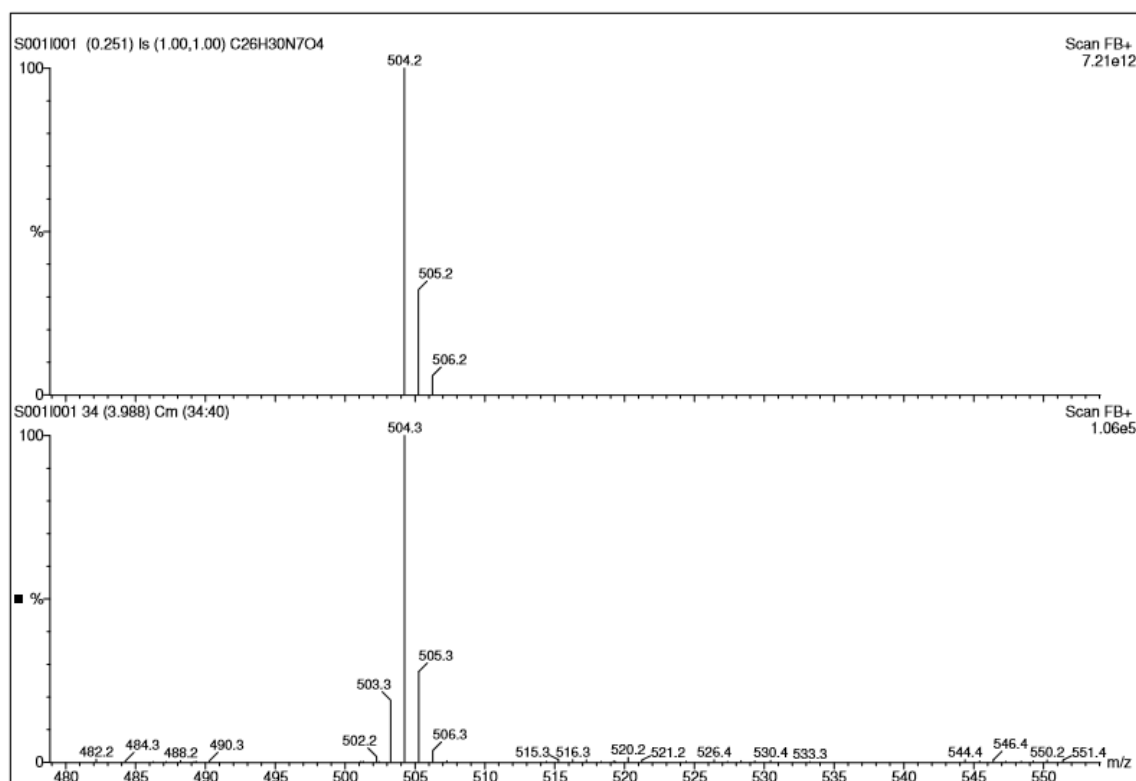


5-amino-*N'*,*N''*-bis(6-butylamidopyridin-2-yl)isophthalamide

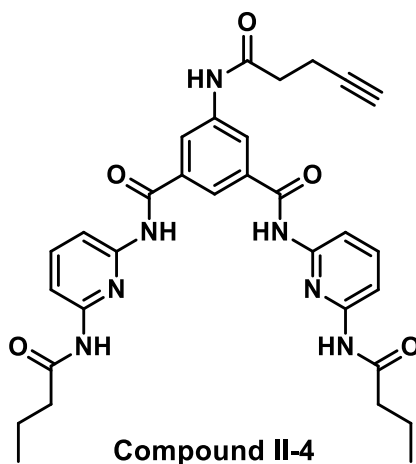


To a solution of **II-2** (0.4 g, 0.75 mmol) in dry THF (34 mL) and MeOH (34 mL) in a round-bottom flask under nitrogen atmosphere, 10% Pd-C (0.4 g) was added and the reaction mixture was heated to 70 °C. Then hydrazine (1.1g, 20.4 mmol) was added to the reaction mixture, which was heated under reflux for 4h. After cooling the reaction mixture to room temperature, Pd-C was removed by filtering it twice through celite, and the filtrate was evaporated under vacuum to give **II-3** as a white solid, 0.3 g, 79%. ¹H NMR ([D₆]dimethyl sulfoxide): δ = 10.18 (s, 2H), 7.80 (m, 6H), 7.70 (m, 1H), 7.31 (d, *J* = 1.4 Hz, 2 H), 5.65 (s, 2H), 2.39 (t, *J* = 7.3 Hz, 2 H), 1.60 (sx, *J* = 7.4 Hz, 2 H), 0.91 (t, *J* = 7.4 Hz, 3 H); ¹³C NMR ([D₆]dimethyl sulfoxide): δ = 172.0 (2C), 165.7 (2C), 150.5 (2C), 150.2 (2C), 149.3 (2C), 140.0 (2C), 138.1, 134.9 (2C), 116.3 (2C), 110.6 (2C), 109.8, 38.0 (2C), 18.4 (2C), 13.6 (2C) ppm. MS *m/z*: calculated for C₂₆H₂₉N₇O₄ [M+H]⁺ 503.6 found FAB 504.3.



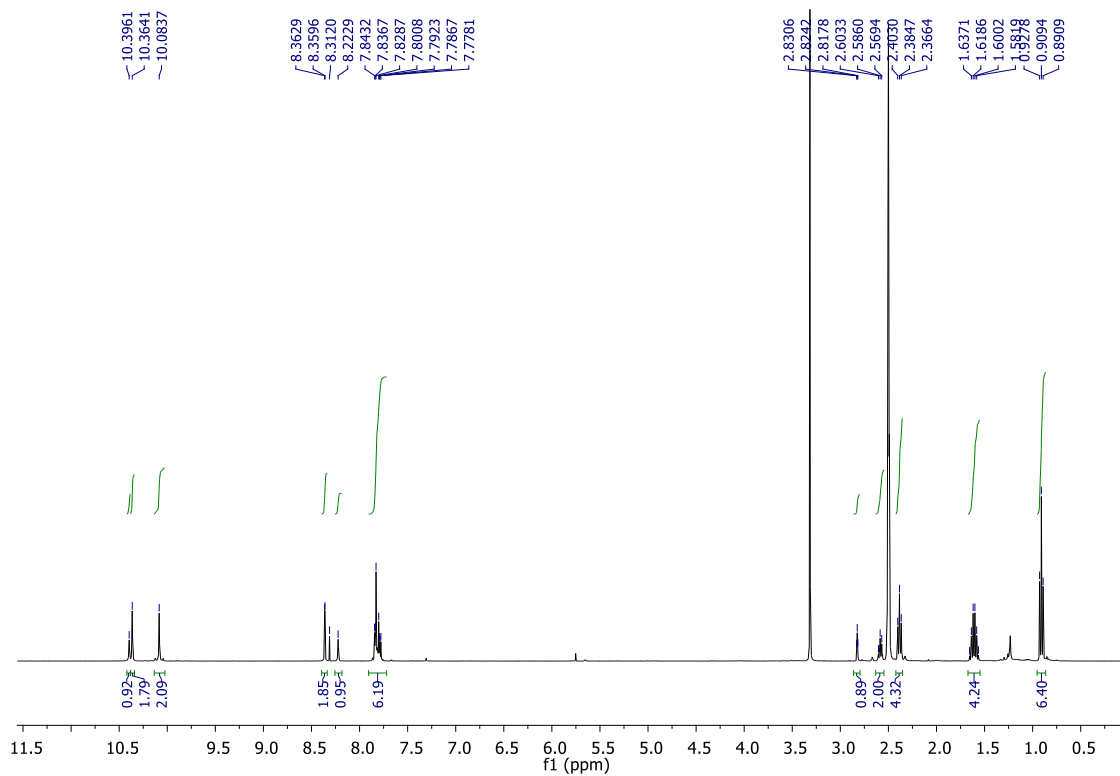


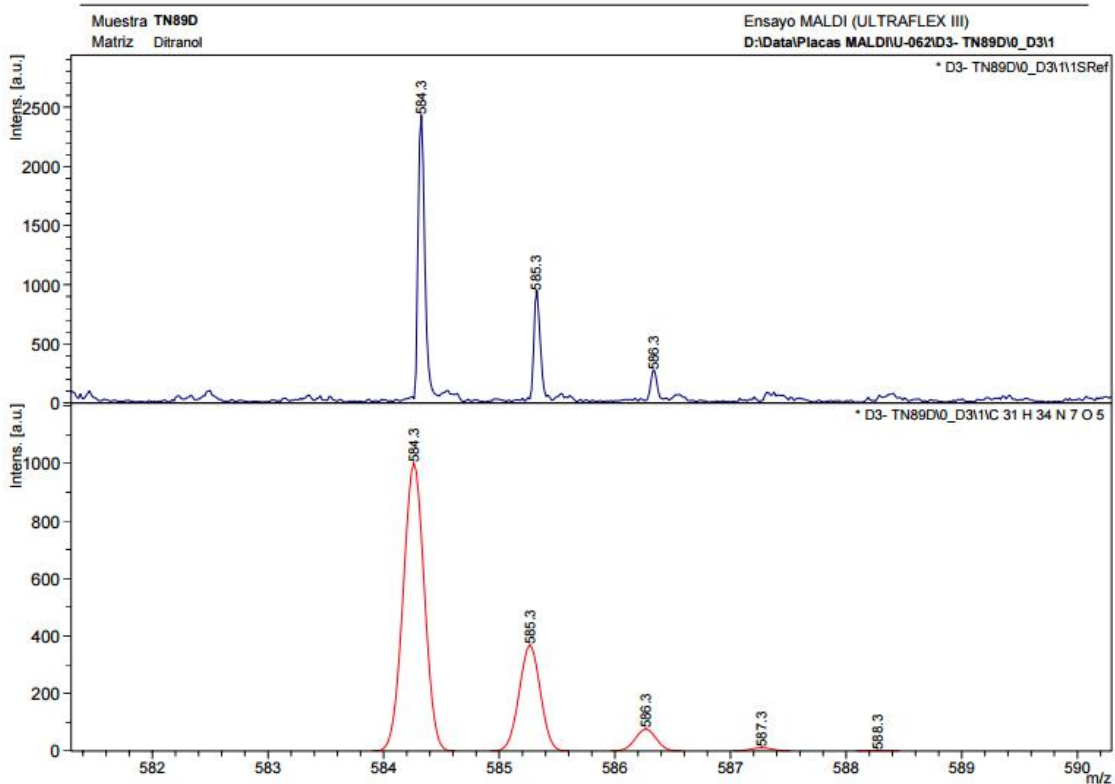
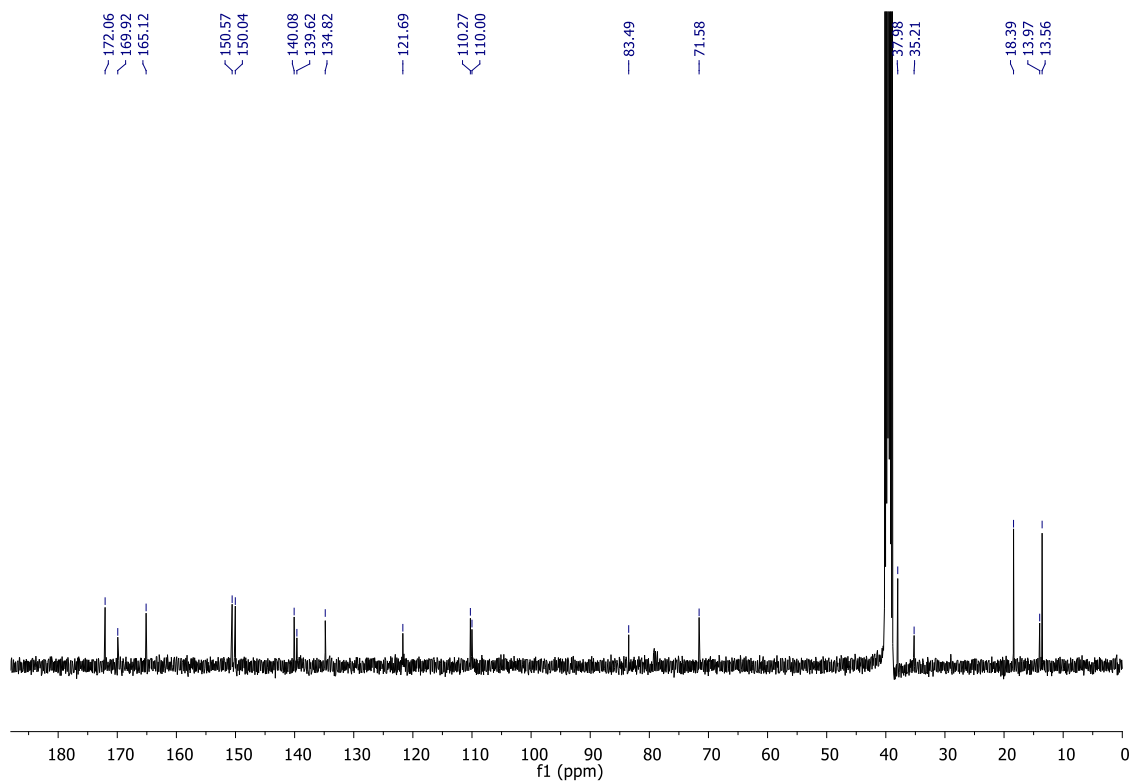
***N'*,*N*³-bis(6-butynamidopyridin-2-yl)-5-(pent-4-ynamido)isophthalamide**

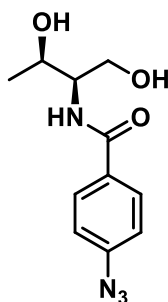


4-pentynoic acid (16 mg, 0.16 mmol) was dissolved in DCM (3.5 mL) and the solution was cooled to 0°C. EDCI.HCl (50 mg, 0.26 mmol) and DMAP (31 mg, 0.26 mmol) were added. The reaction mixture was allowed to stir at room temperature for 30 minutes. A solution of **II-3** (75 mg, 0.15 mmol) in DCM (2 mL) was added to the activated acid. The reaction mixture was stirred for 24h, concentrated under reduced pressure and then DCM was added. The organic layer was washed once with 1M HCl, once with NaHCO₃ (sat., aq.), then concentrated under reduced pressure. The crude material was purified by column chromatography (eluent: DCM: MeOH 25:1) to furnish product **II-4** as white solid, 50mg, 57%. ¹H NMR ([D₆]dimethyl sulfoxide): δ = 10.40 (s, 1H), 10.36 (s, 2H), 10.08 (s, 2H), 8.36 (d, *J* = 1.3 Hz, 2H), 8.22 (m,

1H), 7.81 (m, 6 H), 2.82 (t, $J = 2.6$ Hz, 1 H), 2.58 (m, 2H), 2.38 (t, $J = 7.3$ Hz, 4 H), 1.61 (sx, $J = 7.4$ Hz, 4 H), 0.91 (t, $J = 7.4$ Hz, 6 H); ^{13}C NMR ([D6]dimethyl sulfoxide): $\delta = 172.1$ (2C), 169.9, 165.1 (2C), 150.6 (2C), 150.0 (2C), 140.1 (2C), 139.6 (2C), 134.8 (2C), 121.7, 110.3 (2C), 110.0, 83.5, 71.6, 38.0 (2C), 35.2, 18.4 (2C), 14.0, 13.6 (2C). MS m/z : calculated. for $\text{C}_{31}\text{H}_{33}\text{N}_7\text{O}_4$ $[\text{M}+\text{H}]^+$ 583.6 found MALDI-TOF 584.3.

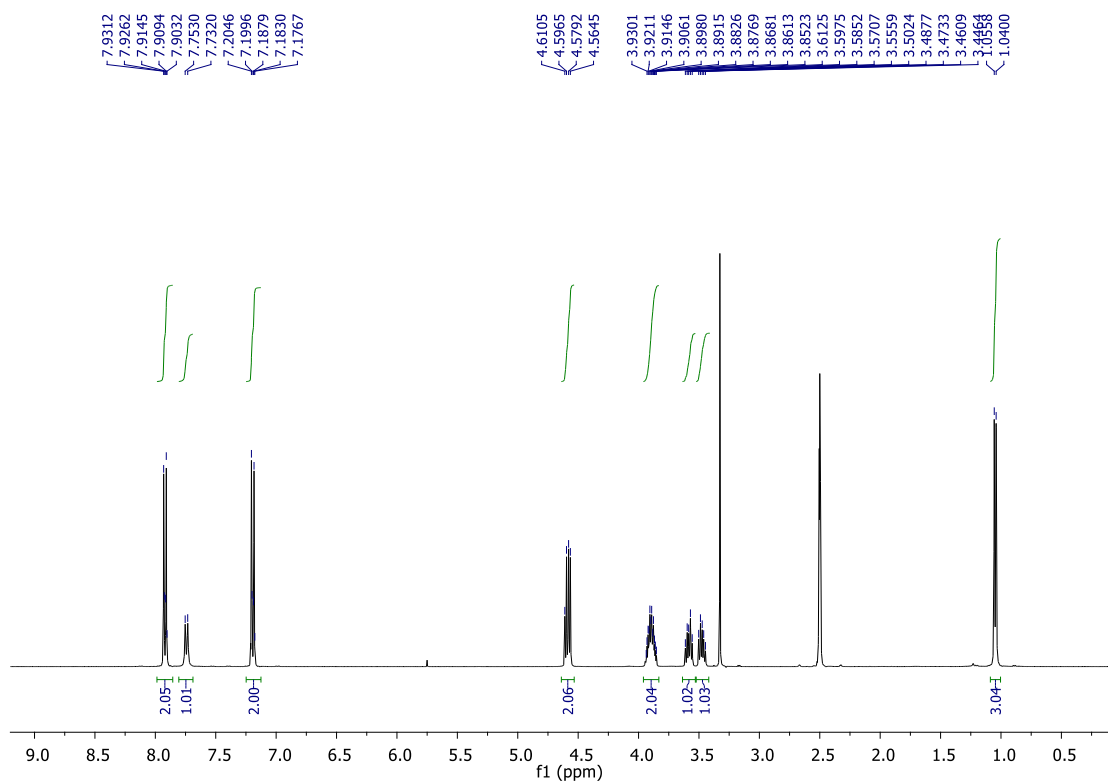


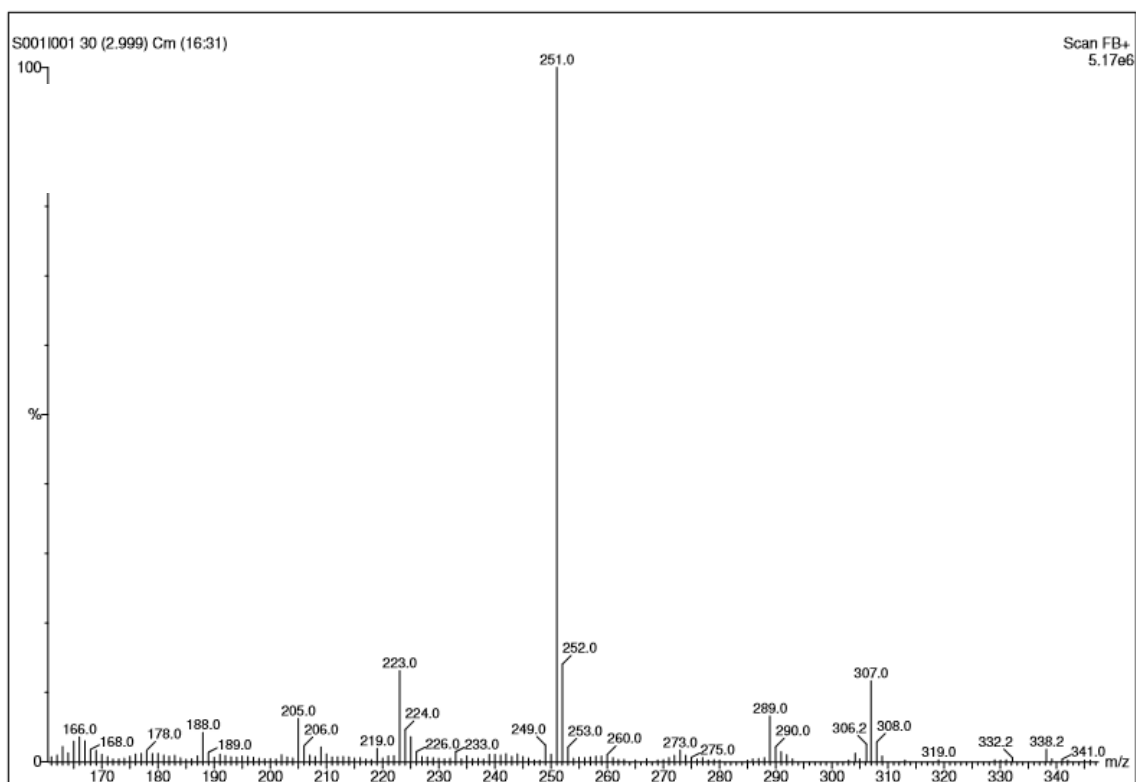
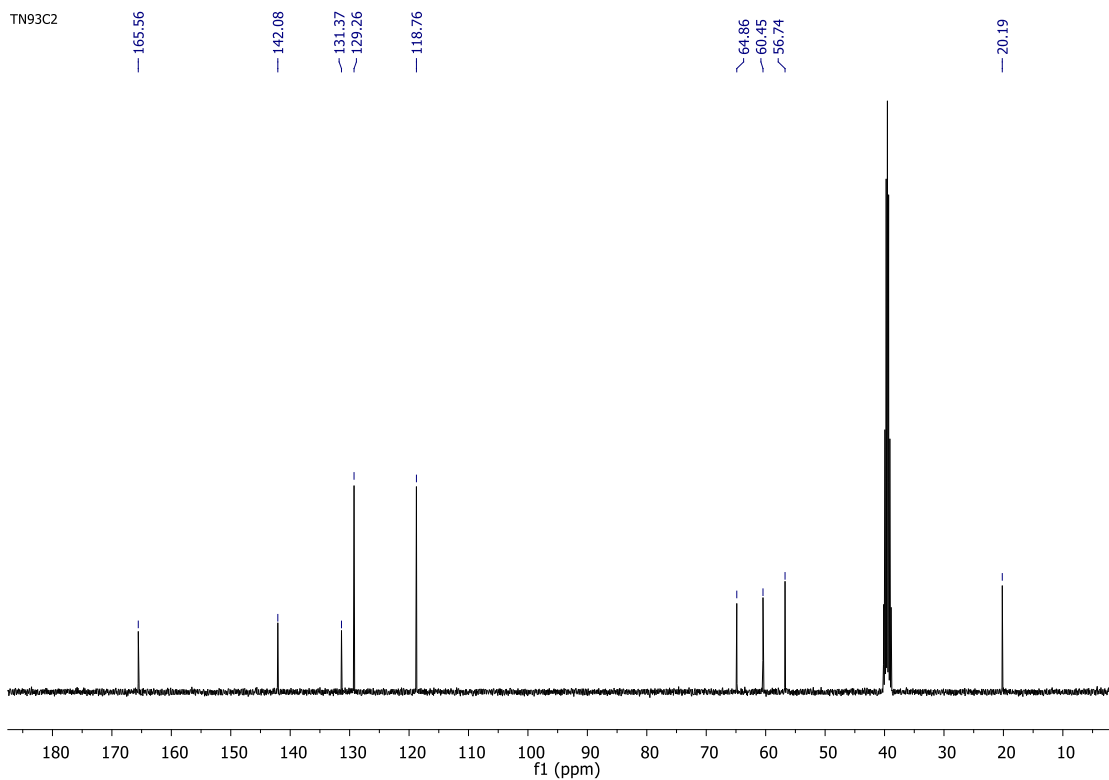


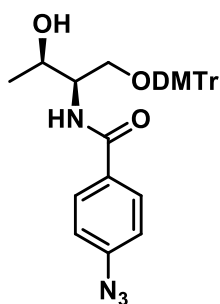
4-azido-*N*-((2*R*,3*R*)-1,3-dihydroxybutan-2-yl)benzamide

Compound II-5

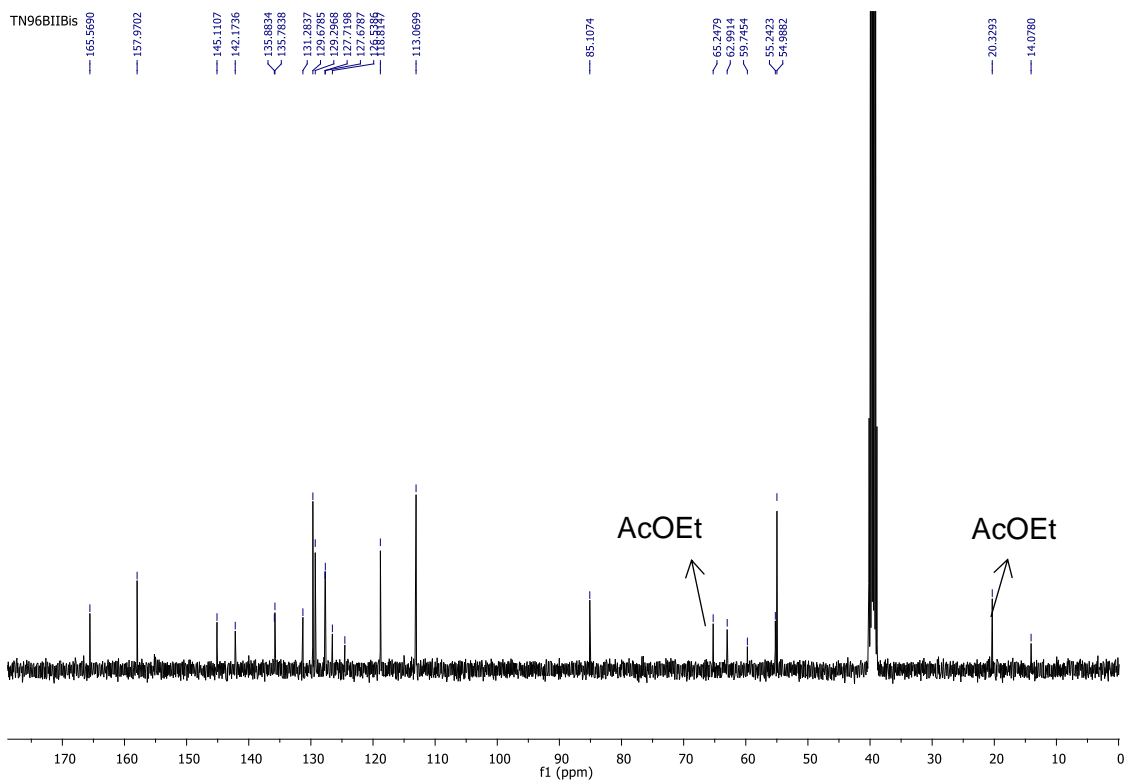
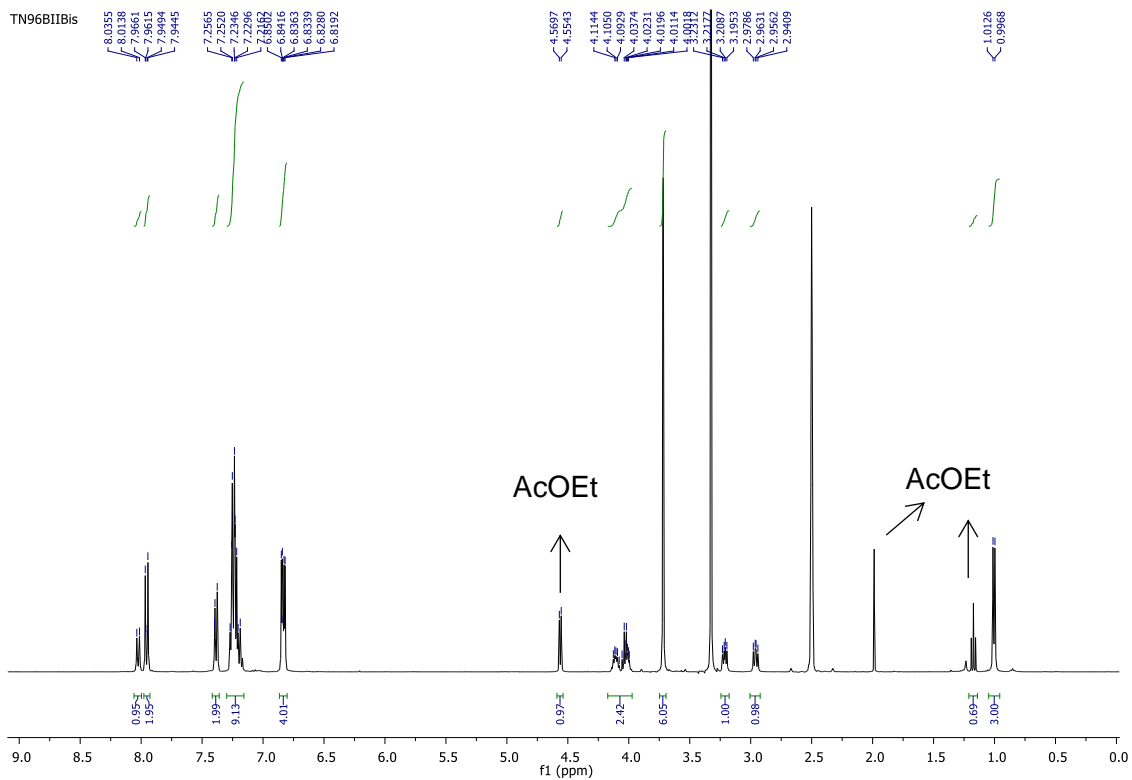
4-Azidobenzoic acid (447 mg, 2.74 mmol) was solved in dry DMF (6.6 mL) under argon atmosphere; then HOBt (339 mg, 2.51 mmol) and DCC (518 mg, 2.51 mmol) were added. After 5 minutes stirring at room temperature *L*-Threoninol (240 mg, 2.28 mmol) was added. The reaction was stirring overnight. The white solid was filtered off and solvent was removed under reduced pressure. The product was purified by column chromatography (gradient elution DCM: MeOH 50:1 to 20:1) to give **II-5** as a yellow solid, 430 mg, 75%. ^1H NMR ([D₆]dimethyl sulfoxide): δ = 7.92 (d, J = 6.7 Hz, 2 H), 7.74 (br d, J = 8.4 Hz, 2 H), 7.19 (d, J = 7.3 Hz, 2H), 4.59 (m, 2H), 3.89 (m, 2H), 3.58 (m, 1H), 3.47 (m, 1H), 1.05 (d, J = 6.3 Hz, 3 H); ^{13}C NMR ([D₆]dimethyl sulfoxide): δ = 165.6, 142.1, 131.4, 129.3, 118.8, 64.9, 60.4, 56.7, 20.2 ppm. MS m/z : calculated. for C₁₁H₁₄N₄O₃ [M+H]⁺ 250.2 found FAB 251.0.

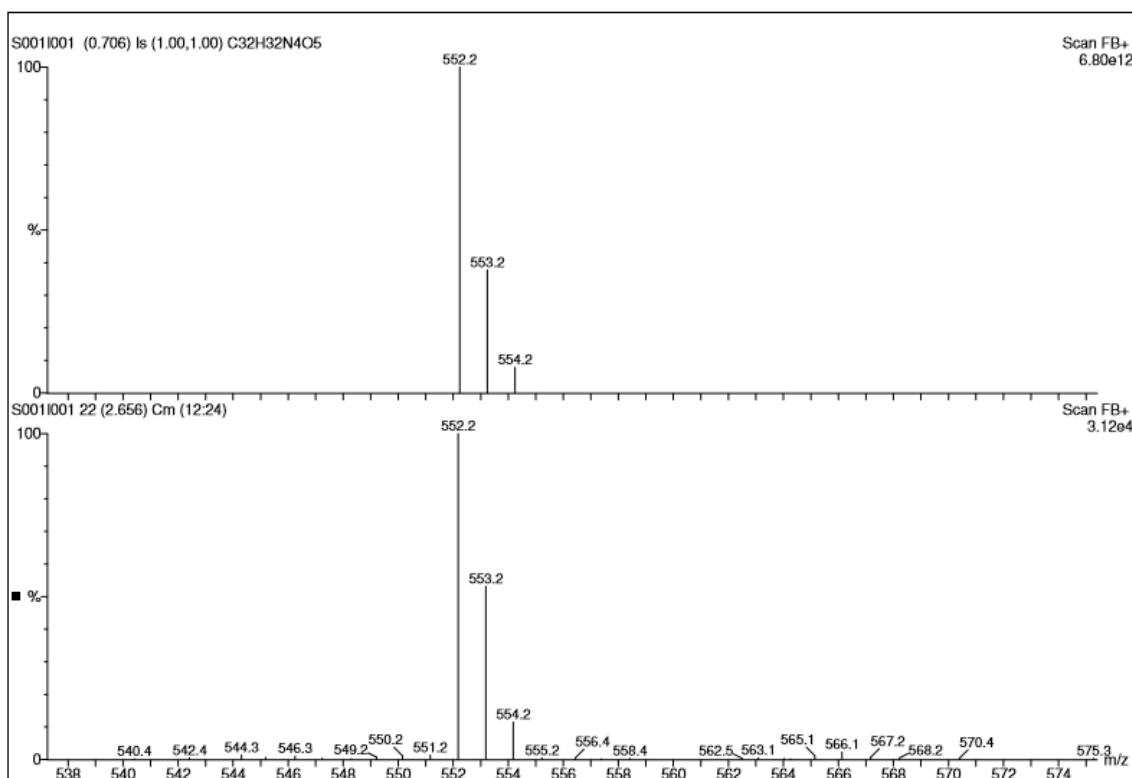




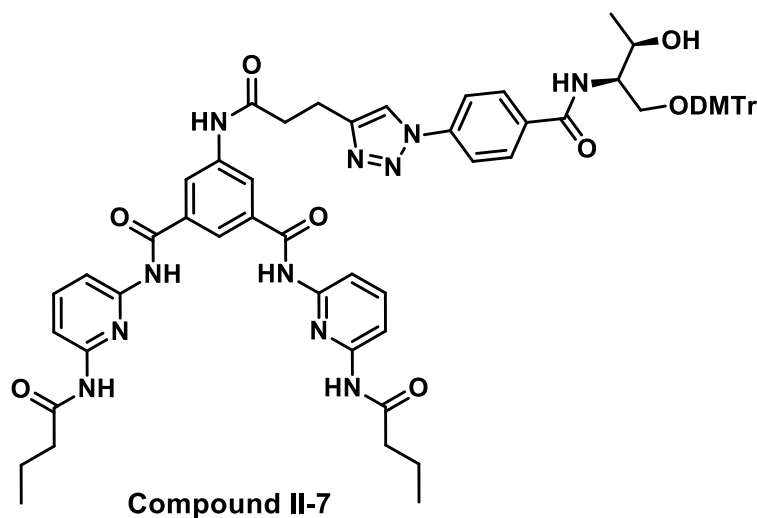
4-azido-*N*-((2*R*,3*R*)-1-(bis(4-methoxyphenyl)(phenyl)methoxy)-3-hydroxybutan-2-yl)benzamide**Compound II-6**

Compound **II-5** (192 mg, 0.77 mmol) was solved in Pyridine (3.8mL) under argon atmosphere. Afterwards DIPEA (149 mg, 1.16 mmol), DMAP (150 mg, 1.16 mmol) and 4,4'-Dimethoxytrityl chloride (313 mg, 0.92 mmol) were added at 0°C. The reaction was stirred overnight. Pyridine was removed under reduced pressure and the desired product was purified by flash column chromatography using neutralized SiO₂ (neutralized with trimethylamine), using gradient elution Hexane: AcOEt 2 : 1 to 1:1 to give **II-6** as a colorless solid, 350 mg, 82%. ¹H NMR ([D₆]dimethyl sulfoxide): δ = 8.02 (d, *J* = 8.7 Hz, 2 H), 7.96 (d, *J* = 8.6 Hz, 2 H), 7.38 (br d, *J* = 8.8 Hz, 2 H), 7.23 (m, 8H), 6.83 (dd, *J* = 8.9, 3.4 Hz, 2 H), 4.55 (d, *J* = 6.2 Hz, 1H), 4.10 (m, 2H), 4.01 (m, 2H), 3.72 (s, 6H), 3.21 (dd, *J* = 9, 5.4 Hz, 1H), 2.96 (dd, *J* = 9, 6.2 Hz, 1H), 1.00 (d, *J* = 6.3 Hz, 3 H); ¹³C NMR ([D₆]dimethyl sulfoxide): δ = 165.6, 158.0 (2C), 145.1, 142.2, 135.9 (2C), 135.7 (2C), 131.3 (2C), 129.7 (2C), 129.3 (2C), 127.7 (2C), 127.7 (2C), 126.5, 124.5, 118.8 (2C), 113.07 (2C), 85.1, 65.2, 63.0, 55.2, 55.0 (2C), 20.3 ppm. MS *m/z*: calculated. for C₃₂H₃₂N₄O₅ [M]⁺ 552.2 found FAB 552.2.



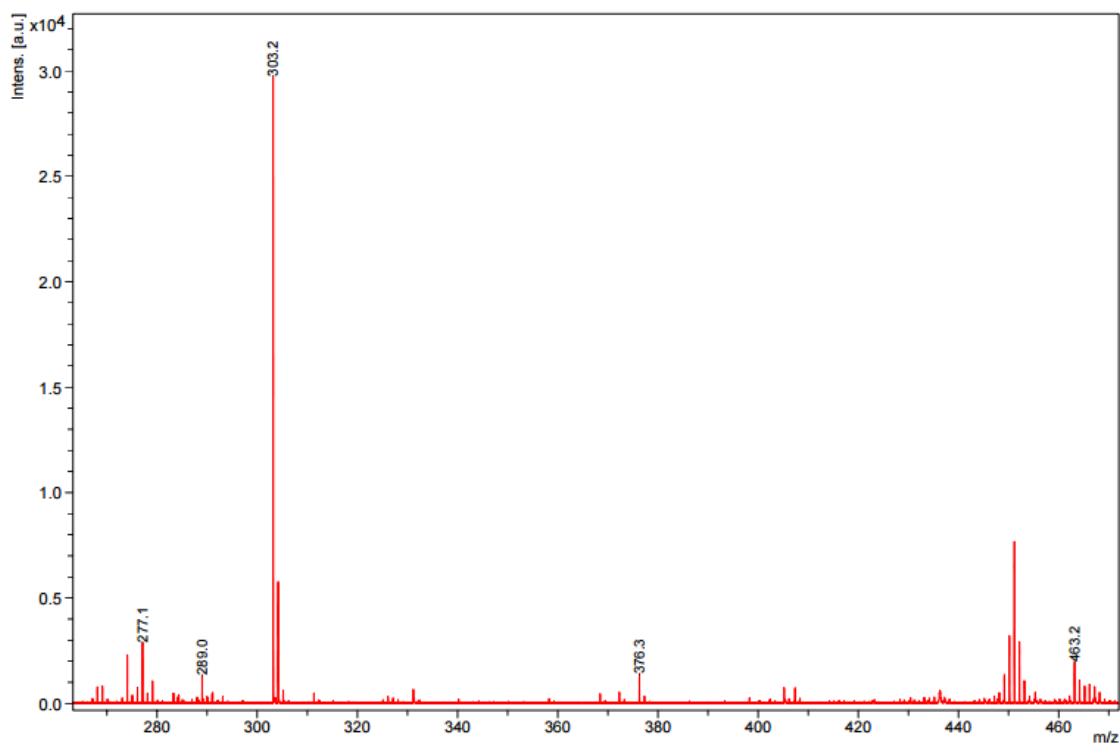
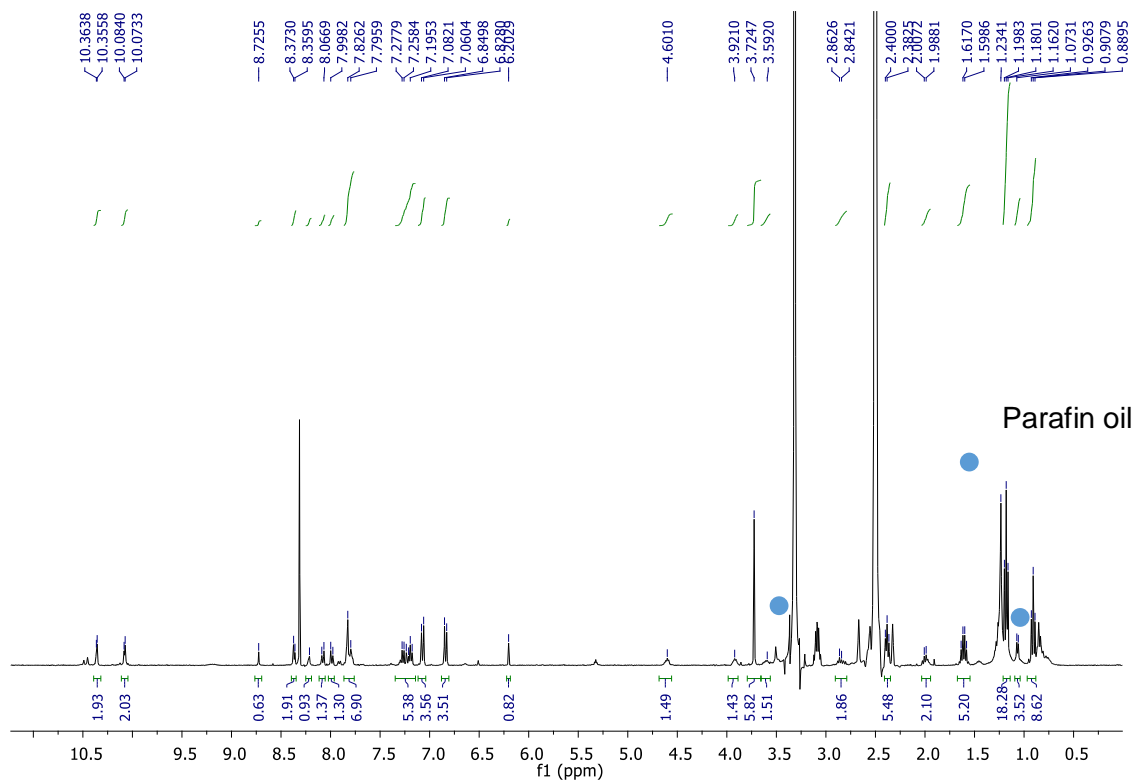


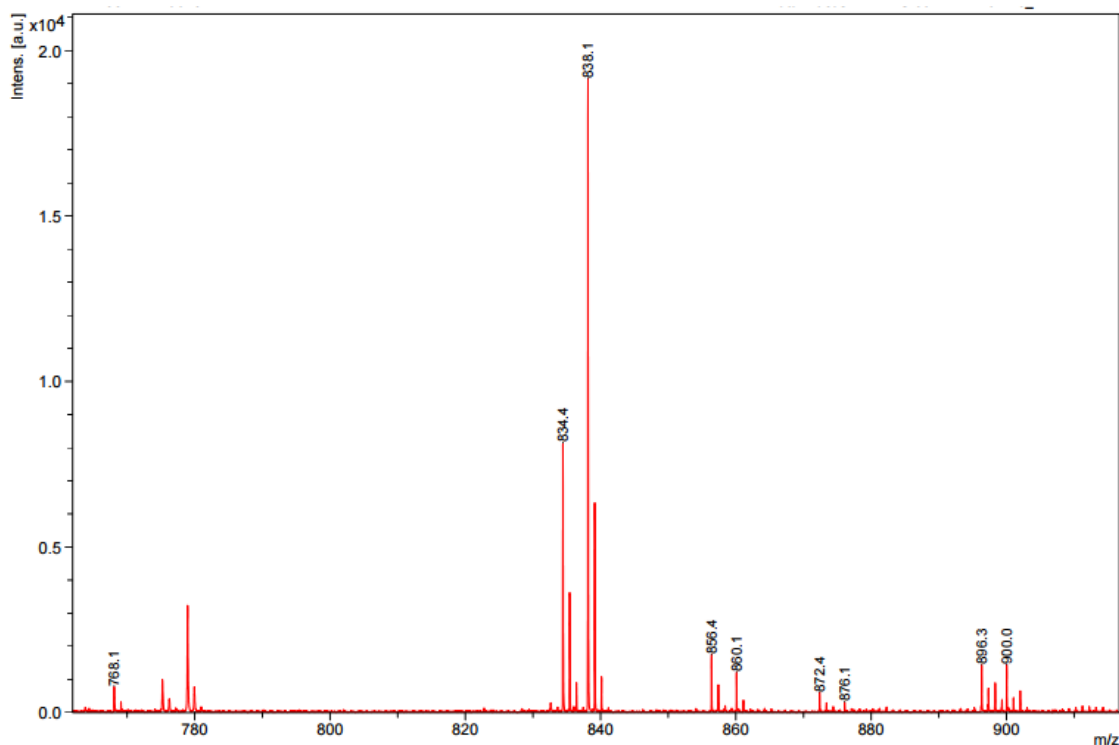
5-(3-(1-(4-(((2R,3R)-1-(bis(4-methoxyphenyl)(phenyl)methoxy)-3-hydroxybutan-2-yl)carbamoyl)phenyl)-1*H*-1,2,3-triazol-4-yl)propanamido)-*N*¹,*N*²-bis(6-butynamidopyridin-2-yl)isophthalamide



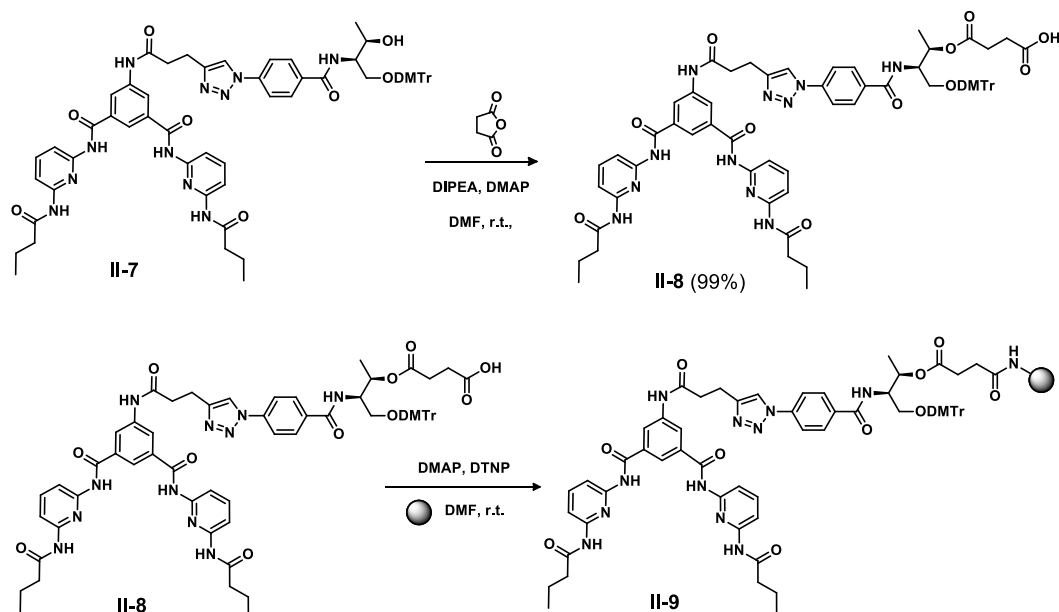
Compound **II-4** (20 mg, 0.034 mmol) and **II-6** (19 mg, 0.034 mmol) were dissolved in anhydrous DMF (1 mL); then DIPEA was added (4.4 mg, 0.034 mmol), followed by the addition of catalytic amount of CuI. The reaction was stirred for 3h. Once it was completed (TLC), the solvent was removed under reduced pressure and the product was purified by flash column chromatography using neutralized SiO₂ (neutralized with trimethylamine), using gradient elution DCM/MeOH 25/1 to 15/1 to give **II-7** as a colorless oil, quantitative yield. ¹H NMR ([D₆]dimethyl sulfoxide): 10.35 (br d, *J* = 3.2 Hz, 2 H), 10.07 (br d, *J* = 4.3 Hz, 2 H), 8.36 (m, 2H), 8.21 (s, 1H), 8.07 (d, *J* = 8.6 Hz, 2 H), 7.80 (m, 7H), 7.23 (m, 4H), 7.07 (d, *J* = 8.7 Hz, 2

H), 6.83 (br d, $J = 8.7$ Hz, 2 H), 6.20 (s, 1H), 4.60 (m, 2H), 3.92 (m, 2H), 3.72 (S, 6H), 3.59 (m, 2H), 2.85 (m, 2H), 2.38 (t, $J = 7.3$ Hz, 1H), 1.60 (sx, $J = 7.3$ Hz, 1H), 1.06 (d, $J = 6.3$ Hz, 3 H), 0.91 (t, $J = 7.3$ Hz, 3 H). MS m/z : calculated for $C_{63}H_{65}N_{11}O_{10}$ [M-DMTr+H] $^+$ 833.9 found MALDI-TOF 834.4.





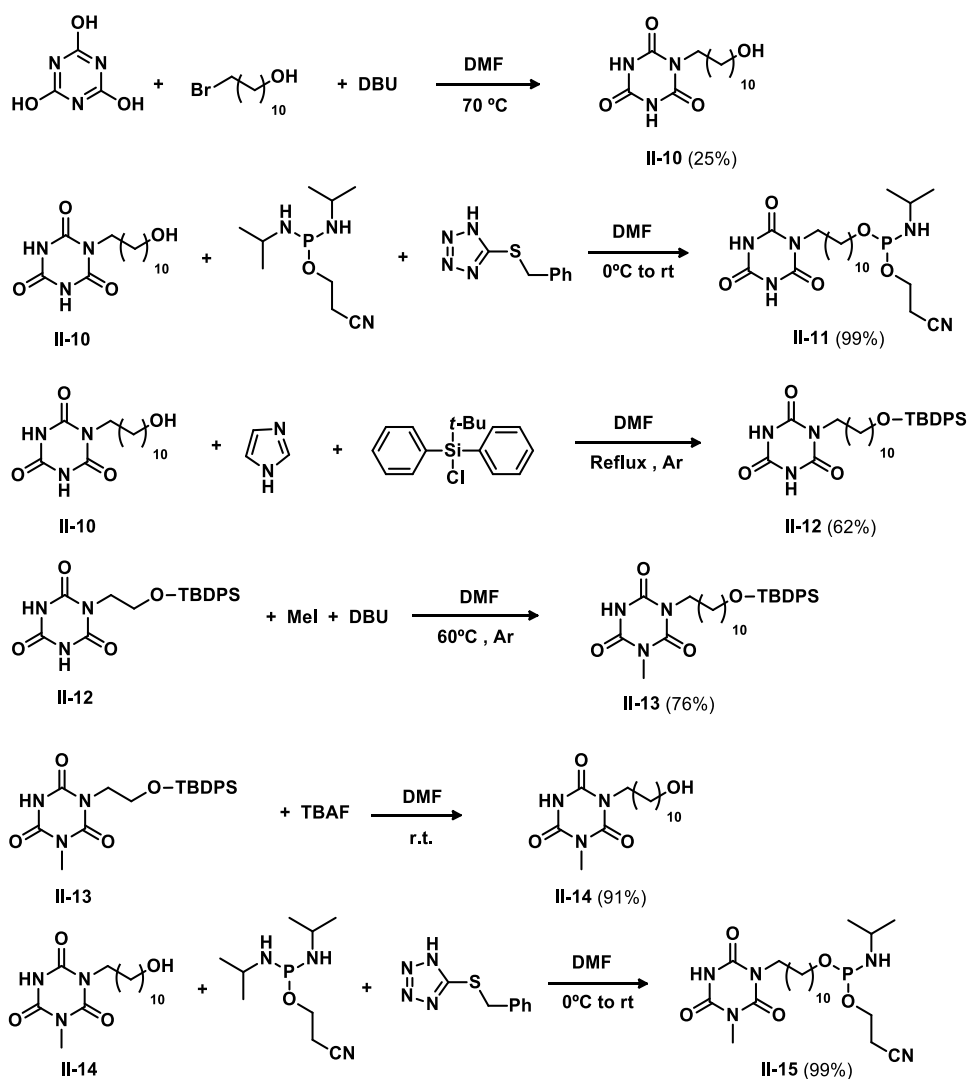
2.3.2. Preparation of modified solid supports



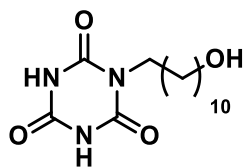
Compound II-8. To a solution of **II-7** (20 mg, 002 mmol) in DMF (0.5 mL), succinic anhydride (3 mg, 0.03 mmol) was then added, followed by the addition of catalytic amount of DMAP and DIPEA (4 mg, 0.03 mmol). The reaction mixture was stirred overnight. The solvent was removed under reduced pressure. The crude material was dissolved in EtOAc and the organic layer was washed with brine (sat. aq.). The product **II-8** was used directly in the next reaction step without further purification.

Compound II-9. 250 mg of commercial solid support (LCAA-CPG-500 Å) were introduced in a specific column. On a round bottom flask, **II-8** (20 mg, 0.016 mmol) was dissolved in dry DMF (0.8 mL), then DCC (5 mg, 0.024 mmol) was added, followed by the addition of HOBT (3 mg, 0.022 mmol); the reaction mixture was introduced quickly in the column with the solid support (ensuring that the column was closed). The column was covered and it was swirling with a vortex every 30min, repeating it for 5h. Then, the excess of liquid was filtered off and the column was washed several times with MeOH and acetonitrile. The modify solid support was treated with 1mL of CAP A (600 μ L of Py, 500 μ L THF, 400 μ L Ac₂O) and 1mL of CAP B (1 mL THF, 400 μ L 1-methylimidazol), reacted for 30 min, and filtered again and washed successively with 10 mL portions of MeOH and MeCN and dried in vacuo. Loading was determined by treating a portion (10 mg) of **II-9** with 1 mL of 18% v/v HClO₄ in EtOH and measuring the absorbance of DMTr cation at 504 nm (η = 75 mL cm⁻¹ μ mol⁻¹). This was found to be 6.7 μ mol/g.

2.3.3. Cyanuric acid derivate synthesis

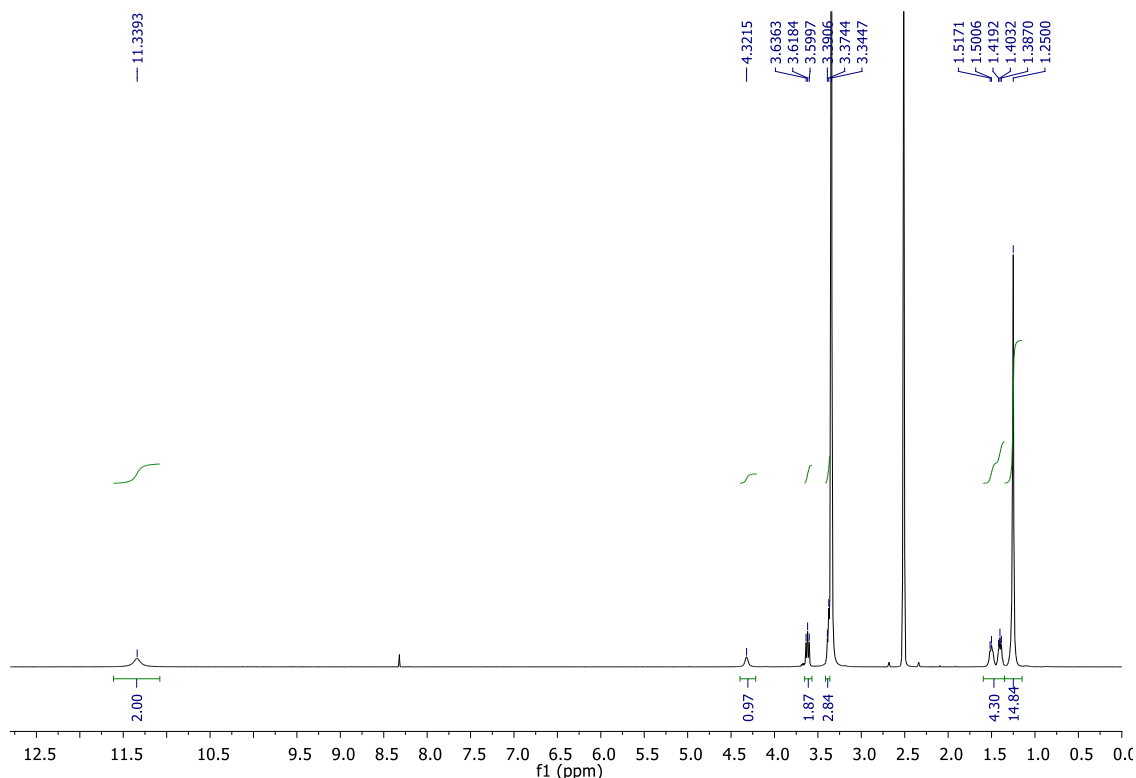


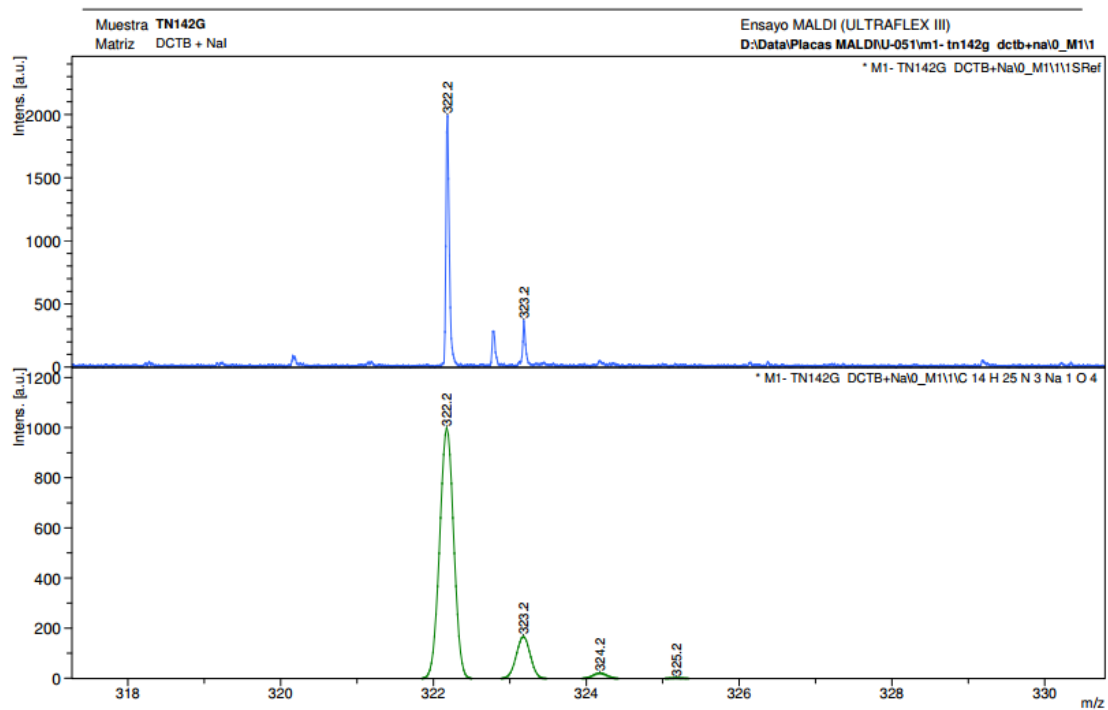
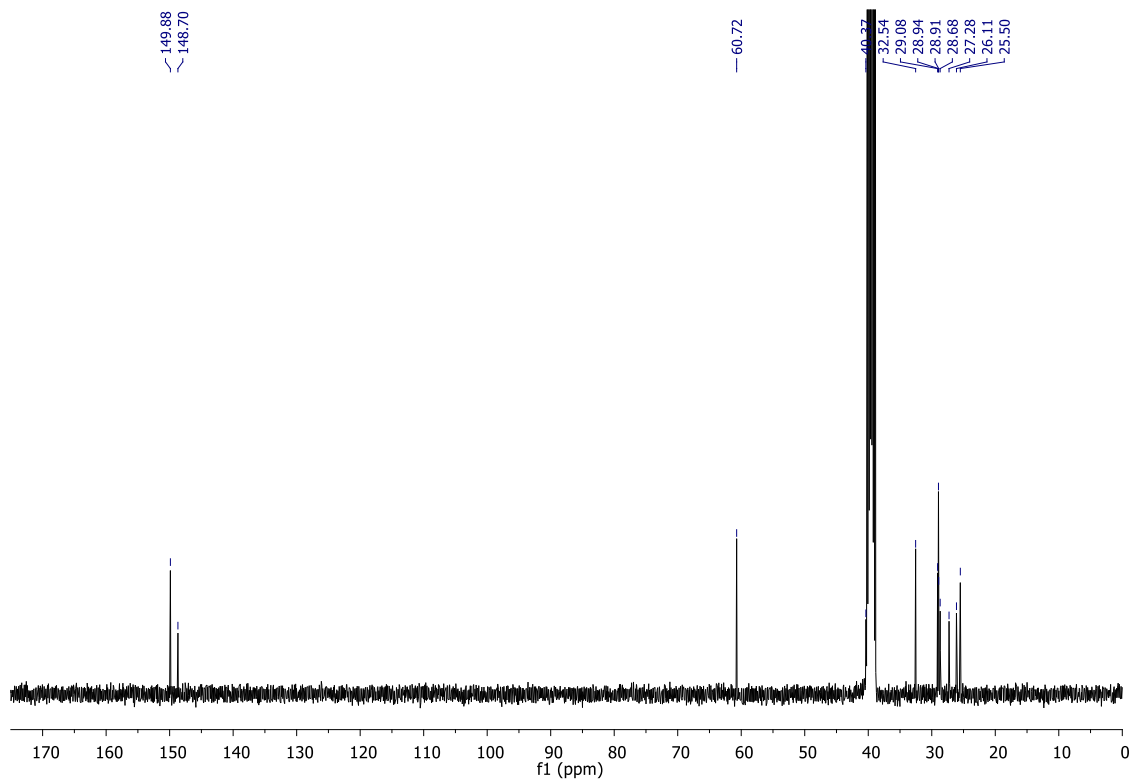
1-(11-hydroxyundecyl)-1,3,5-triazinane-2,4,6-trione

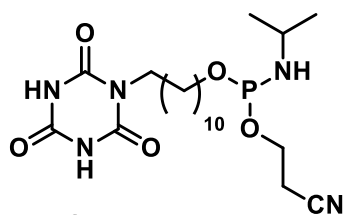


Compound II-10

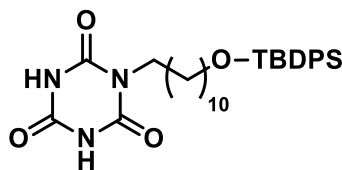
To a solution of cyanuric acid (1.03 g, 7.96 mmol) in DMF (16mL) was added 11-Bromo-1-undecanol (0.5 g, 2 mmol) and 1,8-diazabicycloundec-7-ene (0.32 g, 2 mmol). The reaction mixture was heated under 70°C overnight, poured into the water, and extracted with ethyl acetate. The organic layer was washed with water to eliminate the excess of cyanuric acid, dried with MgSO₄ and filtered. The solvent was removed under reduced pressure and the crude material was purified by column chromatography using DCM : MeOH 15:1 as a eluent to give **II-10** as a white solid, 596 mg, 25%. ¹H NMR ([D₆]dimethyl sulfoxide): δ = 11.34 (br s, 2H), 4.32 (br s, 1H), 3.62 (t, *J* = 7.2 Hz, 2 H), 3.37 (m, 2H), 1.51 (m, 2H), 1.40 (m, 2H), 1.25 (s, 14); ¹³C NMR ([D₆]dimethyl sulfoxide): δ = 149.9 (2C), 148.7, 60.7, 40.4, 32.5, 29.1, 28.9 (2C), 28.9, 28.7, 27.3, 26.1, 25.5.ppm. MS *m/z*: calculated. for C₁₄H₂₅N₃O₄ [M+Na]⁺ 322.4 found MALDI-TOF 322.2.



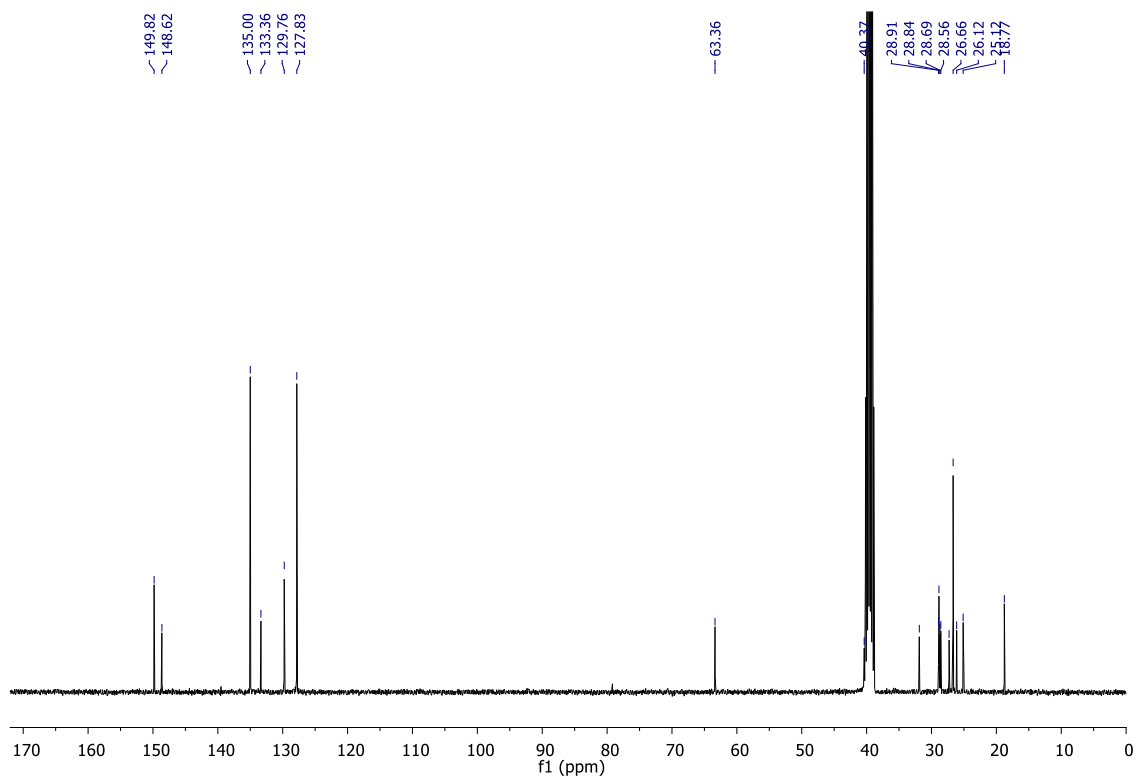
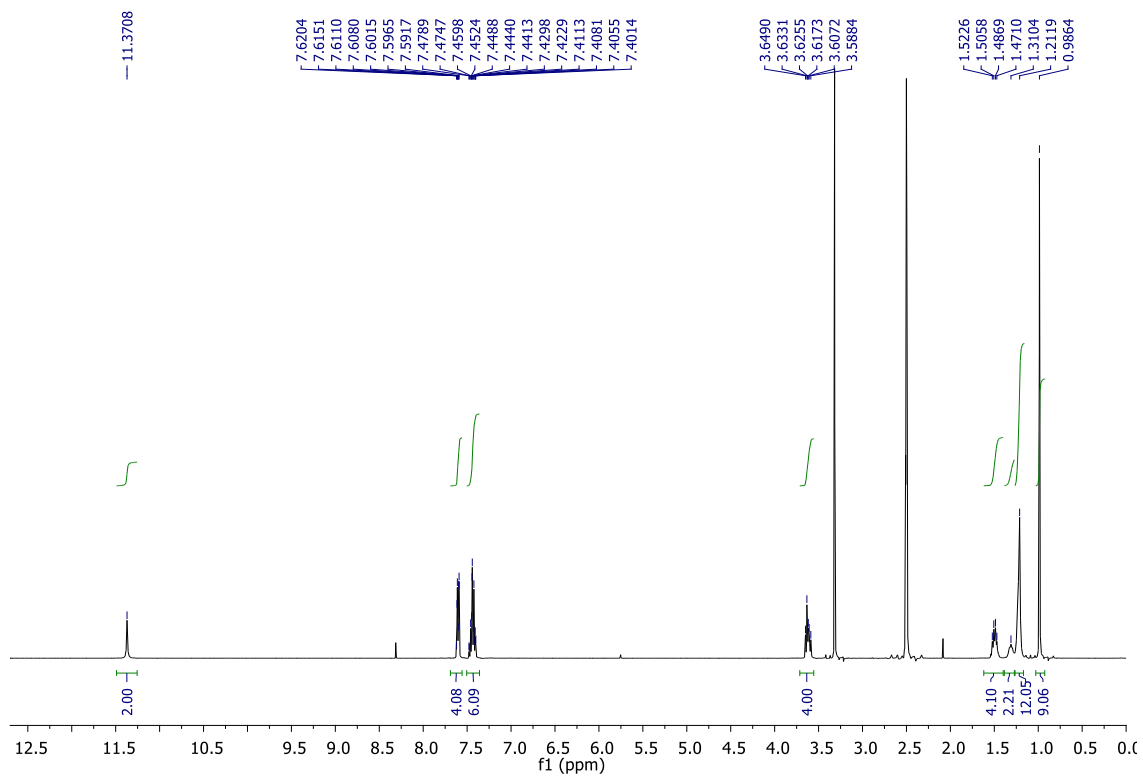


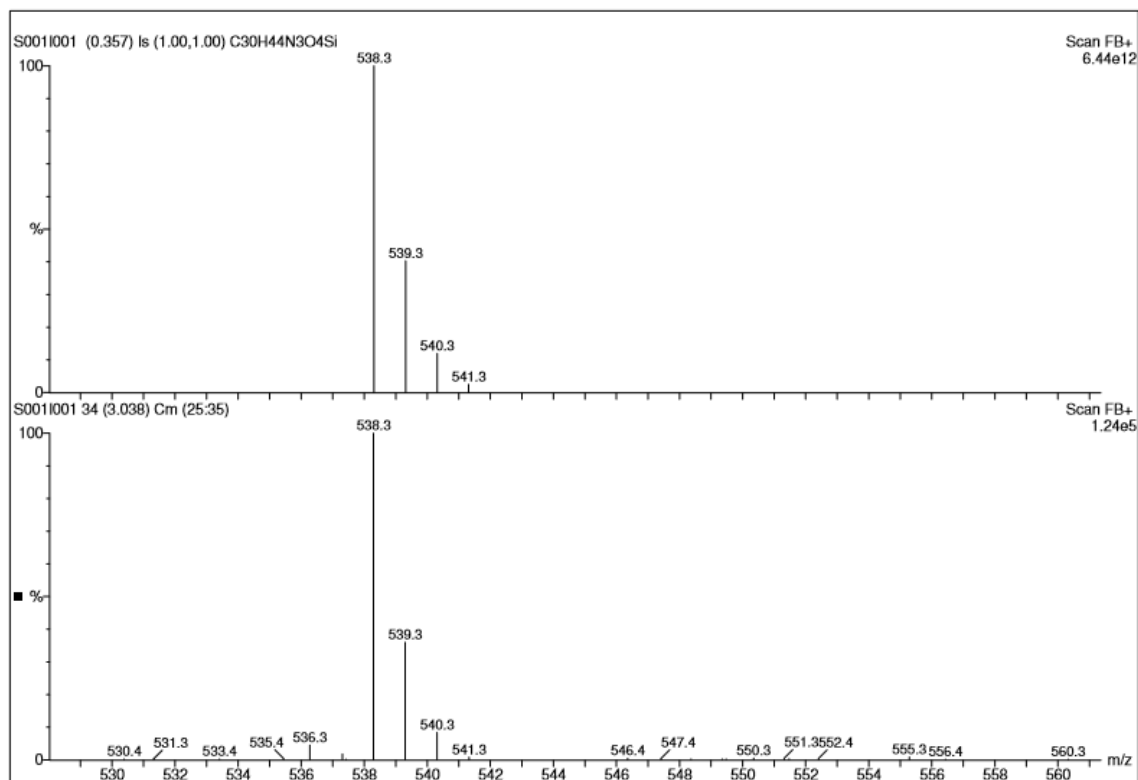
2-cyanoethyl (11-(2,4,6-trioxo-1,3,5-triazinan-1-yl)undecyl) isopropylphosphoramidite**Compound II-11**

Compound **II-10** (100 mg, 0.33 mmol) was solved in dry DMF (1 mL) and the solution was cooled to 0°C. Then, 5-Benzylthio-1-H-tetrazole (76 mg, 0.4 mmol) and the phosphorylating reagent, 2-Cyanoethoxy-bis(N,N-diisopropylamino) phosphine (100 mg, 0.33 mmol), were added. The reaction mixture was allowed to stir at room temperature for 3h under argon atmosphere. When the reaction was completed (followed by TLC), the crude material was using directly, without further purification, in the last step of the automated solid phase synthesis of the corresponding oligonucleotide (oligonucleotide **4** and oligonucleotide **7**), due to **II-11** is a very unstable compound we were not able to isolate it.

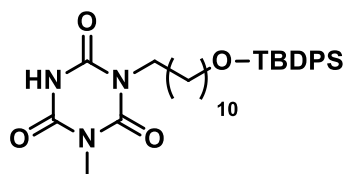
1-(11-((tert-butyldiphenylsilyl)oxy)undecyl)-1,3,5-triazinane-2,4,6-trione**Compound II-12**

Compound **II-10** (310 mg, 1.11 mmol) was solved in dry DMF (6 mL). Imidazole (300 mg, 4.46 mmol) and *tert*-Butyl(chloro)diphenylsilane (337 mg, 1.23 mmol) were added. The reaction mixture was refluxed under argon atmosphere for 3h. The solvent was removed under reduced pressure and the crude material was purified by column chromatography using a gradient elution DCM : MeOH 100 : 1 to 50 : 1 to **II-12** as a white solid, 380mg, 62%. ¹H NMR ([D₆]dimethyl sulfoxide): δ = 11.37 (br s, 2H), 7.61 (m, 4H), 7.44 (m, 6H), 4.32 (br s, 1H), 3.62 (m, 4H), 1.51 (m, 4H), 1.31 (m, 2H), 1.21 (br s, 12), 0.99 (s, 9H); ¹³C NMR ([D₆]dimethyl sulfoxide): δ= 149.8 (2C), 148.6, 135.0 (4C), 133.4 (2C), 129.8 (2C), 127.8 (4C), 63.4, 40.4, 31.9, 28.9, 28.8 (2C), 28.7, 28.6, 27.3, 26.7, 26.1, 25.1, 18.8 (3C) ppm. MS m/z: calculated. for C₃₀H₄₃N₃O₄Si [M+H]⁺ 538.3 found FAB 538.3.



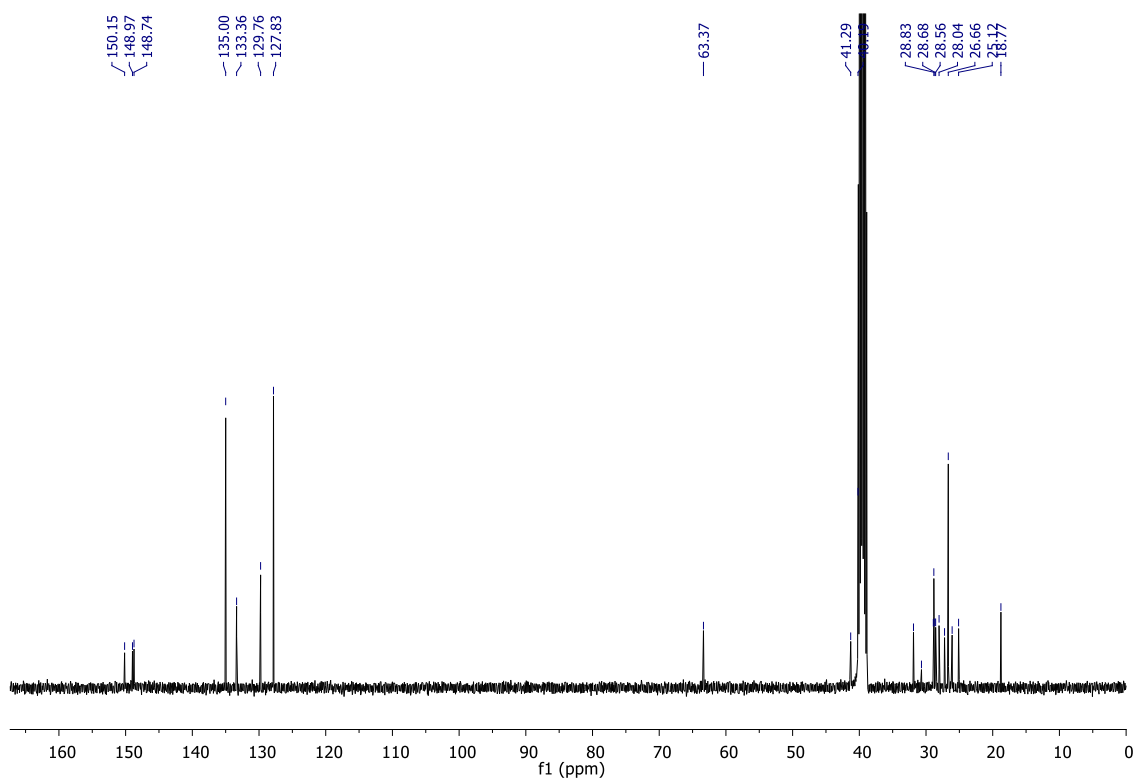
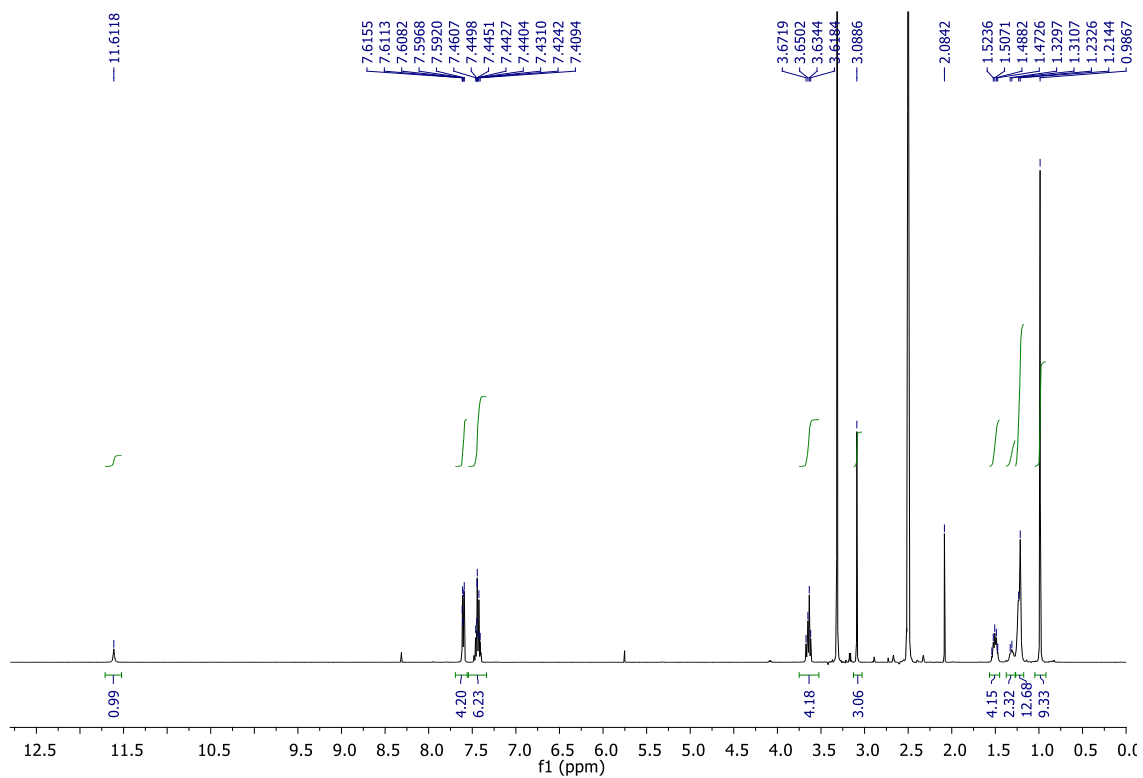


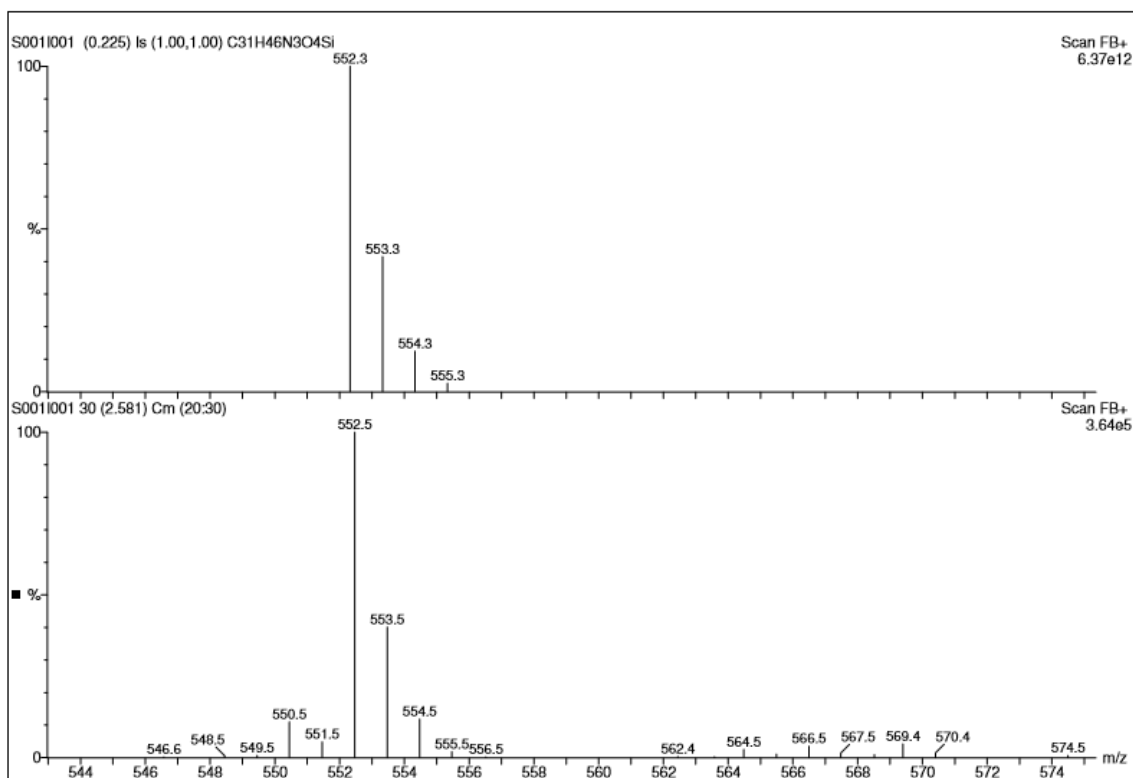
1-(11-((tert-butyldiphenylsilyloxy)undecyl)-3-methyl-1,3,5-triazinane-2,4,6-trione



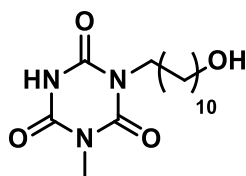
Compound II-13

To a solution of **II-12** (270 mg, 0.5 mmol) in dry DMF (3 mL) were added iodomethane (36 mg, 0.25 mmol) and 1,8-diazabicycloundec-7-ene (40 mg, 0.25 mmol). The reaction mixture was heated at 55 °C overnight. The solvent was removed under reduced pressure and the crude material was purified by column chromatography using DCM : MeOH 100 : 1 as a eluent. To give **II-13** as a colorless oil, (76%). ¹H NMR ([D₆]dimethyl sulfoxide): 11.61 (br s, 1H), 7.60 (m, 4H), 7.43 (m, 6H), 3.64 (m, 4H), 3.09 (s, 3H), 1.51 (m, 4H), 1.31 (m, 2H), 1.22 (br s, 12), 0.99 (s, 9H); ¹³C NMR ([D₆]dimethyl sulfoxide): δ= 150.2, 149.0, 148.7, 135.0 (4C), 133.4 (2C), 129.8 (2C), 127.8 (4C), 63.4, 41.3, 40.3, 31.9, 28.9, 28.8, 28.7, 28.6, 28.0, 26.7 (2C), 26.1, 25.1, 18.8 (3C) ppm. MS m/z: calculated for C₃₁H₄₅N₃O₄Si [M+H]⁺ 552.3 found FAB 552.5.



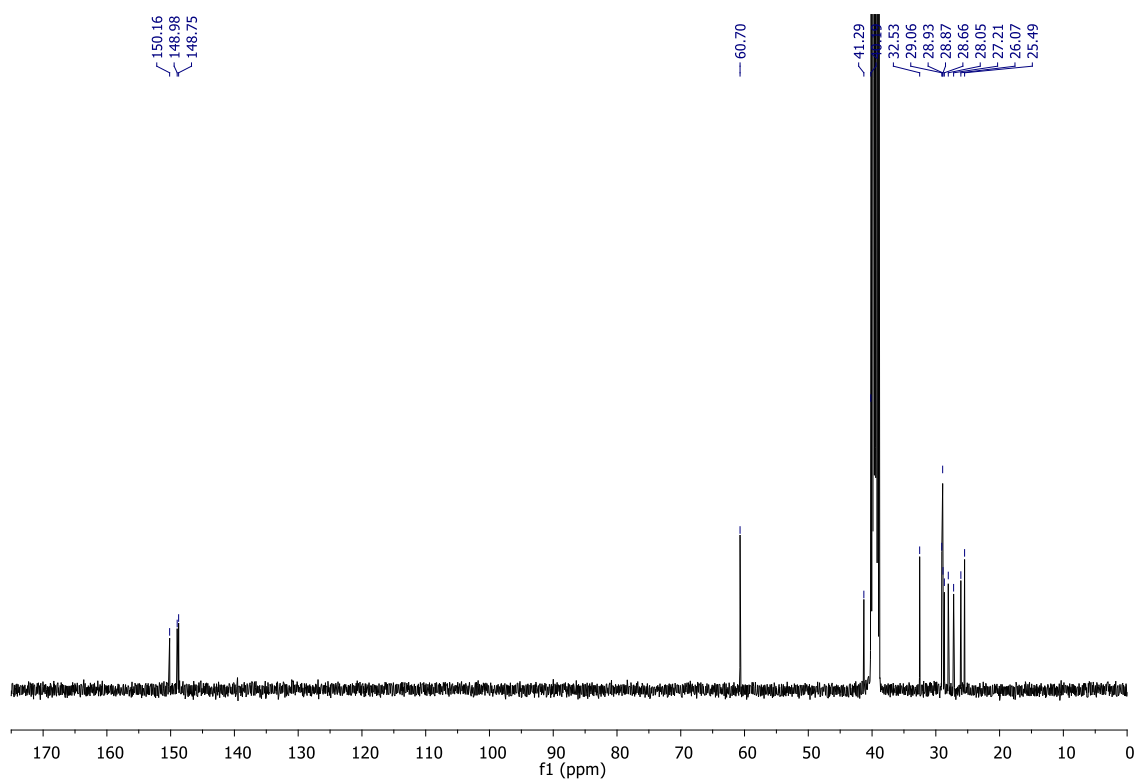
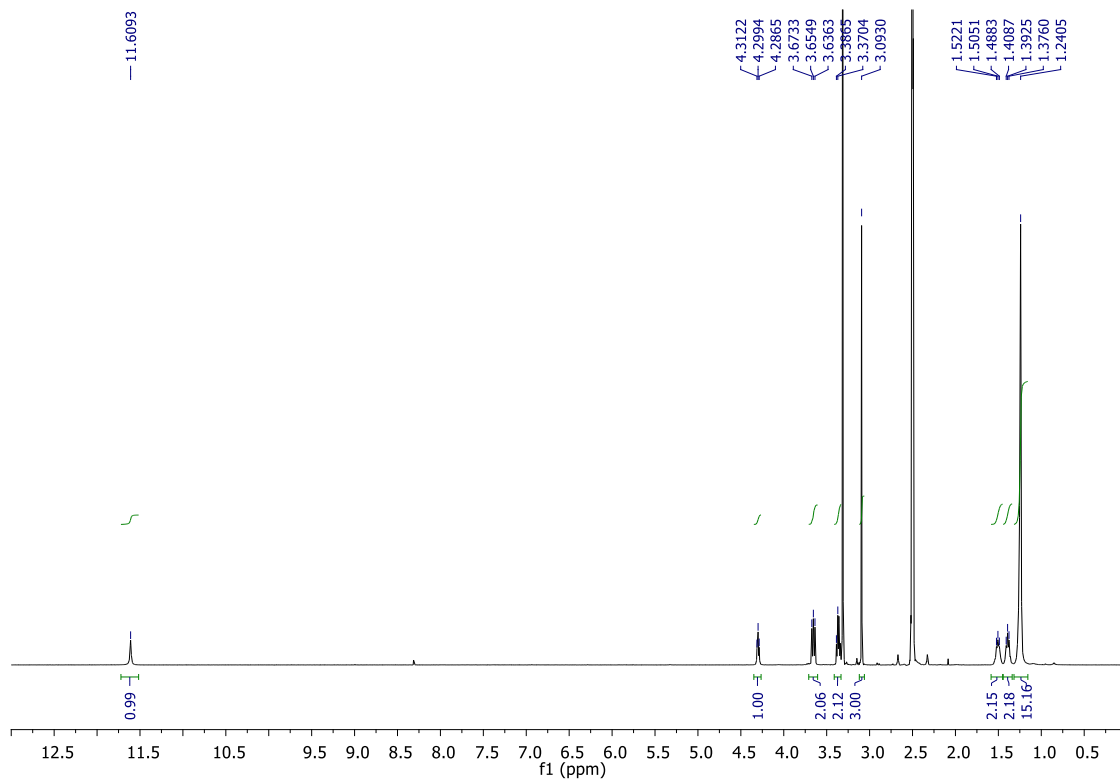


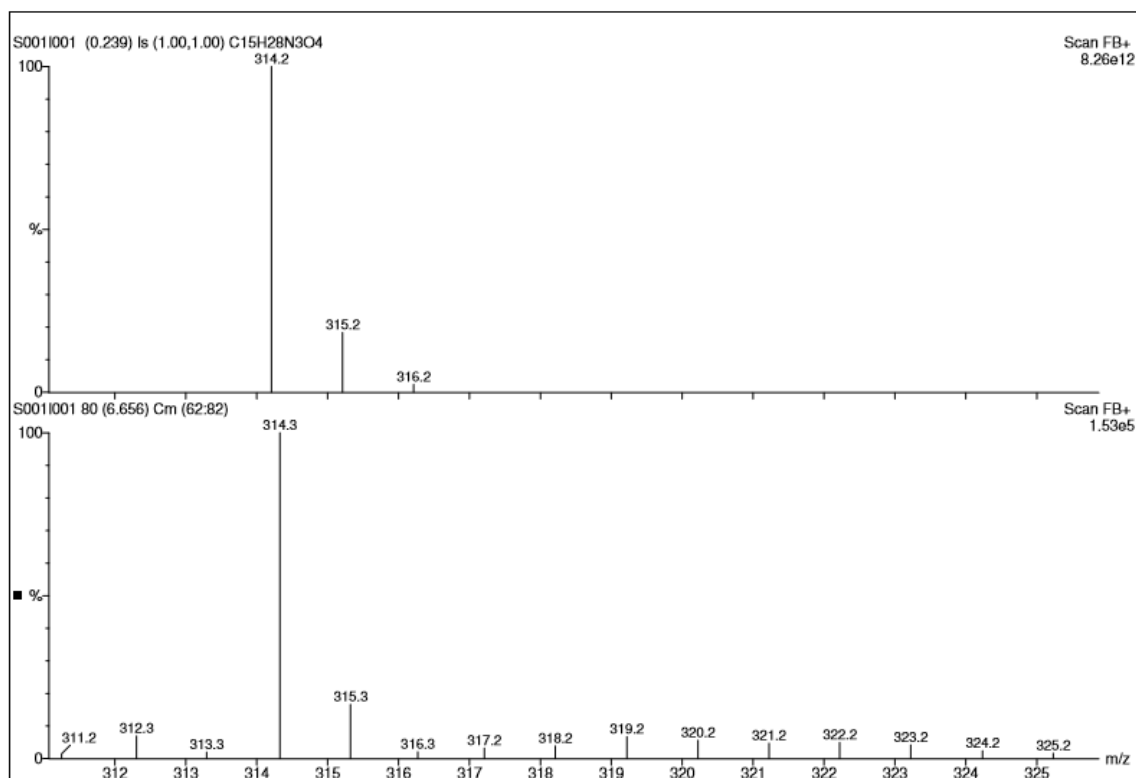
1-(11-hydroxyundecyl)-3-methyl-1,3,5-triazinane-2,4,6-trione



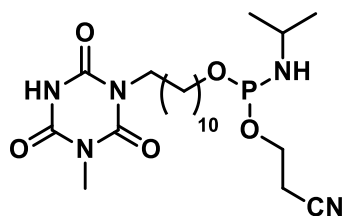
Compound II-14

To a solution of **II-13** (120 mg, 0.22 mmol) in THF was added tetrabutylammonium fluoride solution 1.0 M in THF (0.28 mL). The reaction mixture was stirred for 1h at room temperature. Then the solvent was removed under reduced pressure and the crude material was purified by column chromatography (gradient elution DCM : MeOH 150 : 1 to 50 : 1) to give **II-14** as colorless oil, 63 mg, 91%. ¹H NMR ([D₆]dimethyl sulfoxide): δ = 11.61 (br s, 2H), 4.30 (t, *J* = 5.1 Hz, 2 H), 3.37 (m, 2H), 1.51 (m, 2H), 1.40 (m, 2H), 1.24 (s, 14); ¹³C NMR ([D₆]dimethyl sulfoxide): δ = 150.2, 149.0, 148.7, 60.7, 41.3, 40.2, 32.5, 29.1, 28.9, 28.9 (2C), 28.7, 28.0, 27.2, 26.1, 25.5 ppm. MS *m/z*: calculated for C₁₅H₂₇N₄O₄ [M+H]⁺ 314.4 found FAB 314.4.





**2-cyanoethyl (11-(3-methyl-2,4,6-trioxo-1,3,5-triazinan-1-yl)undecyl)
isopropylphosphoramidite**



Compound II-15

Compound **II-14** (103 mg, 0.33 mmol) was solved in dry DMF (1 mL) and the solution was cooled to 0°C. Then 5-Benzylthio-1-*H*-tetrazole (76 mg, 0.4 mmol) and the phosphitylating reagent, 2-Cyanoethoxy-bis(*N,N*-diisopropylamino) phosphine (100 mg, 0.33 mmol), were added. The reaction mixture was allowed to stir at room temperature for 3h under argon atmosphere. When the reaction was completed (followed by TLC), the crude material was using directly, without further purification, in the last step of the automated solid phase synthesis of the corresponding oligonucleotides (oligonucleotide **5** and oligonucleotide **8**), due to compound **II-15** is a very unstable compound, we were not able to isolate it.

2.3.4. Automated Oligonucleotide synthesis and analytical data of oligonucleotides

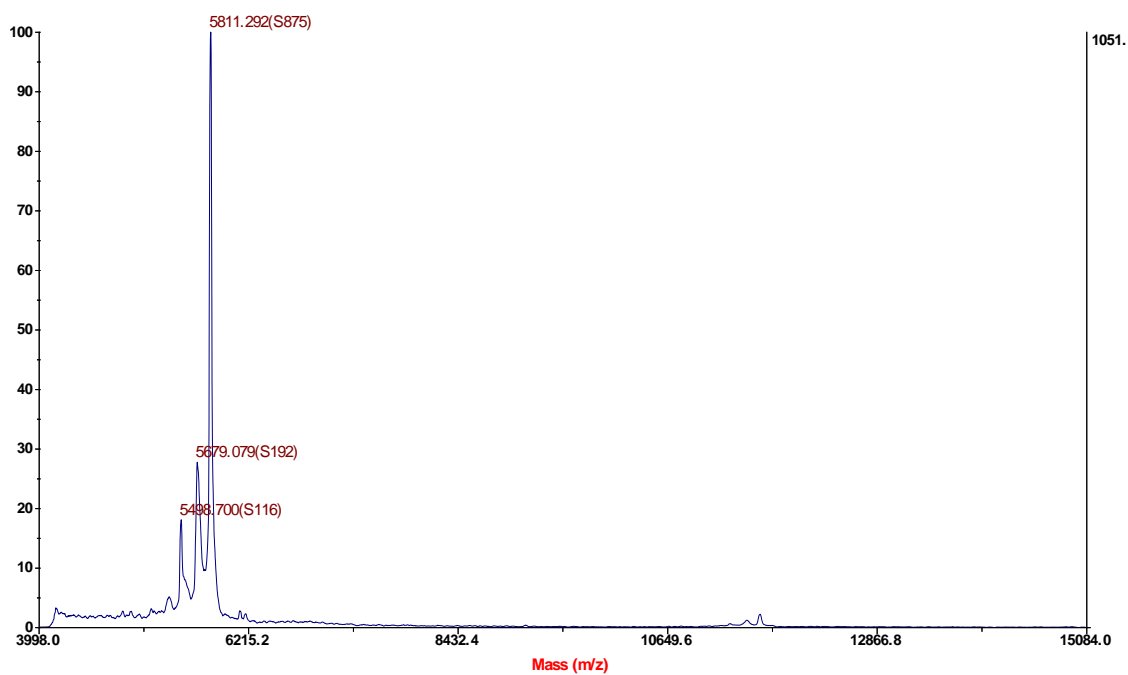
The syntheses of oligonucleotides were performed on a MerMade 4 synthesizer (BioAutomation Corporation). For each oligonucleotide synthesis, columns filled with the corresponding Controlled Pore Glass (CPG) solid support. Anhydrous MeCN was used as solvent. For the cleavage of DMTr protecting groups, the resin was purged with 3 % trichloroacetic acid in anhydrous DCM. The removal of the acid was carried out by purging with anhydrous MeCN. The activation of the phosphoramidite functionality was effected by a 0.25 M benzylthiotetrazole solution in anhydrous MeCN. The coupling time for standard phosphoramidites was 2 min and for cyanuric-acid derivatives 5 min (compound 11 and 15). Oxidation of P(III)-species was attained by alkaline iodine solution (20 mM I₂ in THF/Py/water 7/2/1). For the capping of residual 5'-OH-groups, a mixture of solution A (10% Ac₂O, 10% pyridine, 80% THF) and solution B (10% 1-methylimidazole in THF) was used. After completion of the synthesis, the oligonucleotides were cleaved from the solid support with concomitant removal of the Fmoc and β-cyanoethyl protecting groups by reacting the oligonucleotide-charged solid support with 28 % aq. NH₃ at 55 °C for 20 h. The solution was filtered and the filtrate was concentrated in vacuo. The residue was dissolved in 750 μL water. For purification of this crude oligonucleotide solution, a volume containing ~40 nmol crude oligonucleotide was applied to gel electrophoresis (1 mm, 20% polyacrylamide). The oligonucleotide-containing segments of the gel were visualized by UV-light (260 nm) and separated from the rest of the gel. Oligonucleotides were extracted from the gel using an elutrap system (3 h, 200 V). The solutions were desalted using a NAP-10 column and concentrated in an evaporating centrifuge.

2.3.5. Mass spectral data of synthesized oligonucleotides

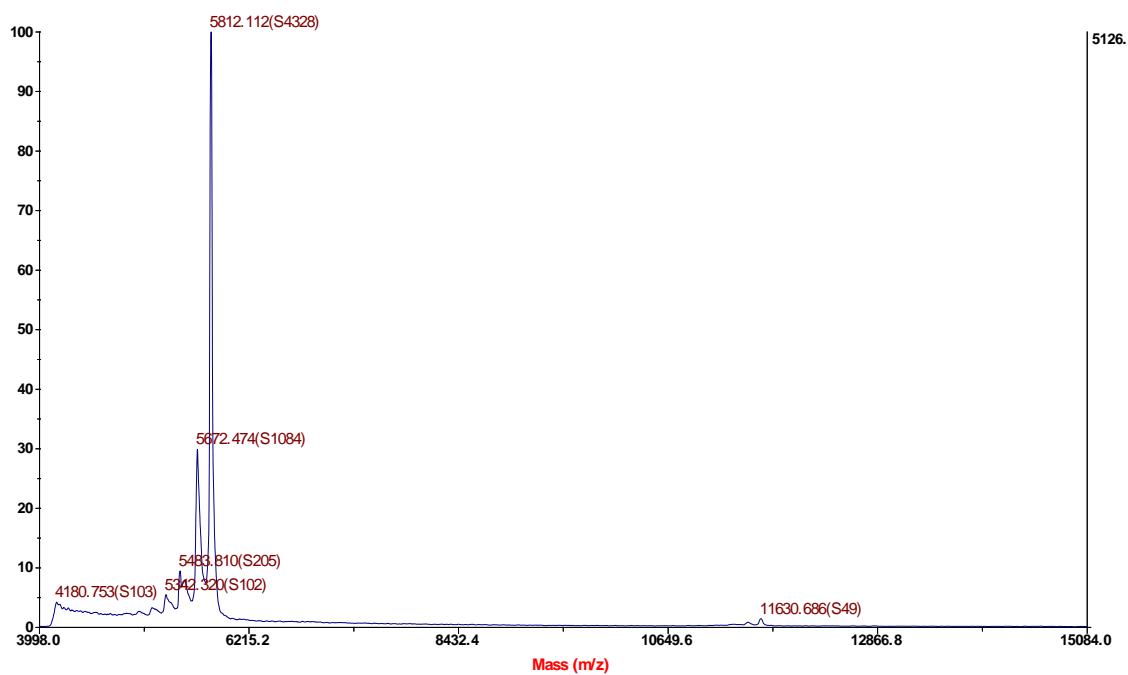
MALDI data was obtained at the Proteomic facility of the National Center for Biotechnology (CNB-CSIC).

Table II-2. MALDI data of synthesized oligonucleotides

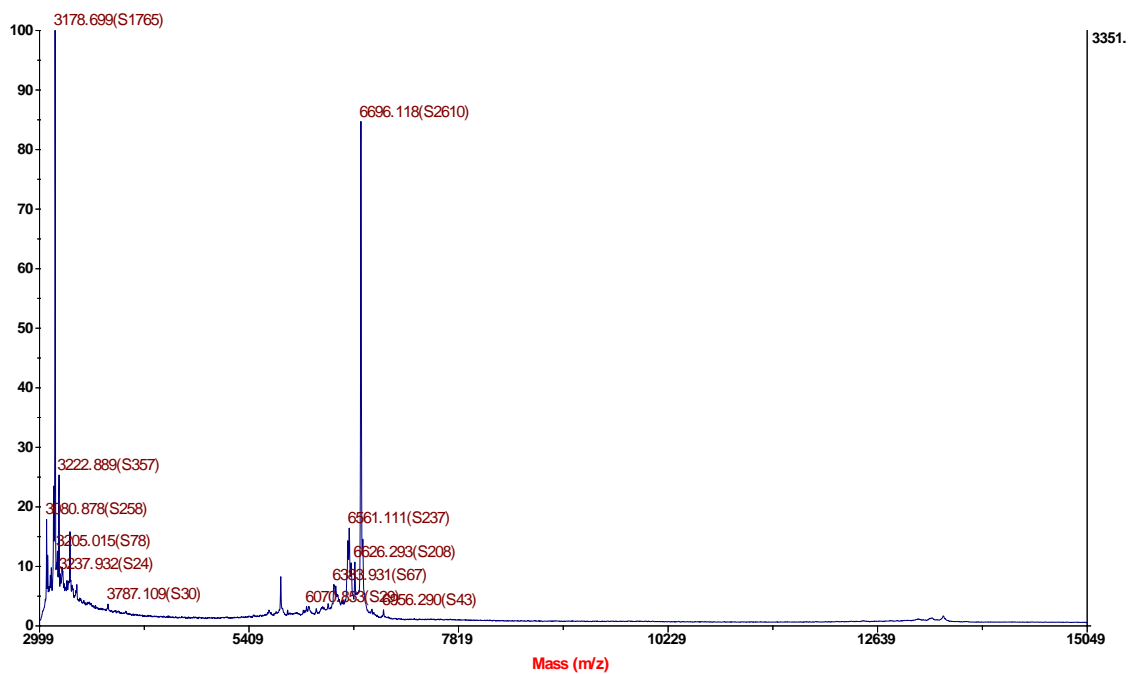
n°.	Sequence	Calculated	Found
1	5'-TCGAATC AGT TTA CAA AAA-3'	5803.9	5811.3
2	5'-TTT TTG TAAACT GAT TCGA-3'	5807.8	5812.1
3	5'-TCGAATC AGT TTA CAA AAA-HR-3'	6699.8	6696.1
4	5'-cy-TTT TTG TAAACT GAT TCGA-3'	6169.1	6165.0
5	5'-cyCH ₃ -TTT TTG TAAACT GAT TCGA-3'	6183.0	6182.0
6	5'-P-TCGAATC AGT TTA CAA AAA-HR-3'	6776.7	6777.2
7	5'-cy-TTT TTG TAAACT GAT-3'	4933.3	4935.5
8	5'-cyCH ₃ -TTT TTG TAAACT GAT-3'	4947.0	4945.6
9	5'-TTT TTG TAAACT GAT-3'	4572.0	4570.4

• Oligonucleotide 1

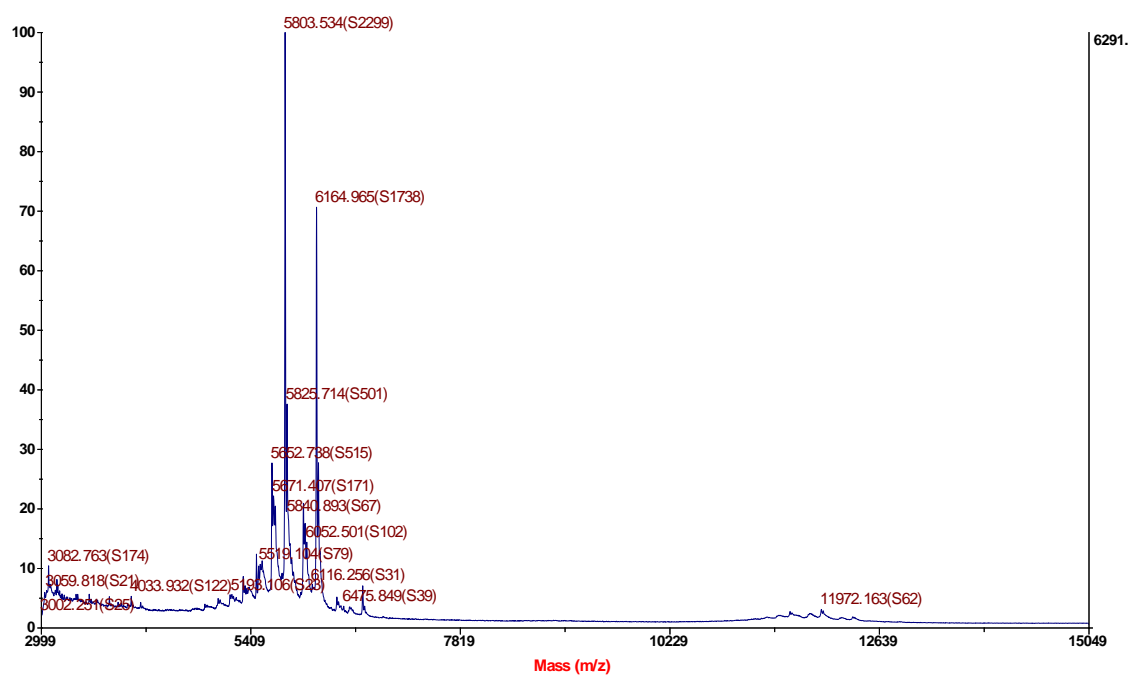
• Oligonucleotide 2



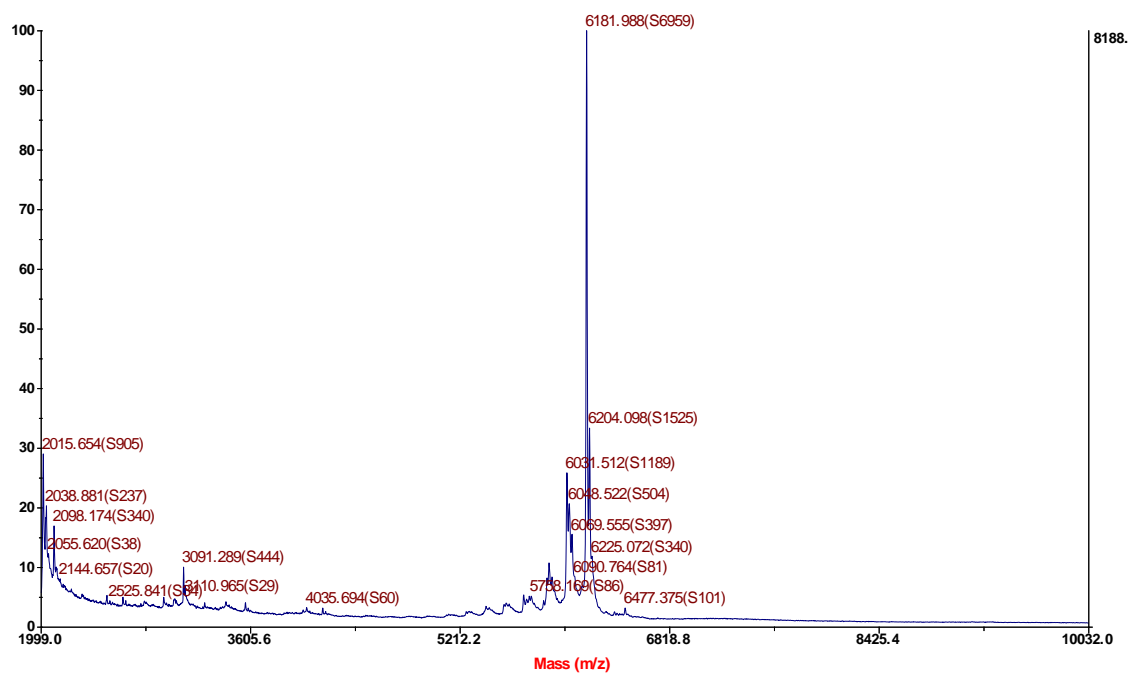
• Oligonucleotide 3



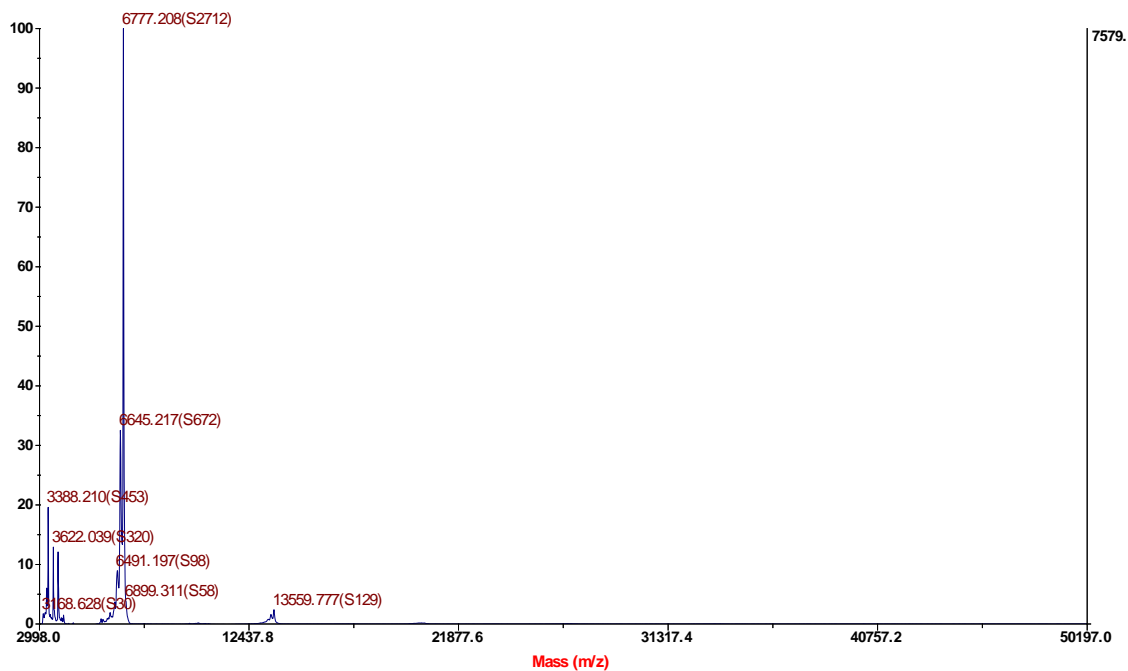
• Oligonucleotide 4



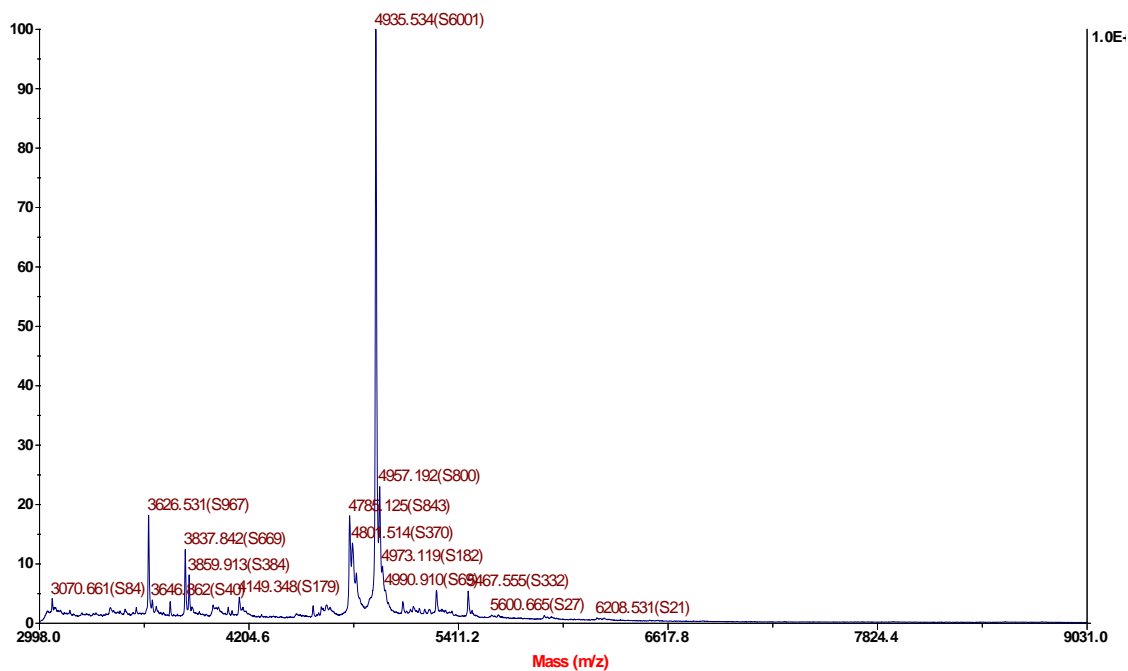
• Oligonucleotide 5



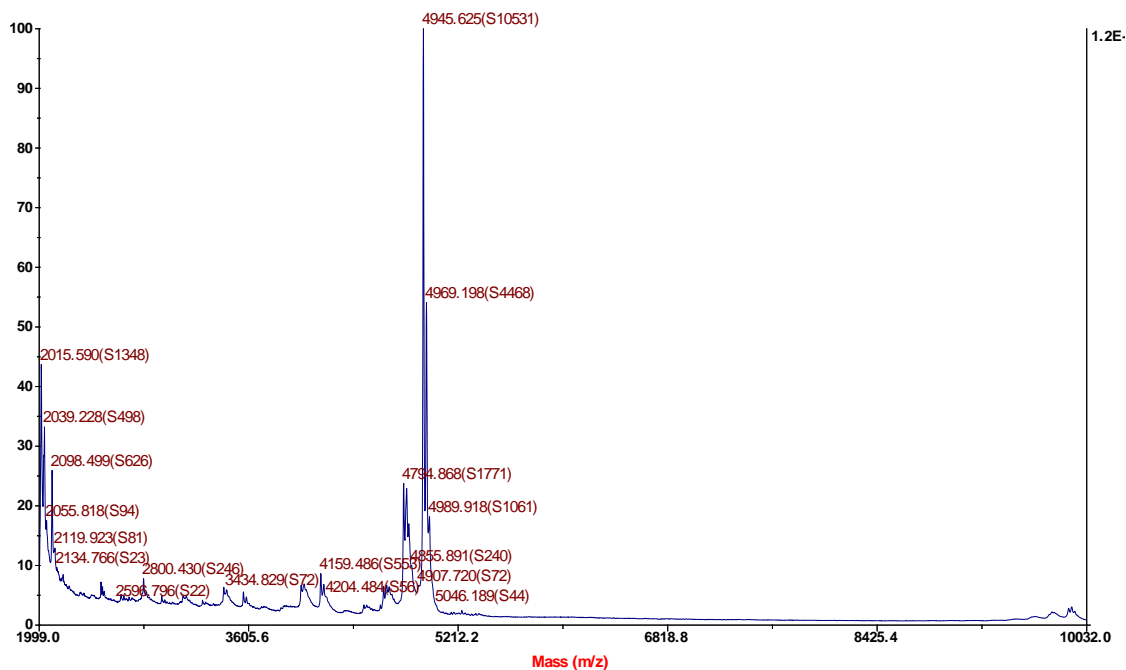
• Oligonucleotide 6



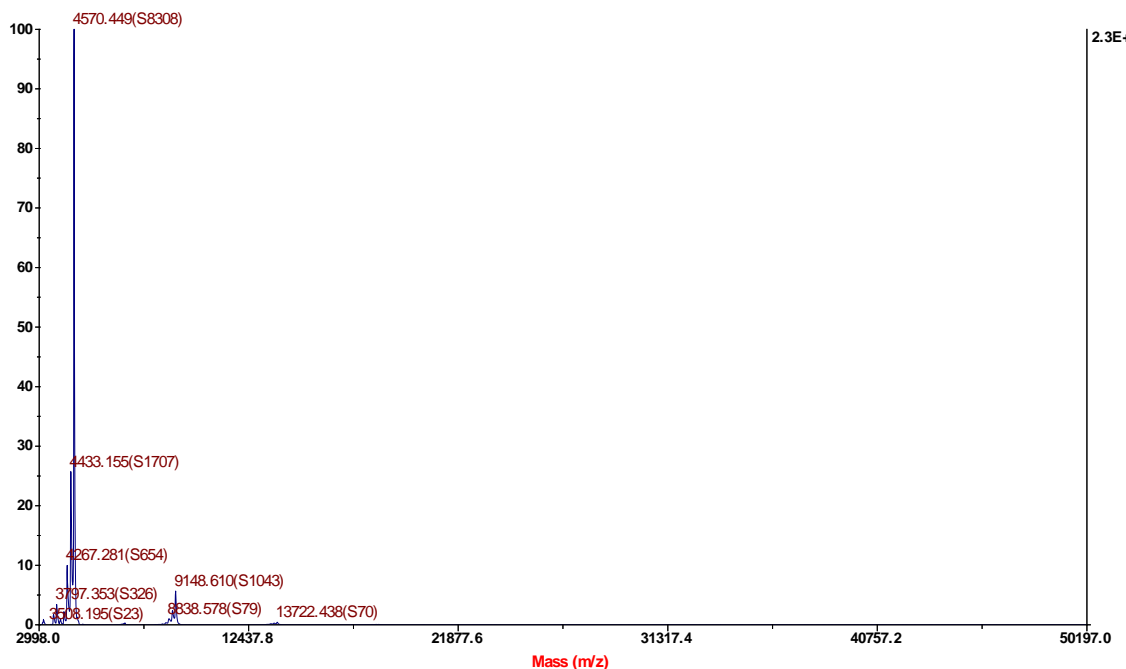
• Oligonucleotide 7



• Oligonucleotide 8



• Oligonucleotide 9



2.3.6. Melting temperatures of duplexes

Melting curves of duplexes were measured on a Cary 5000 UV–Vis-NIR spectrophotometer. For these measurements, buffered aqueous solutions of oligonucleotides were prepared Phosphate Buffered Saline (PBS) (pH = 7, 10 mM NaH₂PO₄/Na₂HPO₄ 1:1, 150 mM NaCl) with oligonucleotide concentrations of 0.2 μM. The volume of each sample was 1000 μL. The samples were heated at a rate of 1 °C/min. For each sample, three melting curves were recorded at a wavelength of 260 nm. Melting temperatures were obtained by calculating the inflexion points of the melting curves.

The melting point was determined for the duplexes a-f, which are structural analogues of the final system (sequences and T_m are summarized in Table II-1).

2.3.7. Synthesis of the DNA construct

The main DNA unwinding segment (410 bp) contains one, two and three repetitions of the GCC cluster separated by 97 bp of a low GC content sequence (Genscript Corp.) The DNA unwinding segment was digested with *EcoRI* and *Sall* restriction endonucleases. The *Sall* end was ligated to the previously described oligonucleotides modified with the HR-cy couple or to a self-annealing oligonucleotide forming a penta-loop (to test the strength of the attachments, see Figure II-7). The *EcoRI* end was ligated to the *EcoRI* end of a short dsDNA linker; the other end of the linker contains non-complementary 5' and 3' protruding strands. The 5' strand is labelled with biotin and the 3' contains the *PstI* restriction endonuclease recognition sequence. After purification of ligation products (Qiagen PCR Purification Kit) a 2686 dsDNA handle (puc19 vector, Novagen) cut with *PstI* and labeled with Digoxigenin at the 5' end was ligated to the *PstI* 3' protruding end of the linker.

2.3.8. Optical tweezers experiments

The DNA construct was bound to Anti-Dig covered beads (Spherotech Co.) by incubating 3 μl of the DNA preparation with 3 μl of the beads for ten minutes at room temperature. The sample was then diluted with 300 μl of the reaction buffer (Tris-HCl 20 mM pH 7.5, 50 mM NaCl) and flowed into the fluidic chamber. The Anti-Dig, DNA covered beads were manipulated with the optical trap and single DNA constructs were obtained by attaching the biotin end of the DNA to the streptavidin bead (Spherotech Co.) previously hold on top of a mobile micropipette. The mechanical properties of the DNA construct allowed identifying single attachments (see experimental force-extension curves below). Data were collected in a dual-beam optical tweezers at 100 Hz at 22 ± 1 °C. Pulling rates were 50 and 200 nm/ s, when indicated.

2.3.9. Experimental force-extension curves

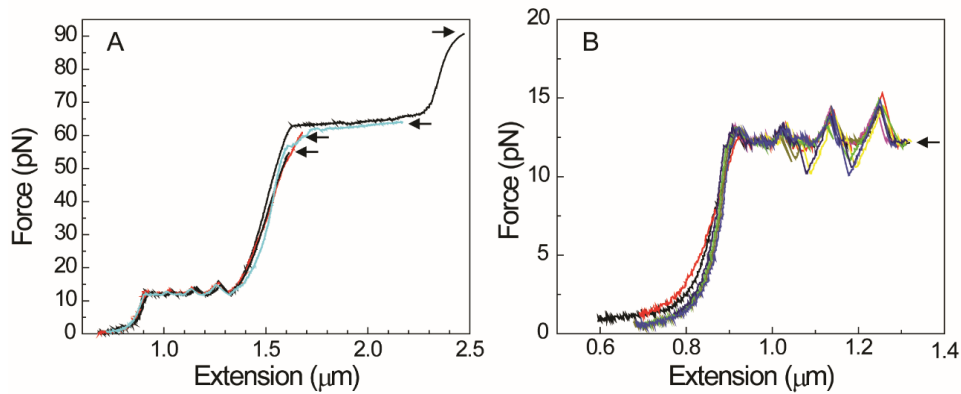


Figure II-6. Independent force-extension curves (FECs) of DNA constructs covalently closed at the *Sall* end by a self-annealing oligonucleotide (see above). Rupture forces (black arrows) indicate the strength of the Dig-AntiDig and/or Biotin/Streptavidin connections used to attach the DNA between the beads (Figure II-3, in Results and Discussion section). The increase in extension at ~60 pN corresponds to the overstretching transition of the dsDNA handle (reference 16 main text). **B**) Alignment of independent FECs without the HR component at the *Sall* end. Disassembly (or rupture force, black arrow) occurred after unzipping of the last GC cluster position. For A) and B) the pulling rate was 50 nm/s.

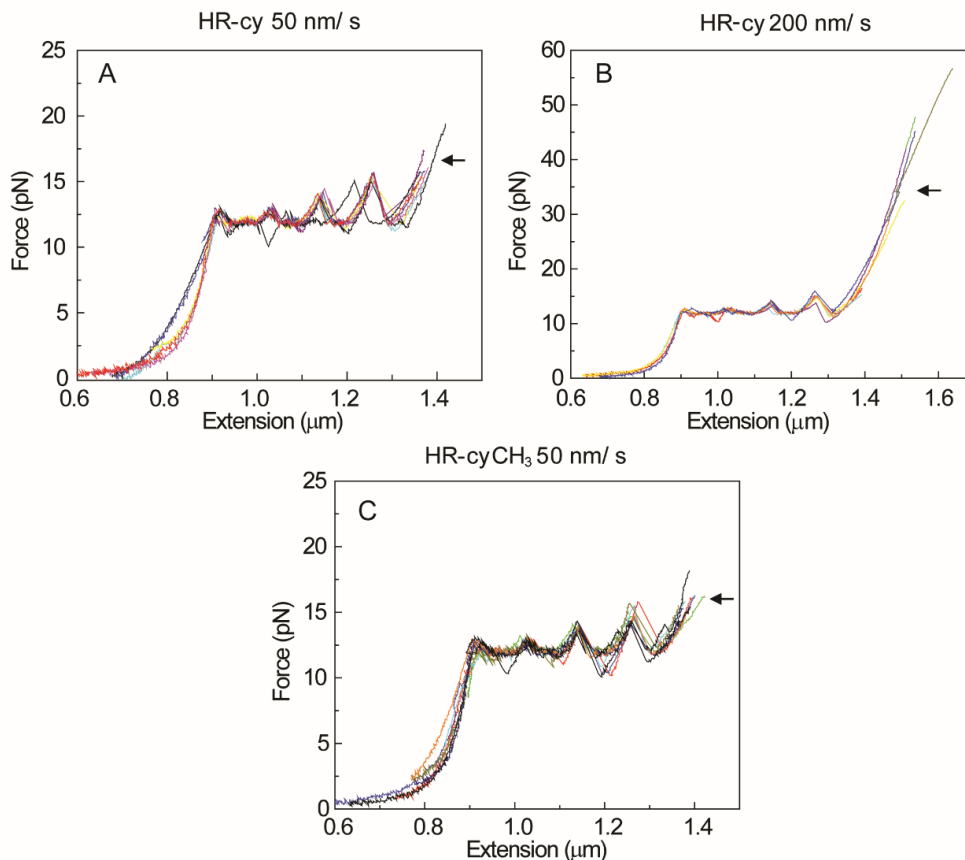


Figure II-7. Alignment of independent FECs of DNA constructs harbouring at the *Sall* end the HR-cy couple (A, pulling rate 50 nm/ s and B, pulling rate 200 nm/ s) or the HR-cyCH₃ couple (C, pulling rate 50 nm/ s). For all plots arrows show the average rupture force at each condition: A) 16.7 ± 1.6 pN, B) 34.0 ± 9.0 pN and C) 15.6 ± 0.7 pN.

2.3.10. Statistical analysis

In order to test quantitatively whether the differences between the values of the rupture forces reported in our work are statistically significant, we applied the statistical hypothesis test known as t-test. The t-test is commonly used to determine whether two independent sets of data are significantly different from each other (Boslaugh S and Watters PA (2008). “The t-test” in Statistics in a nutshell. O’Reilly, 151-165).

As the two samples have unequal sizes and unequal variances, the t statistic to test whether the population averages are different is known as Welch t-test and is calculated as

$$t = \frac{\bar{X}_1 - \bar{X}_2}{\sqrt{s_{1,m}^2 + s_{2,m}^2}}, \quad (1)$$

where \bar{X}_1 is the mean of the sample 1, and $s_{1,m}^2 = s_1^2/n_1$ is the square of the standard deviation of the mean, with s_1 the sample standard deviation and n_1 the size of the sample 1. Analogously, the same quantities with sub-index 2 are defined for the sample 2. For use in significance testing, the distribution of the test statistic is approximated as an ordinary Student's t-bilateral-distribution with the degrees of freedom (df) calculated as:

$$df = \frac{(s_{1,m}^2 + s_{2,m}^2)^2}{s_{1,m}^4/(n_1 - 1) + s_{2,m}^4/(n_2 - 1)} - 2, \quad (2)$$

Once the t value and degrees of freedom are determined, a p -value can be found using a table of values from Student's t-bilateral distribution. The p -value is defined as the probability of obtaining a result equal to or more extreme than what was actually observed. For example, if the p -value obtained is 0.1, the probability of the two data sets to be equal ($\bar{X}_1 \pm s_{1,m} = \bar{X}_2 \pm s_{2,m}$) is 10%. In other words, it can be affirmed with a 90% probability that the two data sets are different ($\bar{X}_1 \pm s_{1,m} \neq \bar{X}_2 \pm s_{2,m}$).

As mentioned above, we run the t-test to determine if the differences between the rupture forces measured for the HR-cy couple at different conditions are ‘real’ or statistically significant. Table S1 below shows the averages and uncertainties of the rupture forces (F_{rup}) measured for each DNA construct (or HR-cy couple) and pulling rate. wt⁵⁰: DNA construct with the HR-cy couple, pulling rate 50 nm/ s. c⁵⁰: DNA construct without the HR-cy couple, pulling rate 50 nm/ s. CH₃⁵⁰: DNA construct with the HR-cyCH₃ couple, pulling rate 50 nm/ s. wt²⁰⁰: DNA construct with the HR-cy couple, pulling rate 200 nm/ s.

The results of the test indicate that the average rupture forces measured for the HR-cy and HR-cyCH₃ couples are statistically different with a ~95 % probability (highlighted in bold in Table II-3).

Table II-3. Statistical analysis of the differences between the rupture forces

X_1 vs X_2	wt ⁵⁰ vs c ⁵⁰	wt ⁵⁰ vs CH ₃ ⁵⁰	wt ⁵⁰ vs wt ²⁰⁰
$F_{rup} X_1$	16.7 ± 1.6	16.7 ± 1.6	16.7 ± 1.6
$F_{rup} X_2$	11.5 ± 0.3	15.6 ± 0.7	34.4 ± 8.5
$F_{rup} X_1 - F_{rup} X_2$	5.2 ± 0.46	1.1 ± 0.51	17.7 ± 2.87
<i>p</i> -value	10 ⁻⁷	0.046	0.0001
$F_{rup} X_1 \neq F_{rup} X_2$			
Probability (%) of $F_{rup} X_1 \neq F_{rup} X_2$	99.99	95.35	99.98

2.3.11. Computational details

Computational calculations were carried out by Belén Nieto-Ortega.

All theoretical calculations were carried out within the density functional theory (DFT) approach by using the C.01 revision of the Gaussian 09 program package.¹⁷⁶ DFT calculations were performed using the long-range corrected ω B97X-D^{177, 178} density functional, which are able to incorporate the dispersion effects by means of a pair-wise London-type potential. The ω B97X-D density functional has emerged as a robust and powerful density functional able to provide accurate structures in supramolecular aggregates dominated by non-covalent interactions of different nature. A Polarizable Continuum Model (PCM) using the integral equation formalism variant (IEF-PCM) was used to represent solvent around solutes via a set of overlapping spheres. This level of DFT has been successfully used for the description of non-covalent interactions in this family of synthetic receptors.¹⁷⁹ The double-zeta Pople's 6-31G(d,p)¹⁸⁰ basis set was employed throughout and the basis set superposition error (BSSE) was corrected according to the counterpoise (CP) scheme of Boys and Bernardi.¹⁸¹

The optimized geometry of HR-cy and HR-cyCH₃ at ω B97X-D/6-31G (d,p) level of theory are shown in Figure II-8. The structure of the system was simplified by substituting the alkyl chain attached to the Hamilton receptor by a hydrogen atom and the alkyl chain attached to the cyanuric acid guest by a shorter chain of $-(CH_2)_2-CH_3$ moiety. As scan coordinate we define the distance between the carbonyl moiety of the cy and the benzene moiety in the HR. In the Figure II-8 the initial optimized structures of both studied system are depicted and also the graphical definition of the scan coordinate.

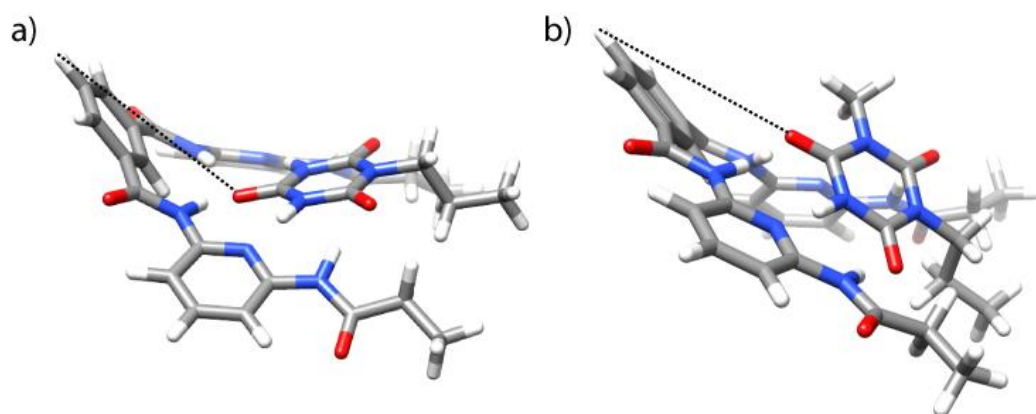


Figure II-8. a) Optimized structure of HR-cy and b) HR-cyCH₃ systems at ω B97X-D /6-31G (d,p) level of theory. In dotted line the scan coordinate is defined.

The potential energy curves (PECs) for HR-cy and HR-cyCH₃ couples were calculated using the SCAN tool implemented in Gaussian software, where single point energy evaluations were performed in each selected internal coordinates. This methodology has been chosen following the literature in the field^{23, 24, 175, 182}. Specifically, our input was design to increase the scan coordinate (see Figure II-8) 50 times with a variation of 0.2 Å between them. The potential energy curves (PECs) for HR-cy and HR-cyCH₃ in two different solvents: water and o-dichlorobenzene are displayed in Figure II-9. In the same figure we show the optimized structures for in the initial stage (completely bonded) and non-interacting state, using a continuous model of water.

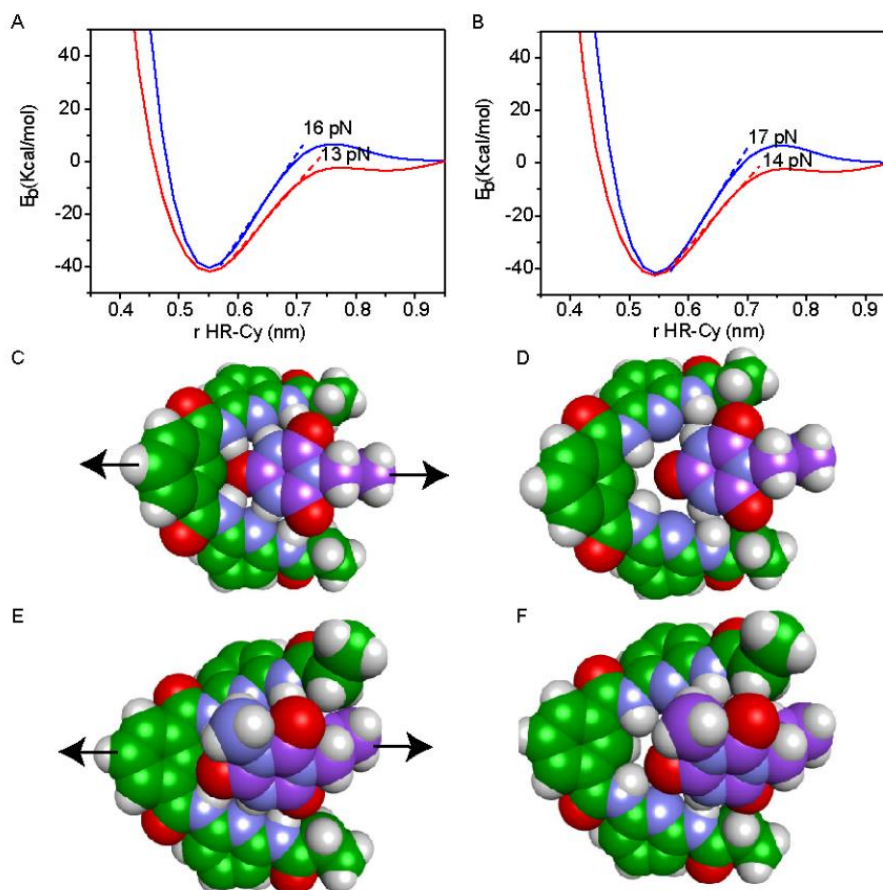


Figure II-9. A) Potential energy curves for HR-cy (blue) and HR-cyCH₃ (red) using a continuous model of water and B) *o*-dichlorobenzene. Energy-minimized molecular models showing the geometry of the C) bound and D) unbound HR-cy. Energy-minimized molecular models showing the geometry of the E) bound and F) unbound HR-cyCH₃.

The curves were calculated by considering the interaction of the two molecular moieties as they are getting closer from an infinite separation. At large distances, interactions are negligible ($E_b = 0$) but attractive interactions grow as host and guest approach each other, reaching a state of equilibrium where the net force (the sum of both attractive and repulsive components) is zero. The PECs indicate the strength of the host-guest interaction based on the depth of the potential well, and the force (F) is the slope of the curve, according to: $F = -dE_b/dr$, where E_b is the binding energy and r the distance between host and guest. At equilibrium, the binding energy for the systems HR-cy and HR-cyCH₃ are calculated to be 40.51 and 41.92 Kcal mol⁻¹ respectively, which are expected binding energies for systems with six and five strong hydrogen bonds in aqueous conditions.

At short distances from the equilibrium state (0-0.03 nm) the potential energy is not affected by a change in the intermolecular distance, but at larger values of r a change in the slope is observed. From this point to the next change in slope, where the cyanuric acid is completely dissociated from the Hamilton's receptor (see Figure II-9D), a value of 16 pN for

the force is obtained. This value is directly related with the force required to split the couple, and is in good agreement with our experimental data, despite all simplification conducted. In the case of the HR-cyCH₃ system, the calculated force was 13 pN, a noticeably lower value than HR-cy, following the same tendency of the experimental results. We also, calculated the rupture force in the case of an organic solvent. We observe an increase in the force, being 17 pN for HR-cy system and 14 pN for HR-cyCH₃.

CHAPTER 3.

Measurement and Manipulation of the Shuttling

Motion of an Individual Molecular Shuttle

3.1. Introduction

Molecular motors are nanoscale devices capable of converting energy into movement and forces, in other words, to perform work at the nanoscale.^{183, 184} Artificial nanomachines are currently the subject of intense research interest due to their many potential applications in diverse fields from biomedicine to nanorobotics. The best way to appreciate the technological potential of controlled molecular-level motion is to recognise that nanomotors and molecular-level machines lie at the heart of every significant biological process. Virtually every biological task involves molecular machines.^{183, 185-195} Catalytic proteins with moving parts able to efficiently convert thermal and chemical energy to work through conformational changes and unidirectional displacements.¹⁸⁴ The construction of miniature, 'nanoscale' machines is a goal of modern science and technology, inspired by Feynman's famous lecture "There's plenty of room at the bottom".¹⁹⁶ The field has advanced to the point that some of the pioneers in the synthesis of molecular machines have been recognized with the Nobel Prize in Chemistry 2016.¹⁹⁷⁻¹⁹⁹ Despite the impressive progress in the field, man-made nanomachines lack efficiency, functionality and are limited to a narrow range of environments and fuels.

Over the last 25 years, researchers have devised an impressive array of switches, ratchets, propellers and more molecular mechanisms that can be plugged together as if they were nanoscale Lego pieces.¹⁵² Recently, the field has reached a turning point; instead of making more motors, top researchers in the field are currently more interested in the practical applications of these motors,²⁰⁰ such as light-activated switches that can release targeted drugs, smart materials that can store mechanical energy (contraction) in response to light or can change their shape acting as an artificial muscle. In the words of Prof. Leigh, one of the top researchers in the field, "In 10 years time, molecular machinery will be seen as a core part of Chemistry and materials design".²⁰⁰ Making the step from molecules to molecular systems, which incorporate several molecular components working in concert to perform complex and integrated functions at different hierarchical levels, will require an exquisite control of the dynamics and mechano-chemical processes (conversion of thermal/chemical energy to motion

and work) governing the operation of these systems at the nanoscale. However, very basic questions about the operation of molecular motors at the nanoscale have still to be answered. In this line arises the aim of this chapter: to quantify the dynamics and mechanochemistry of individual synthetic molecular shuttles under physiological conditions.

Molecular shuttles are perhaps one of the simplest examples of molecular devices, and have long been considered candidates for the construction of molecular motors. Structurally, molecular shuttles are [2]rotaxanes (from the Latin *rota* = wheel and *axis* = axle), chemical species in which one ([2]rotaxanes) or more ([*n*]rotaxanes) macrocycles are threaded onto a dumbbell-shaped component from which de-threading is prevented by bulky “stoppers”.²⁰¹ Although macrocycle and thread are not covalently connected, rotaxanes are molecules, and not supramolecular complexes, since covalent bonds need to be broken to separate their components. The macrocycle can move between two (or more) regions of the thread, called stations, in response to an external stimulus (Figure III-1). Important features of rotaxanes derive from noncovalent interactions between components that contain complementary recognition sites. Such interactions, that are also responsible for the efficient template-directed syntheses of rotaxanes, involve electron-donor/acceptor ability, H-bonds, hydrophobic/hydrophilic character, π - π stacking, coulombic forces and, on the side of the strong interaction limit, metal-ligand bonding.

It is important to note that a molecular shuttle is not a molecular motor, as it cannot convert energy into mechanical work cyclically; it is better classified as a molecular switch, it can be reversibly shifted between its stations, when the stations are dissimilar with each of them addressed by a different external stimulus. However, molecular shuttles are a very closely related model system to molecular motors; and they are characterized by: (i) the kind of energy input supplied to drive them out of equilibrium, (ii) the type of motion (linear, rotatory, oscillatory, ...) performed by their components, (iii) the way in which their operation can be monitored, (iv) the possibility to repeat the operation at will (cyclic process), (v) the time scale needed to complete a cycle, and (vi) the function performed.

In many ways the field of artificial molecular machinery began with Stoddart's first report of a “molecular shuttle” in 1991 (Figure III-1).²⁰² In this rotaxane, the macrocycle (shown in green) moves between two preferred binding sites (the two hydroquinone units, shown in red) by random thermal motion (Brownian motion).

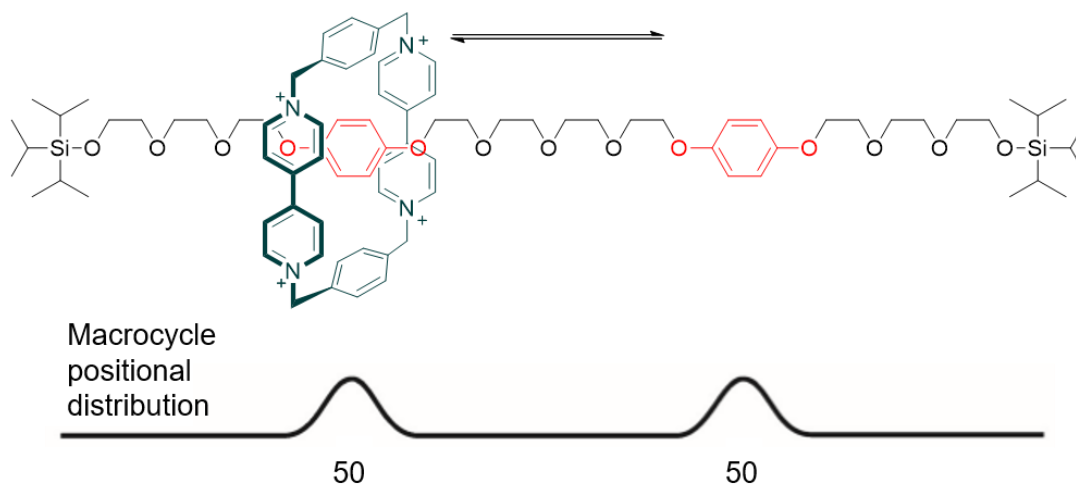


Figure III-1. The first molecular shuttle (Stoddart and co-workers; 1991).²⁰²

When the two recognition sites in the dumbbell component are chemically different, then the rotaxane exist as an equilibrium of two different co-conformations, whose populations reflect their relative free energies as determined primarily by the relative strength of the two different sets of non-covalent bonding interactions in the molecule. Thus, by breaking symmetry of a rotaxane thread to have two different potential stations, its relative affinity for the ring can be switched. Based on this design, Stoddart, Kaifer, and co-workers described the first switchable molecular shuttle, which is arguably also the first artificial molecular Brownian motion machine (Figure III-2).²⁰³ In this molecule, the cationic macrocycle (in green) prefers to reside over the benzidine station (in blue) rather than the biphenol station (in red). However, using stimuli that are either protonation or electrochemical oxidation of the benzidine station, transforms it into a positively charged station (in purple), causing electrostatic repulsion with the tetracationic macrocycle, and rendering the biphenol group the preferred binding site for the macrocycle, thus the ring moves along the thread. This molecule is the first example of a large amplitude, well-defined, controlled switching of the position of a submolecular component along a molecular track.

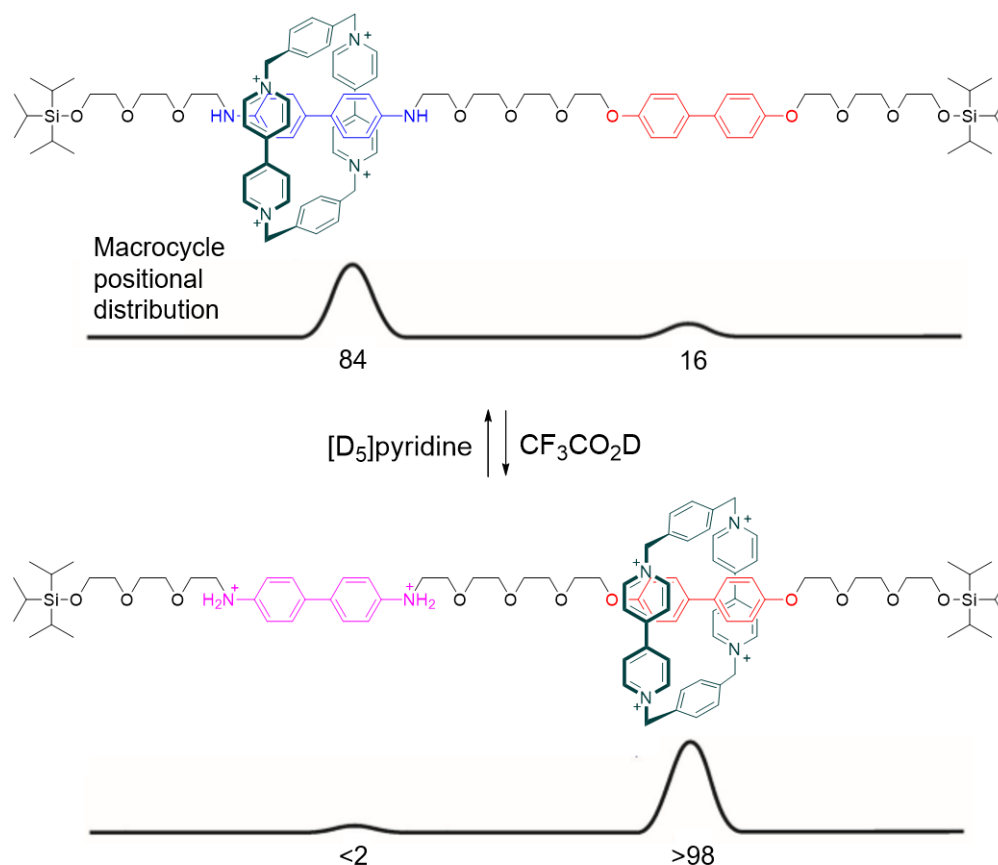


Figure III-2. The first switchable molecular shuttle (Stoddart, Kaifer, and co-workers; 1994).²⁰³

The collective dynamics of molecular shuttles have been studied with increasing structural sensitivity and temporal precision.^{204, 205} In contrast, much of the exquisite and detailed information about how biomolecular machines operate has been obtained from direct measurements made on single molecules using manipulation techniques such as OT or AFM. Such measurements have highlighted many details about their mechanical properties, as we studied in chapter 1.^{169, 206} However, few SMFS investigations have been successively realized on molecular shuttles.^{207, 208} The shortage of such studies comes from the difficulty of developing proper tools and preparing appropriate molecules that can be interfaced with SMFS techniques, especially when one wants to probe sub-molecular motions. Two examples of molecular shuttles were investigated in an irreversible rupture process (de-threading),²⁰⁷ and in reversible cycles that allow the direct measurement of the force generated and the work produced,²⁰⁸ using SMFS. In the first study, Stoddart and co-workers²⁰⁷ pulled the macrocycle over the bulky end groups of a redox-active rotaxane with an AFM tip. They compared the large forces required to de-thread oxidized and unoxidized molecules. The bistable [2]rotaxane R^{4+} (Figure III-3) can switch by the redox-controlled mechanical shuttling of the ring along its thread. The molecule was designed fixing the dumbbell on a surface through a hydroxymethyl

group on one of the stoppers for attachment to SiO_2 via covalent bonds and attaching the ring to an AFM cantilever through a thioctic acid linker. They used SMFS to study the steric and electrostatic interactions present in the ground and oxidized states of R^{4+} . They confirmed that the force associated with the electrostatically driven movement of the cyclobis(paraquat-*p*-phenylene), CB-PQT^{4+} , ring away from tetrathiafulvalene, TTF^{2+} , upon oxidation could be as high as 79 pN.

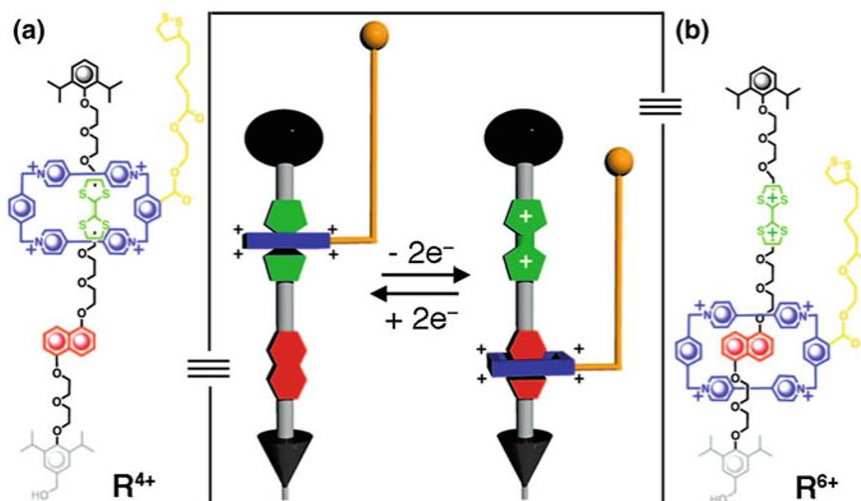


Figure III-3. Chemical structure and schematic representation of bistable [2]rotaxane R^{4+} and the oxidized partner [2]rotaxane R^{6+} . In R^{4+} and R^{6+} an electron-poor cyclobis(paraquat-*p*-phenylene) (CB-PQT^{4+}) ring is confined to a dumbbell containing two electron-rich recognition sites, tetrathiafulvalene (TTF) and 1,5-dioxynaphthalene (DNP), by the presence of bulky 2,6-diisopropylphenyl ether stoppers at each end. One of these stoppers, the one closer to DNP, carries a hydroxymethyl group on its 4-position for subsequent attachment to silicon wafers. (a) The ring, which carries a tether terminated by a thioctic acid ester for attachment to a gold-coated AFM tip, displays a stronger interaction with TTF than with DNP and thus resides selectively on the former. (b) Chemical oxidation of TTF to TTF^{2+} results in a strong charge–charge repulsion between the CB-PQT^{4+} ring and TTF^{2+} , a situation that causes the CB-PQT^{4+} ring to shuttle to DNP in the oxidized [2]rotaxane R^{6+} . Reduction of the TTF^{2+} to its neutral state (TTF) prompts the ring to shuttle back thermally from a metastable state to its ground state. Figure reproduced with permission from *Proc. Natl. Acad. Sci. USA* **2006**, 103 (23), 8583-8588.

A second more recent study realized by the group of Duwez²⁰⁸ on one of Leigh's H-bonded [2]rotaxanes was focused on detecting sub-molecular movement and on measuring the force generated by this molecule against a load during a single shuttling event. They designed a H-bonded molecular shuttle with a tether attached to the ring to track its motion with an AFM cantilever (Figure III-4). The thread bears both fumaramide and succinic amide-ester stations, each of which can bind to the macrocycle through up to four intercomponent hydrogen bonds.²⁰⁹ The ring predominantly resides over the fumaramide site. A mechanical load was applied to the ring of the rotaxane with the AFM cantilever, while simultaneously

following its movement. The rings were stretched in a controlled manner by moving the tip away from the substrate at a fixed pulling rate.

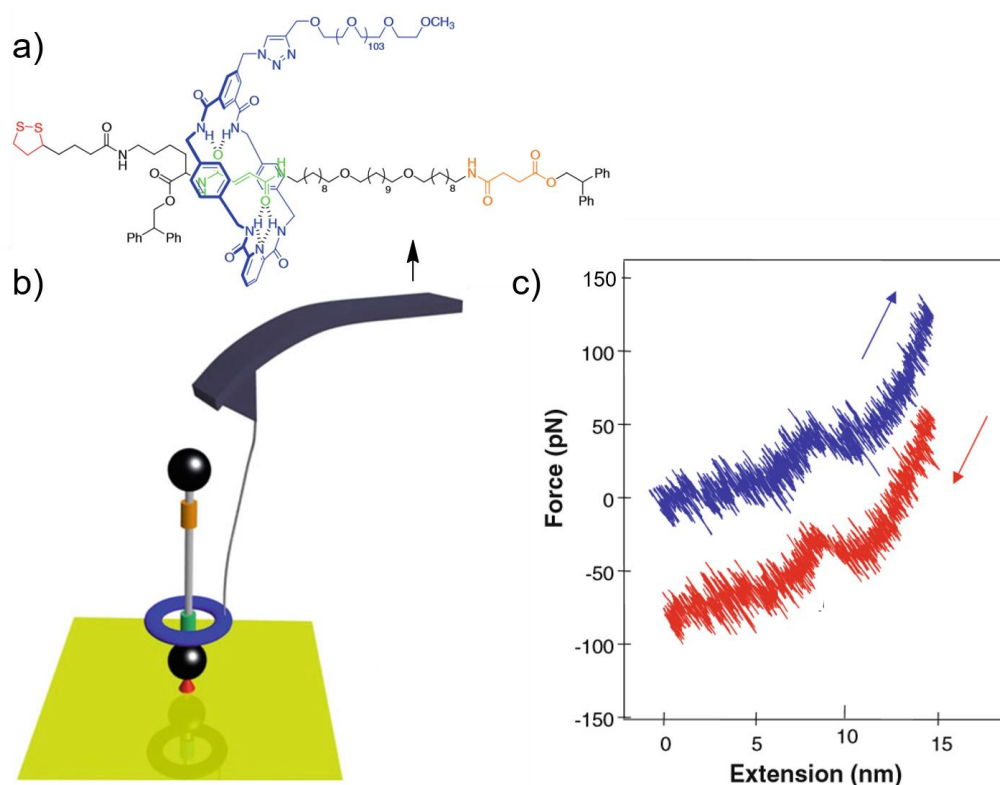


Figure III-4. a) Chemical structure of the rotaxane molecule, which consists of a benzylic amide molecular ring (in blue) mechanically locked onto an axle by bulky diphenylethyl ester groups situated at either end. The axle bears a fumaramide group (in green) and a succinic amide-ester group (in orange), either of which can act as a binding site for the ring through up to four intercomponent H-bonds. Next to the fumaramide binding site, a disulfide group (in red) was introduced to enable the grafting of the molecule onto gold substrates. A 4600 M_n PEO tether (in blue) is attached to the ring in order to link the molecule to the AFM probe and track the motion of the ring along the axle. b) Schematic representation of the rotaxane attached to the AFM set up. c) Pulling (blue) and relaxing (red) force versus extension curves for a single rotaxane–PEO molecule in TCE. The relaxing trace is offset vertically for clarity. This figure was reproduced with permission from **Springer, *Nat. Nanotech.* 2011, 6 (9), 553-557.** Copyright (2011).

They recorded pulling-relaxing cycles (Figure III-4c). During a pulling experiment, the AFM cantilever is exerting force on the PEO tether, if this force is larger than the force of the H-bonds that bind the ring to its preferred site, the H-bonds break apart and the ring detaches from its station. It is then pulled along the axle, away from its most stable binding site, it was observed as the appearance of a “peak “(where no peaks were expected) in the force-extension curve (blue trace in Figure III-4c), and the distance change was compatible with the ring movement between stations. Similarly, in the relaxing cycle (red trace in Figure III-4c) they observed that while relaxing the tension in the PEO tether, the force suddenly increased, with

the appearance of a new “peak” in the force-extension curve, this can be explained by the appearance of force acting on the tether at the other end. This means that the macrocycle has travelled back from the succinic amide-ester site to the fumaramide site and that it is able to generate force of 30 pN against an external load.

Very recently, Duwez et al.²¹⁰ reported on the mechanochemical properties of a donor-acceptor oligotaxane. This molecule arises from the combination of two mechanical interlocked molecules, rotaxane and catenane. In this oligotaxane, the interactions between the mechanically interlocked component parts dictate the single-molecule assembly into a folded secondary structure (Figure III-5).

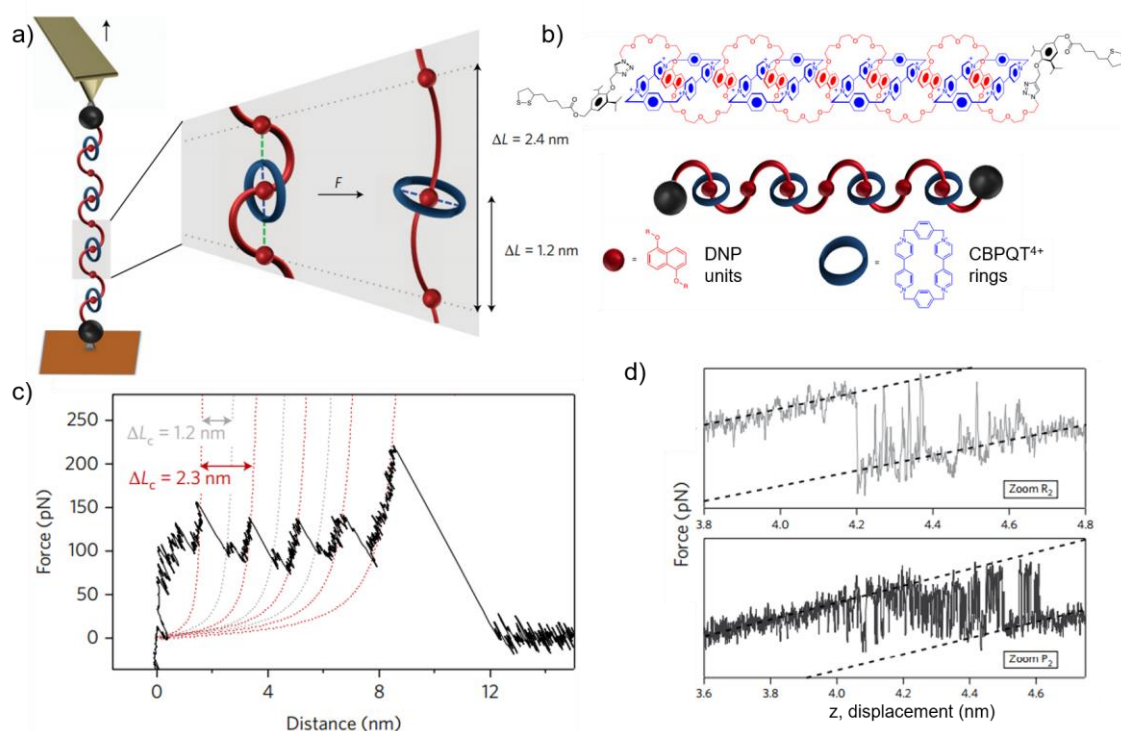


Figure III-5. a) Illustration of the pulling experiment. Mechanical unfolding occurs by retracting the cantilever at a constant velocity. The theoretical variation of length after breaking one interaction between a free DNP and the contiguous ring is about 1.2 nm. b) Structure formula and co-conformation of the [5]rotaxane. In this co-conformation, half of the dioxynaphthalene (DNP) units (in red) are encircled by cyclobis(paraquat-*p*-phenylene) (CBPQT⁴⁺) rings (in blue). The oligorotaxane is terminated by bulky stoppers which prevent the rings from dethreading. c) Example of a force–distance curve obtained at 40 nm s⁻¹ showing a characteristic reproducible sawtooth profile. Each peak is fitted with the WLC model to obtain contour length increment (ΔL_c) values. d) Pulling–relaxing curves showing sequential folding and unfolding of a single interaction in an individual [5]rotaxane molecule in DMF. Hopping from one co-conformation to the other is observable during pulling and relaxing (Pulling at 10 nm s⁻¹ and relaxing at 4 nm s⁻¹). Figure reproduced with permission from **Springer**. *Nat. Nano.* **2018**. Copyright (2018).

They used SMFS-AFM to mechanically unfold oligotaxanes, made of oligomeric dumbbells incorporating 1,5-dioxynaphthalene units encircled by CB-PQT⁴⁺ rings (Figure III-5b). Real-time capture of fluctuations between unfolded and folded states (Figure III-5c and d) reveals that the molecules exert forces of up to 50 pN against a mechanical load of up to 150 pN, and displays transition times of less than 10 μ s.

The SMFS approximation presents the limitations derived from AFM-based techniques; in general, their force resolution is limited by the stiffness of the cantilever to a force range above \sim 20 pN, which is larger than the strength of the weak, non-covalent interactions responsible for remodelling events at the molecular level⁴³ and larger than the forces characteristic of biological molecular motors.²¹¹ For instance, the movement of biological molecular motors that transport cargos uni-directionally (kinesins) is stalled at forces \sim 8 pN²¹² and the hydrogen-bonding holding together the two strands of DNA break at \sim 10 pN.¹⁶² The inability of AFM to access within the range of forces relevant for molecular machinery has prevented the application of this technique to study the operation of these biological systems at the single molecule level. Instead, other techniques, like magnetic and optical tweezers, with force and distances resolution within the 0.1-1 pN and 1-10 nm range respectively, as we explained in chapter 1 of this thesis, are routinely used in to access low force ranges characteristic of noncovalent interactions and molecular dynamics. Moreover, in chemistry, in AFM pulling experiments it can be difficult to discriminate interactions of the AFM tip with the molecule of interest from nonspecific interactions, due to the lack of single molecule reporters in this field.

We arrive at the main objective of this chapter: to measure and manipulate the mechanics and real time kinetics of individual [2]rotaxanes molecules with OT. These experiments will allow us to investigate for the first time:

i) The mechanochemical cycle and dynamics of the system operation when it is driven out of equilibrium by a mechanical load. As a consequence we will extract conclusions about the design of molecular machines at the theoretical level, both to help analyse existing examples and to propose simpler, more efficient machines.

ii) The properties and operation of synthetic molecular shuttles under biocompatible, aqueous conditions. The vast majority of the synthetic devices reported to date have been investigated in organic solvents solutions. The information obtained will be useful to compare synthetic to natural molecular machines under identical conditions, which will shed light on the possibility of creating synthetic-natural hybrids, one of the most ambitious goals in the field.

As mentioned before, we are going to use OT as a single molecule manipulation tool, because it features the force ($<$ 1pN), distance (1-10 nm) and time resolutions (10000 Hz)

required to measure the characteristic forces and displacements that govern noncovalent interactions at molecular level.⁴⁶

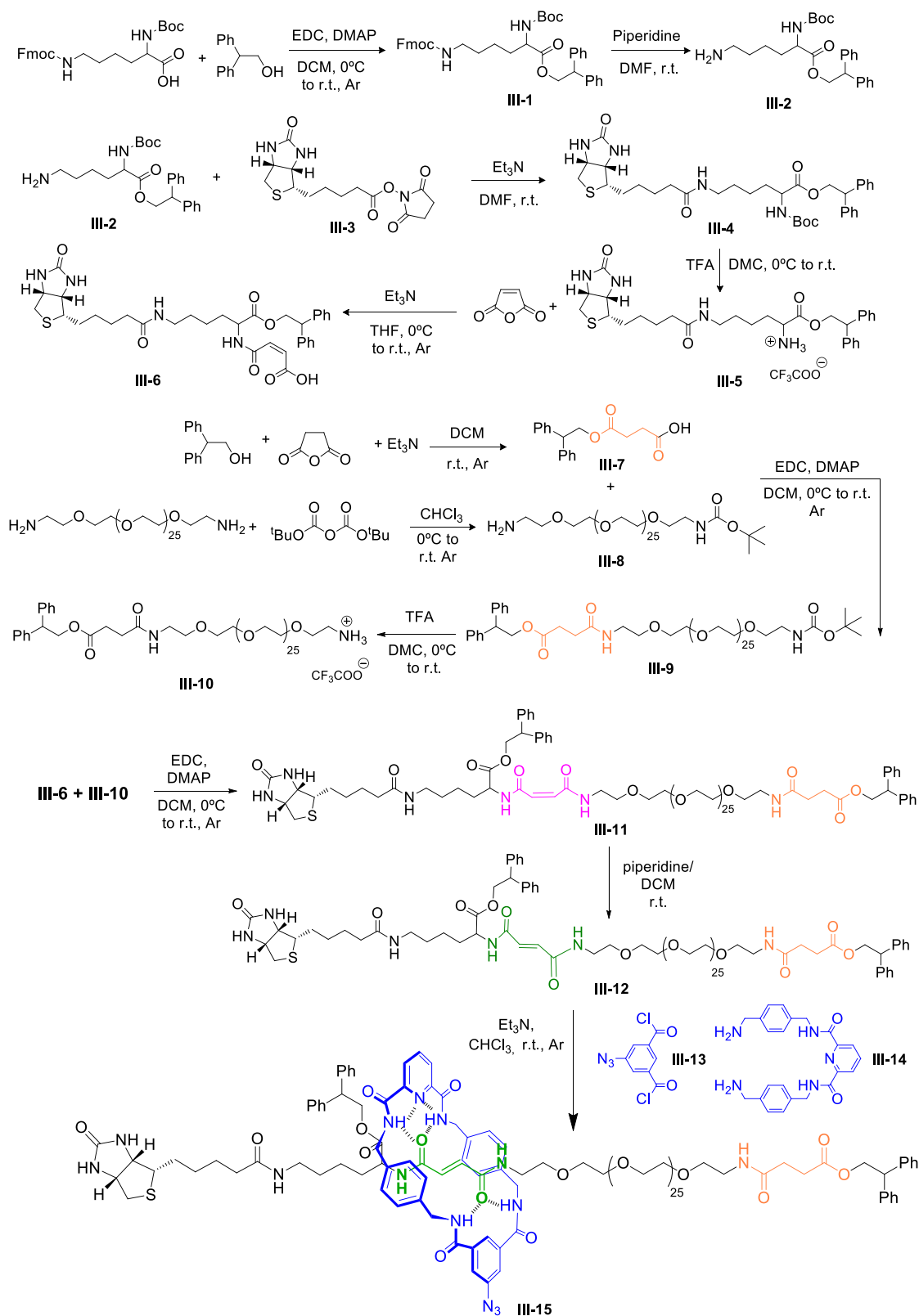
3.2. Results and Discussion

3.3.1. Chemical Design

We have designed a H-bonded Leigh-type²¹³ molecular shuttle with a dsDNA attached to the ring to trace its motion by a dual-beam OT (Figure III-7). Its design and synthesis are detailed below, and represent an authentic tour-de-force in chemistry, including multistep organic chemistry, biochemistry, and controlled supramolecular chemistry.

The chemical structure of the shuttle comprises a strong binding station, namely fumaramide (green in Figure III-6), which is known to be the best fit for a tetraamide macrocycle, because its two amide carbonyls are held by the *trans* double bond in the correct geometry to form four strong hydrogen bonds with the macrocycle. Separated by a polar spacer of approximately 10 nm length, which will provide solubility in water and enough distance for the shuttling to be unambiguously detected by OT, we will place a second station, succinic amide-ester (orange in Figure III-6), which shows less affinity for the macrocycle than the fumaramide station, due to its flexibility and the substitution of one of the amides with an ester, which is a significantly weaker H-bond acceptor. The fumaramide/succinic amide-ester occupancy ratio is larger than 95:5 in several organic solvents at room temperature.²⁰⁹ Two bulky diphenylethyl groups will serve as stoppers. One of the stopper ends is branched to include a biotin fragment that will be initially used to attach the construct to a polystyrene streptavidin-covered microbead, held in place by suction with a micropipette (see below in Figure III-7).

The synthesis of the thread for the shuttle was carried out in 12 steps following Scheme III-1. Macrocyclization around the fumaramide station was performed using a purposely synthesized U-shape (compound **III-14**) and an azide-decorated isophthalic acid chloride derivative (compound **III-13**), to obtain an asymmetric macrocycle with a chemical handle for attachment to the OT, through a dsDNA spacer.



Scheme III-1. Synthetic steps involved in the synthesis of the molecular shuttle, compound III-15.

A synthetic fragment of dsDNA will be used as a handle to control and measure the movement of the ring. The choice of DNA as a linker is based on several facts:

1) dsDNA is a very stable and stiff polymer which has been broadly used to measure tiny conformational changes of biomolecules. DNA handles are used as spacers that prevent non-specific interactions between the force probe (the bead) and the molecule under study.

2) DNA ends can be conveniently modified with many different chemical groups.

3) Its mechanical properties can be used to identify single attachments between the beads.¹⁶⁸ As explained in chapter 1, a single, linear dsDNA molecule presents a characteristic elastic response that can be explained using polymer physics models like the WLC model (Figure I-12b, in chapter 1). When two or more DNA molecules are attached the elastic response (the force-extension curve) changes dramatically.

4) The length of the DNA handle can be adjusted at will.

5) dsDNA handle helps solubilisation of the rotaxane molecule under aqueous conditions.

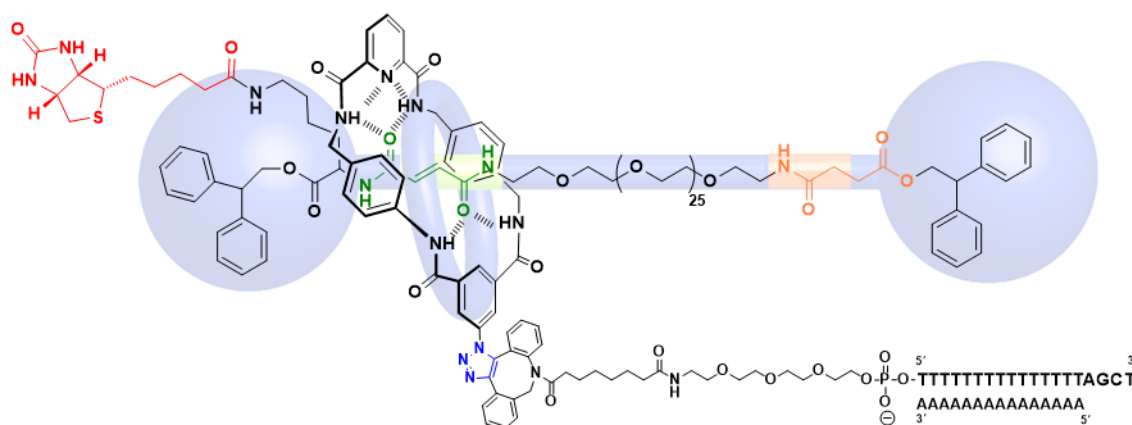


Figure III-6. Chemical structure of the rotaxane molecule. The thread presents a fumaramide group (in green) and a succinic amide-ester group (in orange), either of which can act as a binding site for the benzylic amide macrocycle through up to four hydrogen bonds. Two diphenylethyl ester groups situated at either end act as stoppers. The affinity of the ring for the fumaramide site is much higher than for the succinic amide-ester site, so that the fumaramide/succinic amide-ester occupancy ratio is higher than 95:5.²⁰⁹ Next to the fumaramide binding site, a D-biotin group (in red) was used to enable the linkage of the molecule onto the streptavidin-beads. Through a 1,2,3-triazole group (in blue), the macrocycle is covalently linked to dsDNA. Only the sequence of the dsDNA oligonucleotide is shown. To control the movement of the ring a $\sim 0.9 \mu\text{m}$ dsDNA labelled with Digoxigenin at one end will be ligated to the protruding 3'-end of the oligonucleotide (see Figure III-7).

To attach the dsDNA to the rotaxane we used the following methodology: the 5'-end of a single-stranded DNA (ssDNA) oligonucleotide (polyT) will be covalently linked to a dibenzocyclooctyl (DBCO) phosphoramidite on the last step of a solid support DNA chemical synthesis (see Scheme 2 in Experimental Section). We used a strain-promoted copper-free click reaction^{214, 215} to attach covalently the DBCO reacting group of the oligonucleotide to the azide group in the macrocycle. In this way, we obtained a rotaxane modified with a ssDNA

oligonucleotide through a 1,2,3-triazole group (blue in Figure III-6). We then annealed the rotaxane-oligonucleotide with its complementary DNA strand (polyA), previously synthesized using DNA automated synthesis. The oligonucleotide sequences are designed to provide a protruding 3'-end after annealing. Finally, we ligated a $\sim 0.9 \mu\text{m}$ long dsDNA molecule (2686 bp) containing a protruding 5'-end complementary to the 3'-end of the rotaxane-oligo construct. This dsDNA molecule was labelled with multiple digoxigenines (Dig) at the other end, in order to attach the dsDNA and couple the ring to a polystyrene α -Dig-covered microbeads held in an optical trap (see below in Figure III-7).

In summary, the final product of these reactions will be a rotaxane-DNA complex labelled with biotin at one end and Dig at the opposite end. This construct was coupled to the OT set up as depicted schematically in Figure III-7.

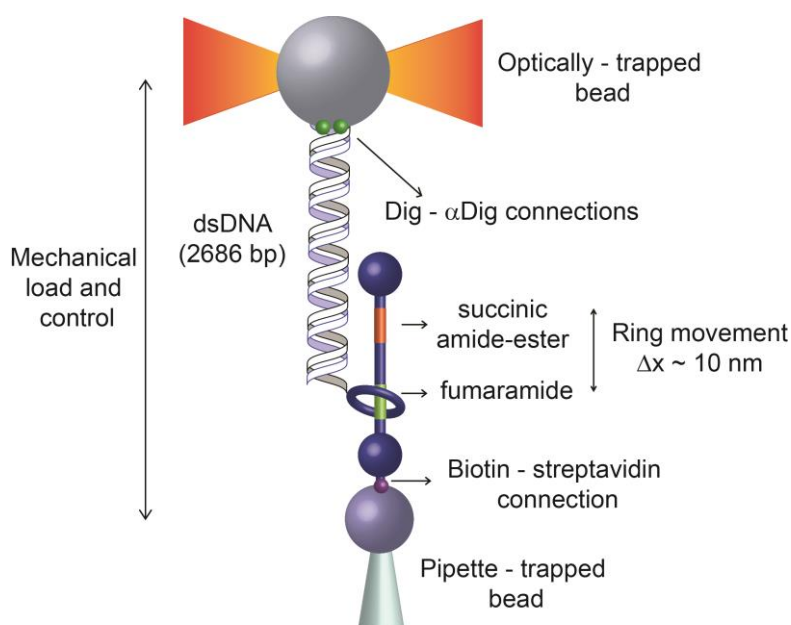


Figure III-7. Schematic representation of the experimental set-up (not to scale). A single rotaxane-DNA construct is attached between an optically trapped α -Dig-coated bead (showing in grey) and a streptavidin-coated bead (showing in blue) immobilized on top of a micropipette. Mechanically force is applied along the vertical axis (moving the optical trap away from the pipette).

3.2.2. Single molecule experiments

Force-extension curves were measured by applying a mechanical load to the ring of the [2]rotaxane and following its movement. Individual molecules were stretched in a controlled manner by moving the optical trap away from the micropipette at a fixed pulling rate, giving a characteristic force-extension profile (Figure III-8b).

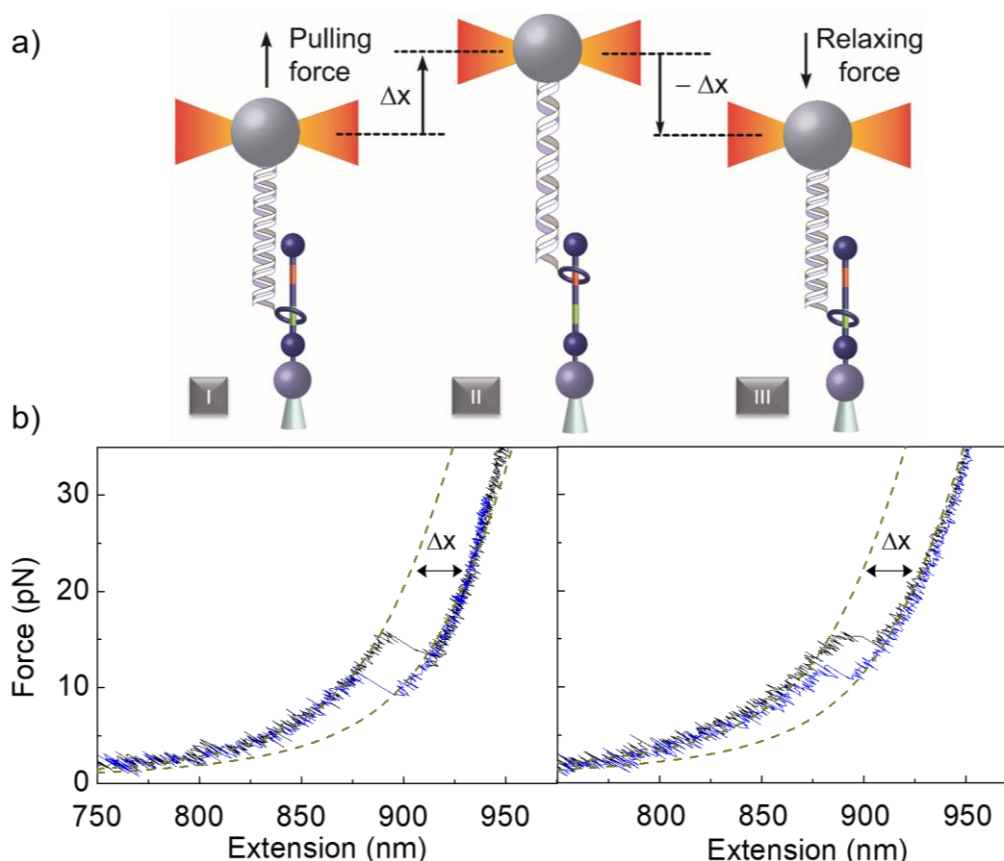


Figure III-8. a) Schematic representation of the experiments carried out to determine the force-extension curves of the molecular shuttle; the shuttle was stretched in a controlled manner by moving the optical trap away from the pipette at a 200 nm/s pulling rate. Initially, the macrocycle is placed on the thermodynamically favoured station (fumaramide, green) (I), application of force along the vertical axis displaces the macrocycle out of its preferred site (II); finally, the ring returns to the original position upon lowering the force (III). b) Force-extension curves of two different and representative individual molecules (pulling rate of 200 nm/s). During the pulling cycle (black trace) there is a peak, at 15.5 pN (for the left example) and 17 pN (for the right example), in the characteristic force-extension curve of the dsDNA (no peaks expected) which corresponds to a change in the contour length of the molecule due to the extension gained when the ring is pulled out the fumaramide station. Likewise, a peak (at 10.9 pN for the left example and 13.5 pN for the right one) during the relaxing cycle (blue trace) is indicating that the macrocycle travels back to the fumaramide station. The yellow dashed lines represent the theoretical force-extension curves obtained using WLC model. The fits of the profile before and after the rupture peak give the increase in length (Δx) of the molecule ($\Delta x = 15$ and 11.5 nm for left and right examples respectively) which is in full agreement with the theoretical length of the fully extended oligoethyleneglycol spacer between the two stations (~ 10 nm).

Figure III-8a shows a schematic representation of the events taking place when pulling on the rotaxane molecule that explain the observed force-extension profile. Figure III-8b shows the pulling-relaxing cycles of two individual rotaxanes. During the pulling experiments (black traces in Figure III-8b), once the force exerted on the macrocycle exceeds the strength of the H-bonds between the ring and the fumaramide station, these H-bonds break apart, giving a

peak in the force-extension curve of the dsDNA. As described in chapter 1, the elastic properties of the dsDNA can be modelled with the WLC model for polymer elasticity (dotted lines in Figure III-8b) and no peaks of force-extension changes are expected below 60 pN of tension. Therefore, this peak corresponds to a change in the contour length of the molecule due to the extension gained when the ring is pulled out of its thermodynamically more stable binding site, and goes to the succinic amide-ester station. This peak appears at 15.5 and 17 pN for the two examples depicted in Figure III-8b, under near physiological conditions (20mM Tris-HCl pH 7.5, 150 mM NaCl, 22 °C). In the relaxing cycle (blue trace in Figure III-8b) we observed that the force suddenly increased, this means that the macrocycle travelled back to the fumaramide station. This result for a single shuttling event can be interpreted as the macrocycle exerting a force against the bead load.²⁰⁸

The fittings of the pulling/relaxing profiles using WLC model, before and after the “rupture peak”, give the increase in length (Δx) of the molecule after rupture of the H-bonds; the Δx value obtained for the molecules showed in Figure III-8b was 15 and 11.5 nm, which is in full agreement with the theoretical length of the fully extended oligoethyleneglycol spacer between the two stations (~10 nm).

Next we decided to perform multiple pulling-relaxing cycles on individual molecules, which are necessary to obtain ΔG of the system. Unexpectedly, we found mechanical fatigue, after few pulling/relaxing cycles the ring was stuck in one of the stations. These experiments rendered poor statistics (Figure III-9b), which may provide a poor estimation of ΔG . In Figure III-9 are depicted the distributions of pulling (black) and relaxing (blue) forces of the rotaxane-DNA construct, in which we observed the macrocycle stop doing shuttling events right after 10 cycles.

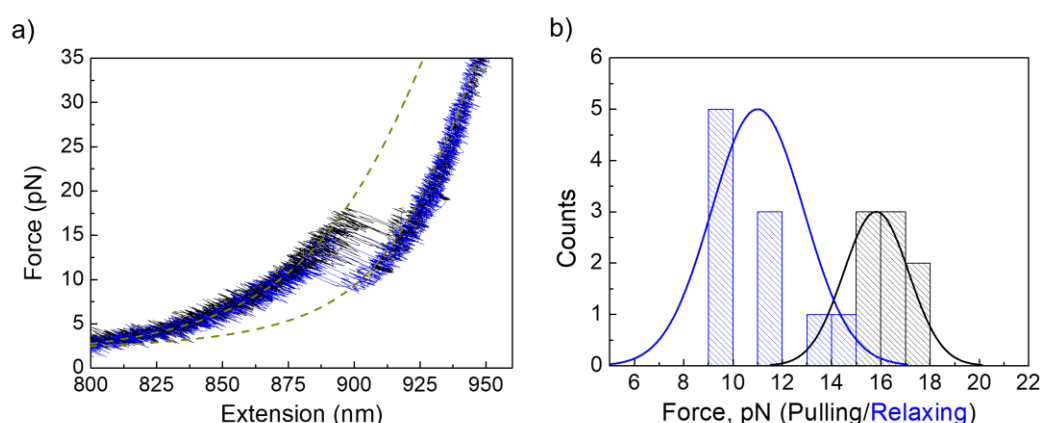


Figure III-9. a) Force-extension curves for ten pulling (black traces)/relaxing (blue traces) cycles of a representative rotaxane molecule using a fixed pulling rate of 200 nm/s. The yellow dashed traces represent the theoretical force-extension curves obtained using WLC model. b) Distributions of the pulling/relaxing forces.

The characteristics of our OT set-up allow us to directly observe the fluctuations (“hopping” events) of the individual macrocycles between the two stations for the very first time. Access to the hopping events will permit a detail characterization of the full set of kinetic parameters describing the force shuttling kinetics and the free energy difference between the two stations. In hopping experiments the kinetics of ring movement between stations can be monitored in real time by keeping constant Force between the beads.

Typical records of extension change under fixed load (Figure III-10 right panels) show two-state hopping behavior. The macrocycle transits between the two stations due to thermal fluctuations. These transitions have been measured as individual shuttling events between the values of extensions corresponding to the fumaramide and succinic amide-ester stations. Again, the extension of the hopping events is in concordance with the distance between the two stations, ~ 10 nm. We were delighted to observe that when the macrocycle explores the succinamide-ester station in one of its thermally induced shuttling trips, it resides over it for a measurable amount of time, in the range of several tenths of a second.

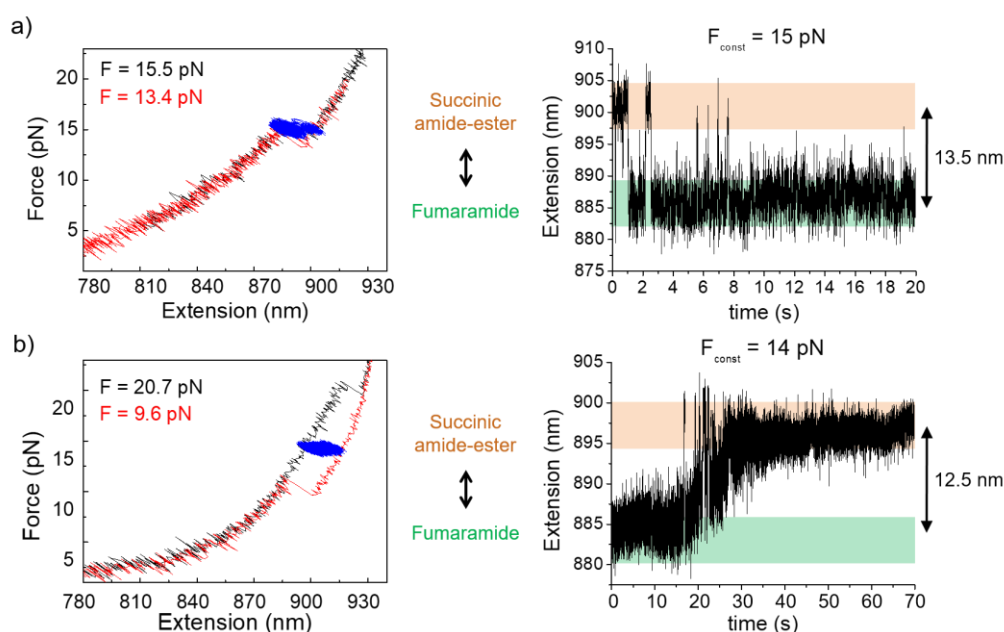


Figure III-10. Representative examples of “hopping” experiments showing mechanical fatigue for two individual rotaxanes a) and b). On the right, pulling (in black) and relaxing (in red) cycles. When we applied a constant force between the rupture and rebinding forces, 15 pN and 14 pN for examples a) and b) respectively, we are able to observe the macrocycle of the rotaxanes “hopping” from the fumaramide station to the succinic amide-ester station in real time. We have monitored this shuttling events through changes in extension with respect the time (graphs in right), which is shows as a blue trace in the force-extension graphs. In both cases the difference in extension obtained in the shuttling events are in accordance with the theoretical length of the fully extended oligoethyleneglycol spacer between the two stations (around 10 nm). Note that after a few seconds shuttling events stop and the ring is stuck at one station. In the example showed in b, the ring gradually spends more time in the succinic amide-ester station, until finally it was stuck at this station.

However, we observed again that our initial design shows fatigue after a few cycles, the macrocycle stopped hopping typically after around 10-20 seconds of measurements, as it is shown in the hopping experiments depicted in Figure III-10. A plausible explanation for these results could be related with the fact that the rotaxane was directly attached to the polystyrene microsphere surface, and the movement of the macrocycle along the track could be inhibited by physisorption onto the bead.

In an attempt to fine-tune the setup and prevent fatigue, we decided to separate the rotaxane from the polystyrene microsphere surface. For this purpose, we used a dsDNA handle (830 bp, $\sim 0.3 \mu\text{m}$) labelled with a streptavidin (via biotin-streptavidin connections) in one end and with a Dig in the other end, that serves as a spacer between the rotaxane and the polystyrene bead. The final set up is schematically depicted in Figure III-11.

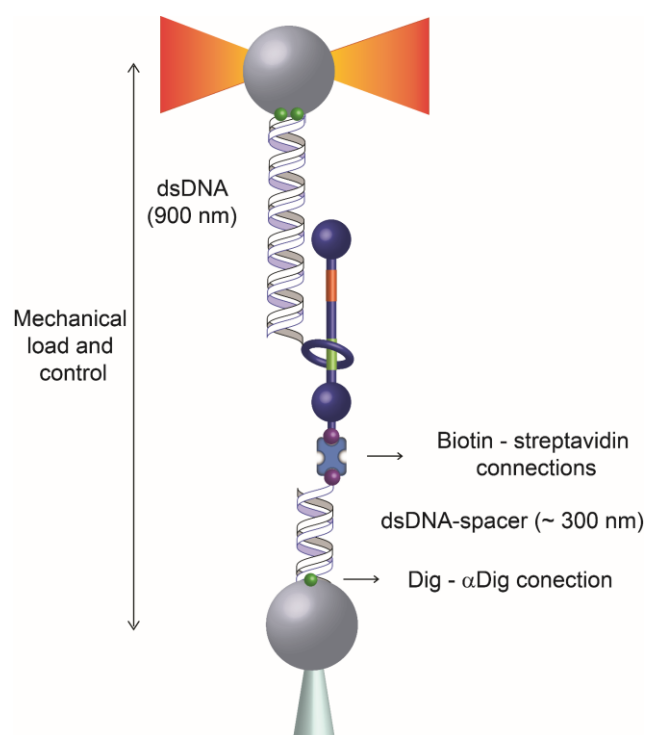


Figure III-11. Schematic representation of the new layout of the rotaxane attachment into the OT set up (not to scale). In the new set-up a dsDNA spacer ($\sim 300 \text{ nm}$), attached to the bead on the micropipette, separates the rotaxane molecule from the surface of the polystyrene microbead.

Individual rotaxane-DNA constructs were stretched in a controlled manner by moving the optical trap away from the micropipette at a fixed pulling rate. The force-extension profiles obtained were in perfect agreement with those obtained with the previous set up, the change in the contour length of the molecule (“the peak”) correspond to the extension gained when the ring moves from one station to the other. With this new experimental set-up, multiple (>90)

stretching-relaxing cycles were performed on a single molecule (Figure III-12b), indicating that separation from the bead helps to decrease the mechanical fatigue observed before. In Figure III-12b are depicted the distributions obtained for 90 pulling/relaxing cycles on a representative molecule.

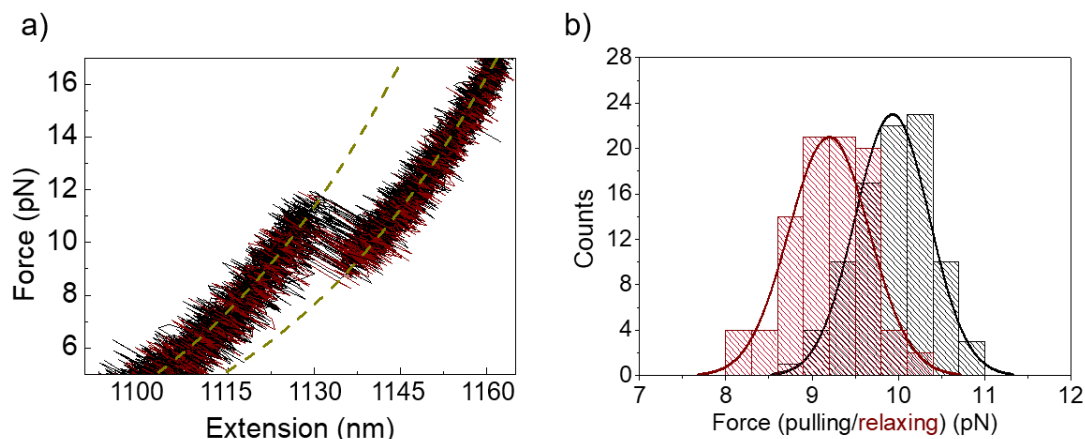


Figure III-12. a) Force-extension curves for 90 consecutive pulling (black traces)/relaxing (blue traces) cycles of a single rotaxane molecule (pulling rate: 200 nm/ s). The dashed lines represent the theoretical force-extension curves obtained using WLC model. b) Distributions of the pulling/relaxing forces.

From the intersection of the rupture forces distributions of the pulling and relaxing cycles, it can be extracted the coexistence force value ($F_{1/2}$) that represents the force under which the macrocycle has an equal probability of being in the fumaramide or succinic amide-ester station. This value was found to be 9.56 pN.

Fluctuation theorems relate the equilibrium free-energy change, ΔG , to non-equilibrium measurements of the work done on a single molecule. The Crook's fluctuation theorem relates ΔG to the probability distributions of the non-equilibrium work measured during the forward and reverse changes that occur when a system is driven away from thermal equilibrium by the action of an external perturbation.²¹⁶ Using CFT, we estimate the free energy driving the macrocycle to bind to the fumaramide station, this value was found to be $38 \pm 3 k_B T$.

Next, we performed the hopping experiments described before. We were glad to observe that, by separating the rotaxane out of the polystyrene surface, we were able to follow the rotaxane movement along minutes in the experiments at constant force, recording hundreds of individual shuttling events; examples of these experiments are depicted in Figure III-13.

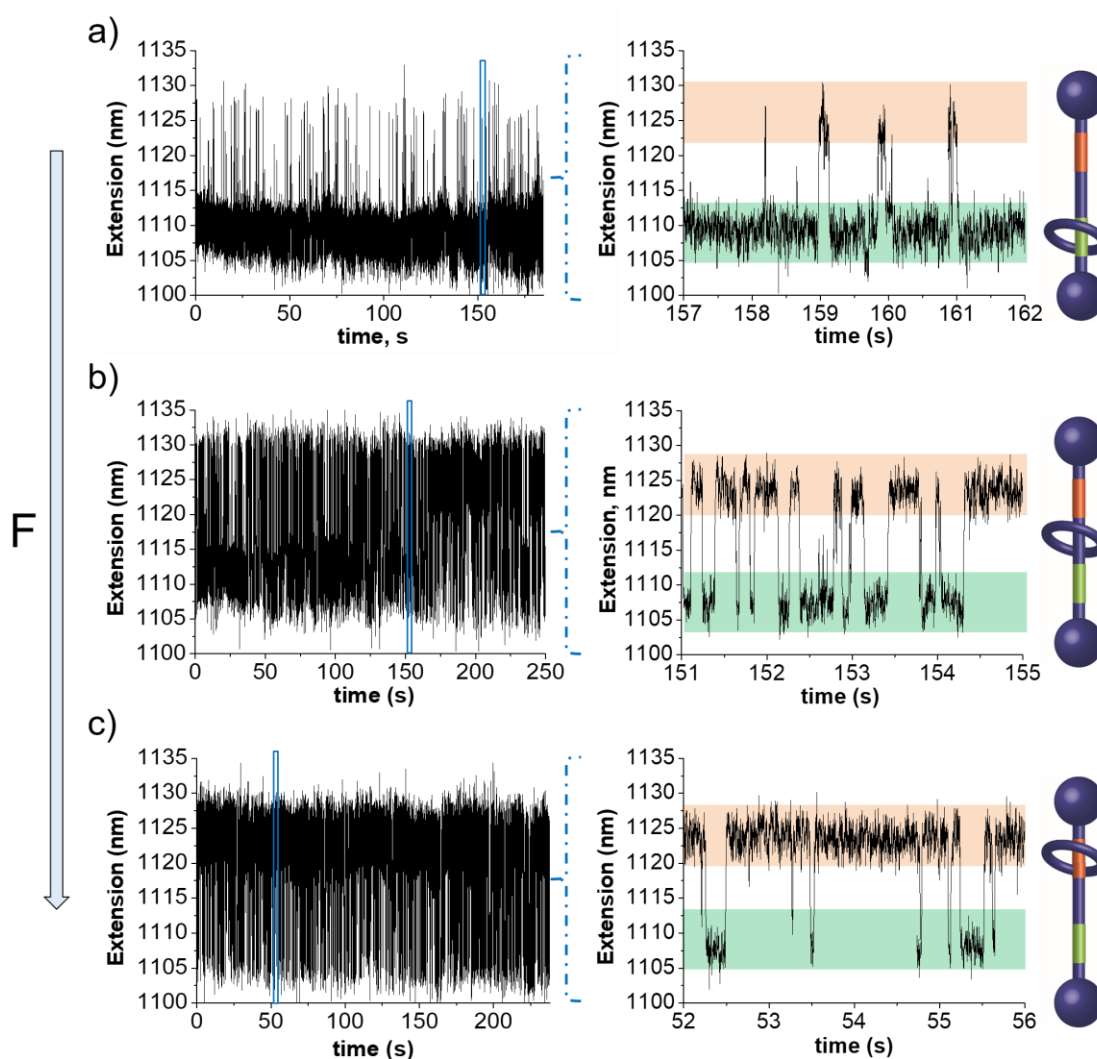


Figure III-13. Experiments carried out at constant force for three individual rotaxanes a to c: a) 8.2 pN; b) 9 pN and c) 10 pN. On the right, are shown the “hopping events” as changes in extension with respect the time. On the left is depicted an expansion of the selected area boxed in blue. The difference in extension gained in the shuttling events is again in concordance with the theoretical length of the fully extended spacer between the two stations (~10 nm). By increasing the force from 8.2 pN in a to 10 pN in c, the macrolyce gradually spends more time in the weak station and less time in the strong one, until finally prefers the succinamide-ester station. On the far right are depicted three schemes of the rotaxane molecule showing the variation of the binding site preference of the macrocycle.

We have seen that the presence of two stations implies that the energy landscape of the rotaxane is dominated by two potential wells separated by a single barrier. The application of force tilts the energy landscape, changing the free-energy difference between the weak and strong stations. The transitions observed at a constant force can be broken into "waiting times" in which the macrocycle undergoes Brownian motion near one station, and a barrier interaction time in which the ring travels from one station to the other. At a glance, we notice that this

transition time is much shorter than the waiting times on either station. This fact is in agreement with natural motors,²¹⁷ and theoretical models.²¹⁸

By increasing the force from 8.2 pN (Figure III-13a) to 10 pN (Figure III-13c) we are able to observe the macrocycle gradually spending more time in the weak succinic amide-ester station and less time in the strong fumaramide station, until finally preferring the weak one (Figure III-13c). In other words, not only can we observe the shuttling events due to thermal fluctuations, but we can also control the average position of the macrocycle, that is, the waiting times spent on each of the stations, favoring one or the other. We were also able to apply a constant force very close to the coexisten force, the force under which the macrocycle has an equal probability of being in the fumaramide or succinic amide-ester station (9 pN, Figure III-13b).

Another related example, depicted in Figure III-14, allowed us to visualize how the macrocycle of a single molecular shuttle changes its preferences by changing the force applied; under 8.3 pN of force the macrocycle resides predominately over the fumaramide station, making scarce hopping to the weak statio. However, by increasing the force to 8.8 pN we were able to see how the macrocycle trend changed exhibiting almost equal preference for both stations.

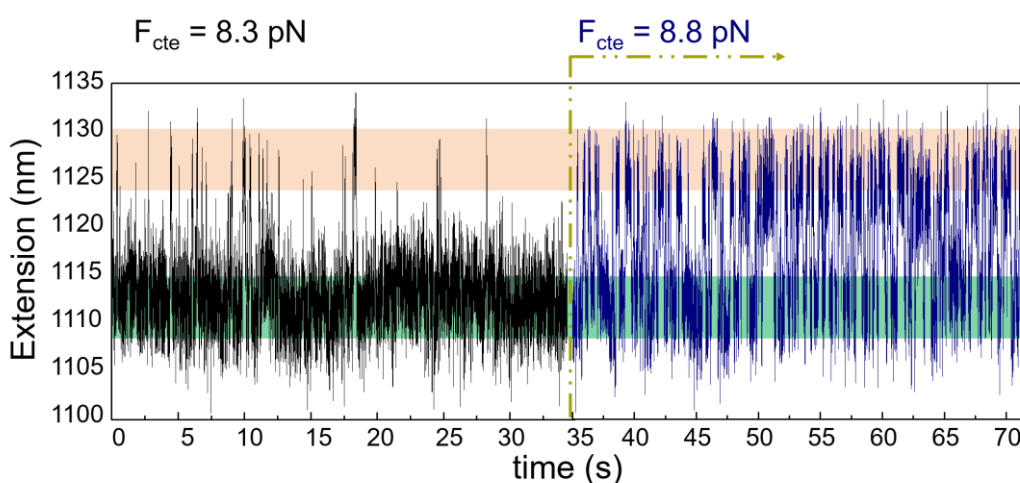


Figure III-14. Extension versus time graphs at a constant force: first we applied a constant force of 8.3 pN (black trace); under which, the macrocycle preffers to stay at the thermodynamic most stable station. By increasing the force to 8.8 pN (blue trace) we were able to observe how this trend change, exhibiting almost equal average lifetimes.

These measurements represent the very first time that a macrocycle “hopping” between stations in an individual molecular shuttle has been observed. Our experimental results fulfill the dream of Stoddart and Astumian in their recent review²¹⁸ where they wished for a “yet undeveloped high resolution microscopic method” that would allow for the observation of 8 to 10 transitions of an individual molecular machine”.

3.2.3. Force-dependent kinetic rates

Through these experiments, in which we apply a constant force, we mechanically induce the ring movement between one station to the other, in other words, force shifts equilibrium from one station to the other. By monitoring the change in contour length of the molecule we are able to feature the ΔG and kinetic rates of the molecule. Ideally, the molecular rates exponentially depend on the applied force according to the Bell-Evans (BE) model. The BE model was the result of Evans' adaptation of the work introduced by Bell in 1978²¹⁹ and adapted for dynamic force spectroscopy,^{40, 42} and had been recently applied to study the kinetics of nucleotide hairpins.²²⁰ This model posited the relationship between force and lifetimes at the single molecular level according to Eqs. 1 and 2:

$$k_f(F) = k_0 \exp\left(-\frac{B - F x_s^\ddagger}{k_B T}\right) = k_m \exp\left(\frac{F x_s^\ddagger}{k_B T}\right) \quad (1)$$

$$k_s(F) = k_0 \exp\left(-\frac{B - \Delta G_{f \rightarrow s} - F x_f^\ddagger}{k_B T}\right) = k_m \exp\left(\frac{\Delta G_{f \rightarrow s} - F x_f^\ddagger}{k_B T}\right) \quad (2)$$

where k_B is the Boltzmann constant; B is the height of the kinetic barrier; $k_m = k_0 \exp(-B/k_B T)$, where k_m is the unfolding kinetic rate at zero force $k_f(0) = k_m$; x_f^\ddagger and x_s^\ddagger are the relative distances between fumaramide station, f , and succinic-amide ester station, s , with respect to the transition state (x^\ddagger) at the coexistence force ($F_{1/2}$); $x_f^\ddagger = x_f - x^\ddagger$, $x_s^\ddagger = x^\ddagger - x_s$. Their sum should be equal to the molecular extension $x_{f \rightarrow s} = x_s^\ddagger + x_f^\ddagger = x_s - x_f$; and $\Delta G_{f \rightarrow s} = F_{1/2} x_{f \rightarrow s}$ is related to the free-energy difference between stations f and s . Note that $k_f(F_{1/2}) = k_s(F_{1/2})$.

We have studied if our molecular shuttle behaves according to the BE model, if a log-normal representation of the unfolding or folding kinetic rates versus force, follow such model. For this, from the hopping experiments, we first extracted the average lifetime (Experimental section) of the macrocycle staying at the fumaramide station τ_f and at the succinic amide-ester station τ_s at every force studied, results are depicted in Table III-1.

Table III-1. Average lifetimes in seconds.

Force, pN	τ_f (fumaramide station)	τ_s (succinic amide-ester Station)
9.69	0.0269	0.4272
9.21	0.0686 ± 0.0145	0.1830 ± 0.0230
8.82	0.0585 ± 0.0185	0.0489 ± 0.0141
8.61	0.1369 ± 0.0329	0.1225 ± 0.0463
8.31	0.1485 ± 0.0127	0.0098 ± 0.0050
8.13	1.0040 ± 0.2520	0.0222 ± 0.0034

From the average lifetimes, we can calculate the kinetic rates for the succinic amide-ester station \rightarrow fumaramide station transition, $k_s(F)$, and viceversa $k_f(F)$, since $k_s = 1/\tau_f$ and $k_f = 1/\tau_s$, at each force (Experimental section).

The experimentally measured $k_s(F)$ and $k_f(F)$ were fitted to Eqs. (1) and (2) along the range of forces available experimentally. Results of such linear fits (in a $\ln k$ versus F representation) are shown in Figure III-15 (solid blue and brown lines). Our molecular shuttle fits reasonably well to the BE model, conforming to a Boltzman distribution. From the fits, we can determine the main parameters that characterize the free energy landscape of the molecular shuttle, according to the BE theory: the unfolding kinetic rate at zero force (k_m), the free energy difference ($\Delta G_{f \rightarrow s}$), the coordinate of the transition state respecting to the strong station (x_f^\ddagger) and the weak station (x_s^\ddagger) and the coexistence force ($F_{1/2}$). The numerical results are summarized in Table III-2.

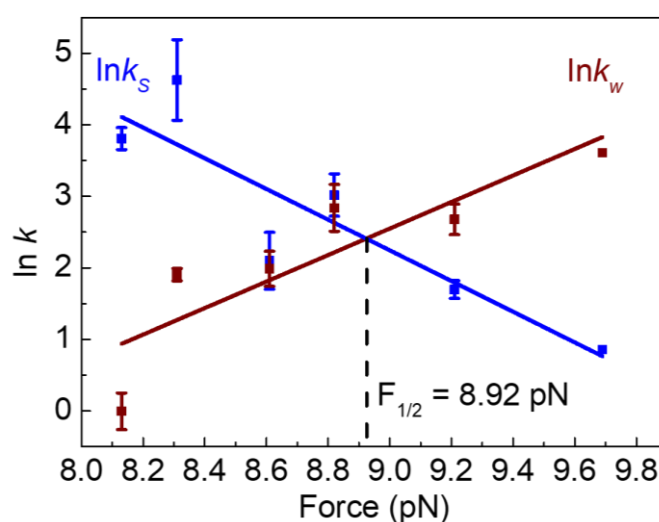


Figure III-15. Representation of $\ln k_s$ and $\ln k_w$ versus force, blue and red dots respectively, showing bar errors. Linear fits to the BE model are shown as blue and brown solid lines.

Table III-2. Kinetic parameters obtained experimentally

k_m, s^{-1}	x_f^\ddagger, nm	x_s^\ddagger, nm	$F_{1/2}, \text{pN}$	$\Delta G_{f \rightarrow s}, k_B T$
$(7.52 \pm 0.01) \times 10^{-7}$	9 ± 2	7 ± 2	8.92	34 ± 2

The difference in free energy between the macrocycle binding to the fumaramide and succinic amide-ester stations, calculated was $34 \pm 2 k_B T$ ($20 \pm 1 \text{ kcal/mol}$; $83 \pm 5 \text{ kJ/mol}$), this result is higher than the $9.3 k_B T$ determined previously by AFM²⁰⁸; however, it should be noticed that we were working under aqueous phase conditions, not comparable with DMF solvent used in the AFM studies; moreover the chemical structure of both molecular shuttles is different in many points.

In conclusion, at the molecular level where thermal fluctuations govern, the dynamics of individual rotaxanes displays fast and stochastic behavior, when subjected to mechanical force. We observe this ‘noisy’ or stochastic behavior experimentally, from single-molecule data, which is an integral part of the mechanism of shuttling and contains important information on the submolecular motion itself. Direct access to the statistical nature of these fluctuations requires appropriate statistical treatment of the data (using the fluctuation theorems previously cited), which is being carried out in collaboration with the laboratory of Prof. Felix Ritort, experts in the field of the non-equilibrium thermodynamics of small systems.

Through this work we have been able to observe experimentally an individual molecular shuttle hopping from one station to the other hundreds of times, along minutes. Such observations have not been possible with other single-molecule techniques, such as AFM, and offer the opportunity to compare the theoretical models with experimental data for the very first time. In particular, we have characterized successfully the mechano-chemical cycle of the operation of a molecular shuttle, by determining the coexistence force, the coupling constants, the velocities and the the coordinate of the transition state. For this we have applied the BE models, so that we probe the relationship between force and residing lifetime of the macrocycle over each station. In this way, we have helped understand how thermal Brownian fluctuations of the macrocycle are converted to submolecular motion. Moreover, we have adapted the molecular shuttle to operate under biocompatible conditions. Our approximation allows comparing the operation system at molecular level of synthetic and biological systems under the same experimental conditions. This is important because strength and dynamics of weak non-covalent interactions are strongly modulated by the surrounding environment. In addition, opens up the possibility to study more complex synthetic-devices at single molecular level under aqueous conditions.

3.3. Experimental Section

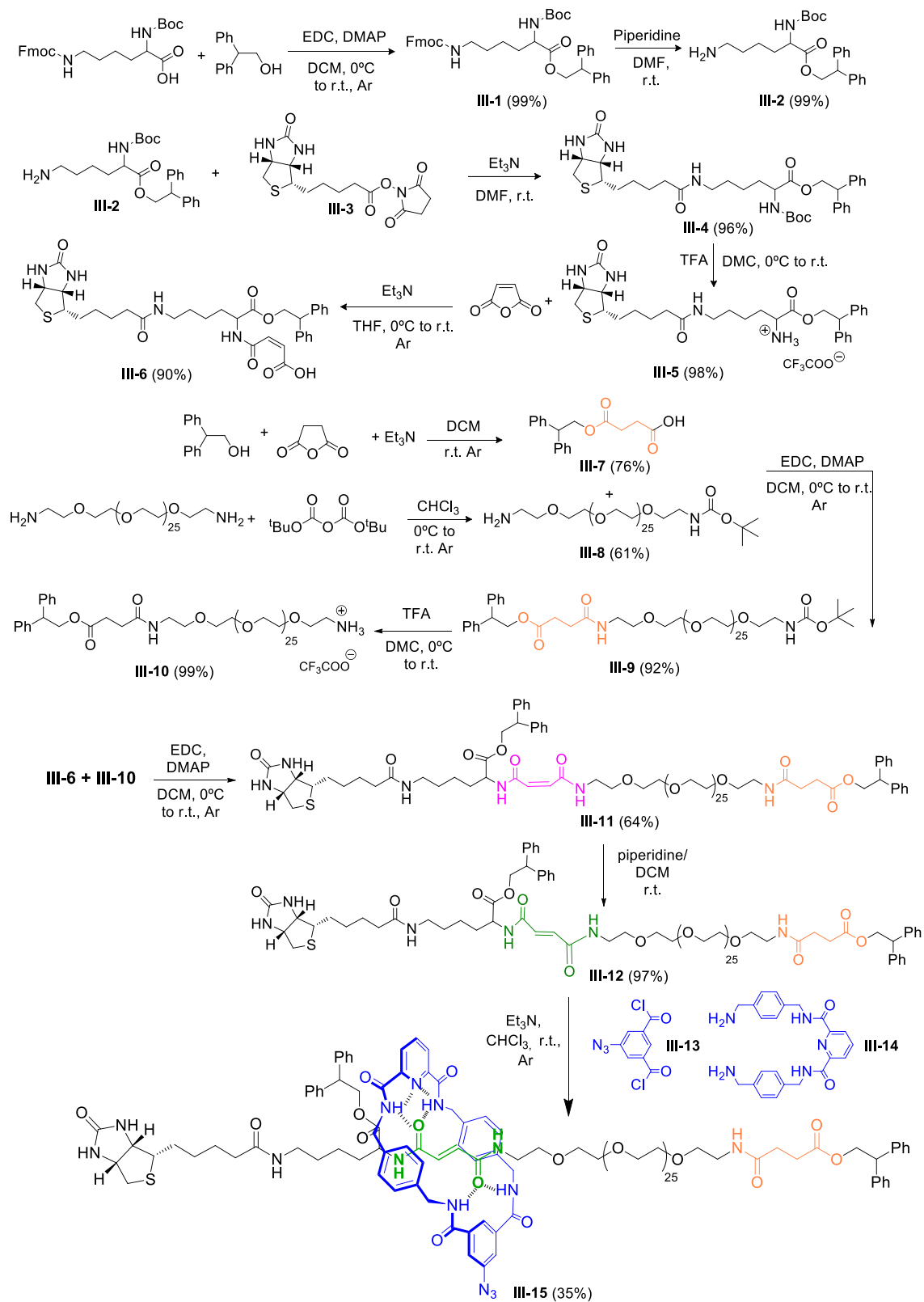
Contents:

- 3.3.1. Rotaxane Synthesis
- 3.3.2. Oligonucleotide synthesis
- 3.3.3. Copper-free click reaction
- 3.3.4. Mass spectral data of synthesized oligonucleotides
- 3.3.5. Synthesis of DNA construct
- 3.3.6. Optical Tweezers experiments
- 3.3.7. Kinetic rates in the Bell-Evans model

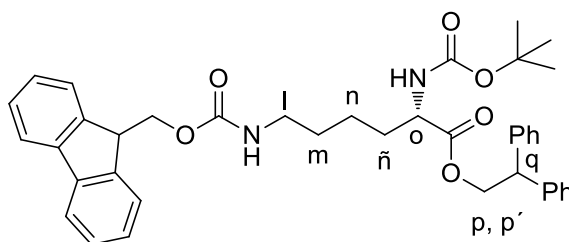
3.3.1. Rotaxane Synthesis

General. All solvents were dried according to standard procedures. Reagents were used as purchased. All air-sensitive reactions were carried out under argon atmosphere. Flash chromatography was performed using silica gel (Merck, Kieselgel 60, 230-240 mesh, or Scharlau 60, 230-240 mesh). Analytical thin layer chromatographies (TLC) were performed using aluminium-coated Merck Kieselgel 60 F254 plates. NMR spectra were recorded on a BrukerAvance 400 (^1H : 400 MHz; ^{13}C : 100 MHz), spectrometer at 298 K, unless otherwise stated, using partially deuterated solvents as internal standards. Coupling constants (J) are denoted in Hz and chemical shifts (δ) in ppm. Multiplicities are denoted as follows: s = singlet, d = doublet, t = triplet, m = multiplet, br = broad. Fast Atom Bombardment (FAB) and Matrix-assisted Laser desorption ionization (coupled to a Time-Of-Flight analyzer) experiments (MALDI-TOF) were recorded on a VS AutoSpec spectrometer and a Bruker ULTRAFLEX III spectrometer, respectively.

Scheme of the rotaxane Synthesis

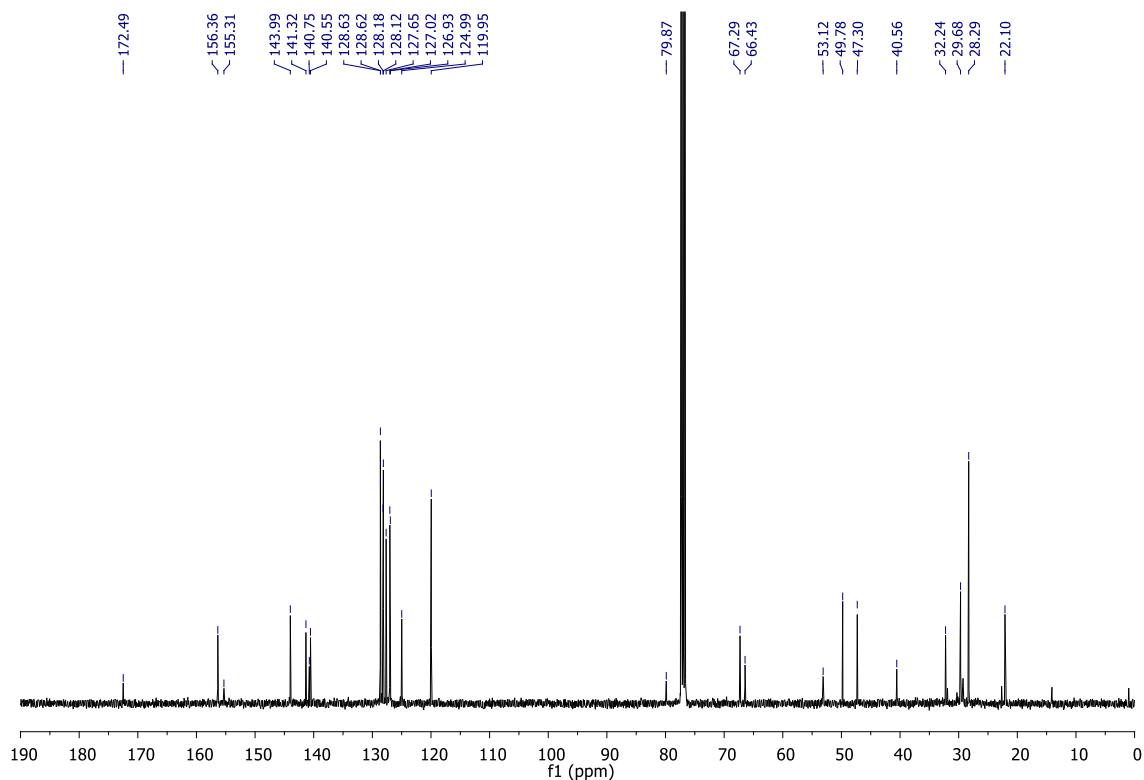
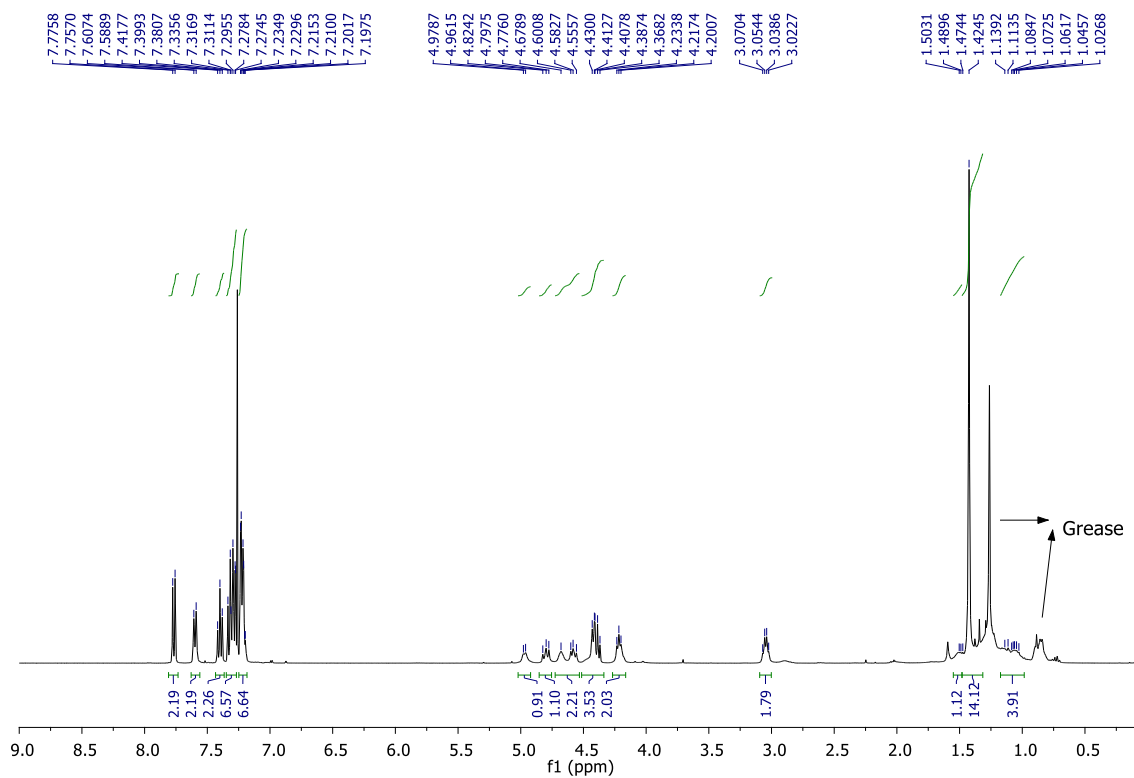


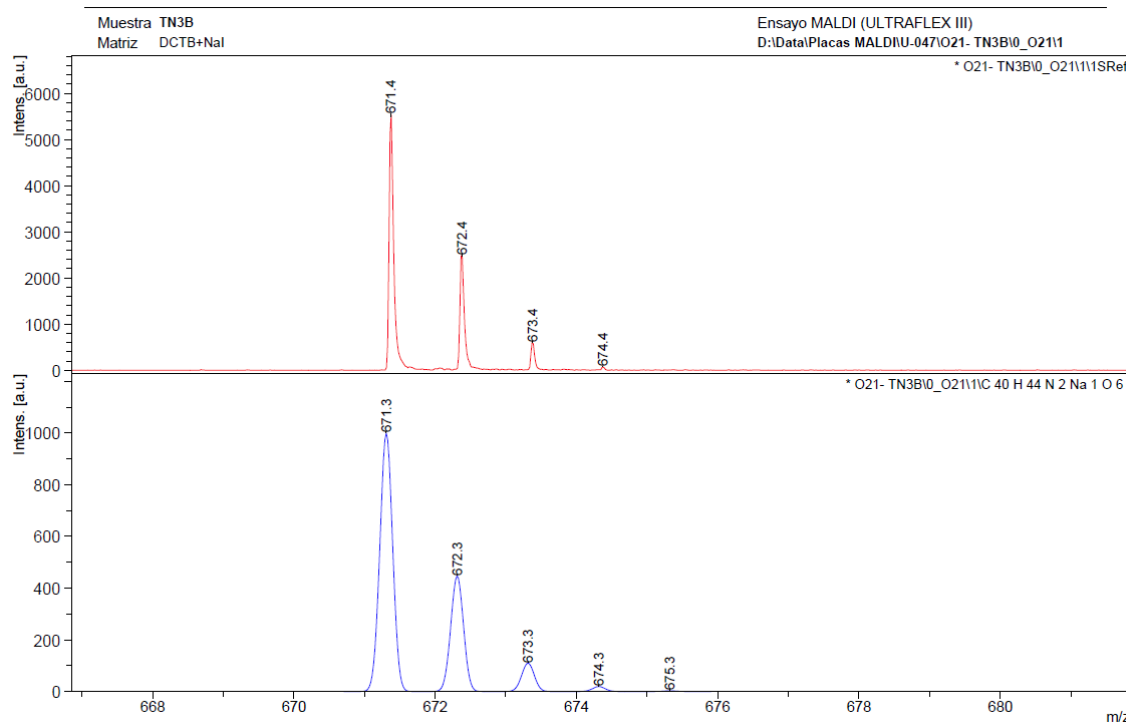
2,2-diphenylethyl 6-(((9H-fluoren-9-yl)methoxy)carbonyl)amino)-2-[(*tert*-butoxy-carbonyl)amino]}hexanoate



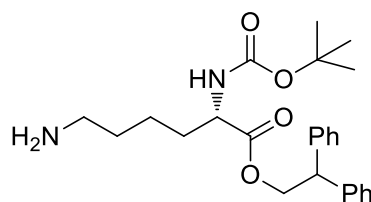
Compound III-1

Boc-D-Lys(Fmoc)-OH (900 mg, 1.92 mmol) was dissolved in DCM (19 mL) and the solution was cooled to 0°C, 1-ethyl-3-(3-dimethylaminopropyl)carbodiimide hydrochloride (EDCI) (732 mg, 3.84 mmol), 4-dimethylaminopyridine (DMAP) (catalytic amount) were added at 0°C. The reaction mixture was allowed to stir at room temperature for 30 min, and then a solution of 2,2-diphenylethanol (457 mg, 2.3 mmol) in DCM (7.7 mL) was added to the activated acid. The reaction mixture was stirred overnight, concentrated under reduced pressure and then diluted with DCM. The organic layer was washed with 1M HCl, with NaHCO₃ (sat. aq.), then further washed with brine (sat. aq.), dried over Na₂SO₄ and concentrated under reduced pressure. The crude material was purified by column chromatography (eluent: hexane: AcOEt 3:1) to furnish the desired product as a colorless oil, 1.12g (quantitative yield). ¹H NMR (CDCl₃): δ = 7.77 (d, *J* = 7.5 Hz, 2H, Fmoc-H), 7.60 (d, *J* = 7.4 Hz, 2H, Fmoc-H), 7.40 (t, *J* = 8 Hz, 2H, Fmoc-H), 7.30 (m, 6 H, Ar-H), 7.22 (m, 6 H, Ar-H, Fmoc-H), 4.97 (m, 1 H, H_{fmoc}), 4.80 (m, 1 H, H_p or H_{p'}), 4.68 (m, 1 H, NH), 4.58 (m, 1 H, H_p or H_{p'}), 4.41 (m, 3 H, H_q, CH₂-Fmoc), 4.22 (m, 2 H, H_o, NH), 3.05 (m, 2 H, H_l), 1.50 (m, 2H, H_m), 1.42 (s, 9 H, Boc-H), 1.07 (m, 4H, H_n, H_ñ); ¹³C NMR (CDCl₃): δ= 172.5, 156.4, 155.3, 144.0 (2C), 141.3 (2C), 140.8, 140.6, 128.6 (2C), 128.6 (2C), 128.2 (2C), 128.1 (2C), 127.7 (2C), 127.0 (2C), 126.9 (2C), 125.0 (2C), 120.0 (2C), 79.9, 67.3, 66.4, 53.1, 49.8, 47.3, 40.6, 32.2, 29.7, 28.3, 22.1 (3C) ppm. MS m/z: calculated for C₄₀H₄₄N₂O₆ [M+Na]⁺ 671.4 found MALDI-TOF 671.3.





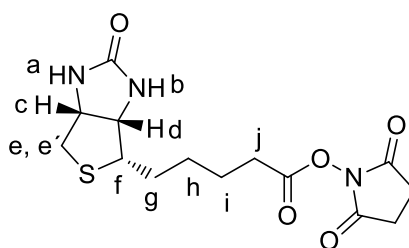
2,2-diphenylethyl 6-((((9H-fluoren-9-yl)methoxy)carbonyl]amino)-2-aminohexanoate



Compound III-2

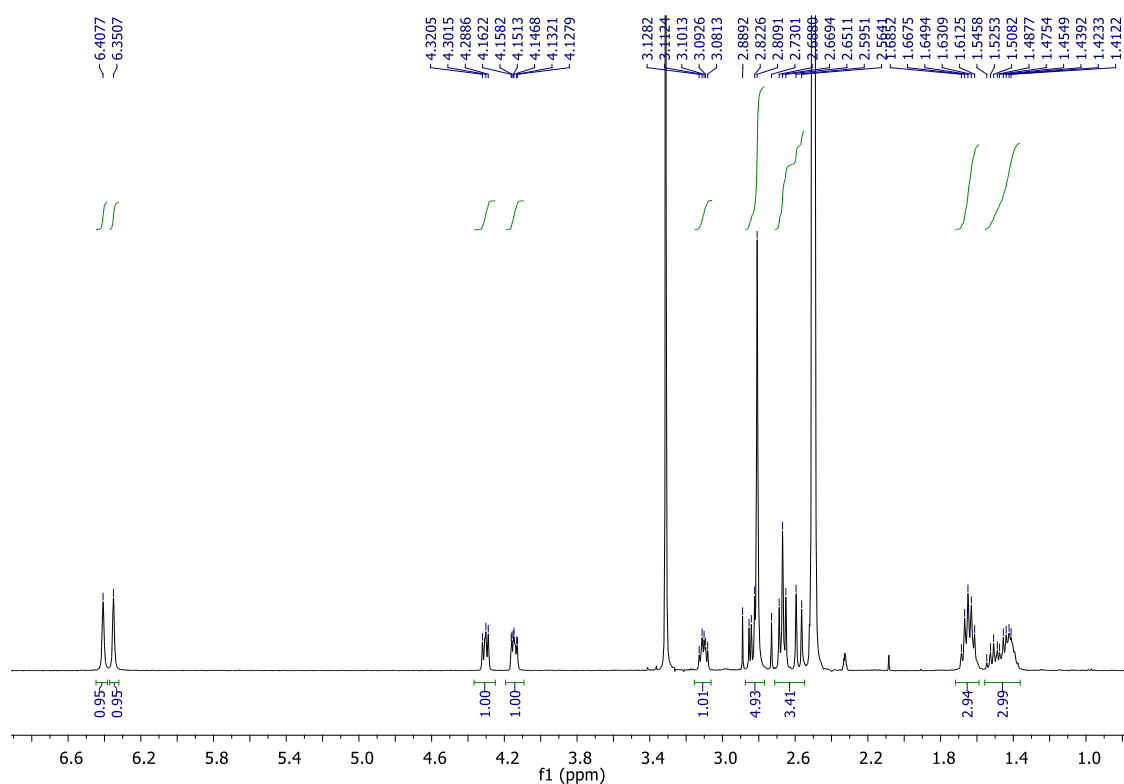
90mg (0.14 mmol) of compound **III-1** was dissolved in 1% pyridine and 1% DBU in DMF (2.8 mL). The reaction mixture was stirred for three hours at room temperature until the reaction was completed (TLC). The solvent was removed under reduced pressure to give compound **III-2** as yellowish oil (quantitative yield) and the crude material was used directly in the next step reaction.

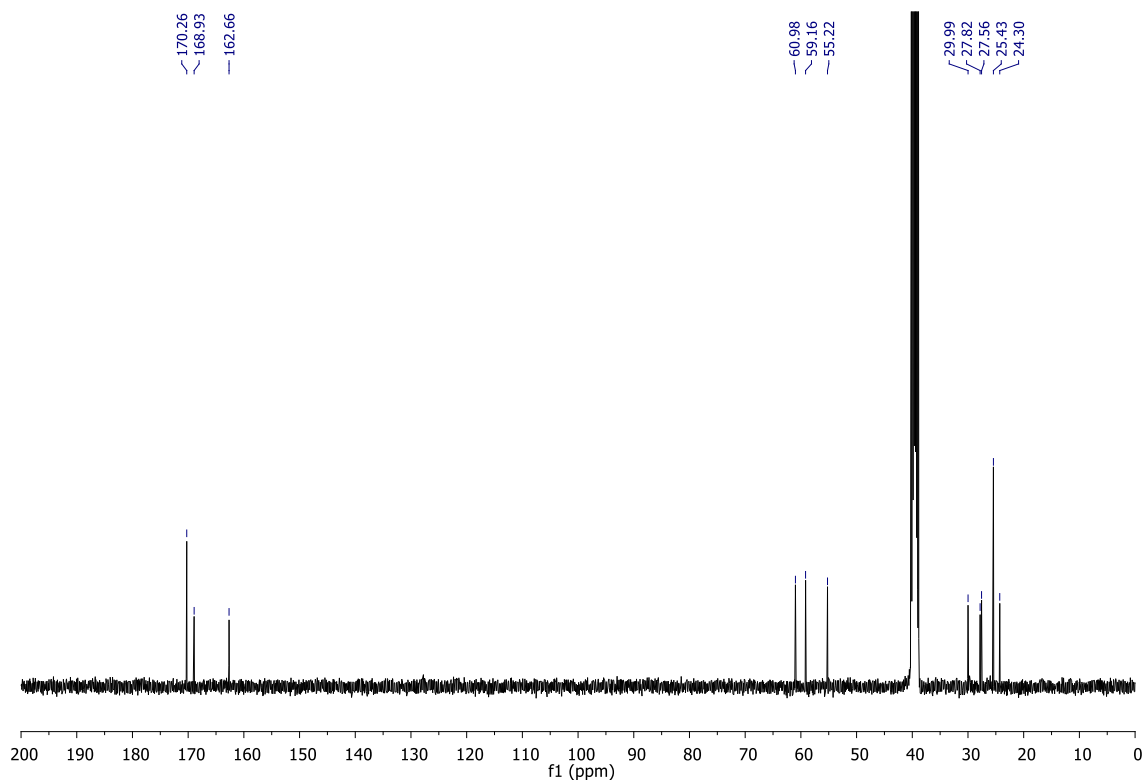
Biotinyl-N-hydroxy-succinimide, N-Hydroxysuccinimidobiotin, N-Succinimidyl D-biotinate, NHS-Biotin



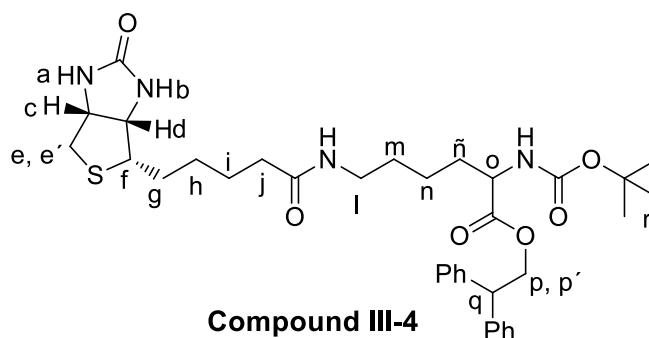
Compound III-3

To a solution of D-biotin (75 mg, 0.31 mmol) and *N*-hydroxysuccinimide (39 mg, 0.34 mmol) in DMF, was added EDCI (71 mg, 0.37 mmol). After being stirred for 24h at room temperature, the reaction solution was concentrated to obtain a white solid. The white solid was washed by methanol several times to furnish compound **III-3** in a 90% yield (96mg, 0.28mmol). ^1H NMR ([D6]dimethyl sulfoxide): δ = 6.41 (s, 1H, H_a), 6.35 (s, 1H, H_b), 4.30 (m, 1H, H_c), 4.15 (m, 1H, H_d), 3.10 (m, 1H, H_f), 2.83 (dd, J = 5.1, 12.5 Hz, 1H, H_e or H_{e'}), 2.81 (s, 4H, succinimida-H), 2.67 (t, J = 7.36 Hz, 2H, H_j), 2.58 (d, J = 12.4 Hz, 1H, H_e or H_{e'}), 1.55 (m, 6H, H_h, H_i, H_j); ^{13}C NMR ([D6]dimethyl sulfoxide): δ = 173.3 (3C), 168.9, 162.7, 61.0, 59.2, 55.2, 30.0, 27.8, 27.6, 25.4 (2C), 24.3 ppm. These data is in concordance with *J. Med. Chem.* 52, **2009**, 7003-7013.



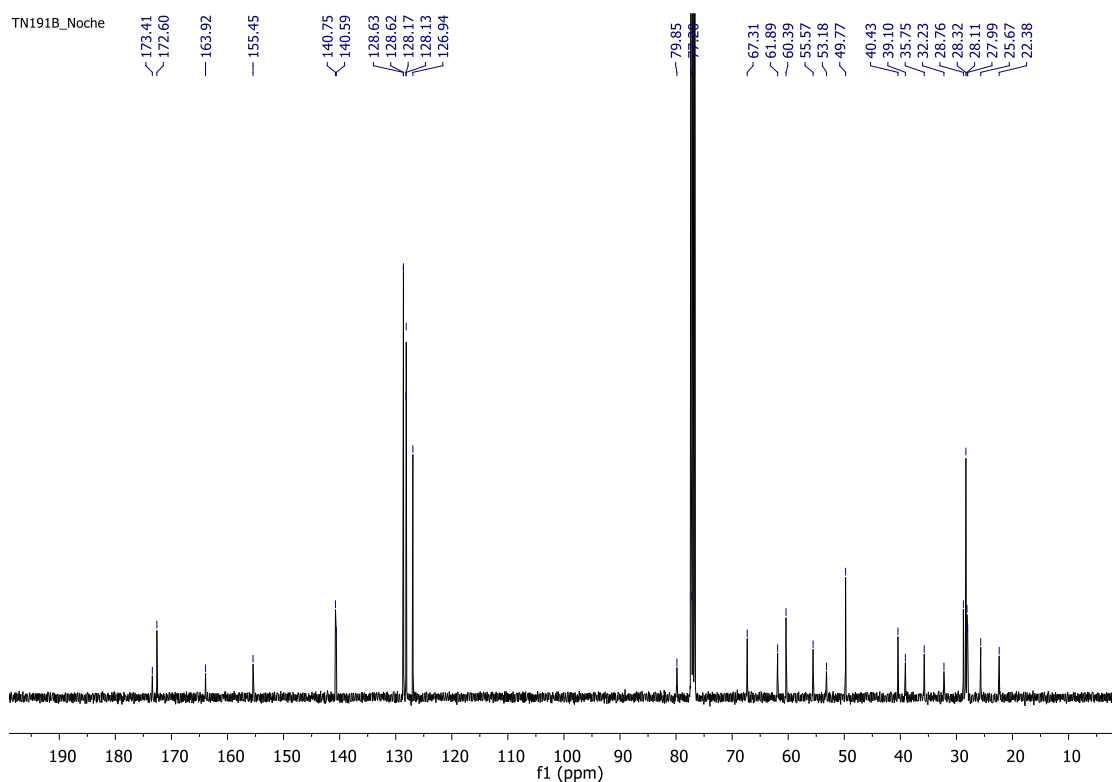
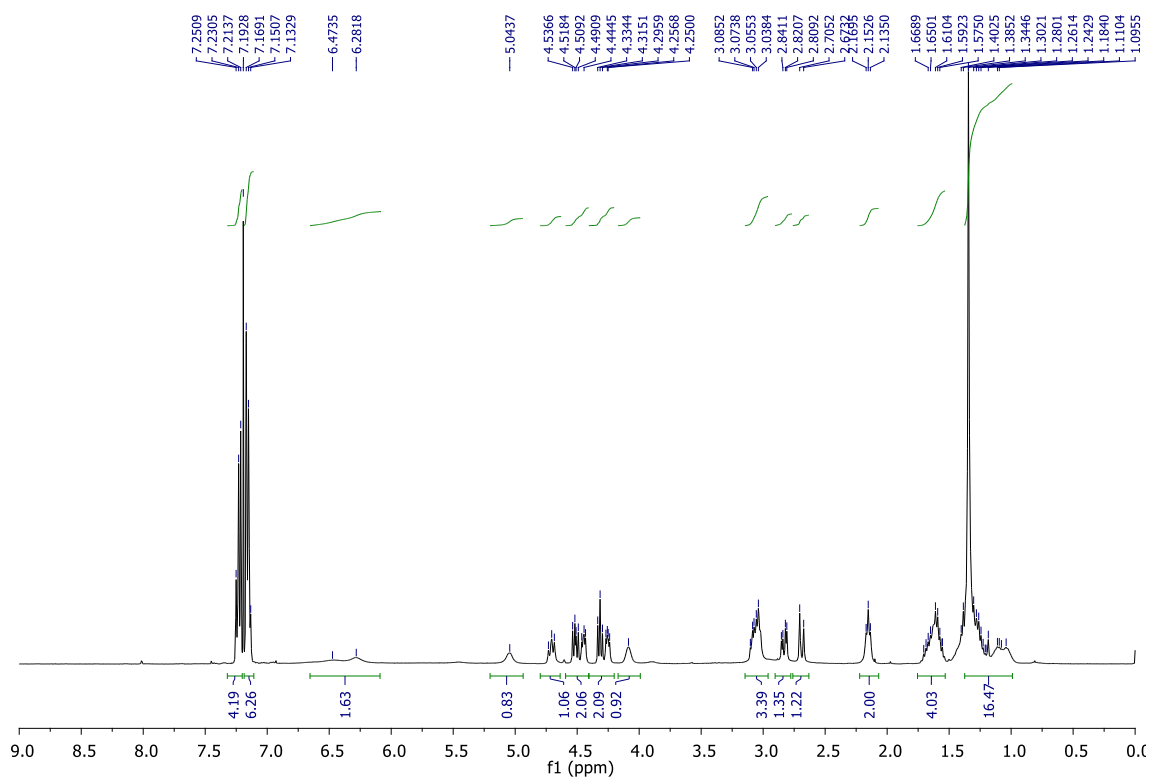


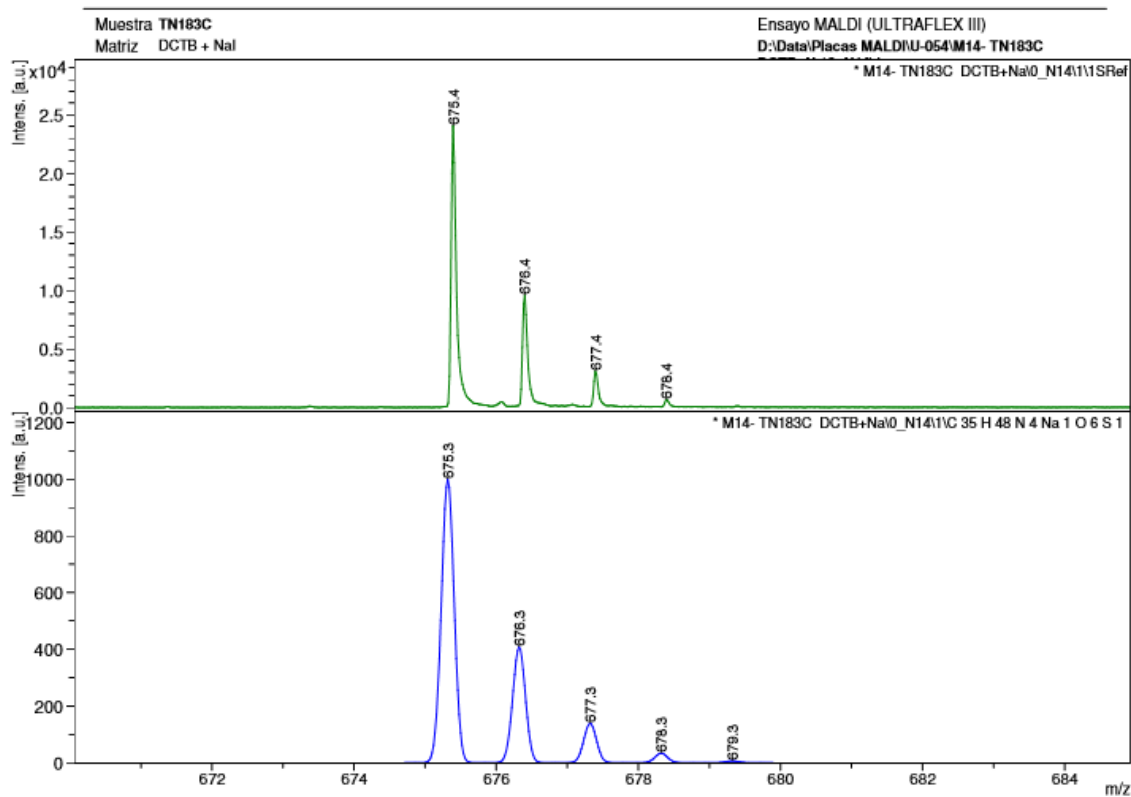
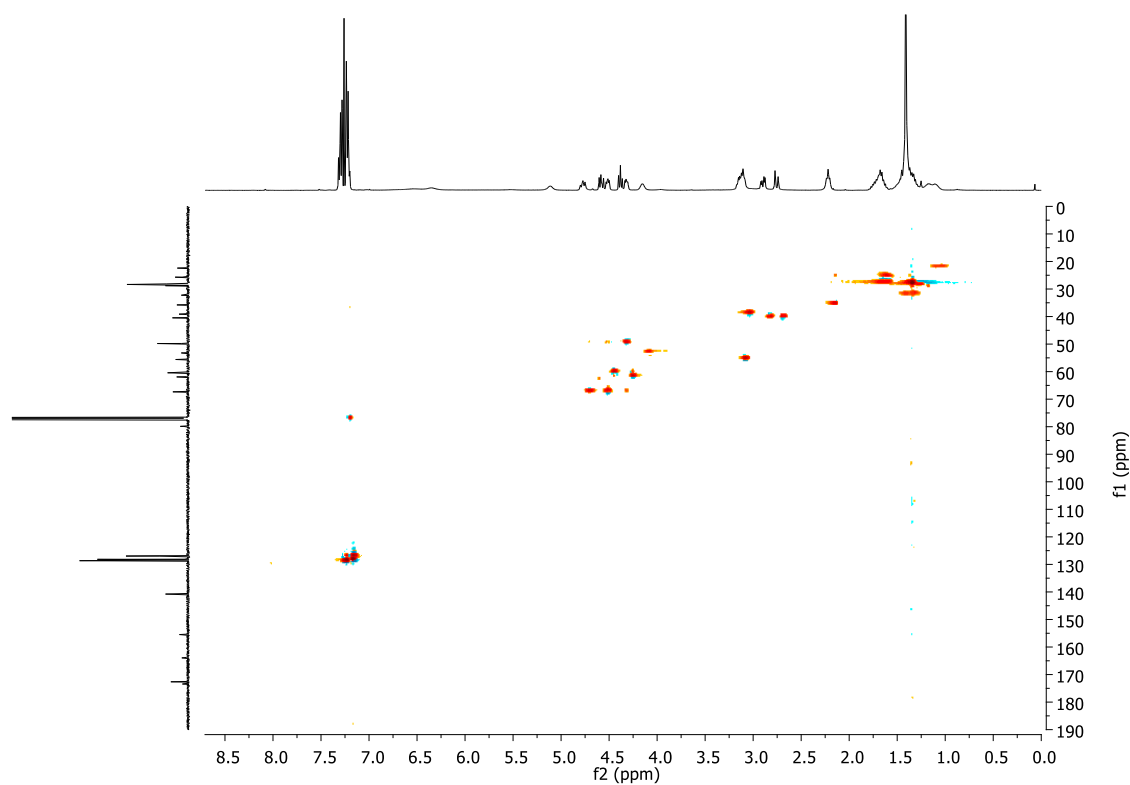
2,2-diphenylethyl 2-[(tert-butoxycarbonyl)amino]-6-(biotinylamino) hexanoate

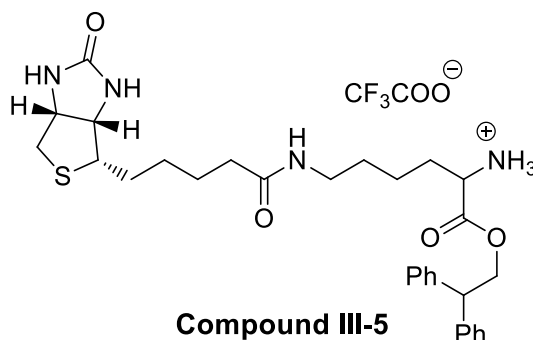


Compounds **III-2** (46 mg, 0.110 mmol) and **III-3** (25 mg, 0.073 mmol) were dissolved in DMF, and then Et₃N (20 μL, 0.144 mmol) was added. The reaction mixture was stirred overnight; then was concentrated in vacuum; the resulting residue was diluted in DCM and washed by water. The crude material was then purified by flash chromatography (using a gradient elution, from CH₃Cl to CH₃Cl/MeOH 9:1) to furnish **III-4** as a colorless oil, 45 mg, 96 %. ¹H NMR (CDCl₃): δ = 7.23 (m, 4 H, Ar-H), 7.14 (m, 6 H, Ar-H), 6.47 (br s, 1 H, H_a), 6.28 (br s, 1 H, H_b), 5.04 (br s, 1 H, NH), 4.71 (m, 1 H, H_p or H_{p'}), 4.52 (dd, *J* = 7.3, 11.0 Hz, 1 H, H_p or H_{p'}), 4.45 (dd, *J* = 4.8, 7.1 Hz, 1 H, H_c), 4.32 (t, *J* = 7.7 Hz, 1 H, H_q), 4.25 (dd, *J* = 4.5, 7.2 Hz, 1 H, H_d), 4.09 (br s, 1 H, H_o), 3.07 (m, 3 H, H_f, H_i), 2.83 (dd, *J* = 4.7, 12.9 Hz, 1 H, H_e or H_{e'}), 2.69 (d, *J* = 12.8 Hz, 1 H, H_{e'} or H_e), 2.17 (t, *J* = 6.8 Hz, 2 H, H_j), 1.61 (m, 4 H, H_g, H_i), 1.34 (s, 9 H, Boc-H), 1.11 (m, 8 H, H_h, H_n, H_m, H_{n̄}); ¹³C NMR (CDCl₃): δ = 173.4, 172.6, 163.9, 155.5, 140.8, 140.6, 128.6 (2C), 128.6 (2C), 128.2 (2C), 128.1 (2C), 126.9 (2C), 79.9, 67.3,

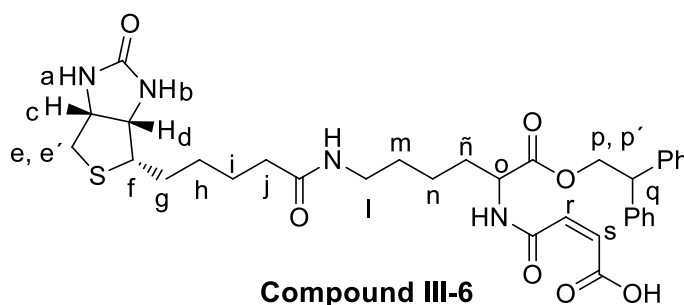
61.9, 60.3, 55.6, 53.2, 49.8, 40.4, 39.1, 35.8, 32.2, 28.8, 28.3 (3C), 28.1, 28.0, 25.7, 22.4 ppm.
MS m/z: calculated for $C_{35}H_{48}N_4O_6S$ $[M+Na]^+$ 675.3 found MALDI-TOF 675.4.



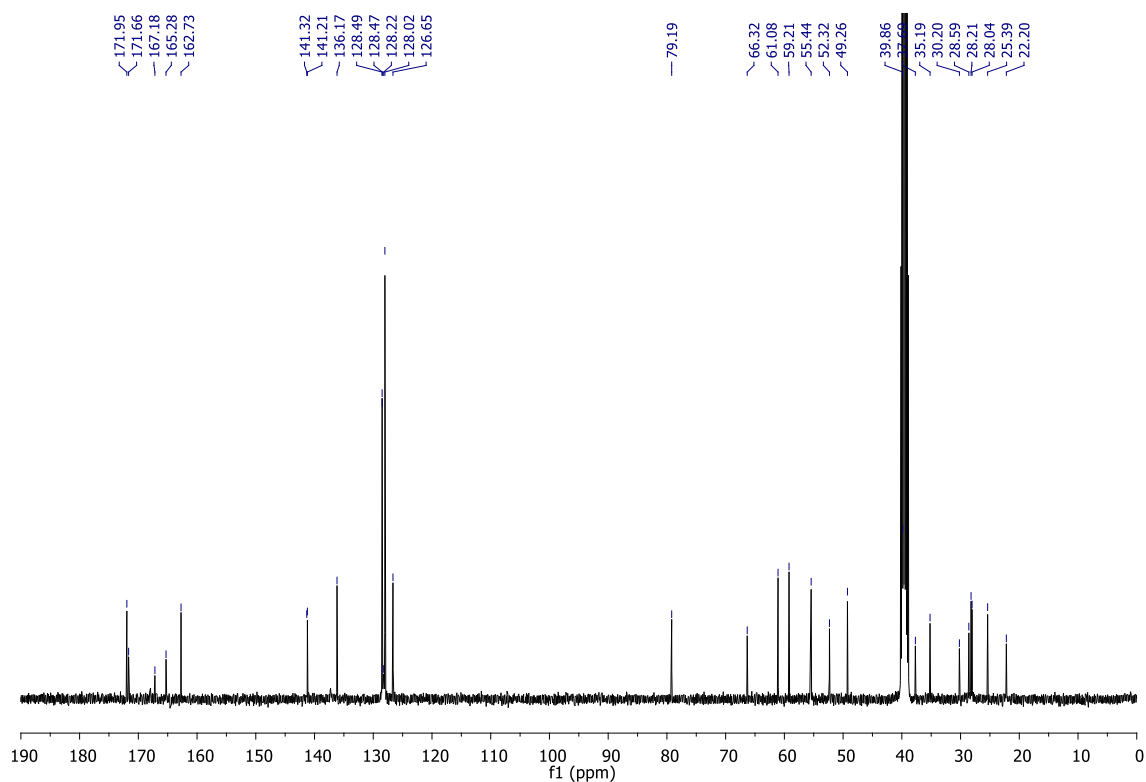
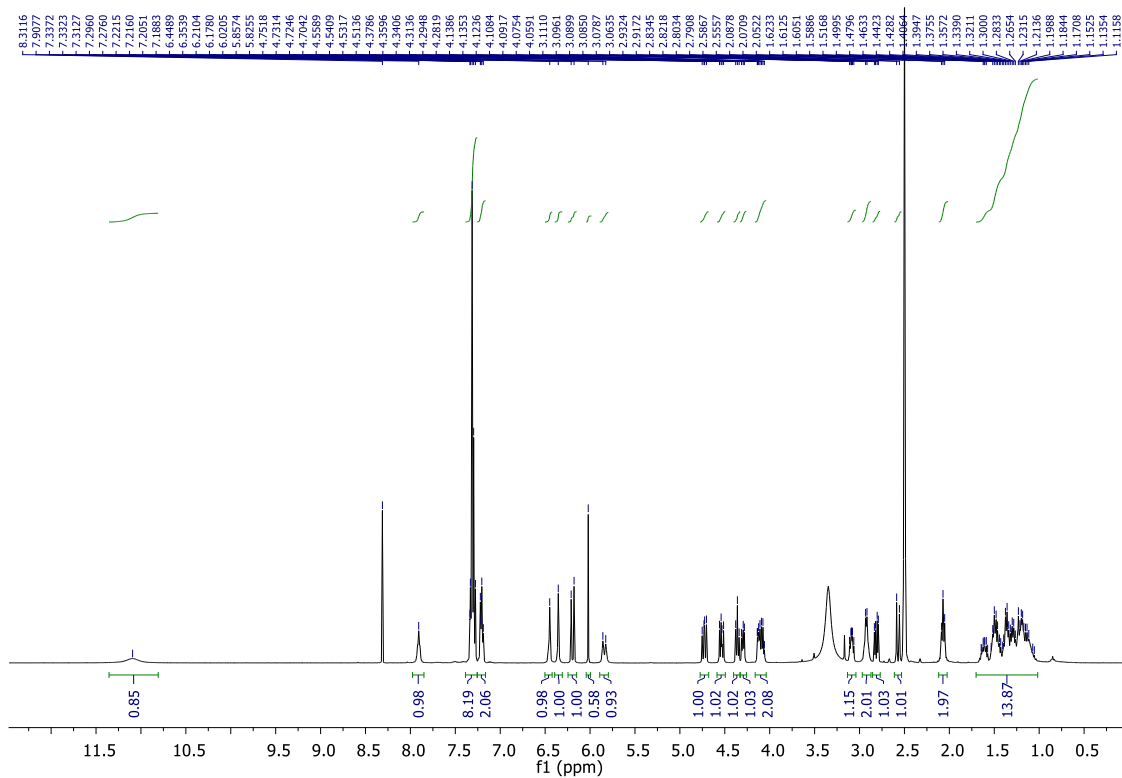


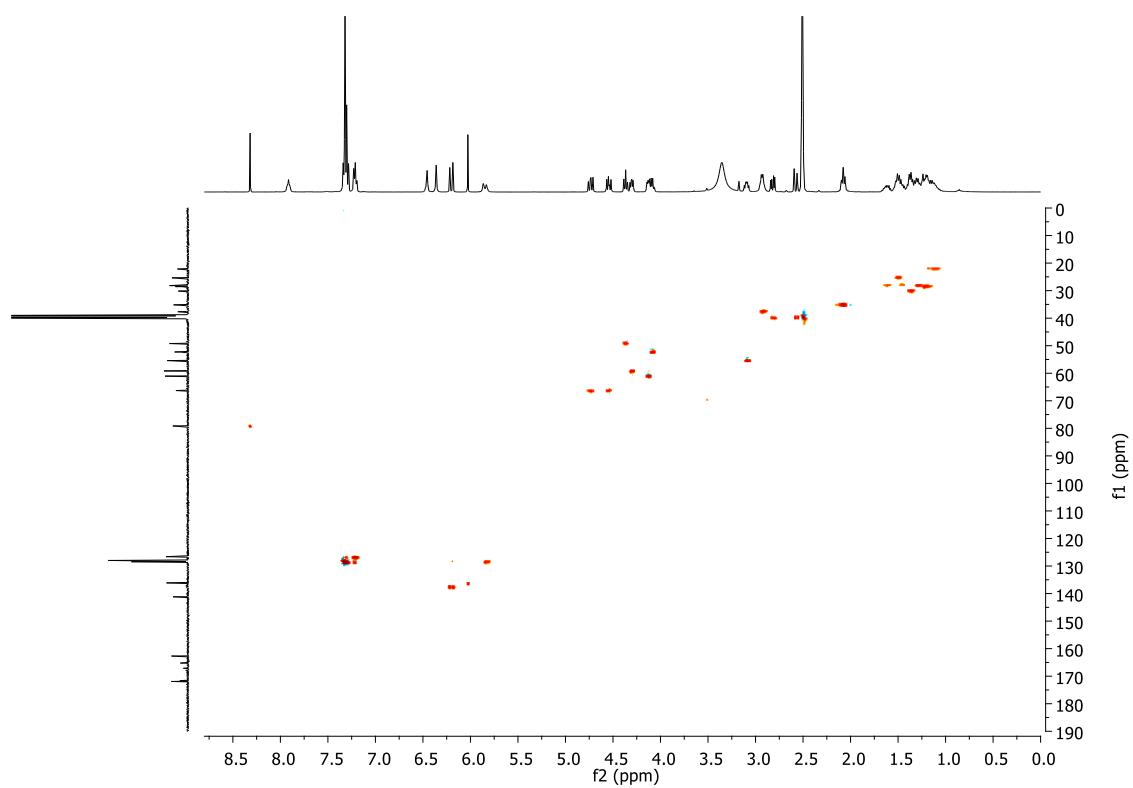
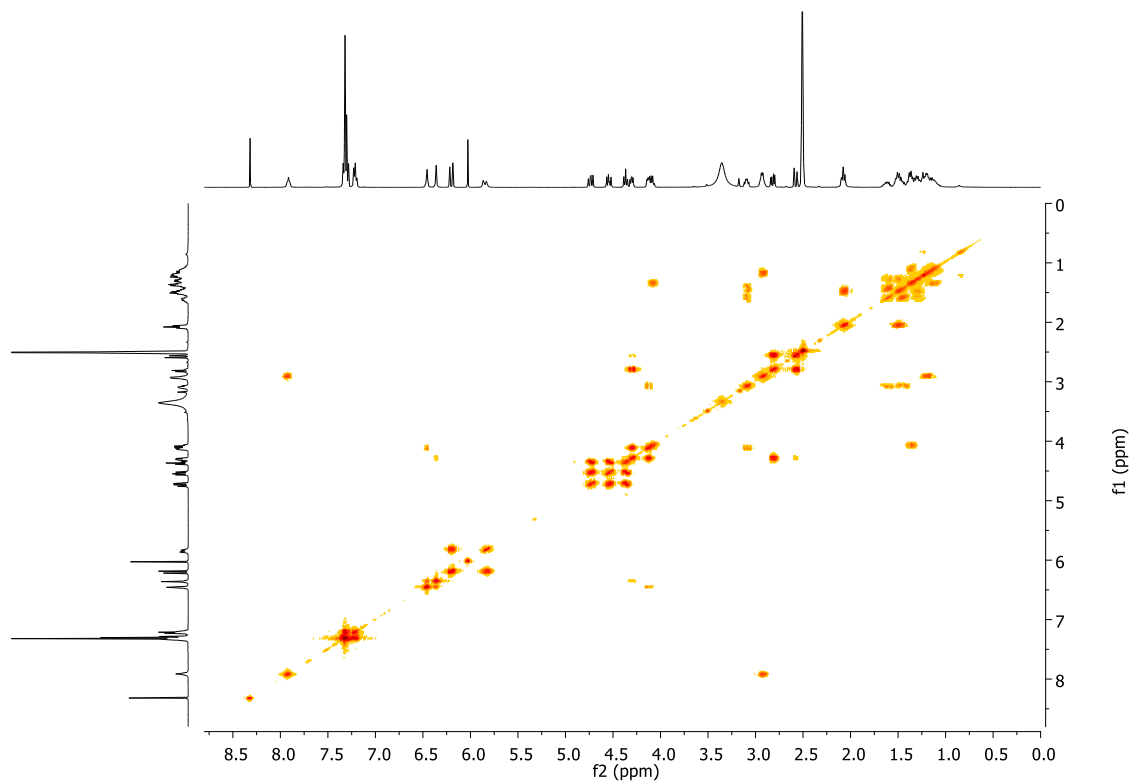
1-(2,2-diphenylethoxy)-1-oxo-6-(biotinylamido)hexan-2-aminium 2,2,2-trifluoroacetate


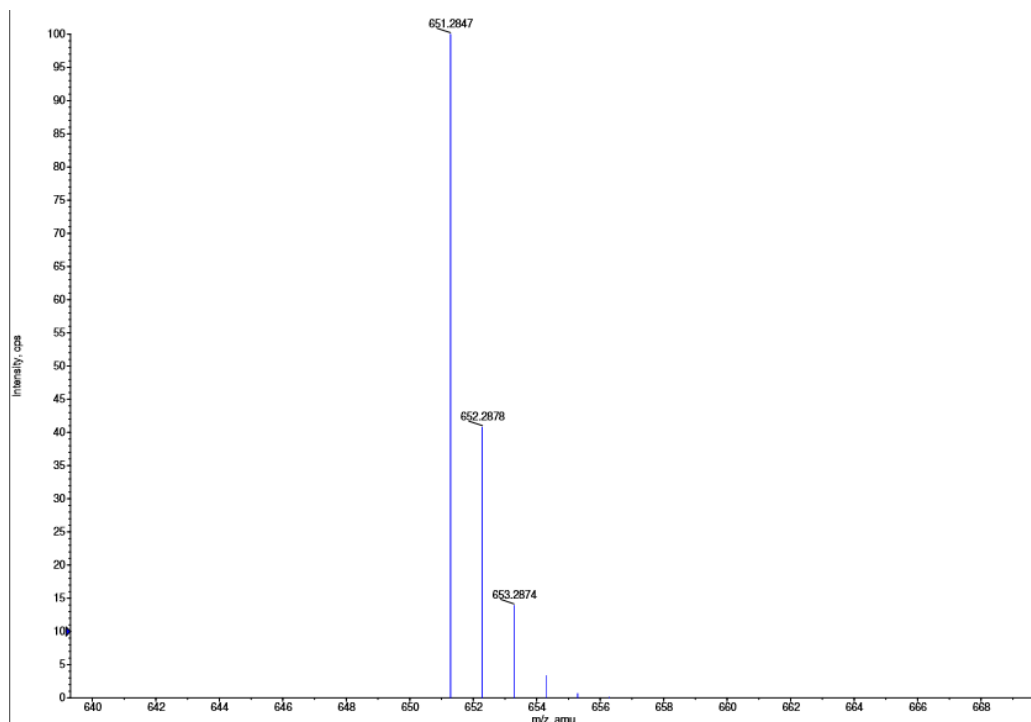
A solution of compound **III-4** (58 mg, 0.09 mmol) in DCM (1.5 mL) was added TFA (0.1 mL) at 0°C. The reaction was stirred at room temperature for 3h until it was completed (followed by TLC). The reaction mixture was concentrated under reduced, then DCM was added and the organic layer was washed with NaHCO₃, further washed with brine, dried over Na₂SO₄ and concentrated under reduced pressure to give compound **5** as a yellowish oil, quantitative yield. The crude material was used directly in the next step reaction.

4-[(1-(2,2-diphenylethoxy)-6-(biotinylamino)-1-oxohexan-2-yl)amino]-4-oxobut-2-enoic acid


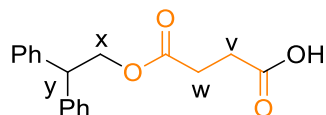
A solution of compound **III-5** (49 mg, 0.09 mmol) and Et₃N (12 μL, 0.093 mmol) in anhydrous THF (1 mL), was cooled to 0°C, then maleic anhydride (9 mg, 0.093 mmol) dissolved in THF (0.4 mL) was added dropwise under nitrogen atmosphere. The solution was allowed to warm up to room temperature and stirred overnight. The solvent was then removed under reduced pressure and the crude material was purified by flash chromatography (using a gradient elution, starting DCM/ MeOH 9:1 and then DCM/ MeOH/ NH₃ 4 : 1: 0.01), to furnish a yellow oil (59 mg 90 % yield). ¹H NMR ([D₆]dimethyl sulfoxide): δ = 11.09 (br s, 1H, OH), 7.91 (m, 1H, NH), 7.30 (m, 8 H, , Ar-H), 7.21 (m, 2 H, , Ar-H), 6.45 (br s, 1 H, H_a), 6.35 (br s, 1 H, H_b), 6.19 (d, J = 13.0 Hz, 1H, H_s), 5.84 (d, J = 12.8 Hz, 1H, H_r), 4.73 (dd, J = 7.9, 10.8 Hz, 1 H, H_p or H_{p'}), 4.53 (dd, J = 7.2, 10.9 Hz, 1 H, H_p or H_{p'}), 4.36 (t, J = 7.6 Hz, 1H, H_q), 4.29 (m, 1 H, H_c), 4.10 (m, 2 H, H_d, H_o), 3.08 (m, 1 H, H_t), 2.92 (m, 2 H, H_i), 2.81 (dd, J = 4.7, 12.9 Hz, 1 H, H_e or H_{e'}), 2.56 (d, J = 12.8 Hz, 1 H, H_e or H_{e'}), 2.07 (t, J = 6.8 Hz, 2 H, H_j), 1.44 (m, 12 H, H_g, H_i, H_h, H_n, H_m, H_n); ¹³C NMR ([D₆]dimethyl sulfoxide): δ = 172.0, 171.7, 167.2, 165.3, 162.7, 141.3, 141.2, 136.2, 128.5 (2C), 128.5 (2C), 128.2, 128.0 (4C), 126.7 (2C), 66.3, 61.1, 59.2, 55.4, 52.3, 49.3, 39.9, 37.7, 35.2, 30.2, 28.6, 28.2, 28.0, 25.4, 22.2 ppm. MS m/z: calculated for C₃₄H₄₂N₄O₇S [M+H]⁺ 650.8 found FAB 651.3.





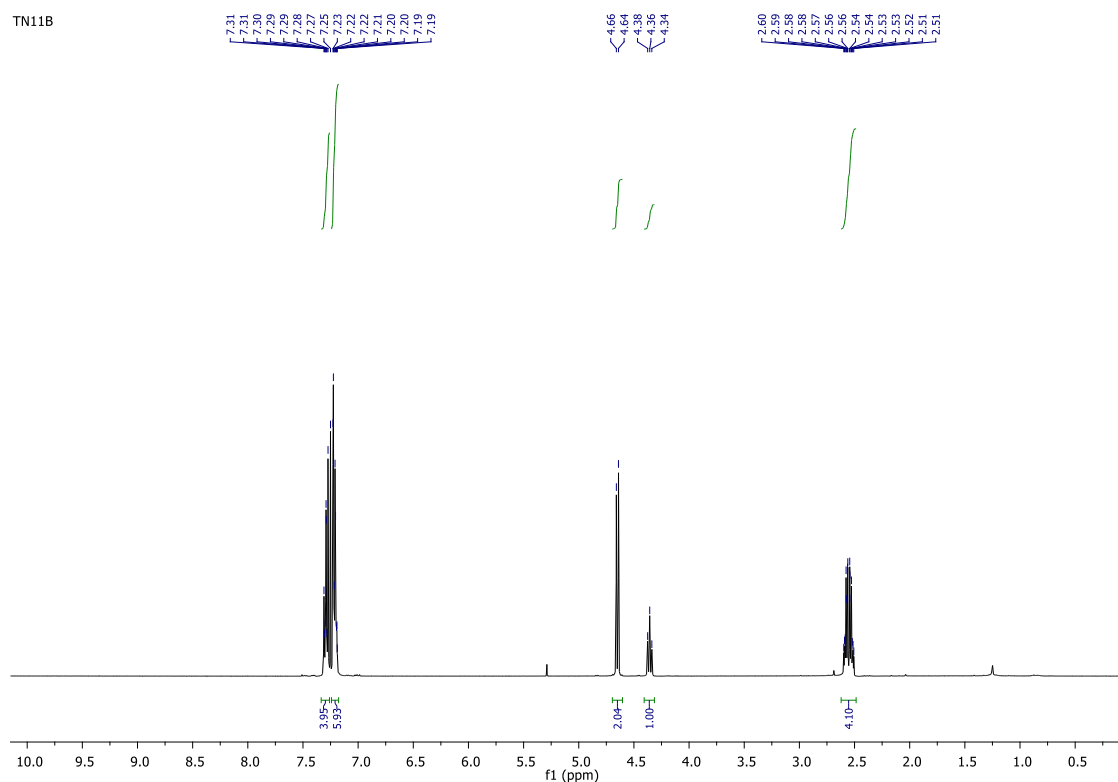


2,2-Diphenylethyl succinic acid mono ester

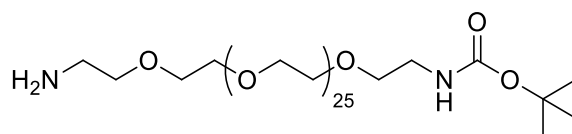


Compound III-7

To a stirred solution of 2,2,-diphenylethanol (1 g, 5.26 mmol) in DCM (53mL) was added one drop of Et₃N and a solution of succinic anhydride (584 mg, 5.83 mmol) in 15 mL DCM, added slowly over 30 min. The reaction mixture was stirred overnight. Once the reaction was completed (follow by TLC), the solvent was removed under reduced pressure and the crude material was purified by column chromatography, eluent: Hexane : AcOEt 2:1, to afford 1.2 g of compound 7 as a white solid (76%). ¹H NMR (CDCl₃): δ = 7.28 (m, 4H, , Ar-H), 7.21 (m, 6H, Ar-H), 4.65 (d, *J* = 7.6 Hz, 2H, H_x), 4.36 (t, *J* = 7.6 Hz, 1H, H_y), 2.55 (m, 4 H, H_v, H_w) ppm. These data is in concordance with *Angew. Chem. Int. Ed.* 42, 2296-2300 (2003).

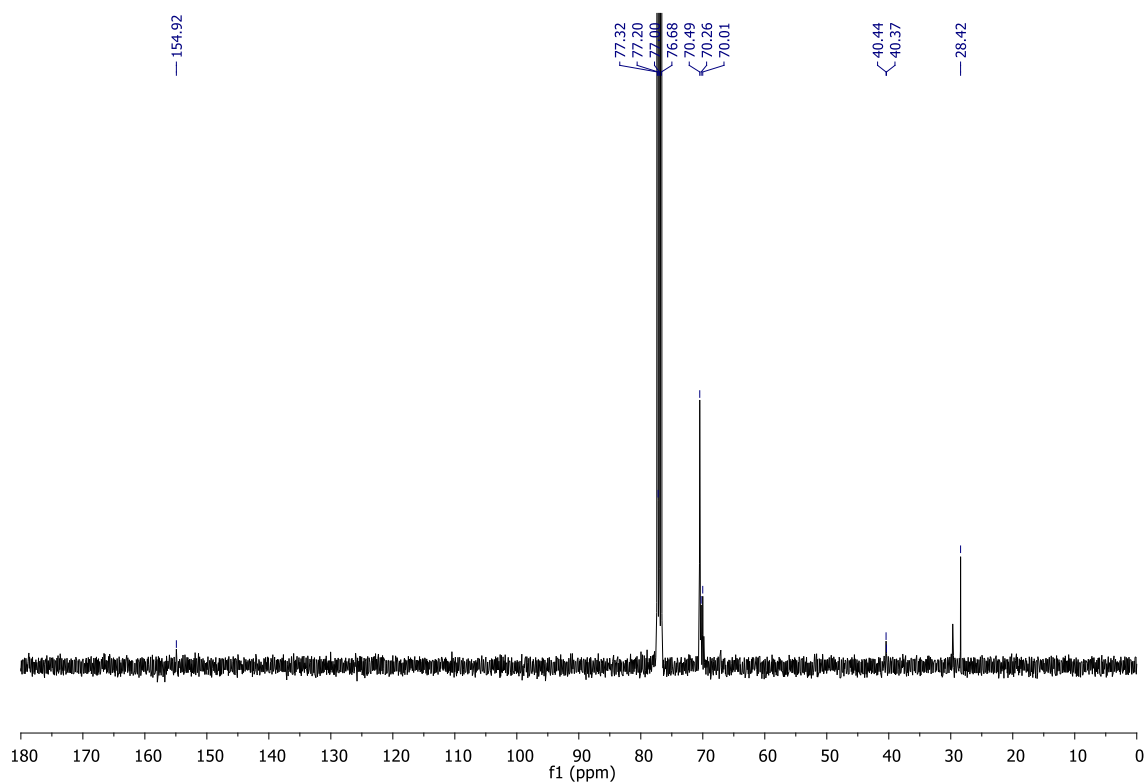
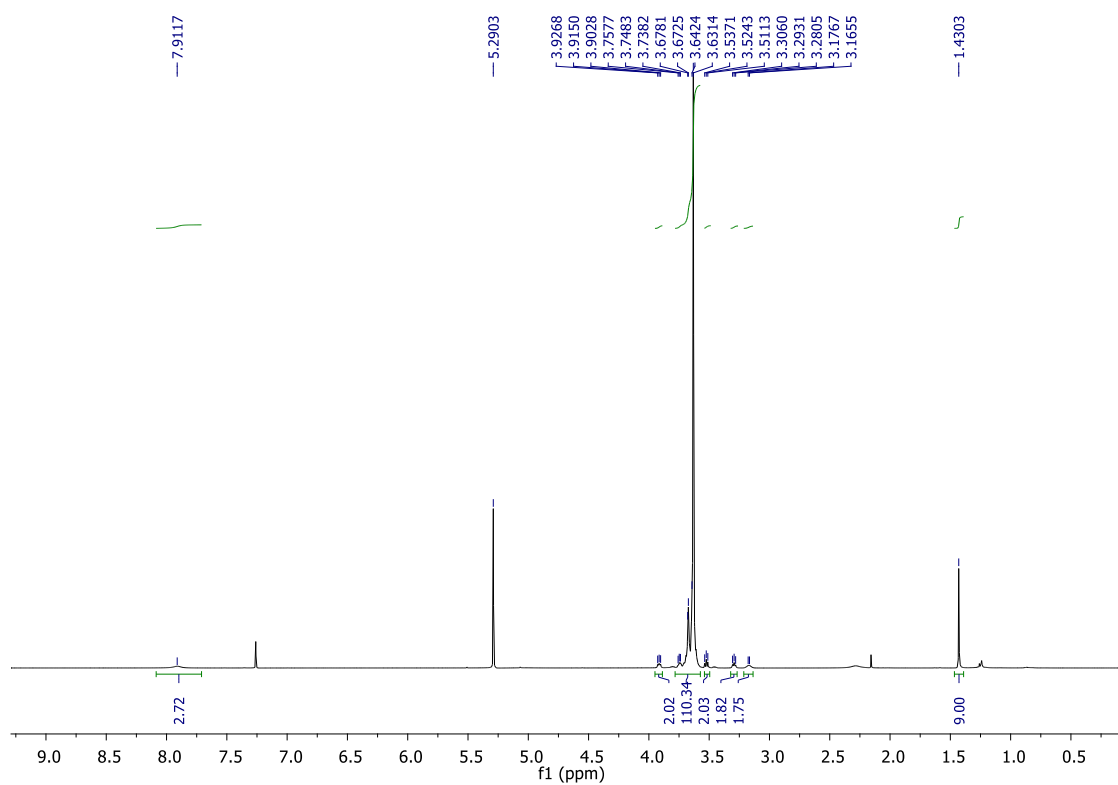


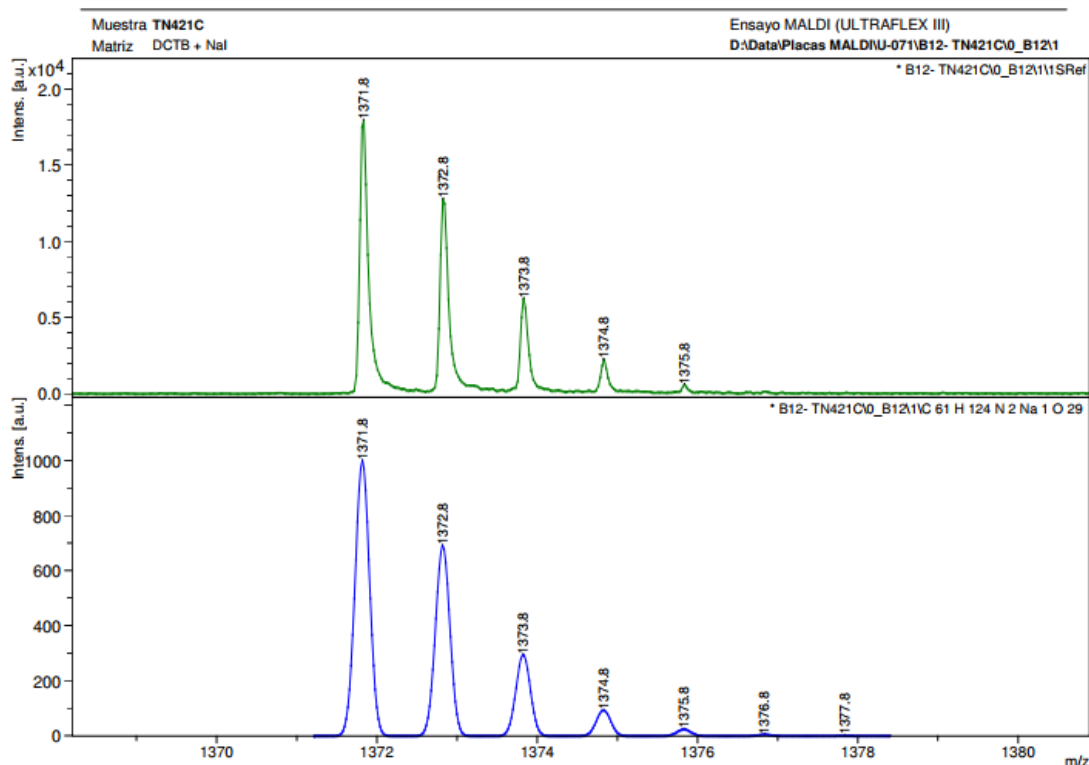
***tert*-Butyl (2-(2-(2-aminoethyl) hexacosaoxy)ethyl) carbamate**



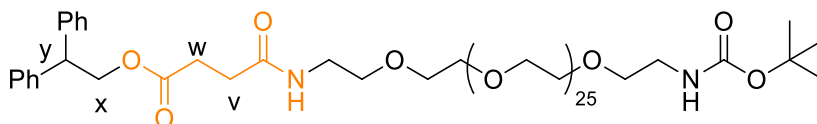
Compound III-8

The reaction was carried out under anhydrous conditions. To 490mg (0.4 mmol) *O,O'*-bis (2-aminoethyl) hexacosaoxy ethylene glycol (EG26) in DCM at 0°C was added di-*tert*-butyl dicarbonate (44mg, 0.2 mmol). The solution was stirred overnight, then the solvent was removed in vacuo and the crude material purified via column chromatography using a gradient elution, starting with CHCl₃/ MeOH 10:1 to 4:1 and finally 1:1, to give a yellowish oil, 165 mg, 61%. ¹H NMR (CDCl₃): δ = 7.91 (br s 3H, 3NH), 3.92 (m, 2H), 3.63 (m, 106H, EG26-H), 3.52 (t, *J* = 5.1, 2H), 3.29 (t, *J* = 5.2, 2H), 3.17 (m, 2H), 1.43 (s, 9H, Boc-H); ¹³C NMR (CDCl₃): δ = 154.9, 79.0, 70.5 (51C), 70.3, 70.0, 69.8, 40.4, 29.7, 40.4 (3C) ppm. MS *m/z*: calculated for C₆₁H₁₂₄N₂O₂₉ [M+Na]⁺ 1371.8 found MALDI-TOF 1371.8.



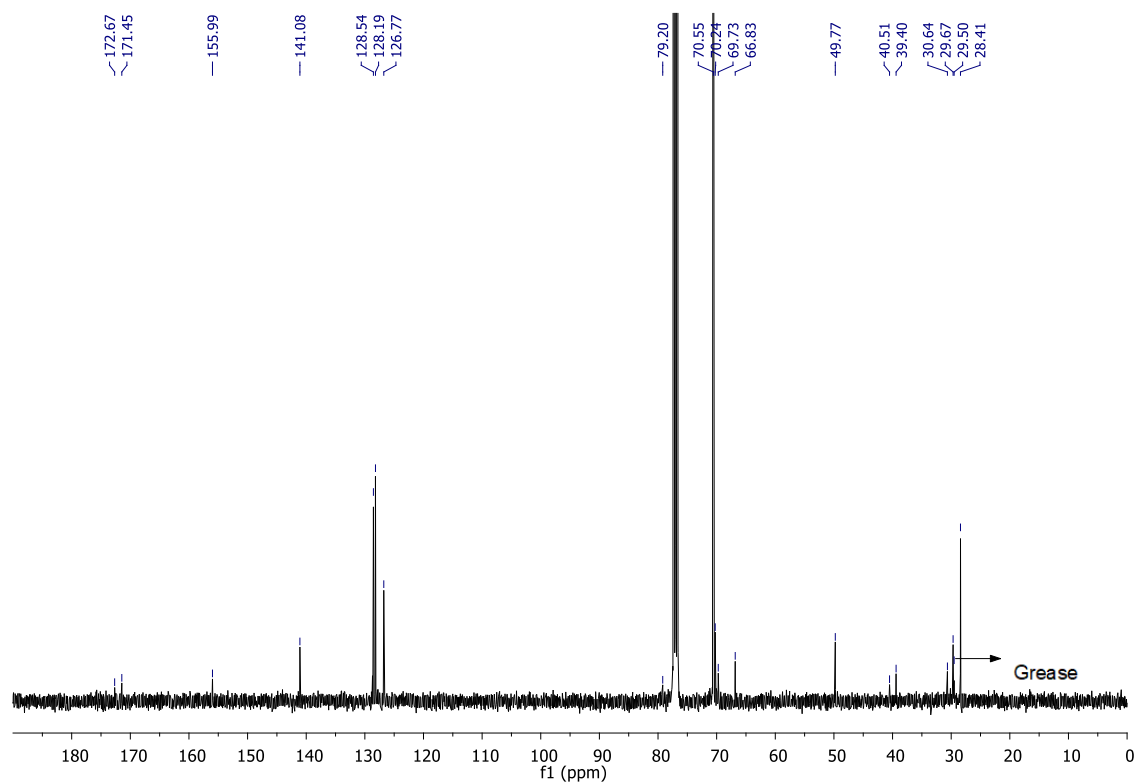
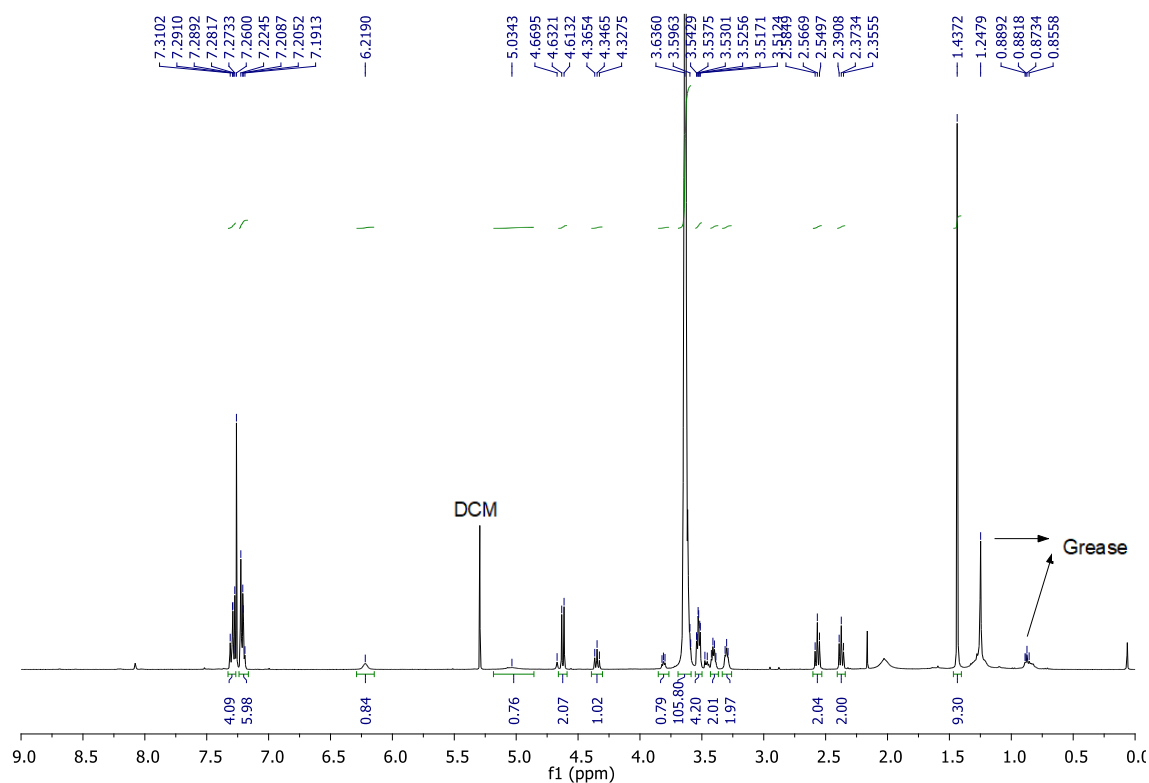


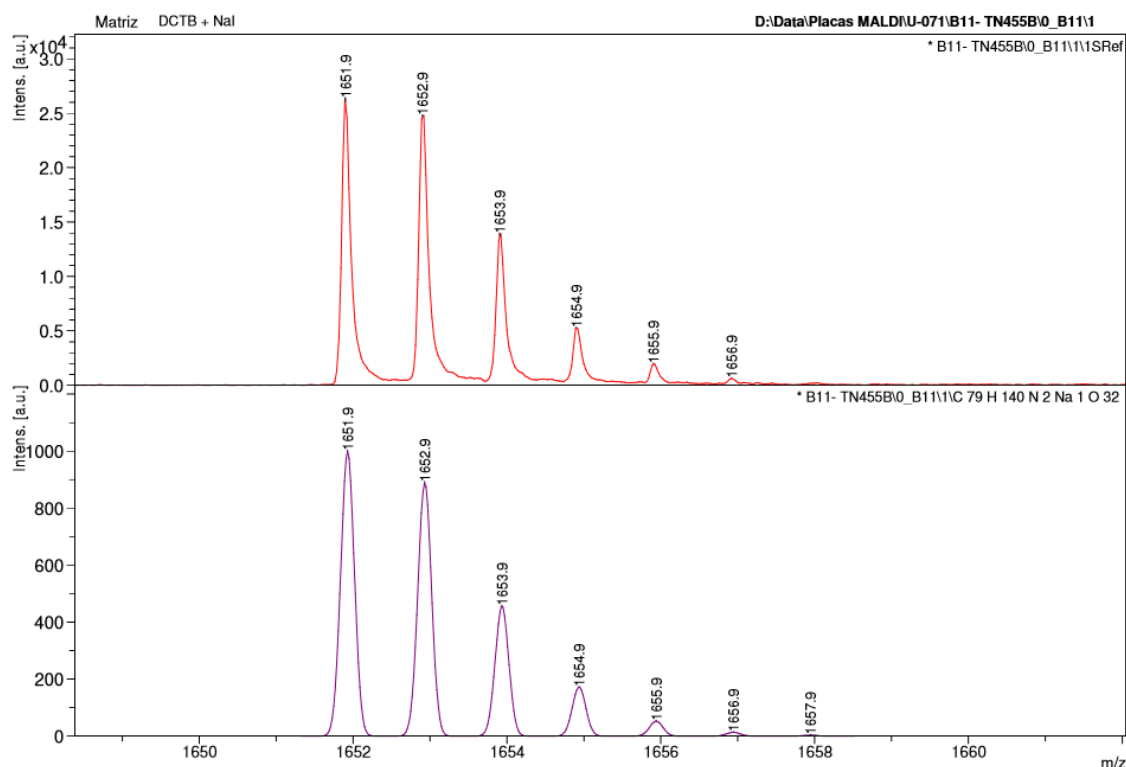
2,2-diphenylethyl 2,2-dimethyl-4,18-dioxo-3,8,11,14-tetraoxa-5,17-diazahenicosan-21-oate



Compound III-9

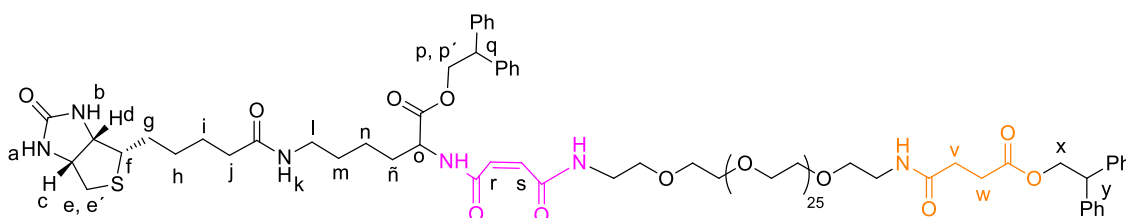
40 mg (0.13 mmol) of compound **III-7** was dissolved in DCM (2 mL) and the solution was cooled down to 0°C. Then EDCI (38 mg, 0.2 mmol) and DMAP (24 mg, 0.2 mmol) were added at 0°C and the reaction mixture was allowed to stir at room temperature for 30min. A solution of compound **III-8** (165mg, 0.12mmol), in DCM (1.5 mL) was added to the activated acid. The reaction mixture was stirred for 24h, concentrated under reduced pressure and then diluted with DCM and washed with 1M HCl, with NaHCO₃ (sat. aq.). The organic layer was further washed with brine (sat.), dried over Na₂SO₄ and concentrated under reduced pressure. The crude material was purified by column chromatography using CHCl₃/ MeOH 15:1 as eluent, to give compound 9 as a colorless oil, 180mg, 92%. ¹H NMR (CDCl₃): δ = 7.28 (m, 4H, Ar-H), 7.21 (m, 6H, Ar-H), 6.23 (br s, 1H, NH), 5.03 (br s, 1H, NH), 4.62 (d, *J* = 7.6 Hz, 2H, H_x), 4.35 (t, *J* = 7.6 Hz, 1H, H_y), 3.81 (m, 1H), 3.63 (m, 103H, EG26-H), 3.53 (m, 4H), 3.40 (m, 2H), 3.30 (m, 2H), 2.57 (t, 2H, *J* = 7.2 Hz, H_w), 2.37 (t, 2H, *J* = 7.0 Hz, H_v), 1.43 (s, 9H, Boc-H); ¹³C NMR (CDCl₃): δ = 172.7, 171.5, 156.0, 141.1 (2C), 128.5 (4C), 128.2 (4C), 126.8 (2C), 79.2, 70.6 (51C), 70.2, 70.2, 69.7, 66.8, 49.8, 40.5, 39.4, 30.6, 29.7, 28.4 (3C) ppm. MS *m/z*: calculated for C₇₉H₁₄₀N₂O₃₂ [M+Na]⁺ 1651.9 found MALDI 1651.9.





Compound III-10. Was synthesized following the same procedure described for compound III-5.

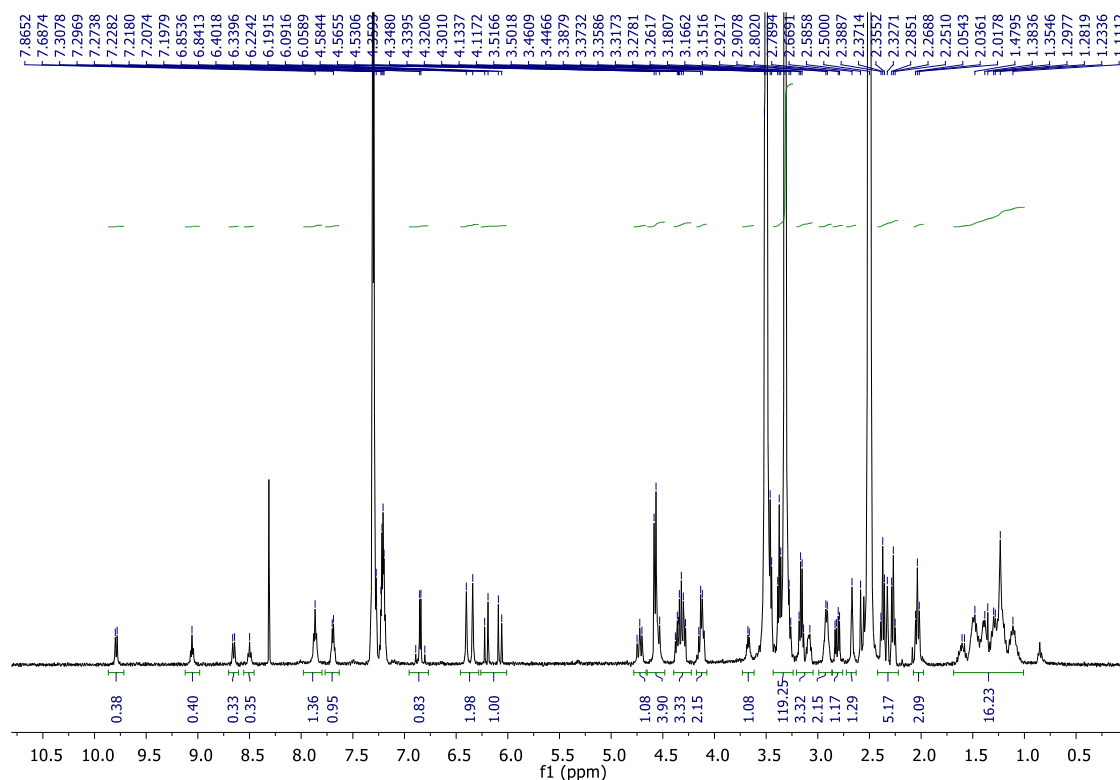
(Z/E 55/45)-Thread

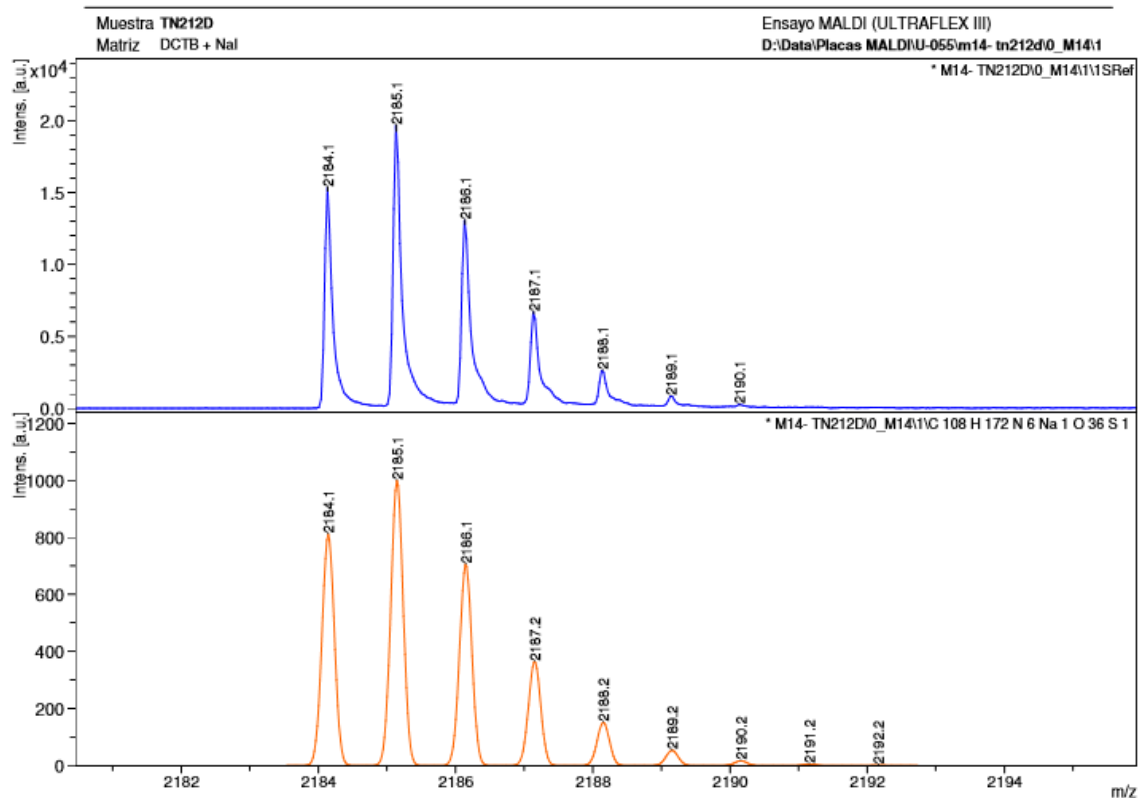
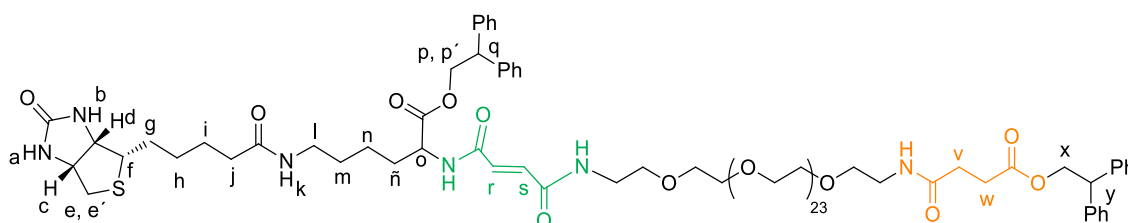


Compound III-11

Compound III-6 (85 mg, 0.13 mmol) was dissolved in DCM (3 mL) and the solution was cooled to 0°C, EDCI (23 mg, 0.19 mmol), DMAP (37 mg, 0.19 mmol) were added at 0°C. The reaction mixture was allowed to stir at room temperature for 30 min, and then a solution of compound III-10 (180 mg, 0.12 mmol) in DCM (7.7 mL) was added to the activated acid. The reaction mixture was stirred overnight, concentrated under reduced pressure and then diluted with DCM. The organic layer was washed with 1M HCl, with NaHCO₃ (sat. aq.), then further washed with brine (sat. aq.), dried over Na₂SO₄ and concentrated under reduced pressure. The crude material was purified by column chromatography (gradient elution: DCM: MeOH 30 : 1 to 9:1) to furnish the desired product as a colorless oil, 166mg, 0.077 mmol (64%).¹H NMR ([D₆]dimethyl sulfoxide) : δ = 8.65 (d, *J* = 7.2 Hz, 1H, NH), 8.50 (t, *J* = 5.6 Hz, 1H, NH), 7.86 (t, *J* = 5,5 Hz, 1H, NH), 7.70 (t, *J* = 5,5 Hz, 1H, NH), 7.27 (m, 16 H, Ar-H), 7.21 (m, 4 H, Ar-H), 6.87 (d, *J* = 15.5 Hz, 0.4 H, H_r or H_s of *E*-isomer), 6.82 (d, *J* = 15.5 Hz, 0.4 H, H_r or H_s of *E*-isomer), 6.40 (br s, 1 H, H_a), 6.34 (br s, 0.5 H, H_b), 6.21 (d, *J* = 13.1 Hz, 0.5 H, H_r or H_s of *Z*-

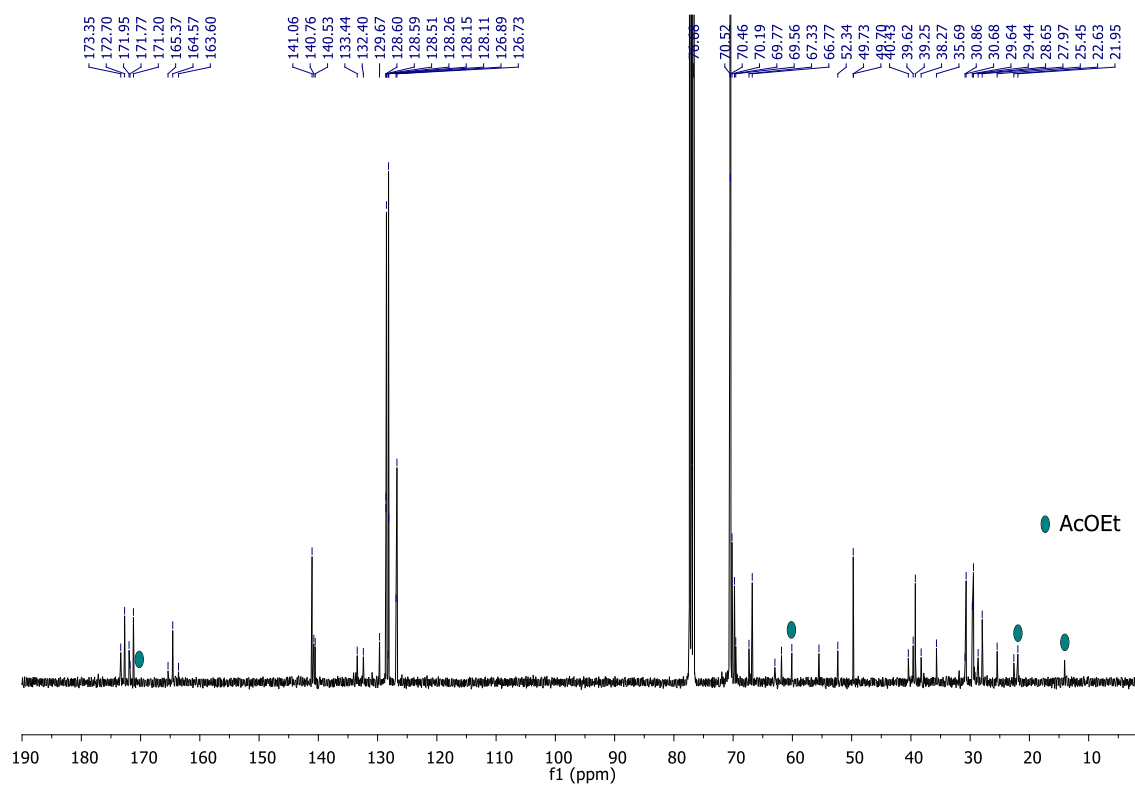
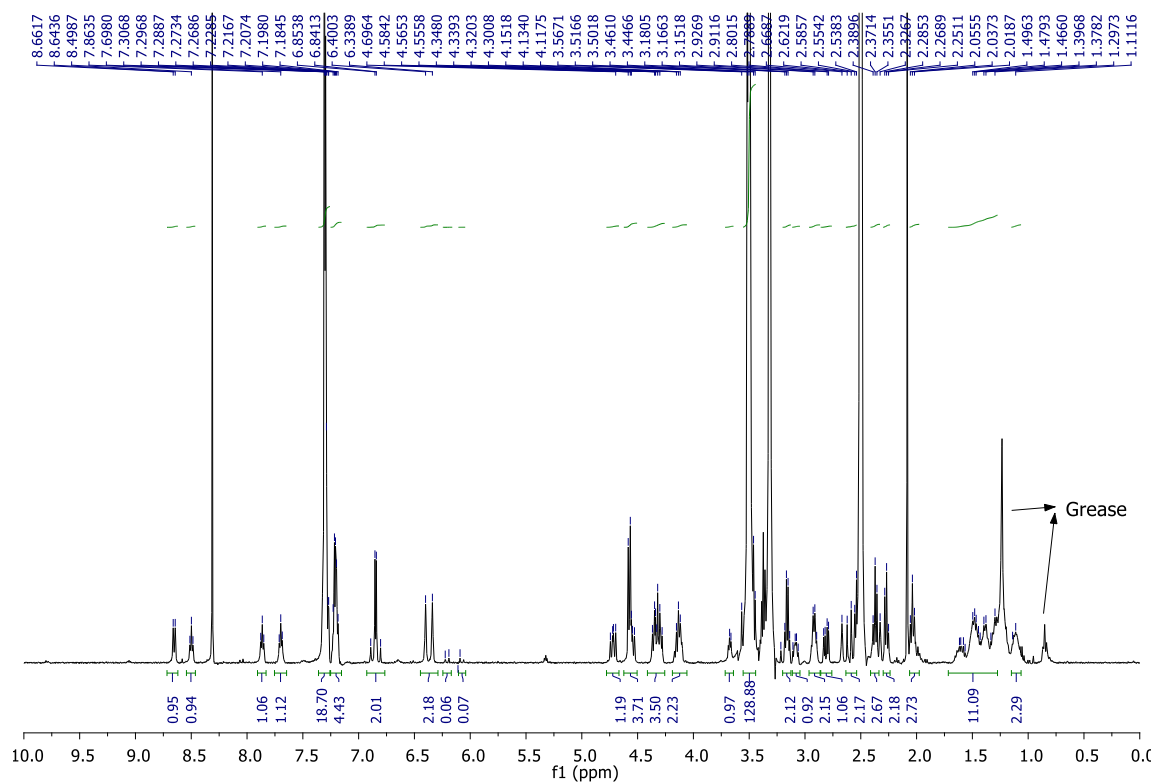
isomer), 6.08 (d, $J = 13.1$ Hz, 1H, H_r or H_s of *Z*-isomer), 4.72 (dd, $J = 8.1, 10.9$ Hz, 1 H, H_p or H_{p'}), 4.55 (m, 3H, H_{p'} or H_p, H_x), 4.33 (m, 3H, H_c, H_y, H_q), 4.12 (m, 2H, H_d, H_o), 3.68 (m, 1H, EG26-H), 3.50 (m, 107H, EG26-H), 3.37 (t, $J = 6.0$ Hz, 2H, EG26-H), 3.17 (dd, $J = 5.8, 11.5$ Hz, 2H, EG26-H), 3.08 (m, 1H, H_f), 2.91 (m, 2 H, H_i), 2.81 (dd, $J = 4.7, 12.9$ Hz, 1 H, H_e or H_{e'}), 2.54 (d, $J = 12.8$ Hz, 1 H, H_{e'} or H_e), 2.37 (t, $J = 6.9$ Hz, 2 H, H_w), 2.27 (t, $J = 6.6$ Hz, 2 H, H_v), 2.04 (t, $J = 6.8$ Hz, 2 H, H_j), 1.44 (m, 12 H, H_g, H_i, H_h, H_n, H_m, H_ñ) (400 MHz, DMSO) ppm. MS m/z : calculated for C₁₀₈H₁₇₂N₆O₃₆S [M+Na]⁺ 2185.1 found MALDI 2185.1.

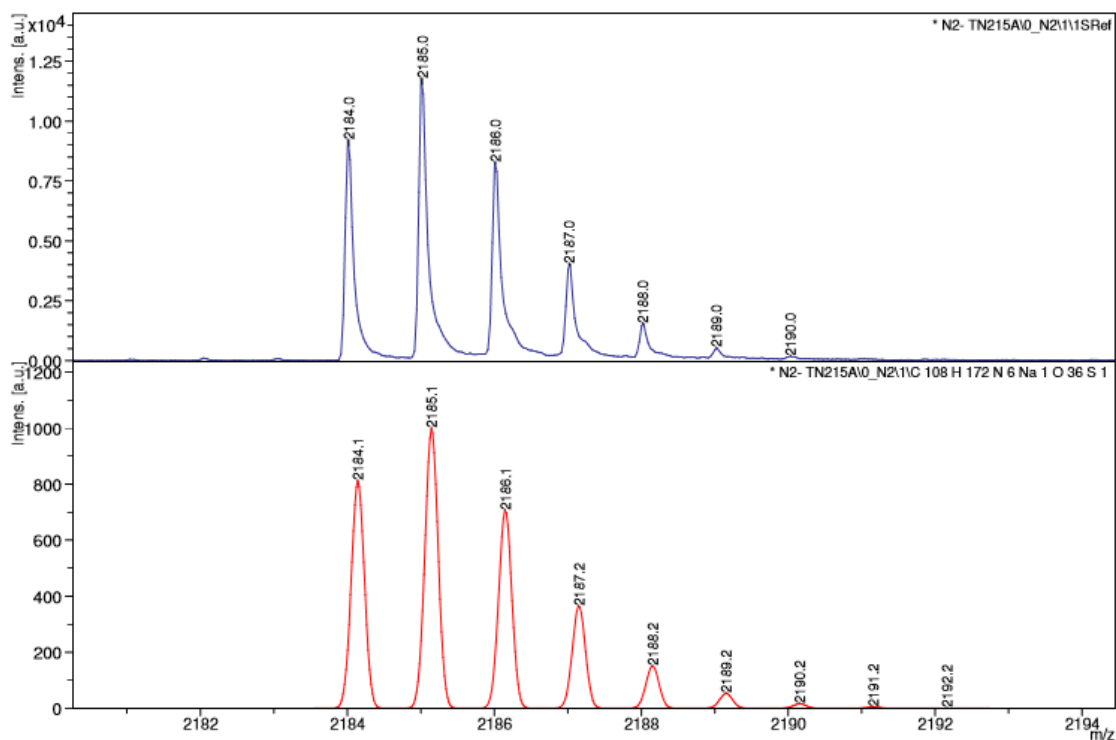


**(E)-Thread****Compound III-12**

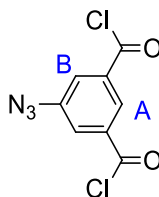
A solution of compound 11 (115 mg, 0.052mmol) and piperidine (4 μ g, 0.006 mmol) in DCM (3 mL) was stirred for 48 h. Then DCM was added and the organic layer was washed twice with 1M HCl. The organic layer was concentrated under reduced pressure to furnish compound 12 as yellowish oil (112 mg, 97%). ^1H NMR ([D₆]dimethyl sulfoxide): δ = 8.65 (d, J = 7.2 Hz, 1H, NH), 8.50 (t, J = 5.6 Hz, 1H, NH), 7.86 (t, J = 5.5 Hz, 1H, NH), 7.70 (t, J = 5.5 Hz, 1H, NH), 7.27 (m, 16 H, Ar-H), 7.21 (m, 4 H, Ar-H), 6.87 (d, J = 15.5 Hz, 1H, H_r or H_s), 6.82 (d, J = 15.5 Hz, 1H, H_r or H_s), 6.40 (br s, 1 H, H_a), 6.34 (br s, 1 H, H_b), 4.72 (dd, J = 8.1, 10.9 Hz, 1 H, H_p or H_{p'}), 4.55 (m, 3H, H_{p'} or H_p, H_x), 4.33 (m, 3H, H_c, H_y, H_q), 4.12 (m, 2H, H_d, H_o), 3.68 (m, 1H, EG26-H), 3.50 (m, 107H, EG26-H), 3.37 (t, J = 6.0 Hz, 2H, EG26-H), 3.17 (dd, J = 5.8, 11.5 Hz, 2H, EG26-H), 3.08 (m, 1H, H_f), 2.91 (m, 2 H, H_l), 2.81 (dd, J = 4.7, 12.9 Hz, 1 H, H_e or H_{e'}), 2.54 (d, J = 12.8 Hz, 1 H, H_{e'} or H_e), 2.37 (t, J = 6.9 Hz, 2 H, H_w), 2.27 (t, J = 6.6 Hz, 2 H, H_v), 2.04 (t, J = 6.8 Hz, 2 H, H_j), 1.44 (m, 12 H, H_g, H_i, H_h, H_n, H_m, H_{n'}); ^{13}C NMR ([D₆]dimethyl sulfoxide): δ = 173.4, 172.7, 171.9, 171.2, 165.4, 164.6, 163.6, 141.1 (2C), 140.8, 140.8, 140.6, 140.5, 133.4, 132.4, 129.7, 128.6 (2C), 128.6 (2C), 128.5 (4C), 128.3, 128.2 (4C), 128.1 (2C), 126.9 (2C), 126.7(2C), 70.5 (50C), 70.5, 70.2, 69.8, 69.6, 67.3, 66.7,

55.5, 52.3, 49.7, 49.7, 40.4, 39.6, 39.3, 38.3, 35.7, 30.9, 30.7, 29.6, 29.4, 28.7, 28.0, 25.5, 22.6, 21.9 ppm. MS m/z: calculated for C₁₀₈H₁₇₂N₆O₃₆S [M+Na]⁺ 2184.0 found FAB 2184.1.





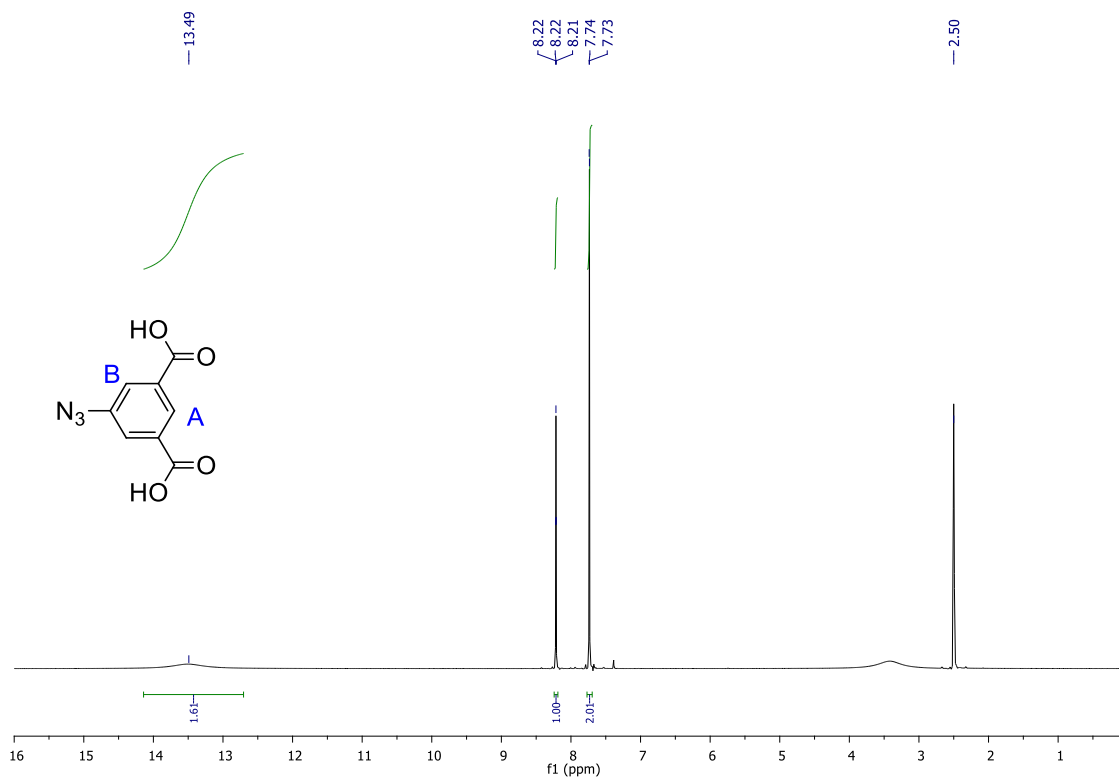
5-azidoisophthaloyl dichloride



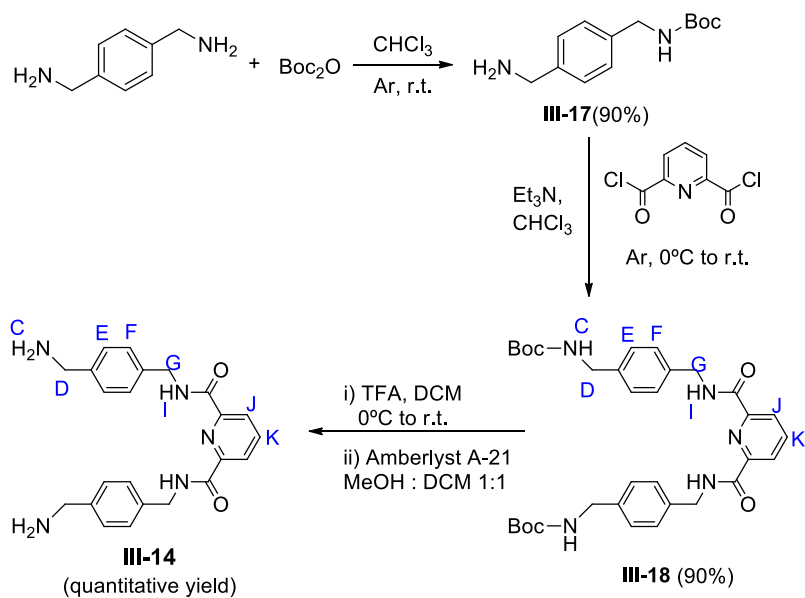
Compound III-13

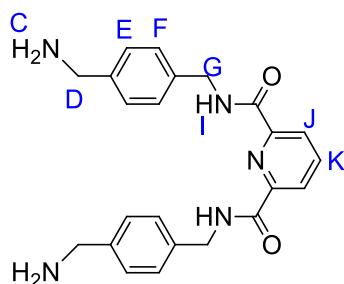
Step i) 5-aminoisophthalic acid (2.5 g, 27.6 mmol) was placed in a flash with water (39 mL), 3 mL of 12M HCl was added dropwise. The mixture was cooled in a ice bath at 0°C. NaNO₂ was dissolved in water and added dropwise to the mixture, which was stirred for 30 min. Then, NaN₃ dissolved in water was added dropwise to the mixture. A yellow solid was formed and gas evolution was observed, making it difficult to keep stirring. The mixture was stirred until gas evolution was no longer detected. The product was then filtered, washed with distilled water and dried under vacuum (3.4g, 60%). ¹H NMR ([D₆]dimethyl sulfoxide): δ = 13.49 (br s, 2H, OH), 8.22 (t, *J* = 1.4 Hz, 1H, Ar-H, H_A), 7.73 (d, *J* = 1.4 Hz, 1H, Ar-H, H_B) ppm. This data is in concordance with *Macromol. Chem. Phys.* **2003**, 214, 2223.

Step ii) To a stirred suspension of 5-azido-isophthalic acid (100 mg, 0.48 mmol) in DCM (2mL) was added two drops of anhydrous DMF and oxalyl chloride (0.15 mL, 1.95 mmol). The reaction mixture was stirred until the product was totally solubilized. The solvent was removed under reduced pressure and the sample was kept 3h under vacuum to remove oxalyl chloride. The crude product was then used directly in the next step.



Scheme for the synthesis of compound III-14

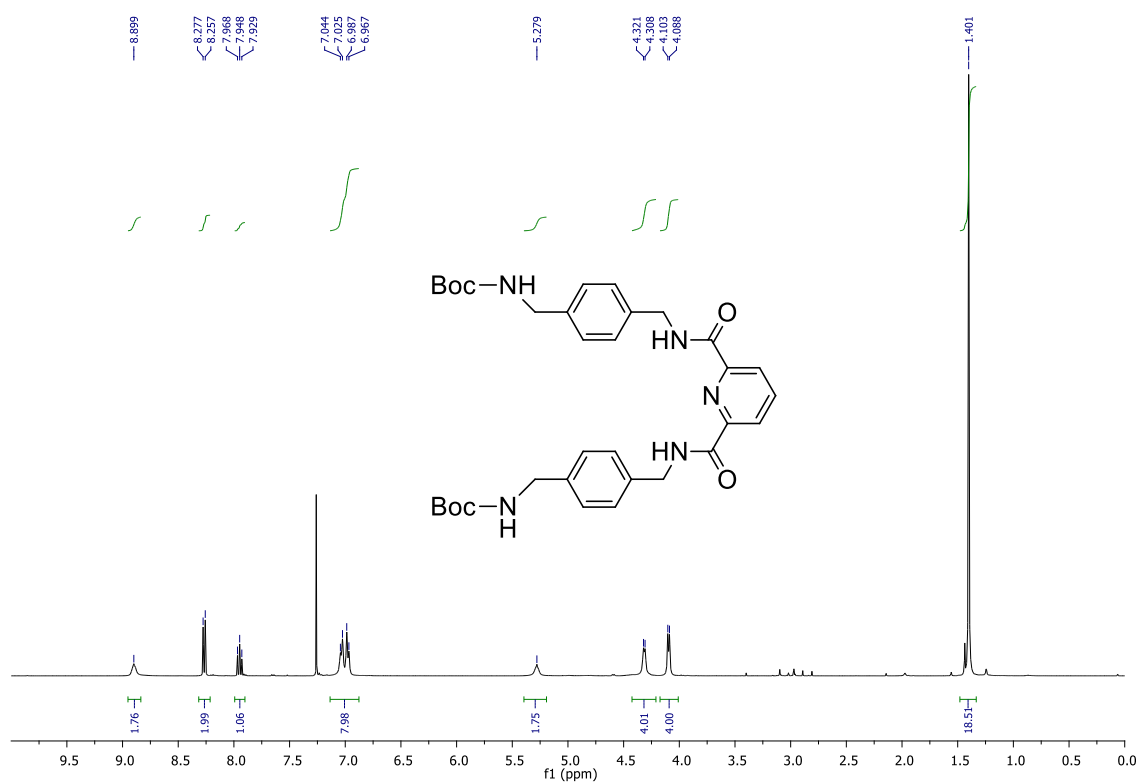
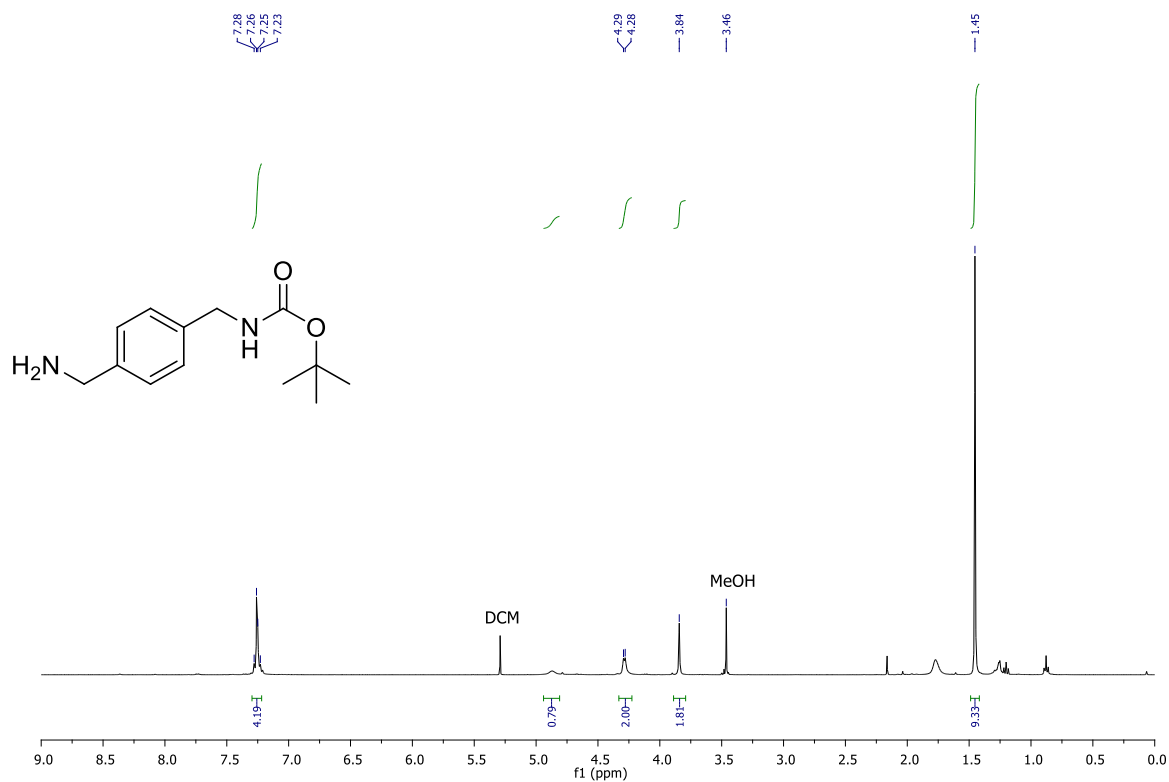


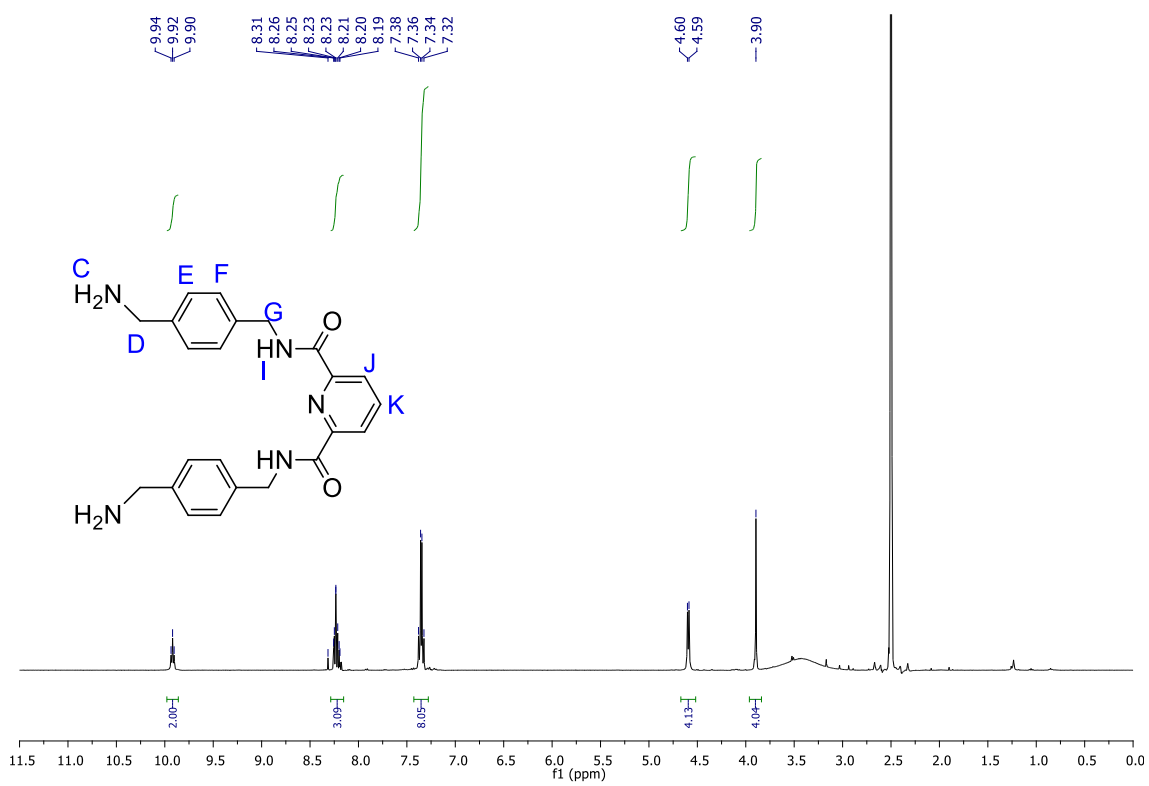
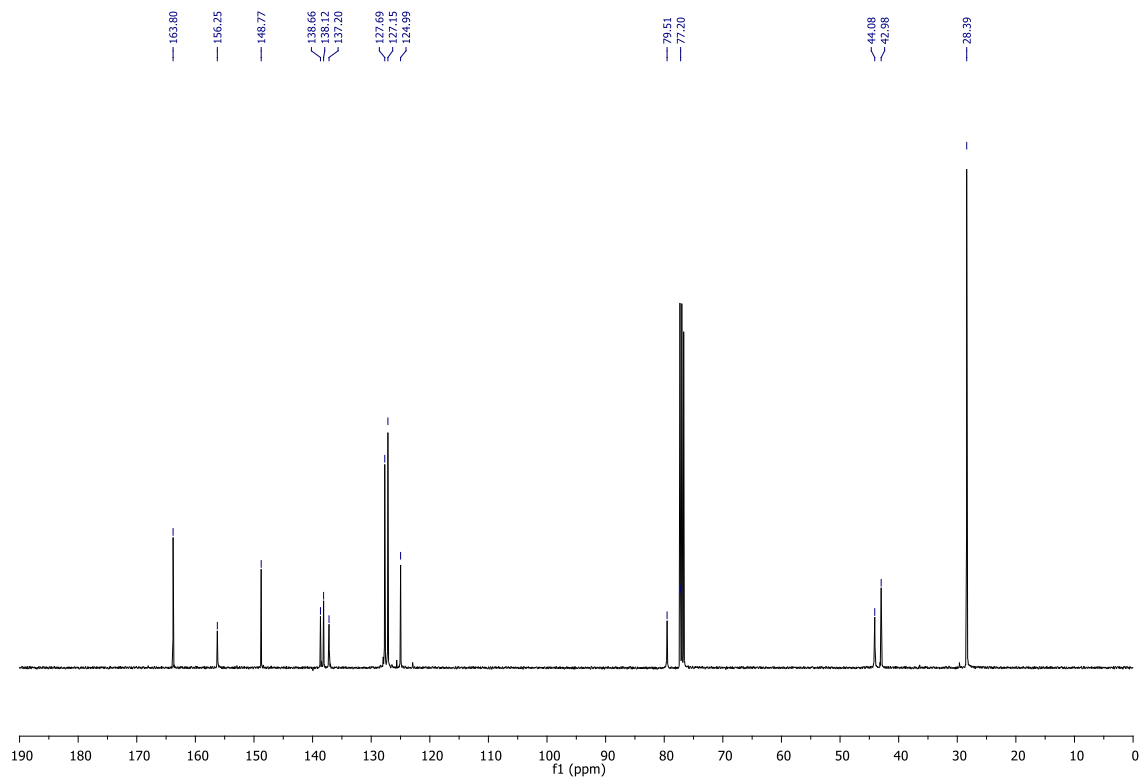
***N*²,*N*⁶-bis(4-(aminomethyl)benzyl)pyridine-2,6-dicarboxamide****Compound III-14**

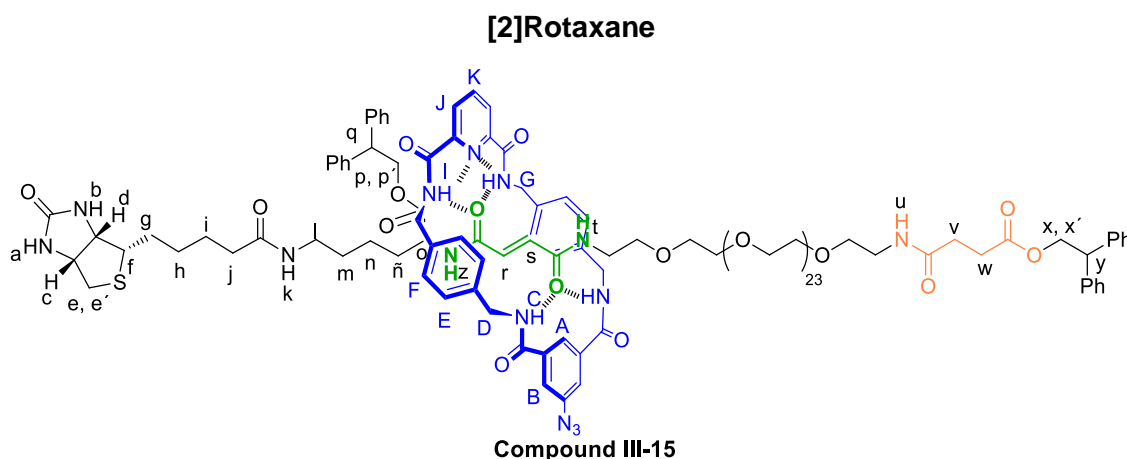
Step i). To a solution of *p*-xylylenediamine (515 mg, 3.78 mmol) in chloroform (60 mL) cooled in an ice bath, a solution of di-*tert*-butyl carbonate (413 mg, 1.89 mmol) in CHCl₃ (45 mL) was added dropwise over a period of 4h. The mixture was stirred overnight under Ar. A white solid was filtered from the solution and washed with cold CHCl₃. The solvent was removed under reduced pressure. To the remaining oil, DCM and water was added. The layers were separated and the aqueous layer was extracted with DCM (x3). The extracts were combined and dried over Na₂SO₄. The crude material was purified using a gradient elution (DCM/ MeOH 15:1 to 6:1) to give compound 14 as yellowish solid (400 mg, 90%) ¹H NMR (CDCl₃): δ = 7.26 (m, 4H, Ar-H), 4.28 (m, 2H), 3.84 (s, 2H) ppm.

Step ii) 2,6-Pyridinedicarboxylic acid (234 mg, 1.4 mmol) was suspended in anhydrous DCM, the mixture was cooled to 0°C with an ice bath, then oxalyl chloride was added dropwise followed by the addition of 2 drops of DMF. The reaction mixture was stirred until the product was totally solubilized. The solvent was removed and the crude solid was dried under high vacuum for 2h. The acid chloride (221 mg, 1.1 mmol) dissolved in CH₂Cl₂, was added dropwise to a solution of compound 14 and Et₃N in CH₂Cl₂. The reaction mixture was stirred overnight. The solvent was removed under reduced pressure. To the remaining oil, DCM and water was added. The layers were separated and the aqueous layer was extracted with DCM (x3). The extracts were combined and dried over Na₂SO₄. The crude material was purified using a gradient elution (DCM : MeOH 15:1 to 6:1) to give compound 14 as yellowish solid (400 mg, 90%) ¹H NMR (CDCl₃): δ = 8.90 (br s, 2H, NH, H_I), 8.27 (d, *J* = 7.8 Hz, 2H, Ar-H, H_J), 7.95 (t, *J* = 7.8 Hz, 1H, Ar-H, H_K), 7.03 (m, 4H, H_F), 6.97 (m, 4H, H_E), 5.28 (br s, 2H, NH, H_C), 4.31 (br d, *J* = 5.5 Hz, 4H, H_G), 4.09 (br d, *J* = 5.9 Hz, 4H, H_D), 1.40 (s, 18H, Boc-H); ¹³C NMR (CDCl₃): δ = 163.8, 156.2, 148.8, 138.7, 138.1, 137.2, 127.7, 127.2, 125.0, 79.5, 44.1, 43.0, 28.4 ppm. This data is in concordance with *Nat. Nanotech.*, 6(9), 2011, 553-557.

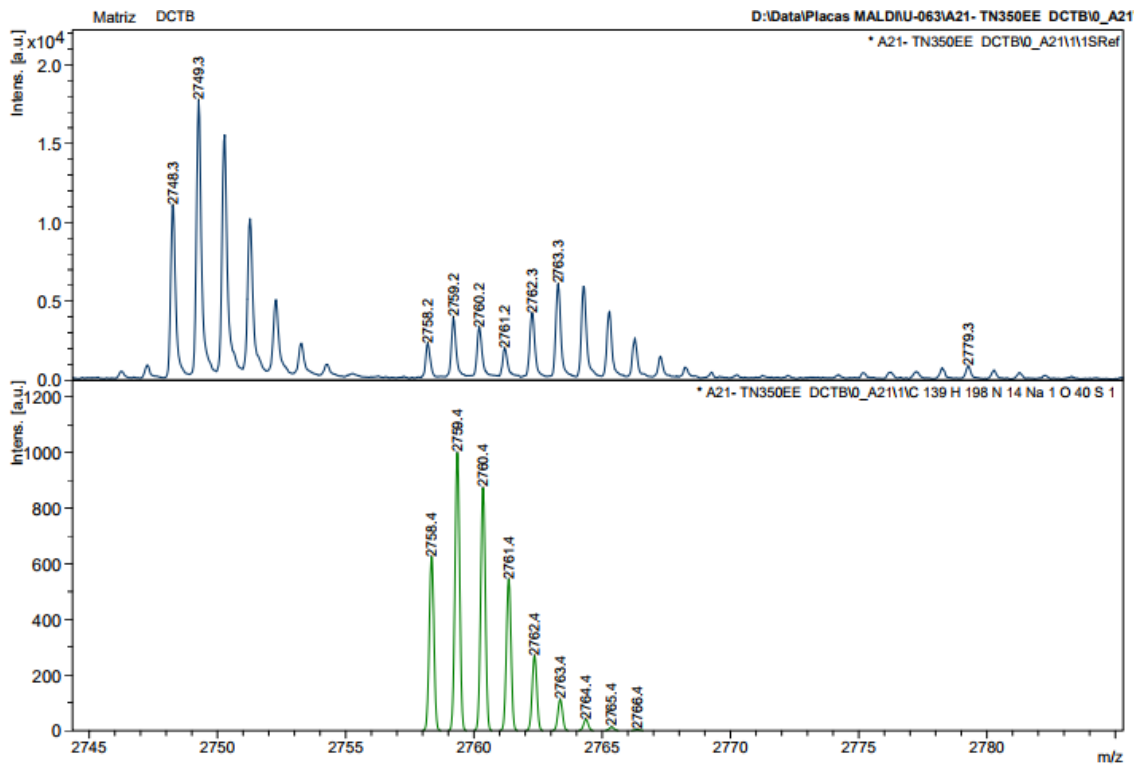
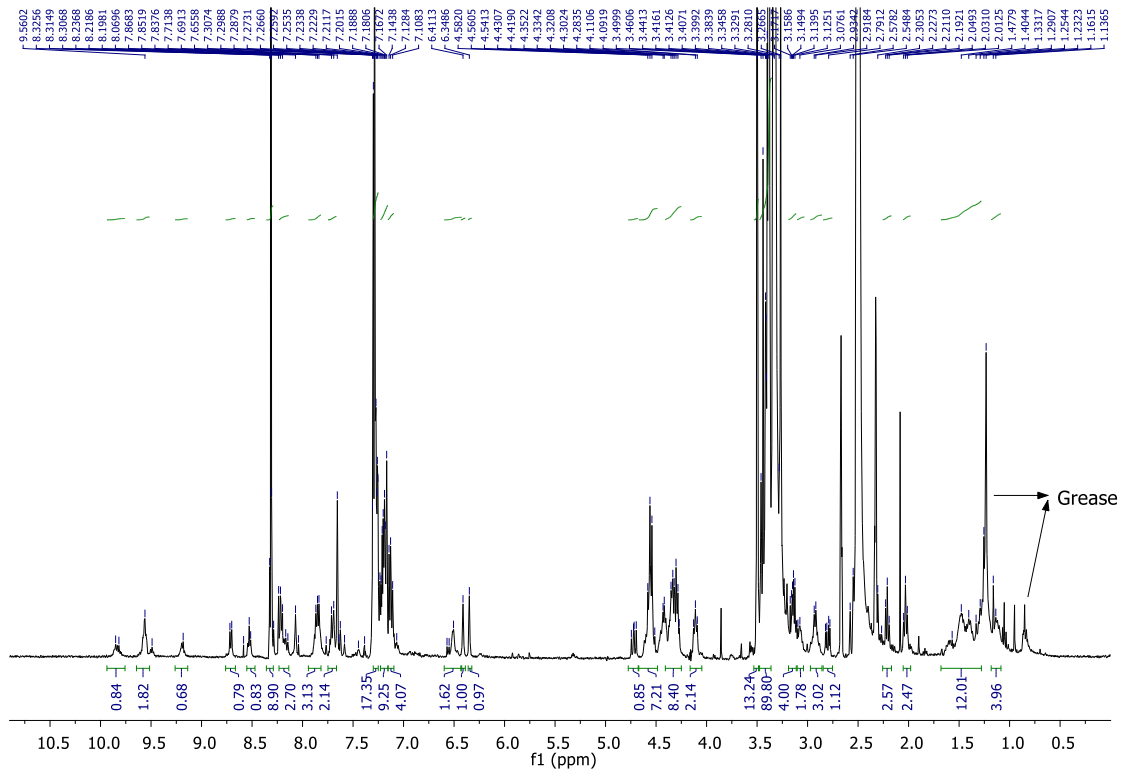
Step iii) Compound was dissolved in DCM, the solution was cooled to 0°C and TFA was added dropwise until the reaction was completed (TLC). Solvent was removed under vacuum. The crude material was dissolved in DCM / MeOH 1/1 v/v ratio and was stirred with Amberlyst A-21 resin for 1h. The solvent was removed under reduced pressure to yield a hygroscopic powder (quantitative yield). ¹H NMR ([D₆]dimethyl sulfoxide): δ = 9.92 (br t, *J* = 6.4 Hz, 2H, NH, H_I), 8.22 (m, 3H, Ar-H, H_J, H_K), 7.37 (m, 4H, H_F), 7.33 (m, 4H, H_E), 4.31 (br d, *J* = 6.4 Hz, 4H, H_G), 4.09 (br s, 4H, H_D).







Thread **III-12** (16 mg, 7.3×10^{-3} mmol), was dissolved in 1.5 mL CHCl_3 (stabilized with amylenes), Et_3N (30 μL , 0.22 mmol) was added and the reaction mixture were stirred vigorously while solutions of the diamine, compound **III-14**, (36 mg, 0.09 mmol) in CHCl_3 (0.7 mL) and the acid chloride, compound **III-13** prepared in step i) (21 mg, 0.09 mmol) (1.07 g, 4.83 mmol) in CHCl_3 (0.7 mL) were simultaneously added over a period of 3 h using motor-driven syringe pumps. After 24h the resulting suspension was filtered and the solvent removed under reduced pressure. The crude material was purified by column chromatography (gradient elution: $\text{DCM} : \text{MeOH}$ 25:1 to 18:1) to furnish rotaxane **III-15** as a colourless oil (7 mg, 35%); ^1H NMR ($[\text{D}_6]$ dimethyl sulfoxide): $\delta = 9.83$ (m, 1H, NH), 9.56 (m, 2H, NH), 9.18 (m, 1H, NH), 8.72 (d, $J = 7.1$ Hz, 1H, NH_t or NH_z), 8.52 (t, $J = 5.7$ Hz, 1H, NH_t or NH_z), 8.31 (m, 1H, Ar-H), 8.22 (m, 2H, Ar-H), 8.11 (m, 1H, NH), 7.82 (m, 1H, NH), 7.70 (m, 1H, NH), 7.63 (m, 2H, Ar-H), 7.28 (m, 16 H, Ar-H), 7.21 (m, 8H, Ar-H), 7.13 (m, 4 H, Ar-H), 6.51 (m, 2H, H_r , H_s), 6.41 (br s, 1 H, H_a), 6.35 (br s, 1 H, H_b), 4.72 (dd, $J = 8.1, 10.9$ Hz, 1 H, H_p or H_p'), 4.56 (m, 7H, H_p or H_p' , H_x , H_x' and H_D or H_G), 4.37 (m, 7H, H_c , H_y , H_q and H_D or H_G), 4.11 (m, 2H, H_d , H_o), 3.50 (m, 14H, EG26-H), 3.40 (m, 90H, EG26-H), 3.17 (m, 2H, EG26-H), 3.08 (m, 1H, H_f), 2.91 (m, 2 H, H_i), 2.81 (m, 1 H, H_e or H_e'), 2.54 (d, $J = 12.8$ Hz, 1 H, H_e or H_e'), 2.32 (m, 2 H, H_w), 2.21 (t, $J = 6.6$ Hz, 2 H, H_v), 2.03 (t, $J = 6.8$ Hz, 2 H, H_j), 1.44 (m, 12 H, H_g , H_i , H_h , H_n , H_m , H_n) MS m/z : calculated for $\text{C}_{108}\text{H}_{172}\text{N}_6\text{O}_{36}\text{S}$ $[\text{M}+\text{Na}]^+$ 2759.4 found MALDI 2759.2.



Comparison of the ^1H NMR spectra of thread, compound **III-12**, and [2]rotaxane compound **III-15** (depicted in Figures III-16 and III-17) in $[\text{D}_6]$ dimethyl sulfoxide (400 MHz, 298K) indicates that the macrocycle predominantly resides over the fumaramide station. The H_r and H_s protons of the fumaramide group are strongly shielded in the rotaxane compared to the thread evidenced by a shift in their peak positions by 0.34 ppm, whereas the chemical shifts of the H_v and H_w protons of the succinic amide-ester group are only slightly shifted by 0.05 ppm.

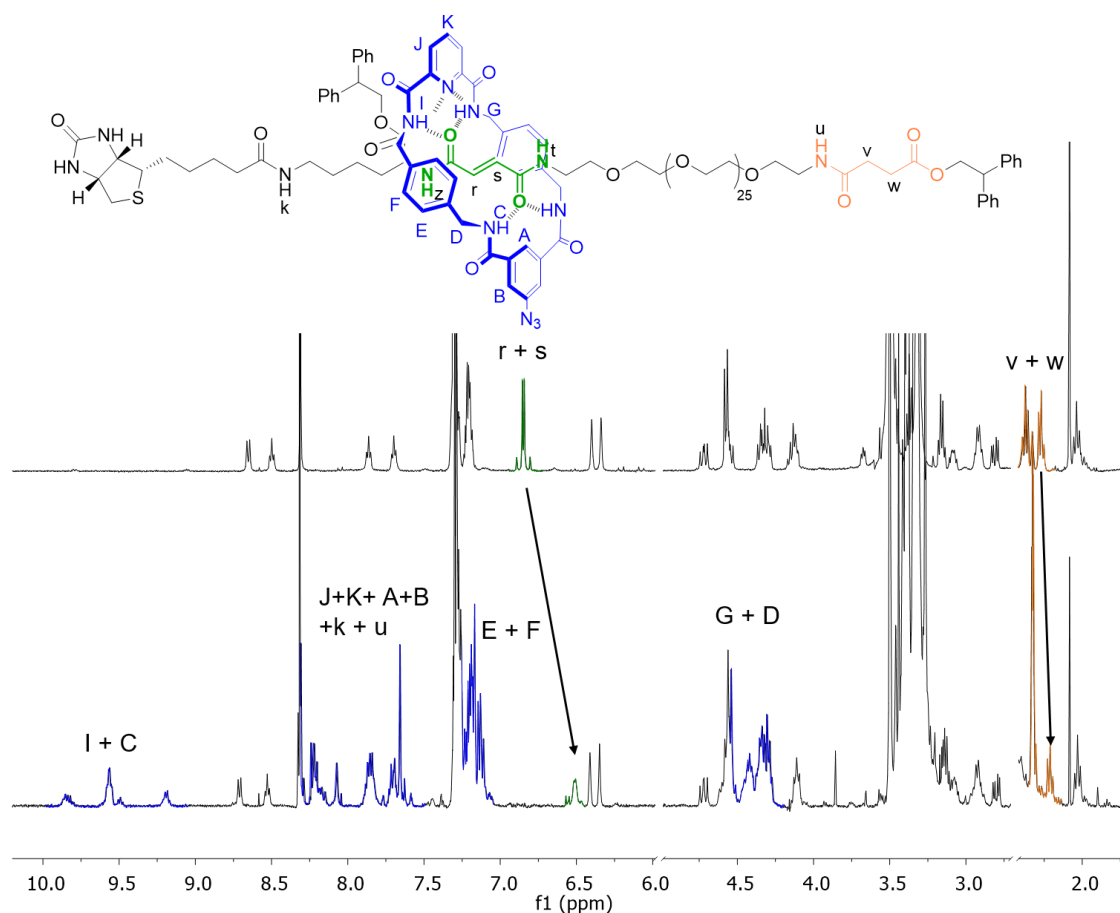


Figure III-16. Comparison of compound **III-12**, (*E*)-thread, (top spectrum) and compound **III-15**, rotaxane molecule, (bottom spectrum) Showing in green the protons corresponding to the fumaramide double bond, which are shifted in 0.34 ppm in the rotaxane molecule; in orange we can find the protons of the succinic-amide ester group, which are shifted only by 0.05 ppm in the rotaxane molecule. Finally we can find the protons corresponding to the macrocycle highlighted in blue.

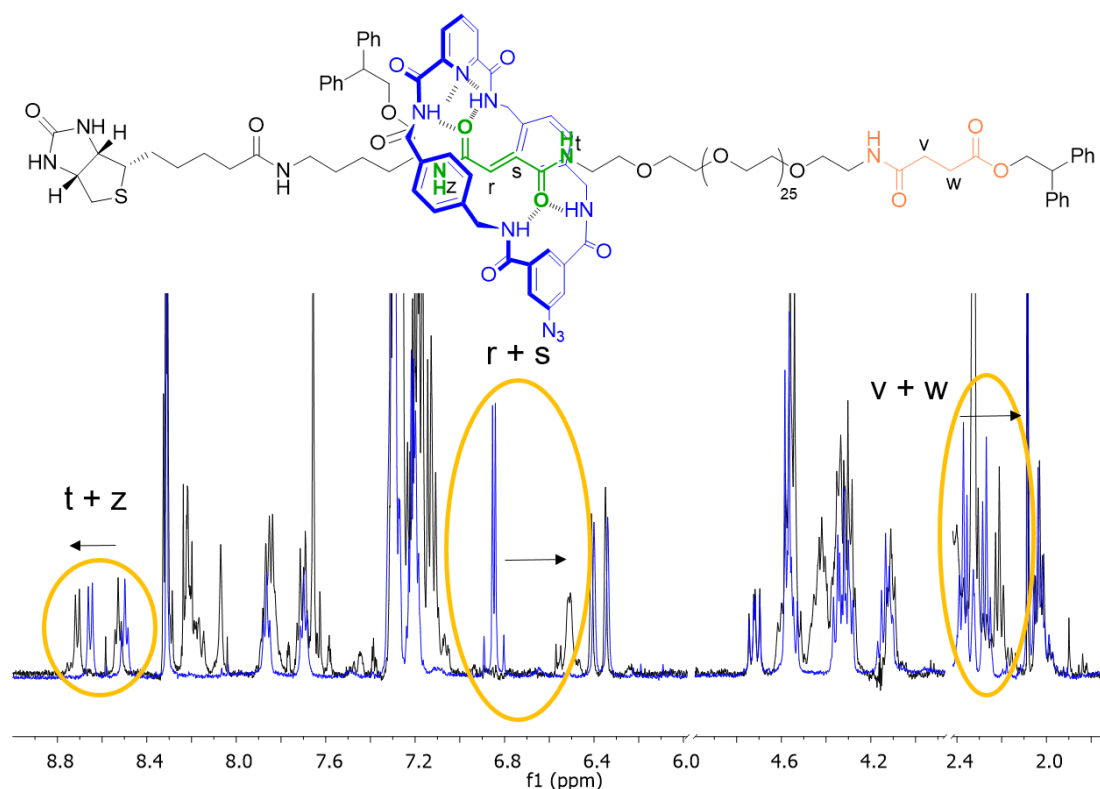


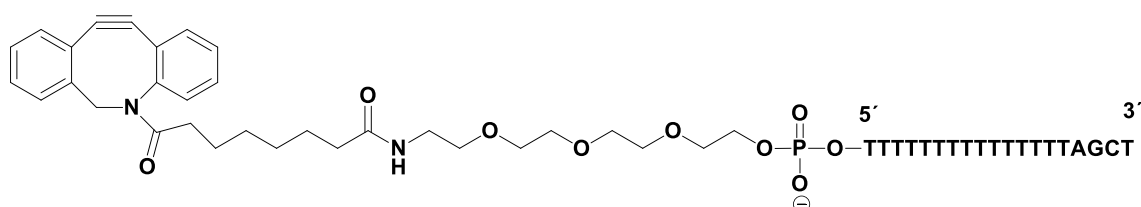
Figure III-17. Comparison of compound **III-12**, (*E*)-thread, (blue spectrum) and compound **III-15**, rotaxane (black spectrum) Showing in yellow circles the protons shifted in the rotaxane molecule.

3.3.2. Oligonucleotide synthesis

The syntheses of oligonucleotides were performed on a MerMade 4 synthesizer (BioAutomation Corporation). For each oligonucleotide synthesis, columns filled with the corresponding Controlled Pore Glass (CPG) solid support. Anhydrous MeCN was used as solvent. For the cleavage of DMTr protecting groups, the resin was purged with 3 % trichloroacetic acid in anhydrous DCM. The removal of the acid was carried out by purging with anhydrous MeCN. The activation of the phosphoramidite functionality was effected by a 0.25 M benzylthiotetrazole solution in anhydrous MeCN. The coupling time for standard phosphoramidites was 2 min and for cyclooctine derivative 5 min. Oxidation of P(III)-species was attained by alkaline iodine solution (20 mM I₂ in THF/Py/water 7/2/1). For the capping of residual 5'-OH-groups, a mixture of solution A (10% Ac₂O, 10% pyridine, 80% THF) and solution B (10% 1-methylimidazole in THF) was used. After completion of the synthesis, the oligonucleotides were cleaved from the solid support with concomitant removal of the Fmoc and β-cyanoethyl protecting groups by reacting the oligonucleotide-charged solid support with 28 % aq. NH₃ at 55 °C for 20 h. The solution was filtered and the filtrate was concentrated in vacuo. The residue was dissolved in 750 μL water. For purification of this crude oligonucleotide solution, a volume containing ~40 nmol crude oligonucleotide was applied to gel

electrophoresis (1 mm, 20% polyacrylamide). The oligonucleotide-containing segments of the gel were visualized by UV-light (260 nm) and separated from the rest of the gel. Oligonucleotides were extracted from the gel using an elutrap system (3 h, 200 V). The solutions were desalted using a NAP-10 column and concentrated in an evaporating centrifuge.

Oligonucleotide 1



Oligonucleotide 2

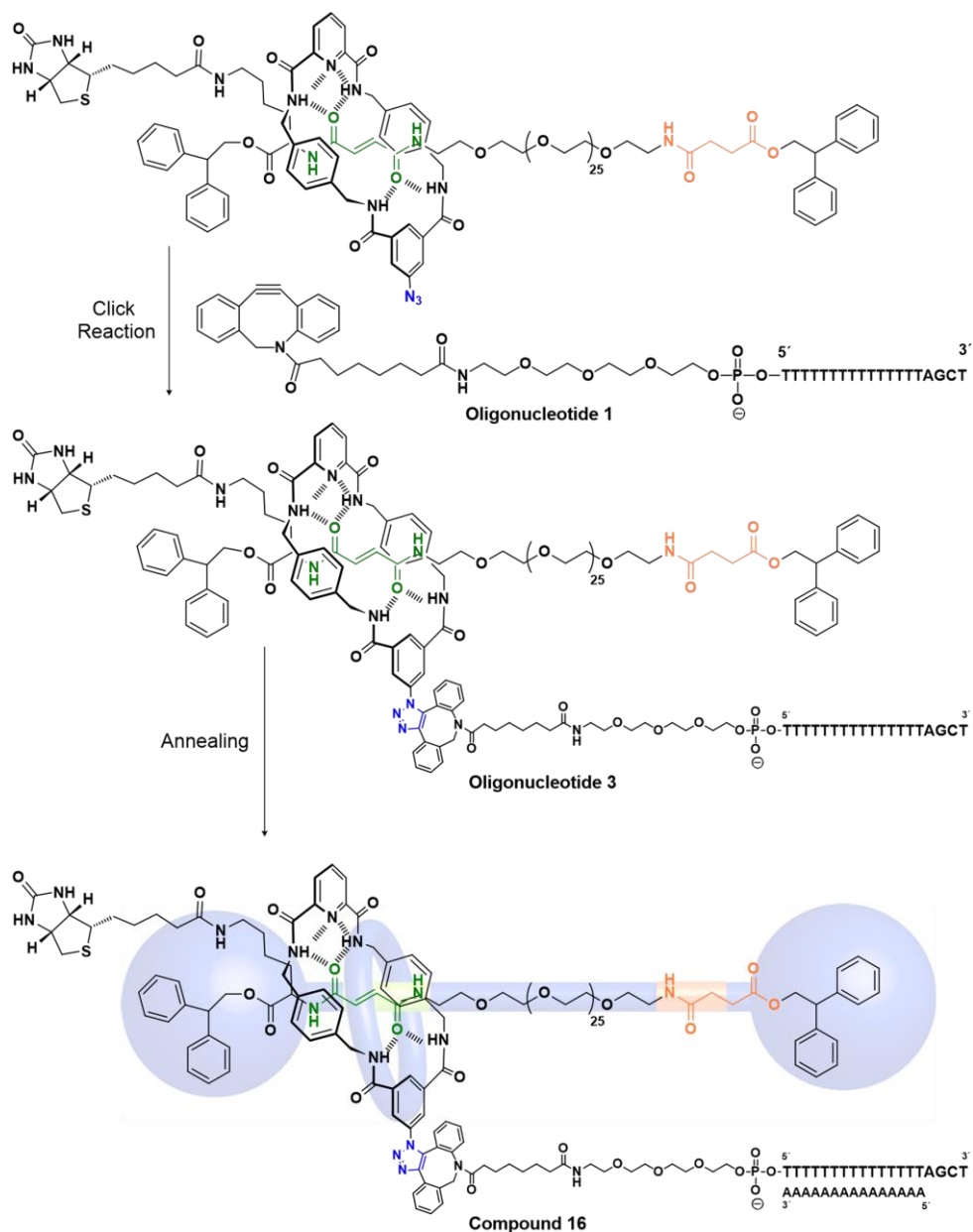


3.3.3. Copper-free click reaction and annealing of oligonucleotides

i) To a stirred solution of oligonucleotide 1 (50 μM) in $\text{H}_2\text{O}/\text{DMF}$ (0.3 mL, 4/1) was added rotaxane 15 (60 μM) in $\text{H}_2\text{O}/\text{DMF}$ (0.3 mL, 4/1). The mixture was allowed to stir overnight at room temperature. Followed and purified by gel electrophoresis (0.2 mm, 20% polyacrylamide). The oligonucleotide-containing segments of the gel were visualized by UV-light (260 nm) and separated from the rest of the gel. Oligonucleotide were extracted from the gel using an elutrap system (3 h, 200 V). The solutions were desalted using a NAP-10 column and concentrated in an evaporating centrifuge, To give the oligonucleotide 3.

ii) 20 μl of each DNA oligonucleotide solution (10 μM) were mixed, and 40 μl of 2 x Annealing Buffer* was added, arriving at a final volume of 80 μL , and a final DNA duplex concentration of 2.5 μM . The mixture was Incubated at 90-95°C for 5 min and gradually/slowly cool down to room temperature (over a period of 12h).

*Annealing buffer: 2 x Annealing buffer concentration: 20 mM Tris-Cl, 100 mM NaCl, 2 mM EDTA.



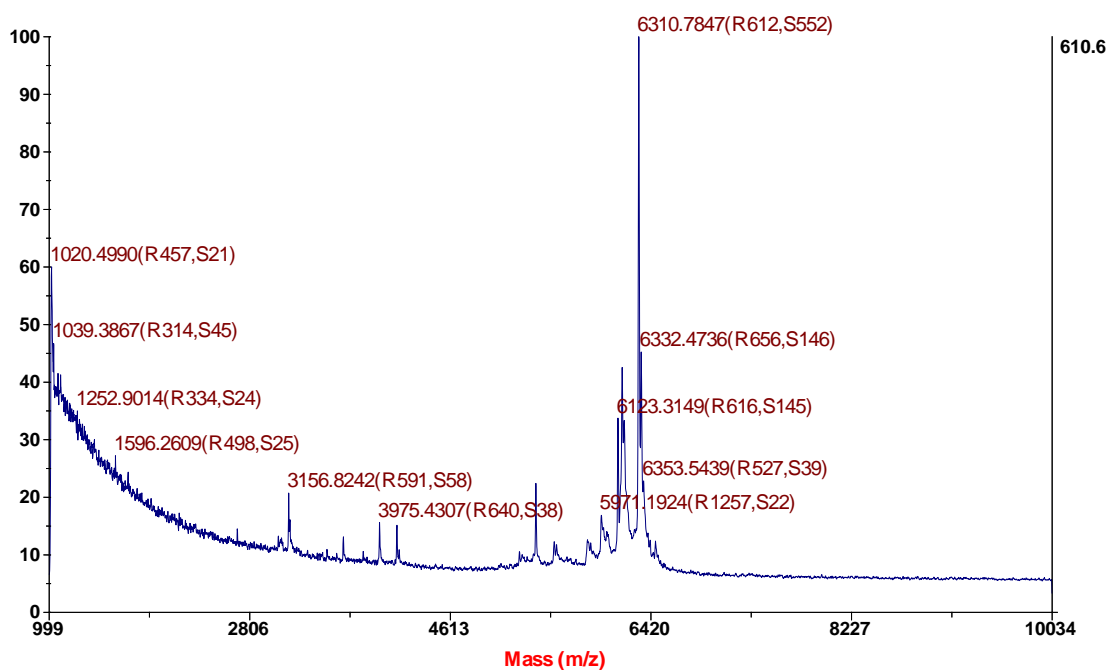
3.3.4. Mass spectral data of synthesized oligonucleotides

MALDI data was obtained at the Proteomic facility of the National Center for Biotechnology (CNB-CSIC).

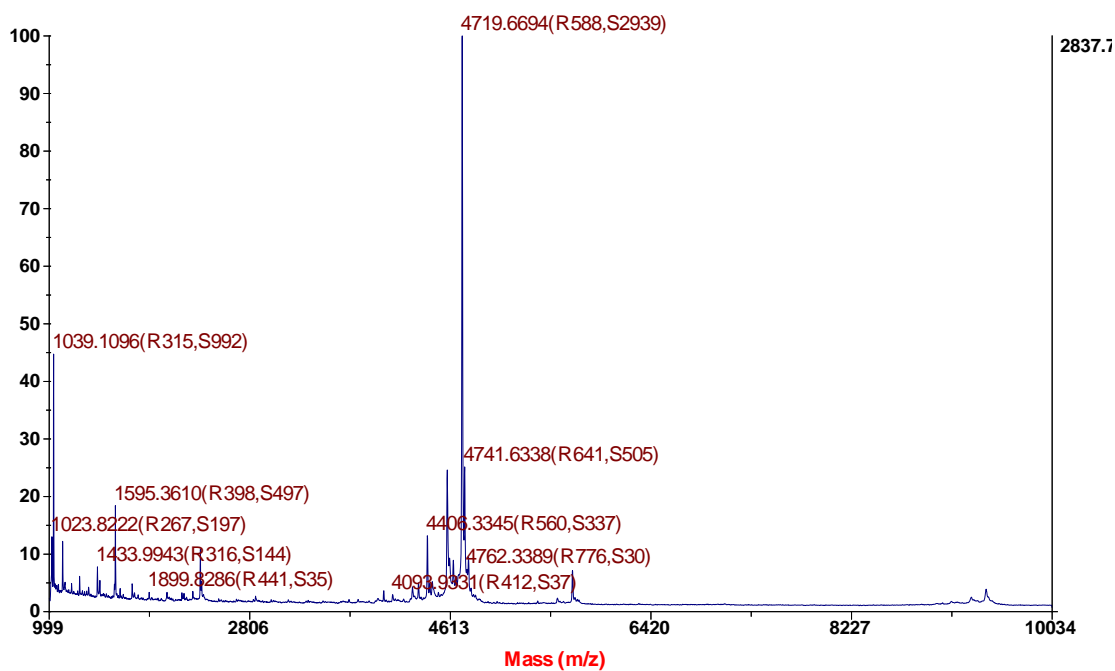
Table III-3. MALDI data of synthesized oligonucleotides

n°.	Sequence	Calculated	Found
1	5'-DBCO-TTT TTT TTT TTT TTT AGCT-3'	6307.4	6310.8
2	5'-AAA AAA AAA AAA AAA-3'	4715.0	4719.7
3	5'-rotax-TTT TTT TTT TTT TTT AGCT-3'	9039.2	9038.8

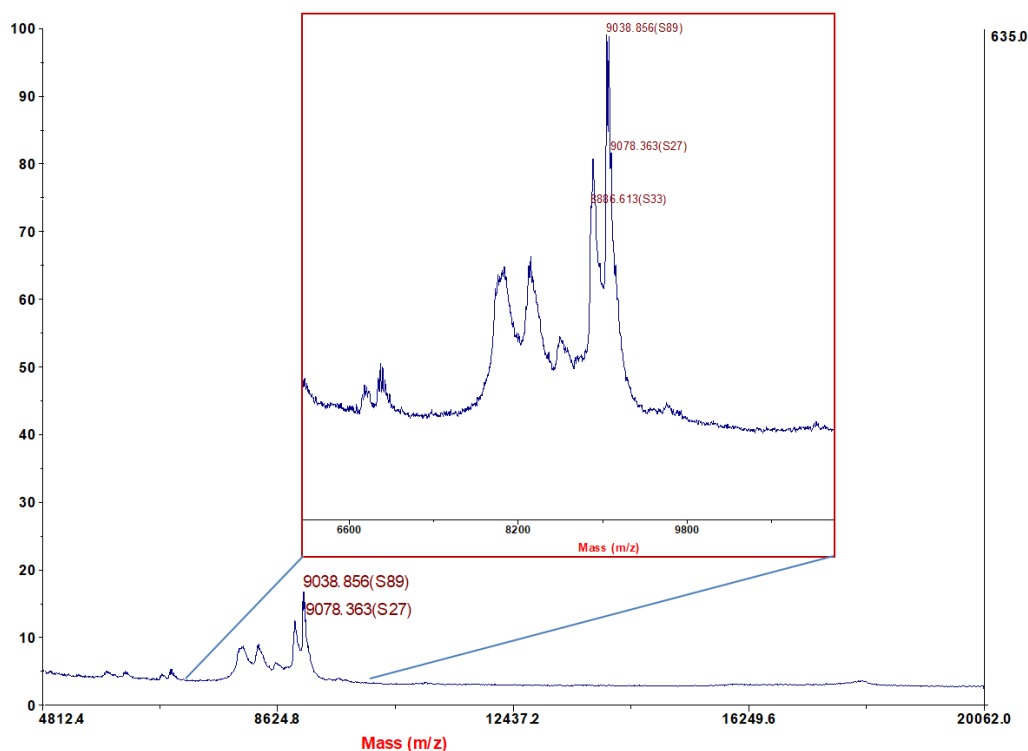
- **Oligonucleotide 1**



- **Oligonucleotide 2**



- **Oligonucleotide 3**



3.3.5. Synthesis of DNA construct

A 2686 dsDNA handle (puc19 vector, Novagen) was cut with *Bam*HI and *Sac*I restriction endonucleases and labeled with Digoxigenin at the *Bam*HI end, and the *Sac*I end was ligated to the previously described oligonucleotide modified with the rotaxane molecule (oligonucleotide 3).

3.3.6. Optical tweezers experiments

Experiments (I). The dsDNA-rotaxane construct was bound to α -Dig covered beads (Spherotech Co.) by incubating 3 μ l of the dsDNA-rotaxane construct with 3 μ l of the beads for 15 min at room temperature. The sample was then diluted with 300 μ l of the reaction buffer (Tris-HCl 20 mM pH 7.5, 150 mM NaCl) and flowed into the fluidic chamber. The α -Dig, DNA covered beads were manipulated with the optical trap and single DNA constructs were obtained by attaching the biotin end of the rotaxane to the streptavidin bead (Spherotech Co.) previously hold on top of a mobile micropipette. The mechanical properties of the DNA construct allowed identifying single attachments (see experimental force-extension curves below). Data were collected in a dual-beam optical tweezers at 100 Hz at 22 ± 1 °C.

Experiments (II): using the dsDNA (830bp) handle

i) The dsDNA-rotaxane construct was bound to α -Dig covered beads (Spherotech Co.) by incubating 3 μ l of the dsDNA-rotaxane construct with 3 μ l of the beads for 15 min at room temperature, then it was diluted with 300 μ l of the reaction buffer (Tris-HCl 20 mM pH 7.5, 150 mM NaCl) and flowed into the flow chamber. These α -Dig (I), DNA covered beads were manipulated with the optical trap

ii) The dsDNA-handle was bound to α -Dig covered beads, by incubating 3 μ l of the dsDNA-handle with 3 μ l of streptavidin (1/10 porportion) and 3 μ l of the beads for 15 min at room temperature, then the sample was diluted; these α -Dig beads were flowed into the fluidic chamber and manipulated with the micropipette.

A single DNA-rotaxane constructs were obtained by attaching the biotin end of the rotaxane to the streptavidin located on the extreme of the dsDNA-handle.

3.3.7. Kinetic rates in the Bell-Evans model

The distances between stations (f = fumaramide, s = succinic amide-ester) were experimentally measured at every force and are depicted in Table III-4:

Force, pN	9.69	9.21	8.82	8.61	8.31	8.13	Mean x_{f-s} , nm
x_{f-s} , nm	14.5	15.1	14.8	15.3	14.5	17.0	15.2 \pm 0.94

Table III-4. Experimental distance x_{f-s} at every force.

In order to calculate average lifetimes of the macrocycle staying in the two stations (fumaramide = Station 1 and succinic amide-ester = Station 2), we used a line $y = y(\text{Station 1}) + \text{treshold} = y(\text{Station 2}) - \text{treshold}$, assuming that all the points above this line belong to the Station 2 and all the points below the line belong to the Station 1. Once the current point is found on the other side of the line, a transition occurs.

Once we have extracted the average lifetimes, we can calculate the kinetic rates for the succinic amide-ester station \rightarrow fumaramide station transition, $k_s(F)$, and viceversa $k_f(F)$, since $k_s = 1/\tau_f$ and $k_f = 1/\tau_s$, at each force (sumarized in Table III-5).

Table III-5. logarithmic scales of the kinetic rates

Force,pN	Ink _s	Ink _f
	fumaramide→suc. amide-ester	suc. amide-ester→fumaramide
9.69	3.61	0.8585
9.21	2.67946±0.21461	1.69827±0.12635
8.82	2.83873±0.32746	3.01798±0.29676
8.61	1.9885±0.24512	2.09964±0.39768
8.31	1.90717±0.08573	4.62537±0.56301
8.13	-0.00399±0.25648	3.80766±0.15437

CHAPTER 4.

Hydrogen Bonds Are Not Shielded In Room Temperature Ionic Liquid

4.1. Introduction

H-bonds are perhaps the most important of noncovalent interactions. The physical properties of water and the information storage in DNA depend on H-bonds, to name just two crucial examples. To this day, however, the balance between the Coulombic and covalent contributions to H-bonds is still the subject of a heated debate.

Current approximations to covalent bonding have proven remarkably accurate based on their good match with state-of-the-art molecule imaging techniques.²²¹⁻²²⁸ Meanwhile, our understanding of noncovalent interactions is much more limited.²²⁹ Supramolecular chemists still argue about the nature, or even the existence,²³⁰ of particular interactions. Specifically, the nature of H-bond is still rather controversial. H-bonds have traditionally been understood as a largely electrostatic interaction,²⁰ but the question of a relevant covalent contribution to H-bonds keeps resurfacing.²³¹⁻²³³ Motivated by this debate, in 2011 the IUPAC moved away from a definition of H-bond that included the very explicit “best considered as an electrostatic interaction” to the much more neutral “is an attractive interaction between a hydrogen atom from a molecule or a molecular fragment X-H in which X is more electronegative than H, and an atom or a group of atoms in the same or a different molecule, in which there is evidence of bond formation”.²³⁴

More recently, Weinhold and Klein presented the ultimate argument in favor of covalent-dominated H-bonds: anti-electrostatic H-bonds between two molecular species with identical charge.²³⁵ They characterized theoretically, using natural bond orbital (NBO) method,²³⁶ a variety of H-bonded anion–anion and cation–cation complexes that demonstrated how the short-range donor-acceptor covalency forces overcome the powerful long-range electrostatic opposition to be expected between ions of like charge.

However, their conclusions were immediately refuted by Frenking and Caramori,²³ who used the energy decomposition analysis (EDA)²³⁷ method to exalt the electrostatic character of the H-bond. Shortly after, it was re-claimed by Weinhold and Klein, who stood by their initial conclusions and argued strongly in favor of a significant covalent contribution to H-bonds.²⁵

From the experimental point of view, Flood and co-workers have very recently provided irrefutable evidence for the existence of stabilizing anion–anion H-bonds in solution, within macrocyclic cavities.²³⁸ The H-bonded bisulfate dimer, $[\text{HSO}_4\cdots\text{HSO}_4]^{2-}$, is stable in solution, encapsulated as a supramolecular complex inside cyanostar macrocycles (Figure IV-1).

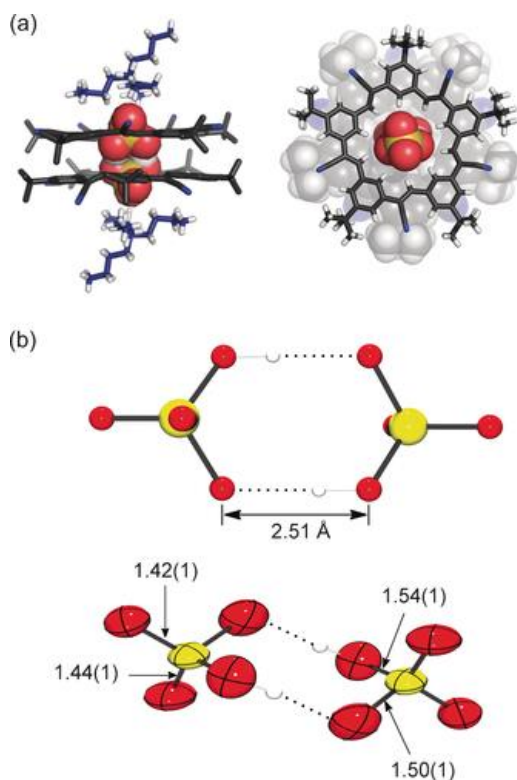


Figure IV-1. a) Crystal structure showing different views the dimer of bisulfate anions that is inside a pair of cyanostars end-capped with two tetrabutylammonium (NBu_4^+) cations producing an overall 2:2:2 complex $\text{CS}_2(\text{HSO}_4)_2(\text{NBu}_4)_2$. b) View of the encapsulated bisulfate dimer showing the self-complementary, anti-electrostatic hydrogen bonding (yellow = S, red = O). Thermal ellipsoids are drawn at 50% probability. Figure reprinted with permission from **WILEY**, *Angew. Chem. Int. Ed.* **2016**, 55 (45), 14057-14062. Copyright (2016).

In other experimental study, Moriarty and co-workers used non-contact atomic force microscopy to image H-bonding networks with sub-molecular resolution, and concluded that the short-range energy force and potential energy landscapes of intermolecular H-bonds were “surprisingly similar” to intramolecular C-C bonds (Figure IV-2).²³⁹

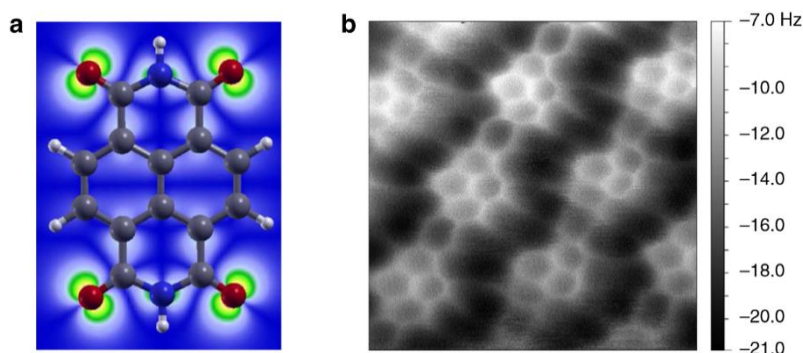


Figure IV-2. a) Ball-and-stick model of naphthalene tetracarboxylic diimide (NTCDI) with a partial charge density isosurface superimposed (Colour coding: grey, carbon; white, hydrogen; red, oxygen; blue, nitrogen); b) Constant height DFM image of a hydrogen-bonded NTCDI island on the Ag. Figure reprinted with permission from **Springer**, *Nat. Comm.* **2014**, 5, 3931.

With all these precedents in mind, we set out to contribute to the question of the nature of the hydrogen bonds. Through this chapter we are going to focus this question from an experimental point of view.

4.2. Results and Discussion

4.2.1. Experimental approach

We are going to compare binding constants (K_a) obtained from titrations on four H-bonded host-guest systems in organic solvents and in room temperature ionic liquid (RTIL), pure salts that are liquid under ambient conditions. As liquids composed entirely of ions, RTILs seem the ideal playground to test the contribution of Coulombic interactions to H-bonding.

First, let's briefly overview the purely electrostatic part of supramolecular interactions. In Table IV-1 are summarized the energy values of the types of electrostatic interactions that will coexist in our experimental design.

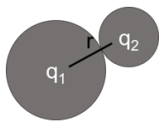
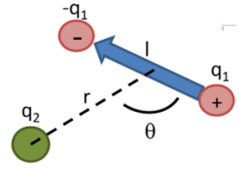
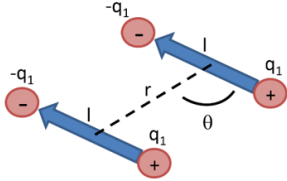
Interaction	Energy	Scheme
Ion pairing	$V(r) = -\frac{q_1 q_2}{4\pi\epsilon_0 r}$	
Ion - Dipole	$V(r, \theta) = -\frac{q_2 \mu_1 \cos\theta}{4\pi\epsilon_0 r^2}$	
Dipole - Dipole	$V(r, \theta) = -\frac{2}{3} \frac{\mu_{12} \mu_{22}}{(4\pi\epsilon_0)^2 k_B T r^6}$	

Table IV-1. Showing the interaction energy between an ion pairing, an ion-dipole and a dipole-dipole couples. Where, a dipole is represented by a vector directed from the positive charge to the negative one. ϵ_0 is the dielectric constant; μ is the dipole moment, which magnitude is $q \cdot \vec{r}$; and θ is the angle between the direction of the molecule axis and the direction between the molecules.

In principle, in RTILs the dipole-dipole electrostatic contribution to H-bonds (proportional to r^{-6}) should be negligible in comparison with dipole-point charge interactions (proportional to r^{-2}). This purely electrostatic picture has been proven true for weak H-bonds in water, which exists in non self-associated form in RTILs, H-bonded to the anions of the RTIL, forming anion-H-O-H-anion associates.²⁴⁰

Herein, we are going to investigate the predominant component in strong H-bonds by comparing association data for several host-guest pairs in organic solvents and RTIL. We hypothesize that if the electrostatic contribution is the most important one, the presence of net charges around should strongly affect the stability of the H-bonded complexes in RTILs. However, if the covalent contribution is significant, this destabilization should be much smaller.

4.2.2. Bulk studies

We have studied the binding constants of four H-bonded host-guest systems with different charge on the main H-bonding motifs (neutral-neutral, anion-neutral and cation-neutral, Table IV-2) in bulk, using UV-vis spectroscopy. The host-guest systems chosen have been thoroughly studied previously, are synthetically accessible, and span a large range of K_a . In particular, we have chosen benzamidine-acetic acid (Ben-AcOH in Table IV-2, neutral-neutral), the Hamilton receptor-cyanuric acid derivative pair (HR-cy in Table IV-2, neutral-

neutral), the 1,4,7,10,13,16-hexaoxacyclooctadecane-ammonium derivative (18_crown_6-Am in Table IV-2, neutral-cation) and *N,N'*-dimethyl thiourea-sodium benzoate (DMTU-BzO⁻ in Table IV-2, neutral-anion). In order to investigate the K_a of the host-guest systems using UV-vis titrations, we tagged them with a visible dye if required (see Experimental Section). Very briefly, we analyse the UV-vis spectrum of a solution of the host with increasing concentration of the guest. To discard dilution effects, we work at constant concentration of the host. The spectral data were fitted using Reactlab™ Equilibria global fitting software (see the Experimental Section). As expected, all data fitted satisfactorily to 1:1 binding models.

The RTIL selected is 1-ethyl-3-methylimidazolium tris(pentafluoroethyl) trifluoro phosphate ([emim][FAP]), which is represented in Figure IV-3. Organic solvents were selected to ensure complete solubility of all species in the host-guest binding equilibrium.

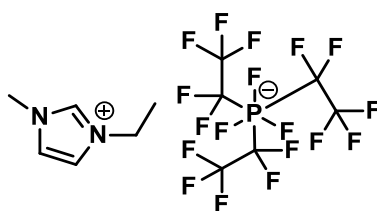


Figure IV-3. RTIL, 1-ethyl-3-methylimidazolium tris(pentafluoroethyl)trifluoro phosphate ([emim][FAP]).

Through these titrations we observed that the four H-bonded host-guest systems associate effectively in [emim][FAP], presenting association constants comparable to those measured in organic solvents, as shown in Table IV-2.

Host-Guest				
log K_a (solvent)	3.4 ± 0.2 (CHCl ₃)	6.5 ± 0.4 (CH ₃ CN)	3.6 ± 0.5 (CH ₃ CN)	4.6 ± 0.1 (CHCl ₃)
log K_a ([emim][FAP])	3.3 ± 0.2	5.8 ± 0.2	3.5 ± 0.4	4.3 ± 0.2

Table IV-2. Structure of the H-bonded host-guest systems and summary of log K_a values (the error values corresponds to three runs).

Examples of the UV-vis titration results for each host-guest pair are depicted in Figure IV-5. It is remarkable that the spectroscopic changes are quantitatively different, but follow similar trends in the organic solvents and [emim][FAP].

For the first couple, Ben-AcOH (Figure IV-5a) the evolution of the spectra in acetonitrile and RTIL during the titration follow similar trends, and are clearly indicative of association. This is one of the most straightforward cases, from the point of view of spectroscopy, as the AcOH guest is completely transparent in the UV-vis region under study. In the titrations performed in acetonitrile, we observe a depletion of the Ben absorption maximum centered at 254 nm, which is accompanied by a blue-shift to 250 nm. These changes are concomitant with the appearance of a new absorption band at around 272 nm, with a clear isosbestic point at 269 nm. In the case of titrations performed using RTIL as solvent, we observe that the absorption band at 271 nm, indicative of Ben H-bonds is already present in the absence of AcOH guest, clearly indicating that the Ben is initially H-bonded, to itself forming a dimer and/or to the RTIL. Upon addition of AcOH, we see the intensity of this band increases significantly and is red-shifted to 274 nm, while the UV maximum at 251 nm is red-shifted to 254 nm. These changes occur without the formation of a clear isosbestic point, in accordance with a picture where Ben coexists as free (or dimerized) species and H-bonded both to the RTIL and to the AcOH guest. However, it is clear from the evolution of the spectra during the titration that the AcOH guest is the strongest binder, and displaces the equilibrium towards Ben-AcOH host-guest complexes. This is also reflected on the good fit to a 1:1 binding model.

For the analysis of the UV-vis spectra of the second and third pairs, that are, HR-cy and 18_Crown_6-Am, cy and Am were tagged with a UV-vis dye, $[\text{Ru}(\text{bpy})_3]^{2+}$, which confers the following spectroscopic properties: $[\text{Ru}(\text{bpy})_3]^{2+}[\text{PF}_6^-]_2$ absorbs UV light and visible light. In acetonitrile the molecule strongly absorbs at 452 ± 3 nm corresponding to the metal to ligand charge transfer (MLCT) transition (extinction coefficient of $14,600 \text{ M}^{-1}\text{cm}^{-1}$), 285 nm corresponding to ligand centered (LC) $\pi^* \leftarrow \pi$ transition and a weak transition around 325 nm (d-d transition).^{241, 242} In Figure IV-4 are depicted this transitions.

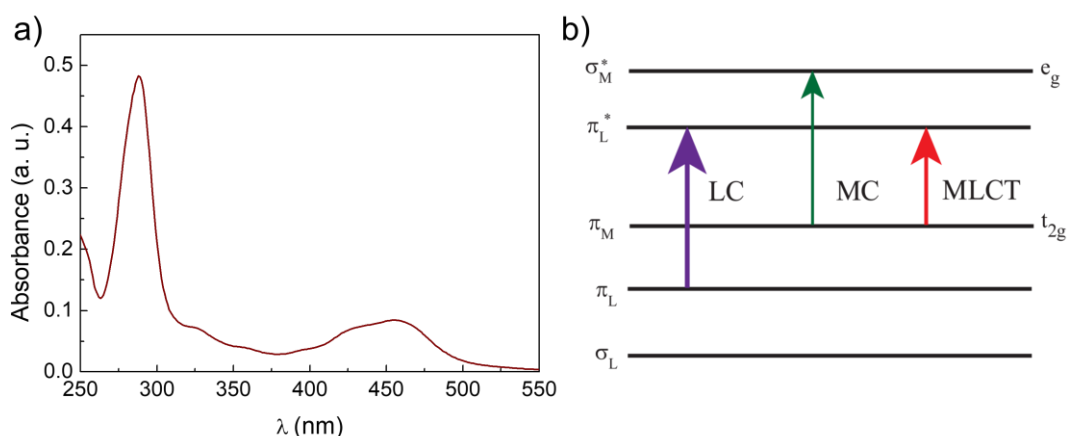


Figure IV-4. a) $[\text{Ru}(\text{bpy})_3]^{2+}[\text{PF}_6^-]_2$ UV-Vis spectrum in acetonitrile. b) Transition of $[\text{Ru}(\text{bpy})_3]^{2+}[\text{PF}_6^-]_2$. Thus, in the UV-vis spectra of this couples, the absorption changes observed are reflected in the strong band located at 285 nm.

For the titration of the HR-cy couple (Figure IV-5b) we carried out additions of HR to a solution of cy. In the case of the titrations carried out in acetonitrile, we observed an increase in absorption in the UV region, noticeable as both an increase in the absorptivity of the maximum at 288 nm and the appearance of a new absorption shoulder at around 320 nm. By comparison with the arithmetic sum of the pure host and guest species, we can safely attribute these changes to HR-cy binding. In the case of the titration performed in the RTIL, we observed similar trends, with the distinction that the absorption shoulder centered at 320 nm was considerable higher.

The changes in the absorption spectra during the titration of the 18_Crown_6-Am couple (Figure IV-5c) are qualitatively similar but quantitatively much smaller. In this case, the titration was carried out adding aliquots of 18_crown_6 over Am (the concentration of Am was kept constant in order to avoid dilution effects). Since 18_crown_6 is transparent in the UV-vis region under study (250-600 nm) spectroscopic changes observed upon the addition of 18_crown_6 correspond to the formation of new species. Both in the titrations carried out in acetonitrile and in those carried out in RTIL, the increase of the absorption band centred in 285 nm was observed, accompanied by a slight increase of the absorption shoulder centered at 320 nm.

Finally, the titration of the DMTU-BzO⁻ couple, depicted in Figure IV-5d, also shows clear spectroscopic changes indicative of strong association, both in chloroform and in RTIL. In the case of titrations carried out in chloroform, addition of DMTU to the BzO⁻ solution causes the UV-vis spectrum to change dramatically. The UV absorption maximum, initially located at 250 nm, is red-shifted and increases in absorption, which occurs together with a significant decrease in the width of the absorption band, approximating the spectrum of BzOH, and supporting the formation of a DMTU-BzO⁻ H-bonded couple beyond reasonable doubt. Similar trends were observed in the titrations carried out in RTIL, in this case, the absorption band centered at 273 nm is already more pronounced even at [DMTU] = 0 and then grows even more upon addition of DMTU.

In all cases, binding constants in [emim][FAP] were smaller but within the same order of magnitude of K_a in organic solvents. Remarkably, this observation holds true both for the whole range of K_a under study, from the very strong HR-cy to the weaker Ben-AcOH. These results indicate that this type of strong, short H-bonds, is not significantly affected by surroundings composed entirely of cations and anions, suggesting that the balance of Coulombic to covalent interactions in H-bonds is not tipped towards the former.

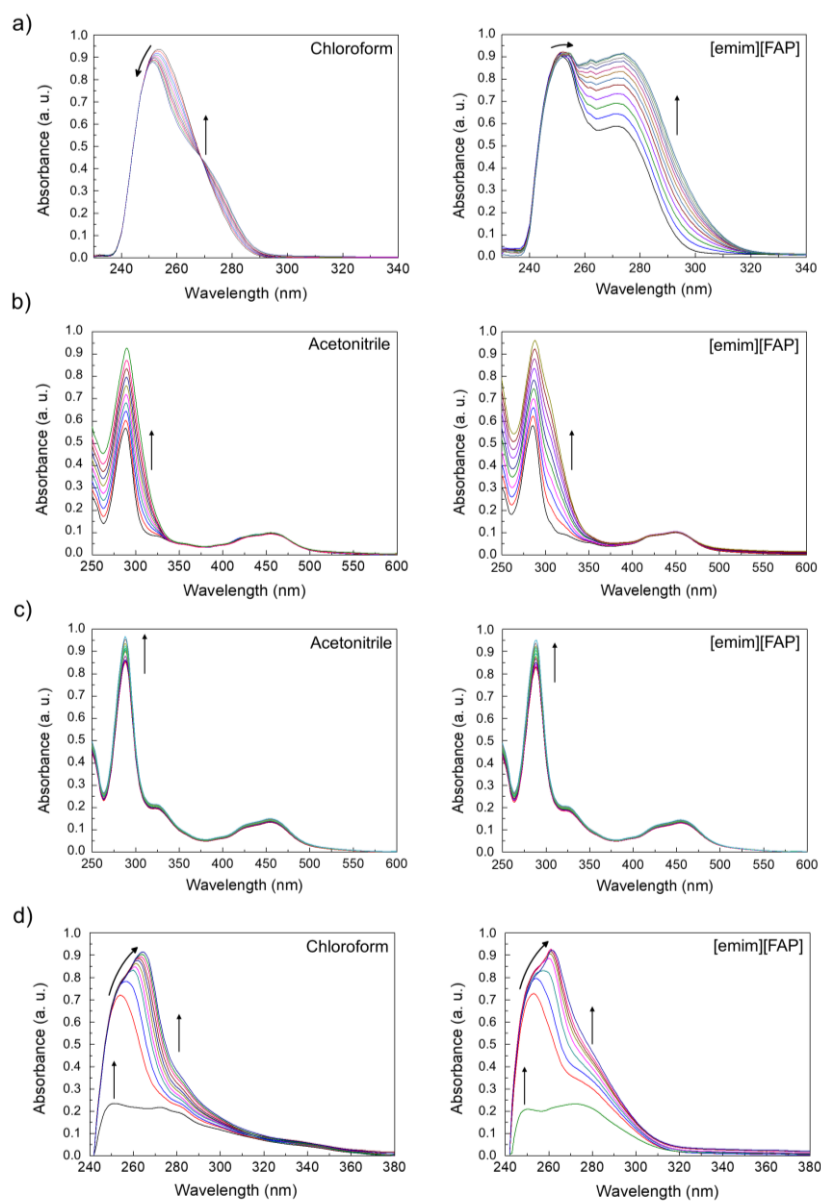


Figure IV-5. UV/Vis titration of a) Ben-AcOH couple in Chloroform (left) and [emim][FAP] (right). UV/vis spectra of Benzamidine (6.5×10^{-4} M) on addition of AcOH (0→3 equiv.), maintaining the concentration of Ben constant, at 298 K. Changes in absorbance reflect changes in the amount of Ben and Ben-AcOH present during the titration experiment and differences in their UV/vis absorption spectra. b) HR-cy couple in acetonitrile (left) and [emim][FAP] (right). UV/vis spectra of cy (4×10^{-6} M) on addition of HR (0→2 equiv.), maintaining the concentration of cy constant, at 298 K. Changes in absorbance reflect changes in the amount of cy and HR-cy present during the titration experiment and differences in their UV/vis absorption spectra. c) 18crown6-Am couple in acetonitrile (left) and [emim][FAP] (right). UV/vis spectra of Am (2.6×10^{-4} M) on addition of 18-crown-6 (0→2 equiv.), at 298 K. Changes in absorbance reflect changes in the amount of Am and 18crown6-Am present during the titration experiment and differences in their UV/vis absorption spectra. d) DMTU-BzO⁻ couple in chloroform (left) and [emim][FAP] (right). UV/vis spectra of BzO⁻ (1×10^{-3} M) on addition of DMTU (0→2 equiv.), at 298 K. Changes in absorbance reflect changes in the amount of BzO⁻ and DMTU-BzO⁻ present during the titration experiment and differences in their UV/vis absorption spectra.

It is important to compare these results with the case of weaker H-bond donors and acceptors, such as water mentioned previously, in which a purely electrostatic picture seems to be coherent with the experimental observations. The ATR spectrum of the RTIL in the presence of water vapour is depicted in Figure IV-6.

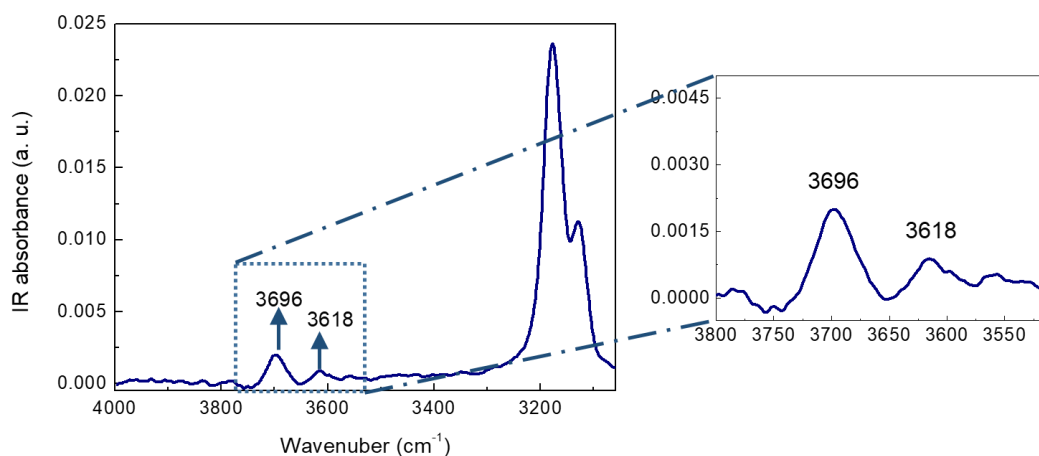


Figure IV-6. ATR-IR spectra of RTIL in the $\nu(\text{O-H})$ region showing the bands of water dissolved in RTIL at 3696 and 3618 cm^{-1} .

It is important to stress that here we investigated the molecular state of water based on the positions of the IR bands of water rather than by comparing their concentrations based on the intensities of these bands. The IR bands corresponding to the antisymmetric (ν_3) and symmetric (ν_1) stretching modes of water usually lie in the region 3000-3800 cm^{-1} , the position and the intensity of these bands are very sensitive to the water environment and to the state of water association via H-bonds. The ν_3 and ν_1 bands in water vapour absorb at 3756 and 3657 cm^{-1} respectively;^{243, 244} these bands shift to lower wavenumber when water interacts with the environment. (e.g. water dissolved in a solvent). The difference in the maximum positions of these bands is ca. 100 cm^{-1} in the case of water bound in symmetric complexes, with both protons of water participating in H-bonds. In the IR spectrum of liquid water the ν_3 and ν_1 bands appear to merge, producing a broad band with a maximum at ca. 3300 cm^{-1} .

Two distinct bands corresponding to the ν_3 and ν_1 modes of water dissolved in [emim][FAP] are seen at 3696 and 3618 cm^{-1} . The position of these two bands of water dissolved in [emim][FAP] indicates that the water molecules are not associated into clusters or pools of water, and can be assigned as “free” water molecules interacting via H-bonds with the [FAP]⁻ anion. This assignment is consistent with the literature data on the spectroscopic manifestation of the formation of symmetrical complexes of water molecules with weak bases.

Spectroscopic characterization of the host-guest systems supported their formation through H-bonds, rather than unspecific solvophobic interactions. In particular, we observed

the fingerprint shifts in the IR spectra for the HR-cy and Ben-AcOH couples. In Figure IV-7, it is clearly observable that the fingerprint of these couples is not the sum of independent species.

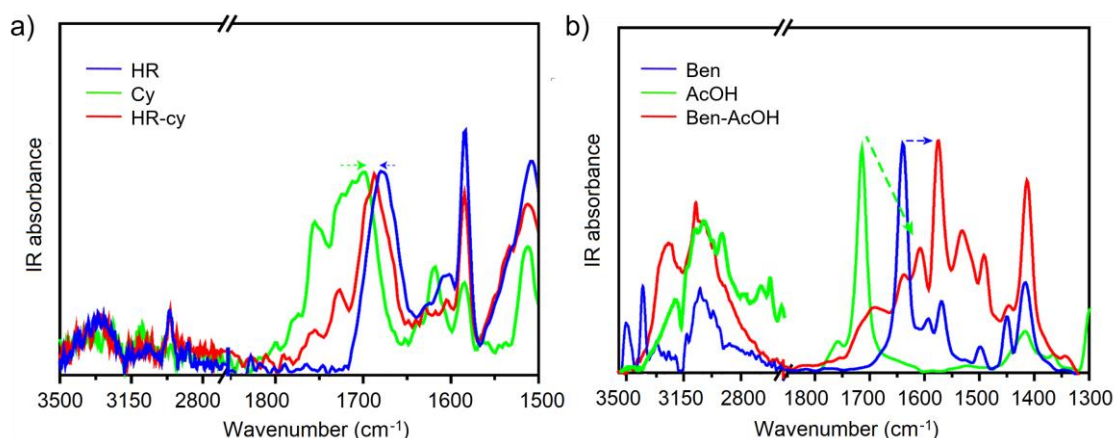


Figure IV-7. ATR-IR spectra in [emim][FAP] of a) HR (blue), cy (green) and the 1:1 molar mixture of both compounds, HR-cy (red) at $7.0 \cdot 10^{-3}$ M. And, b) Ben (blue), AcOH (green) and the 1:1 molar mixture of both compounds Ben-AcOH (red) at 0.1 M. The spectrum of the solvent ([emim][FAP]) has been subtracted in all cases. In both cases we observed the formation of the H-bond couples.

IR spectroscopy, is arguably one of the most powerful methods to give information about the molecular state of H-bond in solution state. Figure IV-7a resents ATR-IR spectra of HR, cy and the 1:1 molar mixture of both compounds, HR-cy at $7.0 \cdot 10^{-3}$ M using [emim][FAP] as solvent. In all the recorded spectra the solvent (RTIL) has been subtracted. HR presents an ATR-IR spectra with the most intense bands in the region of $1700\text{-}1400\text{ cm}^{-1}$, in contrast, the bands around $3500\text{-}3000\text{ cm}^{-1}$ have low intensity, as it is expected, due to the absence of NH_2 and OH groups. Nevertheless, we observe a broad band center around 3310 cm^{-1} , which is assigned to the N-H stretching, $\nu(\text{N-H})$, of secondary amines. Also we observe a sharp band at 2960 cm^{-1} associated to $\nu(\text{C-H})$ of the tert-butyl group. We do not appreciate the pyridine $\nu(\text{C-H})$ stretching, due to the intense vibration of the RTIL in that region. The most interesting band is the $\nu(\text{C=O})$ carbonyl stretching normal mode at 1679 cm^{-1} . The wavenumber of this band indicates a weak C=O double bond character. In the case of the cyanuric acid, we observe a broad band centred a 1714 cm^{-1} with a lower intensity band at higher wavenumber at 1766 cm^{-1} . These bands can be assigned to the different C=O moieties in the molecular structure. Due to the poor intensity of the $3500\text{-}3000\text{ cm}^{-1}$ region, we focus our attention on the carbonyl bands. Interestingly, in the IR spectrum of the 1:1 mixture we observe a broad band with several shoulders, the IR spectrum of the mixture is not the arithmetic sum of the parent IR spectra. We can associate the shoulder a 1696 cm^{-1} with a carbonyl from the cy that is downshifted upon formation of the dimer. On the other hand, the more intense peak, can be

associated with a carbonyl from the HR whose double bond character has been reinforced after the dimer formation. The less intense band at 1729 cm^{-1} , can be associated to a carbonyl of the cy that is not interacting with the HR (see chemical structure of the HR-cy complex). All these changes are in really good agreement with the formation of the expected HR-cy dimer through H-bonds.

As a second example for the IR analysis we analyze the Ben-AcOH couple. The spectrum of ATR-IR spectra of Ben, AcOH and the 1:1 molar mixture of both compounds, Ben-AcOH at 0.1 M using [emim][FAP] as solvent is depicted in Figure IV-7 b). In all the recorded spectra the solvent (RTIL) has been subtracted. The IR spectrum of pure acetic acid is the typical spectrum of the homodimer of acetic acid. A broad spectral feature around 3045 cm^{-1} is observed, assigned to H-Bond OH stretching of a carboxylic acid. Between 2550 and 2800 cm^{-1} , we observe 3 bands assigned as a combination of low energy modes of a cyclic dimer ring with the C-OH bending overtone.²⁴⁵⁻²⁴⁷ We do not observe a narrow band centered at 3540 cm^{-1} that is associated with AcOH monomers. In the fingerprint region, the spectrum is dominated by an intense band centered at 1717 cm^{-1} , assigned to C=O stretching of the carboxylic acid. For the benzamidine, in the region of 3500 - 3000 cm^{-1} the bands are weaker and sharper than those of the O-H stretches. Nevertheless, we can still observe the asymmetric and the symmetric N-H stretch at 3518 and 3422 cm^{-1} for the primary amines (RNH_2). The broad band around 3060 cm^{-1} is associated to the C-H stretch of the aromatic moiety. In the fingerprint, we observe a strong band associated to C=N stretching at 1640 cm^{-1} and at 1572 cm^{-1} a medium intensity band assigned to NH_2 scissoring.

Similarly to the previous example, a new scenario appears when we recorded the spectra in a 1:1 equimolar mixture of both compounds. The spectrum is not the sum of the parent spectra. The bands associated with a cyclic dimer of AcOH and the N-H stretching of primary amine group of Ben are no longer visible. We observe a broad vibrational spectrum between 3400 and 2700 cm^{-1} as it is expected for a doubly H-bonded dimer, with a peak centered at around 3010 cm^{-1} . This broad band is red-shifted with respect to the band of the AcOH homodimer, indicating stronger H-bonds. Both C=X stretching (where X = N or O) suffer a red-shift in frequencies, from 1717 to 1609 cm^{-1} for the C=O and from 1640 to 1578 cm^{-1} for the C=N, as a second clear indication of the formation of strong H-bonds between both compounds. The broad medium-intensity band observed at 1694 cm^{-1} can be assigned to C=O stretching, and belongs to different conformations of the H-bonded heterodimer.

4.2.3. Single molecule experiments

All these data clearly support the formation of the H-bonded host-guest pairs in [emim][FAP]. To gather information of the binding event at the single-molecule level, we turned

to SMFS. In particular, we focused on the HR-cy pair, as benchmark data on SMFS in 1,2-dichlorobenzene (o-DCB) are available from Bassani et al.¹⁶¹ For chemical reasons, we substituted the cy guest with a the barbituric (barb) derivative depicted in Figure IV-8, which has the same H-bonding capabilities. We decorated a gold-coated AFM tip with the barb guest²⁴⁸ (in green in Figure IV-8), and a gold surface with the HR host (in orange in Figure IV-8), using thiol-Au chemistry (See more details in Experimental section). Force-distance measurements were recorded at velocities of 250 nm/s with contact time of 5s. After reaching the maximal force, the two surfaces remained in contact for a time interval of 5 s, after which the direction of the piezo movement was reversed, and the AFM probe was retracted from the surface. Force-distance curves were collected from several different positions on the substrate, and around 50 force-distance curves were measured at each position. These conditions were tested both in o-DCB and in [emim][FAP].

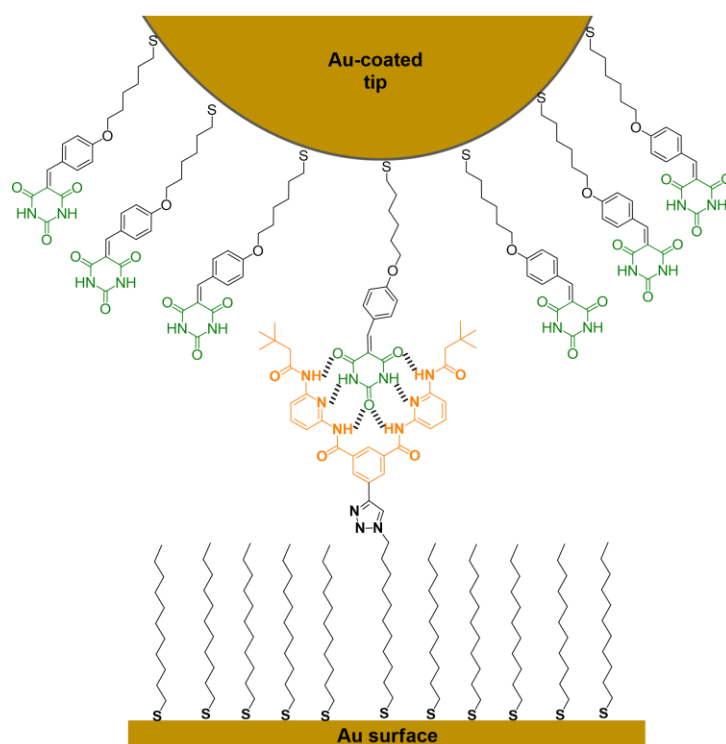


Figure IV-8. Schematic representation of AFM-SMFS of HR-barbituric derivative. Barbituric guest, barb (in green) is immobilized in a gold-coated AFM tip, otherwise the gold-coated surface is functionalized with the HR (in orange).

We first carried out measurements in o-DCB (which are depicted in Figure IV-9), to compare our results with those of Bassani et al.¹⁶¹ From the statistical analysis of 120 curves of three different regions we obtained a binding strength of 434 ± 31 pN for the HR-barb host-guest system, with upper and lower bounds at 164 and 839 pN, respectively (see Figure IV-9a). By subtracting the blank (Figure IV-9b), carried out using a gold-coated tip and a gold-

coated surface without any modification (201 ± 20 pN $n = 120$, 3 regions), we obtain 230 ± 37 pN, which corresponds to the force necessary to break apart the H-bonds between the HR-barb couple; this value is in good agreement with the ~ 180 pN previously reported by Bassani et al.

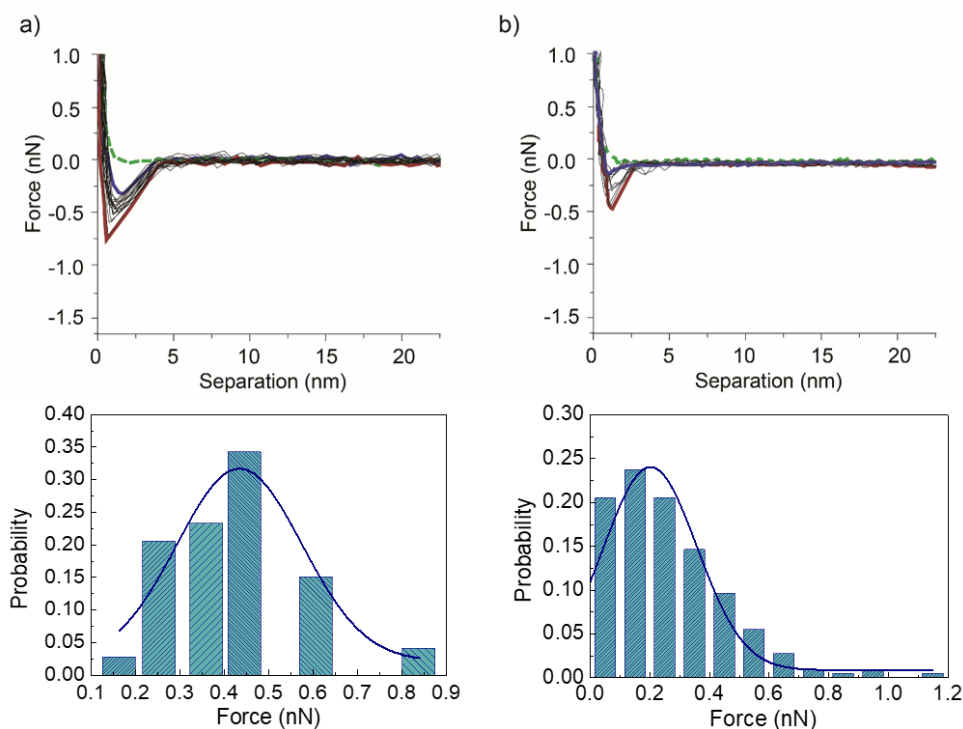


Figure IV-9. a) On the top representative force/distance curves obtained in o-DCB, characterizing the HR-barb interaction. The force profiles represent the interaction forces upon approach (green dash trace) and retraction (twenty aligned black traces, the purple trace represents the lowest breaking force and the red trace corresponds to the highest breaking force) as a function of the separation distance between the surface and the tip. Approaching the sample surface with the AFM probe, no interaction forces were detected, when the retraction take place we can observe a binding event, getting a dissociation force of 431 ± 31 pN ($n = 102$). On the bottom, force histogram fitting to a Gaussian distribution, obtained for 120 curves in three different regions. b) On the top representative force/distance curves obtained in o-DCB, for non-functionalized Au-coated tip and Au-coated surface. The force profiles represent the interaction forces upon approach (green dash trace) and retraction (twenty aligned black traces, the purple trace represents the lowest breaking force and the red trace corresponds to the highest breaking force) as a function of the separation distance between the surface and the tip. Approaching the sample surface with the AFM probe, no interaction forces were detected, when the retraction take place we can observe a binding event, getting a dissociation force of 201 ± 20 pN ($n = 120$). On the bottom, force histogram fitting to a Gaussian distribution, obtained for 200 curves in three different regions.

The retraction curves of the HR-barb system in [emim][FAP] also clearly supported HR-barb binding events (Figure IV-10a), in agreement with the bulk data. The force of the binding event was calculated to be 845 ± 17 pN for 206 binding events in ten different regions, with

upper and lower bounds at 1400 and 500 pN, respectively. These results are explained in light of the control experiments, where no HR-cy binding can take place (Figure IV-10b). In [emim][FAP], for the non-functionalized tip and non-functionalized gold surface, we obtained a peak in the retraction curve that amounts to 751 ± 25 pN, for 200 curves measured in ten different regions (Figure IV-10b). These results show that there is a strong non-specific van der Waals interaction between the tip and the first few layers of RTIL in close contact with the gold surface, in line with literature precedents.²⁴⁹ By subtracting this value, we obtain a breaking force of 94 ± 30 pN, smaller than the value obtained in o-DBC, but within the same order of magnitude.

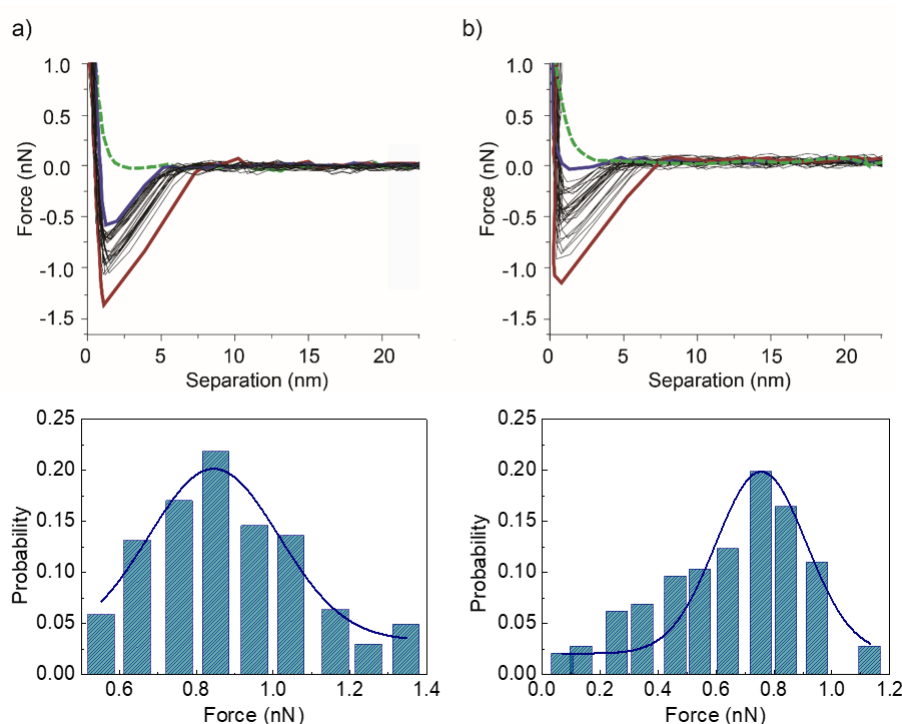


Figure IV-10. a) On the top, representative force/distance curves obtained in [emim][FAP], which characterizes the interaction that occurs between HR-barb couple. The force profiles represent the interaction forces upon approach (green dash trace) and retraction (twenty aligned black traces, showing a purple trace which represents the lowest breaking force and a red trace which corresponds to the highest breaking force) as a function of the separation distance between the surface and the tip. Approaching the sample surface with the AFM probe, no interaction forces were detected, when the retraction take place we can observe a binding event, getting a dissociation force of 845 ± 17 pN. On the bottom, force histogram fitting to a Gaussian distribution, obtained for 206 curves in ten different regions. b) On the top representative force/distance curves obtained in [emim][FAP], for non-functionalized Au-coated tip and Au-coated surface. The force profiles represent the interaction forces upon approach (green dash trace) and retraction (twenty aligned black traces, the purple trace represents the lowest breaking force and the red trace corresponds to the highest breaking force) as a function of the separation distance between the surface and the tip. Approaching the sample surface with the AFM probe, no interaction forces were detected, when the retraction take place we can observe a dissociation force of 751 ± 25 pN ($n = 200$).

On the bottom, force histogram fitting to a Gaussian distribution, obtained for 50 curves in three different regions.

In summary, our data show that strong H-bonds are not completely shielded in [emim][FAP], where electrostatic interactions are expected to play a very minor role. This is opposed to the findings for weaker H-bonds, such as those in water, which are substituted by O-H-anion interactions in RTILs.²⁴⁰ Therefore, our experiments point to a significant covalent contribution to strong H-bonds, which are only weakened, but not completely substituted by the RTIL point charges, and away from a purely electrostatic view of H-bonding. In order to obtain a more complete vision of the problem, and to generalize or disprove our preliminary conclusions, we are now studying the binding constants of the same host-guest systems in a collection of RTILs, in which we systematically vary the size of the cation and anion.

4.3. Experimental Section

Contents:

- 4.3.1. Synthesis of the HR-cy couple
 - 1.a. Cy synthesis
 - 1.b. HR synthesis
- 4.3.2. Synthesis of Am derivative
- 4.3.3. Synthesis HR-barb couple for AFM studies
 - 3.a. HR synthesis
 - 3.b. Barb synthesis
 - 3.c. Synthesis of 11-azidoundecane-1-thiol
- 4.3.4. AFM Tip and surface functionalization
 - 4.a. Barb functionalization of AFM gold-coated Si cantilevers
 - 4.b. HR functionalization of gold-coated surface
- 4.3.5. SAM characterization
 - 5.a. ATR experiments
 - 5.b. Contact angle measurements
- 4.3.6. AFM measurements
- 4.3.7. Description of UV/vis titration experiments
- 4.3.8. Description of ATR experiments with RTIL

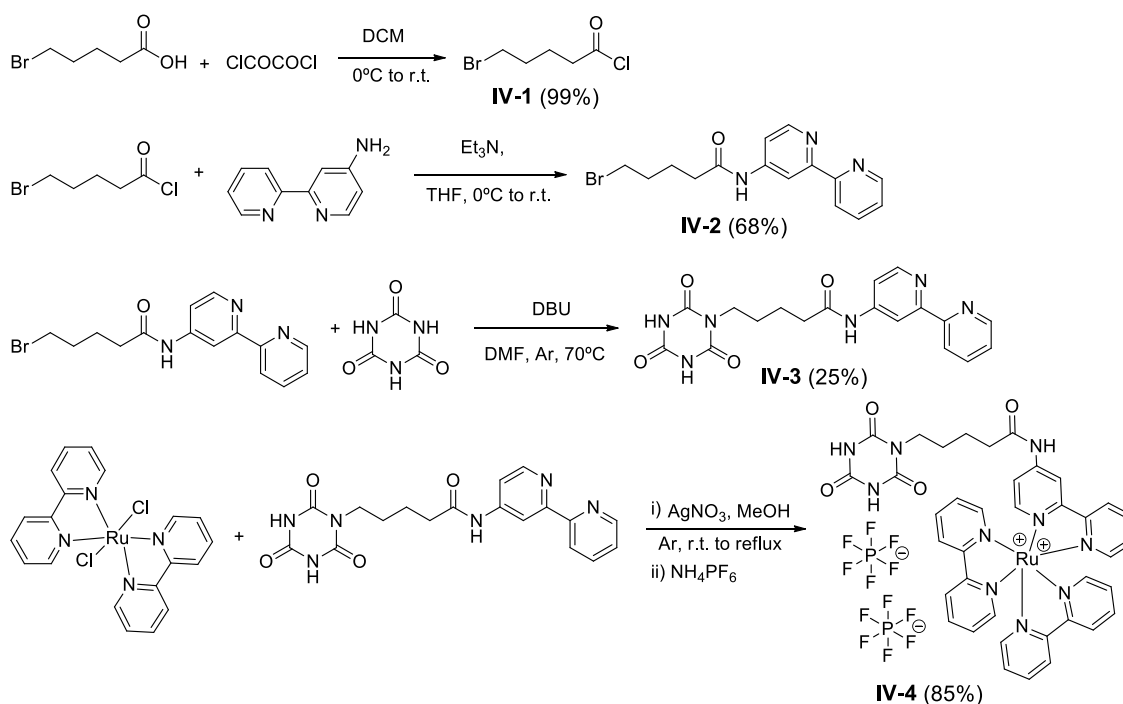
General

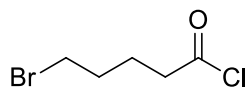
200 nm Gold-coated glass slides (1 cm x 1 cm) were purchased from Ssens bv.

All solvents were dried according to standard procedures. Reagents were used as purchased. All air-sensitive reactions were carried out under argon atmosphere. Flash chromatography was performed using silica gel (Merck, Kieselgel 60, 230-240 mesh, or Scharlau 60, 230-240 mesh). Analytical thin layer chromatographies (TLC) were performed using aluminium-coated Merck Kieselgel 60 F254 plates. NMR spectra were recorded on a BrukerAvance 400 (^1H : 400 MHz; ^{13}C : 100 MHz), spectrometer at 298 K, unless otherwise stated, using partially deuterated solvents as internal standards. Coupling constants (J) are denoted in Hz and chemical shifts (δ) in ppm. Multiplicities are denoted as follows: s = singlet, d = doublet, t = triplet, m = multiplet, br = broad. Fast Atom Bombardment (FAB) and Matrix-assisted Laser desorption ionization (coupled to a Time-Of-Flight analyzer) experiments (MALDI-TOF) were recorded on a VS AutoSpec spectrometer and a Bruker ULTRAFLEX III spectrometer, respectively.

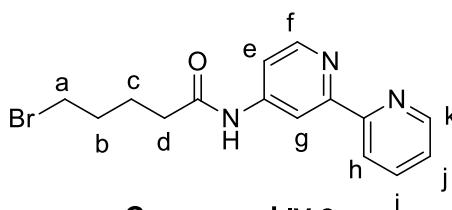
4.3.1. Synthesis of the HR-cy couple

4.3.1.a. Cy synthesis

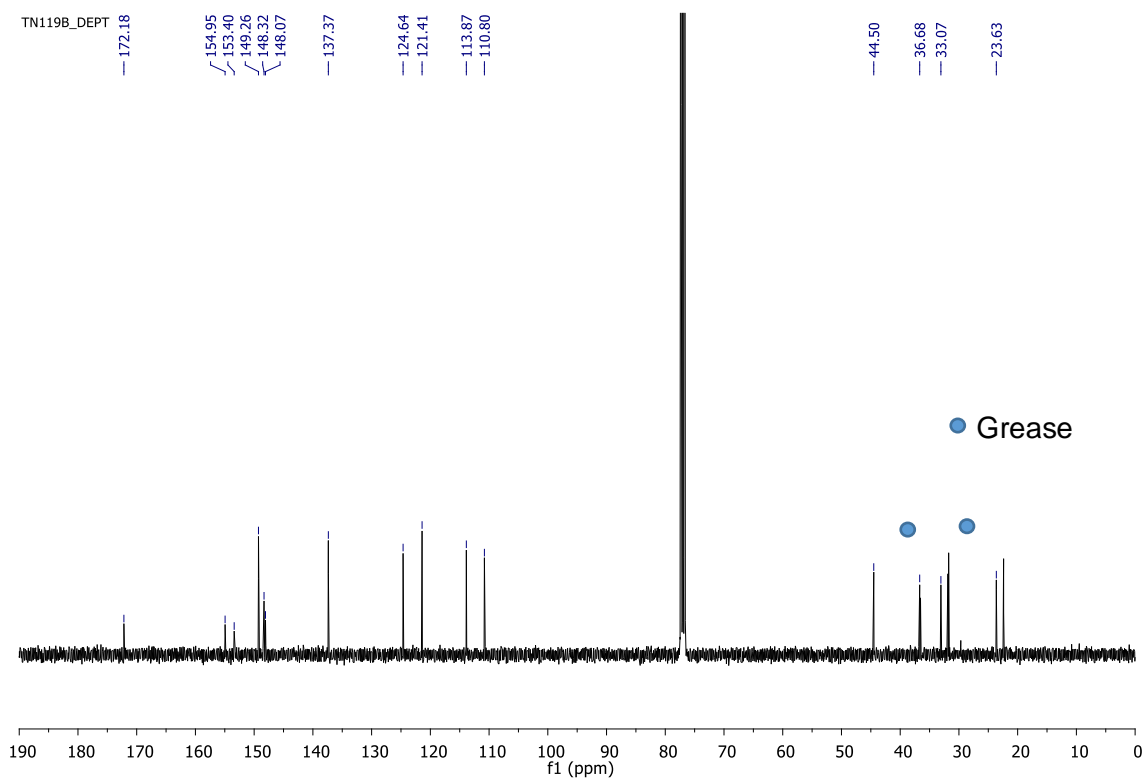
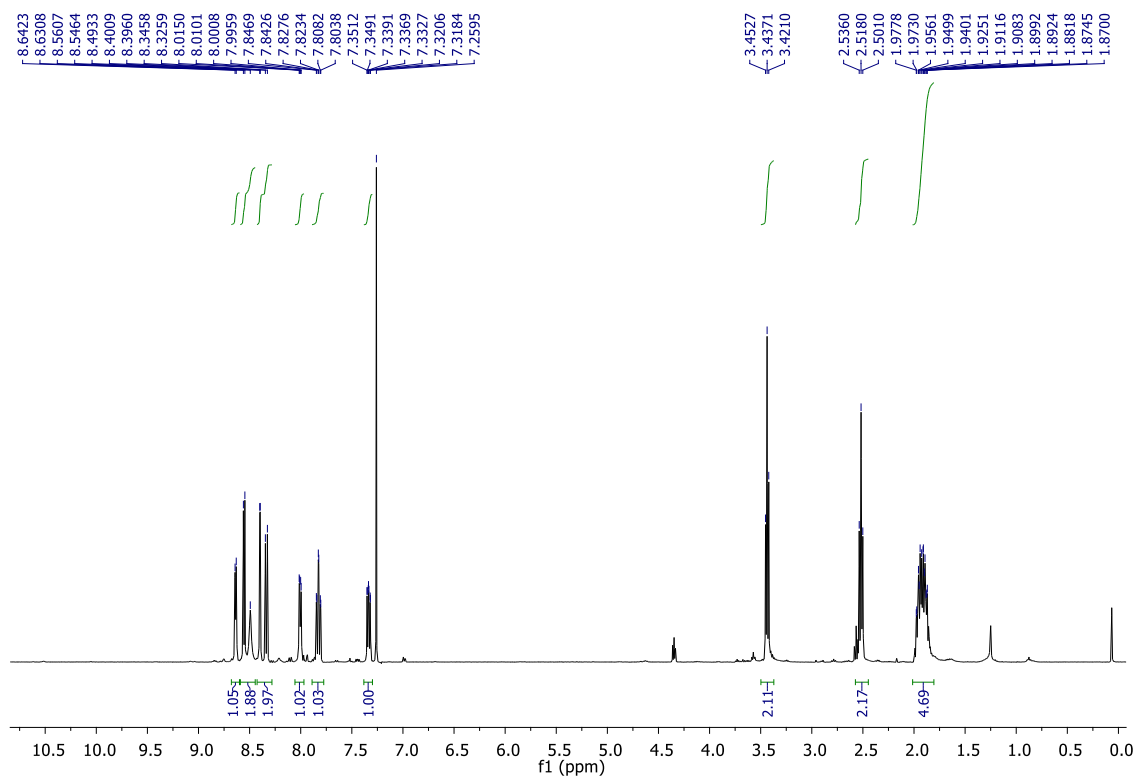


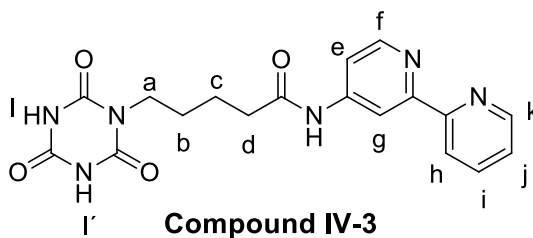
5-bromopentanoyl chloride**Compound IV-1**

5-Bromovaleric acid (200 mg 1.1 mmol) was suspended in anhydrous DCM (4.4 mL), 2 drops of DMF were added and oxalyl chloride (0.12 mL, 1.4 mmol) was added dropwise over a period of 15 min. The reaction was stirred for two hours, then the solvent was removed under reduced pressure and the crude material was directly used in the next step reaction without further purification.

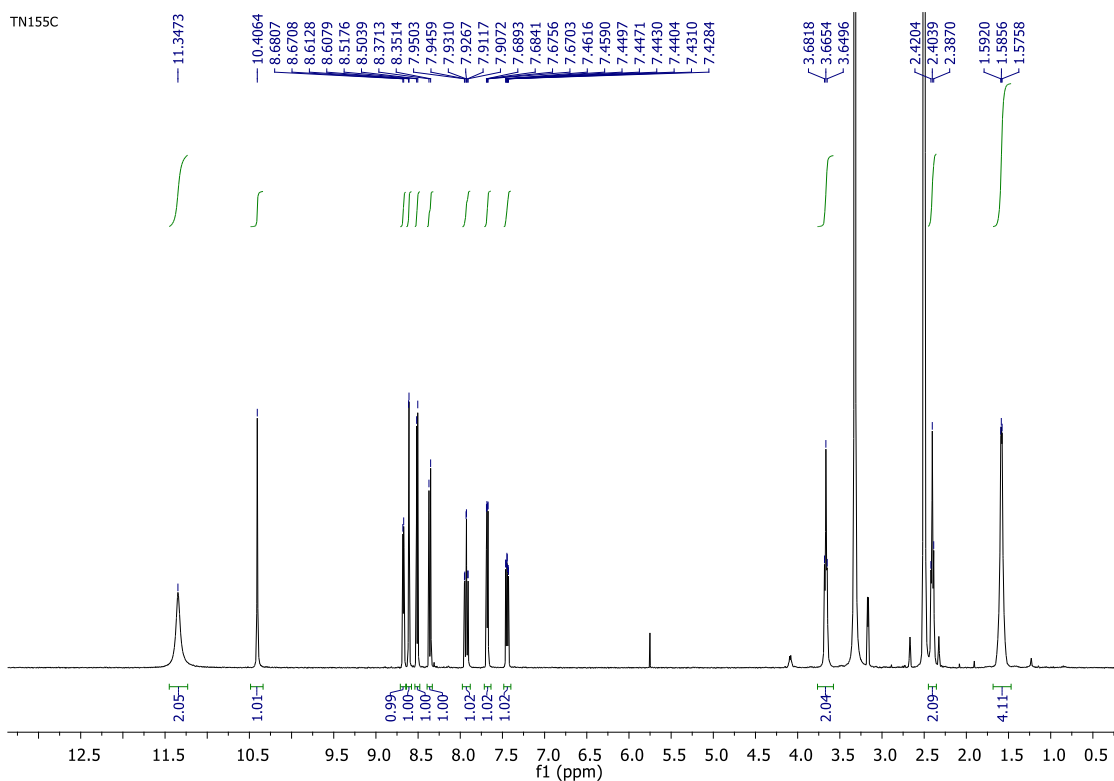
***N*-([2,2'-bipyridin]-4-yl)-5-bromopentanamide****Compound IV-2**

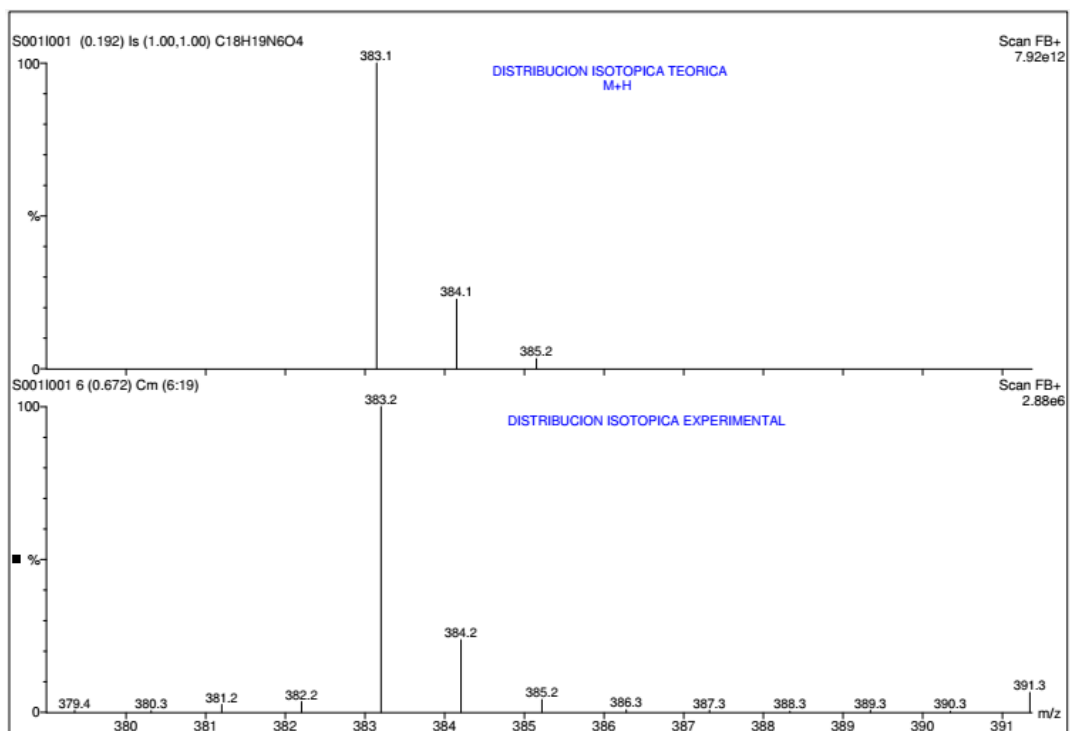
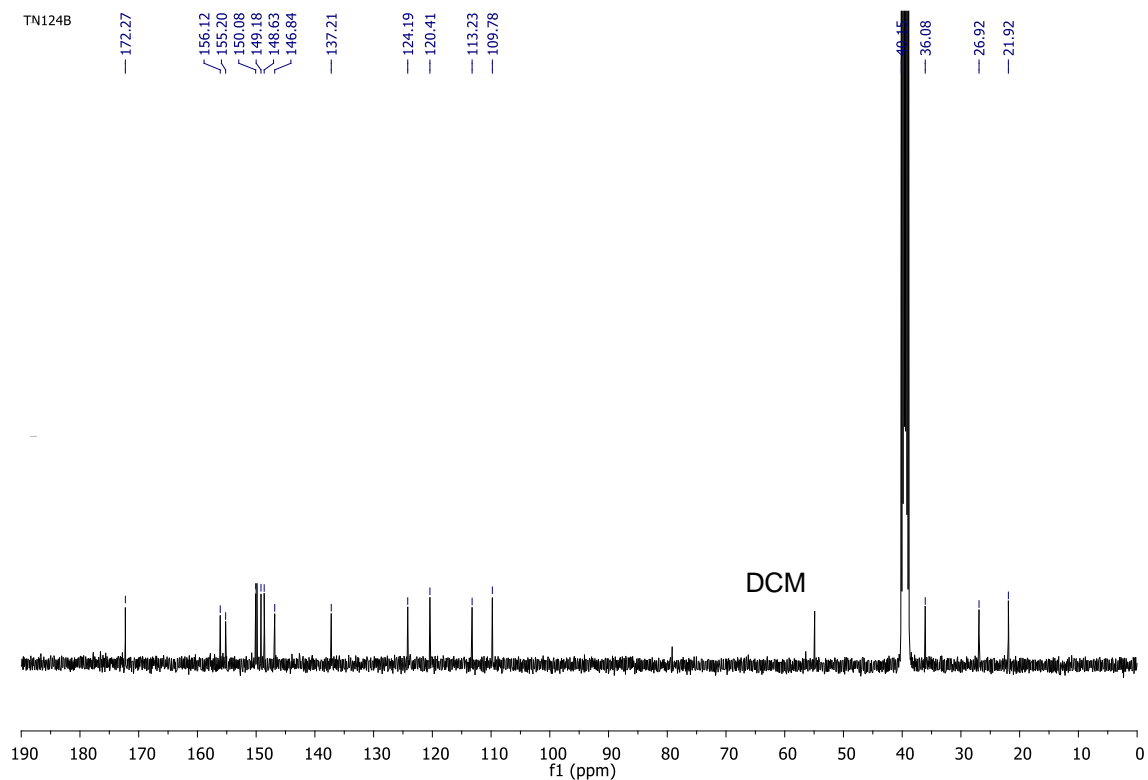
A solution of compound **IV-1** (219 mg, 1.1 mmol) in dry THF (4.5 mL) was added dropwise to a solution of [2,2'-bipyridin]-4-amine (179 mg, 1.05 mmol) and TEA (0.17 mL, 1.26 mmol) in dry THF (4.5 mL) at 0°C under Ar atmosphere. The solution was stirred at r.t. overnight. Then a white residue was filtered off and the solvent removed under reduced pressure. Purification by column chromatography on silica gel (DCM/MeOH 15/1) give compound **IV-2** as yellow oil, 250 mg, 68% yield. ¹H NMR (CDCl₃): δ = 8.64 (d, 1H, *J* = 4.6 Hz, H_k), 8.55 (d, 1H, *J* = 5.7 Hz, H_f), 8.49 (s, 1H, NH), 8.40 (d, 1H, *J* = 2.0 Hz, H_g), 8.33 (d, 1H, *J* = 8.0 Hz, H_h), 8.01 (dd, 1H, *J* = 2.0, 5.7 Hz, H_e), 7.83 (dt, 1H, *J* = 1.7, 7.7 Hz, H_i), 7.34 (ddd, 1H, *J* = 0.8, 4.8, 7.4 Hz, H_j), 3.44 (t, 2H, *J* = 6.2 Hz, CH₂-H_a), 2.52 (t, 2H, *J* = 7.2 Hz, CH₂-H_d); 1.91 (m, 4H, CH₂-H_b, CH₂-H_c); ¹³C NMR (CDCl₃): δ = 172.2, 154.9, 153.4, 149.3, 148.3, 148.1, 137.4, 124.6, 121.4, 113.9, 110.8, 44.5, 36.7, 33.1, 23.6 ppm.



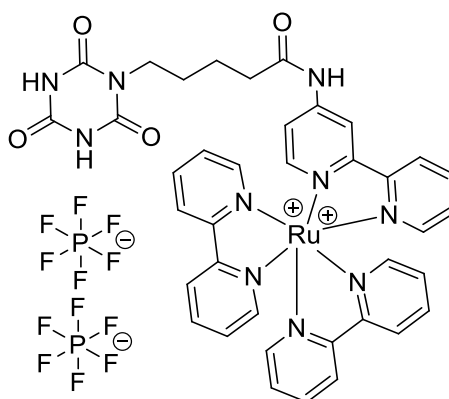
***N*-([2,2'-bipyridin]-4-yl)-5-(2,4,6-trioxo-1,3,5-triazinan-1-yl)pentanamide**

To a solution of cyanuric acid (309 mg, 2.39 mmol) in DMF (5mL) was added compound **IV-2** (200 mg, 0.60 mmol) and 1,8-diazabicycloundec-7-ene (95 mg, 2.39 mmol). The reaction mixture was heated under 70 °C overnight, poured into the water, and extracted with ethyl acetate. The organic layer was washed with water to eliminate the excess of cyanuric acid, dried with MgSO₄ and filtered. The solvent was removed under reduced pressure and the crude material was purified by column chromatography using DCM : MeOH 15:1 as a eluent to give **IV-2** as a white solid, 596 mg, 25%. ¹H NMR ([D₆]dimethyl sulfoxide): δ = 11.35 (br s, 2H, NH-cy), 10.41 (s, 1H, NH-amide), 8.68 (d, 1H, *J* = 4.0 Hz, H_k), 8.61 (d, 1H, *J* = 2.0 Hz, H_g), 8.51 (s, 1H, *J* = 5.5 Hz, H_f), 8.37 (d, 1H, *J* = 8.0 Hz, H_h), 7.93 (dt, 1H, *J* = 1.8, 7.7 Hz, H_i), 7.67 (dd, 1H, *J* = 2.1, 4.0 Hz, H_e), 7.44 (dd, 1H, *J* = 1, 4.8 Hz, H_j), 3.66 (t, 2H, *J* = 6.6 Hz, CH₂-H_a), 2.40 (t, 2H, *J* = 6.8 Hz, CH₂-H_d); 1.59 (m, 4H, CH₂-H_b, CH₂-H_c); ¹³C NMR ([D₆]dimethyl sulfoxide): δ = 172.3, 156.1, 155.2, 150.1 (2C), 149.2, 148.6, 146.8, 137.2, 124.2, 120.4, 113.2, 109.8, 40.2, 36.1, 26.9, 21.9 ppm. MS *m/z*: calculated for C₁₈H₁₈N₆O₄ [M+H]⁺ 383.1 found FAB 383.2.



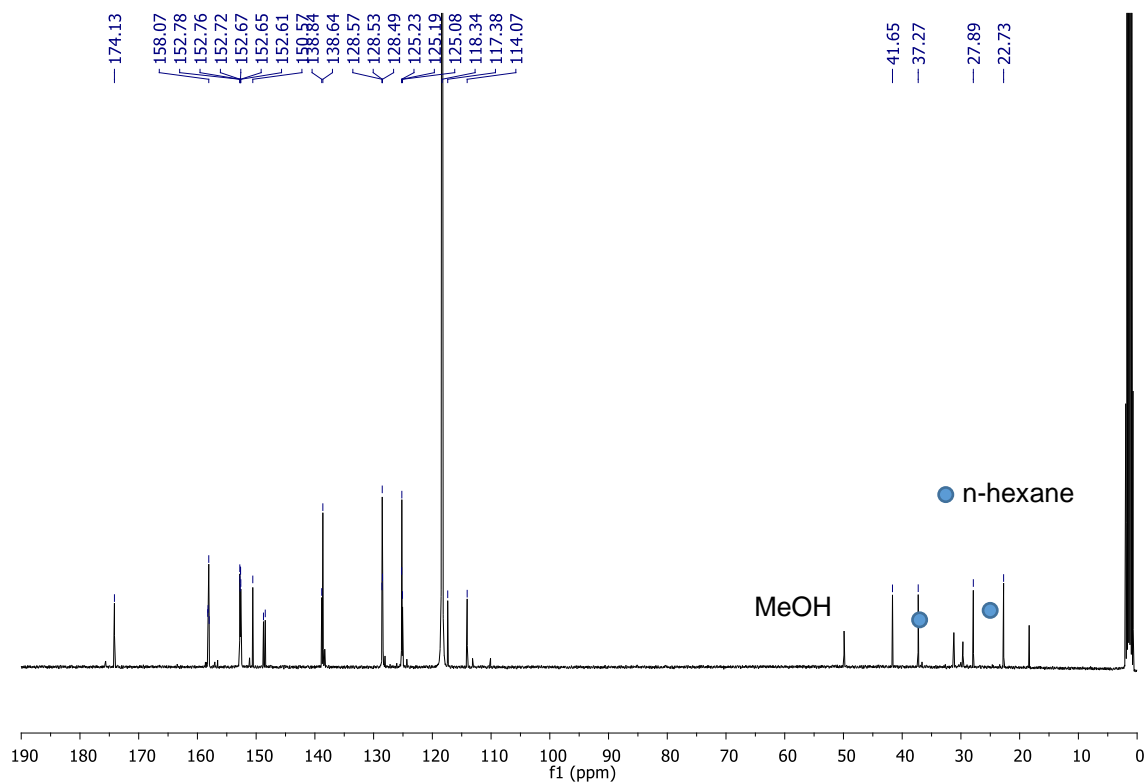
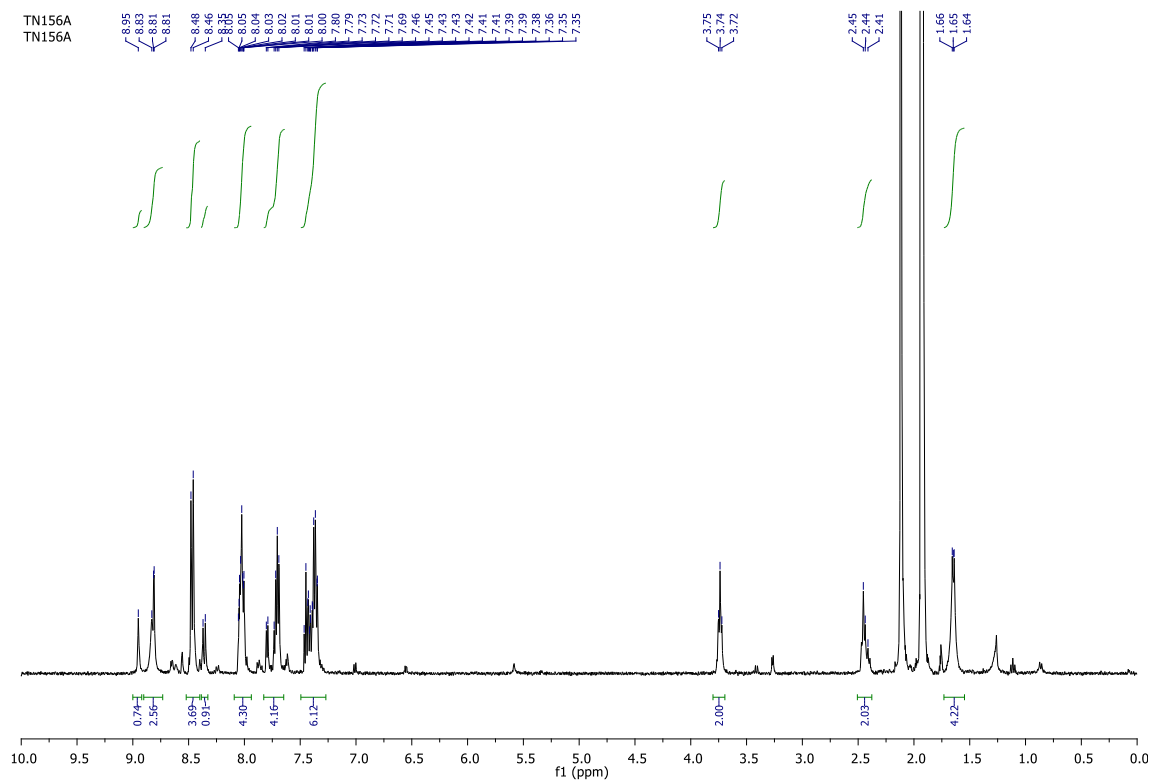


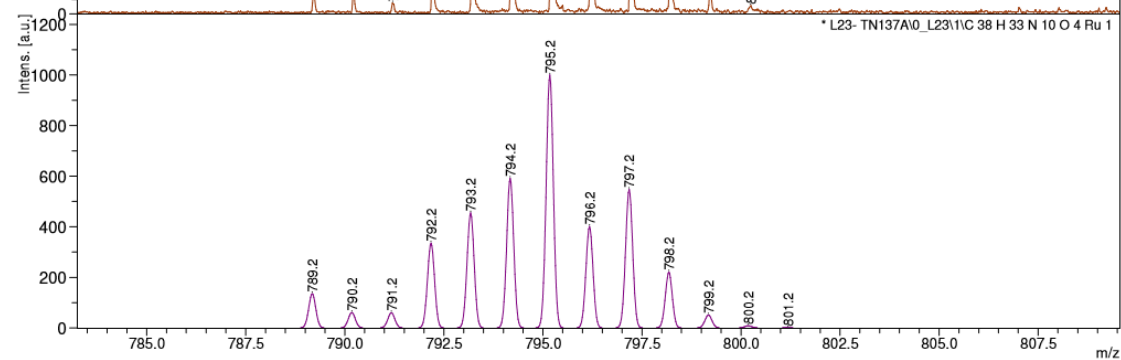
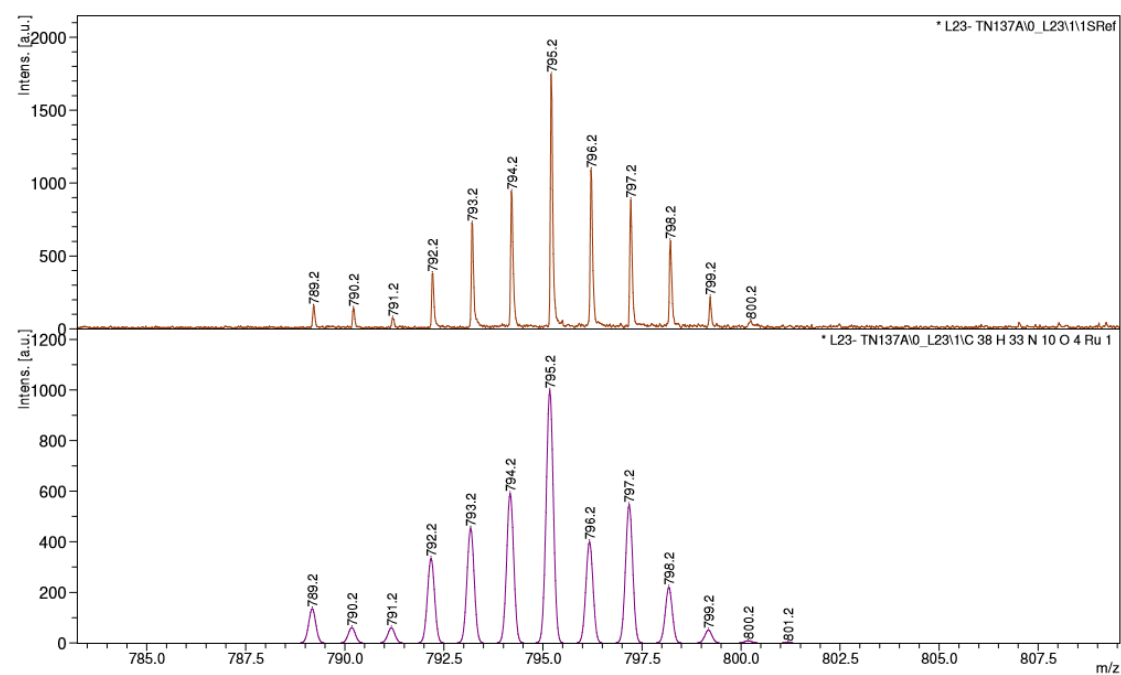
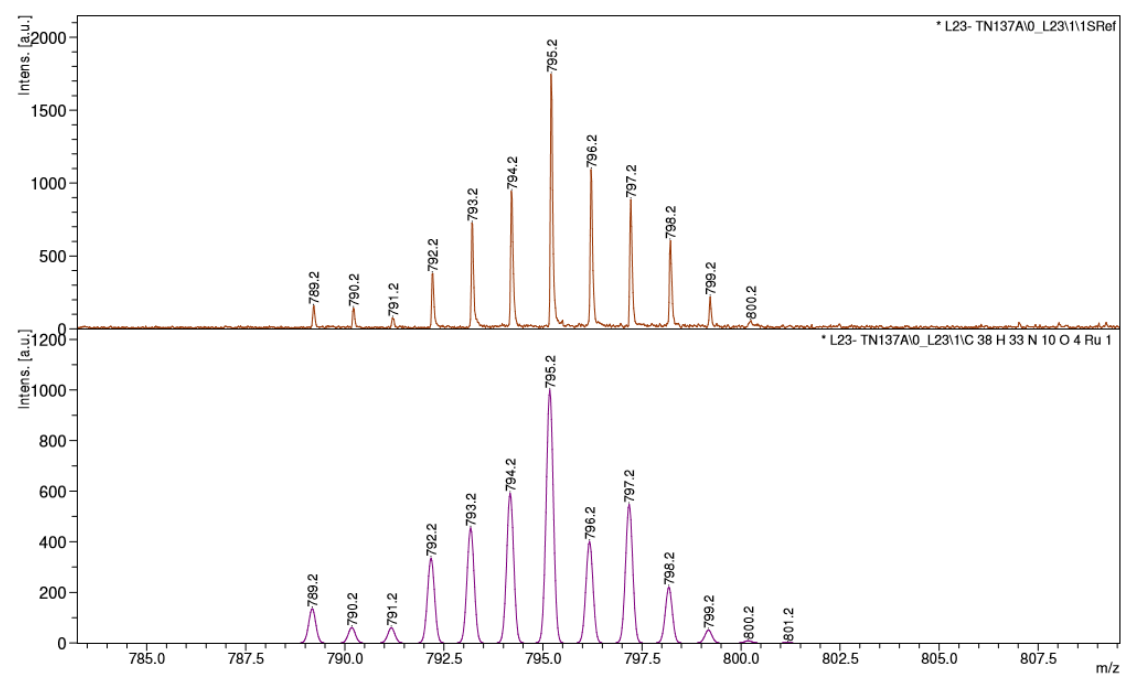
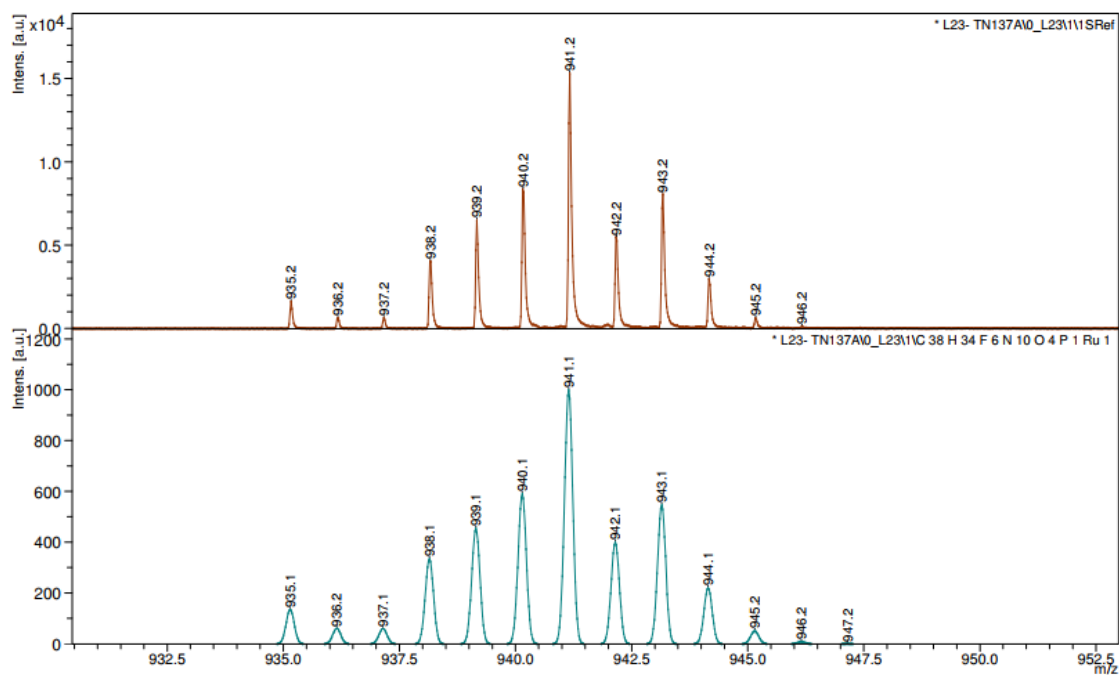
(Bipyridine)₂-(bipyridine-*N*-([2,2'-bipyridin]-4-yl)-5-(2,4,6-trioxo-1,3,5-triazinan-1-yl) pentanamide) ruthenium hexafluorophosphate



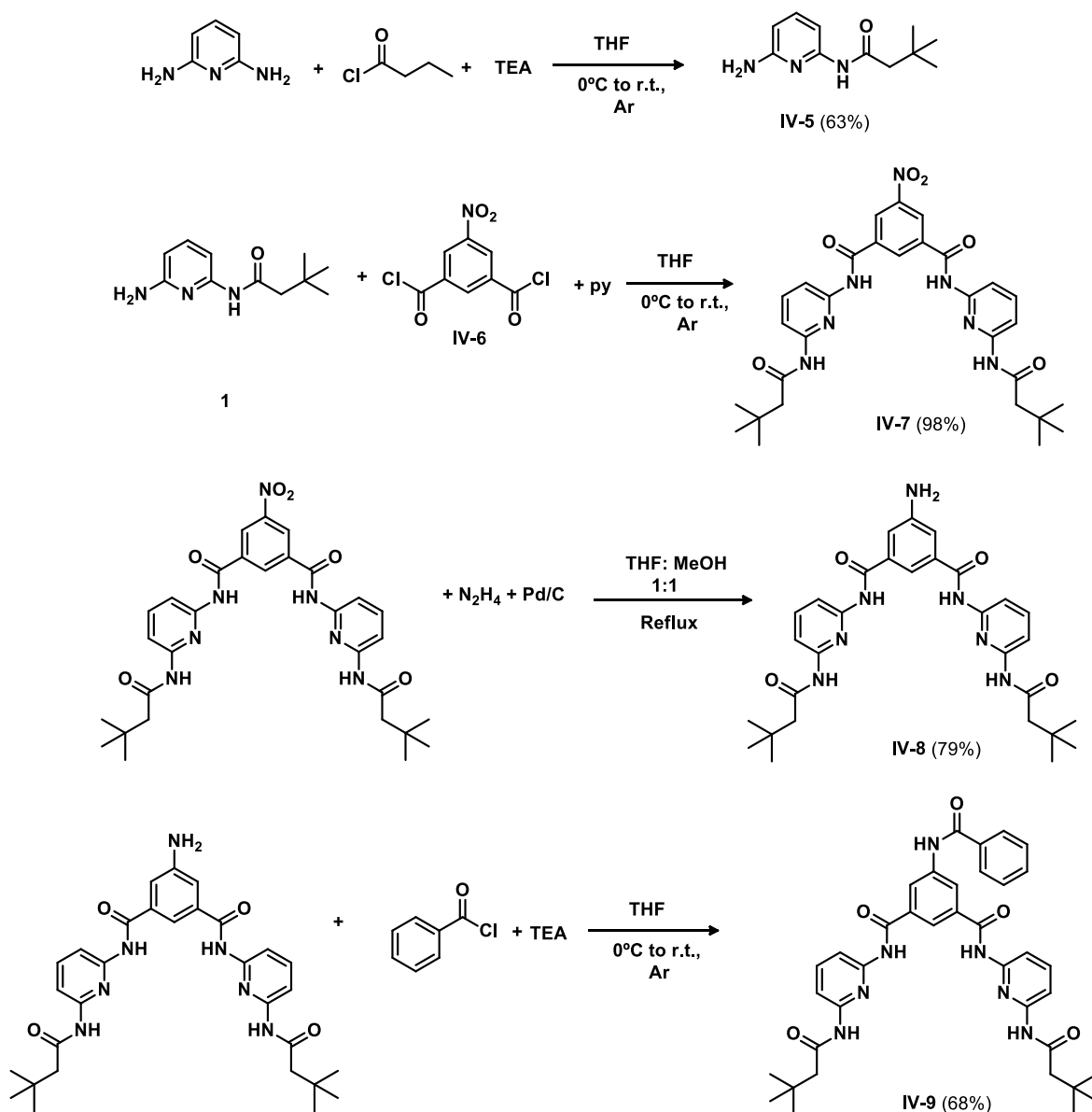
Compound IV-4

[Ru(bpy)₂Cl₂] (54 mg, 0.11 mmol) was reacted with silver nitrate (37 mg, 0.22 mmol) in CH₃OH (5.4 mL) for 3 hours at room temperature under an Ar atmosphere. The suspension was filtered in order to remove the silver salt, and the filtrate was added to compound **IV-3** (47 mg, 0.12 mmol). The solution was heated at reflux in the dark overnight under an Ar atmosphere. The reaction mixture was allowed to reach room temperature and the solvent was evaporated. The remaining solid was re-dissolved in a minimum amount of CH₃OH, and the desired compound was precipitated by dropwise addition of a saturated aqueous solution of ammonium hexafluorophosphate. The precipitate was filtered, washed with water then Et₂O and dried under vacuum to yield 100 mg (85%) of the desired hexafluorophosphate ruthenium complex (compound **IV-4**) as a orange solid. ¹H NMR (CD₃CN): δ = 8.95 (br s, 1H), 8.83 (br s, 1H), 8.81 (d, 2H, *J* = 2.0 Hz, Ar-H), 8.47 (d, 4H, *J* = 8.2 Hz, Ar-H), 8.36 (d, 1H, *J* = 6.7 Hz, Ar-H), 8.03 (m, 4H, Ar-H), 7.79 (d, 1H, *J* = 5.6 Hz, Ar-H), 7.71 (m, 3H, Ar-H), 7.41 (m, 6H, Ar-H), 3.74 (t, 2H, *J* = 5.3 Hz, CH₂), 2.45 (t, 2H, *J* = 6.8 Hz, CH₂), 1.65 (m, 4H, 2CH₂). ¹³C NMR (CD₃CN): δ = 174.1, 158.3, 158.2 (2C), 158.1 (2C), 158.0, 152.8, 152.8, 152.7, 152.7 (2C), 152.6, 152.6, 150.6 (2C), 148.8, 148.5, 138.8, 138.6 (3C), 128.6, 128.5, 128.5 (3C), 125.2, 125.2 (2C), 125.1, 118.3, 117.4, 114.7, 41.7, 37.3, 27.9, 22.7 ppm. MS *m/z*: calculated. for C₃₈H₃₄F₆N₁₀O₄PRu [M+PF₆]⁺ 941.1 found MALDI-TOF 941.2; calculated for C₃₈H₃₄N₁₀O₄Ru [M]⁺ 795.2 found MALDI-TOF 795.2.

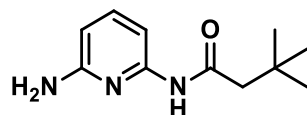




4.3.1.b. HR synthesis



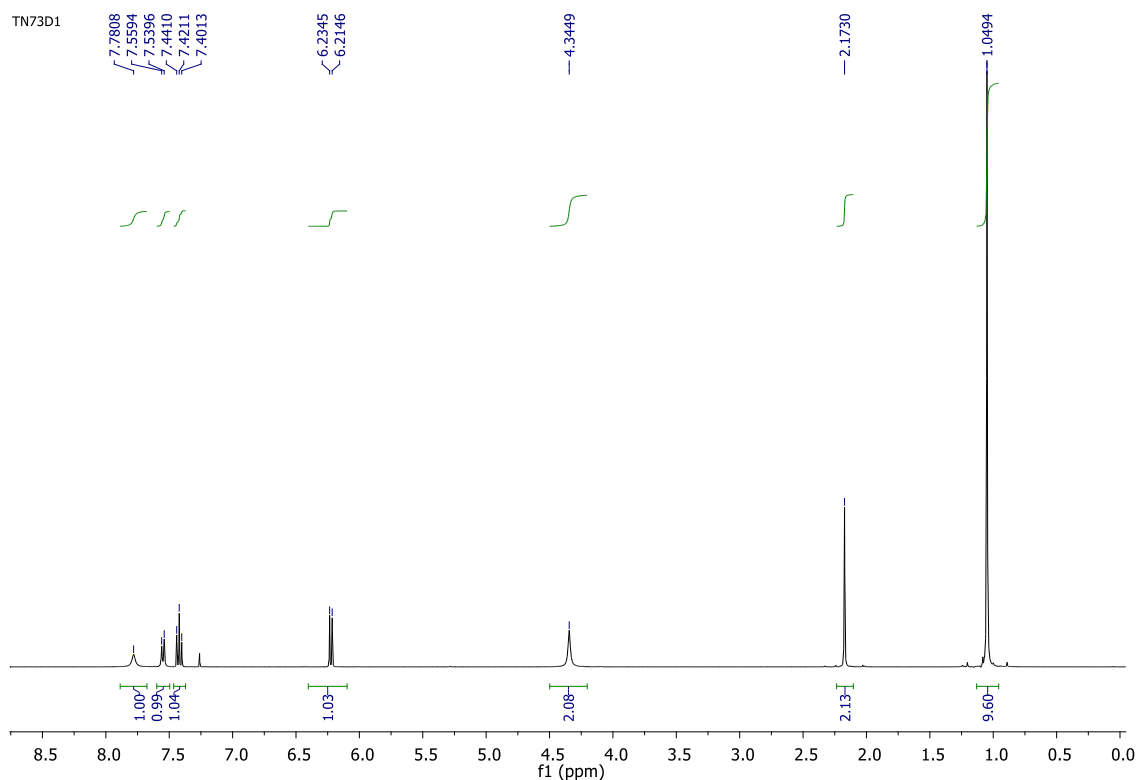
The 5-amino-*N,N'*-bis[6-(3,3-dimethylbutyrylamino) pyridin-2-yl] isophthalamide, compound **IV-8**, was synthesized as described by Dirksen et al.²⁵⁰ The experimental procedures followed are explained below.

***N*-(6-Aminopyridin-2-yl)-3,3-dimethylbutyramide**

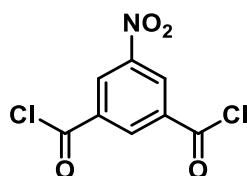
Compound IV-5

A solution of 3,3-dimethyl-butyl chloride (3 g, 22.3 mmol) in dry THF (12 mL) was added to a solution of 2,6-diaminopyridine (2.43 g, 22.3 mmol) and triethylamine (3.1 mL, 22.3

mmol) in dry THF (25 mL) at 0°C under an argon atmosphere over a period of 2 h. The solution was stirred for 60h at room temperature, the residue filtered off, and the solvent removed under reduced pressure. Purification by column chromatography on silica gel (DCM/ethyl acetate 4/1 as eluent) gave a colorless solid (2.9 g, 63%); ¹H NMR (CDCl₃): δ = 7.77 ppm (br s, 1H, CONH), 7.55 (d, 1H, *J* = 7.9 Hz, H_{py}), 7.42 (t, 1H, *J* = 8.0 Hz; H_{py}), 6.22 (d, 1H, *J* = 7.9 Hz, H_{py}), 4.34 (br s, 2H; NH₂), 2.17 (s, 2H; (CH₂C(CH₃)₃), 1.05 (s, 9H; C(CH₃)₃) ppm.

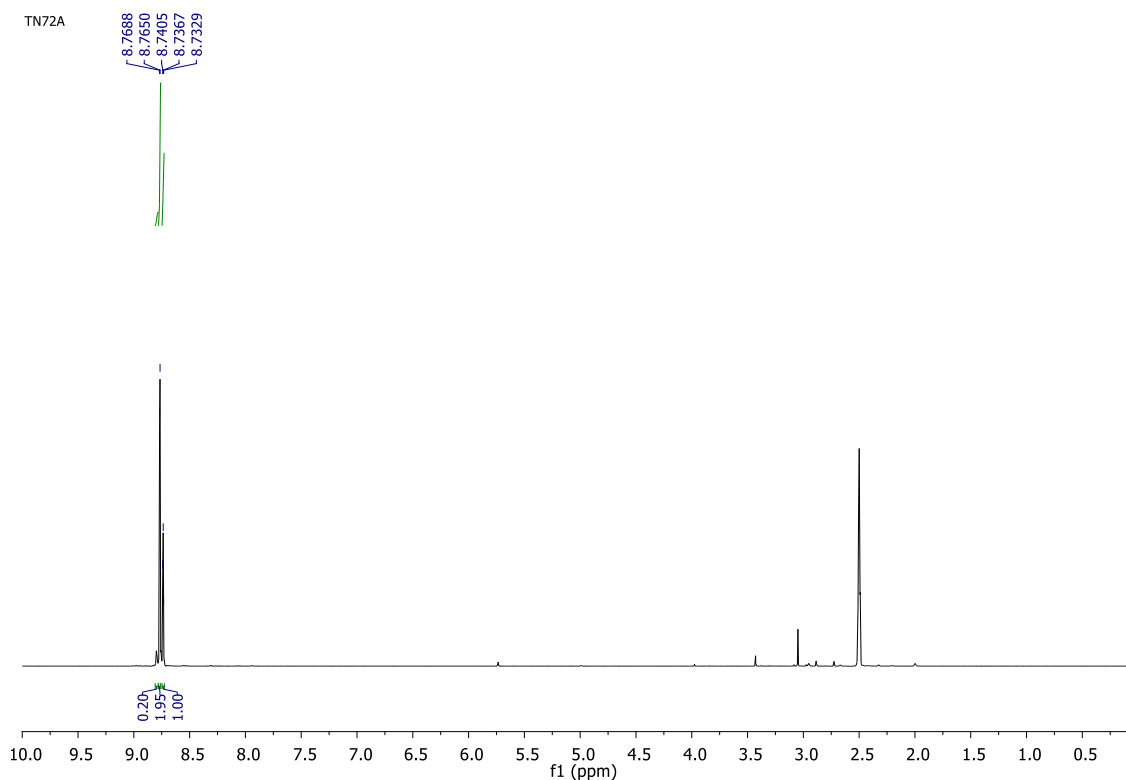


5-Nitroisophthaloyl dichloride

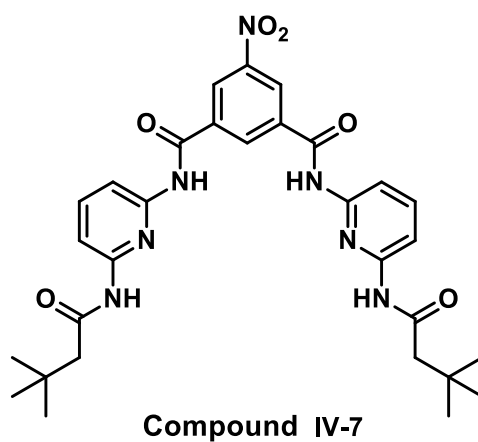


Compound IV-6

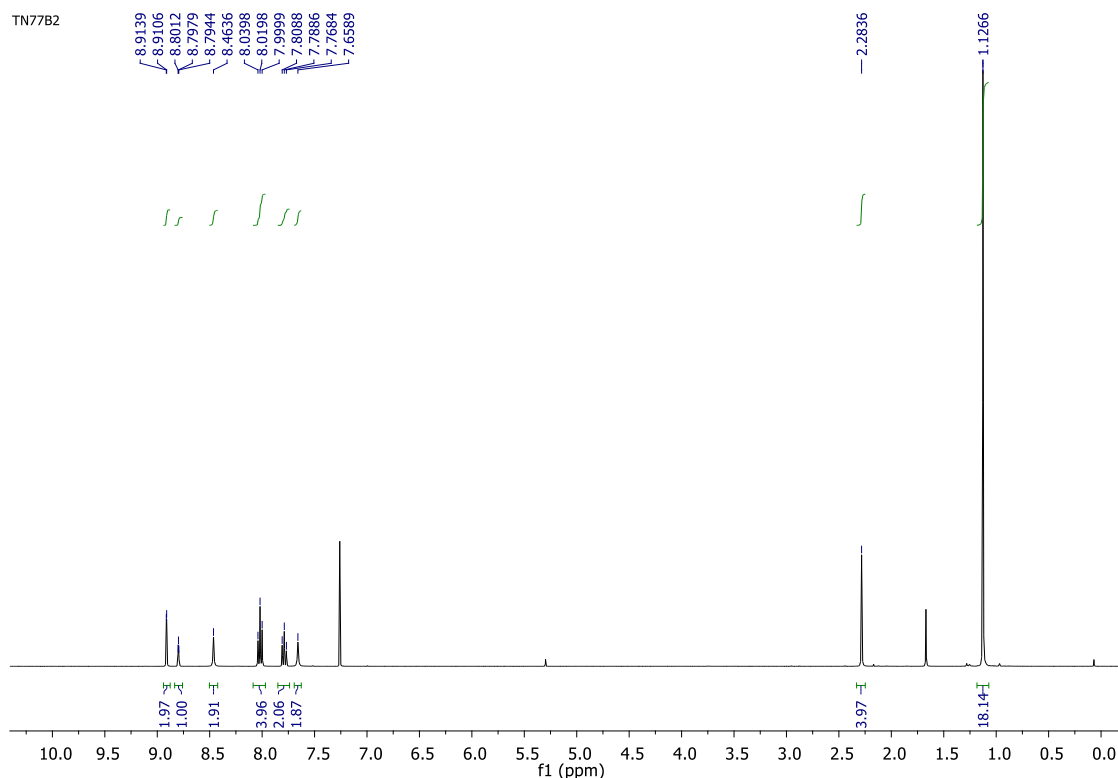
A solution of 5-nitroisophthalic acid (3.0 g, 14.0 mmol) in thionyl chloride (5 mL) and *N,N*-dimethylformamide (five drops) was refluxed for 6 h under dry conditions with subsequent vacuum distillation of the thionyl chloride excess. The residue was dried under high vacuum and yielded a white solid (2.6 g, 98%): ¹H NMR ([D₆]dimethyl sulfoxide): δ = 8.77 (d, *J* = 1.52 Hz, 2H; Ar-H), 8.74 (t, *J* = 1.52 Hz, 1H; Ar-H) ppm.



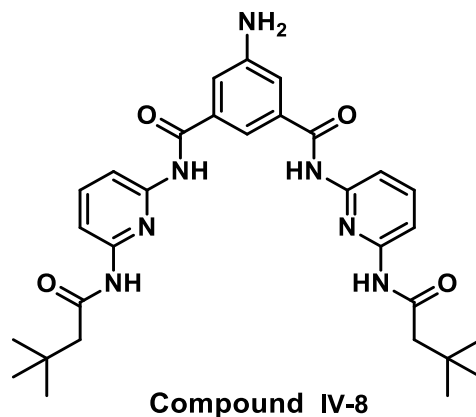
***N,N'*-Bis[6-(3,3-dimethylbutyrylamino)pyridin-2-yl]-5-nitro-isophthalamide**



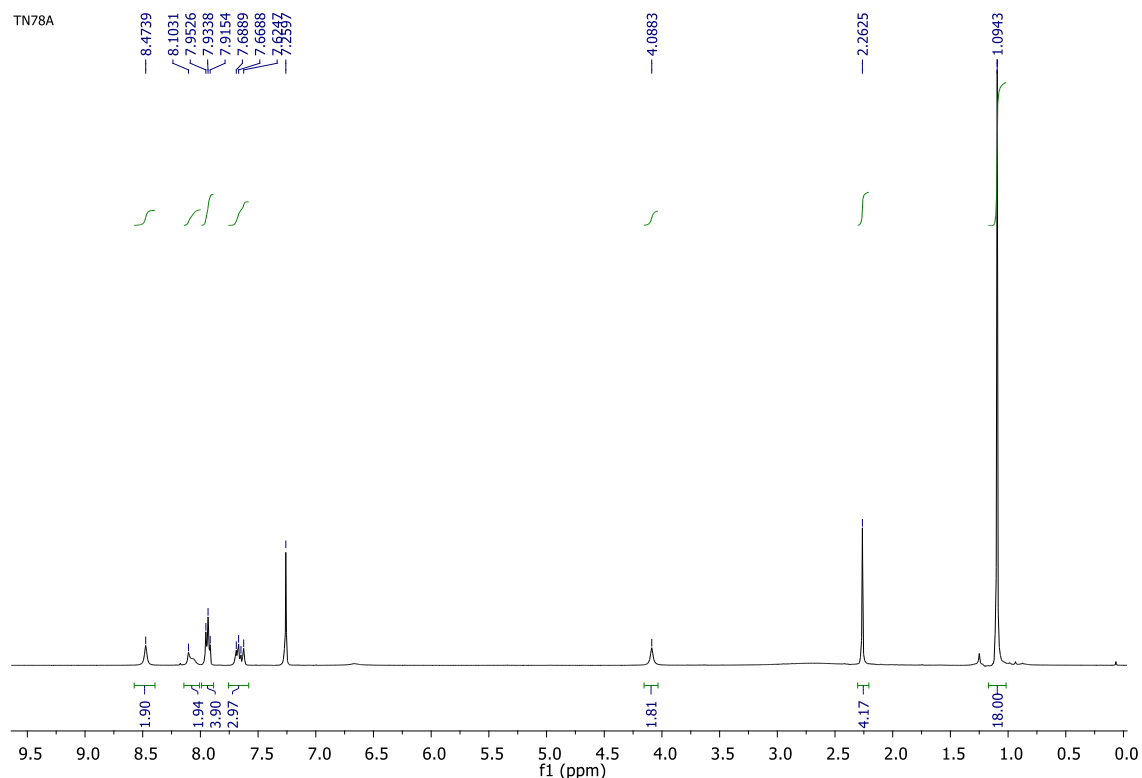
A solution of diacid dichloride **IV-6** (0.9 g, 3.62 mmol) in dry THF (15 mL) was added dropwise to a solution of monosubstituted diaminopyridine **IV-5** (1.5 g, 7.24 mmol) and triethylamine (1 mL, 7.24 mmol) in dry THF (15 mL) at 0°C under an argon atmosphere. The solution was stirred at r.t. for 12 h, the residue filtered off, and the solvent removed under reduced pressure. Purification by column chromatography on silica gel (DCM/ethyl acetate 10/1-3/1 as eluent) gave a yellowish solid (2.1 g, 98%): $^1\text{H NMR}$ (CDCl_3): δ = 8.91 (br d, J = 1.3 Hz, 2H; CONH), 8.80 (br t, J = 1.3 Hz, 1H; Ar-H), 8.46 (br s, 2H; Ar-H), 8.02 (t, J = 8.0 Hz, 4H; Hpy), 7.79 (t, J = 8.0 Hz, 2H; Hpy), 7.66 (br s, 2H; CONH), 2.28 (s, 4H; COCH_2), 1.13 (s, 18H; $\text{C}(\text{CH}_3)_3$) ppm.



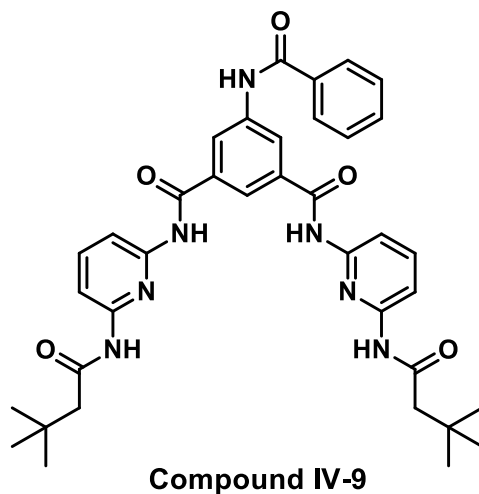
5-Amino-*N,N'*-bis[6-(3,3-dimethylbutyrylamino)pyridin-2-yl]isophthalamide



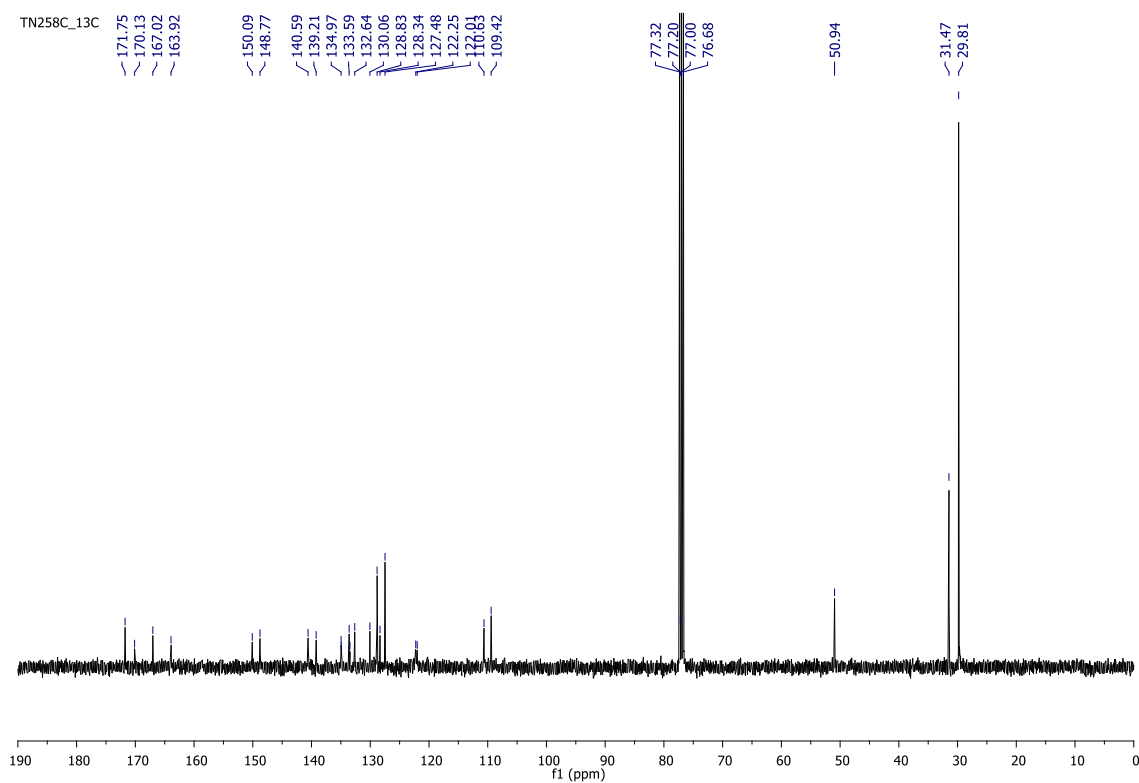
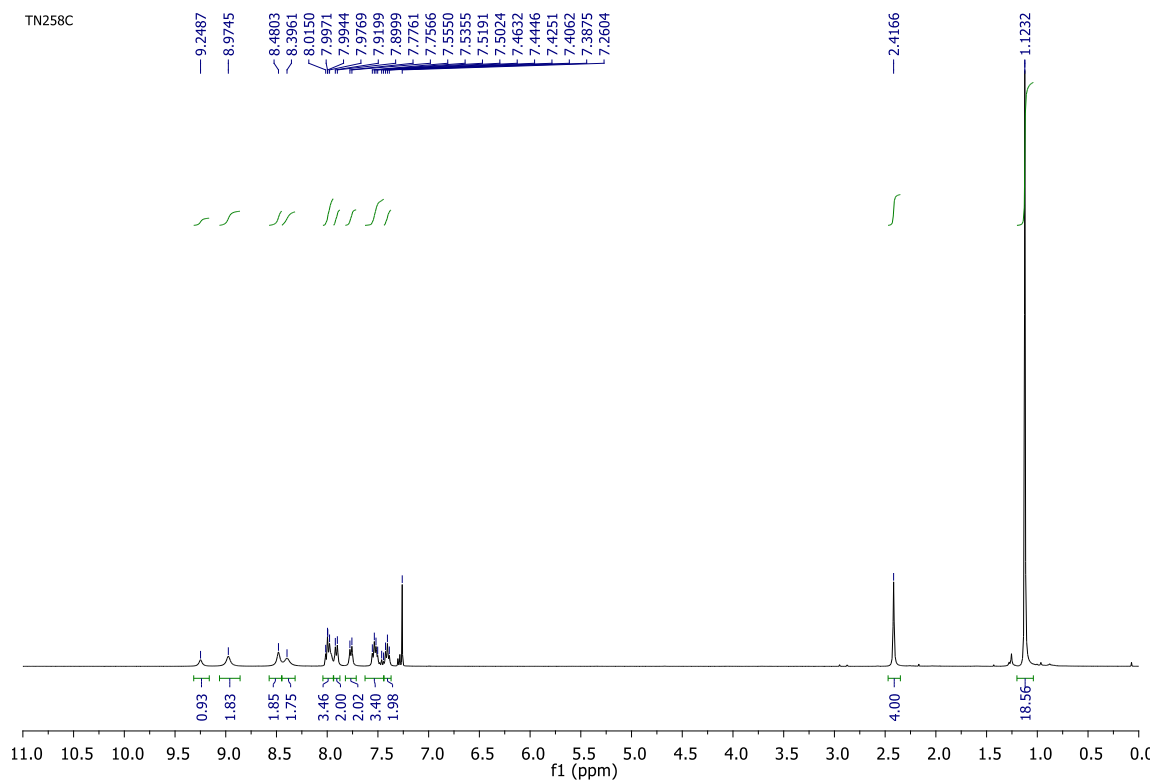
To a solution of compound **IV-7** (0.4 g, 0.68 mmol) in dry THF (34 mL) and MeOH (34 mL) under argon atmosphere, 10% Pd-C (400 mg) was added and the reaction mixture was heated to 70 °C. Then hydrazine (1.1 mL, 20.4 mmol) was added to the reaction mixture, which was heated under reflux for 4h. Once the reaction was completed (TLC). The catalyst was filtered off over celite and the solvent removed under reduced pressure to give a yellowish solid (0.3 g, 79%): $^1\text{H NMR}$ (CDCl_3): δ = 8.47 ppm (s, 2H; CONH), 8.10 (s, 2H; CONH), 7.93 (br t, 4H; Hpy), 7.66 (m, 3H; 2H-py, Ar-H), 4.08 (br s, 2H, NH_2), 2.26 (s, 4H; 2CH_2), 1.11 (s, 18H; $\text{C}(\text{CH}_3)_3$) ppm.



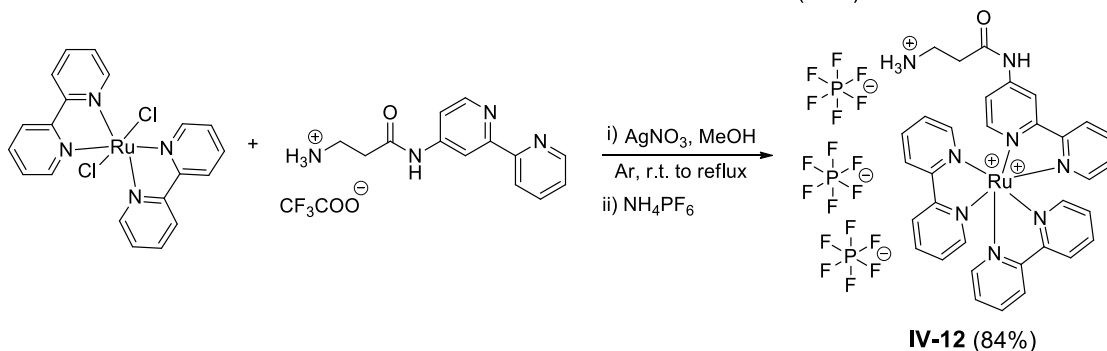
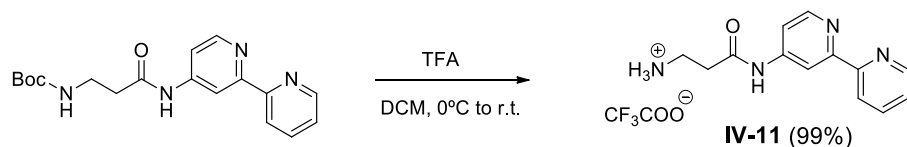
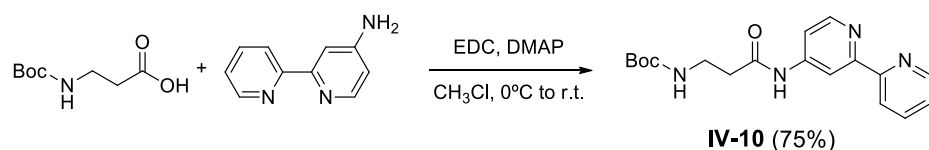
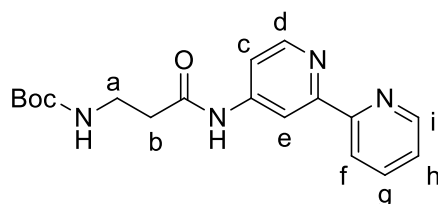
5-benzamido-*N,N*-bis(6-(3,3-dimethylbutyrylamino)pyridin-2-yl)isophthalamide



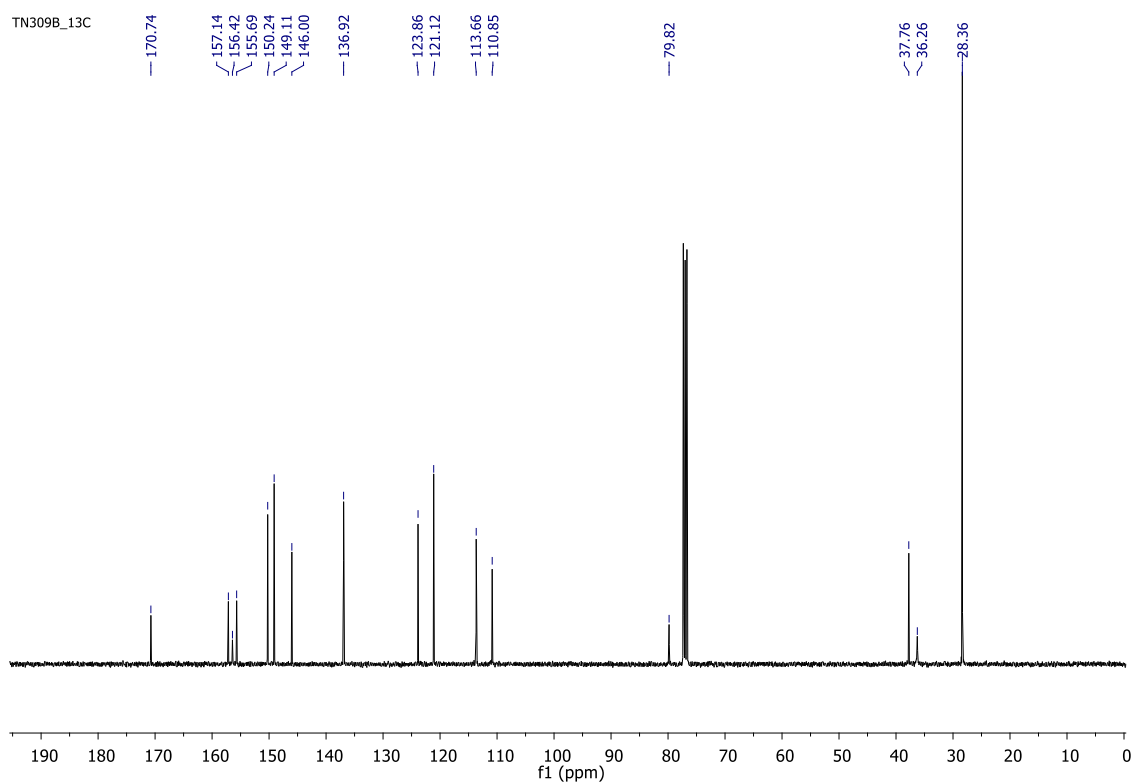
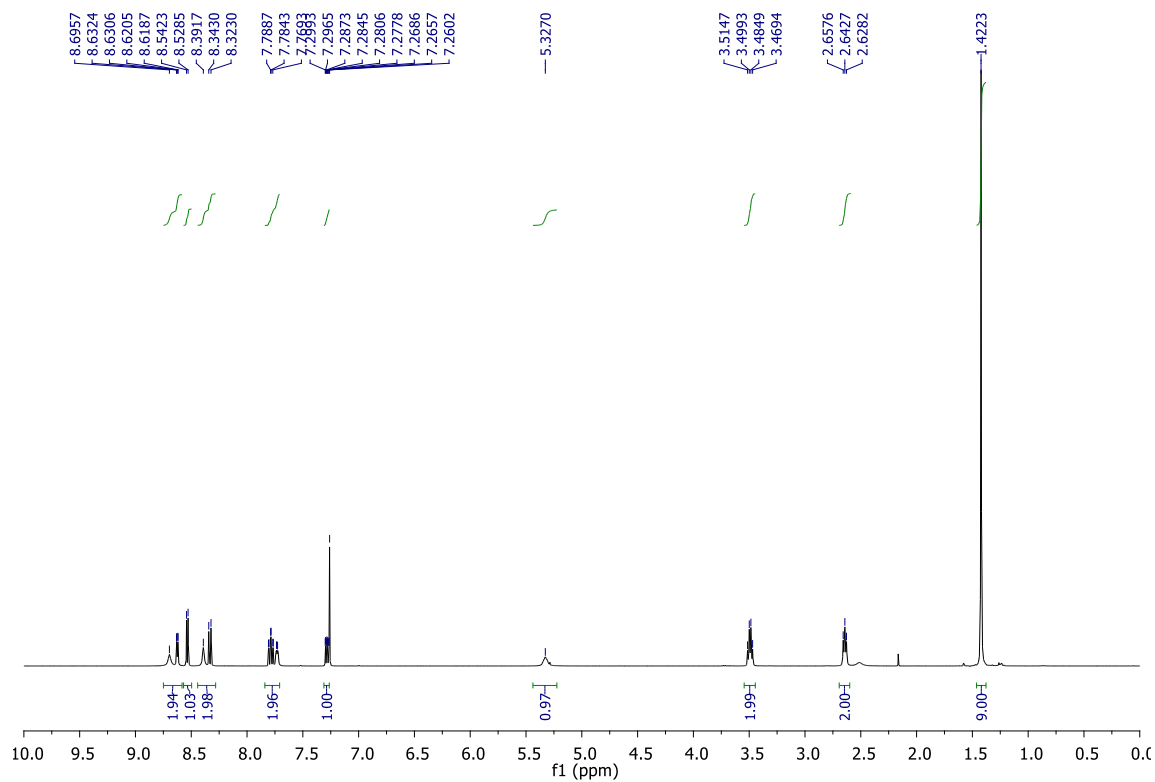
A solution of benzoyl chloride (21 mg, 0.15 mmol) in dry THF (1 mL) was added dropwise to a solution of compound **IV-8** (50 mg, 0.09 mmol) and triethylamine (16 μ L, 0.12 mmol) in dry THF (2 mL) at 0°C under an argon atmosphere. The solution was stirred at r.t. for 12 h, the residue filtered off, and the solvent removed under reduced pressure. Purification by column chromatography on silica gel (DCM/MeOH 15/1 as eluent) gave a yellowish oil (40 mg, 68%): $^1\text{H NMR}$ (CDCl_3): δ = 9.24 (br s, 1H), 8.97 (br s, 2H), 8.48 (br s, 2H), 8.40 (br s, 2H), 7.99 (m, 3H), 7.90 (d, 2H, J = 8.0 Hz), 7.76 (d, 2H, J = 7.8 Hz), 7.53 (m, 3H), 7.41 (t, 2H, J = 7.5 Hz), 2.42 (s, 4H), 1.23 (s, 18H); $^{13}\text{C NMR}$ (CDCl_3): δ = 171.7 (2C), 170.1, 167.0, 163.9, 150.1 (2C), 148.8 (2C), 140.6 (2C), 139.2, 135.0, 133.6, 132.6 (2C), 130.1, 128.8 (2C), 128.3, 127.5 (2C), 122.2, 122.0, 110.6 (2C), 109.4 (2C), 50.9 (2C), 31.5 (2C), 29.8 (6C) ppm.



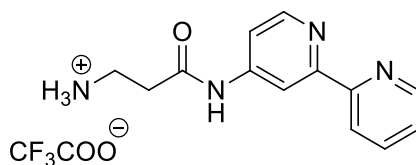
4.3.2. Synthesis of Ammonium derivative (Am)

**tert-butyl (3-((2,2'-bipyridin)-4-ylamino)-3-oxopropyl)carbamate**

3-((*tert*-butoxycarbonyl) amino)propanoic acid (133 mg, 0.70 mmol) was dissolved in CHCl_3 (6 mL) and the solution was cooled to 0°C . EDCI.HCl (168 mg, 0.88 mmol) and DMAP (122 mg, 0.99 mmol) were added. The reaction mixture was allowed to stir at room temperature for 30 minutes. A solution of [2,2'-bipyridin]-4-amine (100 mg, 0.58 mmol) in CHCl_3 (4 mL) was added to the activated acid. The reaction mixture was stirred overnight, concentrated under reduced pressure and the crude material was purified by column chromatography (eluent: DCM/ MeOH 50/1-40/1) to furnish product **IV-10** as colorless oil, 150 mg, 75%. ^1H NMR (CDCl_3): δ = 8.70 (s, 1H, NH), 8.63 (d, 1H, J = 4.8 Hz, H_i), 8.53 (d, 1H, J = 5.5 Hz, H_d), 8.40 (br s, 1H, H_e), 8.33 (d, 1H, J = 8.0 Hz, H_f), 7.78 (dt, 1H, J = 1.8, 7.7 Hz, H_g), 7.73 (m, 1H, H_c), 7.28 (ddd, 1H, J = 0.8, 4.8, 7.5 Hz, H_h), 5.33 (br s, 1H, NH), 3.48 (q, 2H, J = 6.2 Hz, $\text{CH}_2\text{-H}_a$), 2.64 (t, 2H, J = 7.0 Hz, $\text{CH}_2\text{-H}_b$); 1.42 (s, 9H, $3\text{CH}_3\text{-Boc}$); ^{13}C NMR : δ = 170.7, 157.1, 156.4, 155.7, 150.2, 149.1, 146.0, 136.9, 123.9, 121.1, 113.7, 110.9, 79.8, 37.8, 36.3, 28.4 ppm.



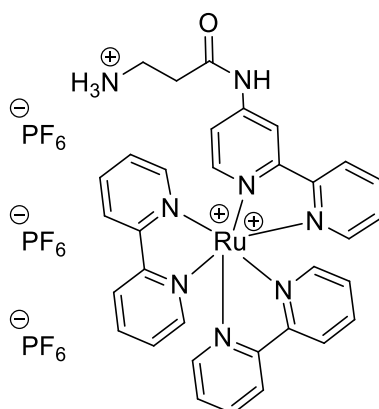
3-([2,2'-bipyridin]-4-ylamino)-3-oxopropan-1-aminium 2,2,2-trifluoroacetate



Compound IV-11

A solution of compound **IV-10** (60 mg, 0.18 mmol) in DCM (1.5 mL) was added TFA (0.1 mL) at 0°C. The reaction was stirred at room temperature for 3h until it was completed (TLC). The reaction mixture was concentrated under reduced, then DCM was added and the organic layer was washed twice with brine, dried over Na₂SO₄, concentrated under reduced pressure and dried under high vacuum to give compound **IV-11** as a yellowish oil, quantitative yield. The crude material was used directly in the next step reaction.

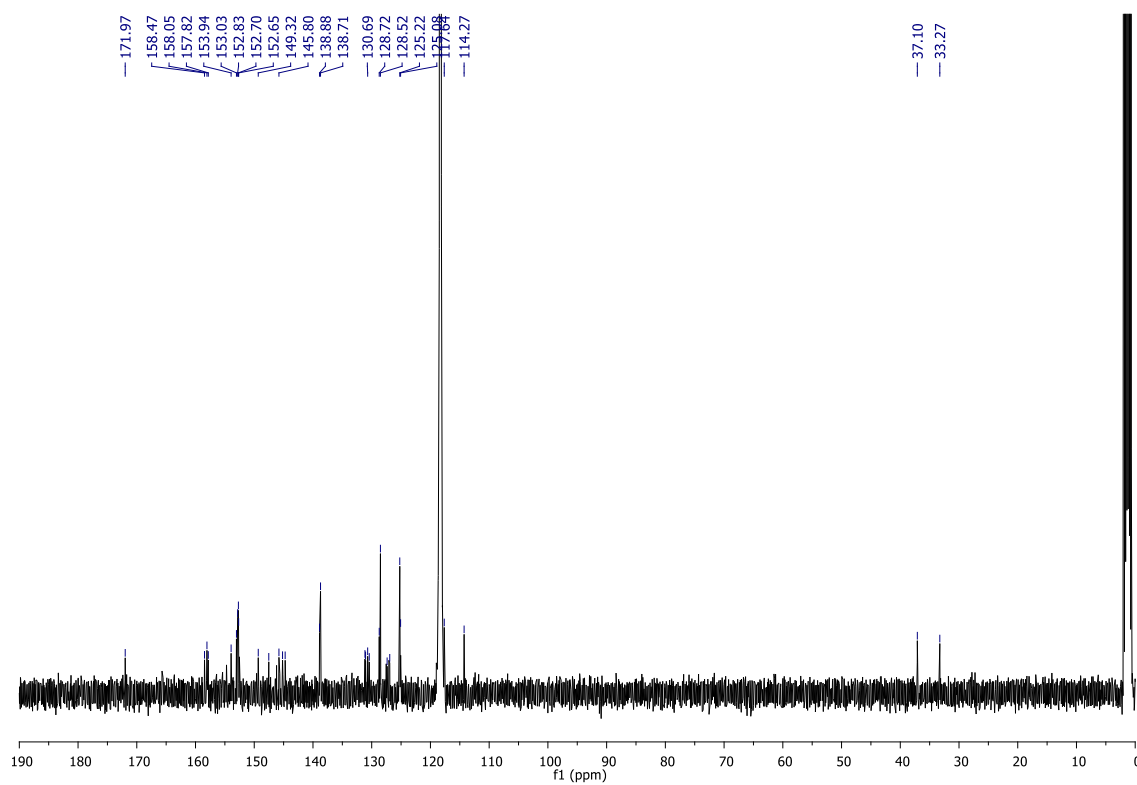
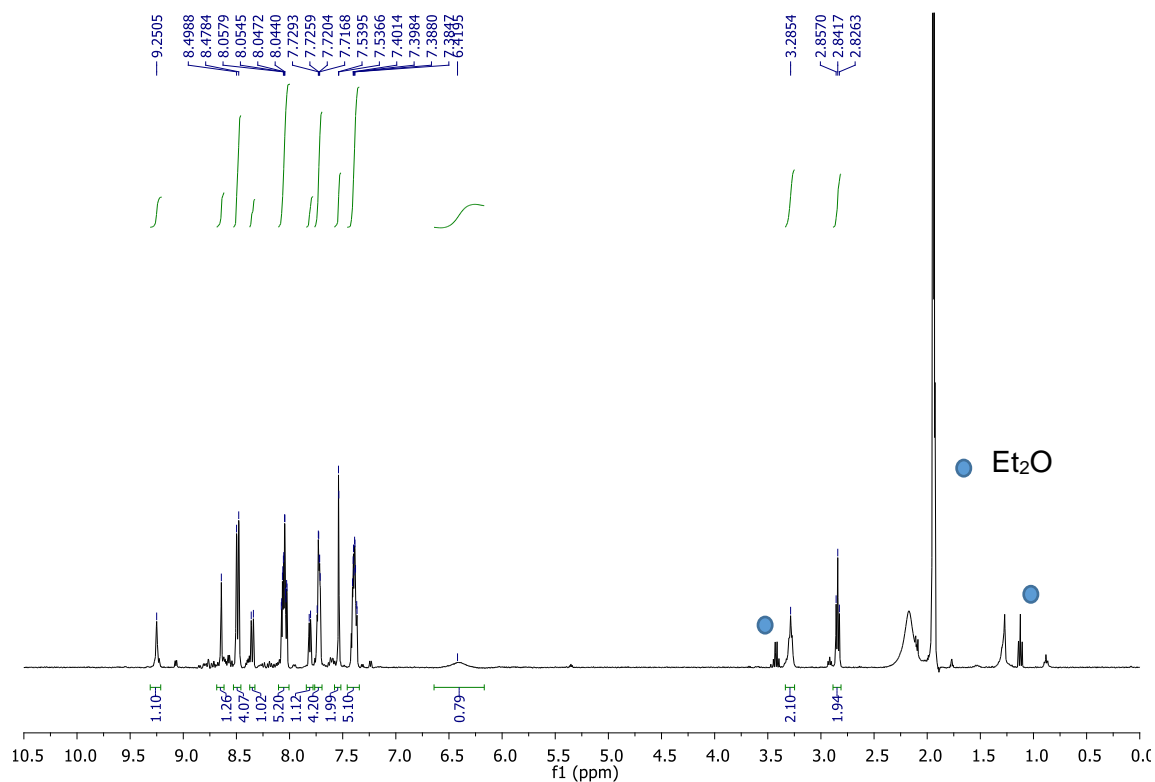
(Bipyridine)₂-(bipyridine-*N*-([2,2'-bipyridin]-4-yl)-5-(2,4,6-trioxo-1,3,5-triazinan-1-yl) pentanamide) ruthenium hexafluorophosphate: Am

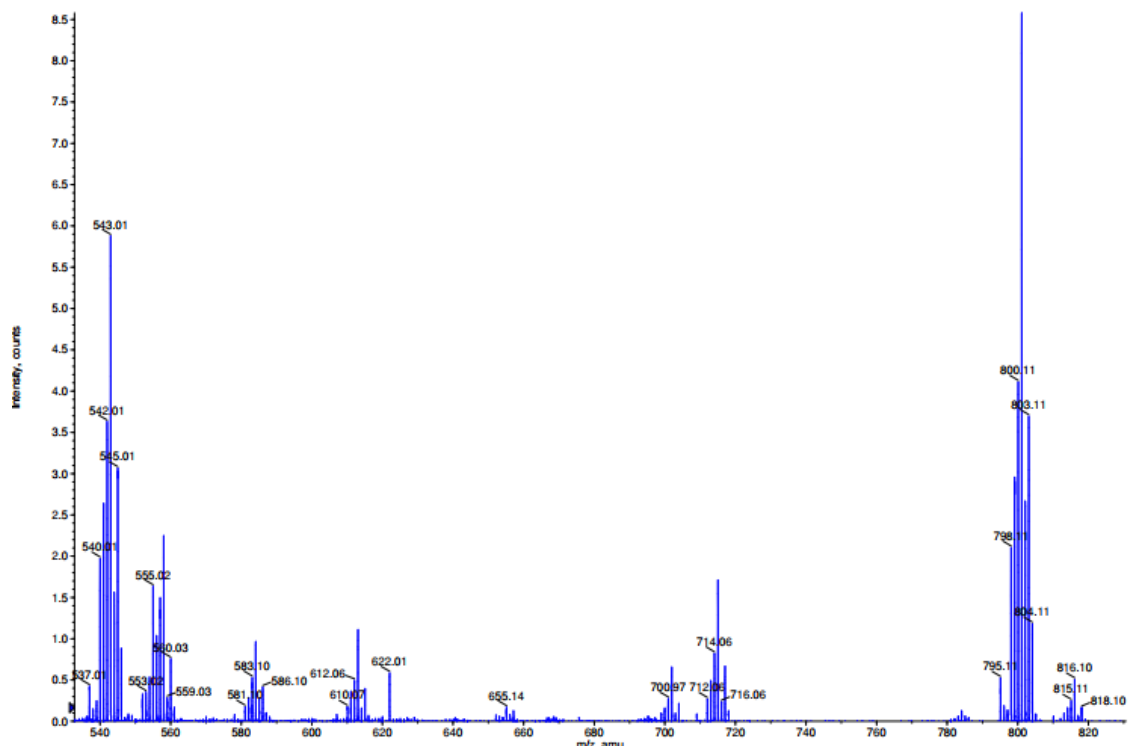


Compound IV-12
Am

[Ru(bpy)₂Cl₂] (54 mg, 0.11 mmol) was reacted with silver nitrate (37 mg, 0.22 mmol) in CH₃OH (5.4 mL) for 3 hours at room temperature under an argon atmosphere. The suspension was filtered in order to remove the silver salt, and the filtrate was added to compound **IV-11** (44 mg, 0.12 mmol). The solution was stirred at room temperature in the dark overnight under an argon atmosphere. The solvent was evaporated. The remaining solid was re-dissolved in a minimum amount of CH₃OH, and the desired compound was precipitated by dropwise addition of a saturated aqueous solution of ammonium hexafluorophosphate. The precipitate was filtered, washed with water then Et₂O and dried under vacuum to yield 97 mg (0.09 mmol, 84%) of the desired hexafluorophosphate ruthenium complex (compound **IV-12**) as a brown solid. ¹H NMR (CD₃CN): δ = 9.25 (br s, 1H, NH), 8.64 (br s, 1H), 8.49 (d, 4H, *J* = 8.2 Hz, Ar-H), 8.35 (d, 1H, *J* = 7.8 Hz, Ar-H), 8.04 (m, 4H, Ar-H), 7.80 (d, 1H, *J* = 5.6 Hz, Ar-H), 7.72 (m, 4H, Ar-H), 7.53 (s, 2H), 7.38 (m, 5H, Ar-H), 6.37 (br s, 3H, NH₃), 3.27 (t, 2H, *J* = 6.2 Hz, CH₂), 2.83 (t, 2H, *J* = 6.2 Hz, CH₂). ¹³C NMR (CD₃CN): δ = 172.0, 158.5, 158.0, 157.8, 153.0, 152.8, 152.7, 152.7, 149.3, 147.5, 145.8, 145.6, 145.2, 144.7, 138.9, 138.7 (2C), 131.1,

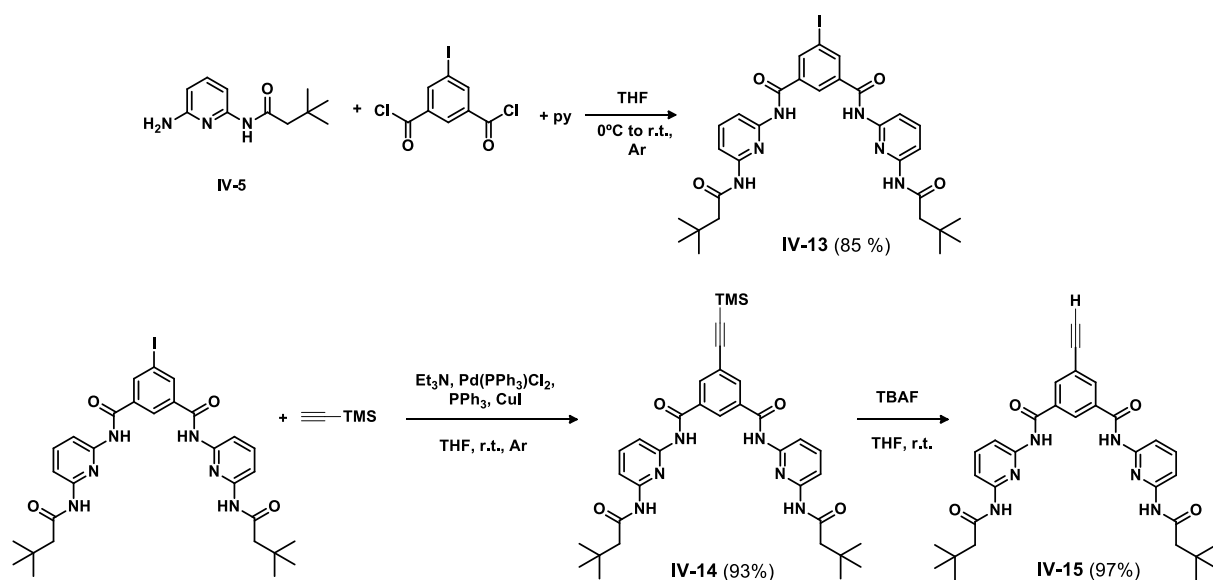
131.0, 130.7, 130.4, 128.7, 128.5 (2C), 127.4, 126.9, 125.2 (2C), 125.1, 117.6, 114.3, 37.1, 33.3 ppm. MS m/z: calculated for $C_{33}H_{31}F_6N_8OPRu$ $[M+PF_6]^+$ 801.7 found ESI⁺ 801.1.

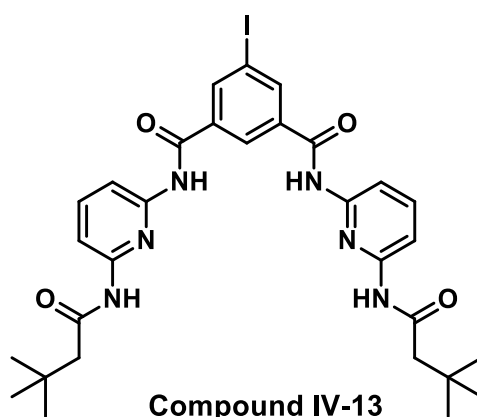




4.3.3. Synthesis HR-barb couple for AFM studies

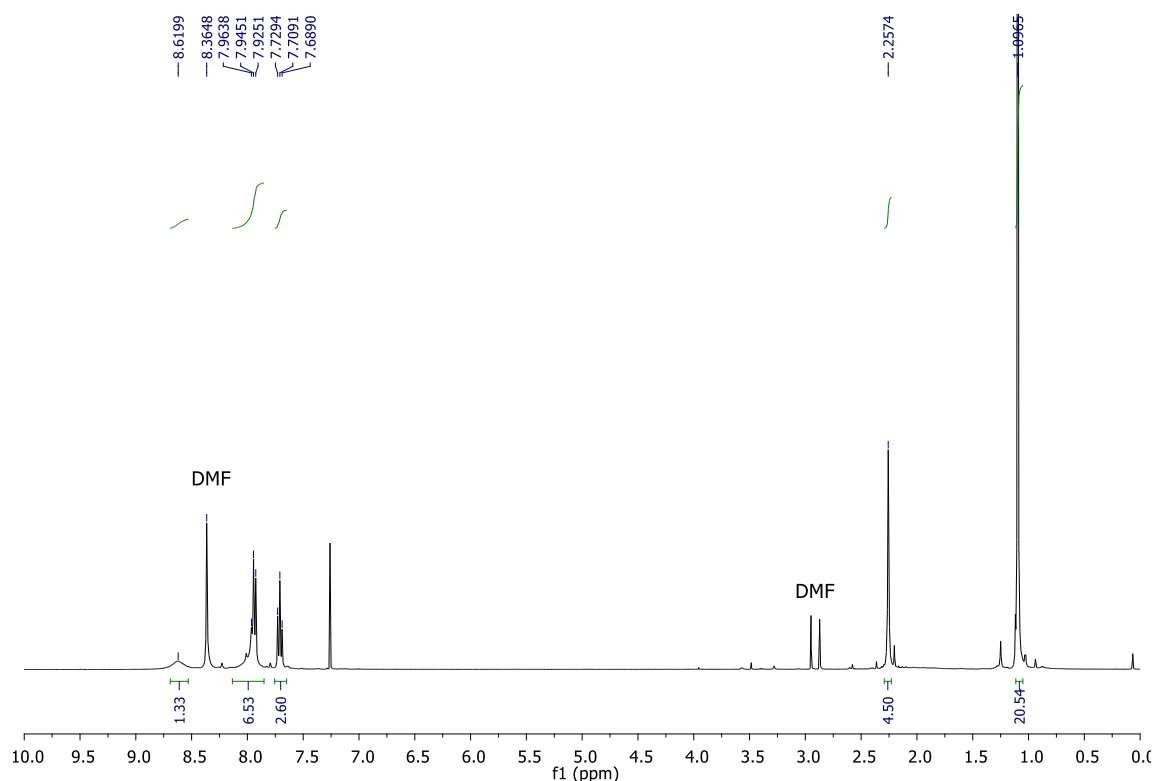
4.3.1.a. HR synthesis



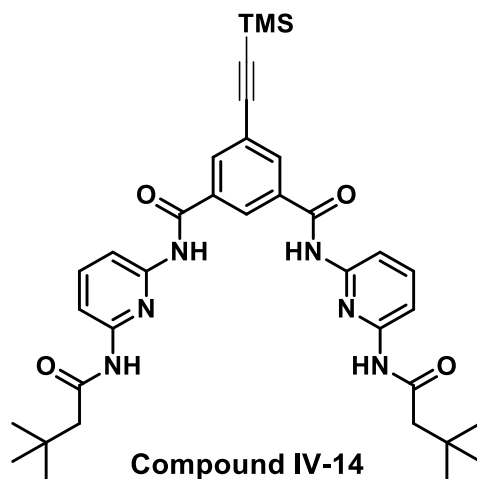
5-Iodo-*N,N'*-Bis[6-(3,3-dimethylbutyrylamino)pyridine-2-yl]isophthalamide

i) 5-iodoisophthalic acid (400mg 1.4 mmol) was suspended in anhydrous DCM (4.4 mL), 2 drops of DMF were added and oxalyl chloride (0.3 mL, 3.6 mmol) was added dropwise over a period of 15 min. The reaction was stirred for two hours, then the solvent was removed under reduced pressure and the crude material was directly used in the next step reaction without further purification.

ii) To the mixture of *N*-(6-aminopyridin-2-yl)-3,3-dimethylbutyramide **IV-5** (500 mg, 2.6 mmol) and triethylamine (0.4 mL, 2.6 mmol) in THF (8 mL) at 0°C, 5-iodo-isophthaloyldichloride 18 (428 mg, 1.3 mmol) in THF (8 mL) was added over 1h. The mixture was stirred at 0°C for 3h and at room temperature for overnight. The mixture was filtered, the solid residue was washed with THF. After removal of the solvent under vacuum, the crude material was purified by column chromatography using dichloromethane and ethyl acetate (3/1) as eluent, to give compound **VI-13** as a white powder (740 mg, 85%). ¹H NMR (CDCl₃): δ = 8.62 (br. s., 1H; NH), 7.95 (m. 6H), 7.71 (t. *J* = 8.1 Hz. 3H), 2.26 (s. 4H; CH₂C(CH₃)₃), 1.10 (s. 18H; CH₂C(CH₃)₃). This data is in concordance with *Organometallics* **2014**, 33 (3), 665-676.²⁵¹

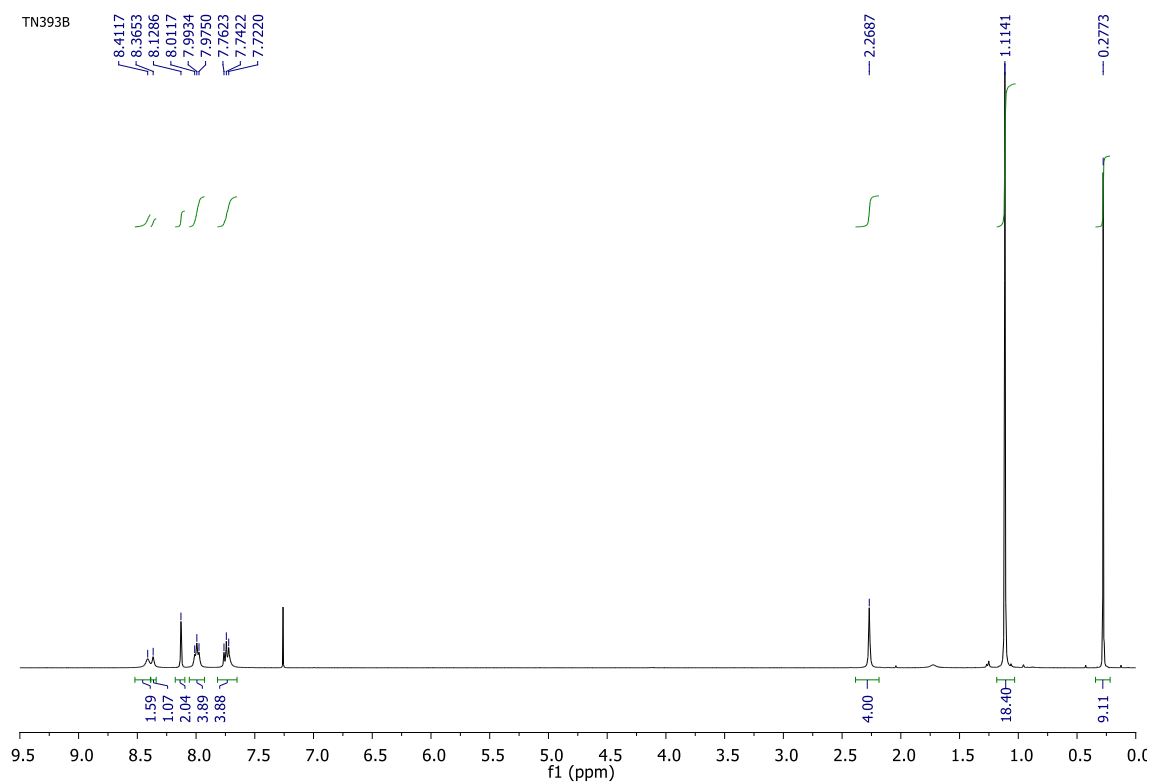


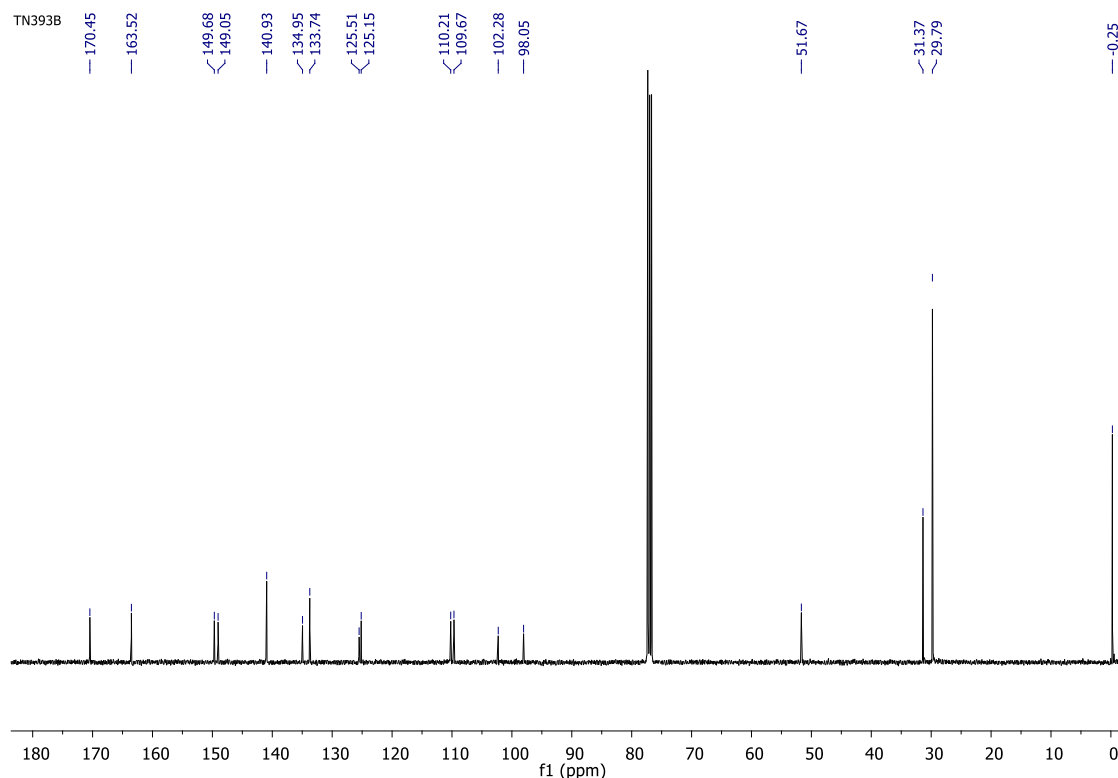
***N,N'*-Bis[6-(3,3-dimethylbutyrylamino)pyridine-2-yl]-trimethylsilyl-ethynyl-isophthalamide**



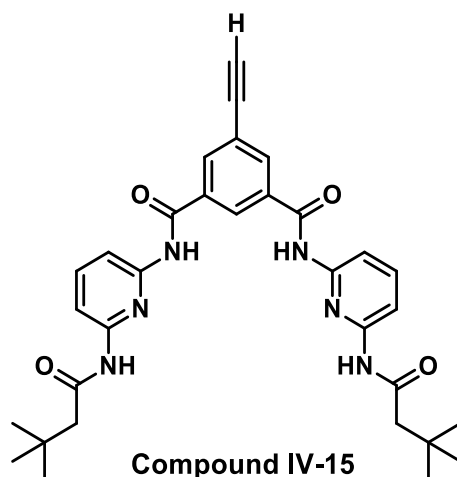
Compound **IV-13** (200 mg, 0.30 mmol) was dissolved in anhydrous THF (5 mL) and distilled NEt_3 (2.2 mL). Then $\text{PdCl}_2(\text{PPh}_3)_2$ (2.1 mg, 0.0032 mmol), CuI (cat. amount) and PPh_3 (0.4 mg, 0.001 mmol) were added. After stirring the reaction mixture for 15 min to dissolve the catalysts, trimethylsilylacetylene (36 mg, 0.36 mmol) was added slowly and dropwise to the suspension. The reaction mixture was then stirred at room temperature for overnight. The solvent was removed under reduced pressure, and the crude material was purified by column chromatography using DCM/EtOAc 8/1-7/1 mixture as a eluent, to furnish compound **IV-14** as a yellow solid 179 mg, 93%. $^1\text{H NMR}$ (CDCl_3): δ = 8.41 (br s, 2H, NH), 8.37 (br s, 1H, NH),

8.13 (s, 2H), 7.99 (t, $J = 4.9$ Hz, 4H), 7.74 (t, $J = 8.0$ Hz, 2H), 2.27 (s, 4H, $\text{CH}_2\text{C}(\text{CH}_3)_3$), 1.11 (s, 18H, $\text{CH}_2\text{C}(\text{CH}_3)_3$), -0.28 (s, 9H, $\text{Si}(\text{CH}_3)_3$). ^{13}C NMR (CDCl_3): $\delta = 170.4$ (2C), 163.5 (2C), 149.7 (2C), 149.0 (2C), 140.9 (2C), 134.9, 133.7, 125.5, 125.2, 110.2 (2C), 109.7 (2C), 102.3, 98.0, 51.7 (2C), 31.4 (2C), 29.8 (6C), -0.3 (3C) ppm. This data is in concordance with *Organometallics* **2014**, 33 (3), 665-676.



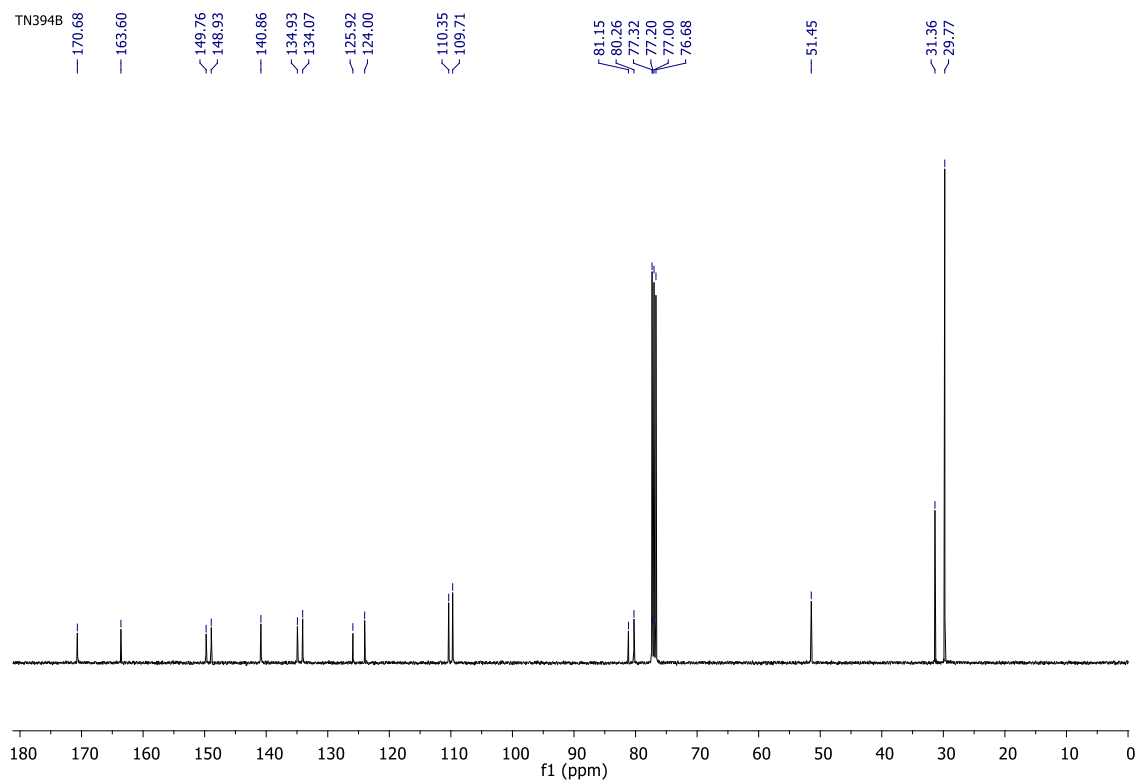
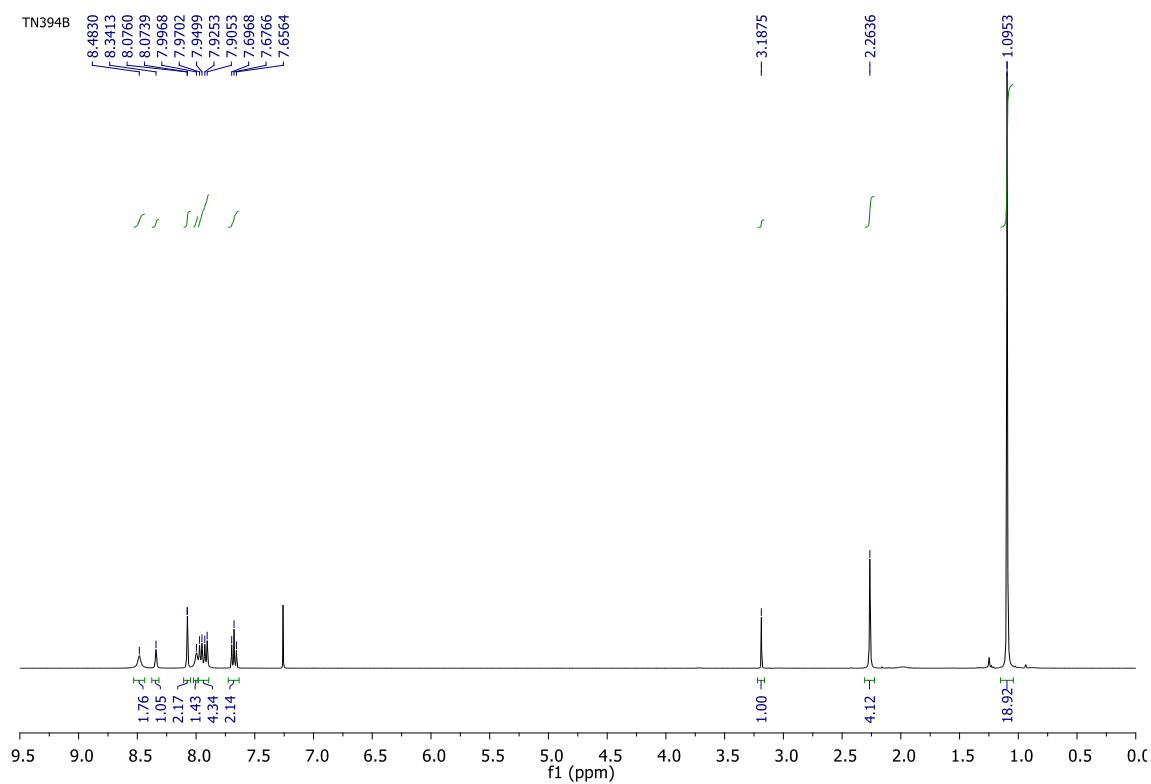


5-Ethynyl-*N,N'*-Bis[6-(3,3-dimethylbutyrylamino)pyridine-2-yl] isophthalamide



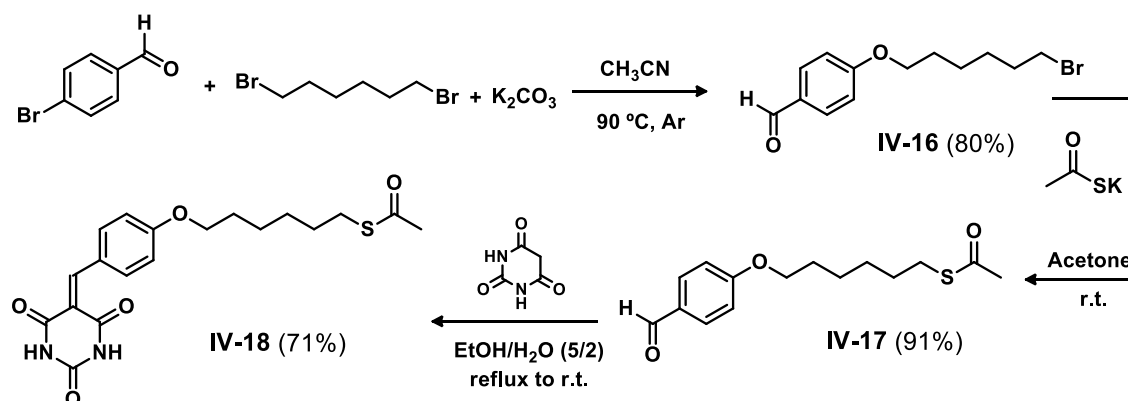
Tetrabutylammonium fluoride solution (TBAF) (74 μ L, 0.26 mmol) in THF was added dropwise to a solution of compound **IV-14** (140 mg, 0.23 mmol) in dry THF (3mL) at room temperature. After stirring for 3h (TLC), solvent was evaporated and the residue purified by column chromatography, using DCM/ AcOEt 4/ 1 as eluent, to furnish compound **IV-15**, 143 mg (97%) as a brown powder. ^1H NMR (CDCl_3): δ = 8.48 (br s, 2H, NH), 8.44 (br s, 1H, NH), 8.07 (s, 1H), 8.00 (s, 2H), 7.98 (d, J = 8.1 Hz, 2H), 7.91 (d, J = 8.0 Hz, 2H), 7.68 (2H J = 8.1 Hz, 2H), 3.19 (s, 1H, $\equiv\text{CH}$), 2.26 (s, 4H, $\text{CH}_2\text{C}(\text{CH}_3)_3$), 1.13 (s, 18H, $\text{CH}_2\text{C}(\text{CH}_3)_3$). ^{13}C NMR (CDCl_3): δ = 170.7 (2C), 163.6 (2C), 149.8 (2C), 148.9 (2C), 140.9 (2C), 134.9 (2C), 134.1

(2C), 125.9, 124.0, 110.4 (2C), 109.7 (2C), 81.2, 80.3, 51.4 (2C), 31.4 (2C), 29.8 (6C). This data is in concordance with *Organometallics* **2014**, 33 (3), 665-676.

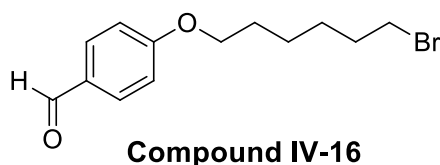


4.3.3.b Barbituric derivative synthesis

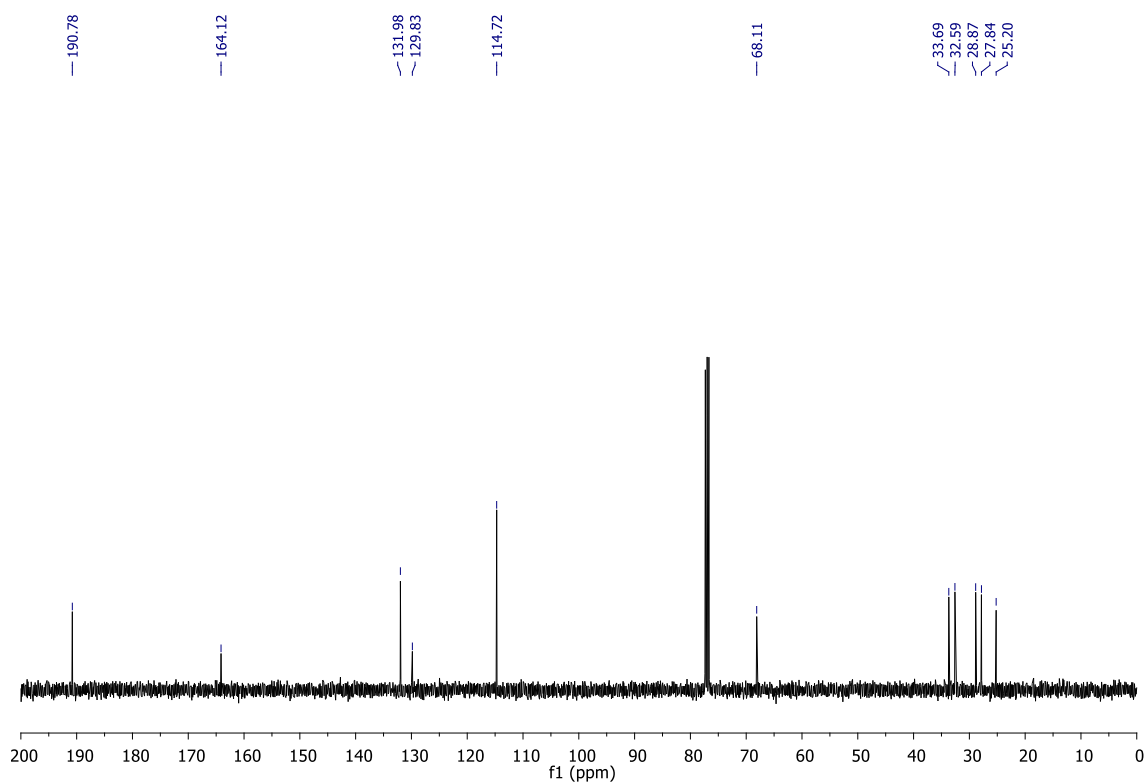
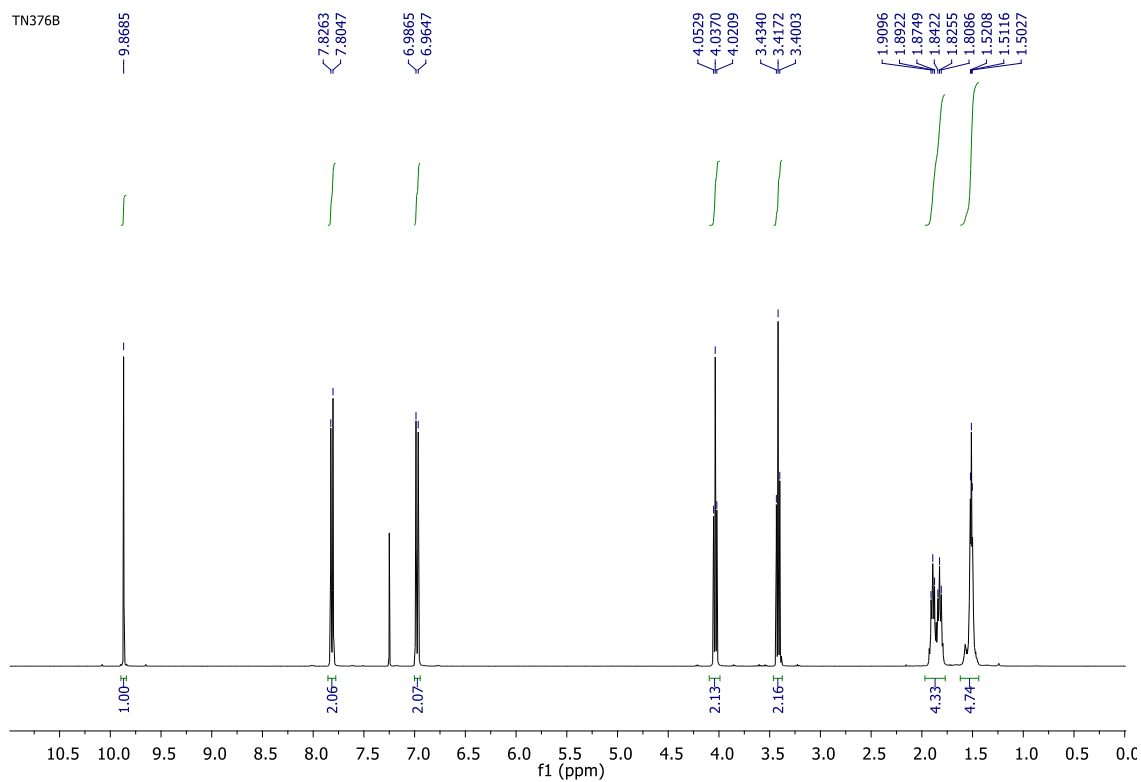
Barbituric derivative (compound **IV-6**) was synthesized following the procedure describe by Huang, C.-H. et al.²⁵²



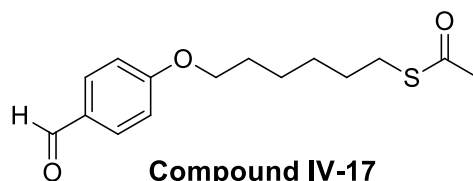
4-((6-bromohexyl)oxy)benzaldehyde



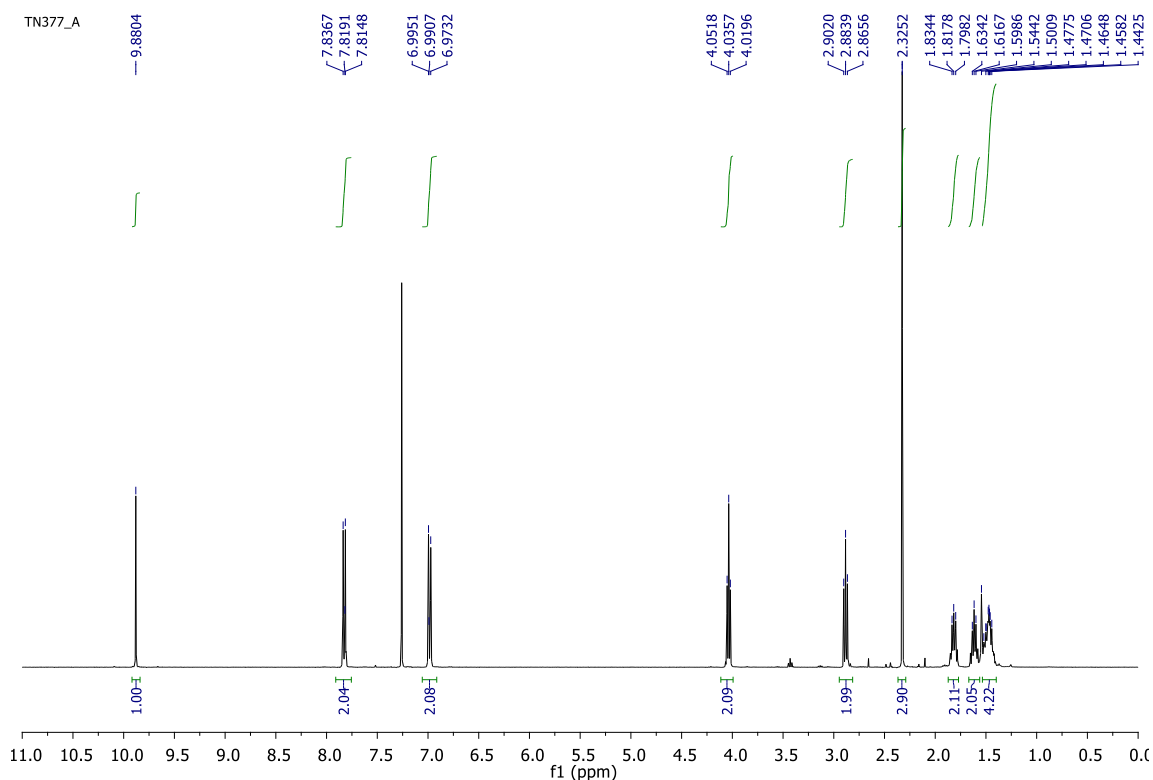
1,6-Dibromohexane (9 g, 36.8 mmol) and K_2CO_3 (6.8 g, 49.2 mmol) were added to a solution of 4-hydroxybenzaldehyde (3 g, 24.6 mmol) in CH_3CN (17 mL). The mixture was refluxed overnight, the white precipitate was filtered off and the filtrate was extracted with CH_2Cl_2 , washed with brine and dried over Na_2SO_4 . The crude material was purified by column chromatography, using DCM/MeOH 200/1-60/1 as eluent; to furnish 5.6 g (80%) as white solid. ^1H NMR (CDCl_3): δ = 9.87 (s, 1H, CHO), 7.81 (d, J = 8.6 Hz, 2H, Ar-H), 6.97 (d, J = 8.7 Hz, 2H, Ar-H), 4.04 (t, J = 6.4 Hz, 2H, OCH_2), 3.42 (t, J = 6.7 Hz, 2H, BrCH_2), 1.89 (m, 2H, CH_2), 1.83 (m, 2H, CH_2), 1.51 (m, 4H, CH_2). ^{13}C NMR (CDCl_3): δ = 190.8, 164.1, 132.0 (2C), 129.8, 114.7 (2C), 68.1, 33.7, 32.6, 28.9, 27.8, 25.2 ppm.



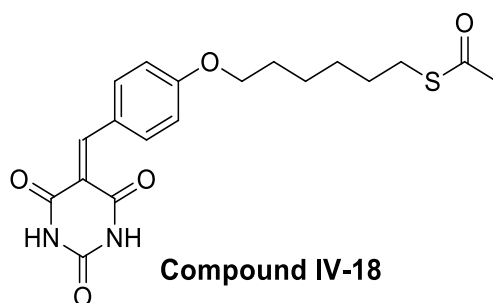
6-(4-formylphenoxy)hexyl thioacetate



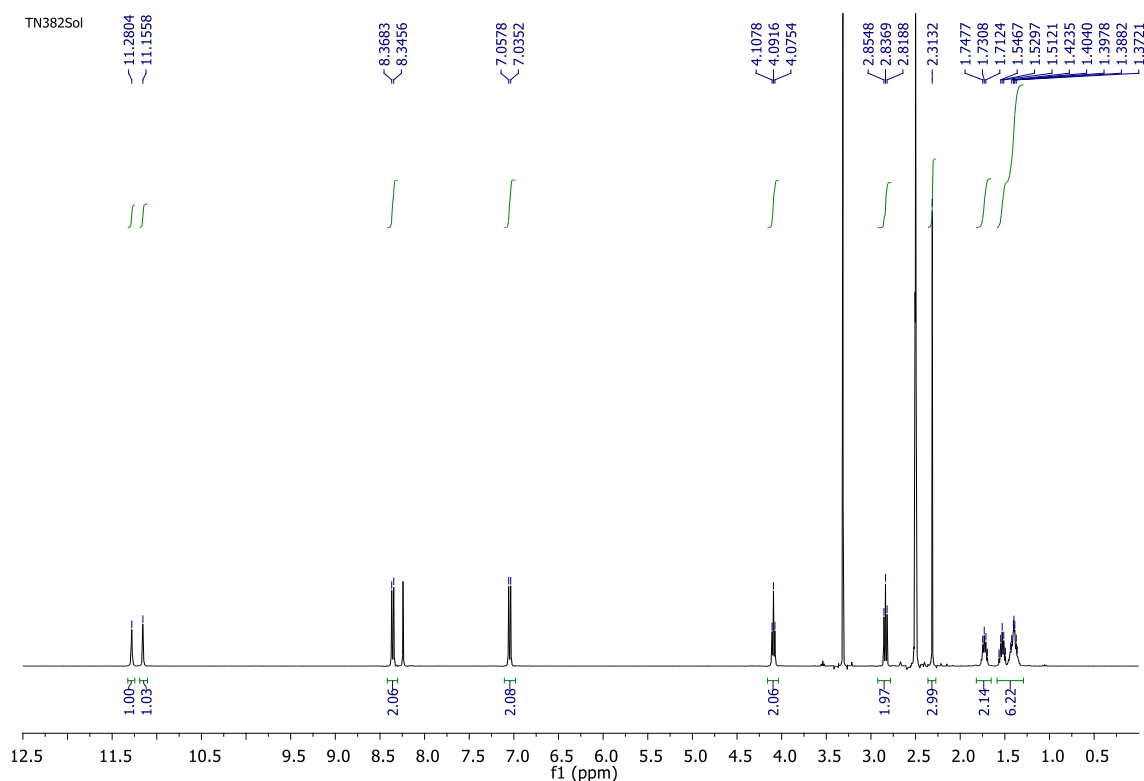
4-(6-Bromohexyloxy)-benzaldehyde (3.44 g, 12.1 mmol) and potassium thioacetate (1.38 g, 12.1 mmol) in acetone (65 mL) were stirred at room temperature overnight. The resulting white precipitate was filtered off and the filtrate was concentrated under reduced pressure to give a white solid (3.08 g, 91%). ^1H NMR (CDCl_3): δ = 9.88 (s, 1H, CHO), 7.82 (d, 2H, J = 8.7 Hz, Ar-H), 6.98 (d, 2H, J = 8.7 Hz, Ar-H), 4.04 (t, 2H, J = 6.3 Hz, OCH_2), 2.88 (t, 2H, J = 7.1 Hz, SCH_2), 2.32 (s, 3H, CH_3), 1.82 (m, 2H), 1.59 (m, 2H), 1.48 (m, 4H).

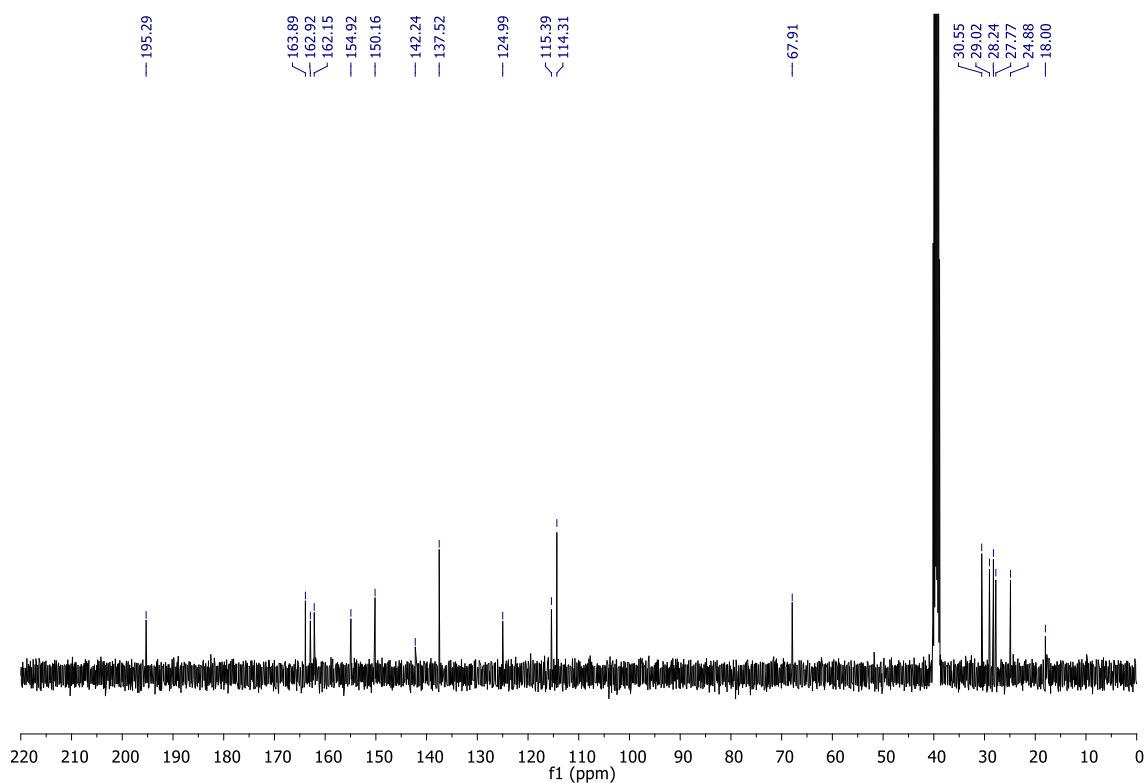


6-{4-[(1,3-Dimethyl-tetrahydro-2,4,6-trioxo-5(2H)-pyrimidinyl)ene)methyl] phenoxy} hexyl thioacetate



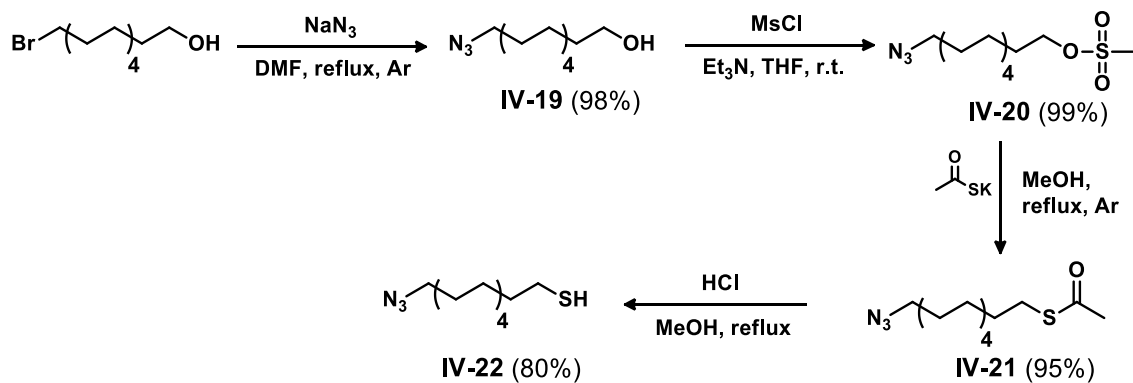
Compound **IV-17** (1.6 g, 5.71 mmol), and barbituric acid (0.73 g, 5.71 mmol) in EtOH/H₂O 5/2 (35 mL) were stirred under reflux for 10 min and then at room temperature overnight. The resulting yellow suspension was filtered, washed with EtOH and dried under reduced pressure to give a yellow solid (1.58 g, 71%). ¹H NMR ([D₆]dimethyl sulfoxide): δ = 11.28 (s, 1H, NH-barb), 11.15 (s, 1H, NH-barb), 8.35 (d, 2H, *J* = 9.1 Hz, Ar-H), 7.04 (d, 2H, *J* = 9.0 Hz, Ar-H), 4.09 (t, 2H, *J* = 6.5 Hz, OCH₂), 2.84 (t, 2H, *J* = 7.2 Hz, SCH₂), 2.31 (s, 3H, CH₃), 1.73 (m, 2H), 1.53 (m, 2H), 1.40 (m, 4H); ¹³C NMR ([D₆]dimethyl sulfoxide): δ = 195.3, 163.9, 162.9, 162.2, 154.9, 150.2, 142.2, 137.5 (2C), 125.0, 115.4, 114.3 (2C), 67.9, 30.6, 29.0, 28.4, 27.8, 24.9 ppm.



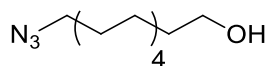


4.3.3.c. Synthesis of 11-azidoundecane-1-thiol

11-azidoundecane-1-thiol (compound **IV-22**) was synthesized following the procedure described by Liu, X. et al.²⁵³



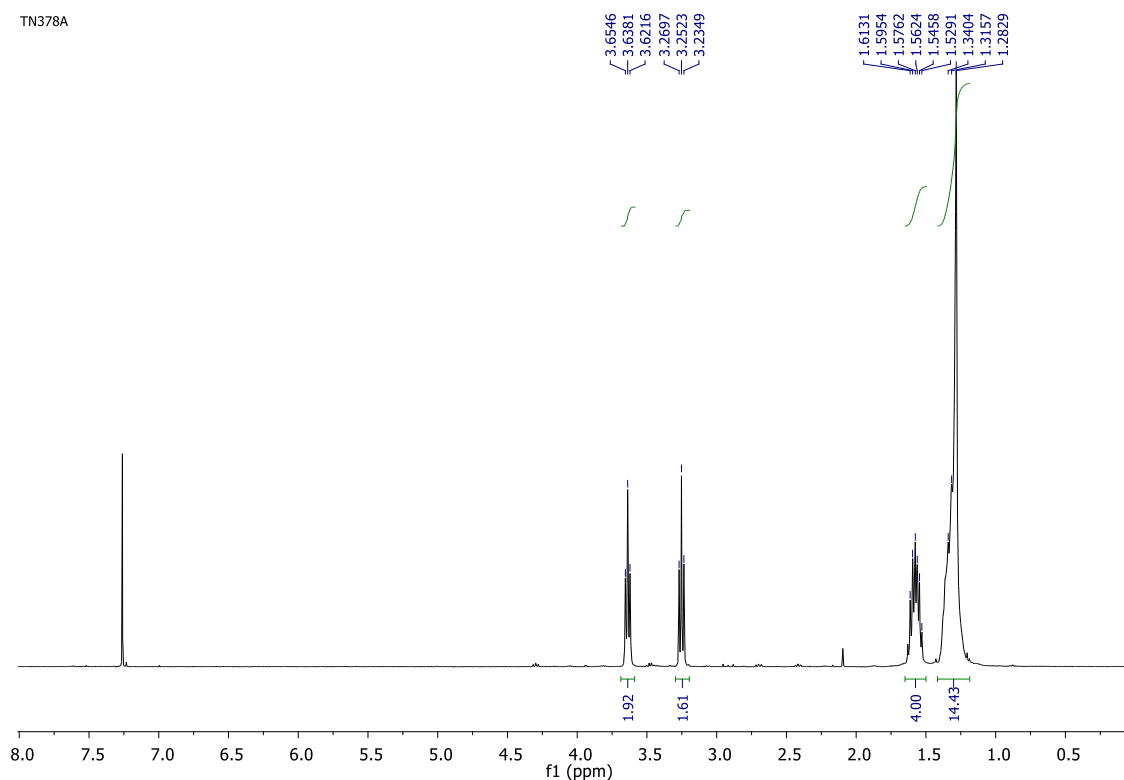
11-azidoundecan-1-ol



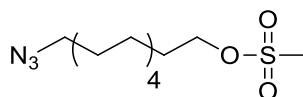
Compound IV-19

Sodium azide (1.43 g, 22.0 mmol) was added to a solution of 11-bromoundecan-1-ol (5 g, 19.9 mmol) in 75 mL DMF. The reaction mixture was stirred under reflux and argon atmosphere overnight. The reaction mixture was allowed to cool to room temperature, followed

by the addition of 75 mL H₂O. The resulting mixture was extracted with diethyl ether. Then the organic phase was combined, dried with MgSO₄, and concentrated under reduced pressure to give compound as a colorless oil (4.25 g, 98%). ¹H NMR (CDCl₃): δ = 3.64 (t, 2H, *J* = 6.5 Hz, OCH₂), 3.25 (t, 2H, *J* = 6.8 Hz, N₃CH₂), 1.56 (m, 4H, CH₂), 1.31 (m, 14H, CH₂).

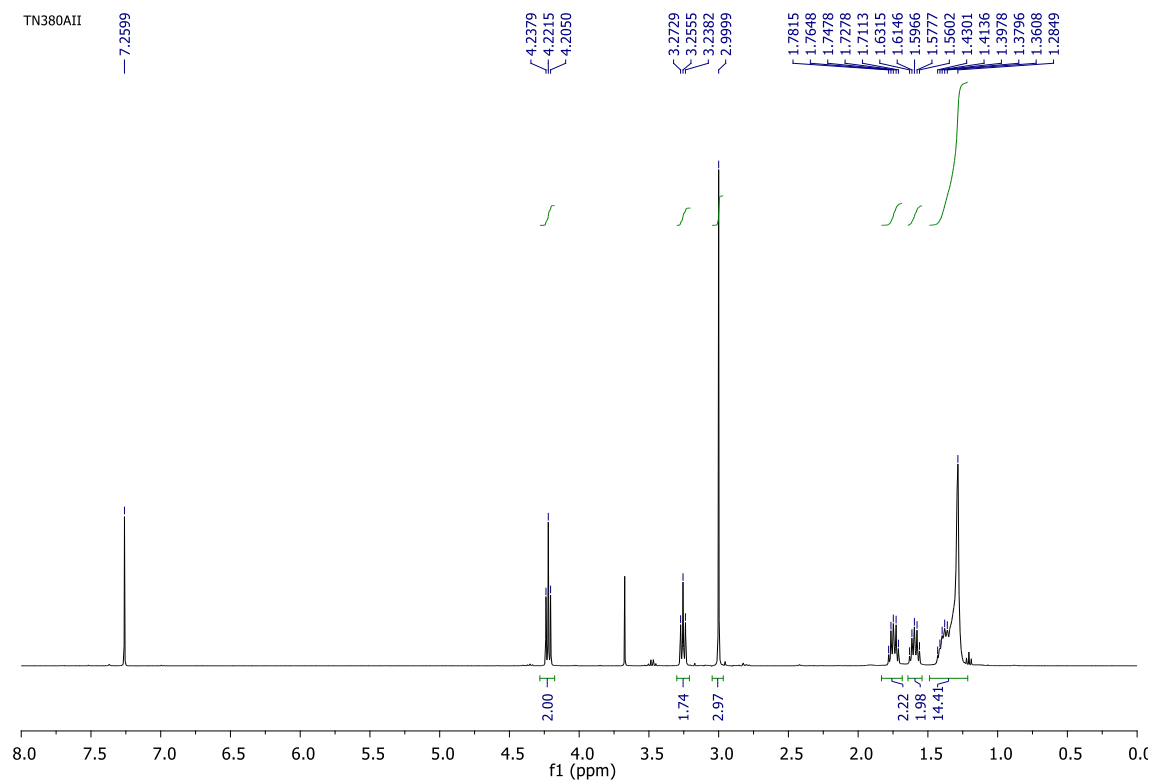


5-azidoundecyl methanesulfonate

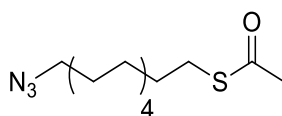


Compound IV-20

To a solution of compound **IV-19** (1.5 g, 6.87 mmol) and NEt₃ (1.9 mL, 13.70 mmol) in THF (52 mL) was added methanesulfonyl chloride (1.5 mL, 19.30 mmol) dropwise in an ice bath. The reaction was stirred at 0 °C for 30 min and at room temperature for another 90 min under argon. Then 52 mL of ice-cold water was added. The aqueous phase was extracted twice with diethyl ether. The combined organic phases were then combined and washed with 1M HCl, H₂O, NaHCO₃ and H₂O. After drying over MgSO₄, the solvent was removed under reduced pressure to yield a colorless oil (2 g, quantitative). ¹H NMR (CDCl₃): δ = 4.22 (t, 2H, *J* = 6.6 Hz, CH₂), 3.26 (t, 2H, *J* = 6.8 Hz, CH₂), 3.00 (s, 3H, CH₃), 1.75 (m, 2H, CH₂), 1.60 (m, 2H, CH₂), 1.36 (m, 14H, CH₂).

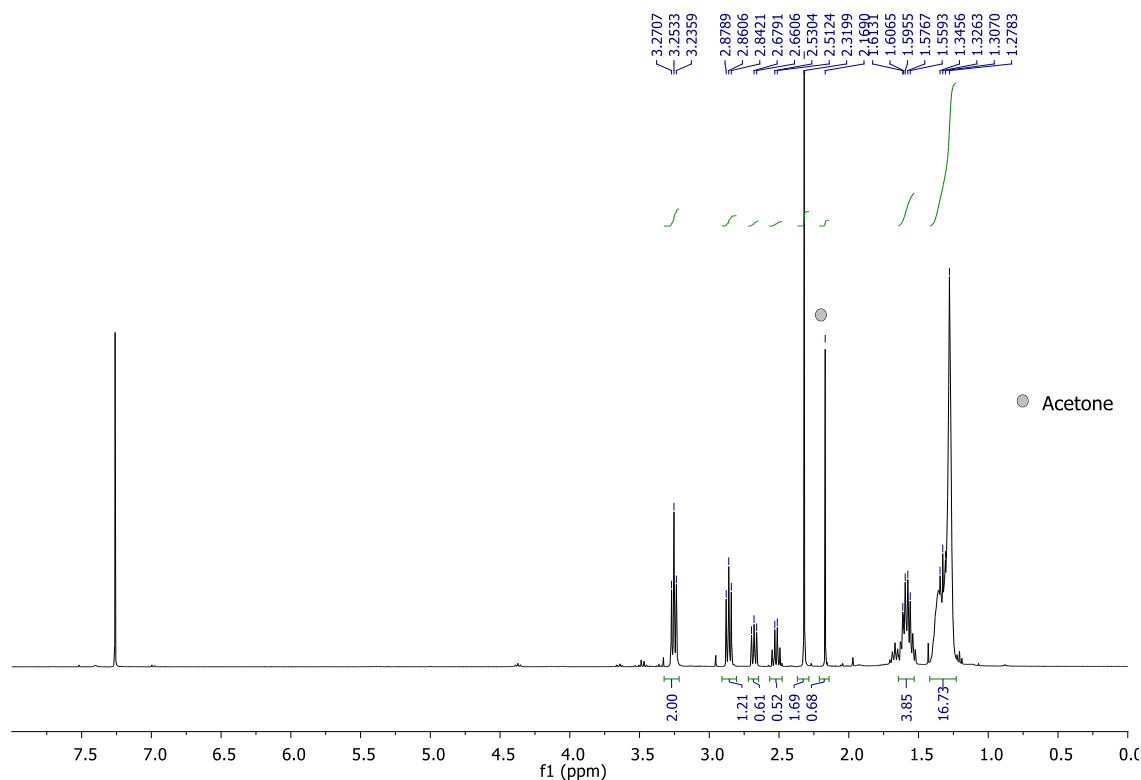


11-azidoundecyl thioacetate

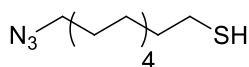


Compound IV-21

Compound **IV-20** (1.7 g, 5.83 mmol) and potassium thioacetate (1.33 g, 11.7 mmol) was dissolved in methanol (50 mL). The reaction mixture was degassed and refluxed under argon for 3h. After cooling to room temperature, excess methanol was removed under reduced pressure and ice water was added. The mixture was extracted with diethyl ether (x3) and washed with H₂O (x3). Then the organic phase was combined, dried with MgSO₄ and concentrated to yield a pale yellow oil (1.61 g, 95%). ¹H NMR (CDCl₃): δ = 3.24 (t, 2H, *J* = 6.88 Hz, CH₂), 2.86 (t, 2H, *J* = 6.88 Hz, CH₂), 2.31 (s, 3H, CH₃), 1.60 (m, 4H, CH₂), 1.33 (m, 14H, CH₂);

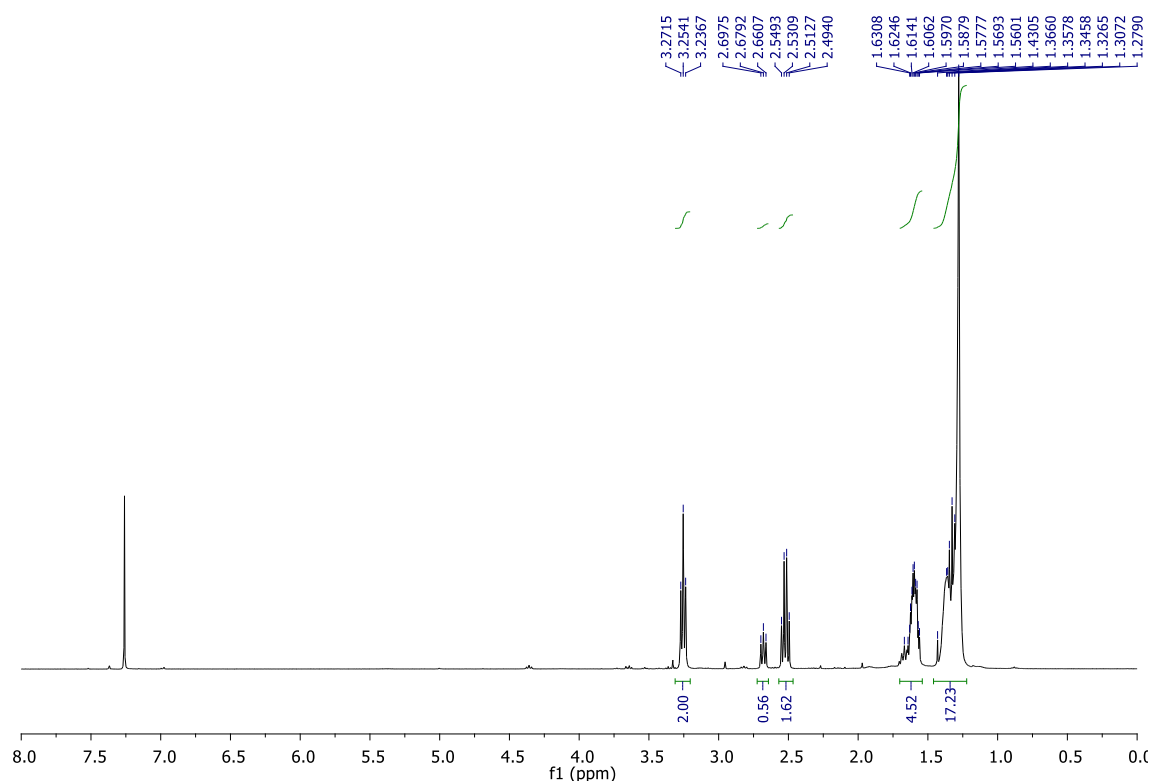


11-azidoundecane-1-thiol



Compound IV-22

To 300 mg of compound **IV-21**, 20mL of methanol was added. The solution was degassed thoroughly and backfilled with N_2 . 1 mL conc HCl was added, and the entire mixture was refluxed for 5h. The reaction mixture was quenched with water and extracted twice with diethyl ether. The organic phase was washed twice with water (x2) and dried over $MgSO_4$. Rotary evaporation yielded a yellow oil. 80% Yield. 1H NMR ($CDCl_3$): δ = 3.25 (t, 2H, J = 7.00 Hz, CH_2), 2.68 (t, 0.6 H, J = 7.25 Hz, CH_2 in disulfide), 2.52 (q, 2H, J = 11.0 Hz, CH_2), 1.61 (m, 4H, CH_2), 1.24 (m, 14H, CH_2).



4.3.4. AFM Tip and surface functionalization

To perform force spectroscopy experiments, the cantilevers were modified with the barbituric acid derivative (compound **IV-22**) and the gold surfaces were functionalized with the Hamilton Receptor (compound **IV-15**).

4.3.4.a Barb functionalization of AFM gold-coated Si cantilevers

AFM gold-coated Si cantilevers were modified by dipping them overnight in a solution of compound **IV-18** (1 mM total concentration in anhydrous THF) at room temperature. 15% Et₃N was used to in situ deprotect the thioacetate groups. After overnight immobilization, the cantilevers were rinsed with THF. To estimate the binding of barbituric acid derivative to the gold-coated AFM tips, gold-coated glass slides acting as test samples were placed into the same immobilization solution followed by THF rinsing under the same conditions.

4.3.4.b HR functionalization of gold-coated surface

SAM-coated gold surfaces were prepared in two steps:

Step i) Functionalization with 11-azidoundecane-1-thiol (compound **IV-22**): By dipping a preliminary cleaned gold surface in a solution of N₃C₁₁H₂₃SH/C₁₁H₂₃SH (0.1 molar ratio) in absolute ethanol at room temperature. The incubation was done overnight and the total thiol concentration was 1 mM. After overnight SAM formation, the gold surfaces were rinsed with ethanol, dried under nitrogen.

Step ii) Click reaction: azide functionalized gold surfaces were immersed at room temperature in a water/ DMSO (1:2) solution containing 0.5 mM alkyne-Hamilton Receptor (compound **IV-15**), 0.5 mM CuSO_4 , 0.5 mM TBTA (tris[(1-benzyl-1*H*-1,2,3-triazol-4-yl)methyl]amine, which is a commonly used ligand for stabilizing the Cu(I) catalyst, and 2.8 mM sodium ascorbate (needed for the Cu(I) catalyst generation) for 4 h. Exposure to light was kept to a minimum. After reaction, the monolayers were rinsed with water and DMSO to ensure all physisorbed molecules to be washed off.

4.3.5. SAM characterization

4.3.5.a Contact angle measurements.

The contact angle of water was measured using a drop shape analysis system DSA100S (Krüss). Contact angle measurements were performed directly on the gold surfaces with a 2 μL drop of ultrapure water. The contact angle value (θ) was calculated from the average of five measurements, with drops being positioned on different places on the surface.

4.3.5.b ATR experiments

ATR spectra were recorded on a Bruker's ALPHA-P FTIR spectrometer at a resolution of 4 cm^{-1} , by coadding 254 scans. ATR experiments were performed using a single-reflection.

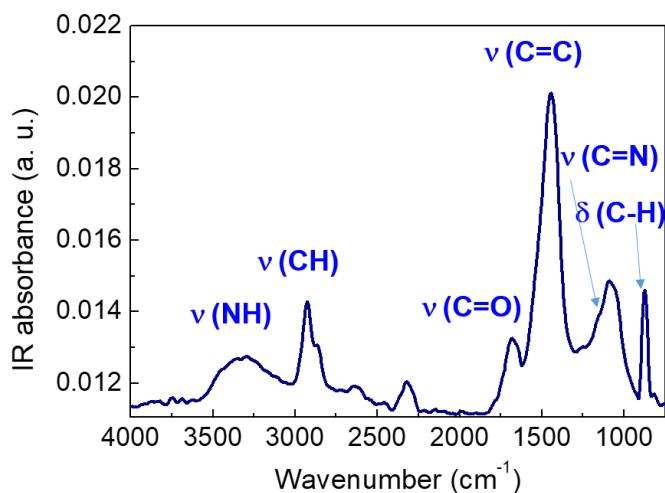


Figure IV-11. ATR-IR spectra of HR-SAM.

4.3.6. AFM measurements.

AFM measurements were acquired with a Nanoscope Multimode IIIa, (Veeco Instruments, Santa Barbara, CA) using gold-coated Si cantilevers Cont-GB (Budget Sensors)

having nominal force constant of 0.2 N/m and resonant frequency of 13 kHz. Force spectroscopy measurements were performed in 1,2-dichlorobenzene and in room temperature ionic liquid as indicated at room temperature.

Force-distance measurements were recorded at velocities of 250 nm/s with contact time of 5s. After reaching the maximal force, the two surfaces remained in contact for a time interval of 5 s, after which the direction of the piezo movement was reversed, and the AFM probe was retracted from the surface. Force distance curves were collected from several different positions on the substrate, and about 60 force curves were measured at each position. The spring constants of all AFM cantilevers were defined using the Sader method.²⁵⁴ Values in the range from 344 to 385 pN/nm were obtained. The same cantilever was used for each set of data, where the interactions between bare or modified AFM tip and bare or functionalized substrates were studied.

4.3.7. Description of UV/vis titration experiments

UV/vis experiments were performed on a Varian Cary® 50 UV/vis spectrometer. Absolute concentrations for each component of a titration experiment were determined by standard calibration curves, and appropriate aliquots added relative to the determined concentrations. All titration were performed with a background concentration of host in the guest solution so as to maintain a constant concentration of host species. Aliquot injections were carried out with MICROMAN™ E positive displacement pipettes into a quartz cuvette (cuvette path length was dependent on concentrations used: 1.0 mm or 10.0 mm) with a Teflon stopper.

Each spectrum was acquired at a resolution of 1.0 nm and an integration time of 0.1 s.

Spectral analyses were performed using the ReactLab™ Equilibria spectral analyses suite (JplusConsulting, www.jplusconsulting.com). Repetitions of the binding experiments for each complex gave association constants within 10% of the values shown, (the error in data fitting for each experiment was <5%).

4.3.8. Description of ATR-IR experiments

ATR-IR measurements were carried out on a Bruker's ALPHA-P FTIR spectrometer for the HR-cy and the Ben-AcOH couples. For the first couple, HR-cy, 1.4×10^{-3} M solutions in RTIL of HR and cy were prepared separately, then 1:1 molar mixture of both compounds, HR-cy at 7.0×10^{-3} M was

For the second couple, Ben-AcOH, 0.2 M solutions in RTIL of Ben and AcOH were prepared separately, then 1:1 molar mixture of both compounds, HR-cy at 0.1 M was measured.

In all the recorded spectra the solvent (RTIL) has been subtracted. Measurements of a small droplet placed on top of the diamond crystal was carried out by coading 254 scans.

CHAPTER 5.

Ingeniering Of Sso7d Protein Looking For A New Solvatochromic Biosensor

The work described in this chapter was carried out in Barbara Imperiali's laboratory at the Massachusetts Institute of Technology (MIT) in Boston, as part of a short internship, in collaboration with Dr. Cristina Zamora.

5.1. Introduction

In the introduction of this thesis we explained what supramolecular chemistry is, emphasizing that intermolecular interactions are responsible for many responses in biology. This internship was a great opportunity to study supramolecular chemistry from a biological point of view.

Keeping this purpose in mind we focused on the evolution of protein-protein interactions ligands in order to develop a new solvatochromic biosensor. Specifically the aim of this work consists of engineering the ultrastable protein Sso7d (from the hyperthermophilic archaeon *Sulfolobus solfataricus*) to find human Epidermal Growth Factor (hEGF) binders, looking for fluorescence increase upon hEGF binding.

Before going into the project itself, I will briefly overview some of the concepts and techniques that will be required for its correct development.

In a solvatochromic fluorophore the effect of solvent polarity on the emission properties are generalized in the Jablonski diagram, which depicts the energies of the different electronic states of the system (Figure V-1). At the beginning, the fluorophore (large oval, green) resides in the electronic ground state (S^0) surrounded by a sphere of solvent molecules (small ovals, white). The electric dipole moment of the fluorophore is indicated by the black arrow. Upon absorbing a photon of the appropriate energy ($h\nu_A$), the system is rapidly promoted to an excited singlet state (S^1). During this event, the system adopts a new electronic configuration with a dipole moment that differs significantly from that of the ground state. In this case, the dipole has increased in magnitude. On the picosecond time-scale, the molecules of the solvent sphere reorient dipoles to accommodate the now larger dipole of the fluorophore, which result in a more ordered arrangement (upper left corner). This step, termed solvent relaxation,

ultimately lowers the energy of the excited singlet state while simultaneously destabilizing the ground state thereby narrowing the energetic gap between the two states. When the system finally returns to the ground state through a fluorescence event, the emitted photon is of a much longer wavelength (i.e. lower energy, $h\nu_F$) than that which was originally absorbed during excitation. The degree of solvent relaxation increases with increasing solvent polarity. In some instances, the fluorophore returns spontaneously to the ground electronic state through a thermal (non-radiative) decay process (k_{nr}) that competes with fluorescence. A common feature among many solvatochromic fluorophores is their tendency to exhibit a marked increase in non-radiative decay as the energy gap that separates the S^{0*} and S^{1*} states is reduced. This effect is apparent particularly in polar protic solvents such as water, and results in a decrease in the fluorescence quantum yield. The mechanisms for such processes are varied and can include a range of events such as internal charge transfer, tautomerization, isomerization, and intersystem crossing to an excited triplet state. When non-radiative decay competes strongly with fluorescence in polar solvents, the fluorophore can exhibit sensitive switch-like emission properties upon perturbations of the ordering of the solvent sphere.²⁵⁵

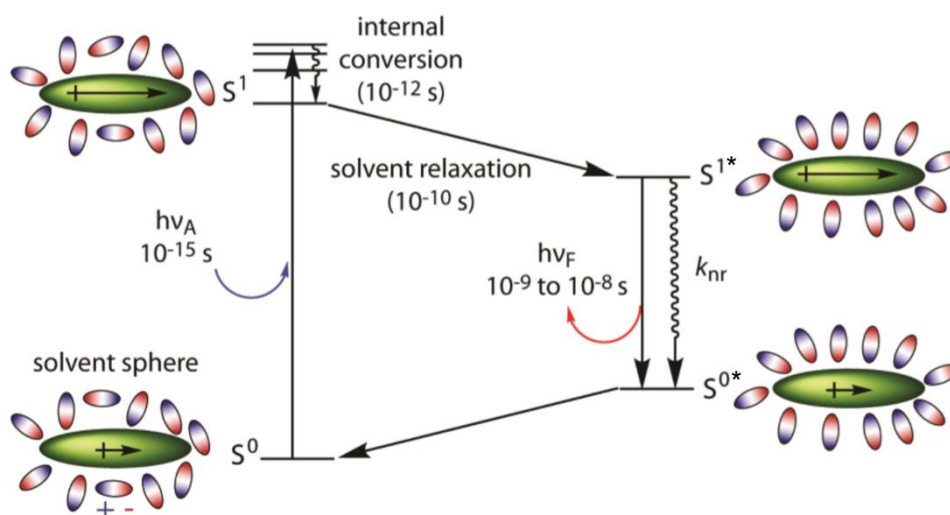


Figure V-1. Origin of solvatochromic effect in fluorescence. Figure reproduced with permission from *Trends in biotechnology* **2010**, 28 (2), 73.

Thereby, solvatochromic fluorophores represent a fascinating class of organic dyes particularly useful for the study of complex biological systems.²⁵⁶⁻²⁶¹ They demonstrate emission properties (e.g. fluorescence lifetimes, emission wavelengths, and quantum yields) that are highly sensitive to the immediate environment; thus, thanks to their sensitivity to local microenvironments, low cost, and ease of handling,²⁶² these compounds present recent applications in the field of proteomics and the study of protein folding and protein-protein interactions.^{255, 263-272} For example, if a solvatochromic fluorophore is appended to the surface of a protein at a site that is involved in a transient interaction or that undergoes a conformational

change, then the probe will report binding or allosteric changes if these events are coupled to modifications in the local solvent sphere. Here, we focus on the incorporation of these tools into small proteins for the development of sensors of protein-protein interactions.

In this class of biosensors, changes in the environment of the fluorophore upon analyte binding (such as solvent shielding) transduce the binding signal into a fluorescence read-out. This concept was introduced for the first time in 1964 by Burr and Koshland.²⁷³

Currently, fluorescence-based biosensors can be designed in three steps. First, a binder is engineered against the intended target using established display technologies²⁷⁴⁻²⁷⁷ and multiple scaffolds,²⁷⁸⁻²⁸⁰ ideally with tailored binding kinetics and affinity.²⁸¹ The second step consists on carefully choosing the labelling site, taking into account that the residue must be: 1) exposed to solvent, 2) non-perturbing to the analyte/scaffold interaction, and 3) close to the binding epitope. Finally, a fluorophore is conjugated to a specific site on the binding protein using established chemical²⁸² or enzymatic²⁸³ techniques.

The insertion of solvatochromic fluorophores in proteins is topologically restricted to sites that preserve its function and activity while permitting the dye to make the necessary contacts that will result in measurable fluorescence changes. This consideration necessitates the use of methods that offer precise control over dye placement within the peptide or protein structure of interest with minimal perturbation. For proteins, the most common methods can broadly be divided into three categories: (i) direct covalent modification; (ii) incorporation of fluorescent amino acids via semi-synthesis (expressed protein ligation); and (iii) incorporation of fluorescent amino acids via suppression of the amber (TAG) stop codon. In this work, we take advantage of the covalent modification, which is clearly explained in the results and discussion section.

Cysteine and lysine reactive agents offer a convenient and direct method for labelling proteins and have been used extensively to conjugate a myriad of auxiliary groups into biomolecules. Most common among these are the thiol-selective electrophiles, such as maleimides and α -halocarbonyl compounds, along with the amine-selective acylating agents such as the O-succinimidyl esters. In general, cysteine residues are ideal since this amino acid occurs relatively infrequently in proteins and possesses excellent nucleophilic properties under most physiological conditions. Proteins with unique cysteines can be readily prepared using standard molecular biology techniques.

Another important point that has to be considered in solvatochromic biosensors, is the undesirable fluorophore pre-activation, which should be attenuated in a rigid protein scaffold. A rigid conformation (characteristic of the β -strands) should reduce the likelihood of fluorophore interactions with the scaffold itself, thereby reducing unwanted background fluorescence (Figure V-2).

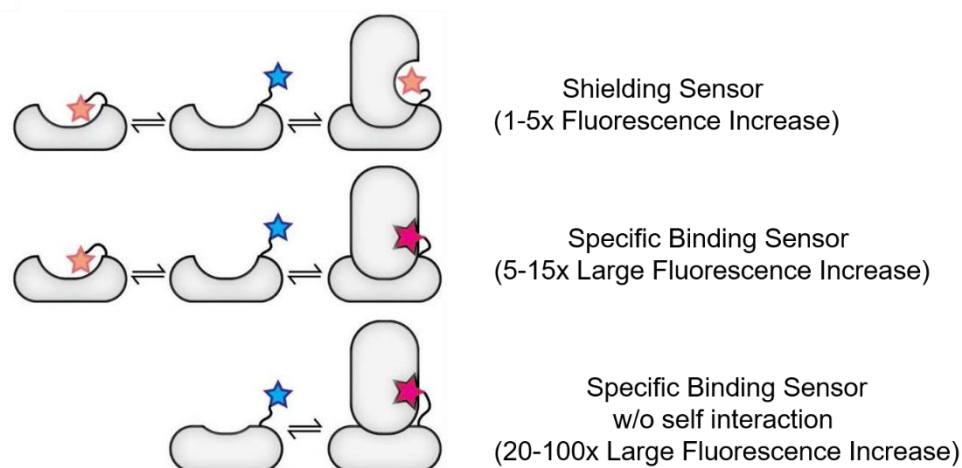


Figure V-2. Mechanistic drawing of the three types of reagentless biosensors. The top one describes a sensors that suffers from pre-activation and the fluorophore undergoes shielding upon binding, yielding a small F/F_0 ratio. The middle one describes a sensor that may have some pre-activation but that alleviates this drawback by having a strong fluorescence enhancement due to a fluorophore binding pocket. The bottom scenario describes a sensor that possesses both ideal properties: little self-interaction and specific binding pocket interaction on the analyte. Extracted from *J. Mol. Biol.* **2016**, 428 (20), 4228-4241.²⁸⁴

Hyperthermophilic proteins are excellent candidates for use as protein scaffolds to engineer molecular recognition. We have selected the ultrastable Sso7d protein from the hyperthermophilic archaeon *Sulfolobus solfataricus* as a versatile scaffold to generate highly stable binding proteins. The Sso7d protein is a small (~7 kDa, 63 amino acids) DNA-binding protein containing an SH3-like fold consisting of an incomplete β -barrel with five β -strands and a C-terminal α -helix.^{285, 286} Sso7d is highly stable with a melting temperature of nearly 100 °C and lacks cysteine.²⁸⁷

Yeast surface display (YSD) has been recently used for engineering proteins based on the Sso7d scaffold.^{288, 289} The yeast display technique was first published by the laboratory of Professor Wittrup. In this methodology, a protein of interest is displayed on the surface of yeast and the protein is away from the cell surface, minimizing potential interactions with other molecules on the yeast cell wall. Briefly, different rounds of positive (against the target binder) and negative (against non-desired binders) magnetic bead selections were used to select for weak binders and to get rid of magnetic bead and non-specific binders. Yeast cells isolated after the magnetic bead-based processes were further screened using FACS (Fluorescence-activated cell sorting) to isolate clones that exhibit higher binding affinity towards the target. Final step is the single clone analysis and characterization (Figure V-3). The whole process is known as directed evolution.²⁹⁰

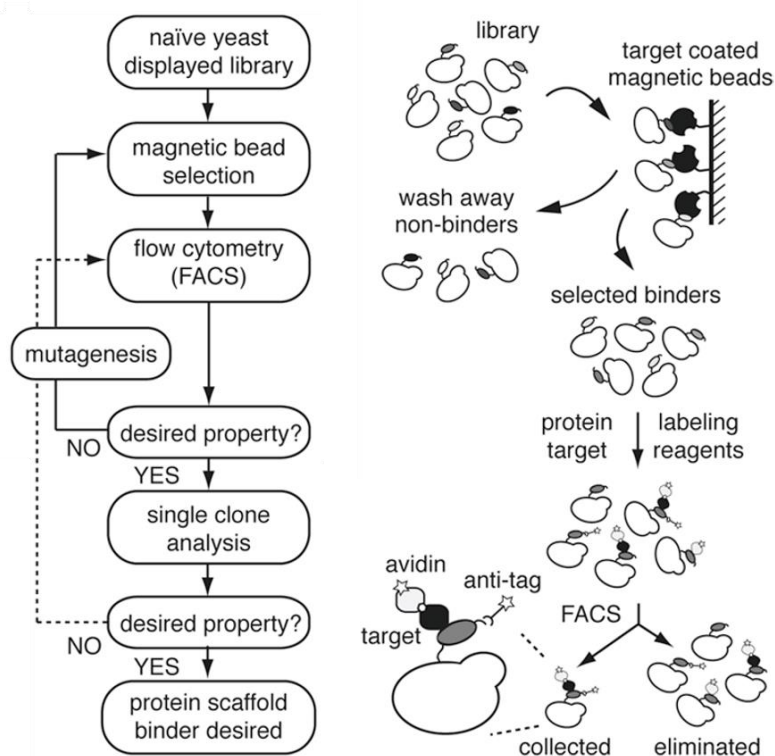


Figure V-3. Schematic representation for selection of protein binders from a naïve yeast display library using magnetic bead screening followed by flow cytometry sorting. Extracted from Angelini A. et al. (2015) Protein Engineering and Selection Using Yeast Surface Display. In: Liu B. (eds) Yeast Surface Display. Methods in Molecular Biology, vol 1319. Humana Press, New York, NY ²⁹¹

Flow cytometry is a technology that simultaneously measures and then analyzes multiple physical characteristics of single particles, usually cells, as they flow in a fluid stream through a beam of light. Any suspended particle or cell from 0.2 to 150 micrometers in size is suitable for analysis. The properties measured include a particle's relative size, relative granularity or internal complexity, and relative fluorescence intensity. These characteristics are determined using an optical-to-electronic coupling system that records how the cell or particle scatters incident laser light and emits fluorescence.

A flow cytometer is made up of three main systems: fluidics (which transports particles in a stream to the laser beam for interrogation), optics (which consists of lasers to illuminate the particles in the sample stream and optical filters to direct the resulting light signals to the appropriate detectors), and electronics (which converts the detected light signals into electronic signals that can be processed by the computer. For some instruments equipped with a sorting feature, the electronics system is also capable of initiating sorting decisions to charge and deflect particles). When particles pass through the laser intercept, they scatter laser light (Figure V-4a). Factors that affect light scattering are the cell's membrane, nucleus, and any granular material inside the cell. Cell shape and surface topography also contribute to the total

light scatter. Forward-scattered light (FSC) is proportional to cell-surface area or size and provides a suitable method of detecting particles greater than a given size, independent of their fluorescence. Side-scattered light (SSC) is proportional to cell granularity or internal complexity. It is collected at approximately 90 degrees to the laser beam by a collection lens and then redirected by a beam splitter to the appropriate detector. Correlated measurements of FSC and SSC can allow for differentiation of cell types in a heterogeneous cell population (Figure V-4b).

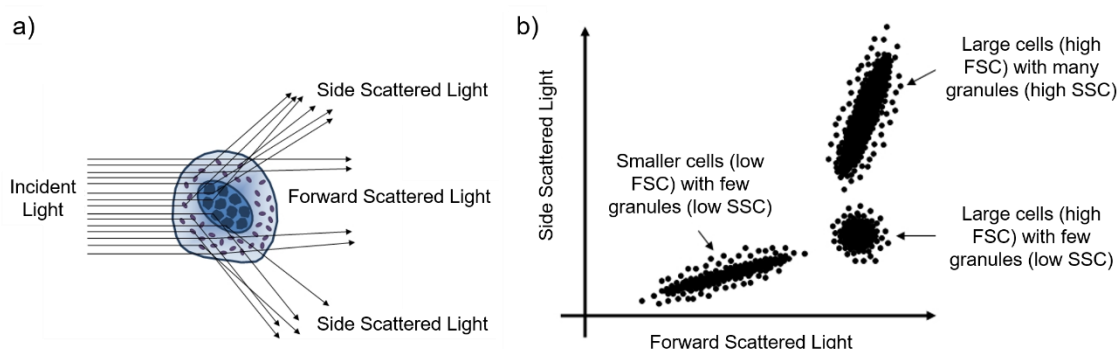


Figure V-4. Light scattering in flow cytometry. a) Light-scattering properties of a cell. b) Cell subpopulations based on FSC vs SSC.

When particles are labelled with fluorophores, the amount of fluorescent signal detected is proportional to the number of fluorophore molecules on the particle. When a fluorescent dye is conjugated to a monoclonal antibody, it can be used to identify a particular cell type based on the individual antigenic surface markers of the cell. In a mixed population of cells, different fluorophores can be used to distinguish separate subpopulations. The staining pattern of each subpopulation, combined with FSC and SSC data, can be used to identify which cells are present in a sample and to count their relative percentages. The cells can also be sorted if desired.

Recently, de Picciotto et al. used an Sso7d-based murine serum albumin (MSA) binder obtained by YSD, and labelled it at seven sites with nitrobenzoxadiaxole-fluorophore. They demonstrated reduced background activation with the Sso7d scaffold, finding 50-fold increases in fluorescence upon addition of MSA.²⁸⁴

The solvatochromic fluorophore 4-*N,N*-dimethylamino-1,8-naphthalimide (4-DMN), developed in Prof. Imperiali's lab, possesses extremely sensitive emission properties due largely to the low intrinsic fluorescence that it exhibits in polar protic solvents such as water.²⁹² This greatly reduces the background signal thereby creating the effect of on-off or switch-like changes in the observed emission intensity with the potential to exceed ratios of 1000-fold. Furthermore, as it was previously reported, it has been determined that this fluorophore possesses significantly greater chemical stability than the other dimethylaminophthalimide

dyes investigated. They showed that the dimethylaminophthalimide series exhibits very little fluorescence in aqueous environments, which is very interesting as even a modest shift in the emission wavelength will typically be accompanied by a significant change in fluorescence intensity.

In another work, also performed in Prof. Imperiali's lab, the performance of 4-DMN cysteine modifying agents with different linker lengths was evaluated. These agents showed very promising results when compared with other five well-established commercially available solvatochromic fluorophores, making them a highly sensitive toolset for the detection of biomolecular interactions.²⁹³

Due to the excellent properties of the 4-DMN fluorophore we selected it to label the Sso7d scaffold.

Finally, the selected target was the human epidermal growth factor (hEGF), a small protein (~6 kDa, 53 amino acids) that binds to the extracellular domain of its receptor (EGFR) and activates the cytoplasmic catalytic function by promoting receptor dimerization and self-phosphorylation on tyrosine residues. Dysregulation of EGF levels has been linked to several diseases including, but not limited to, ovarian cancer and diabetes.

Briefly, in this chapter we focus our efforts on the development of new fluorescence-based sensors. We have used directed evolution to find a Sso7d scaffold that selectively binds hEGF with high affinity. We have then introduced the 4-DMN fluorophore in an adequate position of the Sso7d protein, looking for a fluorescence read-out upon hEGF binding.

5.2. Results and Discussion

First of all we looked for Sso7d-based hEGF binders using yeast surface display and for this, we worked in collaboration with Prof. Wittrup's group.

We used two Sso7d libraries (library 11 and library 18) previously designed in the Wittrup lab. The libraries were generated by the randomized mutation of nine Sso7d residues with 11 (library 11) and 18 (library 18) different amino acids, representing the most common residues found in protein-protein interactions and antibody CDR3 loops. Exclusion of cysteine and proline ensures minimal protein aggregation and Sso7d conformational stability, respectively. Each library is composed of $\sim 10^9$ Sso7d mutants available for panning via yeast surface display.

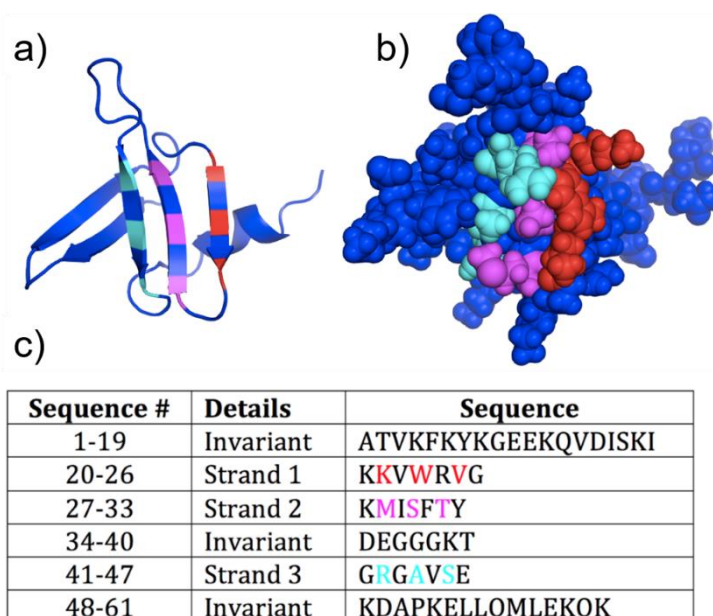


Figure V-5. a) Ribbon diagram showing surface with 9 variable residues. b). Space-filling model of Sso7d module in same pose c) Table showing the Sso7d scaffold sequence. Depicted in red, magenta and blue are the 9 variable positions in strand 1, 2 and 3 respectively.

We worked with the *Saccharomyces Cerevisiae* Aga2 protein system,²⁹⁴ in which Sso7d mutants are genetically encoded as C-terminal fusions to the Aga2p protein (Figure V-6a), linked to the Aga1p surface protein through two disulfide bonds. The gene encoding the Aga1 protein is stably integrated into the yeast chromosome, while the gene encoding the protein scaffold-Aga2 fusion is cloned into a circular yeast display plasmid vector (pCT-CON, Figure V-6b). Galactose-inducible expression of Aga1 and Aga2 results in yeast surface display of Sso7d mutants for selection.

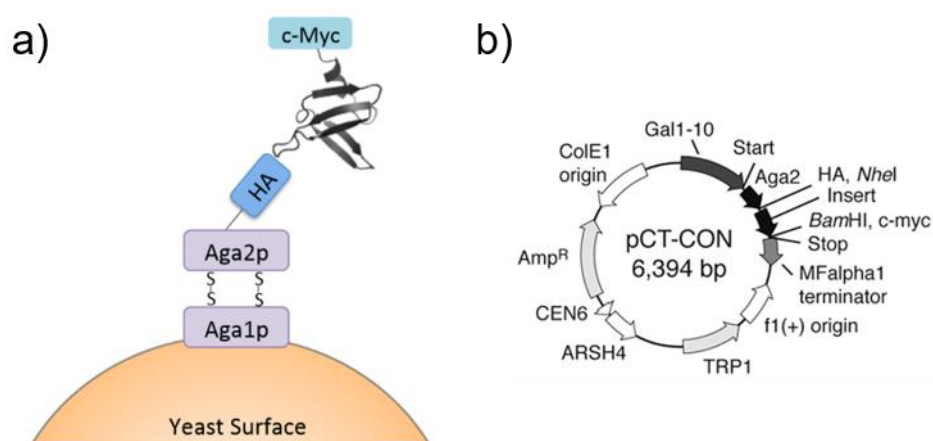


Figure V-6. Schematic representation of yeast surface platform showing. a) The Sso7d scaffold displayed on the surface of yeast. b) Vector map of pCT-CON. The “insert” label indicates the position where the Sso7d gene is inserted.

In our case, the Sso7d scaffolds are flanked by two detection tags: hemagglutinin (HA) epitope tag at the N-terminus, which is used as an expression marker to monitor plasmid incorporation; and c-Myc epitope at the C-terminus, which is used to monitor full length expression of the gene on the yeast surface (Figure V-6a). Using a two-color labeling scheme, with one fluorophore for the expression (anti-HA or c-myc tag) and another for target binder (anti-biotin), protein scaffolds can be engineered for higher affinity and stability binders. HA and c-MYC epitope tags will be used to normalize Sso7d expression levels and ensure full-length expression via flow cytometry.

5.2.1. Selection by magnetic bead sorting

Sso7d selection begins with biotinylated hEGF immobilized on streptavidin magnetic beads (Biotin Binder Dynabeads) incubated with Sso7d yeast libraries. The multivalency of the Dynabeads ($\sim 5 \times 10^6$ biotin-binding sites per bead) and the yeast ($\sim 10^5$ Sso7d per cell) allows for the isolation of weak affinity Sso7d-based binders through avidity interaction.

Sso7d mutants that “capture” bait hEGF via binding interactions are magnetically sorted from non-binders, following exhaustive washes. Sorted yeast clones are grown, Sso7d expression induced once more, and this panning process repeated extensively to enrich hEGF-binding Sso7ds.

After naïve library growth and also after every magnetic sort, we verified full length protein expression by flow cytometry, using primary antibodies against HA and cMyc tags. We used the same secondary antibody for both anti-HA and anti-c-myc detection, so that samples were labeled separately.

In the flow cytometry plots showed in Figure V-7 each dot corresponds to a single yeast cell. The y axis indicates fluorescence intensity of Streptavidin-Alexa Fluor 647, which was used to label the biotinylated hEGF in FACS sorting, while the x axis accounts for fluorescence intensity of Alexa Fluor 488, which we used to label the HA and c-myc tags. Therefore, higher values along the x axis indicated higher display of these tags on the cell surface. Dots that appeared in the Q3 quadrant corresponded to unlabelled cells. Those cells that stained positive in anti-c-myc plots are the ones displaying full length Sso7d protein (dots observed in the Q4 quadrant). In truncations or frame-shift mutants, the c-myc tag detection would be lost and, in the case of plasmid loss, the HA tag would not be detected. As it can be noticed in Figure V-7, after naïve library growth, around 40% of the yeast cells expressed full length protein.

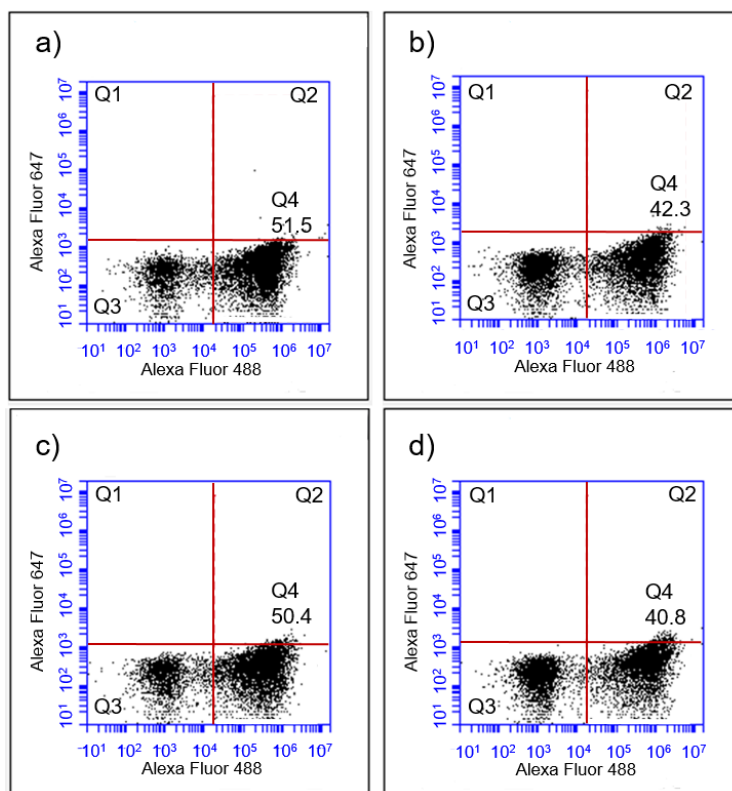


Figure V-7. Flow cytometry plots after naïve library growth: a) and b) Correspond to Library 11, performed against N-terminal HA epitope tags and C-terminal c-myc tags respectively; c) and d) Correspond to Library 18, performed against N-terminal HA epitope tags and C-terminal cMyc tags, respectively. Thanks to this experiment we know that the 42.3 % and 40.8% cells of libraries 11 and 18 respectively have expressed correctly the full length protein.

After a positive magnetic round followed by a negative round and finally a positive magnetic round, we performed 4 FACS sorts. From the last FACS sorting, we selected six mutants and studied them using flow cytometry, in order to find a promising binder. It is important to stress that we studied the behavior of the Sso7d protein on a yeast living cell, in this preliminar study we did not isolated the protein for its study. Thus, we used three different concentrations (5, 50 and 500 nM) of biotinylated hEGF, looking for saturation. In Figure V-8a we can observe that the clone B showed the highest fluorescence values at 500 nM of biotinylated hEGF, so that, we studied it in a wider range of concentrations: 50, 200, 500, 1000 and 2000 nM, exhibiting saturation at 500 nM (Figure V-8b).

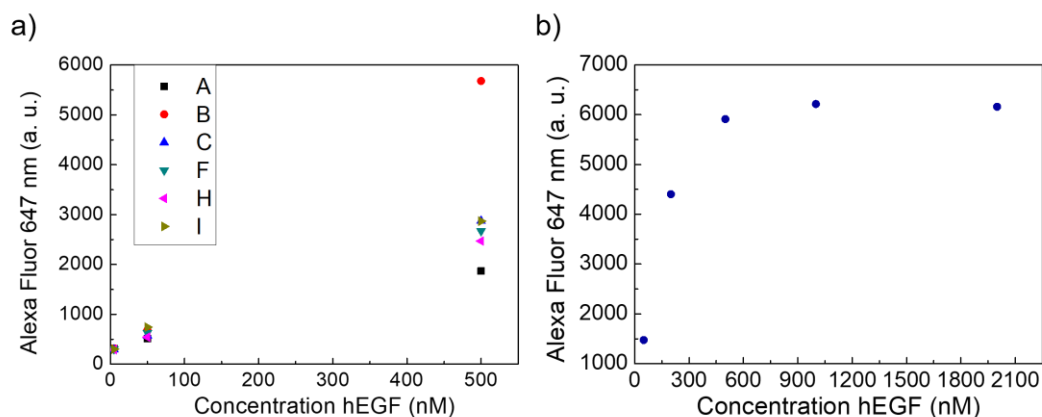


Figure V-8. a) Fluorescence observed of Alexa Fluor 647 for six different clones (A, B, D, F, H and I) at three different concentrations of hEGF (5, 50 and 500 nM). b) Fluorescence observed of Alexa Fluor 647 for clone B. Because of it reached the saturation at 500 nM of biotinylated hEGF, we expected high association constant and we decided to isolate this protein in order to study the association constant by interferometry.

Having identified this promising clone we isolated the plasmid from yeast and sent it for DNA sequencing. The amino acid sequence of the binding Sso7d obtained was:

ATVRFTYRGEERQVGISKIKSVRRYGGQYIAFSYDGGGAGGYGWMSGEDAPKELLQ
MLEKRGS

(Red residues are the nine residues previously randomized)

Dr. Cristina Zamora and Sonya Entova found the optimal conditions to clone this Sso7d sequence into PE-H6 vector. We needed this vector in order to amplify the DNA in *E. coli* and later induce the expression of the Sso7d protein with a His₆ tag and free of the Aga1-fusion.

5.2.2. Protein expression and purification, followed by Sso7d vs hEGF titration studies by interferometry

At this point we were ready to express this Sso7d mutant in *E. coli* to perform interferometry assays in order to determine the affinity of this hEGF binder. Sso7d mutant was expressed in *E. coli* from glycerol stocks and purified using Ni-NTA resin. Protein purity was assessed by SDS-PAGE as shown in Figure V-9.

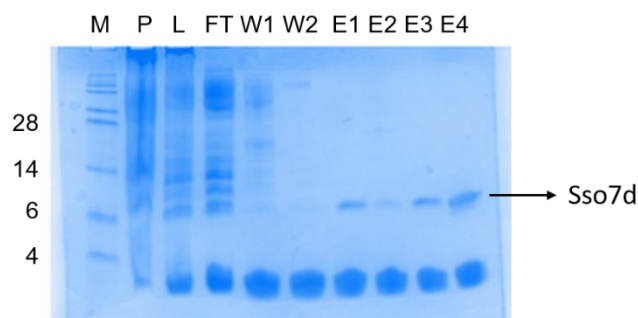


Figure V-9. 16% tricine gels stained with Coomassie for the purification of Sso7d-based mutant. M: marker (See-blue Plus2 prestained), P: pellet, L: lysate, FT: flow-through W: washes, E: elution.

Once we had the protein isolated we could measure binding curves and kinetic parameters for soluble Sso7d binding to immobilized analyte (hEGF). Bio-Layer Interferometry (BLI) is an optical analytical technique that measures interference patterns between waves of light. White light is directed down the fiber-optic biosensor towards two interfaces separated by a thin layer at the tip of the fiber: a biocompatible layer on the surface of the tip, and an internal reference layer (Figure V-10). Light reflects from each of the two layers, and the reflected beams interfere constructively or destructively at different wavelengths in the spectrum. This interference pattern is detected at a CCD array detector.

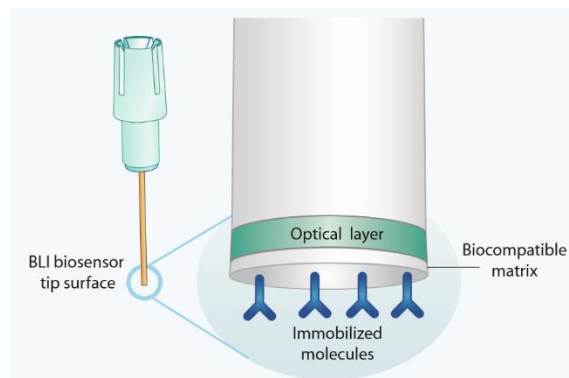


Figure V-10: A Dip and Read biosensor, illustrating the two optical interfaces at the biosensor tip: the internal reference layer (optical layer) and the surface biocompatible matrix on which ligand molecules are immobilized.

When the tip of a biosensor is dipped into a sample in a 96-well microplate, target molecules bind to the 2-dimensional coated surface. This binding forms a molecular layer that increases in thickness as more target molecules bind to the surface. As the thickness at the tip increases, the effective distance between the two reflective layers increases, creating a shift in the interference pattern of the reflected light (Figure V-11). The spectral pattern of the reflected light therefore changes as a function of the optical thickness of the molecular layer, i.e. the number of molecules bound to the biosensor surface. This spectral shift is monitored

at the detector, and reported on a sensorgram as a change in wavelength (nm shift). Monitoring the interference pattern in real time provides kinetic data on molecular interactions.

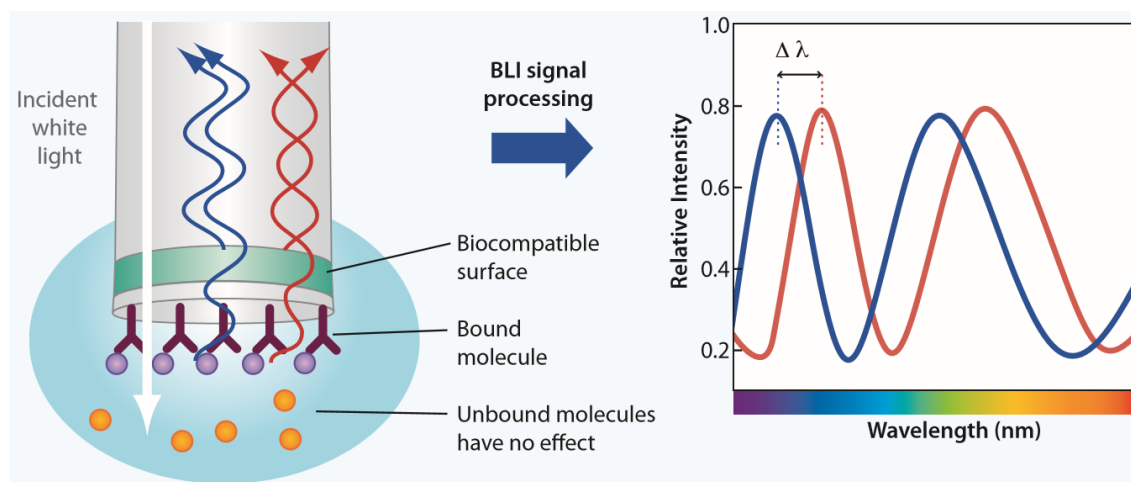


Figure V-11. BLI is an optical analytical technique that analyzes the interference pattern of white light reflected from two surfaces. Changes in the number of molecules bound to the biosensor causes a shift in the interference pattern that is measured in real time.

In our studies we used streptavidin-coated biosensor and the biotinylated hEGF was immobilized. Based on previous experiments performed in Barbara Imperiali's lab, measuring binding constant between hEGF and other Sso7d clones, we carried out the titration experiments.

First, we optimized important parameters, such as the concentration of the analyte (hEGF), and the ligand (Sso7d), association and dissociation times; and we found the best first-order fitting using:

- hEGF concentration of 125 nM in immobilization solution.
- Sso7d concentrations from 6.25 to 150 nM.
- Association times of 60 s.
- Dissociation times of 400 s.

In Figure V-12 we can observe the results obtained for the titration optimized experiment, the fitting curves resulted in a $K_D = (1.90 \pm 0.04) \times 10^{-8}$ M.

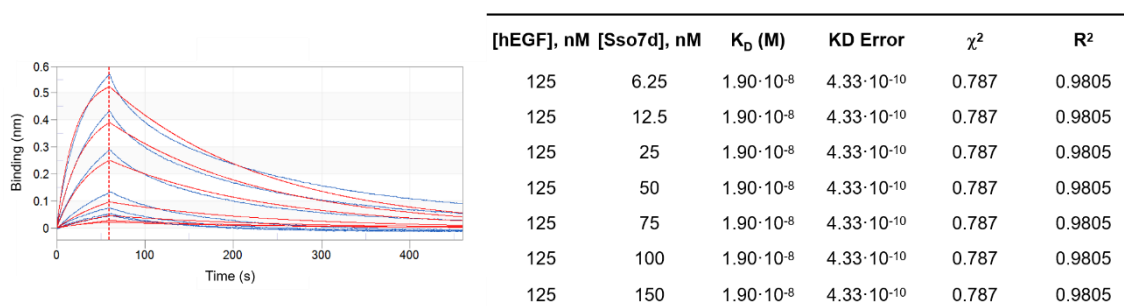


Figure V-12. Association and dissociation curves in blue, showing the fitting in red. The interaction studied corresponds to a 1:1 binding model, where it is assumed that the interaction between ligand and analyte follows pseudo-first-order kinetics. Thus, K_D observed is 19 nM, R^2 : 0.981, χ^2 : 0.787.

The interferometry experiments allowed us to conclude that we had successfully found a hEGF binder with high affinity, presenting the equilibrium dissociation constant (K_D) in the range of 10^{-8} M. The next step was to introduce the fluorescent dye.

5.2.3. Expression and purification of cysteine mutants

The objective was to place cysteine at places carefully determined on Sso7d by S. de Picciotto. These are the positions 31, 33 and 34, labelled in different colors in Figure V-13:

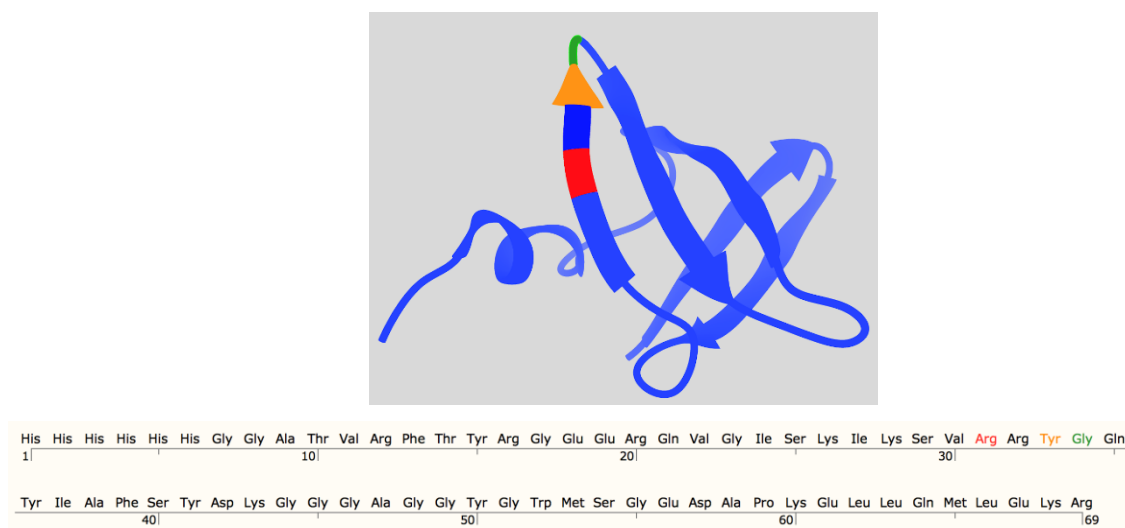


Figure V-13. Ribbon diagram of Sso7d showing the three residues selected for the quick-change, R31C, Y33C and G34C.

We carried out directed mutagenesis to change the selected residues, which are R31, Y33 and G34, to cysteine. Sso7d-based mutants R31C, Y33C and G34C were expressed in *E. coli* and purified using Ni-NTA resin. Protein purity was assessed by SDS-PAGE as shown in Figure V-14.

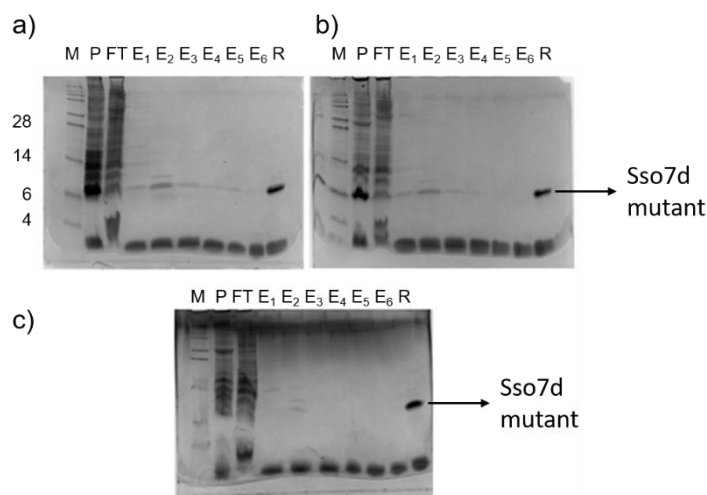


Figure V-14. 16% tricine gels for the IMAC purification of Sso7d-based mutants: a) R31C, b) Y33C, c) G34C. M: marker (See-blue Plus2 prestained), FT: flow-through, E: elution, R : reference.

We obtained good yields for mutants R31C and Y33C, however, this was not the case for G34C, so we decided to continue with the two first mutants.

5.2.4. Labeling of Sso7d cysteine mutants with 4-DMN derivatives

Next step was the labelling of the two Sso7d-based cysteine mutants with the following derivative of 4-DMN (Figure V-15):

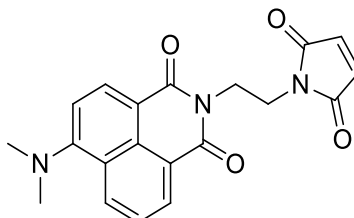


Figure V-15. 4-*N,N*-dimethylamino-1,8-naphthalimide (4-DMN) dye.

Protein labelling was carried out on samples containing 100 μ M Sso7d cysteine mutant, using Tris(2-carboxyethyl)phosphine hydrochloride (TCEP) for thiol reduction. After overnight tumbling at room temperature, the reactions were purified first by buffer exchange using 0.5 mL Centrifugal Filters (3K), adding 300 μ L 50 mM HEPES 5 mM NaCl buffer 4 times. Using these filters we removed a considerable amount of dye and also we got our reactions in the right buffer in order to perform a purification based on ionic exchange. Pure fractions were detected by tricine (16%) gels, Figure V-16.

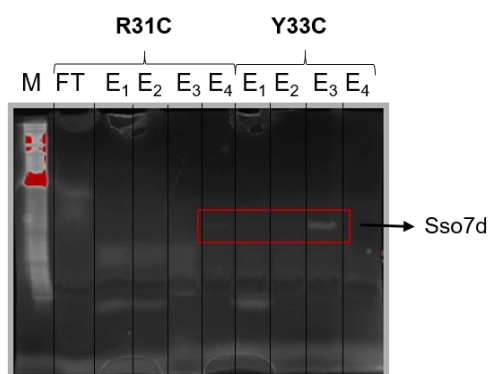


Figure V-16. 16% Tricine gels showing the results for Sso7d mutants R31C and Y33C labelled with 4-DMN.

5.2.5. Fluorescence assays with 4-DMN labelled Sso7d-based cysteine mutants

Spectroscopic assays were performed by measuring the fluorescence intensity increase achieved by the labelled Sso7d mutants upon hEGF binding. We used the same concentrations previously reported by Dr. Seymour De Picciotto²⁸⁴ (300 nM of labelled Sso7d protein and 10 μ M of hEGF). Fluorescence intensity increase was expressed as intensity fold and it was calculated by dividing F/F_0 where F is the maximum fluorescence intensity upon hEGF binding and F_0 is the fluorescence intensity of the free labelled protein measured at the wavelength corresponding to F .

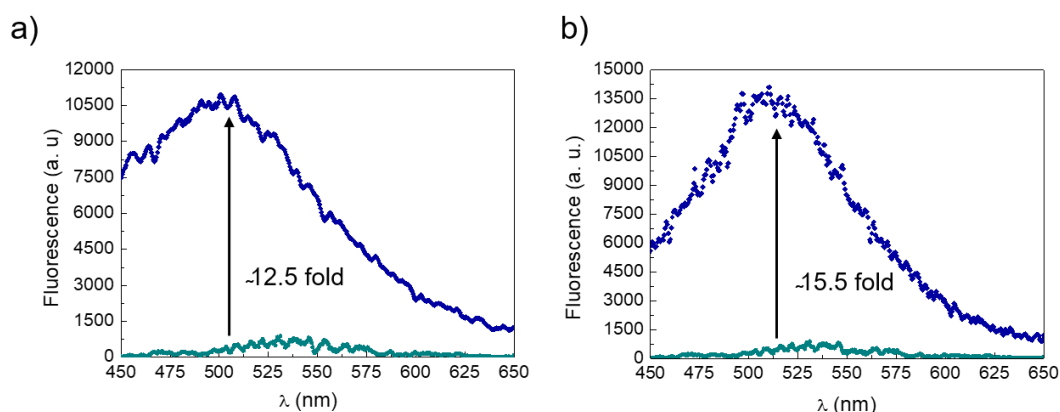


Figure V-17. Graphs for the fluorescence assays performed with 300 nM labeled protein (in green) and 300 nM labeled protein upon addition of 10 μ M hEGF (in blue). with: a) R31C 1 b) Y33C.

The studied mutants labelled with 4-DMN derivative represent a good proof-of-concept and seemed to have the typical properties of specific binding sensors (low fluorescence background and high fluorescence intensity increase upon binding with its partner). However, these Sso7d mutants do not present the 50-fold increases in fluorescence previously reported by De Picotto et al.²⁸⁴ To continue this project, it would be a good point to explore if the 34

position of the Sso7d scaffold presents better fluorescence response. Once this step is completed, it would be necessary to measure the binding constant by interferometry, expecting to maintain values ten times the nM range, as obtained previously.

In conclusion, through directed evolution using YSD, we were able to engineer the Sso7d scaffold and find a specific hEGF binder, which presents binding constant ten times the range of nanomolar. The labelling in two studied positions with the 4-DMN fluorophore showed 15-fold increases in fluorescence. These are promising results and close to find an excellent solvatochromic biosensor.

5.3. Experimental Section

Contents:

5.3.1. Yeast surface display

- 5.3.1.a Reagents set up
- 5.3.1.b Naïve library growth
- 5.3.1.c Magnetic beads selection
- 5.3.1.d Full-length protein expression confirmation
- 5.3.1.e Colony forming units counting
- 5.3.1.f Flow cytometry assays

5.3.2. Identification of individual clones

5.3.3. Expression and purification of Sso7d proteins

5.3.4. Protein labelling with 4-DMN

5.3.5. Fluorescence spectroscopy assays

5.3.6. Sso7d vs hEGF titration studies on Octet

5.3.1. Yeast surface display

5.3.1.a. Reagents set up

- SD-CAA media (pH 4.5)

This media was prepared by dissolving 20 g dextrose, 6.7 g yeast nitrogen base (Difco), 5 g casamino acids (Bacto), 14.7 g sodium citrate and 4.29 g citric acid monohydrate deionized water to a volume of 1 L. This media was then sterilized by filtration. PenStrep 1:100 (Invitrogen) was added to prevent bacterial contamination.

- SG-CAA media (pH 4.5)

This media was prepared by dissolving 20 g glucose, 6.7 g yeast nitrogen base (Difco), 5 g casamino acids (Bacto), 14.7 g sodium citrate and 4.29 g citric acid monohydrate deionized water to a volume of 1 L. This media was then sterilized by filtration. PenStrep 1:100 (Invitrogen) was added to prevent bacterial contamination

- PBSA

This buffer was prepared by dissolving 8 g NaCl, 0.2 g KCl, 1.44 g Na₂HPO₄, 0.24 g KH₂PO₄ and 1 g bovine serum albumin in 1 L of deionized water. pH was adjusted to 7.4 and solution was sterilized by filtration. This solution can be stored for up to 6 months at 4 °C.

- SD-CAA plates

SD-CAA plates were prepared by dissolving 5.4 g Na₂HPO₄, 8.56 g NaH₂PO₄·H₂O, 182 g sorbitol and 15 g agar in deionized water to a volume of 900 mL and autoclave (Solution A).

Another solution was prepared by dissolving 20 g dextrose, 6.7 g yeast nitrogen base (Difco), 5 g casamino acids (Bacto) in deionized water to a volume of 100 mL and sterilize by filtration (Solution B). Then Solution A was cooled with stirring until below 50 °C. Both solutions were mixed and plates were poured.

5.3.1.b. Naïve library growth

Frozen aliquots of Sso7d libraries glycerol stocks (provided by the Wittrup's lab) with 10 x diversity (3×10^{10} cells) were thawed at room temperature and inoculated into 1 L of SD-CAA media. Cells were grown overnight at 30 °C with shaking (250 rpm). Yeast cells typically grow overnight to an OD₆₀₀ = 6-8. Cells were passaged into fresh SD-CAA media by pelleting at least 10 x diversity (3×10^{10} cells) and resuspending them into fresh SD-CAA media. An absorbance of 1 at 600 nm is about 1×10^7 cells/mL. Fresh cells were grown overnight at 30 °C with shaking (250 rpm). Yeasts were passaged again into fresh SD-CAA media as described and grown at 30°C with shaking (250 rpm) until OD₆₀₀ = 2-5. Then at least 10 x diversity cells were pelleted and resuspended in 1L of SG-CAA media with 2 g/L dextrose. Protein expression was induced by incubating overnight at 20 °C with shaking (250 rpm).

5.3.1.c. Magnetic beads selection

First, 4×10^7 Dynabeads Biotin Binder (Invitrogen), for each library, were added to a 2 mL microcentrifuge tube containing 1 mL of ice-cold PBSA. Beads were incubated for 5 min at 4 °C with tumbling. Then microcentrifuge tubes containing magnetic beads were placed on the DynaMag-2 magnet (Invitrogen) for 3 min and supernatant was removed being careful not to touch the beads. Magnetic beads were washed with 1 mL of ice-cold PBSA, incubated for 5 min at 4 °C with tumbling and finally they were placed in the magnet for 3 min to remove the supernatant. Three washes were performed. After supernatant removal 330 pmols of biotinylated-hEGF were combined with the beads in a final volume of 1 mL PBSA. Then beads were incubated at 4 °C with tumbling for 2h. After incubation the microcentrifuge tubes containing hEGF-coated-beads were placed on the magnet for 3 min and supernatant was removed. hEGF-coated-beads were washed again as previously done. Coated-beads were finally resuspended with 550 μ L of ice-cold PBSA. In the meantime, 3×10^{10} cells were pelleted at 3750 rpm for 10 min at 4 °C (at least 10-fold oversampling should be pelleted to reduce the possibility of losing individual clones).

Supernatant was removed and cells were resuspended in 30 mL ice-cold PBSA. Yeast were pelleted again at 3750 rpm for 5 min at 4 °C. Yeast cells were resuspended to a final volume of 10 mL in PBSA and split in 2 mL microcentrifuge tubes (1 mL/tube). 5 μ L of resuspended cells for each library were combined with 495 μ L of ice-cold PBSA and kept at 4°C for full length protein expression analysis. 50 μ L of hEGF-coated magnetic beads were added to each microcentrifuge tube containing yeast cells. Yeast-bead complex was incubated for 2h at 4°C with tumbling. After 2h incubation samples were placed on the magnet for 3 min and supernatant containing non-binders was removed. Magnetic beads containing target binders were washed with PBSA as previously done. Yeast-bead complex was resuspended in SD-CAA media (1 mL/tube) and inoculated into 60 mL SD-CAA media. 1 μ L of this culture was diluted with SD-CAA media to a final volume of 200 μ L, and 50 μ L were plated on SD-CAA plates and incubate at 30 °C. Finally cells were grown at 30 °C with shaking (250 rpm) for 48h.

- Magnetic beads removal

After overnight growing, yeast cell cultures were pelleted at 3750 rpm for 1 min at 4 °C (at least 10 fold library viability should be pelleted). Yeast cells were resuspended in SD-CAA media to a final concentration of 1×10^9 cells/mL and split in 2 mL microcentrifuge tubes (1 mL/tube). Samples were placed on the magnet for 3 min and then supernatant was transferred to a new microcentrifuge tube. This process was repeated twice. Finally supernatant was inoculated into 70 mL SD-CAA media and cells were grown overnight at 30°C with shaking (250 rpm). Cells were passaged and induced as previously done.

5.3.1.d. Full-length protein expression confirmation

Samples kept at 4°C were used to confirm full length protein expression. Antibodies were purchased from Invitrogen. Labeling was done as follows:

	Sample 1 (100 µL)	Sample 2 (100 µL)
[Cells]	2·10 ⁶ cells/mL	2·10 ⁶ cells/mL
Chicken anti-HA IgY	1 : 200 (0.5 µL)	-
Chicken anti-c-myc IgY	-	1 : 200 (0.5 µL)
Alexa Fluor 488-goat anti-chicken IgG	1 : 200 (0.5 µL)	1 : 200 (0.5 µL)

Pelleted yeast cells were combined with primary antibody (chicken anti-HA IgY or chicken anti-c-myc IgY) and ice-cold PBSA was added to a final volume of 100 µL. Samples were incubated for 1.5 h at 4 °C with tumbling. Cells were pelleted by centrifugation at 14000 rpm at 4 °C for 30 s. Primary antibody stained cells were washed twice with 1 mL of ice-cold PBSA and then pelleted by centrifugation at 14000 rpm at 4 °C for 30s. Yeast cells were then combined with the secondary antibody (Alexa Fluor 488-goat anti-chicken IgG) in a final volume of 100 µL ice-cold PBSA. Cells were incubated for 30 min at 4 °C with tumbling. Then samples were washed three times with PBSA and finally pelleted by centrifugation at 14000 rpm at 4 °C for 30s. Cell pellets were kept on ice until analysis. After labeling we ended up with four samples (two per each library) to be analyzed. Cell pellets were resuspended in 1 mL of ice-cold PBSA and labeled samples were analyzed by a BD Accuri™ C6 Plus instrument (from BD Bioscience). Data was analyzed with FlowJo software (See figure 6 in the results and discussion section)

Magnetic beads selection were repeated twice more, one negative magnetic sort to get rid off magnetic-bead binders and a final positive magnetic selection.

5.3.1.e. Colony forming units counting

After cells were grown in SD-CAA plates, colony forming units (CFUs) were counted by visual inspection. The CFUs/mL were calculated using the following equation:

$$\frac{CFUs}{mL} = \frac{\text{number of colonies}}{(\text{dilution factor})(\text{volume plated in mL})}$$

5.3.1.f. Flow cytometry assays

For flow cytometry sorting, cells were doubly labeled with the anti-c-myc tag and with the biotinylated target. For this purpose, two different strategies were used.

	Sample 1 (200 μ L)	Sample 2 (200 μ L)
[Cells]	2·10 ⁷ cells/mL	2·10 ⁷ cells/mL
Chicken anti-c-myc IgY	1 : 200 (1 μ L)	1 : 200 (1 μ L)
Biotinilated hEGF	1 μ M no-preloaded	250 nM preloaded
Alexa Fluor 488-goat anti-chicken IgG	1 : 200 (1 μ L)	1 : 200 (1 μ L)
Streptavidin-Alexa Fluor 647	1 : 200 (1 μ L)	-

- Sample 1 (no-preloaded)

Pelleted yeast cells were combined with the primary antibody (chicken anti-c-myc IgY) and the biotinylated hEGF and ice-cold PBSA was added to a final volume of 200 μ L. Samples were incubated for 1.5 h at 4 °C with tumbling. Cells were pelleted by centrifugation at 14000 rpm at 4 °C for 30 s. Primary antibody stained cells were washed twice with 1 mL of ice-cold PBSA and then pelleted by centrifugation at 14000 rpm at 4 °C for 30 s. Stained cells were then combined with the secondary antibodies (Alexa Fluor 488-goat anti-chicken IgG and Streptavidin-Alexa Fluor 647) in a final volume of 200 μ L ice-cold PBSA. Cells were incubated for 30 min at 4 °C with tumbling. Then samples were washed three times and pelleted by centrifugation at 14000 rpm at 4 °C for 30 s. Cell pellets were kept on ice until analysis. After labeling we ended up with two samples (one per each library) to be analyzed.

- Sample 2 (preloaded)

For the hEGF-preloaded strategy we first incubated Streptavidin-Alexa Fluor 647 with biotinylated-hEGF on ice for 30 min, shielded from light, at a streptavidin/hEGF molar ratio of 1 : 4 in as a small volume as possible. This sample was then mixed with yeast cells and PBSA was added to a final volume of 200 μ L. Labeling with chicken anti-c-myc IgY were performed as previously done and samples were incubated overnight. The secondary labeling was done adding Alexa Fluor 488 goat anti-chicken IgG as previously done. After labeling we ended up with two samples (one per each library) to be analyzed.

- Sorting

Cell pellets were resuspended in 1 mL of ice-cold PBSA immediately before analysis. Samples were analyzed using the FACS Aria™ cell sorter instrument. Yeast cells that were double positive for the HA and target were collected into 5 mL glass tubes and kept on ice. After sorting, collected yeast cells were inoculated into 2 mL of SD-CAA media and grown overnight at 30 °C with shaking. Some yeast cells need more than 48h to completely grow (OD₆₀₀= 6-8). Cells were passaged and induced as previously done.

Data was analyzed using the FlowJo software. Briefly living cells were analyzed by plotting the scattering light (SSC) vs the forward scattering light (FSC) and gating those that presented the correct morphology. Final analysis was done by plotting the binding event (Alexa Fluor-647 emission accounting for hEGF binders) vs the protein displaying event (Alexa Fluor-488 emission accounting for c-myc tag display). Results for the four FACS rounds performed in the Library 18 are shown in Figure V-18.

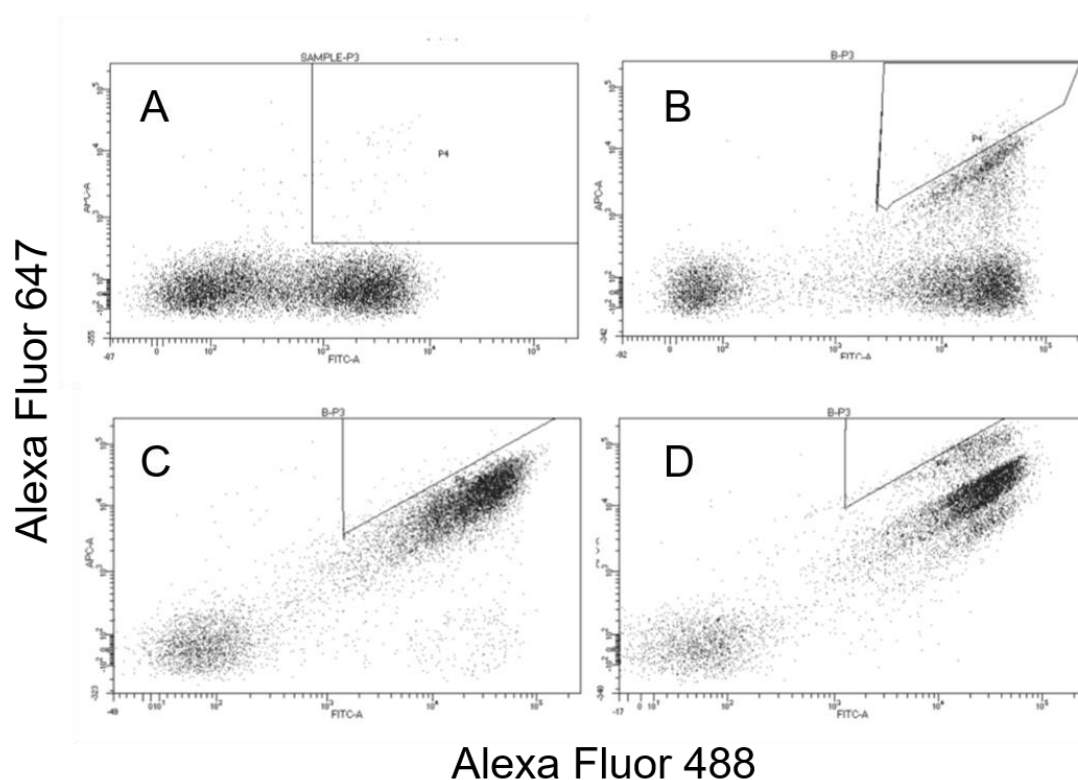


Figure V-18. Flow cytometry plots of FACS sorting from 1st (A) to 4th (D) rounds for the library 18. Performed for Alexa Fluor-647 emission accounting for hEGF binders, depicted in the x axis; versus Alexa Fluor-488 emission accounting for c-myc tag display, y axis.

Yeast cells that show positive staining for both Alexa Fluor 647 and 488 indicate full length protein expression and hEGF binding.

FACS sorts it is recommended to select 1-3% of displaying cells that show detectable binding, we sorted between ~3% of displaying cells showing hEGF-binding (boxed area in Figure V-18A; and triangular area in Figure V-18B-D). Finally in the fourth FACS sorting (Figure V-18D) we were able to enrich for improved hEGF binders, we could clearly see three different diagonals that may contain diverse hEGF binders so we selected the binders placed on the diagonal above

5.3.2. Identification of individual clones

After four subsequent FACS sorting rounds, we selected six candidates and studied by flow cytometer analysis them under increasing concentrations of hEGF.

Sample preparation was done as follows:

	Sample 1 (100 μ L)	Sample 2 (100 μ L)
[Cells]	2·10 ⁶ cells/mL	2·10 ⁶ cells/mL
Chicken anti-c-myc IgY	1 : 200 (0.5 μ L)	1 : 200 (0.5 μ L)
Biotinilated hEGF, nM	5, 50, 500	-
Alexa Fluor 488-goat anti-chicken IgG	1 : 200 (0.5 μ L)	1 : 200 (0.5 μ L)
Streptavidin-Alexa Fluor 647	1 : 200 (0.5 μ L)	-

Pelleted yeast cells were combined with the primary antibody (chicken anti-c-myc IgY) and the biotinylated hEGF and ice-cold PBSA (incubation with primary antibody and hEGF can last from 1.5h up to overnight). Samples were incubated for 1.5 h at 4 °C with tumbling. Cells were pelleted by centrifugation at 14000 rpm at 4 °C for 30 s. Primary antibody stained cells were washed twice with 1 mL of ice-cold PBSA and then pelleted by centrifugation at 14000 rpm at 4 °C for 30 s. Stained cells were then combined with the secondary antibodies (Alexa Fluor 488-goat anti-chicken IgG and Streptavidin-Alexa Fluor 647) in a final volume of 200 μ L ice-cold PBSA. Cells were incubated for 30 min at 4 °C with tumbling. Then samples were washed three times and pelleted by centrifugation at 14000 rpm at 4 °C for 30 s. Cell pellets were kept on ice until analysis. After labeling we ended up with four samples (per concentration of biotinylated hEGF) to be analyzed.

Once analyzed, we obtained the following fluorescence vs hEGF concentration values:

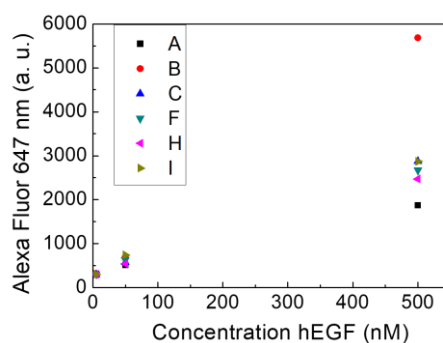


Figure V-18. Fluorescence observed of Alexa Fluor 647 for six different clones (A, B, D, F, H and I) at three different concentrations of hEGF (5, 50 and 500 nM). The clone B present the highest fluorescence value at 500 nM.

Due to clone B exhibited the highest fluorescence values at 500 nM hEGF we studied this clone in a wide range of concentrations (50, 200, 500, 1000 and 2000 nM), using the same procedure described before.

This clone, was sent to sequencing. For this, 1×10^8 yeast cells were pelleted and plasmid DNA was extracted using Zymoprep Yeast Plasmid Miniprep II. To facilitate DNA sequencing, the plasmids extracted from yeasts were amplified in *E. coli* XL1-Blue supercompetent²⁹⁵ cells and isolated using Wizard® Plus SV Minipreps DNA Purification Kit.

5.3.3. Expression and purification of Sso7d proteins

Cristina Zamora and Sonya Entova found the optimal conditions to clone this insert sequence into PE-H6 vector.

DNA extracted from DH5 α cells was used to transform BL21-RIL cells, which were grown on kanamycin/chloramphenicol (KAN/CAM) plates. Single colonies from each plate were picked and grown overnight at 37 °C in 8 mL LB containing KAN, 30 μ g/mL and CAM, 30 μ g/mL. Part of the culture was used to generate Glycerol stocks (1mL) and the rest to inoculate 1L culture containing TB-media with KAN/CAM (30 μ g/mL) and then grown in a 37 °C shaker at 225 rpm. When OD₆₀₀ reached 0.8, protein expression was induced by adding 1mL 1M isopropyl β -D-1-thiogalactopyranoside (IPTG). Cultures were grown overnight at 16 °C with shaking at 225 rpm. Cells were then harvested by centrifugation (5000 g, 4°C) for 30 min. The cell pellet was re-suspended in 35mL buffer containing 50 mM HEPES, 15 mM NaCl, pH 7.2, transferred to a 50 mL conical tubes and re-pelleted at 5000 g for 30 min at 4 °C. The resulting cell pellets were stored at -80°C until purification.

- Lysis and immobilized metal ion affinity chromatography (IMAC) purification

Lysis was done by resuspending the cell pellets in 30mL of 50 mM Tris base, 100 mM NaCl, 1% Triton-X-100, 3% (v/v) glycerol, pH 7.2, and sonicating (3 cycles of 45 s) at 50% amplitude. Finally cells were centrifuged at 41KG for 45 min at 4 °C and the supernatant was incubated with Ni-NTA resin (Qiagen) previously equilibrated with 50 1 x PBS, 10mM imidazole, pH 7.4 buffer. Protein was washed with 50 mM Tris, 100 mM NaCl, 20 mM imidazole. buffer with increasing amounts of imidazole to 40 mM. Protein was finally eluted with the same buffer containing 300 mM imidazole. Pure protein were dialysed in 1 x PBS. Protein purity was assessed by Tris-Tricine electrophoresis (See Figure 7).

- Tris-Tricine electrophoresis (tricine gels)

Tris-tricine electrophoresis was carried out using BioRad system (Mini-protean cell) 16.5 % Tris gel and 100 mM Tris, 100 mM Tricine, 0.1% SDS as running buffer. Sample buffer was 200 mM Tris-HCl, pH 6.8, 2% (w/v) SDS, 40% glycerol, 0.04% Coomassie Brilliant Blue G-250 (ThermoFisher), 2% (v/v) mercaptoethanol (added freshly). Protein molecular weights

were approximated by comparison to a protein marker (See Blue Plus 2 pre-stained protein standard from ThermoFisher). Gels were visualized by Coomassie staining (Imperial Protein Stain from ThermoFisher).

5.3.4. Protein labelling with 4-DMN

Protein labeling was done with samples containing 100 μ M Sso7d cysteine mutants in 50 mM Na_2HPO_4 , 300 mM NaCl, 0.5 M urea, pH 8.0 buffer, adding 10 mM of TCEP (100 equiv) for thiol reduction and 10 equiv of 4-DMN based cysteine modifying agent. Labeling reactions were performed overnight at room temperature with gentle tumbling and protected from light. After overnight tumbling at room temperature, the reactions were purified first by buffer exchange using 0.5 mL Centrifugal Filters (3K), adding 300 μ L 50 mM HEPES 5 mM NaCl buffer 4 times. Using this filters we removed a considerable amount of dye and also we got our reactions in the right buffer in order to perform a purification based on ionic exchange. Using a flow rate 0.5 mL/min. The starting buffer was 50 mM HEPES 5 mM NaCl, once the dye was out of the column 0 concentration of NaCl was increased to 1M. Pure fractions were detected by Tricine gels and combined together (See Figure V-16).

5.3.5. Fluorescence spectroscopy assays

Fluorescence spectroscopy assays, in this work, were performed using a FluoroMax-2 fluorometer with an integration time of 0.1 s, excitation and emission slits set at 5 and 10 nm respectively. Stock solutions of 4-DMN labeled Sso7d mutants were prepared at 600 nM in 1 x PBS at pH 7.4. A stock solution of hEGF at 20 μ M was also prepared in the same buffer. Using these protein stocks, the labeled Sso7d mutant was diluted to 300 nM and exposed to 10 μ M solution of hEGF. The samples were excited at 420 nm and emission collected from 450 - 650 nm. The difference in emission is reported as the fold increase upon hEGF binding. All spectra were corrected for background fluorescence by subtracting a blank scan of the buffer system (See Figure V-17).

5.3.6. Sso7d vs hEGF titration studies on Octet

Interferometry studies were carried out using the Octet RED96 System.

All procedure was performed at 4 $^{\circ}$ C, using 96-well plate (final volume 200 μ L).

The Buffer used was: 50 mM HEPES, 150 mM NaCl, 1% PBSA, 0.05% Tween-20, pH

7.4.

CONCLUSIONS

Throughout this thesis we have addressed some fundamental issues in supramolecular chemistry. For this purpose, we have made use of two single molecule manipulation techniques, which are OT and AFM, as well as bulk studies. According to the results obtained it can be concluded:

1) We have successfully developed a new method to measure the average mechanical strength of H-bonded supramolecular complexes, at the single-molecule level, under non-equilibrium conditions. Our method expands the capabilities of previously described SMFS methods by exploiting the force resolution of OT (0.1-100 pN), which allows measuring the characteristic strength of H-bonds under near-physiological conditions, and by including a DNA reporter that guarantees that the force measurements refer to a single binding event. The modularity and addressability of the DNA construct described here also opens up the possibility of targeting synthetic host-guest couples in controlled orientations and stoichiometry. In this case, we have focused on aqueous conditions, but the system is in principle adaptable to other sets of conditions. This renders our method a versatile and precise tool to address key questions in supramolecular chemistry, like the mechanical strength of hydrogen bonded systems, and its relationship with their thermodynamic stability.

2) We have synthesized a hydrogen-bonded Leigh-type molecular shuttle that comprises a strong binding station, namely fumaramide, separated by a polar spacer of approximately 10 nm length, we placed a second station, succinic amide-ester, which shows less affinity for the macrocycle than the fumaramide station. Two bulky diphenylethyl groups will serve as stoppers. One of the stopper ends is branched to include a biotin fragment that was used to link the molecule to the OT set-up. The other link point to the OT was placed through click reaction between an azide located in the macrocycle and an alkyne modified oligonucleotide; finally this oligonucleotide was ligated to a dsDNA spacer. Individual rotaxane-dsDNA constructs were mechanically manipulated in a controlled manner by a dual-beam OT instrument; thus, for the very first time, we have followed the shuttling motion of single [2]rotaxanes during minutes. We observed the stochastic behaviour of individual molecular shuttles, what allowed us to have access to the statistical nature of these fluctuations and to characterize the mechano-chemical cycle of its system operation, in terms of the free energy difference, the coexistence force, the position of the transition state and the kinetic rates.

Moreover, we have adapted the molecular shuttle to be studied under biocompatible, aqueous conditions, which will shed light on the possibility of creating synthetic-natural hybrids, one of the most ambitious goals in the field.

3) We experimentally observed the formation of H-bonds in four different H-bonded systems, which feature strong H-bond donors and acceptors, benzamidine-acetic acid (Ben-AcOH, neutral-neutral), the Hamilton receptor-cyanuric acid derivative pair (HR-cy, neutral-neutral), the 1,4,7,10,13,16-hexaoxacyclooctadecane-ammonium derivative (18_crown_6-Am, neutral-cation) and *N,N'*-dimethyl thiourea-sodium benzoate (DMTU-BzO⁻, neutral-anion), in [emim][FAP], a RTIL, where electrostatic interactions are expected to play a very minor role, since dipole-dipole electrostatic contribution in H-bonds is proportional to r^{-6} , while dipole-point charge interactions are proportional to r^{-2} . UV-vis spectroscopy titrations of H-Bonded complexes showed that the binding constants are weakened in [emim][FAP] ($K_a(\text{Ben-AcOH}) = 1.99 \times 10^3 \text{ M}^{-1}$; $K_a(\text{HR-cy}) = 3.16 \times 10^6 \text{ M}^{-1}$; $K_a(18_crown_6\text{-Am}) = 3.16 \times 10^3 \text{ M}^{-1}$; $K_a(\text{DMTU-BzO}^-) = 1.99 \times 10^4 \text{ M}^{-1}$), with respect to organic solvents ($K_a(\text{Ben-AcOH}) = 2.51 \times 10^3 \text{ M}^{-1}$ in CH₃Cl; $K_a(\text{HR-cy}) = 6.31 \times 10^5 \text{ M}^{-1}$ in acetonitrile; $K_a(18_crown_6\text{-Am}) = 3.98 \times 10^3 \text{ M}^{-1}$ in acetonitrile; $K_a(\text{DMTU-BzO}^-) = 3.98 \times 10^4 \text{ M}^{-1}$ in CH₃Cl), but still in the same order of magnitude. This trend was also confirmed through IR spectroscopy in two host-guest systems and through single molecule force measurements performed by AFM in one system. These observations are opposed to the findings for weaker H-bonds, such as those in water, which are substituted by O-H-anion interactions in RTILs. Therefore, our experiments point to a significant covalent contribution to strong H-bonds, which is not affected by the RTIL charges, and away from a purely electrostatic view of H-bonding. In order to obtain a more complete vision of the problem, and generalize or disprove our preliminary conclusions, we are now studying binding constants of the same host-guest systems in a collection of RTILs, in which we systematically vary the size of the cation and anion.

4) Through directed evolution using yeast surface display (YSD), we were able to engineer the Sso7d scaffold and find a specific hEGF binder, which presents dissociation constants in the 10⁻⁸ M range. The labelling of the Sso7d protein in two studied positions with the 4-DMN fluorophore showed 15-fold increases in fluorescence; it represented a good proof-of-concept and seemed to have the typical properties of specific binding sensors (low fluorescence background and high fluorescence intensity increase upon binding with its partner). However, these Sso7d mutants do not present the 50-fold increases in fluorescence previously reported by De Picotto et al. To continue this project, it would be a good point to explore if the 34 position of the Sso7d scaffold presents better fluorescence response. In short,

the results obtained until now are promising and close to find an excellent solvatochromic biosensor.

CONCLUSIONES

A lo largo de esta tesis se han abordado algunos temas fundamentales en química supramolecular. Para ello se ha hecho uso de dos técnicas de manipulación de moléculas individuales (pinzas ópticas y AFM) así como de estudios en bulk. De acuerdo con los resultados obtenidos, se puede concluir:

1) Hemos desarrollado con éxito un nuevo método para medir la resistencia mecánica promedio de complejos supramoleculares unidos a través de enlaces de hidrógeno, a nivel de una sola molécula y en condiciones de no equilibrio. Nuestro método expande las capacidades de los métodos SMFS descritos anteriormente, explotando la resolución de fuerza de las pinzas ópticas (0.1-100 pN), que permite medir la fuerza característica de los enlaces de hidrógeno en condiciones cuasi-fisiológicas, e incluyendo un espaciador de ADN que garantiza que las medidas de fuerza se refieren a un único evento de enlace. La modularidad y direccionalidad de la construcción de ADN descrita aquí también abre la posibilidad de estudiar a parejas sintéticas huésped-receptor en orientaciones y estequiometría controladas. En este caso, nos hemos centrado en las condiciones acuosas, pero el sistema es, en principio, adaptable a otros conjuntos de condiciones. Esto hace que nuestro método sea una herramienta versátil y precisa para abordar cuestiones clave en química supramolecular, como la resistencia mecánica de los sistemas de enlace de hidrógeno y su relación con su estabilidad termodinámica.

2) Hemos sintetizado un [2]rotaxano unido a través de enlaces hidrógeno de tipo Leigh, que comprende una estación por la que presenta una afinidad alta, concretamente fumaramida; separado por un espaciador polar de aproximadamente 10 nm de longitud, se encuentra una segunda estación, un éster de succinimida, que presenta menos afinidad por la macrociclo que la estación de fumaramida. Dos grupos voluminosos difeniletilo actúan como “stoppers” impidiendo que el macrociclo se escape. El extremo de un stopper se decoró con una biotina que se usó para unir la molécula a la configuración de las pinzas ópticas. El otro punto de enlace a las pinzas ópticas fue introducido a través de una reacción de click entre una azida localizada en el macrociclo y un oligonucleótido modificado con un alquino; finalmente este oligonucleótido se ligó a un espaciador de dsDNA para facilitar su manipulación en las pinzas ópticas. Construcciones individuales de rotaxano-dsADN se manipularon mecánicamente de una manera controlada mediante un instrumento pinzas

ópticas de doble haz. De este modo, y por primera vez, fuimos capaces de seguir el movimiento de shuttling de moléculas individuales de [2]rotaxanos durante minutos. Observamos el comportamiento estocástico de estas moléculas, lo que permitió tener acceso a la naturaleza estadística de estas fluctuaciones y caracterizar el ciclo mecanoquímico de su sistema de operación, en términos de la diferencia de energía libre de Gibbs, la fuerza de coexistencia, en la que el macrociclo presenta la misma posibilidad de encontrarse en ambas estaciones, la posición del estado de transición y las velocidades cinéticas. Además, hemos adaptado la este dispositivo molecular orgánico para poder estudiarlo en condiciones acuosas biocompatibles, lo que abre las puertas al estudio de híbridos sintéticos naturales más complejos, uno de los objetivos más ambiciosos en el campo.

3) Hemos observado experimentalmente la formación de enlaces hidrógeno en cuatro sistemas diferentes que se unen a través de enlaces de hidrógeno, los cuales presentan dadores y aceptores de enlaces de hidrógeno fuertes: benzamidina-acético acético (Ben-AcOH, neutro-neutro), el receptor de Hamilton-derivado de ácido cianúrico (HR-cy, neutro-neutro), 1,4,7,10,13,16-hexaoxaciclooctadecano- derivado de amonio (18_crown_6-Am, neutro-catión) y *N,N'*-dimetiltiourea-benzoato sódico (DMTU-BzO⁻, neutro-anión), en [emim][FAP], un líquido iónico a temperatura ambiente (RTIL), donde se espera que las interacciones electrostáticas juegasen un papel secundario, ya que la contribución electrostática dipolo-dipolo en enlaces de hidrógeno es proporcional a r^{-6} , mientras que las interacciones de dipolo-carga son proporcionales a r^{-2} . Las valoraciones de espectroscopía UV-vis de los complejos unidos a través de enlace de hidrógeno mostraron que las constantes de asociación se debilitan en [emim][FAP] ($K_a(\text{Ben-AcOH}) = 1.99 \times 10^3 \text{ M}^{-1}$; $K_a(\text{HR-cy}) = 3.16 \times 10^6 \text{ M}^{-1}$; $K_a(18_crown_6\text{-Am}) = 3.16 \times 10^3 \text{ M}^{-1}$; $K_a(\text{DMTU-BzO}^-) = 1.99 \times 10^4 \text{ M}^{-1}$), con respecto a los disolventes orgánicos ($K_a(\text{Ben-AcOH}) = 2.51 \times 10^3 \text{ M}^{-1}$ en CH₃Cl; $K_a(\text{HR-cy}) = 6.31 \times 10^5 \text{ M}^{-1}$ en acetonitrilo; $K_a(18_crown_6\text{-Am}) = 3.98 \times 10^3 \text{ M}^{-1}$ en acetonitrilo; $K_a(\text{DMTU-BzO}^-) = 3.98 \times 10^4 \text{ M}^{-1}$ en CH₃Cl), pero se encuentran en el mismo orden de magnitud. Esta tendencia también se confirmó mediante espectroscopía IR en dos sistemas huésped-receptor y mediante mediciones de fuerza de molécula individual realizadas por AFM en una pareja. Estas observaciones se oponen a los hallazgos de enlaces hidrógeno más débiles, como los que se dan en el agua, que están sustituidos por interacciones O-H-anión en RTIL. Por lo tanto, nuestros experimentos apuntan a una contribución covalente significativa a los fuertes enlaces de hidrógeno, que no se ve afectada por las cargas del RTIL, y se encuentra lejos de una visión meramente electrostática de los enlaces hidrógeno. Para obtener una visión más completa del problema y generalizar o refutar nuestras conclusiones preliminares, ahora estamos estudiando las constantes de asociación de los mismos sistemas huésped-receptor

en una colección de RTILs, en la cual sistemáticamente variamos el tamaño del catión y del anión.

4) A través de evolución dirigida utilizando yeast surface display (YSD), pudimos llevar a cabo la ingeniería de la proteína ultraestable Sso7d (de la archaeon hyperthermophilic *Sulfolobus solfataricus*) y encontrar un binder específico de hEGF, que presenta constantes de disociación en el rango de 10^{-8} M. El marcaje de la proteína Sso7d en dos posiciones estudiadas con el fluoróforo 4-DMN mostró incrementos en la fluorescencia de 15 veces, tras la unión de hEGF; lo que representa una buena prueba de concepto ya que presenta propiedades típicas de sensores de unión específicos (bajo background en fluorescencia y un gran aumento en la intensidad de fluorescencia al unirse con su huésped). Sin embargo, estos mutantes de Sso7d no presentan los aumentos de 50 veces en la fluorescencia previamente descritos por De Picotto et al. Para continuar con este proyecto, sería un buen punto explorar si la posición 34 del scaffold de Sso7d presenta una mejor respuesta de fluorescencia. En resumen, los resultados obtenidos hasta ahora son prometedores y están cerca de encontrar un excelente biosensor solvatocrómico.

REFERENCES

1. Lehn, J. M., Supramolecular chemistry. *Science* **1993**, *260* (5115), 1762.
2. Lehn, J.-M., Supramolecular Chemistry—Scope and Perspectives Molecules, Supermolecules, and Molecular Devices (Nobel Lecture). *Angew. Chem. Int. Ed. Engl.* **1988**, *27* (1), 89-112.
3. Lehn, J.-M., From supramolecular chemistry towards constitutional dynamic chemistry and adaptive chemistry. *Chem. Soc. Rev.* **2007**, *36* (2), 151-160.
4. Lehn, J. M., *Supramolecular Chemistry*. WILEY-VCH Verlag GmbH: 1995; Vol. 1, p 2617-2617.
5. Lehn, J.-M., Perspectives in Supramolecular Chemistry—From Molecular Recognition towards Molecular Information Processing and Self-Organization. *Angewandte Chemie International Edition in English* **1990**, *29* (11), 1304-1319.
6. Lehn, J.-M., Perspectives in Chemistry—Steps towards Complex Matter. *Angewandte Chemie International Edition* **2013**, *52* (10), 2836-2850.
7. Lehn, J.-M., *Supramolecular Chemistry, 1st edn.* Wiley-VCH Verlag GmbH, Weinheim, 1995.
8. Fischer, E., Einfluss der Configuration auf die Wirkung der Enzyme. *Ber. Deutsch. Chem. Ges.* **1894**, *27* (3), 2985-2993.
9. Pedersen, C. J., Cyclic polyethers and their complexes with metal salts. *J. Am. Chem. Soc.* **1967**, *89* (26), 7017-7036.
10. Cram, D. J.; Cram, J. M., Host-Guest Chemistry. *Science* **1974**, *183* (4127), 803-809.
11. Schalley, C. A., *Analytical Methods in Supramolecular Chemistry*. WILEY-VCH Verlag GmbH & Co. KGaA, Weinheim, 2007.
12. Jansen, G., Symmetry-adapted perturbation theory based on density functional theory for noncovalent interactions. *WIREs Comput. Mol. Sci.* **2014**, *4* (2), 127-144.
13. Mulliken, R. S.; Person, W. B., *Molecular complexes : a lecture and reprint volume*. Wiley-Interscience: New York; London, 1969.
14. Müller-Dethlefs, K.; Hobza, P., Noncovalent Interactions: A Challenge for Experiment and Theory. *Chem. Rev.* **2000**, *100* (1), 143-168.
15. Hobza, P.; Selzle, H. L.; Schlag, E. W., Structure and Properties of Benzene-Containing Molecular Clusters: Nonempirical ab Initio Calculations and Experiments. *Chem. Rev.* **1994**, *94* (7), 1767-1785.
16. Hobza, P.; Selzle, H. L.; Schlag, E. W., Potential Energy Surface for the Benzene Dimer. Results of ab Initio CCSD(T) Calculations Show Two Nearly Isoenergetic Structures: T-Shaped and Parallel-Displaced. *The Journal of Physical Chemistry* **1996**, *100* (48), 18790-18794.
17. Hunter, C. A.; Singh, J.; Thornton, J. M., π - π interactions: the geometry and energetics of phenylalanine-phenylalanine interactions in proteins. *Journal of Molecular Biology* **1991**, *218* (4), 837-846.
18. Grabowski, S. J., *Hydrogen Bonding - New Insights*. Springer, 2006.
19. Jeffrey, G. A., and Saenger, W., *Hydrogen bonding in biological structures*. Springer Berlin, 1991.
20. Jeffrey, G. A., and Saenger, W., *An introduction to hydrogen bonding*. Oxford University Press, New York, 1997.
21. Desiraju, G., and Steiner, T., *The weak hydrogen bond in structural chemistry and biology*. Oxford University Press, Oxford, 1999.
22. Scheiner, S., *Hydrogen Bonding. A Theoretical Perspective* Oxford University Press: New York: 1997.
23. Frenking, G.; Caramori, G. F., No Need for a Re-examination of the Electrostatic Notation of the Hydrogen Bonding: A Comment. *Angew. Chem. Int. Ed.* **2015**, *54* (9), 2596-2599.
24. Weinhold, F.; Klein, R. A., Anti-Electrostatic Hydrogen Bonds. *Angew. Chem. Int. Ed.* **2014**, *126* (42), 11396-11399.
25. Weinhold, F.; Klein, R. A., Improved General Understanding of the Hydrogen-Bonding Phenomena: A Reply. *Angewandte Chemie International Edition* **2015**, *54* (9), 2600-2602.
26. Hobza, P.; Špirko, V.; Selzle, H. L.; Schlag, E. W., Anti-Hydrogen Bond in the Benzene Dimer and Other Carbon Proton Donor Complexes. *J. Phys. Chem. A* **1998**, *102* (15), 2501-2504.
27. Hobza, P.; Špirko, V. r.; Havlas, Z.; Buchhold, K.; Reimann, B.; Barth, H.-D.; Brutschy, B., Anti-hydrogen bond between chloroform and fluorobenzene. *Chem. Phys. Lett.* **1999**, *299* (2), 180-186.
28. Lee, J. C.; Peris, E.; Rheingold, A. L.; Crabtree, R. H., An Unusual Type of H.cntdot..cntdot..cntdot.H Interaction: Ir-H.cntdot..cntdot..cntdot.H-O and Ir-H.cntdot..cntdot..cntdot.H-N Hydrogen Bonding and Its Involvement in .sigma.-Bond Metathesis. *J. Am. Chem. Soc.* **1994**, *116* (24), 11014-11019.

29. Richardson, T.; de Gala, S.; Crabtree, R. H.; Siegbahn, P. E. M., Unconventional Hydrogen Bonds: Intermolecular B-H.cntdot..cntdot..cntdot.H-N Interactions. *J. Am. Chem. Soc.* **1995**, *117* (51), 12875-12876.
30. Klooster, W. T.; Koetzle, T. F.; Siegbahn, P. E. M.; Richardson, T. B.; Crabtree, R. H., Study of the N-H...H-B Dihydrogen Bond Including the Crystal Structure of BH₃NH₃ by Neutron Diffraction. *J. Am. Chem. Soc.* **1999**, *121* (27), 6337-6343.
31. Liu, Q.; Hoffmann, R., Theoretical Aspects of a Novel Mode of Hydrogen-Hydrogen Bonding. *J. Am. Chem. Soc.* **1995**, *117* (40), 10108-10112.
32. Ritort, F., Single-molecule experiments in biological physics: methods and applications. *J. Phys.: Condens. Matter* **2006**, *18* (32), R531.
33. Leake, M. C., The physics of life: one molecule at a time. *Philos. Trans. R. Soc. Lond. B. Biol. Sci.* **2013**, *368* (1611), 20120248.
34. Janshoff, A.; Neitzert, M.; Oberdörfer, Y.; Fuchs, H., Force Spectroscopy of Molecular Systems-Single Molecule Spectroscopy of Polymers and Biomolecules. *Angew. Chem. Int. Ed.* **2000**, *39* (18), 3212-3237.
35. Rief, M.; Clausen-Schaumann, H.; Gaub, H. E., Sequence-dependent mechanics of single DNA molecules. *Nat. Struct. Bio.* **1999**, *6*, 346.
36. Marszalek, P. E.; Lu, H.; Li, H.; Carrion-Vazquez, M.; Oberhauser, A. F.; Schulten, K.; Fernandez, J. M., Mechanical unfolding intermediates in titin modules. *Nature* **1999**, *402* (6757), 100-103.
37. Li, Y.; Qin, M.; Li, Y.; Cao, Y.; Wang, W., Single Molecule Evidence for the Adaptive Binding of DOPA to Different Wet Surfaces. *Langmuir* **2014**, *30* (15), 4358-4366.
38. Fuhrmann, A.; Getfert, S.; Fu, Q.; Reimann, P.; Lindsay, S.; Ros, R., Long Lifetime of Hydrogen-Bonded DNA Basepairs by Force Spectroscopy. *Biophys. J.* *102* (10), 2381-2390.
39. Schroeder T; Walhorn V; Mattay J; D, A., Analytical Methods in Supramolecular Chemistry. Volume 1&2, Second Edition
In *Analytical Methods in Supramolecular Chemistry. Volume 1&2, Second Edition*, Wiley-VCH Verlag GmbH & Co. KGaA: 2012; pp I-XVIII.
40. Evans, E., Probing the Relation Between Force—Lifetime—and Chemistry in Single Molecular Bonds. *Annu. Rev. Biophys. Biomol. Struct.* **2001**, *30* (1), 105-128.
41. Wolynes, P.; Onuchic, J.; Thirumalai, D., Navigating the folding routes. *Science* **1995**, *267* (5204), 1619-1620.
42. Evans, E.; Ritchie, K., Dynamic strength of molecular adhesion bonds. *Biophys. J.* **1997**, *72* (4), 1541-1555.
43. Bustamante, C.; Cheng, W.; Mejia, Y. X., Revisiting the Central Dogma One Molecule at a Time. *Cell* **2011**, *144* (4), 480-497.
44. Larson, M. H.; Landick, R.; Block, S. M., Single-molecule studies of RNA polymerase: One singular sensation, every little step it takes. *Molecular cell* **2011**, *41* (3), 249-262.
45. Shen, K.; Arslan, S.; Akopian, D.; Ha, T.; Shan, S.-o., Activated GTPase movement on an RNA scaffold drives cotranslational protein targeting. *Nature* **2012**, *492* (7428), 271-275.
46. Moffitt, J. R.; Chemla, Y. R.; Smith, S. B.; Bustamante, C., Recent Advances in Optical Tweezers. *Ann. Rev. Biochem.* **2008**, *77* (1), 205-228.
47. Brenner, M. D.; Zhou, R.; Ha, T., Forcing a Connection: Impacts of Single-Molecule Force Spectroscopy on In Vivo Tension Sensing. *Biopolymers* **2011**, *95* (5), 332-344.
48. Neuman, K. C.; Nagy, A., Single-molecule force spectroscopy: optical tweezers, magnetic tweezers and atomic force microscopy. *Nat. Methods* **2008**, *5* (6), 491-505.
49. Hummer, G.; Szabo, A., Free Energy Surfaces from Single-Molecule Force Spectroscopy. *Acc. Chem. Res.* **2005**, *38* (7), 504-513.
50. Woodside, M. T.; Behnke-Parks, W. M.; Larizadeh, K.; Travers, K.; Herschlag, D.; Block, S. M., Nanomechanical measurements of the sequence-dependent folding landscapes of single nucleic acid hairpins. *Proc. Natl. Acad. Sci.* **2006**, *103* (16), 6190-6195.
51. Jarzynski, C., Nonequilibrium Equality for Free Energy Differences. *Phys. Rev. Lett.* **1997**, *78* (14), 2690-2693.
52. Cluzel, P.; Lebrun, A.; Heller, C.; Lavery, R.; Viovy, J.-L.; Chatenay, D.; Caron, F., DNA: An Extensible Molecule. *Science* **1996**, *271* (5250), 792-794.
53. Evans, E.; Ritchie, K.; Merkel, R., Sensitive force technique to probe molecular adhesion and structural linkages at biological interfaces. *Biophys. J.* **1995**, *68* (6), 2580-2587.
54. Smith, S.; Finzi, L.; Bustamante, C., Direct mechanical measurements of the elasticity of single DNA molecules by using magnetic beads. *Science* **1992**, *258* (5085), 1122-1126.
55. Kim, S.; Blainey, P. C.; Schroeder, C. M.; Xie, X. S., Multiplexed single-molecule assay for enzymatic activity on flow-stretched DNA. *Nat Meth* **2007**, *4* (5), 397-399.

56. Binnig, G., Quate, C.F. & Gerber, C., Atomic force microscope. *Phys. Rev. Lett.* **1986**, *56*, 930–933.
57. Dai P., W. S., Taub H., Buckley J.E., Ehrlich S.N., Larese J.Z., Binnig G., Smith D.P., X-ray-diffraction and scanning-tunneling-microscopy studies of a liquid-crystal film adsorbed on single-crystal graphite. *Phys. Rev. B Condens. Matter* **1993**, (47), 7401–7407.
58. Binnig, G., Garcia, N., Rohrer H., Conductivity sensitivity of inelastic scanning tunneling microscopy. *Phys. Rev. B Condens. Matter* **1985**, (32), 1336–1338
59. Marti, O.; Elings, V.; Haugan, M.; Bracker, C. E.; Schneir, J.; Drake, B.; Gould, S. A. C.; Gurley, J.; Hellemans, L.; Shaw, K.; Weisenhorn, A. L.; Zasadzinski, J.; Hansma, P. K., Scanning probe microscopy of biological samples and other surfaces. *J. Microsc.* **1988**, *152* (3), 803-809.
60. Engel, A., Biological Applications of Scanning Probe Microscopes. *Annual Review of Biophysics and Biophysical Chemistry* **1991**, *20* (1), 79-108.
61. Lindsay, S. M., Biological scanning probe microscopy comes of age. *Biophysical Journal* **1994**, *67* (6), 2134-2135.
62. Shao, Z.; Yang, J.; Somlyo, A. P., Biological Atomic Force Microscopy: From Microns to Nanometers and Beyond. *Annual Review of Cell and Developmental Biology* **1995**, *11* (1), 241-265.
63. Fisher, T. E.; Marszalek, P. E.; Fernandez, J. M., Stretching single molecules into novel conformations using the atomic force microscope. *Nat Struct Mol Biol* **2000**, *7* (9), 719-724.
64. Carrion-Vazquez, M.; Oberhauser, A. F.; Fisher, T. E.; Marszalek, P. E.; Li, H.; Fernandez, J. M., Mechanical design of proteins studied by single-molecule force spectroscopy and protein engineering. *Prog. Biophys. Mol. Biol.* **2000**, *74* (1), 63-91.
65. Zlatanova, J.; Lindsay, S. M.; Leuba, S. H., Single molecule force spectroscopy in biology using the atomic force microscope. *Prog. Biophys. Mol. Biol.* **2000**, *74* (1), 37-61.
66. Fisher, T. E.; Oberhauser, A. F.; Carrion-Vazquez, M.; Marszalek, P. E.; Fernandez, J. M., The study of protein mechanics with the atomic force microscope. *Trends Biochem.Sci.* *24* (10), 379-384.
67. Scheuring, S.; Fotiadis, D.; Möller, C.; Müller, S. A.; Engel, A.; Müller, D. J., Single Proteins Observed by Atomic Force Microscopy. *Single Mol.* **2001**, *2* (2), 59-67.
68. Rief, M.; Oesterhelt, F.; Heymann, B.; Gaub, H. E., Single Molecule Force Spectroscopy on Polysaccharides by Atomic Force Microscopy. *Science* **1997**, *275* (5304), 1295-1297.
69. Rief, M.; Gautel, M.; Oesterhelt, F.; Fernandez, J. M.; Gaub, H. E., Reversible Unfolding of Individual Titin Immunoglobulin Domains by AFM. *Science* **1997**, *276* (5315), 1109-1112.
70. Cumpson, P. J., Zhdan, P. & Hedley, J., Calibration of AFM cantilever stiffness: a microfabricated array of reflective springs. *Ultramicroscopy* **2004**, (100), 241–251.
71. Leake, M. C., Wilson, D., Gautel, M. & Simmons, R.M., The elasticity of single titin molecules using a two-bead optical tweezers assay. *Biophys. J.* **2004**, (87), 1112–1135.
72. Kellermayer, M. S., Delayed dissociation of in vitro moving actin filaments from heavy meromyosin induced by low concentrations of Triton X-100. *Biophys. Chem.* **1997**, (67), 199–210.
73. Smith, S. B.; Cui, Y.; Bustamante, C., Overstretching B-DNA: The Elastic Response of Individual Double-Stranded and Single-Stranded DNA Molecules. *Science* **1996**, *271* (5250), 795-799.
74. Florin, E.; Moy, V.; Gaub, H., Adhesion forces between individual ligand-receptor pairs. *Science* **1994**, *264* (5157), 415-417.
75. Yasuda, R.; Noji, H.; Kinoshita, K., Jr.; Yoshida, M., F1-ATPase is a highly efficient molecular motor that rotates with discrete 120 degree steps. *Cell* **1998**, *93* (7), 1117-1124.
76. Rief, M.; Gautel, M.; Schemmel, A.; Gaub, H. E., The mechanical stability of immunoglobulin and fibronectin III domains in the muscle protein titin measured by atomic force microscopy. *Biophys. J.* **1998**, *75* (6), 3008-3014.
77. Katz, E.; Willner, I., Biomolecule-Functionalized Carbon Nanotubes: Applications in Nanobioelectronics. *ChemPhysChem* **2004**, *5* (8), 1084-1104.
78. Lee, G.; Chrisey, L.; Colton, R., Direct measurement of the forces between complementary strands of DNA. *Science* **1994**, *266* (5186), 771-773.
79. Marszalek, P. E.; Oberhauser, A. F.; Pang, Y.-P.; Fernandez, J. M., Polysaccharide elasticity governed by chair-boat transitions of the glucopyranose ring. *Nature* **1998**, *396* (6712), 661-664.
80. Marszalek, P. E.; Pang, Y.-P.; Li, H.; Yazal, J. E.; Oberhauser, A. F.; Fernandez, J. M., Atomic levers control pyranose ring conformations. *Proc. Nat. Acad. Sci. USA* **1999**, *96* (14), 7894-7898.
81. Camesano, T. A.; Wilkinson, K. J., Single Molecule Study of Xanthan Conformation Using Atomic Force Microscopy. *Biomacromolecules* **2001**, *2* (4), 1184-1191.
82. Brockwell, D. J.; Paci, E.; Zinober, R. C.; Beddard, G. S.; Olmsted, P. D.; Smith, D. A.; Perham, R. N.; Radford, S. E., Pulling geometry defines the mechanical resistance of a β -sheet protein. *Nature Struct. Biol.* **2003**, *10*, 731.
83. Carrion-Vazquez, M.; Li, H.; Lu, H.; Marszalek, P. E.; Oberhauser, A. F.; Fernandez, J. M., The mechanical stability of ubiquitin is linkage dependent. *Nature Struct. Biol.* **2003**, *10*, 738.

84. Dietz, H.; Berkemeier, F.; Bertz, M.; Rief, M., Anisotropic deformation response of single protein molecules. *Proc. Natl Acad. Sci. USA* **2006**, *103* (34), 12724-12728.
85. Lee, G.; Abdi, K.; Jiang, Y.; Michaely, P.; Bennett, V.; Marszalek, P. E., Nanospring behaviour of ankyrin repeats. *Nature* **2006**, *440* (7081), 246-249.
86. Schwaiger, I.; Sattler, C.; Hostetter, D. R.; Rief, M., The myosin coiled-coil is a truly elastic protein structure. *Nat. Mater* **2002**, *1* (4), 232-235.
87. Becker, N.; Oroudjev, E.; Mutz, S.; Cleveland, J. P.; Hansma, P. K.; Hayashi, C. Y.; Makarov, D. E.; Hansma, H. G., Molecular nanosprings in spider capture-silk threads. *Nat. Mater* **2003**, *2* (4), 278-283.
88. Cao, Y.; Li, H., Polyprotein of GB1 is an ideal artificial elastomeric protein. *Nat. Mater* **2007**, *6* (2), 109-114.
89. Schönherr, H.; Beulen, M. W. J.; Bügler, J.; Huskens, J.; van Veggel, F. C. J. M.; Reinhoudt, D. N.; Vancso, G. J., Individual Supramolecular Host-Guest Interactions Studied by Dynamic Single Molecule Force Spectroscopy. *J. Am. Chem. Soc.* **2000**, *122* (20), 4963-4967.
90. Kado, S.; Kimura, K., Single Complexation Force of 18-Crown-6 with Ammonium Ion Evaluated by Atomic Force Microscopy. *J. Am. Chem. Soc.* **2003**, *125* (15), 4560-4564.
91. Auletta, T.; de Jong, M. R.; Mulder, A.; van Veggel, F. C. J. M.; Huskens, J.; Reinhoudt, D. N.; Zou, S.; Zapotoczny, S.; Schönherr, H.; Vancso, G. J.; Kuipers, L., β -Cyclodextrin Host-Guest Complexes Probed under Thermodynamic Equilibrium: Thermodynamics and AFM Force Spectroscopy. *J. Am. Chem. Soc.* **2004**, *126* (5), 1577-1584.
92. Liu, Y.; Wang, Z.; Zhang, X., Characterization of supramolecular polymers. *Chem. Soc. Rev.* **2012**, *41* (18), 5922-5932.
93. Auletta, T.; van Veggel, F. C. J. M.; Reinhoudt, D. N., Self-Assembled Monolayers on Gold of Ferrocene-Terminated Thiols and Hydroxyalkanethiols. *Langmuir* **2002**, *18* (4), 1288-1293.
94. Evans, E. A.; Calderwood, D. A., Forces and Bond Dynamics in Cell Adhesion. *Science* **2007**, *316* (5828), 1148-1153.
95. Merkel, R.; Nassoy, P.; Leung, A.; Ritchie, K.; Evans, E., Energy landscapes of receptor-ligand bonds explored with dynamic force spectroscopy. *Nature* **1999**, *397* (6714), 50-53.
96. Kienberger, F.; Kada, G.; Gruber, H. J.; Pastushenko, V. P.; Riener, C.; Trieb, M.; Knaus, H.-G.; Schindler, H.; Hinterdorfer, P., Recognition Force Spectroscopy Studies of the NTA-His6 Bond. *Single Mol.* **2000**, *1* (1), 59-65.
97. Kudera, M.; Eschbaumer, C.; Gaub, H. E.; Schubert, U. S., Analysis of Metallo-Supramolecular Systems Using Single-Molecule Force Spectroscopy. *Adv. Func. Mater.* **2003**, *13* (8), 615-620.
98. Kersey, F. R.; Yount, W. C.; Craig, S. L., Single-Molecule Force Spectroscopy of Bimolecular Reactions: System Homology in the Mechanical Activation of Ligand Substitution Reactions. *J. Am. Chem. Soc.* **2006**, *128* (12), 3886-3887.
99. Zou, S.; Schönherr, H.; Vancso, G. J., Stretching and Rupturing Individual Supramolecular Polymer Chains by AFM. *Angew. Chem. Int. Ed.* **2005**, *44* (6), 956-959.
100. Zou, S.; Schönherr, H.; Vancso, G. J., Force Spectroscopy of Quadruple H-Bonded Dimers by AFM: Dynamic Bond Rupture and Molecular Time-Temperature Superposition. *J. Am. Chem. Soc.* **2005**, *127* (32), 11230-11231.
101. Embrechts, A.; Schönherr, H.; Vancso, G. J., Forced Unbinding of Individual Urea-Aminotriazine Supramolecular Polymers by Atomic Force Microscopy: A Closer Look at the Potential Energy Landscape and Binding Lengths at Fixed Loading Rates. *J. Phys. Chem. B* **2012**, *116* (1), 565-570.
102. Embrechts, A.; Velders, A. H.; Schönherr, H.; Vancso, G. J., Self-Complementary Recognition of Supramolecular Urea-Aminotriazines in Solution and on Surfaces. *Langmuir* **2011**, *27* (23), 14272-14278.
103. Zhang, Y.; Liu, C.; Shi, W.; Wang, Z.; Dai, L.; Zhang, X., Direct Measurements of the Interaction between Pyrene and Graphite in Aqueous Media by Single Molecule Force Spectroscopy: Understanding the π - π Interactions. *Langmuir* **2007**, *23* (15), 7911-7915.
104. Iliafar, S.; Mittal, J.; Vezenov, D.; Jagota, A., Interaction of Single-Stranded DNA with Curved Carbon Nanotube Is Much Stronger Than with Flat Graphite. *J. Am. Chem. Soc.* **2014**, *136* (37), 12947-12957.
105. Ashkin, A.; Dziedzic, J. M.; Bjorkholm, J. E.; Chu, S., Observation of a single-beam gradient force optical trap for dielectric particles. *Opt. Lett.* **1986**, *11* (5), 288-290.
106. Svoboda, K.; Block, S. M., Biological Applications of Optical Forces. *Annu. Rev. Biophys. Biomol. Struct.* **1994**, *23* (1), 247-285.
107. Neuman, K. C.; Block, S. M., Optical trapping. *Rev. Sci. Instrum.* **2004**, *75* (9), 2787-2809.
108. Ashkin, A.; Dziedzic, J., Optical trapping and manipulation of viruses and bacteria. *Science* **1987**, *235* (4795), 1517-1520.

109. Ashkin, A.; Dziedzic, J. M.; Yamane, T., Optical trapping and manipulation of single cells using infrared laser beams. *Nature* **1987**, *330* (6150), 769-771.
110. Ashkin, A.; Dziedzic, J. M., Internal cell manipulation using infrared laser traps. *Proceedings of the National Academy of Sciences* **1989**, *86* (20), 7914-7918.
111. Hormeño, S.; Ibarra, B.; Carrascosa, José L.; Valpuesta, José M.; Moreno-Herrero, F.; Arias-Gonzalez, J. R., Mechanical Properties of High-GC Content DNA with A-Type Base-Stacking. *Biophys. J.* **100** (8), 1996-2005.
112. Hormeño, S.; Ibarra, B.; Valpuesta, J. M.; Carrascosa, J. L.; Ricardo Arias-Gonzalez, J., Mechanical stability of low-humidity single DNA molecules. *Biopolymers* **2012**, *97* (4), 199-208.
113. Herrero-Galán, E.; Fuentes-Perez, M. E.; Carrasco, C.; Valpuesta, J. M.; Carrascosa, J. L.; Moreno-Herrero, F.; Arias-Gonzalez, J. R., Mechanical Identities of RNA and DNA Double Helices Unveiled at the Single-Molecule Level. *J. Am. Chem. Soc.* **2013**, *135* (1), 122-131.
114. Arias-Gonzalez, J. R., Single-molecule portrait of DNA and RNA double helices. *Integrative Biology* **2014**, *6* (10), 904-925.
115. Woodside, M. T.; Behnke-Parks, W. M.; Larizadeh, K.; Travers, K.; Herschlag, D.; Block, S. M., Nanomechanical measurements of the sequence-dependent folding landscapes of single nucleic acid hairpins. *Proc. Nat. Acad. Sci. USA* **2006**, *103* (16), 6190-6195.
116. Svoboda, K.; Schmidt, C. F.; Schnapp, B. J.; Block, S. M., Direct observation of kinesin stepping by optical trapping interferometry. *Nature* **1993**, *365* (6448), 721-727.
117. Peterman, E. J. G.; Gittes, F.; Schmidt, C. F., Laser-Induced Heating in Optical Traps. *Biophys. J.* **2003**, *84* (2), 1308-1316.
118. Seol, Y.; Carpenter, A. E.; Perkins, T. T., Gold nanoparticles: enhanced optical trapping and sensitivity coupled with significant heating. *Opt. Lett.* **2006**, *31* (16), 2429-2431.
119. Hormeño, S.; Gregorio-Godoy, P.; Pérez-Juste, J.; Liz-Marzán, L. M.; Juárez, B. H.; Arias-Gonzalez, J. R., Laser Heating Tunability by Off-Resonant Irradiation of Gold Nanoparticles. *Small* **2014**, *10* (2), 376-384.
120. Neuman, K. C.; Chadd, E. H.; Liou, G. F.; Bergman, K.; Block, S. M., Characterization of Photodamage to Escherichia coli in Optical Traps. *Biophys. J.* **1999**, *77* (5), 2856-2863.
121. Hormeño, S.; Arias-Gonzalez, J. R., Exploring mechanochemical processes in the cell with optical tweezers. *Biol. Cell* **2006**, *98* (12), 679-695.
122. Gilli, G.; Gilli, P.; Editors, *The Nature of Hydrogen Bond: Outline of a Comprehensive Hydrogen Bond Theory*. Oxford University Press: 2009; p 330 pp.
123. Buntkowsky, G.; Shenderovich, I. G.; Weisz, K.; Editors, *Facets of Hydrogen Bonding and Hydrogen Transfer. (Dedicated to Professor Hans-Heinrich Limbach on the Occasion of His 70th Birthday)*. [In: *Z. Phys. Chem. (Muenchen, Ger.)*, 2013; 227(6-7)]. Oldenbourg Wissenschaftsverlag GmbH: 2013; p 342 pp.
124. Rekharsky, M.; Inoue, Y.; Tobey, S.; Metzger, A.; Anslyn, E., Ion-Pairing Molecular Recognition in Water: Aggregation at Low Concentrations That Is Entropy-Driven. *J. Am. Chem. Soc.* **2002**, *124* (50), 14959-14967.
125. Prins, L. J.; Reinhoudt, D. N.; Timmerman, P., Noncovalent synthesis using hydrogen bonding. *Angew. Chem., Int. Ed.* **2001**, *40* (13), 2382-2426.
126. Prins, L. J.; Timmerman, P.; Reinhoudt, D. N., Amplification of Chirality: The "Sergeants and Soldiers" Principle Applied to Dynamic Hydrogen-Bonded Assemblies. *J. Am. Chem. Soc.* **2001**, *123* (42), 10153-10163.
127. Garzoni, M.; Baker, M. B.; Leenders, C. M. A.; Voets, I. K.; Albertazzi, L.; Palmans, A. R. A.; Meijer, E. W.; Pavan, G. M., Effect of H-Bonding on Order Amplification in the Growth of a Supramolecular Polymer in Water. *J. Am. Chem. Soc.* **2016**, *138* (42), 13985-13995.
128. Hosono, N.; Kushner, A. M.; Chung, J.; Palmans, A. R. A.; Guan, Z.; Meijer, E. W., Forced Unfolding of Single-Chain Polymeric Nanoparticles. *J. Am. Chem. Soc.* **2015**, *137* (21), 6880-6888.
129. Abbel, R.; Grenier, C.; Pouderoijen, M. J.; Stouwdam, J. W.; Leclere, P. E. L. G.; Sijbesma, R. P.; Meijer, E. W.; Schenning, A. P. H. J., White-Light Emitting Hydrogen-Bonded Supramolecular Copolymers Based on π -Conjugated Oligomers. *J. Am. Chem. Soc.* **2009**, *131* (2), 833-843.
130. Dankers, P. Y. W.; Harmsen, M. C.; Brouwer, L. A.; Van Luyn, M. J. A.; Meijer, E. W., A modular and supramolecular approach to bioactive scaffolds for tissue engineering. *Nat. Mater.* **2005**, *4* (7), 568-574.
131. Montoro-Garcia, C.; Camacho-Garcia, J.; Lopez-Perez, A. M.; Mayoral, M. J.; Bilbao, N.; Gonzalez-Rodriguez, D., Role of the Symmetry of Multipoint Hydrogen Bonding on Chelate Cooperativity in Supramolecular Macrocyclization Processes. *Angew. Chem., Int. Ed.* **2016**, *55* (1), 223-227.

132. Bilbao, N.; Destoop, I.; De Feyter, S.; Gonzalez-Rodriguez, D., Two-Dimensional Nanoporous Networks Formed by Liquid-to-Solid Transfer of Hydrogen-Bonded Macrocycles Built from DNA Bases. *Angew. Chem., Int. Ed.* **2016**, *55* (2), 659-663.
133. Panman, M. R.; Bakker, B. H.; den Uyl, D.; Kay, E. R.; Leigh, D. A.; Buma, W. J.; Brouwer, A. M.; Geenevasen, J. A. J.; Woutersen, S., Water lubricates hydrogen-bonded molecular machines. *Nat. Chem.* **2013**, *5* (11), 929-934.
134. Chatterjee, M. N.; Kay, E. R.; Leigh, D. A., Beyond Switches: Ratcheting a Particle Energetically Uphill with a Compartmentalized Molecular Machine. *J. Am. Chem. Soc.* **2006**, *128* (12), 4058-4073.
135. Fioravanti, G.; Haraszkiwicz, N.; Kay, E. R.; Mendoza, S. M.; Bruno, C.; Marcaccio, M.; Wiering, P. G.; Paolucci, F.; Rudolf, P.; Brouwer, A. M.; Leigh, D. A., Three State Redox-Active Molecular Shuttle That Switches in Solution and on a Surface. *J. Am. Chem. Soc.* **2008**, *130* (8), 2593-2601.
136. Kay, E. R.; Leigh, D. A., Hydrogen bond-assembled synthetic molecular motors and machines. *Top. Curr. Chem.* **2005**, *262* (Molecular Machines), 133-177.
137. Lussis, P.; Svaldo-Lanero, T.; Bertocco, A.; Fustin, C.-A.; Leigh, D. A.; Duwez, A.-S., A single synthetic small molecule that generates force against a load. *Nat. Nanotechnol.* **2011**, *6* (9), 553-557.
138. Panman, M. R.; Bodis, P.; Shaw, D. J.; Bakker, B. H.; Newton, A. C.; Kay, E. R.; Brouwer, A. M.; Buma, W. J.; Leigh, D. A.; Woutersen, S., Operation Mechanism of a Molecular Machine Revealed Using Time-Resolved Vibrational Spectroscopy. *Science (Washington, DC, U. S.)* **2010**, *328* (5983), 1255-1258.
139. Camara-Campos, A.; Musumeci, D.; Hunter, C. A.; Turega, S., Chemical Double Mutant Cycles for the Quantification of Cooperativity in H-Bonded Complexes. *J. Am. Chem. Soc.* **2009**, *131* (51), 18518-18524.
140. Sun, H.; Hunter, C. A.; Navarro, C.; Turega, S., Relationship between Chemical Structure and Supramolecular Effective Molarity for Formation of Intramolecular H-Bonds. *J. Am. Chem. Soc.* **2013**, *135* (35), 13129-13141.
141. Hunter, C. A.; Misuraca, M. C.; Turega, S. M., Solvent effects on chelate cooperativity. *Chem. Sci.* **2012**, *3* (2), 589-601.
142. Hunter, C. A.; Misuraca, M. C.; Turega, S. M., Dissection of Complex Molecular Recognition Interfaces. *J. Am. Chem. Soc.* **2011**, *133* (3), 582-594.
143. Hunter, C. A.; Misuraca, M. C.; Turega, S. M., Influence of H-Bond Strength on Chelate Cooperativity. *J. Am. Chem. Soc.* **2011**, *133* (50), 20416-20425.
144. Hubbard, T. A.; Brown, A. J.; Bell, I. A. W.; Cockroft, S. L., The Limit of Intramolecular H-Bonding. *Journal of the American Chemical Society* **2016**.
145. Shalit, A.; Ahmed, S.; Savolainen, J.; Hamm, P., Terahertz echoes reveal the inhomogeneity of aqueous salt solutions. *Nat. Chem.* **2016**, Ahead of Print.
146. Thordarson, P., Determining association constants from titration experiments in supramolecular chemistry. *Chemical Society Reviews* **2011**, *40* (3), 1305-1323.
147. Brynn Hibbert, D.; Thordarson, P., The death of the Job plot, transparency, open science and online tools, uncertainty estimation methods and other developments in supramolecular chemistry data analysis. *Chemical Communications* **2016**.
148. The workings of molecular machines are typically governed by modulation of noncovalent interactions under non-equilibrium conditions: see references 28-30.
149. Kassem, S.; van Leeuwen, T.; Lubbe, A. S.; Wilson, M. R.; Feringa, B. L.; Leigh, D. A., Artificial molecular motors. *Chem. Soc. Rev.* **2017**, *46* (9), 2592-2621.
150. Astumian, R. D., How molecular motors work - insights from the molecular machinist's toolbox: the Nobel prize in Chemistry 2016. *Chem. Sci.* **2017**, *8* (2), 840-845.
151. Astumian, R. D., Microscopic reversibility as the organizing principle of molecular machines. *Nat. Nano.* **2012**, *7*, 684.
152. Feringa, B. L., The Art of Building Small: From Molecular Switches to Molecular Motors. *J. Org. Chem.* **2007**, *72* (18), 6635-6652.
153. Juette, M. F.; Terry, D. S.; Wasserman, M. R.; Altman, R. B.; Zhou, Z.; Zhao, H.; Blanchard, S. C., Single-molecule imaging of non-equilibrium molecular ensembles on the millisecond timescale. *Nat Meth* **2016**, *13* (4), 341-344.
154. Jarzynski, C., Single-molecule experiments: Out of equilibrium. *Nat Phys* **2011**, *7* (8), 591-592.
155. Vera, A. M.; Carrión-Vázquez, M., Direct Identification of Protein-Protein Interactions by Single-Molecule Force Spectroscopy. *Angewandte Chemie International Edition* **2016**, n/a-n/a.
156. Merkel, R.; Nassoy, P.; Leung, A.; Ritchie, K.; Evans, E., Energy landscapes of receptor-ligand bonds explored with dynamic force spectroscopy. *Nature* **1999**, *397*, 50.

157. Stock, P.; Monroe, J. I.; Utzig, T.; Smith, D. J.; Shell, M. S.; Valtiner, M., Unraveling Hydrophobic Interactions at the Molecular Scale Using Force Spectroscopy and Molecular Dynamics Simulations. *ACS Nano* **2017**, *11* (3), 2586-2597.
158. Huang, W.; Zhu, Z.; Wen, J.; Wang, X.; Qin, M.; Cao, Y.; Ma, H.; Wang, W., Single Molecule Study of Force-Induced Rotation of Carbon–Carbon Double Bonds in Polymers. *ACS Nano* **2017**, *11* (1), 194-203.
159. Wang, J.; Kouznetsova, T. B.; Craig, S. L., Single-Molecule Observation of a Mechanically Activated Cis-to-Trans Cyclopropane Isomerization. *J. Am. Chem. Soc.* **2016**, *138* (33), 10410-10412.
160. Kawai, S.; Nishiuchi, T.; Kodama, T.; Spijker, P.; Pawlak, R.; Meier, T.; Tracey, J.; Kubo, T.; Meyer, E.; Foster, A. S., Direct quantitative measurement of the C=O...H–C bond by atomic force microscopy. *Sci. Adv.* **2017**, *3* (5).
161. Liang, C.-K.; Dubacheva, G. V.; Buffeteau, T.; Cavagnat, D.; Hapiot, P.; Fabre, B.; Tucker, J. H. R.; Bassani, D. M., Reversible Control over Molecular Recognition in Surface-Bound Photoswitchable Hydrogen-Bonding Receptors: Towards Read–Write–Erase Molecular Printboards. *Chem. Eur. J.* **2013**, *19* (38), 12748-12758.
162. Essevaz-Roulet, B.; Bockelmann, U.; Heslot, F., Mechanical separation of the complementary strands of DNA. *Proc. Nat. Acad. Sci. USA* **1997**, *94* (22), 11935-11940.
163. Yeonee, S.; Keir, C., N., SnapShot: force spectroscopy and single-molecule manipulation. *Cell* **2013**, *153* (5), 1168-1168.
164. Chang, S. K.; Hamilton, A. D., Molecular recognition of biologically interesting substrates: synthesis of an artificial receptor for barbiturates employing six hydrogen bonds. *Journal of the American Chemical Society* **1988**, *110* (4), 1318-1319.
165. Morin, J. A.; Cao, F. J.; Lázaro, J. M.; Arias-Gonzalez, J. R.; Valpuesta, J. M.; Carrascosa, J. L.; Salas, M.; Ibarra, B., Active DNA unwinding dynamics during processive DNA replication. *Proc. Nat. Acad. Sci. USA* **2012**, *109* (21), 8115-8120.
166. Smith, S. B.; Cui, Y.; Bustamante, C., Optical-trap force transducer that operates by direct measurement of light momentum. In *Methods Enzymol.*, Academic Press: 2003; Vol. 361, pp 134-162.
167. Note that unzipping of more than one DNA construct would require forces larger than 20 pN under our experimental conditions.
168. Bustamante, C.; Marko, J.; Siggia, E.; Smith, S., Entropic elasticity of lambda-phage DNA. *Science* **1994**, *265* (5178), 1599-1600.
169. Bustamante, C.; Chemla, Y. R.; Forde, N. R.; Izhaky, D., Mechanical Processes in Biochemistry. *Annu. Rev. Biochem.* **2004**, *73* (1), 705-748.
170. Strunz, T.; Oroszlan, K.; Schäfer, R.; Güntherodt, H.-J., Dynamic force spectroscopy of single DNA molecules. *Proc. Nat. Acad. Sci. USA* **1999**, *96* (20), 11277-11282.
171. Ke, C.; Jiang, Y.; Rivera, M.; Clark, R. L.; Marszalek, P. E., Pulling Geometry-Induced Errors in Single Molecule Force Spectroscopy Measurements. *Biophys. J.* **2007**, *92* (9), L76-L78.
172. Vander Wal, M.; Kamper, S.; Headley, J.; Sinniah, K., Effects of Contact Force and Salt Concentration on the Unbinding of a DNA Duplex by Force Spectroscopy. *Langmuir* **2006**, *22* (3), 882-886.
173. Chai, J.-D.; Head-Gordon, M., Systematic optimization of long-range corrected hybrid density functionals. *J. Chem. Phys.* **2008**, *128* (8), 084106.
174. Padmavathi, D. A., Potential Energy Curves & Material Properties. *Materials Sciences and Applications* **2011**, *2*, 97-104.
175. Dutta, A.; Sherrill, C. D., Full configuration interaction potential energy curves for breaking bonds to hydrogen: An assessment of single-reference correlation methods. *J. Chem. Phys.* **2003**, *118* (4), 1610-1619.
176. Frisch, M. J.; Trucks, G. W.; Schlegel, H. B.; Scuseria, G. E.; Robb, M. A.; Cheeseman, J. R.; Scalmani, G.; Barone, V.; Mennucci, B.; Petersson, G. A.; Nakatsuji, H.; Caricato, M.; Li, X.; Hratchian, H. P.; Izmaylov, A. F.; Bloino, J.; Zheng, G.; Sonnenberg, J. L.; Hada, M.; Ehara, M.; Toyota, K.; Fukuda, R.; Hasegawa, J.; Ishida, M.; Nakajima, T.; Honda, Y.; Kitao, O.; Nakai, H.; Vreven, T.; Montgomery Jr., J. A.; Peralta, J. E.; Ogliaro, F.; Bearpark, M. J.; Heyd, J.; Brothers, E. N.; Kudin, K. N.; Staroverov, V. N.; Kobayashi, R.; Normand, J.; Raghavachari, K.; Rendell, A. P.; Burant, J. C.; Iyengar, S. S.; Tomasi, J.; Cossi, M.; Rega, N.; Millam, N. J.; Klene, M.; Knox, J. E.; Cross, J. B.; Bakken, V.; Adamo, C.; Jaramillo, J.; Gomperts, R.; Stratmann, R. E.; Yazyev, O.; Austin, A. J.; Cammi, R.; Pomelli, C.; Ochterski, J. W.; Martin, R. L.; Morokuma, K.; Zakrzewski, V. G.; Voth, G. A.; Salvador, P.; Dannenberg, J. J.; Dapprich, S.; Daniels, A. D.; Farkas, Ö.; Foresman, J. B.; Ortiz, J. V.; Cioslowski, J.; Fox, D. J. *Gaussian 09 Revision C.01*, Gaussian, Inc.: Wallingford, CT, USA, 2009.
177. Chai, J.-D.; Head-Gordon, M., Long-range corrected hybrid density functionals with damped atom-atom dispersion corrections. *Physical Chemistry Chemical Physics* **2008**, *10* (44), 6615-6620.

178. Chai, J.-D.; Head-Gordon, M., Systematic optimization of long-range corrected hybrid density functionals. *The Journal of Chemical Physics* **2008**, *128* (8), 084106.
179. McGrath, J. M.; Pluth, M. D., Understanding the Effects of Preorganization, Rigidity, and Steric Interactions in Synthetic Barbiturate Receptors. *J. Org. Chem.* **2014**, *79* (2), 711-719.
180. Francl, M. M.; Pietro, W. J.; Hehre, W. J.; Binkley, J. S.; Gordon, M. S.; DeFrees, D. J.; Pople, J. A., Self-consistent molecular orbital methods. XXIII. A polarization-type basis set for second-row elements. *J. Chem. Phys.* **1982**, *77* (7), 3654-3665.
181. Boys, S. F.; Bernardi, F., The calculation of small molecular interactions by the differences of separate total energies. Some procedures with reduced errors. *Mol. Phys.* **1970**, *19* (4), 553-566.
182. Padmavathi, D. A., Potential Energy Curves & Material Properties. *Materials Sciences and Applications* **2011**, 97-104.
183. Kay, E. R.; Leigh, D. A.; Zerbetto, F., Synthetic Molecular Motors and Mechanical Machines. *Angew. Chem. Int. Ed.* **2007**, *46* (1-2), 72-191.
184. Schliwa, M., *Molecular Motors*. Wiley-VCH, Weinheim, 2003.
185. Balzani, V.; Credi, A.; Raymo, F. M.; Stoddart, J. F., Artificial Molecular Machines. *Angew. Chem. Int. Ed.* **2000**, *39* (19), 3348-3391.
186. Special Issue Molecular Machines *Acc. Chem. Res.* **2001**, *34* (6), 409-522.
187. Kinbara, K.; Aida, T., Toward Intelligent Molecular Machines: Directed Motions of Biological and Artificial Molecules and Assemblies. *Chem. Rev.* **2005**, *105* (4), 1377-1400.
188. Browne, W. R.; Feringa, B. L., Making molecular machines work. *Nat. Nanotech.* **2006**, *1* (1), 25-35.
189. V. Balzani, M. V., A. Credi, *Molecular Devices and Machines. Concepts and Perspectives for the Nanoworld, 2nd ed.* Wiley-VCH, Weinheim, 2008.
190. Ma, X.; Tian, H., Bright functional rotaxanes. *Chem. Soc. Rev.* **2010**, *39* (1), 70-80.
191. von Delius, M.; Leigh, D. A., Walking molecules. *Chem. Soc. Rev.* **2011**, *40* (7), 3656-3676.
192. Bruns, C. J.; Stoddart, J. F., Rotaxane-Based Molecular Muscles. *Acc. Chem. Res.* **2014**, *47* (7), 2186-2199.
193. Kay, E. R.; Leigh, D. A., Rise of the Molecular Machines. *Angew. Chem. Int. Ed.* **2015**, *54* (35), 10080-10088.
194. Cheng, C.; Stoddart, J. F., Wholly Synthetic Molecular Machines. *ChemPhysChem* **2016**, *17* (12), 1780-1793.
195. Wilson, M. R.; Solà, J.; Carlone, A.; Goldup, S. M.; Lebrasseur, N.; Leigh, D. A., An autonomous chemically fuelled small-molecule motor. *Nature* **2016**, *534* (7606), 235-240.
196. Feynman, R. P., *Eng. Sci.* **1960**, *23*, 22-36.
197. Sauvage, J.-P., From Chemical Topology to Molecular Machines (Nobel Lecture). *Angew. Chem. Int. Ed.* **2017**, *56* (37), 11080-11093.
198. Feringa, B. L., The Art of Building Small: From Molecular Switches to Motors (Nobel Lecture). *Angew. Chem. Int. Ed.* **2017**, *56* (37), 11060-11078.
199. Stoddart, J. F., Mechanically Interlocked Molecules (MIMs)—Molecular Shuttles, Switches, and Machines (Nobel Lecture). *Angew. Chem. Int. Ed.* **2017**, *56* (37), 11094-11125.
200. Peplow, M., The tiniest Lego: a tale of nanoscale motors, rotors, switches and pumps. *Nature* **2015**, *525* (7567), 18-21.
201. J.-P. Sauvage, C. O. D.-B., *Molecular Catenanes, Rotaxanes and Knots: A Journey Through the World of Molecular Topology*. Wiley-VCH, Weinheim, 1999.
202. Anelli, P. L.; Spencer, N.; Stoddart, J. F., A molecular shuttle. *J. Am. Chem. Soc.* **1991**, *113* (13), 5131-5133.
203. Bissell, R. A.; Cordova, E.; Kaifer, A. E.; Stoddart, J. F., A chemically and electrochemically switchable molecular shuttle. *Nature* **1994**, *369* (6476), 133-137.
204. Panman, M. R.; Bodis, P.; Shaw, D. J.; Bakker, B. H.; Newton, A. C.; Kay, E. R.; Brouwer, A. M.; Buma, W. J.; Leigh, D. A.; Woutersen, S., Operation Mechanism of a Molecular Machine Revealed Using Time-Resolved Vibrational Spectroscopy. *Science* **2010**, *328* (5983), 1255-1258.
205. Rijs, A. M.; Sändig, N.; Blom, M. N.; Oomens, J.; Hannam, J. S.; Leigh, D. A.; Zerbetto, F.; Buma, W. J., Controlled Hydrogen-Bond Breaking in a Rotaxane by Discrete Solvation. *Angew. Chem. Int. Ed.* **2010**, *49* (23), 3896-3900.
206. Bustamante, C., In singulo Biochemistry: When Less Is More. *Ann. Rev. Biochem.* **2008**, *77* (1), 45-50.
207. Brough, B.; Northrop, B. H.; Schmidt, J. J.; Tseng, H.-R.; Houk, K. N.; Stoddart, J. F.; Ho, C.-M., Evaluation of synthetic linear motor-molecule actuation energetics. *Proc. Natl. Acad. Sci. USA* **2006**, *103* (23), 8583-8588.

208. Lussis, P.; Svaldo-Lanero, T.; Bertocco, A.; Fustin, C.-A.; Leigh, D. A.; Duwez, A.-S., A single synthetic small molecule that generates force against a load. *Nat. Nanotech.* **2011**, *6* (9), 553-557.
209. Altieri, A.; Bottari, G.; Dehez, F.; Leigh, D. A.; Wong, J. K. Y.; Zerbetto, F., Remarkable Positional Discrimination in Bistable Light- and Heat-Switchable Hydrogen-Bonded Molecular Shuttles. *Angew. Chem. Int. Ed.* **2003**, *42* (20), 2296-2300.
210. Sluysmans, D.; Hubert, S.; Bruns, C. J.; Zhu, Z.; Stoddart, J. F.; Duwez, A.-S., Synthetic oligorotaxanes exert high forces when folding under mechanical load. *Nat. Nano.* **2018**.
211. Carlos Bustamante; Yann R. Chemla; Nancy R. Forde, a.; Izhaky, D., Mechanical Processes in Biochemistry. *Annu. Rev. Biochem.* **2004**, *73* (1), 705-748.
212. Svoboda, K.; Block, S. M., Force and velocity measured for single kinesin molecules. *Cell* **77** (5), 773-784.
213. Leigh, D. A.; Venturini, A.; Wilson, A. J.; Wong, J. K. Y.; Zerbetto, F., The Mechanism of Formation of Amide-Based Interlocked Compounds: Prediction of a New Rotaxane-Forming Motif. *Chem. Eur. J.* **2004**, *10* (20), 4960-4969.
214. Mukhortava, A.; Schlierf, M., Efficient Formation of Site-Specific Protein–DNA Hybrids Using Copper-Free Click Chemistry. *Bioconjugate Chem.* **2016**, *27* (7), 1559-1563.
215. van Delft, P.; Meeuwenoord, N. J.; Hoogendoorn, S.; Dinkelaar, J.; Overkleeft, H. S.; van der Marel, G. A.; Filippov, D. V., Synthesis of Oligoribonucleic Acid Conjugates Using a Cyclooctyne Phosphoramidite. *Org. Lett.* **2010**, *12* (23), 5486-5489.
216. Crooks, G. E., Entropy production fluctuation theorem and the nonequilibrium work relation for free energy differences. *Phys. Rev. E* **1999**, *60* (3), 2721-2726.
217. Astumian, R. D.; Mukherjee, S.; Warshel, A., The Physics and Physical Chemistry of Molecular Machines. *ChemPhysChem* **2016**, *17* (12), 1719-1741.
218. Pezzato, C.; Cheng, C.; Stoddart, J. F.; Astumian, R. D., Mastering the non-equilibrium assembly and operation of molecular machines. *Chem. Soc. Rev.* **2017**, *46* (18), 5491-5507.
219. Bell, G., Models for the specific adhesion of cells to cells. *Science* **1978**, *200* (4342), 618-627.
220. Alemany, A.; Ritort, F., Force-Dependent Folding and Unfolding Kinetics in DNA Hairpins Reveals Transition-State Displacements along a Single Pathway. *J. Phys. Chem. Lett.* **2017**, *8* (5), 895-900.
221. Clair, S.; Abel, M.; Porte, L., Growth of boronic acid based two-dimensional covalent networks on a metal surface under ultrahigh vacuum. *Chem. Comm.* **2014**, *50* (68), 9627-9635.
222. Kong, H.; Yang, S.; Gao, H.; Timmer, A.; Hill, J. P.; Díaz Arado, O.; Mönig, H.; Huang, X.; Tang, Q.; Ji, Q.; Liu, W.; Fuchs, H., Substrate-Mediated C–C and C–H Coupling after Dehalogenation. *J. Am. Chem. Soc.* **2017**, *139* (10), 3669-3675.
223. Kocić, N.; Liu, X.; Chen, S.; Decurtins, S.; Krejčí, O.; Jelínek, P.; Repp, J.; Liu, S.-X., Control of Reactivity and Regioselectivity for On-Surface Dehydrogenative Aryl–Aryl Bond Formation. *J. Am. Chem. Soc.* **2016**, *138* (17), 5585-5593.
224. Krüger, J.; Pavliček, N.; Alonso, J. M.; Pérez, D.; Guitián, E.; Lehmann, T.; Cuniberti, G.; Gourdon, A.; Meyer, G.; Gross, L.; Moresco, F.; Peña, D., Tetracene Formation by On-Surface Reduction. *ACS Nano* **2016**, *10* (4), 4538-4542.
225. Mönig, H.; Hermoso, D. R.; Díaz Arado, O.; Todorović, M.; Timmer, A.; Schüer, S.; Langewisch, G.; Pérez, R.; Fuchs, H., Submolecular Imaging by Noncontact Atomic Force Microscopy with an Oxygen Atom Rigidly Connected to a Metallic Probe. *ACS Nano* **2016**, *10* (1), 1201-1209.
226. Eder, G.; Smith, E. F.; Cebula, I.; Heckl, W. M.; Beton, P. H.; Lackinger, M., Solution Preparation of Two-Dimensional Covalently Linked Networks by Polymerization of 1,3,5-Tri(4-iodophenyl)benzene on Au(111). *ACS Nano* **2013**, *7* (4), 3014-3021.
227. Kawai, S.; Takahashi, K.; Ito, S.; Pawlak, R.; Meier, T.; Spijker, P.; Canova, F. F.; Tracey, J.; Nozaki, K.; Foster, A. S.; Meyer, E., Competing Annulene and Radialene Structures in a Single Anti-Aromatic Molecule Studied by High-Resolution Atomic Force Microscopy. *ACS Nano* **2017**, *11* (8), 8122-8130.
228. Majzik, Z.; Cuenca, A. B.; Pavliček, N.; Miralles, N.; Meyer, G.; Gross, L.; Fernández, E., Synthesis of a Naphthodiazaborinine and Its Verification by Planarization with Atomic Force Microscopy. *ACS Nano* **2016**, *10* (5), 5340-5345.
229. Hunter, C. A., Quantifying intermolecular interactions: Guidelines for the molecular recognition toolbox. *Angewandte Chemie, International Edition* **2004**, *43* (40), 5310-5324.
230. Grimme, S., Do special noncovalent π - π stacking interactions really exist? *Angew. Chem., Int. Ed.* **2008**, *47* (18), 3430-3434.
231. Grabowski, S. J., What Is the Covalency of Hydrogen Bonding? *Chem. Rev. (Washington, DC, U. S.)* **2011**, *111* (4), 2597-2625.
232. Gilli, G.; Gilli, P., Towards an unified hydrogen-bond theory. *J. Mol. Struct.* **2000**, *552*, 1-15.

233. Alkorta, I.; Elguero, J., Non-conventional hydrogen bonds. *Chemical Society Reviews* **1998**, *27* (2), 163-170.
234. Arunan, E.; Desiraju, G. R.; Klein, R. A.; Sadlej, J.; Scheiner, S.; Alkorta, I.; Clary, D. C.; Crabtree, R. H.; Dannenberg, J. J.; Hobza, P.; Kjaergaard, H. G.; Legon, A. C.; Mennucci, B.; Nesbitt, D. J., Defining the hydrogen bond: an account (IUPAC Technical Report). *Pure Appl. Chem.* **2011**, *83* (8), 1619-1636.
235. Weinhold, F.; Klein, R. A., Anti-Electrostatic Hydrogen Bonds. *Angew. Chem., Int. Ed.* **2014**, *53* (42), 11214-11217.
236. Reed, A. E.; Curtiss, L. A.; Weinhold, F., Intermolecular interactions from a natural bond orbital, donor-acceptor viewpoint. *Chem. Rev.* **1988**, *88* (6), 899-926.
237. T. Ziegler, A. R., *Theor. Chem. Acc.* **1977**, (47), 333-341.
238. Fatila, E. M.; Twum, E. B.; Sengupta, A.; Pink, M.; Karty, J. A.; Raghavachari, K.; Flood, A. H., Anions Stabilize Each Other inside Macrocyclic Hosts. *Angew. Chem. Int. Ed.* **2016**, *55* (45), 14057-14062.
239. Sweetman, A. M.; Jarvis, S. P.; Sang, H.; Lekkas, I.; Rahe, P.; Wang, Y.; Wang, J.; Champness, N. R.; Kantorovich, L.; Moriarty, P., Mapping the force field of a hydrogen-bonded assembly. *Nature Communications* **2014**, *5*, 3931.
240. Cammarata, L.; Kazarian, S. G.; Salter, P. A.; Welton, T., Molecular states of water in room temperature ionic liquids. *Phys. Chem. Chem. Phys.* **2001**, *3* (23), 5192-5200.
241. Kalyanasundaram, K., Photophysics, photochemistry and solar energy conversion with tris(bipyridyl)ruthenium(II) and its analogues. *Coordination Chemistry Reviews* **1982**, *46* (Supplement C), 159-244.
242. Montalti, M. A. C. L. P. M. T. G., *Handbook of Photochemistry (3rd ed.)*. 6000 Broken Sound Prkway NW, Suite 200 Boca Raton, FL: CRC press Taylor & Francis Group., 2006.
243. Conrad, M. P.; Strauss, H. L., Nearly free rotation of water and ammonia in alkanes and other weakly interacting solvents. *J. Phys. Chem.* **1987**, *91* (6), 1668-1673.
244. Backx, P.; Goldman, S., Water/water-d₂ solubility isotope effects. An estimate of the extent of nonclassical rotational behavior of water, when dissolved in benzene or carbon tetrachloride. *J. Phys. Chem.* **1981**, *85* (20), 2975-2979.
245. Emmeluth, C.; Suhm, M. A.; Luckhaus, D., A monomers-in-dimers model for carboxylic acid dimers. *The Journal of Chemical Physics* **2003**, *118* (5), 2242-2255.
246. Fischer, S., Franck-Condon Factors and the Method of Steepest Descent. *The Journal of Chemical Physics* **1971**, *55* (12), 5844-5844.
247. Hu, Y. J.; Fu, H. B.; Bernstein, E. R., IR plus vacuum ultraviolet spectroscopy of neutral and ionic organic acid molecules and clusters: Acetic acid. *The Journal of Chemical Physics* **2006**, *125* (18), 184308.
248. In order to work with exactly the same conditions as previously reported by Bassani et al. we decided the gold-coated tip with a barbituric guest instead of the cyanuric derivative, which only differs from the first in the N1.
249. Gebbie, M. A.; Smith, A. M.; Dobbs, H. A.; Lee, A. A.; Warr, G. G.; Banquy, X.; Valtiner, M.; Rutland, M. W.; Israelachvili, J. N.; Perkin, S.; Atkin, R., Long range electrostatic forces in ionic liquids. *Chem. Comm.* **2017**, *53* (7), 1214-1224.
250. Dirksen, A.; Hahn, U.; Schwanke, F.; Nieger, M.; Reek, J. N. H.; Vögtle, F.; De Cola, L., Multiple Recognition of Barbiturate Guests by "Hamilton-Receptor"-Functionalized Dendrimers. *Chem. Eur. J.* **2004**, *10* (8), 2036-2047.
251. Gatri, R.; Ouerfelli, I.; Efrat, M. L.; Serein-Spirau, F.; Lère-Porte, J.-P.; Valvin, P.; Roisnel, T.; Bivaud, S.; Akdas-Kilig, H.; Fillaut, J.-L., Supramolecular Ruthenium-Alkynyl Multicomponent Architectures: Engineering, Photophysical Properties, and Responsiveness to Nitroaromatics. *Organometallics* **2014**, *33* (3), 665-676.
252. Huang, C.-H.; McClenaghan, N. D.; Kuhn, A.; Bravic, G.; Bassani, D. M., Hierarchical self-assembly of all-organic photovoltaic devices. *Tetrahedron* **2006**, *62* (9), 2050-2059.
253. Liu, X.; Wang, Y.; Chen, C.; Tintaru, A.; Cao, Y.; Liu, J.; Ziarelli, F.; Tang, J.; Guo, H.; Rosas, R.; Giorgio, S.; Charles, L.; Rocchi, P.; Peng, L., A Fluorinated Bola-Amphiphilic Dendrimer for On-Demand Delivery of siRNA, via Specific Response to Reactive Oxygen Species. *Adv. Funct. Mater.* **2016**, *26* (47), 8594-8603.
254. Sader, J. E.; Chon, J. W. M.; Mulvaney, P., Calibration of rectangular atomic force microscope cantilevers. *Rev. Sci. Instrum.* **1999**, *70* (10), 3967-3969.
255. Loving, G. S.; Sainlos, M.; Imperiali, B., Monitoring protein interactions and dynamics with solvatochromic fluorophores. *Trends in biotechnology* **2010**, *28* (2), 73.

256. Diwu, Z.; Lu, Y.; Zhang, C.; Klaubert, D. H.; Haugland, R. P., Fluorescent Molecular Probes II. The Synthesis, Spectral Properties and Use of Fluorescent Solvatochromic Dapoxyl Dyes. *Photochem. Photobiol.* **1997**, *66* (4), 424-431.
257. Ding, B.; Yin, N.; Liu, Y.; Cardenas-Garcia, J.; Evanson, R.; Orsak, T.; Fan, M.; Turin, G.; Savage, P. B., Origins of Cell Selectivity of Cationic Steroid Antibiotics. *J. Am. Chem. Soc.* **2004**, *126* (42), 13642-13648.
258. Uchiyama, S.; Takehira, K.; Yoshihara, T.; Tobita, S.; Ohwada, T., Environment-Sensitive Fluorophore Emitting in Protic Environments. *Org. Lett.* **2006**, *8* (25), 5869-5872.
259. Gonçalves, M. S. T., Fluorescent Labeling of Biomolecules with Organic Probes. *Chemical Reviews* **2009**, *109* (1), 190-212.
260. Adams, M. M.; Anslyn, E. V., Differential Sensing Using Proteins: Exploiting the Cross-Reactivity of Serum Albumin To Pattern Individual Terpenes and Terpenes in Perfume. *J. Am. Chem. Soc.* **2009**, *131* (47), 17068-17069.
261. Sinkeldam, R. W.; Greco, N. J.; Tor, Y., Fluorescent Analogs of Biomolecular Building Blocks: Design, Properties, and Applications. *Chemical Reviews* **2010**, *110* (5), 2579-2619.
262. Lakowicz, J. R., *Principles of Fluorescence Spectroscopy*, 3rd ed. Springer: New York, 2006.
263. Vázquez, M. E.; Nitz, M.; Stehn, J.; Yaffe, M. B.; Imperiali, B., Fluorescent Caged Phosphoserine Peptides as Probes to Investigate Phosphorylation-Dependent Protein Associations. *J. Am. Chem. Soc.* **2003**, *125* (34), 10150-10151.
264. Toutchkine, A.; Kraynov, V.; Hahn, K., Solvent-Sensitive Dyes to Report Protein Conformational Changes in Living Cells. *J. Am. Chem. Soc.* **2003**, *125* (14), 4132-4145.
265. Vázquez, M. E.; Blanco, J. B.; Imperiali, B., Photophysics and Biological Applications of the Environment-Sensitive Fluorophore 6-N,N-Dimethylamino-2,3-naphthalimide. *J. Am. Chem. Soc.* **2005**, *127* (4), 1300-1306.
266. Royer, C. A., Probing Protein Folding and Conformational Transitions with Fluorescence. *Chem. Rev.* **2006**, *106* (5), 1769-1784.
267. Lata, S.; Gavutis, M.; Tampé, R.; Piehler, J., Specific and Stable Fluorescence Labeling of Histidine-Tagged Proteins for Dissecting Multi-Protein Complex Formation. *J. Am. Chem. Soc.* **2006**, *128* (7), 2365-2372.
268. Loving, G.; Imperiali, B., A Versatile Amino Acid Analogue of the Solvatochromic Fluorophore 4-N,N-Dimethylamino-1,8-naphthalimide: A Powerful Tool for the Study of Dynamic Protein Interactions. *J. Am. Chem. Soc.* **2008**, *130* (41), 13630-13638.
269. Pazos, E.; Vazquez, O.; Mascarenas, J. L.; Eugenio Vazquez, M., Peptide-based fluorescent biosensors. *Chem. Soc. Rev.* **2009**, *38* (12), 3348-3359.
270. Loving, G.; Imperiali, B., Thiol-Reactive Derivatives of the Solvatochromic 4-N,N-Dimethylamino-1,8-naphthalimide Fluorophore: A Highly Sensitive Toolset for the Detection of Biomolecular Interactions. *Bioconj. Chemistry* **2009**, *20* (11), 2133-2141.
271. Sainlos, M.; Iskenderian, W. S.; Imperiali, B., A General Screening Strategy for Peptide-Based Fluorogenic Ligands: Probes for Dynamic Studies of PDZ Domain-Mediated Interactions. *J. Am. Chem. Soc.* **2009**, *131* (19), 6680-6682.
272. Lee, H. S.; Guo, J.; Lemke, E. A.; Dimla, R. D.; Schultz, P. G., Genetic Incorporation of a Small, Environmentally Sensitive, Fluorescent Probe into Proteins in *Saccharomyces cerevisiae*. *J. Am. Chem. Soc.* **2009**, *131* (36), 12921-12923.
273. Burr, M.; Koshland, D. E., use of "reporter groups" in structure-function studies of proteins. *Proceedings of the National Academy of Sciences of the United States of America* **1964**, *52* (4), 1017-1024.
274. Chao, G.; Lau, W. L.; Hackel, B. J.; Sazinsky, S. L.; Lippow, S. M.; Wittrup, K. D., Isolating and engineering human antibodies using yeast surface display. *Nat. Protoc.* **2006**, *1*, 755.
275. Hanes, J.; Plückthun, A., In vitro selection and evolution of functional proteins by using ribosome display. *Proc. Nat. Acad. Sci. USA* **1997**, *94* (10), 4937-4942.
276. Roberts, R. W.; Szostak, J. W., RNA-peptide fusions for the in vitro selection of peptides and proteins. *Proc. Natl. Acad. Sci. USA* **1997**, *94* (23), 12297-12302.
277. Clackson, T.; Hoogenboom, H. R.; Griffiths, A. D.; Winter, G., Making antibody fragments using phage display libraries. *Nature* **1991**, *352*, 624.
278. Koide, A.; Bailey, C. W.; Huang, X.; Koide, S., The fibronectin type III domain as a scaffold for novel binding proteins¹¹ Edited by J. Wells. *J. Mol. Biol.* **1998**, *284* (4), 1141-1151.
279. Binz, H. K.; Amstutz, P.; Kohl, A.; Stumpp, M. T.; Briand, C.; Forrer, P.; Grütter, M. G.; Plückthun, A., High-affinity binders selected from designed ankyrin repeat protein libraries. *Nat. Biotechnol.* **2004**, *22*, 575.

280. Liao, X.; Rabideau, A. E.; Pentelute, B. L., Delivery of Antibody Mimics into Mammalian Cells via Anthrax Toxin Protective Antigen. *Chembiochem* **2014**, *15* (16), 2458-2466.
281. de Picciotto, S.; Imperiali, B.; Griffith, L. G.; Wittrup, K. D., Equilibrium and dynamic design principles for binding molecules engineered for reagentless biosensors. *Anal. biochem.* **2014**, *0*, 9-15.
282. Spicer CD, D. B., Selective chemical protein modification. *Nat Commun.* **2014**, *5*, 1–14.
283. Rashidian, M.; Dozier, J. K.; Distefano, M. D., Chemoenzymatic Labeling of Proteins: Techniques and Approaches. *Bioconjug. chem.* **2013**, *24* (8), 1277-1294.
284. de Picciotto, S.; Dickson, P. M.; Traxlmayr, M. W.; Marques, B. S.; Socher, E.; Zhao, S.; Cheung, S.; Kiefer, J. D.; Wand, A. J.; Griffith, L. G.; Imperiali, B.; Wittrup, K. D., Design Principles for SuCESSful Biosensors: Specific Fluorophore/Analyte Binding and Minimization of Fluorophore/Scaffold Interactions. *J. Mol. Biol.* **2016**, *428* (20), 4228-4241.
285. Baumann, H.; Knapp, S.; Lundbäck, T.; Ladenstein, R.; Härd, T., Solution structure and DNA-binding properties of a thermostable protein from the archaeon *Sulfolobus solfataricus*. *Nat. Struct. Biol.* **1994**, *1*, 808.
286. Baumann, H.; Knapp, S.; Karshikoff, A.; Ladenstein, R.; Härd, T., DNA-binding Surface of the Sso7d Protein from *Sulfolobus solfataricus*. *J. Mol. Biol.* **1995**, *247* (5), 840-846.
287. Knapp, S.; Karshikoff, A.; Berndt, K. D.; Christova, P.; Atanasov, B.; Ladenstein, R., Thermal Unfolding of the DNA-binding Protein Sso7d from the Hyperthermophile *Sulfolobus solfataricus*. *J. Mol. Biol.* **1996**, *264* (5), 1132-1144.
288. Gera, N.; Hussain, M.; Wright, R. C.; Rao, B. M., Highly Stable Binding Proteins Derived from the Hyperthermophilic Sso7d Scaffold. *J. Mol. Biol.* **2011**, *409* (4), 601-616.
289. Gera, N.; Hill, A. B.; White, D. P.; Carbonell, R. G.; Rao, B. M., Design of pH Sensitive Binding Proteins from the Hyperthermophilic Sso7d Scaffold. *PLOS ONE* **2012**, *7* (11), e48928.
290. Ackerman, M.; Levary, D.; Tobon, G.; Hackel, B.; Orcutt, K. D.; Wittrup, K. D., Highly avid magnetic bead capture: An efficient selection method for de novo protein engineering utilizing yeast surface display. *Biotechnol. Prog.* **2009**, *25* (3), 774-783.
291. Angelini, A. e. a., *Protein Engineering and Selection Using Yeast Surface Display*. Humana Press, New York, NY, 2015; Vol. 1319.
292. Loving, G.; Imperiali, B., A Versatile Amino Acid Analogue of the Solvatochromic Fluorophore 4-N,N-Dimethylamino-1,8-naphthalimide: A Powerful Tool for the Study of Dynamic Protein Interactions. *J. Am. Chem. Soc* **2008**, *130* (41), 13630-13638.
293. Loving, G.; Imperiali, B., Thiol-Reactive Derivatives of the Solvatochromic 4-N,N-Dimethylamino-1,8-naphthalimide Fluorophore: A Highly Sensitive Toolset for the Detection of Biomolecular Interactions. *Bioconjug. chem.* **2009**, *20* (11), 2133-2141.
294. de Nobel, H., Pike, J., Lipke, P.N. & Kurjan, J. , Genetics of a-agglutinin function in *Saccharomyces cerevisiae*. *Mol. Gen. Genet.* **1995**, *247*, 409-415.
295. These competent cells enable a highly efficient, rapid, and reproducible method for introducing random mutations in a cloned gene of interest. This method involves propagating the cloned gene into XL1-Red Competent Cells; an *Escherichia coli*